Transport of microparticles in spatially and time-dependent flows

Von der Universität Bayreuth
zur Erlangung des Grades eines
Doktors der Naturwissenschaften (Dr. rer. nat.)
genehmigte Abhandlung

von

Matthias Laumann

geboren in Buchen (Odenwald)

1. Gutachter: Prof. Dr. Walter Zimmermann
2. Gutachter: Prof. Dr. Igor Aronson, Penn State University
3. Gutachter: Prof. Dr. Arthur Peeters

Tag der Einreichung: 11.04.2019
Tag des Kolloquiums: 05.08.2019

Zusammenfassung

Diese Dissertation beschäftigt sich mit der Mikrofluidik und insbesondere der Dynamik von Mikrometer großen Teilchen, wie z.B. Polymeren, Kapseln und roten Blutzellen, in Strömungen bei kleiner Reynoldszahl. Dabei wird vor allem der Transport der Teilchen senkrecht zur Strömung betrachtet, die sogenannte transversale Migration. Klassische Beispiele sind die Migration eines deformierbaren Teilchens zum Zentrum einer Poiseuille-Strömung oder die Migration durch die abstoßende Wechselwirkung mit einer Kanalwand. Jedoch kann eine Migration durch viele weitere Mechanismen verursacht bzw. durch äußere Einflüsse gezielt gesteuert werden, was in dieser Arbeit untersucht wird. Diese Migrationsmechanismen könnten zur Teilchentrennung in mikrofluidischen Systemen, z.B. von gesunden Zellen und Krebszellen, genutzt werden. Mikrofluidische Systeme sind eine vielversprechende Technologie in der Biotechnologie, Pharmakologie, medizinische Diagnose und Grundlagenforschung.

Eine Möglichkeit zur Erzeugung einer Migration sind gekrümmte Stromlinien, wie z.B. in einem Kanal mit sinusförmig modulierten Wänden, was anhand einer Kapsel und einer roten Blutzelle gezeigt wird. Diese nicht parallelen Stromlinien in Verbindung mit der endlichen Größe des Teilchens führt dazu, dass es senkrecht zur Strömung migriert, was zu einem zweiten Attraktor führt. Da dieser Effekt von den Teilcheneigenschaften abhängt, können damit Teilchen untersucht und getrennt werden, wie z.B. kranke (Krebs-) und gesunde Zellen.

Weiterhin ist es interessant, den Einfluss einer Zeitabhängigkeit der Strömung auf die Migration zu untersuchen. Es wird gezeigt, dass bereits ein linearer Scherfluss zu einer Migration führen kann, wenn er zeitabhängig ist und das sich darin befindliche Teilchen eine intrinsische Asymmetrie besitzt.

Oszilliert ein zeitabhängiger Fluss schnell genug, so ist die Trägheit eines sich darin befindlichen Teilchens nicht länger vernachlässigbar. Ein asymmetrisches, deformierbares Teilchen mit einer anderen Dichte als das umgebende Fluid kann sich in in diesem Fluss im Mittel bewegen, selbst wenn der Fluss keine mittlere Geschwindigkeit besitzt. In dieser Arbeit wird anhand einer Januskapsel gezeigt, dass der Effekt ausreichend stark ist, um die Gravitation zu überwinden und dass man durch einen asymmetrischen Fluss auch einen Nettofortschritt eines symmetrischen Teilchen, z.B. einer homogenen Kapsel, erhält.

Neben dem Einfluss der Strömung auf die Migration ist es interessant, wie sich äußere Kräfte auf den Transport von Teilchen auswirken. Dazu wird der bereits bekannte Fall eines deformierbaren Teilchens in der Poiseuille-Strömung untersucht und dabei um eine externe Kraft ergänzt, wie sie z.B. bei einer Kapsel auftritt, die innerhalb eine höhere Dichte als das umgebende Fluid aufweist. Durch die Deformation im Poiseuille-Fluss oder im linearen Scherfluss wird der

Reibungskoeffizient anisotrop, sodass eine externe Kraft in Flussrichtung auch eine Bewegung senkrecht zum Fluss bewirkt. Im Poiseuille-Fluss findet man, je nach der Richtung der externen Kraft, entweder eine Migration zum Zentrum oder zur Wand, was mit der abstoßenden Wandwechselwirkung zu einem Attraktor führt.

Der Transport eines Teilchens in einer Flüssigkeit durch äußere Kräfte erlaubt es zudem die Eigenschaften des Teilchens zu bestimmen. Dadurch wurde das magnetische Moment des magnetotaktischen Bakteriums Magnetospirillum gryphiswaldense gemessen, indem es mit Hilfe eines bekannten Magnetfeldes durch eine ruhende Flüssigkeit bewegt wurde. Mit den hier verwendeten Modellen wurden die Reibungskoeffizienten der spiralförmigen Bakterien bestimmt, die für die Messung benötigt wurden. Durch diese Art der Messung konnte die Form der einzelnen Bakterien berücksichtigt werden. Die Ergebnisse können zum genaueren Verständnis der Biosynthese des Magnetosoms und des resultierenden magnetischen Moments beitragen.

In dieser Arbeit wird zudem untersucht, wie sich ein Gradient in der Viskosität auf die Migration von Teilchen auswirkt. Solch ein Gradient lässt sich direkt durch einen Temperaturgradienten erzeugen, da die Viskosität stark von der Temperatur abhängt. Zudem findet man bei Strömungen scherverdünnender Flüssigkeiten durch einen Kanal eine räumlich abhängige Viskosität. Im Falle eines deformierbaren Teilchens und eines Gradienten senkrecht zu einem linearen Scherfluss ergibt sich eine Migration hin zur geringeren Viskosität, bzw. mit der Wandwechselwirkung zu einem Attraktor. Im Poiseuille-Fluss findet man einen zweiten Attraktor in Wandnähe, neben dem Attraktor im Zentrum.

Betrachtet man Teilchen die kleiner sind als die vorher genannten, so kann das thermische Rauschen den Transport in einer Strömung beeinflussen. Ein Beispiel hierfür sind semiflexible Polymere oder Filamente, die eine Migration im parabolischen Poiseuille-Fluss aufweisen. Je nach Steifheit des Polymers migriert es entweder überall weg vom Zentrum oder unterhalb eines kritischen Wertes zu einem Attraktor. Hier wird der Einfluss des Rauschens auf diesen Attraktor untersucht: Durch das Rauschen wird der kritische Wert vergrößert. Zudem wird der Einfluss der Wand bei endlichen Rauschen untersucht.

Als Anhang folgt eine Diskussion der einfachen Kugel-Modelle, die zur Simulation von weichen Teilchen in Mikroströmungen verwendet wurden (neben der Lattice Boltzmann Methode). Diese Kugel-Modelle erlauben einerseits effiziente Simulationen und andererseits stimmen sie gut mit bereits vorhandener Literatur und mit anderen Methoden überein. Darüber hinaus erlauben sie genäherte, semi-analytische Berechnungen um die Migrationsgeschwindigkeit eines deformierbaren Teilchens in einem Fluss grob abzuschätzen und die Mechanismen, die zu einer Migration führen, anzugeben.

Abstract

This thesis deals with microfluidics and especially with the dynamics of micrometers sized particles like polymers, capsules, and red blood cells in flows of low Reynolds number. Thereby especially the transport of the particles perpendicular to the stream lines is studied, the so-called cross-streamline migration. A classical example is the migration of a soft particle to the center of a Poiseuille flow or the migration due to the repulsive interaction with a channel boundary. However, a migration can be caused by many further effects or can be controlled by external influences, what is studied in this thesis. These mechanisms of migration can be used in microfluidic devices to separate different kinds of particles, for example of healthy and cancer cells. Such microfluidic devices are promising tools in biotechnology, pharmacology, medical diagnostics and basic research.

A possibility to generate a migration are curved stream lines, which are found for example in a channel with sinusoidally modulated boundaries, which is shown with a capsule and a red blood cell. These non-parallel stream lines in combination with the finite size of the particle lead to a cross-stream migration, what results in a second attractor. Because this effect depends on the properties of the particles, it can be used to analyze and separate particles like malignant (cancer) and healthy cells.

Furthermore it is interesting to study the influence of a time-dependent flow on the migration. It is shown that even a linear shear flow can lead to a migration, if it is time-dependent and if the particle has an intrinsic asymmetry.

If a time-dependent flow oscillates fast enough, then the inertia of an immersed particle is no longer negligible. An asymmetric deformable particle with a different density than the surrounding fluid may move on average in such a flow, even if the flow has a vanishing mean velocity. This thesis shows that the effect is strong enough to overcome gravity with the help of a Janus capsule and that one can achieve a net motion of a symmetric particle, e.g. a homogeneous capsule, by an asymmetric flow.

Besides the influence of the flow on the migration, it is interesting how external forces affect the transport of particles. For this purpose the well-known migration of a soft particle in a Poiseuille flow is investigated in presence of an additional external force, for example a buoyancy force due to different densities of the fluid inside the capsule and of the surrounding fluid. Because of the deformation in the Poiseuille flow or in a linear shear flow the friction coefficient becomes anisotropic so that a force in flow direction leads also to a motion perpendicular to the flow. In a Poiseuille flow one finds a migration towards the center or the wall which leads in combination with the repulsive wall interaction

to an attractor.

The transport of particles in a fluid due to external forces allows furthermore to determine properties of the particle. In this way the magnetic moment of the magnetotactic bacterium Magnetospirillum gryphiswaldense was measured by moving it with the help of a known magnetic field through a quiescent fluid. With the models used here the friction coefficient of the spiral shaped bacteria was determined, what is needed for the measurement. With this kind of measurement it is possible to consider the shape of individual bacteria. The results may contribute to a deeper understanding of the Biosynthesis of the magnetosome and the resulting magnetic moments.

In this work is also investigated how a gradient in the viscosity influences the migration of particles. Such a gradient can be generated directly by a temperature gradient because the viscosity of fluids strongly depends on the temperature. Additionally, one finds also in flows of shear thinning fluid through a channel a spatially dependent viscosity. In case of a deformable particle and a gradient perpendicular to a linear shear flow, on finds a migration to the lower viscosity and an attractor if the wall interaction is considered. In a Poiseuille flow one finds a second attractor close to the wall besides the one at the channel center.

If particles are investigated that are smaller than those mentioned before, then the thermal noise can affect the transport in a flow. An example are here semi-flexible polymers or filaments, which display also a migration in a parabolic Poiseuille flow. Depending on the stiffness of the polymer, it migrates outwards or below a critical value to an attractor. In this thesis the effect of the noise is investigated. The noise increases this critical value. Furthermore the influence of the wall is studied.

As appendix follows a discussion of simple bead models used to simulate soft particles in microflows (besides the Lattice Boltzmann Method). These bead models allow on the one hand efficient simulations and on the other hand they agree well with the literature and with other methods. In addition, they allow semi-analytical approximations which allow to roughly estimate the migration of a deformable particle in a flow and to determine the mechanisms that lead to a migration.

Contents

Extended abstract

Motivation

Theoretical microfluidics investigates the dynamics of fluids or suspensions in submillimeter sized systems. It is a broad field and many such submillimeter sized systems exist. Examples are, among other things, the study of blood and especially the dynamics of red blood cells in flows or other type of cells [1–5], or the behavior of microswimmers (artificial ones or bacteria), e.g. the question how microswimmers achieve a net motion at low Reynolds numbers without inertial effects [6, 7]. Further examples are DNA sorting or polymer processing [4, 5, 8, 9].

Another reason for the scientific and technological interest in microfluidics is the rapidly evolving field of lab-on-a-chip (LOC) systems [10]. Hereby the technology developed to produce microelectronics is used to assemble the LOC systems. Such a LOC system consist for example of components like microchannels (where the fluid streams through) and micro-pumps. Other components can be mixers, chemical reaction chambers, optical devices (e.g. lasers and waveguides), or microelectronics (like photo-diodes) [10–12]. Such devices can be used to analyze chemical or biological systems like cells. Microfluidics and LOC systems are a promising technology in biotechnology, pharmacology, medical diagnostics, forensics, environmental monitoring and basic research [2, 4, 8, 10, 13–20].

This thesis addresses the transport of particles in microflows. For example it is possible that particles do not follow simply the streamlines of the flow, but move also additionally perpendicular to the flow. This is called cross-stream migration (CSM). Segre and Silberberg reported in 1961 that rigid particles in a tube flow with finite Reynolds number do not solely follow the flow but move also perpendicular to the flow and gather at an position between the center of the tube and the walls [21]. Such effects of a non-zero Reynolds number are used in inertial microfluidics e.g. to focus or sort different kinds of particles like cells in microfluidic devices [20, 22–26]. But also at zero Reynolds number a CSM of soft particles can be found. A well-known example is the migration of soft particles away from channel boundaries due to the repulsive interaction of soft particles and the boundaries in linear shear flows and Poiseuille flows [2, 27–31]. Also far away from boundaries a CSM of soft particles is found in a Poiseuille flow which is caused by the spatially dependent shear rate. Examples of such soft particles are dumbbells [32, 33], droplets [34, 35], vesicles and capsules [36–38].

In this thesis, new mechanisms of CSM and particle transport are shown, for example in microchannels by a modulation of the walls or by time-dependent flows. Possible applications may be the sorting of different kinds of particles or cells with respect to their properties, like their size or stiffness, in microfluidic devices. Such a sorting is useful in diagnostics [20] because the stiffness of a

cell is an important biomarker for detecting diseases like malaria [39], diabetes [40], and cancer [41]. Especially cancer cells [42] have a different stiffness than healthy cells or the stiffness of red blood cell is affected by diseases like anaemia [43]. Hence the cross-stream migration of deformable particles is usefull method to determine the deformability and sort e.g. healthy and infected cells [20].

Methods

The equation of motion for fluids

The dynamics of fluids is governed by the Navier-Stokes equation [44]. The equation connects the velocity of a fluid $\boldsymbol{u}(\boldsymbol{r}, t)$ with the pressure p. It is given by

$$\rho(\partial_t + \boldsymbol{u} \cdot \nabla)\boldsymbol{u} = -\nabla p + \eta \Delta \boldsymbol{u}\,, \tag{1}$$

whereby ρ and η denote the density and the viscosity of the fluid, respectively. Typical values of the viscosity and the density of fluids e.g. of water are $\eta = 1\,\mathrm{mPas}$ and $\rho = 10^3\,\mathrm{kg/m^3}$. To solve the equation it must be extended with an equation of state and the mass conservation. In the most simple case of an incompressible fluid the conservation of mass becomes

$$\nabla \cdot \boldsymbol{u} = 0\,. \tag{2}$$

It is helpful to rescale the equations to receive a nondimensional equation. With the help of a system's typical length L and velocity U one can define $\boldsymbol{u} = U\boldsymbol{u}'$, $\partial_t \boldsymbol{u} = U^2/L \partial_{t'} \boldsymbol{u}'$ and $p' = \rho U^2 p$ (other terms analogue) which leads to the equation

$$\partial_{t'} \boldsymbol{u}' + (\boldsymbol{u}' \cdot \nabla')\boldsymbol{u}' = -\nabla' p' + \frac{1}{\mathrm{Re}} \Delta' \boldsymbol{u}' \tag{3}$$

with the Reynolds number

$$\mathrm{Re} = \frac{\rho U L}{\eta}\,. \tag{4}$$

The Reynolds number compares the inertial force and the viscous force. If it is much smaller than one then the viscous forces dominate and the inertial terms can be neglected. This leads to the Stokes equation

$$-\nabla p + \eta \Delta \boldsymbol{u} = 0\,. \tag{5}$$

It is possible that external forces like gravity act on the fluid. In this case the equation becomes

$$-\nabla p + \eta \Delta \boldsymbol{u} + \boldsymbol{f} = 0 \tag{6}$$

with the external force density $\mathbf{f}$.

Bead-spring models

The Oseen Tensor and its extensions

The Stokes equation of an incompressible fluid, i.e. eqs. (2) and (6), can be solved for an arbitrary force density. This can be done for example by a Fourier transformation of these linear equations [45]. This lead to the flow field of a point force $\boldsymbol{f} = \boldsymbol{F}\delta(\boldsymbol{r})$ located at the origin

$$\boldsymbol{u}(\boldsymbol{r}) = \boldsymbol{O}(\boldsymbol{r}) \cdot \boldsymbol{F}\,, \text{ with } \boldsymbol{O}(\boldsymbol{r}) = \frac{1}{8\pi\eta r}\left(\mathbf{1} + \frac{\boldsymbol{r}\boldsymbol{r}}{r^2}\right)\,, \tag{7}$$

whereby the boundary condition is that the flow vanishes at infinity. Hereby $\boldsymbol{O}(\boldsymbol{r})$ is called the Oseen tensor. It is the Greens function of the Stokes equation. The flow field of an arbitrary force density is then obtained by

$$\boldsymbol{u}(\boldsymbol{r}) = \int \boldsymbol{O}(\boldsymbol{r} - \boldsymbol{r}') \cdot \boldsymbol{f}(\boldsymbol{r}')\mathrm{d}^3\mathrm{r}'\,. \tag{8}$$

The flow field of the Oseen tensor given by eq. (7). It can be used to approximate the flow around a particle, as long as it can be treated as a point particle, i.e. as long as the diameter of the particle is small compared to the distance between the particle and the point at which the flow is evaluated. The approximation can be improved by assuming a sphere with radius a and including corrections in the radius. This is done by the method of reflections and Faxén's law and results in the so called Rotne-Prager matrix [46–49]

$$\boldsymbol{P}(\boldsymbol{r}) = \begin{cases} \frac{1}{8\pi\eta r}\left[\left(1 + \frac{2a^2}{3r^2}\right)\mathbf{1} + \left(1 - \frac{2a^2}{r^2}\right)\frac{\boldsymbol{r}\boldsymbol{r}}{r^2}\right] & \text{with } r > 2a\,, \\ \frac{1}{6\pi\eta r}\left[\left(1 - \frac{9r}{32a}\right)\mathbf{1} + \frac{3r}{32a}\frac{\boldsymbol{r}\boldsymbol{r}}{r^2}\right] & \text{with } r \leq 2a\,. \end{cases} \tag{9}$$

A further advantage besides the correction of the flow is that this tensor does not diverge at $r \to 0$.

The Oseen tensor is derived with the boundary condition that the flow vanishes at infinity. Therefore it can not be used e.g. in presence of a wall. In this case the velocity vanishes at the wall and not at infinity. Similar as the derivation of the Rotne-Prager tensor also the boundary condition of a vanishing velocity at a plane, e.g. a flat wall can be included [50]. The location of the force $\boldsymbol{r}_\mathrm{f}$ is important here and especially its distance to the wall. This leads to the so called Blake tensor [50] given by

$$\boldsymbol{B}(\boldsymbol{r}, \boldsymbol{r}_\mathrm{f}) = {}^{S}\mathbf{O}(\mathbf{r} - \mathbf{r}_\mathrm{f}) - {}^{S}\mathbf{O}(\mathbf{r} - \mathbf{r}'_\mathrm{f}) + {}^{D}\mathbf{H}(\mathbf{r}, \mathbf{r}'_\mathrm{f}) - {}^{SD}\mathbf{H}(\mathbf{r}, \mathbf{r}'_\mathrm{f})\,, \tag{10}$$

where $\mathbf{r}'_\mathrm{f} = (x_\mathrm{f}, y_\mathrm{f}, -z_\mathrm{f})$ is the position of the force mirrored at the boundary which is located at the plane given by $z = 0$. The first tensor in eq. (10) is

the Oseen tensor. The second contribution is the Oseen tensor with the mirror image of the point force. It is now helpful to define the distance

$$\tilde{\mathbf{r}} \;=\; \mathbf{r} - \mathbf{r}'_{\mathrm{f}} = \tilde{r}\hat{\tilde{\mathbf{r}}} \tag{11}$$

between the point where the flow is evaluated and the mirrored force. The components of the vectors $\mathbf{r}$ and $\tilde{\mathbf{r}}$ are denoted by r^α and $\tilde{r}^\alpha$ with $\alpha = x, y, z$. In eq. (10) the contribution

$${}^{D}\mathbf{H}_{ij}^{\alpha\beta}(\mathbf{r}_i, \mathbf{r}'_j) = \frac{1}{4\pi\eta\tilde{r}_{ij}^3}\, z_j^2(1-2\delta_{\beta z}) \left(\delta_{\alpha\beta} - 3\frac{\tilde{r}_{ij}^\alpha \tilde{r}_{ij}^\beta}{\tilde{r}_{ij}^2}\right) \tag{12}$$

is the Stokes doublet (D) and

$${}^{SD}\mathbf{H}_{ij}^{\alpha\beta}(\mathbf{r}_i, \mathbf{r}'_j) = \frac{z_j(1-2\delta_{\beta z})}{4\pi\eta\tilde{r}_{ij}^3} \left(\delta_{\alpha\beta}\tilde{r}_{ij}^z - \delta_{\alpha z}\tilde{r}_{ij}^\beta + \delta_{\beta z}\tilde{r}_{ij}^\alpha - 3\frac{\tilde{r}_{ij}^\alpha \tilde{r}_{ij}^\beta \tilde{r}_{ij}^z}{\tilde{r}_{ij}^2}\right) \tag{13}$$

is the source doublet (SD). The complete Blake tensor given by eq. (10) is the solution of the flow generated by a point force in presence of a wall. But often a channel is simulated which includes two walls. In this case one can use the Blake tensor for each wall as a reasonable approximation if the ratio between the wall-wall distance and the particle extension is larger than 5 [51].

Stokesian dynamics simulations

Bead-spring models are a simple method to simulate e.g. polymers, fibers, red blood cells, or capsules in a flow. An overview of bead-spring models and their applications is given here and more detailed in *pub8*. These models consist of a number of beads with radius a which cover the surface of a particle, e.g. a capsule. The model uses different equations that connect the deformation of the particle and the force $\boldsymbol{f}_i$ acting on the i-th beads. The Stokesian dynamics of the beads [46] is given by the equation of motion

$$\dot{\boldsymbol{r}}_i = \boldsymbol{u}_0(\boldsymbol{r}_i, t) + \frac{1}{6\pi\eta a}\boldsymbol{f}_i + \sum_{j,j\neq i} \boldsymbol{H}_{i,j} \cdot \boldsymbol{f}_j \text{ with } \boldsymbol{H}_{i,j} = \boldsymbol{O}(\boldsymbol{r}_i - \boldsymbol{r}_j)\,. \tag{14}$$

Hereby $\boldsymbol{r}_i$ means the location of the i-th bead (and $\dot{\boldsymbol{r}}_i$ its velocity), $\boldsymbol{u}_0(\boldsymbol{r}, t)$ denotes the undisturbed flow without the particle, $\boldsymbol{f}_i/6\pi\eta a$ is the Stokes friction of a sphere and the last term describes the flow disturbance generated by the presence of the other beads. Instead of the Oseen tensor (eq. (7)), also the Rotne-Prager (eq. (9)) tensor or the Blake tensor (eq. (10)) can be chosen, as discussed above. This flow disturbance created by one bead and influencing another is called hydrodynamic interaction between the beads. In certain cases it can be interesting to compare simulations with and without hydrodynamic interaction to determine its influence.

The Lattice Boltzmann Method

Kinetic theory of gases

A different method to calculate flows is the Lattice Boltzmann Method (LBM). One should note that the LBM solves the full Navier-Stokes equation unlike simulations using the Oseen tensor. Here a short introduction based on [52] is given.

The LBM originates from the mesoscopic kinetic theory of gases. Mesoscopic means here that the gas is neither described by single particles (microscopic) nor solely by macroscopic quantities like the density or the flow velocity. Instead a particle distribution function f is used which specifies the density of particles which are located at $\boldsymbol{r}$ and have the velocity $\boldsymbol{\xi}$ at time t, i.e. $f = f(\boldsymbol{r}, \boldsymbol{\xi}, t)$. This distribution function allows to calculate macroscopic quantities by its moments, for example

$$\text{the density} \qquad \rho(\boldsymbol{r}, t) = \int f(\boldsymbol{r}, \boldsymbol{\xi}, t) \mathrm{d}^3\xi \,, \tag{15}$$

$$\text{the momentum density} \qquad \boldsymbol{u}(\boldsymbol{r}, t)\rho(\boldsymbol{r}, t) = \int \boldsymbol{\xi} f(\boldsymbol{r}, \boldsymbol{\xi}, t) \mathrm{d}^3\xi \,, \tag{16}$$

$$\text{and the energy density} \qquad \boldsymbol{E}(\boldsymbol{r}, t)\rho(\boldsymbol{r}, t) = \int |\boldsymbol{\xi}|^2 f(\boldsymbol{r}, \boldsymbol{\xi}, t) \mathrm{d}^3\xi \,. \tag{17}$$

The distribution function of a gas, e.g. consisting of colliding single atoms, can be calculated in certain cases: It is reasonable to assume that a system can reach an equilibrium if it is not disturbed by external influences. One can assume that the distribution function of the equilibrium f^{eq} does not depend on the spatial coordinates, and is isotropic in the velocities. If one assumes further that f^{eq} can be written in a separable form $f^{\mathrm{eq}}(\boldsymbol{r}, \boldsymbol{\xi}, t) = f^{\mathrm{eq}}_{1\mathrm{D}}(\boldsymbol{\xi}_{\mathrm{x}}) f^{\mathrm{eq}}_{1\mathrm{D}}(\boldsymbol{\xi}_{\mathrm{y}}) f^{\mathrm{eq}}_{1\mathrm{D}}(\boldsymbol{\xi}_{\mathrm{z}})$ (other derivations are possible [53]) one can derive the Maxwell-Boltzmann distribution

$$f^{\mathrm{eq}}(\boldsymbol{r}, \boldsymbol{\xi}, t) = \rho \left(\frac{\rho}{2\pi p} \right)^{\frac{3}{2}} \exp\left(-\frac{p|\xi|^2}{2\rho} \right) . \tag{18}$$

It is furthermore interesting how the gas can reach this equilibrium, i.e. how the distribution function changes over time and what is its equation of motion. The total derivative of f yields

$$\frac{\mathrm{d}f}{\mathrm{d}t} = \frac{\partial f}{\partial t} + \frac{\partial f}{\partial r_\beta}\frac{\mathrm{d}r_\beta}{\mathrm{d}t} + \frac{\partial f}{\partial \xi_\beta}\frac{\mathrm{d}\xi_\beta}{\mathrm{d}t} \,, \tag{19}$$

$$= \frac{\partial f}{\partial t} + \frac{\partial f}{\partial r_\beta}\xi_\beta + \frac{\partial f}{\partial \xi_\beta}\frac{F_\beta}{\rho} \tag{20}$$

with the force on the particle given by $\boldsymbol{F}$. One has to consider here that the distribution function changes if the particles collide. This collisions are described

by a collision operator $\Omega(f)$ which leads to the Boltzmann equation

$$\frac{\partial f}{\partial t} + \frac{\partial f}{\partial r_\beta}\xi_\beta + \frac{\partial f}{\partial \xi_\beta}\frac{F_\beta}{\rho} = \Omega(f)\,. \tag{21}$$

This collision operator is non-trivial. But one can determine the properties of this operator: It must conserve the mass, the momentum and the total energy. Furthermore it must lead to an equilibrium state. A most simple ansatz that fulfills all these requirements is the approximation of Bhatnagar, Groos and Krook [54], which is the so called BGK operator. It is given by

$$\Omega(f) = \frac{1}{\tau}\left(f - f^{\mathrm{eq}}\right)\,. \tag{22}$$

The Lattice Boltzmann Method

Overview The LBM is inspired by the mesoscopic kinetic theory of gases described above. It uses a discretized distribution function and a discretized Boltzmann equation to simulate the flow of fluids numerically [52, 55]. Hereby the space, the time and the velocity of the distribution function is discretized. Usually hereby the lattice distance $\Delta x = 1$ and the time step $\Delta t = 1$ is chosen. The discrete velocities are denoted by $\boldsymbol{c}_i$. The discretization is generally classified as DdQq with the number of dimensions d and the number of discrete velocities of the distribution function q. Most common are D2Q9 and D3Q19. As example D3Q19 means a three dimensional simulation with a set of 19 different vectors $\boldsymbol{c}_i$. The discrete velocity function is then written as $f_i(\boldsymbol{r}, t)$ and denotes the density of particles moving with velocity $\boldsymbol{c}_i$ at the position $\boldsymbol{r}$ and time t. This allows to calculate the macroscopic flow velocity and the density by

$$\rho(\boldsymbol{r}, t) = \sum_i f_i(\boldsymbol{r}, t)\,, \tag{23}$$

$$\boldsymbol{u}(\boldsymbol{r}, t)\rho(\boldsymbol{r}, t) = \sum_i \boldsymbol{c}_i f_i(\boldsymbol{r}, t)\,. \tag{24}$$

To calculate f_i the discretized version of the Boltzmann equation is solved, which is given by

$$f_i(\boldsymbol{r} + \boldsymbol{c}_i\Delta t, t + \Delta t) = f_i(\boldsymbol{r}, t) + \Omega_i(\boldsymbol{r}, t)\,, \tag{25}$$

whereby at first an external force is neglected. The values of $\boldsymbol{c}_i$ are chosen such that $\boldsymbol{r} + \boldsymbol{c}_i\Delta t$ lies on a lattice grid. For the collision operator one can chose among many possibilities, but the most common is the BGK collision operator [52, 54, 55] given by

$$\Omega_i = -\frac{f_i - f_i^{\mathrm{eq}}}{\tau}\Delta t\,. \tag{26}$$

Hereby also the equilibrium distribution function is discretized. Often the discretization up to the second order is used [52, 55] which is given by

$$f_i^{\mathrm{eq}} = w_i \rho \left(1 + \frac{\boldsymbol{u} \cdot \boldsymbol{c}_i}{c_s^2} + \frac{(\boldsymbol{u} \cdot \boldsymbol{c}_i)^2}{2c_s^4} - \frac{\boldsymbol{u} \cdot \boldsymbol{u}}{2c_s^2} \right) \text{ with } c_s = \frac{1}{\sqrt{3}} \frac{\Delta x}{\Delta t} \tag{27}$$

and with the weights w_i that depend on the used discretization. Equation (25) becomes with the BGK collision operator

$$f_i(\boldsymbol{r} + \boldsymbol{c}_i \Delta t, t + \Delta t) = f_i(\boldsymbol{r}, t) - \frac{\Delta t}{\tau} \left[f_i(\boldsymbol{r}, t) - f_i^{\mathrm{eq}}(\boldsymbol{r}, t) \right] \tag{28}$$

with the relaxation time τ. This is the lattice Boltzmann equation. It can be divided in two steps [52, 55]. On can calculate at first the right hand side and define

$$f_i^*(\boldsymbol{r}, t) = f_i(\boldsymbol{r}, t) - \frac{\Delta t}{\tau} \left[f_i(\boldsymbol{r}, t) - f_i^{\mathrm{eq}}(\boldsymbol{r}, t) \right] \tag{29}$$

which is called the collision step because the collision operator is calculated. The next step is then the calculation of

$$f_i(\boldsymbol{r} + \boldsymbol{c}_i \Delta t, t + \Delta t) = f_i^*(\boldsymbol{r}, t) \,. \tag{30}$$

It means that the distribution function (or the particles) move with their according velocity to the neighboring lattice sides.

These equations allow to calculate the distribution function and hence the flow numerically. But it is not trivial that these equations solve indeed the Navier-Stokes equation, i.e. that they describe the motion of a fluid. This can be shown by the so-called Chapman-Enskog analysis. The full calculation is not reproduced here and can be found in e.g. [52, 56, 57] and only the idea is given. The distribution function is expanded in terms of a small parameter ε by

$$f_i = f_i^{\mathrm{eq}} + \varepsilon f_i^{(1)} + \varepsilon^2 f_i^{(2)} + ... \tag{31}$$

Hereby ε represents a measure of the Knudsen number Kn$= l_{\mathrm{mfp}}/l$ which is the ratio of the mean free path of the particles (the mean distance moved between two collision) and the typical size of the system considered. Usually only the first order is considered and one does not look close at orders higher than $f_i^{(1)}$. These expansion is used together with eq. (28) which leads to a set of semi-independent equations for the $f_i^{(j)}$. One assumes that each $f_i^{(j)}$ fulfills the conservation laws. Then these equations are taylor-expanded and the mean value and the first moment is calculated. This results in the conservation of the mass and the Navier-Stokes equation. Hence the LBM can describe a fluid. Further results are firstly that the pressure and the density is connected by the equation $p = c_s^2 \rho$, secondly that c_s as given in eq. (27) is the speed of sound and thirdly that the viscosity is given by

$$\eta = \rho c_s^2 \left(\tau - \frac{\Delta t}{2} \right) . \tag{32}$$

Implementation in this thesis Up to here the basics of the LBM are described by giving a brief summery of the book of T. Krüger et. al. [52]. In the following the concrete implementation used for the work in this thesis and further necessary details are described like the treatment of external forces and boundary conditions, e.g. walls. The common D3Q19 [52] discretization is used together with the Bhatnagar-Gross-Krook (BGK) collision operator [54, 55]. The equation of the temporal evolution of the probability distribution with an external force F_i is given by [57]

$$f_i(\mathbf{r} + c_i\Delta t, t + \Delta t) = f_i(\mathbf{r}, t) - \frac{\Delta t}{\tau}\left(f_i(\mathbf{r}, t) - f_i^{\mathrm{e}}(\mathbf{r}, t)\right) + \Delta t F_i\,. \quad (33)$$

The equilibrium distribution is given by eq. (27) and the weighting factors w_i of D3Q19 can be found in [52, 55]. The probability distribution function allows to calculate the density and the velocity of the fluids via its moments. With an external force a correction term is needed [57] so that the equations become

$$\rho(\mathbf{r}, t) = \sum_i f_i(\mathbf{r}, t)\,, \quad (34)$$

$$\rho(\mathbf{r}, t)\mathbf{u}(\mathbf{r}, t) = \sum_i \mathbf{c}_i f_i(\mathbf{r}, t) + \frac{1}{2}\Delta t\mathbf{F}(\mathbf{r})\,. \quad (35)$$

The external forces are used to drive the flow instead of a pressure gradient because this results in the same flow and allows to use periodic boundaries in flow direction [52]. This is useful especially to simulate a particle in a micro channel because the particle can simply pass the periodic boundary which mimics an infinite channel. A pressure gradient however implies a pressure boundary, i.e. a fixed pressure, at both ends of the channel (the simulation box). But the presence of a particle immersed in the flow changes the pressure, i.e. the particle must be placed far away from the boundaries. Especially it can not pass the boundaries to avoid an interaction with the fixed pressure boundary condition. This means a large box must be chosen which results in a long simulation time. Therefore it is much more practicable to drive the flow by an external force and to use periodic boundary conditions. Also in this case the box must large enough to avoid self-interactions of the particle, but can be chosen shorter.

Besides the external force also the channel walls must be included in the LBM, i.e. no slip boundary conditions. This is done in the streaming step: If the distribution function would stream into a lattice side that is considered as a part of a wall the particles are reflected and come back to the node they came from. But they have now a reversed velocity [52, 55]. Also periodic boundary conditions can be used which can be applied straightforwardly in the streaming step.

Furthermore the soft particles, e.g. capsules must be included in the LBM. The particle consists of a set of nodes located at $\boldsymbol{r}_j$ on the surface of the particle and certain laws that allows to calculate the forces on this nodes due to the deformation of the particle. One must consider thereby that the nodes of the particle not necessarily lie on the lattice sides of the LBM grid at the points $\boldsymbol{r}_{\mathrm{LBM},i}$. Therefore a method is needed to calculate the flow at the position of the particle's nodes and also to couple the forces of the particle to the flow, i.e. to the LBM grid. This is done by the immersed boundary method [52, 58]. The forces acting on the particle's surface, i.e. on its nodes, are distributed to neighboring LBM grid nodes by the function ϕ: With the help of this function the force on a LBM lattice site denoted by $\boldsymbol{F}(\boldsymbol{r}_{\mathrm{LBM},i})$ can be calculated with the forces $\boldsymbol{f}_j$ acting on the particle's node at $\boldsymbol{r}_j$ via

$$\boldsymbol{F}(\boldsymbol{r}_{\mathrm{LBM},i}) = \sum_j \phi\left(\boldsymbol{r}_{\mathrm{LBM},i} - \boldsymbol{r}_j\right) \boldsymbol{f}_j \tag{36}$$

with the sum over all forces of the particle. Also the velocity at the position of the nodes of the particle must be calculated. With the velocity $\boldsymbol{u}(\boldsymbol{r}_{\mathrm{LBM},j})$ calculated with the LBM at the LBM grid points one can calculate the velocity $\boldsymbol{v}_i$ at the position of the particle's nodes at $\boldsymbol{r}_i$ by

$$\boldsymbol{v}_i = \sum_j \phi\left(\boldsymbol{r}_i - \boldsymbol{r}_{\mathrm{LBM},j}\right) \boldsymbol{u}(\boldsymbol{r}_{\mathrm{LBM},j}) \,. \tag{37}$$

Now an appropriate choice of ϕ must be chosen. One assumes at first that ϕ can be written as the product

$$\phi(\mathbf{r}) = \frac{1}{(\Delta x)^3} \tilde{\phi}\left(\frac{x}{\Delta x}\right) \tilde{\phi}\left(\frac{y}{\Delta x}\right) \tilde{\phi}\left(\frac{z}{\Delta x}\right) \,. \tag{38}$$

with the distance of the grid points Δx of the LBM. It is reasonable that $\tilde{\phi}(r)$ (r denotes $\frac{x}{\Delta x}, \frac{y}{\Delta x}$ or $\frac{z}{\Delta x}$) should fulfill the following requirements

$$\tilde{\phi}(r) \text{ is continous for all real values of r} \tag{39}$$

$$\tilde{\phi}(r) = 0 \text{ for } |r| \geq 2 \tag{40}$$

$$\sum_{j \text{ even}} \tilde{\phi}(r-j) = \sum_{j \text{ odd}} \tilde{\phi}(r-j) = \frac{1}{2} \tag{41}$$

$$\sum_j (r-j)\tilde{\phi}(r-j) = 0 \tag{42}$$

$$\sum_j \tilde{\phi}^2(r-j) = const. \tag{43}$$

The idea behind this requirements is that no sudden jumps in the force or the velocity should appear while the particle moves through the LBM grid (eq. (39)). The force is also only distributed to near neighbors (eq. (40)) so that the only over a few points of the grid must be summed (eqs. (36) and (37)). Equation (41) ensures a higher numerical stability if finite differences are used (as done in [58]). It implies also

$$\sum_j \tilde{\phi}(r-j) = 1 \tag{44}$$

so that the force distributed to the neighboring grid nodes is equal to the force on the particle. The eqs. (42) and (43) ensure that linear functions are interpolated exactly. With these requirements the function ϕ becomes a delta peak if the grid distance Δx goes to zero. Hence it can describe point forces. This system of equations can be solved for ϕ which leads to a cumbersome expression. It can be extremely well [58] approximated by

$$\tilde{\phi}(R) = \begin{cases} \frac{1}{4}\left(1+\cos(\frac{\pi R}{2})\right) & \text{if } |R| \leq 2 \\ 0 & \text{else} \end{cases} . \tag{45}$$

This allows now to calculate the flow with the LBM with an immersed particle. The nodes of the particle follow the flow and their equation of motion is

$$\dot{\boldsymbol{r}}_i = \boldsymbol{v}_i \tag{46}$$

with the interpolation given by eq. (37).

Modeling of particles

The particles are discretized and consist of a number of beads or nodes on the surface of the particles and a set of equations that allow to calculate the forces on the particle due to the deformation. The flow around the particle and its motion can be simulated either with the Oseen tensor with eq. (14) or with the LBM and the immersed boundary method with eq. (46). The calculation of the forces due to the deformation is the same in both methods.

Polymers and semi-flexible fibers

To simulate polymers or semi-flexible fibers in this thesis N beads are arranged in a line in the equilibrium position. They are connected by simple springs and a bending potential. Also other force laws for the bending or springs with finite extensibility, so called FENE springs (finitely extensible non-linear elastic

springs, cf. e.g. [59]) are used in other studies. The forces are derived from potentials via $\boldsymbol{f}_i = -\nabla V$. The potential of a spring is given by

$$V_{\text{str}} = \frac{k}{2} \sum_{i=1}^{N-1} \left[b - r_{ij} \right]^2 , \qquad \text{with} \qquad j = i + 1 \tag{47}$$

with the bead to bead distance $\boldsymbol{r}_{ij} = \boldsymbol{r}_i - \boldsymbol{r}_j$, the spring constant k and the equilibrium distance b between two neighboring beads. The bending potential [60] is given by

$$V_{\text{b}} = -\frac{\kappa}{2} \sum_{i=2}^{N-1} \ln \left(1 + \cos \beta_i \right) \tag{48}$$

with the bending stiffness κ, the inner product

$$\cos(\beta_i) = \hat{\boldsymbol{r}}_{(i-1)i} \cdot \hat{\boldsymbol{r}}_{i(i+1)} \tag{49}$$

and the unit vectors $\hat{\boldsymbol{r}}_i = \boldsymbol{r}_i / |\boldsymbol{r}_i|$. Furthermore a truncated Lennard-Jones potential [60, 61]

$$V_{\text{LJ}} = \varepsilon \sum_{i=1}^{N-1} \sum_{j=i+1}^{N} \left[\frac{1}{2} \left(\frac{r_c}{r_{i,j}} \right)^{12} - \left(\frac{r_c}{r_{i,j}} \right)^{6} \right] \Theta(r_c - r) , \tag{50}$$

can be used to avoid that the beads overlap. Hereby ε and r_c denote the strength and the cut-off length, respectively.

If small particles like polymers are studied also the Brownian motion, i.e. the thermal noise can play a role. In this case a stochastic force $\boldsymbol{f}^{\text{s}}$ must be included besides the deterministic forces due to the deformation. The stochastic force [46, 62, 63] has a vanishing mean value and its amplitude is given by the fluctuation dissipation theorem [64, 65] which means

$$\left\langle \boldsymbol{f}_j^{\text{s}}(t) \right\rangle = 0 , \qquad \left\langle \boldsymbol{f}_i^{\text{s}}(t) \boldsymbol{f}_j^{\text{s}}(t') \right\rangle = 2 k_{\text{B}} T \boldsymbol{H}_{ij} \delta(t - t') \tag{51}$$

with Boltzmann's constant k_B and the temperature T. This noise is included in the equations of motion (eq. (14)) via

$$\dot{\boldsymbol{r}}_i = \boldsymbol{u}_0(\boldsymbol{r}) + \sum_j \boldsymbol{H}_{i,j} \cdot \boldsymbol{f}_j + \boldsymbol{f}_i^{\text{s}}(t) . \tag{52}$$

with

$$\boldsymbol{H}_{i,j} = \begin{cases} \boldsymbol{O}(\boldsymbol{r}_i - \boldsymbol{r}_j) \text{ for } i \neq j \\ \frac{1}{6\pi\eta a} \text{ for } i = j \end{cases} . \tag{53}$$

Instead of the Oseen tensor (eq. (7)) also the Rotne-Prager tensor (eq. 9) or the Blake tensor (eq. (10)) can be chosen.

Capsules

A capsule consists of a fluid that is encapsulated by an elastic membrane [66]. Artificial capsules can be assembled e.g. by polymerization of a liquid droplet which leads to spherical particles with a thin, solid membrane. Such capsules are used for example in pharmaceutical, cosmetic, and food industries. Besides the artificial capsules also natural particles can be found that can be approximately modeled as capsules. Examples are simple models of cells like cancer cells or red blood cells [1, 66, 67].

To model the capsule, assumptions of the membrane and its shape are made [66]: First it is assumed that the membrane can be treated as a two dimensional surface, because the thickness of the membrane is much smaller than the diameter of the capsule. Secondly, the membrane is impermeable for the fluid. Thirdly, in this work, the equilibrium shape of the capsule is assumed to be spherical.

To simulate the capsule, its surface must be discretized, which can be done in many ways. A solution that leads to sufficient homogeneous distribution of nodes works as follows [68, 69]: One starts with an icosahedron and refines it by adding new nodes at the center of each edge. The new edges are shifted then outwards to the surface of the sphere. This process can be repeated until the surface of the sphere has a sufficient resolution. A typical value is a number of $N = 642$ nodes. The reason for starting with an icosahedron is that it consists of equilateral triangles. Also the same number of triangles meet at all vertexes of the icosheadron. This properties lead to a homogeneous distribution of nodes of the refined meshes.

Also the forces acting on a deformed capsule must be calculated. An often used model of the elastic forces is the neo-Hookean law [66, 70, 71]. It describes a rubber like material with a constant elastic modulus. It is derived by assuming an thin, incompressible membrane. Incompressible means that a streching of the area of the membrane is balanced by a thinning of its thickness. Hence the neo-Hookean force law can not describe particles with a conserved surface. The derivation involves the surface displacement gradient $\boldsymbol{S}$ defined via $\mathrm{d}\boldsymbol{x} = \boldsymbol{S} \cdot \mathrm{d}\boldsymbol{X}$ with the line elements $\mathrm{d}\boldsymbol{x}$ and $\mathrm{d}\boldsymbol{X}$ of the deformed and undeformed surface, respectively. This allows to calculate the Green-Lagrange strain tensor

$$\boldsymbol{e} = \frac{1}{2}\left(\boldsymbol{S}^{\mathrm{T}} \cdot \boldsymbol{S} - \mathbf{1} + \boldsymbol{n}\boldsymbol{n}\right) \tag{54}$$

with the unit normal vector of the deformed surface $\boldsymbol{n}$. The eigenvalues of this tensor are called principal extension ratios λ_1, λ_2. With their help on can define

two deformation invariants

$$I_1 = \mathrm{tr}(\boldsymbol{S}^{\mathrm{T}} \cdot \boldsymbol{S}) - 2 = \lambda_1^2 + \lambda_2^2 - 2\,, \tag{55}$$

$$I_2 = \det(\boldsymbol{S}^{\mathrm{T}} \cdot \boldsymbol{S}) - 1 = \lambda_1^2 \lambda_2^2 - 1\,. \tag{56}$$

The product $\lambda_1 \lambda_2$ is the ratio of the deformed and the undeformed surface. The potential of the neo-Hookean law is then given by

$$V_{\mathrm{NH}} = \frac{G}{2}\left(I_1 - 1 + \frac{1}{1+I_2}\right) \tag{57}$$

with the elastic modulus G. The according force can be calculated by the gradient of the potential which involves the derivatives of I_1 and I_2 with respect to the coordinates. How this is done numerically, i.e. with the help of the discretized mesh, is explained in detail in [69]. It is useful to measure the stiffness of the capsule by a dimensionless number, the capillary number, which is given by

$$\mathrm{Ca} = \frac{\eta R}{G}\dot{\gamma} \tag{58}$$

with the radius of the capsule R, the viscosity η and the shear rate of the flow $\dot{\gamma}$. It compares the causes of a deformation, e.g. the friction forces on the capsule due to the viscosity and the shear rate with the strength of the elastic restoring forces, i.e. the elastic modulus. A high value of the capillary number means the capsule is relatively soft and displays a strong deformation.

Besides the Neo-Hookean law, also other forces are considered. A resistance to a bending of the membrane [72] is described by the potential

$$V_{\mathrm{b}} = \frac{\kappa}{2}\sum_{i,j}\left[1 - \cos\left(\beta_{i,j}\right)\right] \tag{59}$$

whereby κ means the bending stiffness, $\beta_{i,j}$ denotes the angle between two normal vectors of neighbouring triangles of the discretized surface and the sum is over neighbouring triangles. At last one must take care about that the membrane is usually impermeable for the fluid, i.e. the volume of the capsule is conserved. This can be implemented by a penalty potential [73] given by

$$V_{\mathrm{V}} = \frac{k_{\mathrm{V}}}{\mathcal{V}_0}\left(\mathcal{V}(t) - \mathcal{V}_0\right)^2 \tag{60}$$

with the volume $\mathcal{V}(t)$ and the reference volume $\mathcal{V}_0$. A sufficient high value of the stiffness k_{V} of the potential ensures small changes in the volume over the time of the simulation.

Main results

Here, a summary of the main results of the thesis is given. At first, it is discussed how the properties of the flow (like curved stream lines in *pub1* or a time-dependence in *pub2* and *pub3*) can generate a cross-streamline migration or a transport of an immersed particle. Furthermore, the effect of external forces on a particle in a flow are examined (*pub4*) and are used to measure properties of bacteria (*pub5*). Then follows an investigation of the influence of a viscosity gradient (e.g. due to a temperature gradient or shear-thinning, cf. *pub6*) and of the thermal noise (*pub7*). As appendix, the simple bead spring model, which is used among other simulations, is compared to other methods. Also a semi-analytical approximation of migration velocities is shown (*pub8*).

Influence of the flow on particle transport

Modulated microchannels

It is well-known that soft particles in a Poiseuille flow at low Reynolds number, e.g. in a micro channel, migrate across the straight stream lines towards the center of the channel, even in the bulk without considering the wall interaction. Examples of such particles are dumbbells [32, 33], droplets [34, 35], vesicles and capsules [36–38]. This cross-stream migration is caused by the deformability and the spatially dependent shear rate. It is now an interesting question whether a modulation of the channel walls can lead to a qualitatively different behavior than a migration to the center. Such modulated channels have been studied before, but in the case of nonzero Reynolds number flows [20, 22–26] or with a complex shear thinning fluid [74]. But little is known about the particle dynamics in a flow through a modulated channel at low Reynolds number and with a Newtonian fluid.

The idea why a particle displays a different migration behavior in a modulated channel than in a straight one is the following: A particle in a plane Poiseuille flow lags behind the flow (see e.g. [38]). This can be explained by a simple approximation just by averaging the undisturbed Poiseuille flow over the surface of the particle. This average of the Parabolic flow profile is smaller than the velocity at the particle's center. Hence the particle migrates laterally and lags behind due to its finite size. One can now think about how this effect can be utilized to cause a cross-stream migration. To achieve this, the stream lines must not be parallel, which can be achieved by a channel with modulated walls. The migration in such a channel is discussed in *pub1*. The walls are modulated

sinusoidally and are given by

$$y = d\left[1 + \varepsilon \sin\left(\frac{2\pi}{\lambda}x\right)\right] \tag{61}$$

with the channel's mean diameter d, the modulation amplitude ε and the modulation's wavelength λ. The flow streams in a diverging section of the channel away from the center and in a converging part towards the center. A lag behinds means now that the particle can not follow the flow: Hence, while it moves through a converging part and the flow streams towards the center of the channel, the particle can not follow completely and migrates towards the walls. A stiff particle would migrate exactly the same distance towards the center in the following diverging part of the channel, which results in no net effect. A soft particle however displays a different deformation in the converging and diverging section of the channel, which breaks this symmetry and results in a net effect towards the walls. This migration due to the curved stream lines competes with the common migration in a Poiseuille flow to the center of the channel.

The considerations are proofed by simulations, whereby both Stokesian dynamics simulations and Lattice Boltzmann simulations are used. Hereby a capsule and a red blood cell is utilized. This allows to show that the effect is both found with an artificial capsule and a biological red blood cell. Furthermore a capsule can also represent a cancer cell [67].

Indeed the both models showed a migration away from the center: Particles that are positioned initially close to the center of the channel migrate to the center as in a flat flow. But particles with a sufficient distance to the center migrate away from it towards a second, off-center attractor. Hence in a wavy channel a second, off-center attractor coexists with the attractor at the center and both are separated by a repeller. The second attractor is found without wall interactions (Stokesian dynamics) and with wall interactions (Lattice Boltzmann). The reason for this coexistence is that close to the center the streamlines are nearly straight so that the common center-migration, as found in a flat Poiseuille flow, dominates. Closer to the walls the stream lines are more curved and the migration due to the curved stream lines dominates.

The second attractor is only found at certain parameters: The wavelength of the channel must be chosen to be approximately 10 times larger than the particle radius. If the wavelength is much higher or lower than this value then the curvature of the flow plays no role at the length of the particle and the effect of the curved streamlines on the particles migration vanishes. In this case a center-migration as in a flat Poiseuille flow is found. Also the modulation of the channel must be sufficiently high so that the migration to the center can be overcome. Hence only above a critical value of the modulation amplitude an

attractor is found, i.e. at $\varepsilon > \varepsilon_c$ (cf. eq. (61)). For example with a wavelength of 12 times the particle radius the critical modulation amplitude is $\varepsilon_c = 0.14$ for the investigated particle. If the wavelength is less well adjusted the critical modulation amplitude becomes higher, e.g. with a wavelength of 20 times the particle radius the value is $\varepsilon_c = 0.23$. If the modulation amplitude is increased beyond the critical value the attractor is shifted closer towards the walls the repeller comes closer to the center due to the stronger migration induced by the curved stream lines. Besides the particles size the critical modulation amplitude depends also on the particle's stiffness: The critical modulation amplitude increases with the cell's stiffness.

A possible application is the sorting of particles with respect to their properties like their size or stiffness. Especially a sorting of cells with different stiffness is useful because the health status of cells correlates with the cell's stiffness for example at cancer cells [75].

Time-dependent, linear shear flow

It is well-known that in a flow with parallel stream lines a curvature of the flow (e.g. in a Poiseuille flow) is necessary to find a migration of a soft particle. Examples are the cross-stream migration of dumbbells [32, 33], droplets [34, 35], vesicles and capsules [36–38]. Another well-studied effect is the migration of soft particles in a linear shear flow or a Poiseuille flow near a boundary [2, 27–31]. Besides this, also the influence of particle properties, like a viscosity contrast [76] or a chirality of the particle [77] was investigated. But less is known about the migration of soft particles in time-dependent flows. It is now an interesting question whether and under which conditions a migration in a linear shear flow can be reached, if the flow is time-dependent. This is discussed in *pub2*.

The time-dependent, linear shear flow is chosen as follows

$$\boldsymbol{u}(y,t) = \begin{cases} \dot{\gamma} y \hat{\boldsymbol{e}}_y & \text{at } 0 \leq t < \frac{T}{2}\,, \\ -\dot{\gamma} y \hat{\boldsymbol{e}}_y & \text{at } \frac{T}{2} \leq t < T\,, \end{cases} \tag{62}$$

which is continued periodically. This means the linear shear flow changes periodically its flow direction with a period length of T but has a constant magnitude and shear rate. To study the migration in this time-dependent, linear shear flow three models are used. The first model is a simple dumbbell consisting of two beads with different radii, connected by a spring. The second one is a ring, i.e. six beads connected by springs and a bending potential with a different stiffness at both halves of the ring. These both models are simulated with the Stokesian Dynamics simulations. The third model is a capsule with a Neo-Hookean force

and bending potential, which differs at both halves of the capsule. The capsule was simulated with the LBM.

The simulations of all three models showed qualitatively the same behavior. A symmetric particle, i.e. dumbbell with equally sized beads and a ring or a capsule with the same strength of the bending potential at both halves, follows the stream lines completely and no migration is found. The reason is the point-symmetric deformation of the particle. An asymmetric particle in constant flow (i.e. without switching the flow's direction) already displays a cross-stream migration because the particles are not point symmetric due to the intrinsic asymmetry. The dumbbell displays a migration towards the smaller bead and the capsule and the ring migrate towards the stiffer half. But the particles also show a tank-treading motion. This means the particle migrates after one full turn the same distance in both the positive and negative y-direction (perpendicular to the flow). Hence there is no net effect. But if the flow changes its direction periodically than the smaller bead or the stiffer half points always in positive (or negative) y-direction which leads to a net effect. Hence both the asymmetry of the particles and a periodical change of the flow direction is essential.

One can now study the reason of the migration, at first with the dumbbell. The center of the dumbbell weighted with the drag coefficients ζ_i of both beads is given by

$$\boldsymbol{r}_c = \frac{\zeta_1 \boldsymbol{r}_1 + \zeta_2 \boldsymbol{r}_2}{\zeta_1 + \zeta_2} \,. \tag{63}$$

Its equation of motion is given by

$$\dot{\boldsymbol{r}}_c = \boldsymbol{u}(y_c, t) - \frac{\zeta_2 - \zeta_1}{\zeta_1 + \zeta_2} \frac{1}{4\pi\eta R} \boldsymbol{f}(R) \tag{64}$$

with the drag coefficients $\zeta_1 < \zeta_2$, the distance of the beads $\boldsymbol{R}$ (pointing from the larger to the smaller bead), the unit vector $\hat{\boldsymbol{e}}_R = \boldsymbol{R}/R$ and the spring force $\boldsymbol{f}(R) = k(R - b)\hat{\boldsymbol{e}}_R$ with the equilibrium length b. The derivation of eq. (64) shows that the hydrodynamic interaction, i.e. the Oseen-tensor is essential for the migration. Without interaction of the beads, i.e. if just their Stokes friction with the undisturbed flow is considered one receives $\dot{\boldsymbol{r}}_c = \boldsymbol{u}(y_c, t)$, which means the center follows the stream lines. One can see furthermore that the migration vanishes if both beads have the same radius. Moreover eq. (64) shows that if the spring is compressed the particle migrates parallel to the spring and towards the smaller bead, i.e. $\boldsymbol{R}$. This means if the spring is compressed and the dumbbell is asymmetric it can exert a force on the fluid: The larger bead pushes fluid in one direction and the dumbbell moves in the other direction. Thus the migration is caused by the asymmetry and the interaction with the fluid.

The migration of the ring and the capsule can be understood similar. They do not consist of different sized beads but their shape is not symmetric due to the different strength of the bending potential. Also the migration of the ring and the capsule caused by the asymmetry and the interaction with the fluid.

After discussing the mechanism also the dependence on the period length is investigated. Again all three models show qualitatively the same behavior. At very short periods the particles can not follow the flow and display nearly no migration. At longer periods the particle is deformed by the flow, but do not reach an equilibrium shape before the flow is switched. Nevertheless a migration is found. If the period is further increased an equilibrium state is reached and the tank-treading motion sets in. In this range of T the migration is maximal. At higher values of the T the tank-treading rotates the particle by a large angle. The stable mean orientation is in this case oriented such that the small bead (or the stiff half) is the same duration above and below the center of the particle, such that the migration vanishes. This causes an unsteady drop of the migration velocity as function of the period. The migration velocity falls from a nonzero migration velocity to zero above a critical value of the period.

Furthermore the magnitude of the migration velocity does not depend on the initial condition because the particles reorient to certain stable orientations. After a transient the same magnitude is found independent of the initial conditions. Only the direction, i.e. positive or negative y-direction, depends on the initial orientation.

A possible application of this kind of migration may be the sorting of asymmetric or inhomogeneous particles from symmetric particles with a linear, time-dependent shear flow.

Particles with finite inertia in time-dependent flows

A time-dependent flow raises also the question whether the inertia of the particle (not of the fluid, i.e. at low flow Reynolds number) plays a role and how the inertia can be used to achieve a net motion. This is especially interesting because many studies investigate how a microswimmer can achieve a net motion at low Reynolds number. Such a motion can not be created easily at low Reynolds number. A simple swimmer with one reciprocally changing degree of freedom, e.g. a shell that opens and closes periodically can achieve a net motion at a high Reynolds number, but does not move in total at low Reynolds number. This result is often referred to as Purcell's scallop theorem [6]. Many studies deal with the question of how to break the scallop theorem, which can be done by active microswimmers by using two degrees of freedom [78–81], by amoeboid swimming [82–84] or nonreciprocal motion of cillia [85–87] and flagella [88–90],

among many other examples.

Another way to break the scallop theorem is to include the inertia of the particle. In this case a swimmer can achieve a net motion by an active shape deformation even if the motion is reciprocal [91] because the scallop theorem assumes no inertia of the particle. This leads to the question if a completely passive particle with inertia can display a net motion in a time-dependent flow, which can be seen as a kind of artificial microswimmer driven by the external flow (with zero mean flow). It was shown recently that a passive particle shows a net motion in a sinusoidal oscillating, spatially homogeneous flow, if the particle is asymmetric [92]. Hereby a simple model of two rods, which are connected by a torsion spring with an equilibrium angle of $\pi/4$, was used. This simple model clearly demonstrated the effect. However, gravity was neglected. This raises the question of whether the effect is relevant if gravity is included.

The effect was studied further by another paper [93]: A capsule was simulated that is filled with another fluid than the surrounding one and also a small bead with the density of gold was inserted in the capsule. This bead is connected by springs with the membrane of the capsule. Such a particle may be non-trivial to assemble. This particle can be tuned such, that the mean density inside the capsule fits nearly the density of the surrounding fluid, which solves the problem of the sinking due to gravity. This particle displays a non-reciprocal deformation of its surface due to the asymmetric density distribution inside the capsule, which leads to a net motion upwards. The paper also studied a capsule that has inside a mean density (of the fluid inside and the bead) that is higher than the surrounding fluid. In this case the effect is explained by the time-dependent drag. But the effect found with this particle is to weak to overcome gravity.

Thus the question is open if simple particles exists that can overcome gravity in shaken liquids. Such particles are presented in *pub3*: A Janus capsule that has a stiff and a soft half displays a net motion in a time-dependent flow. It is shown also that an even simpler particle, a isotropic capsule can also rise in a shaken liquid against gravity if an appropriate flow is used, i.e. a flow that streams short and fast in one direction and slower and longer in the other direction (with zero mean flow). The effect is also explained in detail by simple bead-spring models of the asymmetric particle, a tetrahedron, and a isotropic particle, a ring.

The models are simulated with the help of the Maxey and Riley equation [94], which describes the motion of one rigid sphere with finite inertia in a flow at low Reynolds number. The interaction between the beads of the model are described with the time-dependent Oseen tensor [95]. The capsules are simulated with a multi-relaxation-time lattice Boltzmann method with an extension to describe

a density contrast inside and outside the capsule [55, 57, 58, 96–99].

At first a short analytical consideration is given to explain the effect in detail and to determine reasonable parameters. Hereby only the most important terms of the Maxey and Riley equation are considered which leads to

$$M\frac{dv(t)}{dt} = \zeta(t)\left[u(t) - v(t)\right] + M_f\frac{du(t)}{dt} \tag{65}$$

with the external time-dependent flow $u(t) = U\sin(\omega t)$, the mass of the particle M the displaced mass M_f and its velocity $v(t)$. The friction coefficient of the particle is assumed to be time-dependent and is given by

$$\zeta(t) = \begin{cases} \zeta_1 & \text{at } 0 \le t < \frac{T}{2}\,, \\ \zeta_2 & \text{at } \frac{T}{2} \le t < T\,, \end{cases} \tag{66}$$

which is periodically continued. The time-dependence of ζ is caused by a deformation of the particle due to the inertia and the time-dependent flow and the asymmetric shape. The deformation is not calculated directly here but the simulations confirm that ζ is indeed time-dependent.

This approximation yields the velocity at each half period

$$v_{1,2}(t) \;=\; C_{1,2}(t)e^{-\frac{\zeta_{1,2}t}{m}} + UB_{1,2}\sin(\omega t) + UD_{1,2}\cos(\omega t) \tag{67}$$

with

$$B_i \;=\; \frac{MM_f\omega^2 + \zeta_i^2}{\omega^2M^2 + \zeta_i^2}\,, \tag{68a}$$

$$D_i \;=\; \frac{\omega\zeta_i(M_f - M)}{\omega^2M^2 + \zeta_i^2}\,, \tag{68b}$$

which can be continued periodically. The boundary conditions

$$v_1(0) = v_2(T),\; v_1\left(\frac{T}{2}\right) = v_2\left(\frac{T}{2}\right) \tag{69}$$

allows to determine $C_{1,2}$

$$C_1 \;=\; U\omega\Gamma\frac{(\omega^2M - \zeta_1\zeta_2)(e^{-\frac{2\zeta_2\pi}{\omega M}} + e^{-\frac{\zeta_2\pi}{\omega M}})}{e^{-\frac{\pi(\zeta_1+2\zeta_2)}{\omega M}} - e^{-\frac{\zeta_2\pi}{\omega m}}}\,, \tag{70}$$

$$C_2 \;=\; U\omega\Gamma\frac{(\omega^2M - \zeta_1\zeta_2)(1 + e^{-\frac{\zeta_1\pi}{\omega M}})}{e^{-\frac{\pi(\zeta_1+2\zeta_2)}{\omega M}} - e^{-\frac{\zeta_2\pi}{\omega m}}} \tag{71}$$

with the constant

$$\Gamma = \frac{(\zeta_1 - \zeta_2)(M - M_f)}{(\omega^2M^2 + \zeta_2^2)(\omega^2M^2 + \zeta_1^2)}\,. \tag{72}$$

The mean velocity of the particle is given by

$$\langle v(t)\rangle_T = \frac{\int_0^T v(t)dt}{T} = \frac{U\omega^2 M\Gamma}{2\zeta_1\zeta_2\pi\left(e^{\frac{\pi(\zeta_1+\zeta_2)}{\omega M}}-1\right)} \cdot \left[(\zeta_1+\zeta_2)(\zeta_1\zeta_2+\omega^2M^2)\left(1-e^{\frac{\pi(\zeta_1+\zeta_2)}{\omega m}}\right) + (\zeta_1-\zeta_2)(\omega^2M^2-\zeta_1\zeta_2)\left(e^{\frac{\zeta_1\pi}{\omega M}}-e^{\frac{\zeta_2\pi}{\omega M}}\right)\right] . \quad (73)$$

This allows to determine the requirements of a net motion after one period of the flow. Firstly, the density of the particle must differ from the one of the fluid, i.e. $\langle v(t)\rangle_T = 0$ with $M = M_f$ ($\Gamma = 0$). Secondly the frequency must be high enough so that the inertia plays a role. The influence of the inertia can be measured by comparing the velocity relaxation time of the particle $\tau_v = \frac{M}{\zeta}$ and the frequency of the flow ω. Equation (73) shows that the net velocity vanishes if the inertia is negligible due to a low frequency, i.e. $\langle v(t)\rangle_T \to 0$ at $\frac{M}{\zeta_{1,2}}\omega \to 0$ and $\frac{M_f}{\zeta_{1,2}}\omega \to 0$. Thirdly, the drag coefficient must change over time and must be in one half period larger than in the following, i.e. $\langle v(t)\rangle_T = 0$ with $\zeta_1 = \zeta_2$. For example the particle must have a higher drag while the flow streams upwards. In this calculation a time-dependent drag is assumed. Such a time-dependence can be achieved by the deformation of an asymmetric particle. To get a high deformation the frequency of the flow must be in the same range than the spring's relaxation time (for a tetrahedron) $\tau_k = \frac{M}{k}$ with the spring stiffness k and the mass M, e.g. one must choose $\frac{M}{k}\omega \approx 1$. All three conditions must be fulfilled to get a net motion. In this calculation, a symmetric (sinusoidal) flow is used. Also a symmetric particle in an asymmetric flow can be used which is shown in the following by the simulations.

The calculation helps to explain why the particle investigated in [92] would be sinking if gravity is included: With the small parameters $\frac{M}{\zeta_{1,2}}\omega = 0.063 \ll 1$ the inertial effect is weak.

These results are confirmed by simulations. The tetrahedron shows that the drag is indeed time-dependent which leads to a net velocity and it rises against gravity. Hereby the frequency of the flow must both fit the spring relaxation time and also $\tau_v\omega$ is chosen not too small. Also the flow's velocity must be higher than a certain value so that the net velocity induced by the external flow is higher than the sinking velocity. The Janus capsule shows qualitatively the same behavior. Also the asymmetry of the capsule can be varied, i.e. the ratio of the stiffness of both halves. Here the net velocity as function of the ratio shows that the asymmetry is necessary. A symmetric capsule with equal halves in a symmetric flow is only sinking, due to the gravity.

Also symmetric particles in an asymmetric flow are investigated. The flow is

given by

$$\mathbf{u}_0(t) = U\ [\sin(\omega t) + \varepsilon \cos(2\omega t)]\, \hat{e}_y\,, \tag{74}$$

It is flowing long and slow in one direction and fast and short in the other one, so that the mean velocity is zero. This flow induces an asymmetric drag of a symmetric particle due to the different flow velocities. Therefore the same effect is found as for the asymmetric particles. Also the symmetric particle can rise against gravity. This is confirmed by simulations of a ring and of a capsule. It is found that the asymmetry of the flow ε must be high enough to induce an upwards net motion, besides a sufficient high flow velocity U and a frequency that fits the velocity relaxation time and the elastic relaxation time. The sign of ε determines if the net velocity induced by the flow is directed upwards or downwards which means the particle's motion can be controlled by the flow.

A possible application of this effect could by the assembly of artificial microswimmers. The microswimmers investigated here are driven by the background flow which is a new method compared with the well known actuation of artificial microswimmers like the actuation by magnetic [100–103], electric [104, 105], chemical [106, 107] or optical [108] forces. It is shown here that the an actuation by the background flow can be achieved with simple particles, e.g. with a capsule. A further application is the sorting of different particles: For example biological cells have a different density than e.g. water [109] and healthy and malignant cells differ in their stiffness [75]. Hence they may be sorted in a shaken fluid because the inertia induced velocity depends on their stiffness.

Transport due to external forces

Transport of soft particles due to external forces in flows

Besides the properties of the flow studied in the previous section also external forces can influence the transport of particles in flows. An external force on a particle can be realized e.g. by using lighter or heavier particles than the fluid, which results in a buoyancy force. Such systems have been studied previously: For example heavy and rigid particles at finite Reynolds number in a flow downwards or upwards a gravity field migrate away from or to the tubes center, respectively [110]. Also the effects of axial forces on the transport of soft particles in a flow with a finite Reynolds number through a tube was studied [111–113]. Further examples are the effect of forces on polymers in Poiseuille flows, e.g. electrical forces on charged polymers [114, 115]. Also the shape and the characteristic deformation of sedimenting heavy vesicles have been investigated recently [116–118]. But very little is known about the dynamics of soft and non-neutrally buoyant particles in vertical Stokes flows, which is studied in

pub4.

Here the transport of a soft capsule is studied in a linear shear flow and a Poiseuille flow

$$\boldsymbol{u}(\boldsymbol{r}) = U\left[1 + \left(\frac{y}{d}\right)^2\right]\hat{\boldsymbol{e}}_x \tag{75}$$

with the Poiseuille flows maximal velocity U, the viscosity η and the center to wall distance d. This is done by an analytical calculation and with simulations of a soft capsule. Thereby Stokesian dynamics simulations are used with the Oseen tensor, which neglects wall interactions, and with the Blake tensor that includes the wall interaction. Also LBM simulations are utilized.

At first an explanation of the dynamics is given. In a linear shear flow the capsule is deformed and adopts the shape of an ellipsoid. The shape in a Poiseuille flow is approximately also an ellipsoid. An ellipsoid has an anisotropic drag coefficient. Due to the anisotropic drag a force in flow direction results also in a transport perpendicular to the flow. In *pub4* the migration due to the force was calculated approximately (cf. also *pub8* and eq. (91)). The shape of a soft capsule in a linear shear flow was calculated by D. Barthès-Biesel for small capillary numbers, i.e. small deformations [66, 70]. By using the expression of the shape together with the drag coefficient of an ellipsoid given in [119], here the velocity due to the external force is calculated approximately. This results in

$$v_{m,f} \approx \frac{5}{96}\frac{F_x^{ext}}{\pi\eta R} \tag{76}$$

with the particle radius R. Thus a transport perpendicular to the flow due to a force in flow direction is already found in a linear shear flow. In a Poiseuille flow one can approximately use the local shear rate of the Poiseuille flow which results in

$$v_{m,f} \approx -\frac{5}{48}\frac{F_x^{ext} U y_c}{\pi G d^2} \approx -0.0331\frac{F_x^{ext} U y_c}{G d^2} \tag{77}$$

with the particle's distance to the center y_c and the Neo-Hookean stiffness G of the capsule. The result is similar to eq. (91) and the small difference is due to the different approximations. This allows to determine the direction of the migration induced by the external force in flow direction: For example if the particle is heavier than the fluid (e.g. $F_x^{ext} < 0$) and the flow streams upwards ($U > 0$) then the particle migrates to the walls ($v_{m,f} > 0$ with y_c). This means the particle migrates to the walls if the external force is antiparallel to the flows direction. A change in the flow direction ($U < 0$) or the usage of a lighter particle ($F_x^{ext} > 0$) results in a reversal of the migration velocity. In this case the force and the flow direction is parallel.

The simulations allow to verify the calculations, to use larger deformations and to include the wall interaction. All simulation methods show a good agree-

ment with the calculations as long as the deformation is small and at a sufficient distance to the wall. The migration velocity as function of the capillary number without walls displays a linear increase with the capillary number and a saturation at a sufficient high capillary number. If the external force is parallel to the flow the migration to the center is enhanced and if both are antiparallel the migration is directed towards the walls. The walls can be included by using the Blake tensor. In this case the inwards migration due to a force parallel to the flow is enhanced by the wall repulsion. The outwards migration due to a force antiparallel to the flow is canceled by the wall repulsion at a certain distance to the wall. Hence this distance is an attractor. The location of this attractor depends on the parameters like the capillary number or the external force.

This effect can be used to sort different kinds of particles. For example biological cells have a 5% to 15% higher density than water [109]. The simulations show that this density difference is enough to achieve a migration to the walls. Moreover healthy and malignant cancer cells differ in their stiffness [75], so that the stiffness is an indicator of the health status. Because the location of the off-center attractor depends on the capillary number the effect may be used to sort cells with respect to their stiffness.

Measurement of the magnetic moment of bacteria

Here another example of the transport of particles due to an external force is given but without an external flow of the fluid. *pub5* shows that a transport due to an external force allows to determine properties of particles. More precisely, the magnetic moment of a magnetotactic bacterium, Magnetospirillum gryphiswaldense, is measured.

Among many other organism like algae, bees, pigeons and mice [120], also bacteria [121] like Magnetospirillum gryphiswaldense use the magnetic field of the earth for navigation and orientation. To do this, Magnetospirillum gryphiswaldense synthesizes magnetosomes which are intracellular organelles that comprise membrane-enclosed magnetite (Fe_3O_4) nanoparticles [122–125]. These magnetosomes allow to navigate and to align along the geomagnetic field [126]. The bacterium has a helical shape with the length of several micrometers and a diameter of a half micrometer. It was studied previously, e.g. its motility [127], its swimming in presence of magnetic fields [128, 129] and the magnetotaxis and aerotaxis [130]. Also the molecular mechanism underlying the magnetosome biosynthesis and intracellular alignment has been studied [123, 125, 126, 131–139].

But the physical property that makes magnetotaxis possible, the magnetic moment, was not studied at a single cell level before. This previous studies

used a complete population to measure the average magnetic moment of Magnetospirillum gryphiswaldense by assuming all bacteria have the same shape. Moreover the shape was approximated as a cylinder or an ellipsoid. The results of this studies differ by more than one order of magnitude [129, 140, 141]. This raises the question why these results show this large spread. A possible reason is that the shape and the dimensions of the individual cells must be considered instead of using simplified, averaged shapes. Another study suggested furthermore that the noise induced by living bacteria can lead to a systematical error of the measurement [142]. Therefore dead bacteria are used.

pub5 shows a method to determine the magnetic moment taking each individual shape into account, whereby more than 350 individual cells were used. Inhomogeneous switchable magnetic fields are generated by magnetic tweezers. Such magnetic tweezers are often used in single molecule and cellular studies [143–149]. This allows to measure the motion of the bacteria in the magnetic field. The translational motion due to the magnetic force is studied with a magnetic gradient field and a rotational motion by an alternating field. The magnetization can now be determined by the force balance of the magnetic field and the viscous forces because the field strength and the drag coefficient is known and the trajectories are measured by microscopy.

The drag coefficient must hereby be determined by the measured shape of the bacteria. Here comes the bead models into play, which allows to calculate the drag coefficient of an arbitrary shaped particle [45, 46, 150]. The drag was also calculated by the boundary integral method [151–153].

Besides this measurement with the magnetic tweezers a second method was used, which allows to compare both methods. Hereby images of the bacteria were generated by transmission electron microscopy. This allows to determine the volume of the magnetosomes. By using the volume and the known saturation magnetization of magnetite this allows to compare both methods and to show that they are consistent.

The results of the average magnetic moments of Magnetospirillum gryphiswaldense were firstly $\mu = (2.4 \pm 1.1) \cdot 10^{-16}\,\mathrm{Am}^2$ at $B = 6 - 23\,\mathrm{mT}$ obtained with by measuring the rotation of the bacteria in the alternating fluid, secondly $\mu = (7.7 \pm 3.4) \cdot 10^{-16}\,\mathrm{Am}^2$ at $B = 90 - 130\,\mathrm{mT}$ by measuring the translation of the bacteria and thirdly $\mu = (9.9 \pm 2.6) \cdot 10^{-16}\,\mathrm{Am}^2$ by measuring the volume of the magnetosomes with the transmission electron microscope and using the saturation magnetization of magnetite for large external fields.

The study allows to answer the raised questions. At first it is discussed if the helical shape must be taken into account. Therefore the results obtained with the drag of a helix is compared with the results obtained by assuming an averaged cylinder and neglecting individual shapes. The study shows an error

of 10% of the average magnetization of all bacteria if the helical shape is not considered. If distribution of magnetization of individual bacteria is investigated the individual shape is even more important. For example if the magnetic moment of the shortest bacterium is determined the error between a measurement using the individual helical shape and the average shape using a cylinder is 29%. For the longest bacterium the error is -22%.

A further question was whether dead or living cells should be used for measurement. The study used only dead cells so that no final answer can be given. But a comparison with other studies [129, 154] that uses dead bacteria shows a good agreement, especially compared with large spread of the studies using living cells mentioned above. Hence one can conclude that the measurement of dead cells provides more consistent results.

Cross-stream migration due to a viscosity gradient

Besides the mechanisms of cross-stream migration discussed above, also complex, non-Newtonian fluids can cause a cross-stream migration. This was studied in channels with flat or modulated walls [20, 74, 155–160]. The dynamics of particles immersed in such viscoelastic and shear-thinning fluids is rather complex and is caused and influenced by many effects like the fluid elasticity, wall interaction, shear thinning and the particle's deformability. This can lead to a migration to the channel walls. But it is difficult to determine the cause of the migration to the walls in a complex fluid. For example, no explicit expression of the force on the particle due to the fluids elasticity is known in presence of a non-constant viscosity [157]. Therefore a more simple fluid is investigated in *pub6*, where a fluid with constant gradient in the viscosity is used. It can be seen as a first approximation of a viscosity profile of a shear thinning fluid without considering elastic forces. This allows to show that a viscosity contrast alone can lead to a migration towards a wall in simple shear flows and Poiseuille flows: A migration towards the lower viscosity is found, if the viscosity varies perpendicular to the flow. This simplified system can help to better understand the migration in complex fluids. Another advantage is that such a viscosity gradient can be also realized experimentally with a temperature gradient, because the viscosity of a fluid often strongly depends on the temperature. A temperature gradient can easily be created in microfluidic devices [161].

To investigate the migration in a flow with a viscosity gradient, the viscosity profile $\eta(\boldsymbol{r})$ with a constant gradient $\boldsymbol{G}_\eta$ is used

$$\eta(\boldsymbol{r}) = \eta_0 + \boldsymbol{G}_\eta \cdot \boldsymbol{r} \text{ with } \nabla\eta = \boldsymbol{G}_\eta \,. \tag{78}$$

Only flows at low Reynolds number are considered in *pub6*, which are determined

by solving the Stokes equation

$$-\nabla p + \nabla \cdot \left\{\eta[\nabla \mathbf{u} + (\nabla \mathbf{u})^T]\right\} + \mathbf{f} = 0 \tag{79}$$

with the flow velocity $\mathbf{u}$ and the pressure p for two setups: The flow can be driven by a moving plate or a pressure gradient. If the flow is driven by a pressure gradient it results in the parabolic flow profile without the viscosity gradient, whereas with gradient the maximum of the flow velocity is shifted towards the lower viscosity.

To investigate the influence of the gradient in the viscosity on the transport of particles, a capsule is utilized. The capsule is simulated with the Stokesian dynamics method which neglects wall interactions and the lattice Boltzmann method where the wall interaction is included. To use the Stokesian dynamics method, the Oseen tensor is required which can only be used with a constant viscosity. Therefore, a generalized Oseen tensor is derived in first order of the viscosity gradient. The calculation is given in the appendix of *pub6*.

At the beginning, *pub6* gives a simple explanation why a migration in a linear shear flow is found for a gradient in the viscosity. This is done by considering the symmetries of the flow and the capsule and by calculating the forces on the particle numerically. At first a rigid spherical particle is discussed (cf. fig 1). Such a particle rotates in a linear shear flow and it follows the stream line through its center. Due to the symmetry of the flow and the capsule the net force on the particle is zero. But if this motion, i.e. the rotation, is performed in presence of a viscosity gradient then the symmetry is broken. As example, the gradient is oriented here perpendicular to the flow and lies inside the shear plane (y-direction). This results in a non vanishing net force $\boldsymbol{F}_{net} = \oint \boldsymbol{F}_f dA$ (of the friction force due to the rotation). But this force is parallel to the flow and thus no cross-stream migration is found with a rigid capsule (only a lateral migration). The situation in case of a deformable particle is similar. But the deformable particle is not spherical and adopts the shape of an ellipsoid. Due to this shape, the net force in presence of the gradient has a component perpendicular to the flow, which leads to a cross-streamline migration. It is oriented towards the lower viscosity.

These findings are confirmed by the simulations. In a flow driven by a moving plate a cross-stream line migration is only found with a gradient in the viscosity and with a soft particle. The migration is directed towards the lower viscosity and increases with the gradient and with the capillary number. A comparison of the Stokesian dynamics simulations using the LBM and the generalized Oseen tensor shows a good agreement (an error of 10%) as long as the viscosity varies not too much, i.e. 15% over the size of the particle. With the LBM the wall interaction is included so that the particle migrates until the wall repulsion stops

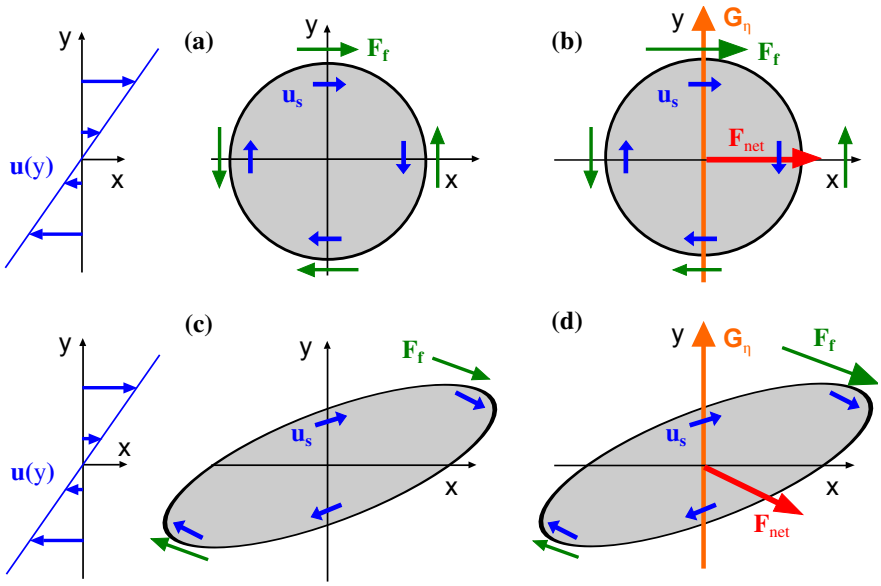

Figure 1: (a) A sketch of a rigid, spherical capsule in a linear shear flow. Its surface rotates with the velocity $\mathbf{u}_s$ due to the flow $\mathbf{u}$. This motion leads to a friction force $\boldsymbol{F}_f$, whereby the net force is zero. (b) If the same motion is performed with a gradient, the friction force at the half with the higher viscosity is higher than at the other half, which leads to a non-vanishing net force. The force is parallel to the flow because the system is still symmetric to the yz-plane. (c) A deformable capsule performs a tank-treading motion in the flow and is deformed to an ellipsoid. It has a point symmetry which prevents a net force without gradient. (d) If this motion is performed with a gradient then the point symmetry is broken which causes a net force. This force has a component perpendicular to the flow, towards the region with the lower viscosity.

the migration at a certain distance to the wall. This distance depends on the particle's properties.

Also in a Poiseuille flow a temperature gradient and therefore a viscosity gradient can be applied which is also simulated with Stokesian dynamics (without the wall interaction) and with the LBM (with the wall interaction). Due to the viscosity gradient, the maximal flow velocity is shifted towards the lower viscosity. In a Poiseuille flow both the spatially varying shear rate (found also without a gradient) and the gradient in the viscosity causes a migration. Therefore, without wall interaction, the particle migrates either to the maximal flow velocity or to the wall with the lower viscosity, depending on the initial condition. Also the migration is faster, compared to the case without gradient. But if the wall interaction is included, the particles migrate for every initial position

to the maximal flow velocity. The reason is that the wall interaction is stronger than the migration due to the viscosity gradient in this flow profile.

But another viscosity profile is also possible: In a flow of a shear thinning fluid the viscosity is maximal in the center and minimal at the boundaries. Therefore a fixed viscosity profile is used with a maximum at the center and a linear decrease towards the walls, which is an approximation of a shear thinning behavior. It reproduces a flow profile that is characteristic for shear thinning fluids, i.e. a flow profile with the maximal velocity at the center, a nearly constant velocity close to the center and a fast decrease of the velocity close to the walls. This system is simulated with the lattice Boltzmann method. Here particles close to the center migrate to the center and particles further away from the center migrate towards the lower viscosity, i.e. towards the walls until the wall repulsion stops the migration. Hence the attractor at the center and the attractor at the walls coexist.

A possible application of the focusing of particles, found in the linear shear flow with a viscosity gradient, may be the sorting of different particles. This is possible because the migration velocity and the attractor's distance to the wall depend on the particle properties, e.g. on their stiffness. The linear temperature gradient applied to a Poiseuille flow helps to enhance the migration velocity and allows to position the particles via the shift of the maximal velocity. The simulations with the viscosity profile that approximates the one of shear thinning fluids show a migration towards the walls. Hence the viscosity gradient (with the deformability of the particle) alone can already lead to a wall migration. This may help to understand the migration behavior in more complex fluids, where it is not easy to determine which of many possible effects leads to the wall migration.

Influence of noise on the cross-stream migration

In the previous part of this thesis, systems are investigated in which thermal noise can be neglected. In systems of smaller size like semi-flexible polymers or small fibers in a Poiseuille flow, the noise can become important and one can ask how the cross-stream migration of deformable particles is affected by noise effects. This is studied in *pub7*.

These kinds of particles are often investigated in previous studies. For example early observations of an enhanced polymer concentration near a channel wall [162] were explained by polymer kinetic theories for bead-spring chain models in inhomogeneous flows [163, 164]. Also lift forces were predicted for flexible polymers near a wall (as for vesicles [28, 29]) in simulations [165] and are found in experiments [166]. For Brownian fibers a small off-center concentration peak

was predicted [167, 168] and experiments showed such a peak with actin filaments [169]. Also the distribution of semi-flexible polymers was investigated in many simulations which investigate especially the influence of the boundary effects [170–173]. It was shown recently that fibers can also migrate without a wall interaction and how the wall influences the migration. This system was investigated without noise in [9, 174, 175]. In *pub7* also the migration without the boundary and the influence of the wall interaction on the migration of fibers or semi-flexible polymers is investigated, whereby here especially the influence of the noise on the migration is discussed.

The study in this thesis continues the research of Steffen Schreiber [176]. Semi-flexible polymers or fibers in *pub7* are simulated with a bead-spring model. Hereby a chain of beads is used which is connected by springs and a bending potential is used. As mobility matrix the Rotne-Prager tensor is used and wall interactions with the Blake tensor are included. Besides the deterministic forces due to the springs and the bending potential, also stochastic forces, i.e. the thermal noise, are included. The chain consists of three beads and is confirmed by simulations with five beads, that show qualitatively the same results. The flow is a planar Poiseuille flow.

At first semi-flexible bead-spring models are studied without the interactions with the wall. With low thermal noise a cross-streamline migration to an off-center attractor is found. The particles migrate to this attractor if they are positioned initially not too close to the wall. If the particles are closer to the wall, they migrate towards the wall and leave the channel due to the missing wall interaction. This means also a repeller exists between the off-center attractor and the channel wall. At higher thermal noise the dynamics is different: Here, the particles migrate towards the attractor at all initial positions in the channel, i.e. no repeller is found. The same qualitative results are also found in a tube flow.

After identifying the attractor and the repeller, it is investigated how their position depend on the parameters. At first is discussed how the position depends on the bending stiffness at low thermal noise. At increasing stiffness the attractor is shifted away from the center and the repeller comes closer to the center. Above a critical value of the stiffness the attractor and repeller vanishes. In this case, the particles migrate everywhere away from the center of a parabolic flow profile. These results are found in the simulations performed for this thesis and also in [176].

It is especially investigated how the attractor is affected by the noise: At high thermal noise the attractor exists at higher values of the stiffness than without noise, i.e. the critical value is increased.

A closer look on the dynamics of the chain allows to give a criterion which

determines the migration direction. A chain is a long time oriented parallel to a stream line until it is a bit inclined due to the noise. Then it rotates very fast due to the shear rate and is then again oriented parallel to the flow. But due to the spatially dependent shear rate in a Poiseuille flow the chain does not only rotate but is also bend by the flow. The simulations show that the maximal bending angle during one flip determines the migration direction. A maximal bending angle lower than $\pi/2$ leads to a migration to the center and an angle above $\pi/2$ to a migration away from the center.

This criterion can explain why the attractor vanishes at a high bending stiffness and exists at a low stiffness. At a low stiffness the situation is the following: Close to the center the shear rate is small and the particle is bend less, i.e. it migrates outward. Further away from the center the shear rate is higher and the chain is more bend, i.e. it migrates towards the center. This explains the attractor. In the region close to the wall the shear rate is even higher. In this case the chain rotates very fast and is less bend. Hence the chain migrates towards the wall and not to the attractor which explains the repeller. At a higher bending stiffness the chain is bend less at all initial positions. Hence it migrates everywhere away from the center of the parabolic flow profile. Therefore no attractor exists at a high bending stiffness above the critical value. At a high noise the situation is different: The interplay between the high noise and the shear rate increases the deformation and the bending. Thus the noise stabilizes the attractor.

The migration of the semi-flexible bead-spring models is also investigated with the wall interaction. One could expect that the particles, which migrate away from the center of the flow profile are hindered by the wall, so that one new attractor appears. But interestingly two new attractors appear at low values of the noise: At small values of the bending stiffness three attractors are found. If the bending stiffness is increased two attractors vanish and one attractor is found at all values of the bending stiffness.

With a high thermal noise only two attractors are found at a low bending stiffness. The third attractor found at low noise has a small basin of attraction so that particles at a high noise can be pushed out of the basin by the noise. It is therefore not found in the case of large noise amplitudes. At higher values of the bending stiffness one attractor vanishes and the other is found at all values of the bending stiffness. It is at the same location as in case of a lower thermal noise.

This can be again explained with the criterion of the maximal bending angle. The wall interaction influences the maximal bending angle during one flip because the bead which is located the closest to the wall is slowed down by the wall interaction. The bead chain is thus influenced on the one hand by the spatially

dependent shear rate and also by the wall interaction. The interplay between both determines the maximal bending angle and the migration direction which leads to the new attractors. The details of this dynamics are given in *pub7*.

Hence it is shown in *pub7* that the noise is important and can change the behavior qualitatively. For example it can stabilize an attractor in the case without wall effects. Also with wall effects the behavior with high and low noise is different.

Describing cross-streamline migration by bead-spring models

In this thesis bead-spring models are used, besides LBM-simulations, to model the cross-stream migration of soft particles in flows. Such simple models are helpful to understand the mechanisms leading to a cross-streamline migration. This approach was for example used by Watari and Larson to show in a very clear way that a chirality of soft particles leads to a CSM even in a linear shear flow [77]. Besides this, bead-spring models can even describe vesicles, also with an viscosity contrast [9, 177], or red blood cells [178] in a very efficient way. Further examples are the modeling of DNA [179], cilia [180], flexible filaments, [181], proteins [182, 183], general colloidal particles [184] and microswimmers [185–187]. Also conceptual work was done in the last years to improve bead models further [188, 189].

The bead model of a capsule used in this thesis was not used before. Therefore *pub8* compares the model quantitatively with other methods as a benchmark test. Besides the capsule also other simple models of deformable particles, i.e. a triangle, a tetrahedron, and a ring of beads, are investigated to demonstrate the minimal requirements that a bead-spring model must have to describe the cross-stream migration qualitatively. Furthermore, the simple bead-spring models are used to derive a semi-analytical expression for the cross-streamline migration. A viscosity contrast is not used in the models in this thesis.

The models are compared with the results of other studies found for a two dimensional vesicle [36] and a three dimensional capsule [38] in a flow with parallel stream lines. The results of these studies are firstly that a migration is not found in a linear shear flow, but in a Poiseuille flow. The Poiseuille flow has a non-vanishing second derivative, e.g. a curvature of the flow profile, and thus the shear rate varies across the particle. Secondly the migration is directed to the center of the flow, i.e. towards the maximal flow velocity. Thirdly, no migration is found at a vanishing capillary number (cf. eq. (58)), e.g. the deformation is necessary for a migration. The migration increases with the capillary number until it reaches a constant value above a certain value of the

capillary number.

The findings of these studies are compared with the two dimensional bead-spring models, at first with the triangle. It is a simple model and consists of three beads that are connected by springs. Already this simple model displays a migration. It is not found in a linear shear flow, but in a Poiseuille flow where it displays a migration to the center. The migration velocity as function of the capillary number (Ca) shows that the migration vanishes if the capillary number approaches zero (i.e. a very rigid triangle), which means the deformability is necessary. At higher values of the capillary number at the order of one the migration is maximal and at values larger than one the migration becomes slower and vanishes with an increasing Ca due to the high deformation. This means the simple triangle fits the findings of the vesicle at low values of the capillary number. At higher values the vesicle's area conservation prevents a high deformation and the migration becomes independent of Ca whereas the deformation of the triangle becomes large and its migration vanishes.

The ring behaves similar to the triangle, except that its bending potential prevents high deformations at high values of Ca. Thus the ring can also reproduce the plateau at high values of Ca found with the vesicle and agrees qualitatively well with the vesicle.

The findings with the three dimensional models are similar to the two dimensional models: The tetrahedron agrees quantitatively well with [38] at low capillary numbers, but the migration of the tetrahedron vanishes at high values of Ca due to the high deformations. In case of the bead capsule model the high deformation is prevented by the volume conservation and the plateau at high values of Ca is reproduced well.

The bead capsule model can also be compared to other capsule models. Barthès-Biesel [66] has shown that the Taylor parameter D= $\frac{L-B}{L+B}$ with the long and the short half axis L and B of the deformed, ellipsoidal capsule, is given by D = $\frac{25}{12}$Ca in case of small deformations. Simulations of the bead capsule model fit this result. A further benchmark was a comparison with the migration velocity of a capsule in a pipe flow calculated by Helmy and Barthès-Biesel [66, 190] in case of small deformations, which the simulations also agree with. A third test was a comparison with a LBM simulation of a capsule in a flat Poiseuille flow. To compare the bead model with the LBM, the Blake tensor is used because the LBM solves the full equations, i.e. includes also the wall interaction. Here a good agreement between the two models is found. Thus the bead capsule model can describe the CSM of capsules well.

Besides the fast simulations, the models can also be used for semi-analytical calculations. The migration velocity is defined as difference between the particles

velocity $\dot{\boldsymbol{r}}_c$ and the flow's velocity $\boldsymbol{u}(\boldsymbol{r}_c)$ at the particles center $\boldsymbol{r}_c$

$$\boldsymbol{v}_m = \dot{\boldsymbol{r}}_c - \boldsymbol{u}(\boldsymbol{r}_c)\,. \tag{80}$$

With the help of the bead-spring models one can show that the migration is given by

$$\boldsymbol{v}_m = \boldsymbol{u}_m - \boldsymbol{u}(\boldsymbol{r}_c) + \boldsymbol{\zeta}^{-1}(\boldsymbol{F}^{ext} - \boldsymbol{F}^{u} - \boldsymbol{F}^{tt}) \tag{81}$$

or with $\mathbf{u}_u = \boldsymbol{\zeta}^{-1}\boldsymbol{F}^{u}$ and $\mathbf{u}_{tt} = \boldsymbol{\zeta}^{-1}\boldsymbol{F}^{tt}$ by

$$\boldsymbol{v}_m = \boldsymbol{u}_m - \boldsymbol{u}(\boldsymbol{r}_c) + \mathbf{u}_u + \mathbf{u}_{tt} + \boldsymbol{\zeta}^{-1}\boldsymbol{F}^{ext}\,, \tag{82}$$

which allows to discuss the origin of the cross-streamline migration (the complete calculation is given in *pub8*): The first term $\boldsymbol{u}_m - \boldsymbol{u}(\boldsymbol{r}_c)$ means that a particle can migrate if the flow's mean velocity, i.e. the undisturbed flow without the particle averaged over the surface of the particle is not equal to the flow at the particles center. For example in a flat Poiseuille flow the average is lower than the flow at the particles center which leads to a lag behind of the particle (cf. e.g. [38]). But because the flow points everywhere in the same direction, also the average points in flow direction, which means this term can only lead to a lateral migration. This is not the case in a flow with non-parallel stream lines, e.g. in a channel with modulated walls (cf. *pub1*). The second term $\boldsymbol{\zeta}^{-1}\boldsymbol{F}^{ext}$ describes the Stokes friction, i.e. the effect of an externally applied force $\boldsymbol{F}^{ext}$ with the friction matrix $\boldsymbol{\zeta}$ (cf. *pub4*). The other forces $\boldsymbol{F}^{u}$ and $\boldsymbol{F}^{tt}$ describe the friction between the fluid and the particle. The force $\boldsymbol{F}^{tt}$ describes the friction that is caused by the tank-treading motion in the fluid. The force $\boldsymbol{F}^{u}$ is exerted on the particle by the external flow, e.g. a Poiseuille flow, that streams around the particle. As example in a homogeneous flow eq. (82) becomes

$$\boldsymbol{v}_m = \boldsymbol{\zeta}^{-1}\boldsymbol{F}^{ext}\,, \tag{83}$$

which means

$$\dot{\boldsymbol{r}}_c = \boldsymbol{u} + \boldsymbol{\zeta}^{-1}\boldsymbol{F}^{ext}\,. \tag{84}$$

This describes just the Stokes friction. In a Poiseuille flow, which is spatially dependent, the particle is deformed so that the term $\boldsymbol{F}^{u}$ is non-zero. Also a tank-treading occurs and $\boldsymbol{F}^{tt}$ is non-zero. The terms can be calculated numerically (cf. *pub8*) which shows that both terms contribute to the migration to the center. Hence the migration is caused both by the friction due to the spatially dependent flow that streams around the deformed capsule $\boldsymbol{F}^{u}$ and by the tank-treading motion $\boldsymbol{F}^{tt}$.

The migration can also be calculated semi-analytically. The details of the calculation are given in *pub8*. The flow is Taylor-expanded around the position of the particle at $\boldsymbol{r}_c$ which results in

$$\boldsymbol{u}_0 \approx \sum_{n=0}^{2} \frac{1}{n!} \left[(x-x_c)\partial_x + (y-y_c)\partial_y\right]^n_{x=x_c,y=y_c} \boldsymbol{u}_0 \,, \tag{85}$$

$$= \sum_{k,l=0}^{k+l\leq 2} \boldsymbol{b}_{k,l}(x-x_c)^k(y-y_c)^l \,. \tag{86}$$

and small deformations are assumed. This allows to calculate the migration velocity in dependence of the Taylor coefficients $\boldsymbol{b}_{k,l}$ of the flow, the viscosity and of the stiffness and the radius of the particle. For the sake of simplicity a translational independence is assumed in one spatial direction, i.e. the flow depends only on two spatial coordinates. The calculation shows that the contributions of the flow around the particle and the tank-treading to the migration are

$$(\mathbf{u}_u + \mathbf{u}_{tt}) \propto \mathrm{Ca}\, C \,. \tag{87}$$

Also the contribution of the mean flow $\boldsymbol{u}_m - \boldsymbol{u}(\boldsymbol{r}_c)$ can be calculated but this term does not contribute in a planar flow with parallel stream lines. Thus the migration in a planar flow is proportional to the capillary number $\mathrm{Ca} = \frac{\eta R}{G_s} b_\sigma$, whereby b_σ is a Taylor coefficient that contains a first derivative of the flow (cf. eq. (86)). The migration is furthermore proportional to the curvature of the flow profile $C = R^2 b_{\sigma'}$, whereby $b_{\sigma'}$ denotes a Taylor coefficient containing a second derivative of the flow (cf. eq. (86)). This means the migration is caused by the particle's deformability, i.e. by a nonzero value of Ca and by a shear rate that varies across the particle, i.e. by a nonzero value of C which is the curvature of the flow profile. The proportionality factors are calculated numerically and are given in *pub8*. Also the Stokes friction matrix $\boldsymbol{\zeta}^{-1}$ and the mean velocity $\boldsymbol{u}_m$ can be calculated as function of the Taylor-coefficients of the flow, the viscosity and the particles parameters.

This allows for example to discuss why no migration is found in a linear shear flow. Here the second derivative of the flow is zero, i.e. $C = 0$ and the migration vanishes. In a planar Poiseuille flow

$$\boldsymbol{u}_0 = U\left[1 - \left(\frac{y}{d}\right)^2\right]\hat{\boldsymbol{e}}_y \tag{88}$$

the Taylor coefficients are

$$\boldsymbol{b}_\sigma = -2U\frac{y_c}{d^2}\hat{\boldsymbol{e}}_y \text{ and } \boldsymbol{b}_{\sigma'} = -\frac{U}{d^2}\hat{\boldsymbol{e}}_y \,. \tag{89}$$

With eqs. (82) and (87) and the proportionality constant given in the appendix of *pub8* follows the cross-streamline migration velocity

$$v_{m,y} = u_{u,y} + u_{tt,y} + (\boldsymbol{\zeta}^{-1}\boldsymbol{F}^{ext}) \cdot \hat{\boldsymbol{e}}_y \,, \tag{90}$$

$$= -0.8875\, U^2 \frac{\eta y_c R^3}{G_s d^4} + 0.0527 \frac{F_y^{ext}}{\eta R} - 0.0388 \frac{U y_c F_x^{ext}}{G_s d^2} \,. \tag{91}$$

Hence the calculation reproduces the migration to the center in a Poiseuille flow and the Stokes friction with $0.0527\frac{F_y^{ext}}{\eta R} \approx \frac{F_y^{ext}}{6\pi\eta R}$. Due to the deformation of the soft particle in the Poiseuille flow to an ellipsoid also the force in x-direction contributes to the CSM in y-direction, which is described by the last term in eq. (91) (cf. also *pub4*).

Furthemore the results can be compared e.g. with the work Helmy and Barthès-Biesel for the migration velocity of capsules in pipe flow [190]. The calculation with the bead-spring model shows an error of 10% compared with the more exact calculation of Helmy and Barthès-Biesel which needs less approximations. But the easier bead-spring model allows the calculation in the more general, Taylor-expanded flow.

Bibliography

[1] Misbah C 2012 *J. Phys. Conf. Ser.* **392** 012005

[2] Secomb T W 2017 *Annu. Rev. Fluid Mech.* **49** 443

[3] Geislinger T M and Franke T 2014 *Adv. Colloid Interface Sci.* **208** 161

[4] Sajeesh P and Sen A K 2014 *Microfluid. Nanofluid.* **17** 1

[5] Misbah C 2014 *J. Fluid Mech.* **760** 1

[6] Purcell E M 1977 *Am. J. Phys.* **45** 3

[7] Bechinger C, Leonardo R D, Löwen H, Reichardt C, Volpe G and Volpe G 2016 *Rev. Mod. Phys.* **88** 045006

[8] Graham M D 2011 *Annu. Rev. Fluid Mech.* **43** 273

[9] Farutin A, Piasecki T, Slowicka A M, Misbah C, Wajnryb E and Ekiel-Jeżewska M L 2016 *Soft Matter* **12** 7307

[10] Bruus H 2007 *Theoretical Microfluidics* Oxford master series in condensed matter physics (Oxford: Oxford University Press)

[11] Thorsen T, Maerkl S J and Quake S R 2002 *Science* **298** 580

[12] Balslev S, Jorgensen A M, Bilenberg B, Mogensen K B, Snakenborg D, Geschke O, Kutter J P and Kristensen A 2006 *Lab Chip* **6** 213

[13] Squires T M and Quake S R 2005 *Rev. Mod. Phys.* **77** 977

[14] Kirby B J 2010 *Micro- and Nanoscale Fluid Mechanics* (Cambridge, England: Cambridge University Press)

[15] Nguyen N T and Wereley S T 2010 *Fundamentals and Applications of Microfluidics* (Boston: Artech House)

[16] Popel A S and Johnson P C 2005 *Annu. Rev. Fluid Mech.* **37** 43

[17] Sackmann E K, Fulton A L and Beebe D J 2014 *Nature* **507** 181

[18] Dahl J B, Lin J M G, Muller S J and Kumar S 2015 *Annu. Rev. Chem. Biomol. Eng.* **6** 293

[19] Amini H, Lee W and Carlo D D 2014 *Lab Chip* **14** 2739

[20] Karimi A, Yazdi S and Ardekani A M 2013 *Biomicrofluidics* **7** 021501

[21] Segré G and Silberberg A 1961 *Nature* **189** 209

[22] Wu Z, Chen Y, Wang M and Chung A J 2016 *Lab Chip* **16** 532

[23] Zhang J, Yan S, Sluyter R, Li W, Alici G and Nguyen N T 2014 *Sci. Rep.* **4** 4527

[24] Carlo D D 2009 *Lab Chip* **9** 3038

[25] Carlo D D, Irima D, Tompkins R G and Toner M 2007 *Proc. Natl. Acad. Sci. U. S. A.)* **104** 18892

[26] Zhang J, Yan S, Yuan D, Alici G, Nguyen N T, Ebrahimi Warkiani M and Li W 2016 *Lab Chip* **16** 10

[27] Jhon M S and Freed K F 1985 *J. Polym. Sci., Polym. Phys. Ed.* **23** 955

[28] Cantat I and Misbah C 1999 *Phys. Rev. Lett.* **83** 880

[29] Seifert U 1999 *Phys. Rev. Lett.* **83** 876

[30] Abkarian M, Lartigue C and Viallat A 2002 *Phys. Rev. Lett.* **88** 068103

[31] Grandchamp X, Goupier G, Srivastav A, Minetti C and Podgorski T 2013 *Phys. Rev. Lett.* **110** 108101

[32] Sekhon G, Armstrong R and Jhon M S 1982 *J. Polym. Sci., Polym. Phys. Ed.* **20** 947

[33] Brunn P O 1983 *Int. J. Multiphase Flow* **9** 187

[34] Leal L G 1980 *Annu. Rev. Fluid Mech.* **12** 435

[35] Mandal S, Bandopadhyay A and Chakraborty S 2015 *Phys. Rev. E* **92** 023002

[36] Kaoui B, Ristow G H, Cantat I, Misbah C and Zimmermann W 2008 *Phys. Rev. E* **77** 021903

[37] Coupier G, Kaoui B, Podgorski T and Misbah C 2008 *Phys. Fluids* **20** 111702

[38] Doddi S K and Bagchi P 2008 *Int. J. Multiphase Flow* **34** 966

[39] Dondorp A M, Kager P A, Vreeken J and White N J 2000 *Parasitol. Today* **16** 228

[40] Mokken F C, Kedaria M, Henny C P, Hardeman M R and Gelb A W 1992 *Ann. Hematol.* **64** 113

[41] Cross S E, Jin Y S, Rao J and Gimzewski J K 2007 *Nat. Nanotechnol.* **2** 780

[42] Suresh S 2007 *Acta Mater.* **55** 3989

[43] Ballas S K 1991 *Am. J. Hematol.* **36** 122

[44] Landau L and Lifshitz E 1987 *Fluid Mechanics* Course of Theoretical Physics (Oxford: Pergamon Press)

[45] Doi M and Edwards S F 1986 *The Theory of Polymer Dynamics* (Oxford: Clarendon Press)

[46] Dhont J K G 1996 *An Introduction to Dynamics of Colloids* (Amsterdam: Elsevier)

[47] Yamakawa H 1970 *J. Chem. Phys.* **53** 436

[48] Rotne J and Prager S 1969 *J. Chem. Phys.* **50** 4831

[49] Wajnryb E, Mizerski K A, Zuk P J and Szymczak P 2013 *J. Fluid Mech.* **731** R3

[50] Blake J R 1971 *Proc. Camb. Philos. Soc.* **70** 303

[51] Jones R B 2004 *J. Chem. Phys.* **121** 483

[52] Krüger T, Kusumaatmaja H, Kuzmin A, Shardt O, Silva G and Viggen E M 2016 *The Lattice Boltzmann Method - Principles and Practice* (Berlin: Springer)

[53] Gombosi T 1994 *Gaskinetic Theory* (Cambridge: Cambridge University Press)

[54] Bhatnagar P L, Gross E P and Krook M 1954 *Phys. Rev.* **94** 511

[55] Aidun C K and Clausen J R 2010 *Annu. Rev. Fluid. Mech* **42** 439

[56] Chapman S and Cowling T 1952 *The Mathematical Theory of Non-uniform Gases* (Cambridge: Cambridge University Press)

[57] Guo Z, Zheng C and Shi B 2002 *Phys. Rev. E* **65** 046308

[58] Peskin C S 2002 *Acta Numer.* **11** 479

[59] Wedgewood L E, Ostrov D N and Bird R 1991 *J. Non-Newtonian Fluid Mech.* **40** 119

[60] Hendricks J, Kawakatsu T, Kawasaki K and Zimmermann W 1995 *Phys. Rev. E* **51** 2658

[61] Grest G S and Kremer K 1986 *Phys. Rev. A* **33** 3628

[62] Honerkamp J 1994 *Stochastic dynamical systems* (New York, NY: VCH)

[63] van Kampen N G 2007 *Stochastic Processes in Physics and Chemistry* (Amsterdam: Elsevier)

[64] Gardiner C W 1983 *Handbook of stochastic methods for physics, chemistry and the natural sciences* Springer series in synergetics (Berlin: Springer)

[65] Öttinger H C 1996 *Stochastic processes in polymeric fluids* (Berlin: Springer)

[66] Barthès-Biesel D 2016 *Annu. Rev. Fluid Mech.* **48** 25

[67] Wang G, Mao W, Byler R, Patel K, Henegar C, Alexeev A and Sulchek T 2013 *PLoS One* **8** e75901

[68] Krueger T, Varnik F and Raabe D 2011 *Comput. Math. Appl.* **61** 3485

[69] Krüger T 2012 *Computer Simulation Study of Collective Phenomena in Dense Suspensions of Red Blood Cells under Shear* (Wiesbaden: Springer Spektrum)

[70] Barthès-Biesel D 1981 *J. Fluid Mech.* **113** 251

[71] Ramanujan S and Pozrikidis C 1998 *J. Fluid Mech.* **361** 117

[72] Gompper G and Kroll D M 1996 *J. Phys. I (France)* **6** 1305

[73] Krueger T, Gross M, Raabe D and Varnik F 2013 *Soft Matter* **9** 9008

[74] Schlenk M, Drechsler M, Karg M, Zimmermann W, Trebbin M and Förster S 2018 *Lab Chip* **18** 3163

[75] Guck J, Schinkinger S, Lincoln B, Wottawah F, Ebert S, Romeyke M, Lenz D, Erickson H M, Ananthakrishnan R, Mitchell D, Käs J, Ulvick S and Bilby C 2005 *Biophys. J.* **88** 3689

[76] Farutin A and Misbah C 2014 *Phys. Rev. E* **89** 042709

[77] Watari N and Larson R G 2009 *Phys. Rev. Lett.* **102** 246001

[78] Becker L E, Koehler S A and Stone H A 2003 *J. Fluid Mech.* **490** 15

[79] Tam D and Hosoi A E 2007 *Phys. Rev. Lett.* **98** 068105

[80] Or Y 2012 *Phys. Rev. Lett.* **108** 258101

[81] Wiezel O and Or Y 2016 *Proc. Royal Soc. A* **472** 20160425

[82] Farutin A, Rafaï S, Dysthe D K, Duperray A, Peyla P and Misbah C 2013 *Phys. Rev. Lett.* **111** 228102

[83] Wu H, Thiébaud M, Hu W F, Farutin A, Rafaï S, Lai M C, Peyla P and Misbah C 2015 *Phys. Rev. E* **92** 050701

[84] Wu H, Farutin A, Hu W F, Thiébaud M, Rafaï S, Peyla P, Lai M C and Misbah C 2016 *Soft Matter* **12** 7470

[85] Eloy C and Lauga E 2012 *Phys. Rev. Lett.* **109** 038101

[86] Guo H, Nawroth J, Ding Y and Kanso E 2014 *Phys. Fluids* **26** 091901

[87] Guo H and Kanso E 2016 *Phys. Rev. E* **93** 033119

[88] Berg H C 2003 *Annu. Rev. Biochem.* **72** 19

[89] Berg H C 2000 *Phys. Today* **53** 24

[90] Berg H C 2004 *E. Coli in Motion* (Springer Science & Business Media)

[91] Gonzalez-Rodriguez D and Lauga E 2009 *J. Phys. Condens. Matter* **21** 204103

[92] Jo I, Huang Y, Zimmermann W and Kanso E 2016 *Phys. Rev. E* **94** 063116

[93] Morita T, Omori T and Ishikawa T 2018 *Phys. Rev. E* **98** 023108

[94] Maxey M R and Riley J J 1983 *Phys. Fluids* **26** 883

[95] Español P, Rubio M A and Zúñiga I 1995 *Phys. Rev. E* **51** 803

[96] Ladd A J C 1994 *J. Fluid Mech.* **271** 285

[97] d'Humières D, Ginzburg I, Krafczyk M, Lallemand P and Luo L S 2002 *Philos. Trans. Royal Soc. A* **360** 437

[98] Shao J Y and Shu C 2015 *Int. J. Numer. Methods Fluids* **77** 526

[99] Premnath K N and Abraham J 2007 *J. Comput. Phys.* **224** 539

[100] Sitti M 2009 *Nature* **458** 1121

[101] Dreyfus R, Baudry J, Roper M L, Fermigier M, Stone H A and Bibette J 2005 *Nature* **437** 862

[102] Cheang U K, Roy D, Lee J H and Kim M J 2010 *Appl. Phys. Lett.* **97** 213704

[103] Snezhko A and Aranson I S 2011 *Nat. Mater.* **10** 698

[104] Chang S T, Paunov V N, Petsev D N and Velev O D 2007 *Nat. Mater.* **6** 235

[105] Loget G and Kuhn A 2011 *Nat. Commun.* **2** 535

[106] Jiang H R, Yoshinaga N and Sano M 2010 *Phys. Rev. Lett.* **105** 268302

[107] Thutupalli S, Seemann R and Herminghaus S 2011 *New J. Phys.* **13** 073021

[108] Leoni M, Kotar J, Bassetti B, Cicuta P and Lagomarsino M C 2009 *Soft Matter* **5** 472

[109] Milo R and Phillips R 2016 *Cell biology by the numbers* (New York, NY: Garland Science)

[110] Jeffrey R C and Pearson J R A 1965 *J. Fluid Mech.* **22** 721

[111] Kim Y W and Yoo J Y 2009 *Lab Chip* **9** 1043

[112] Prohm C and Stark H 2014 *Lab Chip* **14** 2115

[113] Schaaf C and Stark H 2017 *Soft Matter* **13** 3544

[114] Zheng J and Yeung E S 2002 *Anal. Chem.* **74** 4536

[115] Usta O B, Butler J E and Ladd A J C 2007 *Phys. Rev. Lett.* **98** 098301

[116] Huang Z H, Abkarian M and Viallat A 2011 *New J. Phys.* **13** 035026

[117] Peltomäki M and Gompper G 2013 *Soft Matter* **9** 8346

[118] Boltz H H and Kierfeld J 2015 *Phys. Rev. E* **92** 033003

[119] Happel J and Brenner H 1981 *Low Reynolds Number Hydrodynamics* (Englewood Cliffs: Prentice-Hall)

[120] Frankel R B 1984 *Annu. Rev. Biophys. Bioeng.* **13** 85

[121] Blakemore R 1975 *Science* **190** 377

[122] Schleifer K H, Schüler D, Spring S, Weizenegger M, Amann R, Ludwig W and Köhler M 1991 *Syst. Appl. Microbiol.* **14** 379

[123] Faivre D and Schüler D 2008 *Chem. Rev.* **108** 4875

[124] Katzmann E, Scheffel A, Gruska M, Plitzko J M and Schüler D 2010 *Mol. Microbiol.* **77** 208

[125] Toro-Nahuelpan M, Müller F D, Klumpp S, Plitzko J M, Bramkamp M and Schüler D 2016 *BMC Biol.* **14** 88

[126] Schüler D 2008 *FEMS Microbiol. Rev.* **32** 654

[127] Schultheiss D, Kube M and Schüler D 2004 *Appl. Environ. Microbiol.* **70** 3624

[128] Erglis K, Wen Q, Ose V, Zeltins A, Sharipo A, Janmey P A and Cebers A 2007 *Biophys. J.* **93** 1402

[129] Reufer M, Besseling R, Schwarz-Linek J, Martinez V, Morozov A, Arlt J, Trubitsyn D, Ward F and Poon W 2014 *Biophys. J.* **106** 37

[130] Popp F, Armitage J P and Schüler D 2014 *Nat. Commun.* **5** 5398

[131] Grünberg K, Wawer C, Tebo B M and Schüler D 2001 *Appl. Environ. Microbiol.* **67** 4573

[132] Bazylinski D A and Frankel R B 2004 *Nat. Rev. Microbiol.* **2** 217

[133] Grünberg K, Müller E C, Otto A, Reszka R, Linder D, Kube M, Reinhardt R and Schüler D 2004 *Appl. Environ. Microbiol.* **70** 1040

[134] Scheffel A, Gruska M, Faivre D, Linaroudis A, Plitzko J M and Schüler D 2006 *Nature* **440** 110

[135] Faivre D, Böttger L H, Matzanke B F and Schüler D 2007 *Angew. Chem., Int. Ed.* **46** 8495

[136] Rong C, Huang Y, Zhang W, Jiang W, Li Y and Li J 2008 *Res. Microbiol.* **159** 530

[137] Jogler C and Schüler D 2009 *Annu. Rev. Microbiol.* **63** 501

[138] Ding Y, Li J, Liu J, Yang J, Jiang W, Tian J, Li Y, Pan Y and Li J 2010 *J. Bacteriol.* **192** 1097

[139] Fdez-Gubieda M L, Muela A, Alonso J, Garcia-Prieto A, Olivi L, Fernández-Pacheco R and Barandiarán J M 2013 *ACS Nano* **7** 3297

[140] Erglis K, Alberte L and Cebers A 2008 *Magnetohydrodyn.* **44** 223

[141] Logofătu P C, Ardelean I, Apostol D, Iordache I, Bojan M, Moisescu C and Ioniţă B 2008 *J. Appl. Phys.* **103** 094911

[142] Nadkarni R, Barkley S and Fradin C 2013 *PLoS One* **8** 1

[143] Wang N, Butler J P and Ingber D E 1993 *Science* **260** 1124

[144] Bausch A R, Möller W and Sackmann E 1999 *Biophys. J.* **76** 573

[145] Fabry B, Maksym G N, Butler J P, Glogauer M, Navajas D and Fredberg J J 2001 *Phys. Rev. Lett.* **87** 148102

[146] Tanase M, Biais N, Sheetz M, eds: Wang Y L and Discher D E 2007 *Cell Mechanics* (*Methods in Cell Biology* vol 83) (Amsterdam: Elsevier Academic Press Inc)

[147] De Vlaminck I and Dekker C 2012 *Annu. Rev. Biophys.* **41** 453

[148] Irmscher M, de Jong A M, Kress H and Prins M W 2012 *Biophys. J.* **102** 698

[149] Irmscher M, de Jong A M, Kress H and Prins M W J 2013 *J. R. Soc., Interface* **10** 20121048

[150] Leal L G 2007 *Advanced Transport Phenomena* (Cambridge: Cambridge University Press)

[151] Pozrikidis C 1992 *Boundary Integral and Singularity Methods for Linearized Viscous Flow* (Cambridge: Cambridge University Press)

[152] Saad Y and Schultz M 1986 *SIAM J. Sci. and Stat. Comput.* **7** 856

[153] Daddi-Moussa-Ider A, Guckenberger A and Gekle S 2016 *Phys. Rev. E* **93** 012612

[154] Fischer H, Mastrogiacomo G, Löffler J F, Warthmann R J, Weidler P G and Gehring A U 2008 *Earth Planet. Sci. Lett.* **270** 200

[155] D'Avino G, Tuccillo T, Maffettone P, Greco F and Hulsen M 2010 *Comput. Fluids* **39** 709

[156] Yuan D, Zhao Q, Yan S, Tang S Y, Alici G, Zhang J and Li W 2018 *Lab Chip* **18** 551

[157] Del Giudice F, Sathish S, D'Avino G and Shen A Q 2017 *Anal. Chem.* **89** 13146

[158] Lu X, Liu C, Hu G and Xuan X 2017 *J. Colloid. Interf. Sci.* **500** 182

[159] Faridi M A, Ramachandraiah H, Banerjee I, Ardabili S, Zelenin S and Russom A 2017 *J. Nanobiotechnol.* **15** 3

[160] D'Avino G, Greco F and Maffettone P L 2017 *Annu. Rev. Fluid Mech.* **49** 341

[161] Miralles V, Huerre A, Malloggi F and Jullien M C 2013 *Diagnostics* **3** 33

[162] Agarwal U S, Dutta A and Mashelkar R A 1994 *Chem. Eng. Sci.* **49** 1693

[163] Brunn P O and Kaloni P N 1985 *J. Chem. Phys.* **83** 2497

[164] Brunn P O 1985 *J. Polym. Sci. Polym. Phys.* **23** 89

[165] Ma H and Graham M D 2005 *Phys. Fluids* **17** 083103

[166] Stein D, von der Heyden F J J, Koopmans J A and Dekker C 2006 *Proc. Natl. Acad. Sci. (USA)* **103** 15853

[167] Nitsche L C and Hinch E J 1997 *J. Fluid Mech.* **332** 1

[168] Schiek R L and Shaqfeh E S G 1997 *J. Fluid Mech.* **332** 23

[169] Steinhauser D R, Köster S and Pfohl T 2012 *ACS Macro Lett.* **1** 541

[170] Saintillan D, Shaqfeh E S G and Darive E 2006 *J. Fluid Mech.* **557** 297

[171] Chelakkot R, Winkler R G and Gompper G 2010 *EPL* **91** 14001

[172] Chelakkot R, Winkler R G and Gompper G 2011 *J. Phys. Cond. Mat* **23** 184117

[173] Reddig S and Stark H 2011 *J. Chem. Phys.* **135** 165101

[174] Słowicka A M, Ekiel-Jeżewska M L, Sadlej K and Wajnryb E 2012 *J. Chem. Phys.* **136** 044904

[175] Słowicka A M, Wajnryb E and Ekiel-Jeżewska M L 2013 *Eur. Phys. J. E* **36** 31

[176] Schreiber S 2012 *The dynamics of hydrodynamically interacting particles in external fields and near solid boundaries* Doctoral thesis (Bayreuth: Universität Bayreuth)

[177] Mourad I and Aline L L 2014 *Int. J. Numer. Methods Fluids* **76** 835

[178] Lingling S, Tsorng-Whay P and Roland G 2012 *Int. J. Numer. Methods Fluids* **68** 1393

[179] Pandey H and Underhill P T 2015 *Phys. Rev. E* **92** 052301

[180] Nasouri B and Elfring G J 2016 *Phys. Rev. E* **93** 033111

[181] Bailey A G and Lowe C P 2017 *Phys. Rev. E* **96** 062417

[182] Blanco P M, Via M, Garcés J L, Madurga S and Mas F 2017 *Entropy* **19** 105

[183] Chow E and Skolnick J 2017 *Biophys. J.* **112** 2261

[184] Swan J W and Wang G 2016 *Phys. Fluids* **28** 011902

[185] Watari N and Larson R G 2010 *Biophys. J.* **98** 12

[186] Kong M, Wu Y, Li G and Larson R G 2015 *Soft Matter* **11** 1572

[187] Küchler N, Löwen H and Menzel A M 2016 *Phys. Rev. E* **93** 022610

[188] Mizerski K A, Wajnryb E, Zuk P J and Szymczak P 2014 *J. Chem. Phys.* **140** 184103

[189] Zuk P J, Wajnryb E, Mizerski K A and Szymczak P 2014 *J. Fluid Mech.* **741** R5

[190] Helmy A and Barthès-Biesel D 1982 *J. Mecanique theorique appliquee* **1** 859

Acknowledgment

At first I want to thank Prof. Dr. Walter Zimmermann for the opportunity to write this thesis in his group, for his supervision, the possibility to learn from him and many ideas for projects.

I thank also Prof. Dr. Chaouqi Misbah for giving me the possibility to visit Grenoble, the ideas for the wavy channel paper I received in Grenoble and at conferences.

I want to thank Prof. Stephan Gekle too for his help and advice in writing two of the publications.

Furthermore I want to thank Dr. Diego Kienle for supervising me at the beginning of time as PhD student and for writing papers with me.

Additionally I want to give thanks to the complete TP 1 group for the good atmosphere: A large thank goes to Winfried Schmidt for the good company in the office (Wortwitz-Winni) and for his help with the english language (wandelndes Wörtebuch) and for his time spend with proof-reading of papers. I also want to thank Andre Förtsch for the good company at many conferences and the cooperation in writing papers. Great thanks goes also to Markus Hilt for the assistance in technical problems, Claudia Brandt for all the administrative work like the billing of travel expenses, Lisa Rapp for many discussion on interesting topics, all the other people in the group and last but not least Aurora 22 for the great coffee.

I also want to say thanks to all my friends and especially to Markus Holzinger, Joe Schultheiß and the boardgame group. It is always a funny and good company and a nice opportunity to talk about something else than the work.

A large thanks goes to my family and especially my brother Daniel for long skype talks, visits in Bayreuth and Darmstadt and also for the proof-reading, even if not all creative corrections could be included.

Publications

List of included publications and the author's contributions

pub1 *Emerging Attractor in Wavy Poiseuille Flows Triggers Sorting of Biological Cells*
M. Laumann, W. Schmidt, A. Farutin,
D. Kienle, S. Förster, C. Misbah, and W. Zimmermann,

Phys. Rev. Lett. **122**, 128002 (2019)

individual contributions:
M.L. and W.Z. designed the research;
M.L. wrote the source code and performed the simulations of the capsule;
W.S. added the red blood cells to the code and performed
the simulations of the red blood cell;
all authors discussed and interpreted the results and wrote the paper.

pub2 *Cross-stream migration of asymmetric particles driven by oscillating shear*
M. Laumann, P. Bauknecht, S. Gekle,
D. Kienle and W. Zimmermann,

2017 EPL **117** 44001

individual contributions:
S.G., D.K., M.L. and W.Z. designed the research;
M.L. wrote the source code of the dumbbell;
M.L. performed the simulations of the dumbbell and the ring;
P.B. performed the simulations of the capsule;
all authors discussed and interpreted the results and wrote the paper.

pub3 *Engineering passive swimmers by shaking liquids*
M. Laumann , A. Förtsch, E. Kanso and W. Zimmermann

submitted to New J. Phys. on 2019-03-15 (with referees)
manuscript number NJP-110170
preprint on arXiv (https://arxiv.org/abs/1903.11510)

individual contributions:
E.K., M.L. and W.Z. designed the research;
M.L. performed the analytical calculations;
M.L. wrote the source code and performed the simulations
of the bead models with the Maxey and Riley equations;
A.F. wrote the source code and performed the LBM simulations
of the capsules with different density than the surrounding fluid;
all authors discussed and interpreted the results and wrote the paper.

pub4 *Migration reversal of soft particles in vertical flows*
A. Förtsch, M. Laumann, D. Kienle and W. Zimmermann

2017 EPL **119** 64003

individual contributions:
D.K., M.L. and W.Z. designed the research;
A.F. wrote the source code and performed the simulations of the ring;
M.L. wrote the source code and performed the simulations
of the capsule with the bead model and the LBM;
all authors discussed and interpreted the results and wrote the paper.

pub5 *Measurement of the magnetic moment of single Magnetospirillum gryphiswaldense cells by magnetic tweezers*
C. Zahn, S. Keller, M. Toro-Nahuelpan, P. Dorscht, W. Gross, M. Laumann, S. Gekle, W. Zimmermann, D. Schüler and H. Kress,

Sci. Rep. **7**, 3558 (2017)

individual contributions:
H.K. and D.S. designed the research;
P.D. built the magnetic tweezers setup;
C.Z., P.D. and W.G. characterized the magnetic tweezers setup;
M.T.-N. prepared the samples and performed the electron microscopy experiments;
C.Z. performed the magnetic tweezers experiments;
S.K. and C.Z. wrote the data analysis software;
C.Z. and M.T.-N. analyzed the experimental data;
M.L., W.Z. and S.G. calculated the viscous drag coefficients and analyzed the simulation data;
all authors discussed the results and wrote the paper.

pub6 *Focusing and splitting of particle streams in microflows via viscosity gradients*
M. Laumann and W. Zimmermann,

submitted to Eur. Phys. J. E on 2019-01-24 (with referees)
manuscript number e190030
preprint on arXiv (https://arxiv.org/abs/1903.11018)

individual contributions:
M.L. and W.Z. designed the research;
M.L. performed the calculations and the simulations and wrote the source code;
M.L. and W.Z. interpreted and discussed the results and wrote the paper.

pub7 *Noise-controlled particle focusing in Poiseuille flows*
M. Laumann, S. Schreiber, W. Zimmermann,

draft

individual contributions:
M.L. and W.Z. designed the research
S. Schreiber wrote the simulation program;
M.L. and S. Schreiber performed the simulations;
all authors discussed and interpreted the results and wrote the paper.

pub8 *Understanding Cross-Stream Migration with Basic Bead-Spring Models*
M. Laumann, M. Holzinger, and W. Zimmermann,

draft

individual contributions:
M.L. and W.Z. designed the research;
M.H. performed the simulations of the tetrahedron and the triangle;
M.L. and performed the simulations of the ring and the capsule;
M.L. performed the semi-analytical calculations;
all authors discussed and interpreted the results and wrote the paper;

Contributions to conferences

- 2019: Spring meeting of the German physical society, Regensburg (talk)
- 2018: Self-Organization in Active Matter: from Colloids to Cells, Erice (poster)
- 2018: Workshop Living Fluids, meeting of the Franco-German University, Münster (talk)
- 2018: Spring meeting of the German physical society, Berlin (talk and poster)
- 2017: Workshop Living Fluids, meeting of the Franco-German University, Paris (talk and poster)
- 2017: Spring meeting of the German physical society, Dresden (talk and poster)
- 2016: Spring meeting of the German physical society, Regensburg (talk and poster)
- 2016: Patterns in Nature - Functions, Variations and Control, Bayreuth (poster)
- 2016: Active Complex Matter, Cargese (poster)
- 2015: Workshop Living Fluids, meeting of the Franco-German University, Saarbrücken (talk)
- 2015: Spring meeting of the German physical society, Berlin (poster)
- 2014: Workshop Living Fluids, meeting of the Franco-German University, Marrakech (talk)

Publication 1

Emerging Attractor in Wavy Poiseuille Flows
Triggers Sorting of Biological Cells
M. Laumann, W. Schmidt, A. Farutin,
D. Kienle, S. Förster, C. Misbah, and W. Zimmermann,
Phys. Rev. Lett. **122**, 128002 (2019)

DOI: 10.1103/PhysRevLett.122.128002

Emerging Attractor in Wavy Poiseuille Flows Triggers Sorting of Biological Cells

Matthias Laumann,[1,2] Winfried Schmidt,[1] Alexander Farutin,[2] Diego Kienle,[1] Stephan Förster,[3] Chaouqi Misbah,[2,1] and Walter Zimmermann[1,*]

[1]*Theoretische Physik I, Universität Bayreuth, 95440 Bayreuth, Germany*
[2]*Universite Grenoble Alpes/CNRS UMR 5588, LIPhy, 38041 Grenoble, France*
[3]*JNCS-1/ICS-1, Forschungszentrum Jülich, 52428 Jülich, Germany*

(Received 28 November 2018; published 26 March 2019)

Microflows constitute an important instrument to control particle dynamics. A prominent example is the sorting of biological cells, which relies on the ability of deformable cells to move transversely to flow lines. A classic result is that soft microparticles migrate in flows through straight microchannels to an attractor at their center. Here, we show that flows through wavy channels fundamentally change the overall picture. They lead to the emergence of a second, coexisting attractor for soft particles. Its emergence and off-center location depends on the boundary modulation and the particle properties. The related cross-stream migration of soft particles is explained by analytical considerations, Stokesian dynamics simulations in unbounded flows, and Lattice-Boltzmann simulations in bounded flows. The novel off-center attractor can be used, for instance, in diagnostics, for separating cells of different size and elasticity, which is often an indicator of their health status.

DOI: 10.1103/PhysRevLett.122.128002

Microfluidics attracts great attention across several disciplines [1–9]. The field includes important physics-based strategies to understand the dynamics of particles in microflows and the mechanics of (deformable) cells with a great variety of applications in life science and technology. For example, studies of soft particles in suspension and their cross-streamline migration (CSM) in low Reynolds-number linear shear and Poiseuille flows provide important insights about blood flow, cell dynamics, DNA sorting, and polymer processing, among others [8–13]. Furthermore, a surprising splitting of streams of wormlike colloids in shear-thinning fluids through modulated channels was found [14]. In modulated channels with secondary flows [15] or in serpentine [16] or curved channels [17,18], for instance, particle dynamics and separation may also be driven by inertia. Very little is known about the behavior of soft microparticles such as (red blood) cells in pressure driven Newtonian fluid flows at low Reynolds number through microchannels with modulated walls. For this case, we describe the emergence of a novel second attractor for soft particles. This may give rise to promising applications in particle separation, such as biological cells with differing elasticity or size.

Segré and Silberberg reported in 1961 on CSM of rigid particles in low Reynolds-number flows through pipes [19]. Such finite Reynolds-number effects are exploited in inertial microfluidics [17,20]. When particles and channels approach the micrometer scale, it is also possible that fluid inertia does not matter and particles follow the Stokesian dynamics. In this limit, there is no CSM of rigid particles but of soft particles which are deformed by the local shear rate. This drives, for instance, tank-treading vesicles away from walls in Poiseuille and linear shear flows [9,21–25]. Away from walls the spatially varying shear rate in bulk Poiseuille flows breaks the fore-aft symmetry of the

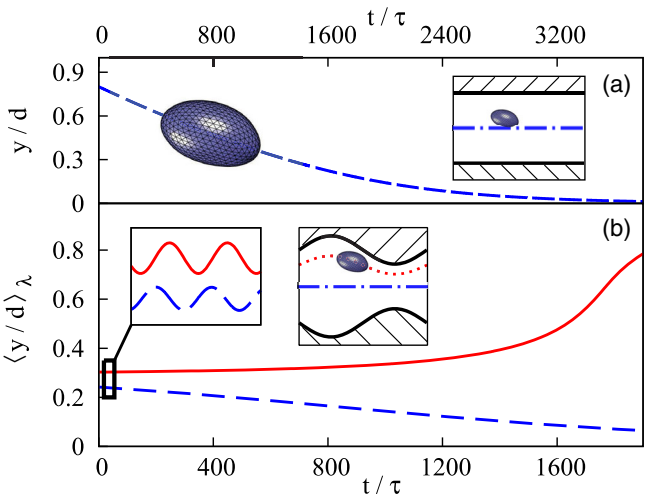

FIG. 1. (a) The trajectory of a soft capsule (dashed line) in plane Poiseuille flow approaches the attractor at the channel center at $y = 0$: The inset shows the channel cross section with the particle attractor (dash-dotted line). (b) A soft capsule in a wavy channel moves to either the off-center attractor (solid line) or to the center, depending on its initial position. The left inset shows the particle's wavy motion around the trajectory's mean (cf. animations in the Supplemental Material [38]). The right inset shows the wavy off-center particle attractor (dotted line) and the attractor at the channel center (dash-dotted line). For parameters, see [39].

deformed particle, so that dumbbells [26,27], droplets [28,29], vesicles, and capsules [30–32] exhibit bulk CSM, even in unbounded Poiseuille flows where the interaction with the channel boundaries is neglected. Such parity breaking mechanisms may be induced spontaneously by viscosity contrast [33] or chirality [34], which are not considered here. Surprisingly, CSM of soft particles can be also reversed by gravitational effects [35]. Recently, migration was also found for nonsymmetric soft particles in time-periodic linear shear flows [36] and even in time-periodic homogeneous plug flows when particle inertia is considered [37].

As we show, soft particles in flows through wavy channels experience a periodically altering local shear rate; therefore they are periodically deformed. However, they adopt a different shape during each half period of a wavy flow. This nonsymmetric deformation causes an off-center attractor for soft particles in Newtonian fluid flow that coexists with the particle attractor at the channel center, as indicated in Fig. 1 (cf. animations in the Supplemental Material [38]).

We consider red blood cells (RBCs) and soft capsules in flows through a channel with modulated walls at

$$y_b = \pm d[1 + \varepsilon \sin(Kx)] \quad \text{with} \quad K = \frac{2\pi}{\lambda}, \tag{1}$$

with the mean boundary distance $2d$, the modulation amplitude ε, and the wavelength λ. The resulting wavy flow field $\mathbf{u}(\mathbf{r}) = (u_x, u_y, 0)$ is determined up to first order in the modulation amplitude ε (see Supplemental Material [38]) [40]

$$u_x = \tilde{u}\left(1 - \frac{y^2}{d^2} + 2\varepsilon \sin(Kx) \times [B_1 Ky \sinh(Ky) + (B_1 + B_2)\cosh(Ky)]\right), \tag{2a}$$

$$u_y = -2\tilde{u}\varepsilon \cos(Kx)[B_1 Ky \cosh(Ky) + B_2 \sinh(Ky)], \tag{2b}$$

with the flow amplitude $\tilde{u}$. The soft particle's surface is represented by N beads with radius a and located at $\mathbf{r}_i$. Their Stokesian dynamics [41] is described by a set of equations

$$\dot{\mathbf{r}}_i = \mathbf{u}(\mathbf{r}_i) + \sum_{j=1}^{N} \mathbf{H}_{ij} \cdot \mathbf{F}_j. \tag{3}$$

The particle center is at $\mathbf{r}_c = \sum_{i=1}^{N} \mathbf{r}_i/N$ and particle-wall interactions are neglected. The force on the jth bead is given by $\mathbf{F}_j = -\nabla_j V(\mathbf{r})$ with the total potential $V(\mathbf{r})$, and $\mathbf{H}_{ij}$ denoting the mobility matrix (see the Supplemental Material [38]) [42–44].

For the capsule, the total potential is $V(\mathbf{r}) = V_{\mathrm{NH}} + V_b + V_v$ with the neo-Hookean part V_{NH}, that describes rubberlike materials with a constant surface shear-elastic modulus G [45,46]. The beads form triangles as indicated in the Supplemental Material [38]. With the angles $\beta_{i,j}$ enclosed by the normal vectors at neighboring triangles and the bending elasticity κ, the bending potential is $V_b = \kappa/2\sum_{i,j}(1 - \cos\beta_{i,j})$ [47]. The potential $V_v = k_v[\mathcal{V}(t) - \mathcal{V}_0]^2/\mathcal{V}_0$ keeps the capsules volume $\mathcal{V}(t)$ close to the reference volume $\mathcal{V}_0 = 4/3\pi R^3$ of a spherical capsule of radius R with volume stiffness k_v [48].

For the RBC we use as total potential $V(\mathbf{r}) = V_{\mathrm{Sk}} + V_{b,R} + V_v + V_a$ [48]. V_{Sk} denotes the potential of the Skalak law which describes the elastic forces of a RBC with the shear and area resistance κ_s and κ_α (see [48,49]). The bending potential is given by $V_{b,R} = \sqrt{3}\kappa_R/2\sum_{i,j}(\beta_{i,j} - \beta_{i,j}^{(0)})^2$ where $\beta_{i,j}^{(0)}$ denotes the angles of the equilibrium shape, whereby we use the typical biconcave shape (see the Supplemental Material [38] and Ref. [50]). The potentials $V_v = k_v/\mathcal{V}_0[\mathcal{V}(t) - \mathcal{V}_0]^2$ and $V_a = k_a/\mathcal{A}_0[\mathcal{A}(t) - \mathcal{A}_0]^2$ keep deviations of $\mathcal{V}(t)$ and $\mathcal{A}(t)$ from the reference values $\mathcal{V}_0$ and $\mathcal{A}_0$ small [48]. The (dimensionless) parameters are given in Ref. [39].

We use also simulations for the particle dynamics with a standard lattice Boltzmann method (LBM) with the Bhatnager-Gross-Krook collision and the immersed boundary method [51–55]. Hereby, the effects of the channel boundary on the particle dynamics are fully taken into account.

The migration velocity $\mathbf{v}_m$ of a particle is the difference between the particle velocity $\dot{\mathbf{r}}_c$ and the undistorted flow velocity $\mathbf{u}(\mathbf{r}_c)$ at the particle's position $\mathbf{r}_c$, leading to

$$\mathbf{v}_m = \dot{\mathbf{r}}_c - \mathbf{u}(\mathbf{r}_c) = \underbrace{\sum_i \frac{\mathbf{u}(\mathbf{r}_i)}{N} - \mathbf{u}(\mathbf{r}_c)}_{=\mathbf{v}_m^f} + \underbrace{\frac{1}{N}\sum_{i,j}\mathbf{H}_{ij} \cdot \mathbf{F}_j}_{=\mathbf{v}_m^{\mathrm{HI}}}.$$

The contribution $\mathbf{v}_m^f$ is the difference between the undisturbed flow, averaged over the particle's surface, and the undisturbed flow at its center. In Poiseuille flow, the shear gradient varies across an extended particle and accordingly the particle does not follow a single streamline. The second contribution $\mathbf{v}_m^{\mathrm{HI}}$ describes the flow disturbance due to a particle.

In plane Poiseuille flow, $\mathbf{v}_m^f$ is antiparallel to the straight flow direction and causes a lag behind of particles with respect to the undistorted, local flow, but does not contribute to CSM. The classical CSM to the channel center is induced by $\mathbf{v}_m^{\mathrm{HI}}$. In a wavy channel, $\mathbf{v}_m^f$ contributes also to the migration perpendicular to the channel axis. In the diverging parts of the channel, a particle lags behind the outward directed streamline. Accordingly, the particle migrates towards a streamline closer to the center. In the

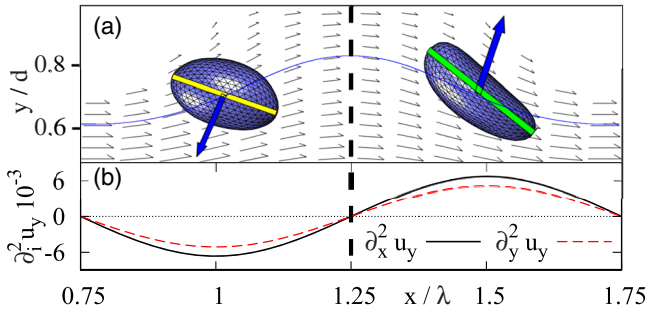

FIG. 2. (a) Two snapshots of a capsule are shown, resulting from their Stokesian dynamics simulation in an unbounded wavy flow field (black arrows). The flow is symmetric to the dashed vertical line, but the deformed particle is not (see, e.g., colored bars). (b) shows the second derivatives $\partial_x^2 u_y(x)$ and $\partial_y^2 u_y(x)$ of the vertical flow velocity u_y at $y = 0.7d$.

converging flow section the opposite is the case: The particle migrates to a streamline farther away from the center. For a rigid spherical particle in a periodically alternating diverging and converging flow at low Reynolds number, the migration steps inside and outside compensate each other and there is no net migration. However, the situation with deformable particles is different: The particle's shape is nonreciprocal during the periodically alternating converging and the diverging channel sections as indicated by the two snapshots for a capsule from Stokesian dynamics simulations in Fig. 2. This leads altogether to a net contribution of $\mathbf{v}_m^f$ to the migration away from the channel axis.

We demonstrate by a simple analytical consideration that the outward directed net migration caused by $\mathbf{v}_m^f$ may become larger than the classical inward migration driven by $\mathbf{v}_m^{\mathrm{HI}}$. By a Taylor expansion of $\mathbf{u}(\mathbf{r})$ around $\mathbf{r}_c$ and with the relations

$$\sum_i (\mathbf{r}_i - \mathbf{r}_c) = 0, \qquad \sum_i \underbrace{(x_i - x_c)(y_i - y_c)}_{\text{changes sign}} \ll \sum_i \underbrace{(x_i - x_c)^2}_{>0}$$

we obtain for the y component of $\mathbf{v}_m^f$

$$v_{m,y}^f = \frac{1}{N}\sum_i [\mathbf{u}(\mathbf{r}_i) - \mathbf{u}(\mathbf{r}_c)] \cdot \mathbf{e}_y \approx \frac{\partial_x^2 u_y}{2N}\sum_i (x_i - x_c)^2 + \frac{\partial_y^2 u_y}{2N}\sum_i (y_i - y_c)^2. \quad (4)$$

The signs of the curvatures $\partial_x^2 u_y$ and $\partial_y^2 u_y$ of the wavy flow determine the local direction of the migration velocity $v_{m,y}^f$. Their values for the imposed flow evaluated at $y/d = 0.7$ are shown in Fig. 2(b). The two sums in Eq. (4) are shape factors. They indicate that the local migration velocity increases with the deformation. In a widening channel section the signs of both curvatures are negative and therefore the migration direction points to the flow center ($v_{m,y}^f < 0$).

In the following section, the flow is converging and the signs of the curvatures are positive; i.e., the direction of $v_{m,y}^f$ points in this section away from the flow center. During the converging half period, the soft particle is stretched in flow direction with a maximum of the shape factors of about ($\sum_i (x_i - x_c)^2 = 22.8$ and $\sum_i (y_i - y_c)^2 = 17.7$). Both factors are larger than their maxima during the diverging flow part, ($\sum_i (x_i - x_c)^2 = 21.4$ and $\sum_i (y_i - y_c)^2 = 11.2$), where the capsule is compressed in the flow direction. Both shapes in Fig. 2(a) are not mirror symmetric to the dashed vertical line. Therefore, the migration velocity averaged over one spatial period, $\langle v_{m,y}^f \rangle_\lambda$, points for these parameters away from the channel center.

The curvature of the flow lines vanishes at the channel center. The local migration velocity $v_{m,y}^f$ increases at every x position with the distance from the channel center and with the boundary-modulation amplitude ε. Above a critical boundary-modulation amplitude ε_c the contribution $v_{m,y}^f$ may outweigh the classical inward migration described by $v_{m,y}^{\mathrm{HI}}$. In this case the resulting off-center attractor coexists with the attractor at the channel center at $y = 0$. Depending on the initial value of y, particles migrate either to the center or to the off-center attractor.

The trends of cross-stream migration illustrated by analytical considerations are characterized by Stokesian dynamics simulations of models for capsules and red blood cells in unbounded wavy flows and by simulations using the LBM in bounded flows. In Fig. 3, the averaged CSM velocity $\langle v_{m,y} \rangle_\lambda$ of capsules and RBCs is shown as a function of λ/R and in units of $\tilde{u}$ for two values $\tilde{u} = 5, 11$. This averaged CSM velocity is obtained by a linear fit (over a sufficient number of periods) of the lateral particle position $y(t)$, whereby the mean values of each period are used. For an initial particle position of $y = d/2$ in Fig. 3, the averaged migration direction $\langle v_{m,y} \rangle$ points to the channel center in the range of small and large values of λ/R. This means capsules and RBCs migrate in both ranges towards the channel center, similar as in unmodulated channel flows. Here, the averaged modulation-induced outward CSM, $\langle v_{m,y}^f \rangle_\lambda$, becomes small and cannot outweigh anymore the common inward migration $\langle v_{m,y}^{\mathrm{HI}} \rangle_\lambda$. This can be understood from Fig. 2: The flow's curvature plays a role only if the modulation wavelength is not much larger and not much shorter than the particle size, such as in the intermediate range of λ/R in Fig. 3. For the flow amplitude $\tilde{u} = 5$, capsules migrate in the range $7R \lesssim \lambda \lesssim 25R$ away from the channel center and the outward CSM velocity reaches a maximum at $\lambda \approx 12R$. For a larger flow velocity at the channel center $\tilde{u} = 11$, the respective ranges for capsules and RBCs are slightly shifted to larger values of λ/R. With increasing particle distance y from the channel center, the λ/R range of outward migration increases.

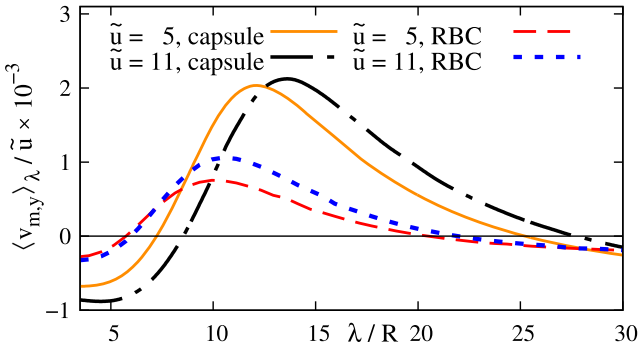

FIG. 3. The averaged CSM velocity $\langle v_{m,y}\rangle_\lambda$ of capsules and RBCs in unbounded wavy Poiseuille flow as a function of λ/R. $\langle v_{m,y}\rangle_\lambda$ is given for two amplitudes $\tilde{u} = 5$, 11. It is negative for small and rather large values of λ/R and the particles migrate to the channel center. $\langle v_{m,y}\rangle_\lambda$ is positive in the intermediate range of λ/R, where particles migrate away from the channel center. For further parameters, cf. [39].

Importantly, the qualitative behavior of the CSM velocity for capsules and RBCs is equivalent.

Figure 4 shows the averaged CSM velocity $\langle v_{m,y}\rangle_\lambda$ of a capsule in units of the flow amplitude $\tilde{u}$ and as a function of the y position of the capsule for three amplitudes $\varepsilon = 0$, 0.2, 0.3. Here, the CSM velocity results from LBM simulations of the capsule in a wavy channel, fully accounting for wall effects. In a flat channel with $\varepsilon = 0$ the capsule migrates from every $0 < y < d$ to the channel center. Beyond a critical modulation amplitude, e.g., for $\varepsilon = 0.2$, the CSM velocity is negative at $y \lesssim 0.15d$ and beyond one finds an outward migration. The zero crossing of $\langle v_{m,y}\rangle_\lambda$ at $y \approx 0.15d$ marks the position of a repeller. When a soft particle approaches the channel wall, its migration changes to the inward direction again. This means particles with $y \gtrsim 0.15d$ migrate for $\varepsilon = 0.2$ to the off-center attractor at $y \approx 0.4d$ where the migration velocity vanishes again. For a larger modulation amplitude $\varepsilon = 0.3$ the repeller is moved closer to the channel center and the attractor closer to the wall as indicated by the dashed line in Fig. 4. Hence, the results from LBM simulations for bounded Poiseuille flows confirm the analytical considerations and the results obtained by Stokesian dynamics simulations for unbounded flows.

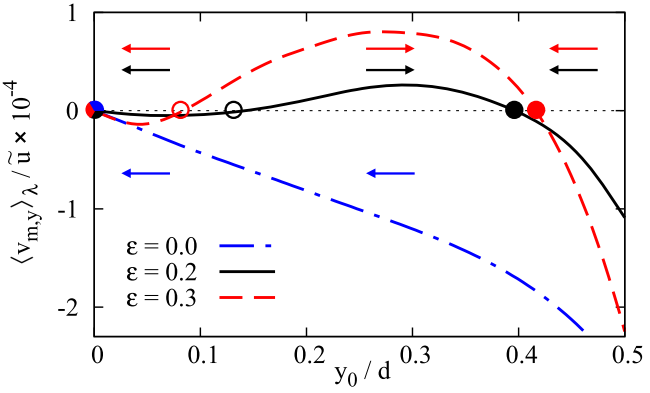

FIG. 4. The averaged migration velocity $\langle v_{m,y}\rangle_\lambda/\tilde{u}$ for capsules in bounded flows obtained by LBM simulations as a function of the particle's y position and for the modulation amplitudes $\varepsilon = 0.0$, 0.2, 0.3. The capsule migrates toward the center ($y = 0$) at small y below the repeller (empty circles) and otherwise to the second attractor (solid circles), confirming the analytical considerations and Stokesian dynamics simulations in unbounded flows. The arrows mark the migration direction, i.e., the sign of $\langle v_{m,y}\rangle_\lambda$. For further parameters, cf. [56].

Figure 5 shows the y positions of the off-center particle attractors (solid lines) and its repeller (dashed line) as a function of the boundary-modulation amplitude ε for unbounded Poiseuille flows and for three ratios $\lambda/R = 12$, 16, 20. In each case, the second attractor and the repeller appear if ε is larger than the respective critical value $\varepsilon_c = 0.14$, 0.19, 0.23. Capsules starting at a y position below the repeller migrate towards the channel center, while capsules starting above the repeller migrate to the off-center attractor. Figure 5 shows that the y positions of the second attractor and the repeller move closer to the channel center with increasing λ/R, i.e., with decreasing particle size for a given modulation wavelength λ. The off-center attractor and the repeller move also closer to the channel center with increasing stiffness of the capsules, as shown in the Supplemental Material [38].

The emergence of the second attractor for soft particles in low Reynolds-number flows through wavy channels is different to the inertia driven off-center attractors [7]. It coexists with an attractor at the channel center and this suggests a novel method for separating soft particles according to their sizes and elasticities. For instance, if two different sized particles with different radii R with $R = \lambda/20$ and $R = \lambda/12$ are injected at $y \geq 0.5d$ in a

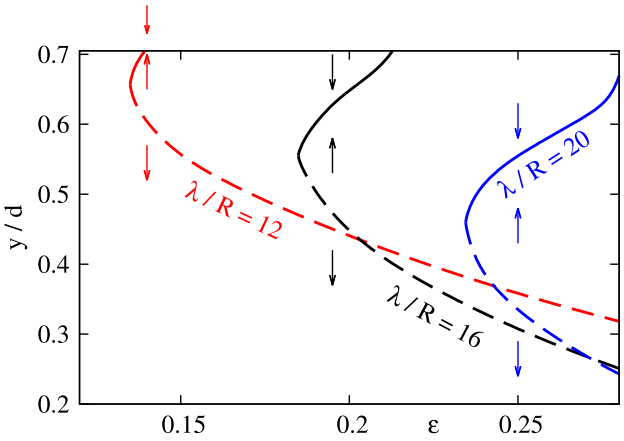

FIG. 5. The y position of the *second attractors* (solid lines) and the repellers (dashed lines) of capsules as a function of ε for $\lambda/R = 12$, 16, 20. Particles with an initial position below the repeller migrate to the channel center. The second attractor occurs for ε larger than the respective critical values $\varepsilon_c = 0.14$, 0.19, 0.23, which increase with increasing wavelength.

channel with $\varepsilon \approx 0.22$ they will be separated: The smaller particle with $R = \lambda/20$ migrates to the channel center, whereas the larger particle with $R = \lambda/12$ migrates to the off-center attractor. Hence, they can be separated with two different outlets, one at the channel center and one off center. These trends are confirmed by taking fully into account the boundary effects. For example, a capsule of radius $R = 6.6$ ($\lambda/R \approx 17$) at $y = 0.3$ migrates in LBM simulations to the wall for parameters as in Fig. 4 and a larger particle with $R = 20$ ($\lambda/R = 5.5$) to the channel center. We also remark that the migration direction does not depend on the flow direction. This allows us to utilize shorter channels simply by reversing the flow's direction in experiments.

The discovered cross-stream migration of soft particles in Newtonian fluids through wavy channels is controlled by the amplitude of the boundary modulation and the ratio of the particle size and the modulation wavelength. The origin of this CSM is the interplay between a lag behind of a particle with respect to the local flow and its asymmetric deformation in each half-period of the channel modulation. It can outweigh the classical CSM to the channel center [30–32] and induce a second, coexisting off-center attractor. This generic CSM for soft particles may play also an important role for the recently observed splitting of streams of wormlike colloids in shear thinning fluids through wavy channels [14]. Furthermore, the emergence of the second attractor allows us to separate soft particles also with respect to their stiffness (see also the Supplemental Material [38]). Since the health status of cells has been shown to affect the cell elasticity [57], our proposed approach may improve further the separation of healthy cells from malignant (e.g., cancer) cells.

For support we thank the French-German University (Grant No. CFDA-Q1-14, "Living fluids"); A. F. and C. M. the Centre National d'Etudes Spatiales; W. S. and W. Z. the Elite Study Program Biological Physics.

*Corresponding author.
walter.zimmermann@uni-bayreuth.de

[1] T. M. Squires and S. R. Quake, Rev. Mod. Phys. **77**, 977 (2005).
[2] B. J. Kirby, *Micro- and Nanoscale Fluid Mechanics* (Cambridge University Press, Cambridge, England, 2010).
[3] N.-T. Nguyen and S. T. Wereley, *Fundamentals and Applications of Microfluidics* (Artech House, Boston, 2010).
[4] A. S. Popel and P. C. Johnson, Annu. Rev. Fluid Mech. **37**, 43 (2005).
[5] E. K. Sackmann, A. L. Fulton, and D. L. Beebe, Nature (London) **507**, 181 (2014).
[6] J. B. Dahl, J.-M. G. Lin, S. J. Muller, and S. Kumar, Annu. Rev. Chem. Biomol. Eng. **6**, 293 (2015).
[7] H. Amini, W. Lee, and D. D. Carlo, Lab Chip **14**, 2739 (2014).
[8] M. D. Graham, Annu. Rev. Fluid Mech. **43**, 273 (2011).
[9] T. W. Secomb, Annu. Rev. Fluid Mech. **49**, 443 (2017).
[10] T. M. Geislinger and T. Franke, Adv. Colloid Interface Sci. **208**, 161 (2014).
[11] P. Sajeesh and A. K. Sen, Microfluid. Nanofluid. **17**, 1 (2014).
[12] C. Misbah, J. Fluid Mech. **760**, 1 (2014).
[13] A. Farutin, T. Piasecki, A. M. Slowicka, C. Misbah, E. Wajnryb, and M. L. Ekiel-Jeżewska, Soft Matter **12**, 7307 (2016).
[14] M. Schlenk, M. Drechsler, M. Karg, W. Zimmermann, R. Trebbin, and S. Förster, Lab Chip **18**, 3163 (2018).
[15] Z. Wu, Y. Chen, M. Wang, and A. J. Chung, Lab Chip **16**, 532 (2016).
[16] J. Zhang, S. Yan, R. Sluyter, W. Li, G. Alici, and N.-T. Nguyen, Sci. Rep. **4**, 4527 (2014).
[17] D. D. Carlo, Lab Chip **9**, 3038 (2009).
[18] D. D. Carlo, D. Irima, R. G. Tompkins, and M. Toner, Proc. Natl. Acad. Sci. U.S.A. **104**, 18892 (2007).
[19] G. Segré and A. Silberberg, Nature (London) **189**, 209 (1961).
[20] J. Zhang, S. Yan, D. Yuan, G. Alici, N.-T. Nguyen, M. Ebrahimi Warkiani, and W. Li, Lab Chip **16**, 10 (2016).
[21] M. S. Jhon and K. F. Freed, J. Polym. Sci., Polym. Phys. Ed. **23**, 955 (1985).
[22] I. Cantat and C. Misbah, Phys. Rev. Lett. **83**, 880 (1999).
[23] U. Seifert, Phys. Rev. Lett. **83**, 876 (1999).
[24] M. Abkarian, C. Lartigue, and A. Viallat, Phys. Rev. Lett. **88**, 068103 (2002).
[25] X. Grandchamp, G. Coupier, A. Srivastav, C. Minetti, and T. Podgorski, Phys. Rev. Lett. **110**, 108101 (2013).
[26] G. Sekhon, R. Armstrong, and M. S. Jhon, J. Polym. Sci., Polym. Phys. Ed. **20**, 947 (1982).
[27] P. O. Brunn, Int. J. Multiphase Flow **9**, 187 (1983).
[28] L. G. Leal, Annu. Rev. Fluid Mech. **12**, 435 (1980).
[29] S. Mandal, A. Bandopadhyay, and S. Chakraborty, Phys. Rev. E **92**, 023002 (2015).
[30] B. Kaoui, G. H. Ristow, I. Cantat, C. Misbah, and W. Zimmermann, Phys. Rev. E **77**, 021903 (2008).
[31] G. Coupier, B. Kaoui, T. Podgorski, and C. Misbah, Phys. Fluids **20**, 111702 (2008).
[32] S. K. Doddi and P. Bagchi, Int. J. Multiphase Flow **34**, 966 (2008).
[33] A. Farutin and C. Misbah, Phys. Rev. E **89**, 042709 (2014).
[34] N. Watari and R. G. Larson, Phys. Rev. Lett. **102**, 246001 (2009).
[35] A. Förtsch, M. Laumann, D. Kienle, and W. Zimmermann, Europhys. Lett. **119**, 64003 (2017).
[36] M. Laumann, P. Bauknecht, S. Gekle, D. Kienle, and W. Zimmermann, Europhys. Lett. **117**, 44001 (2017).
[37] I. Jo, Y. Huang, W. Zimmermann, and E. Kanso, Phys. Rev. E **94**, 063116 (2016).
[38] See Supplemental Material at http://link.aps.org/supplemental/10.1103/PhysRevLett.122.128002 for animations and for the calculation of the flow. Also details of the modeling and of the CSM of the capsule and the RBC are given.
[39] Parameters for Stokesian dynamics: (a) Flow: $u_0 = 5.0$, $d = 50$, $\lambda = 80.0$, $\varepsilon = 0.3$, $\eta = 1.0/6.0$; (b) Capsule: $G = 0.2$, $\kappa_c = 1.0$, $k_v = 1.0$, $a = 0.4$, $N = 642$, $b = 1.0$,

$R = 6.6$; (c) RBC: $\kappa_\alpha = 175.5$, $\kappa_s = 3.51$, $\kappa_R = 0.23$, $k_v = 1.0$, $k_a = 1.0$, $a = 0.2$, $N = 642$, $b = 1.0$, $R = 6.6$.
[40] S. Tsangaris and E. Leiter, J. Eng. Math. **18**, 89 (1984).
[41] J. K. G. Dhont, *An Introduction to Dynamics of Colloids* (Elsevier, Amsterdam, 1996).
[42] H. Yamakawa, J. Chem. Phys. **53**, 436 (1970).
[43] J. Rotne and S. Prager, J. Chem. Phys. **50**, 4831 (1969).
[44] E. Wajnryb, K. A. Mizerski, P. J. Zuk, and P. Szymczak, J. Fluid Mech. **731**, R3 (2013).
[45] S. Ramanujan and C. Pozrikidis, J. Fluid Mech. **361**, 117 (1998).
[46] D. Barthès-Biesel, Annu. Rev. Fluid Mech. **48**, 25 (2016).
[47] G. Gompper and D. M. Kroll, J. Phys. I (France) **6**, 1305 (1996).
[48] T. Krüger, M. Gross, D. Raabe, and F. Varnik, Soft Matter **9**, 9008 (2013).
[49] R. Skalak, A. Tozeren, R. P. Zarda, and S. Chien, Biophys. J. **13**, 245 (1973).
[50] E. Evans and Y. Fung, Microvasc. Res. **4**, 335 (1972).
[51] T. Krueger, F. Varnik, and D. Raabe, Comput. Math. Appl. **61**, 3485 (2011).
[52] P. L. Bhatnagar, E. P. Gross, and M. Krook, Phys. Rev. **94**, 511 (1954).
[53] C. K. Aidun and J. R. Clausen, Annu. Rev. Fluid Mech. **42**, 439 (2010).
[54] Z. Guo, C. Zheng, and B. Shi, Phys. Rev. E **65**, 046308 (2002).
[55] C. S. Peskin, Acta Numer. **11**, 479517 (2002).
[56] Model parameters for LBM simulations: $\lambda = 110$, channel diameter in y and z direction $d_y = 120$ (modulated walls), $d_z = 120$ (flat side walls), $\tilde{u} = 0.03$, density $\rho = 1.0$, $\eta = 1.0$; capsule: $k_v = 0.1$, $\kappa = 0.002$, $G = 0.002$, $b = 1$, $R = 6.6$, particle Reynolds number $\mathrm{Re_p} = 0.4$.
[57] J. Guck, S. Schinkinger, B. Lincoln, F. Wottawah, S. Ebert, M. Romeyke, D. Lenz, H. M. Erickson, R. Ananthakrishnan, D. Mitchell, J. Käs, S. Ulvick, and C. Bilby, Biophys. J. **88**, 3689 (2005).

Supplementary Information

Matthias Laumann,[1,2] Winfried Schmidt,[1] Alexander Farutin,[2] Diego Kienle,[1] Stephan Förster,[3] Chaouqi Misbah,[2,1] and Walter Zimmermann[1]

[1] *Theoretische Physik I, Universität Bayreuth, 95440 Bayreuth, Germany*
[2] *Universite Grenoble Alpes/CNRS UMR 5588, LIPhy, 38041 Grenoble, France*
[3] *JNCS-1/ICS-1, Forschungszentrum Jülich, 52428 Jülich, Germany*

(Dated: February 27, 2019)

SECONDARY ATTRACTORS AS FUNCTION OF DEFORMABILITY

Besides their size, the coexisting off-center attractor allows separation of soft particles due to elasticity as well. For capsules, the surface shear-elastic modulus G serves as a measure for the latter. Fig. 1 shows values of vanishing averaged migration velocity $\langle v_{\mathrm{m},y}\rangle_\lambda$ as a function of the modulation amplitude ε and the capsule's y-position in the channel in units of the mean channel diameter d. Analogously to Fig. 5 (main text), solid lines indicate attractors (lateral positions with a negative migration velocity above and a positive one below) and dashed lines repellers (lateral positions with a positive migration velocity above and a negative one below). The graphs for three different values of G are shown. Increasing values of G (increased stiffness of the capsule) result in a shift of both the attractor and repeller to smaller values of y. I. e. for a channel with $\varepsilon = 0.2$, a capsule with $G = 0.1$ entering the channel at $y \approx 0.45d$ will migrate towards its center, whereas a capsule with four times this surface shear-elastic modulus located at the same lateral position will move in the opposite direction towards the walls. In addition, Fig. 1 indicates that the critical value ε_c increases with growing G (a coexisting off-center attractor occurs for larger values of ε, the stiffer the capsule is).

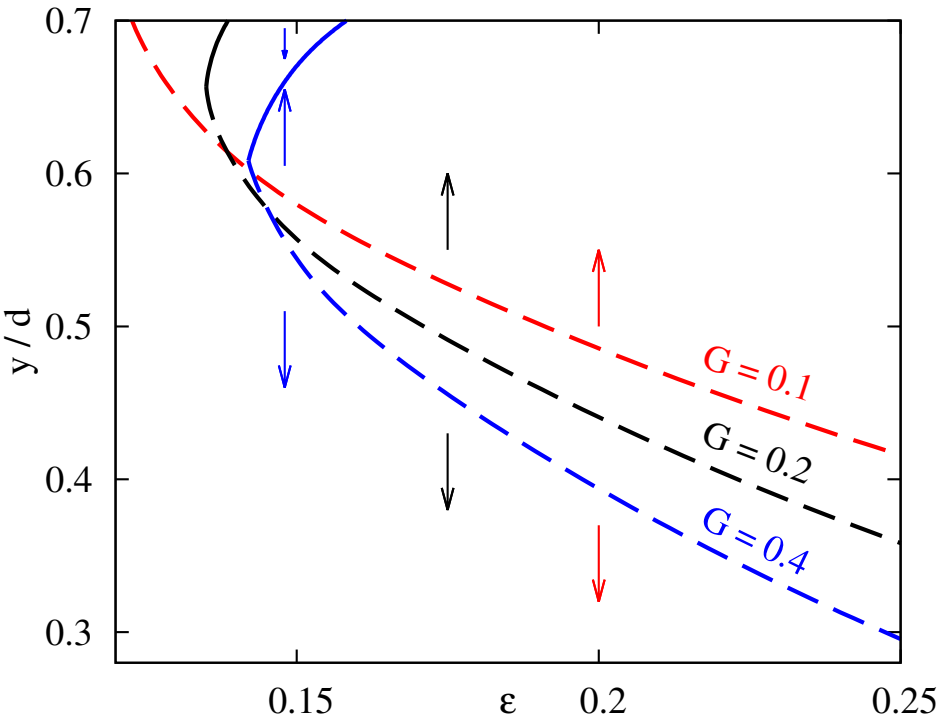

FIG. 1. The y-position of *secondary attractors* (solid lines) and repellers (dashed lines) of capsules as function of ε for three different values of the stiffness $G = 0.1, 0.2, 0.4$. Similar as in Fig. 5 (main text), capsules with an initial position below the repeller migrate to the channel center and capsules with an initial position above move to the secondary off-center attractor. The secondary attractor occurs beyond the respective critical values $\varepsilon_c = 0.122, 0.135, 0.142$ which increase with growing stiffness.

SECONDARY ATTRACTORS OF RBC

Fig. 2 complements Fig. 5 (main text) for Stokesian dynamics simulations of RBCs in unbounded flows. The secondary attractor and the repellers are shifted to the center with increasing wavelength. This behavior agrees quantitatively with the capsule, especially at a ratio of the channel wavelength and the capsule's radius of $\lambda/R = 12$, but the attractor and repeller are found closer to the center compared to the capsule. Especially at $\lambda/R = 20$ the repeller is shifted towards the center of the flow. Furthermore the red blood cells displays a new repeller at initial positions close to the wall at $\lambda/R = 16$ and $\lambda/R = 20$. An initial orientation of the RBC with its rotational symmetry axis along the flow vorticity (cf. RBC sketch I) in Fig. 4) has been used.

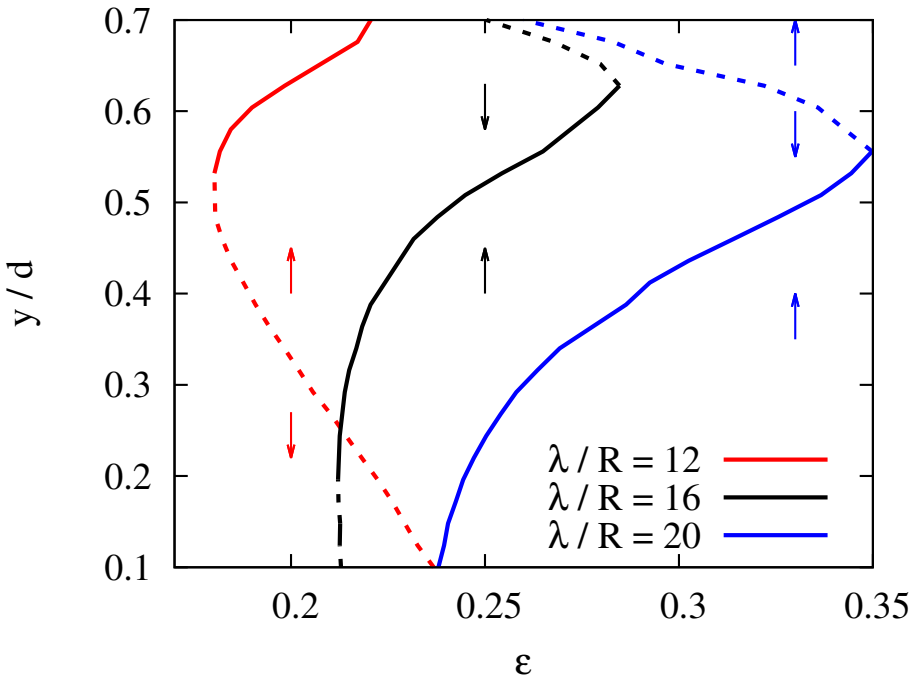

FIG. 2. The y-position of the *secondary attractors* (solid lines) and repellers (dashed lines) of RBCs as function of the dimensionless modulation amplitude ε for three different values of the wavelength to particle size ratio $\lambda/R = 12, 16, 20$. The secondary attractor occurs if the value of ε is larger than a critical value $\varepsilon_c = 0.17, 0.21, 0.23$ which increases with increasing wavelength.

INFLUENCE OF INITIAL CONDITIONS OF RBC

The red blood cell has no spherical symmetry, the migration velocity thus depends on the initial orientation. Therefore we give here again the migration velocity in dependence of the wavelength as shown Fig. 3 in the main text but with different initial orientations. We start with the red blood cell's rotational symmetry axis in the x-y-plane (cf. orientation II) in Fig. 4, whereas in the main text we used an initial orientation as in Fig. 4, I)) and determine the migration velocity. We use eight simulations with different angles φ between the symmetry axis and the x-direction and average the migration velocity over them. The resulting migration velocity is shown in Fig. 3. We observe small local maxima at $\lambda\,/\,R = 11, 16, 26$ which are not found with the initial orientation used in the main text. The reason are the more complex trajectories which show e.g. a tumbling motion (rotational symmetry axis of RBC perpendicular to the flow's vorticity) whereas in the main text the red blood cell displays a tank-treading motion (rotational symmetry axis of RBC parallel to the flow's vorticity). But besides this local maxima we find the same qualitative shape of the curve as given in Fig. 3 in the main text: The red blood cell displays a migration to the center if the wavelength is short with $\lambda \lesssim 5R$ or much longer than the cell with $\lambda \gtrsim 27R$. At intermediate values we find a migration to the walls with a maximum at $\lambda \approx 10R$. Thus the qualitative behavior does not depend on the orientation.

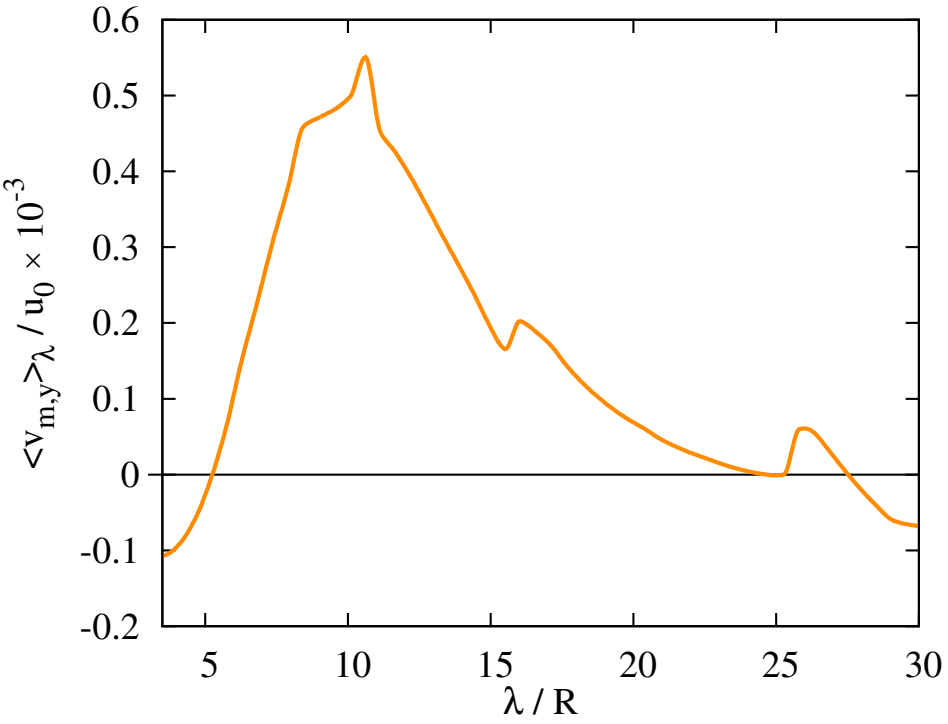

FIG. 3. The lateral migration of a red blood cell is shown as function of the ratio between modulation wavelength λ and the particle radius R. The initial position is $y_0 = d/2$. To get a migration away from the center (positive values of $\langle v_m \rangle_\lambda$) the wavelength must be adjusted to the particle's size. If the wavelength is too small compared to the particle's radius or too large the waviness of the flow plays no role and the particle migrates to center as in a flat channel. At $\lambda \approx 10R$ the wavelength is well adjusted and the migration away from the center reaches it maximum.

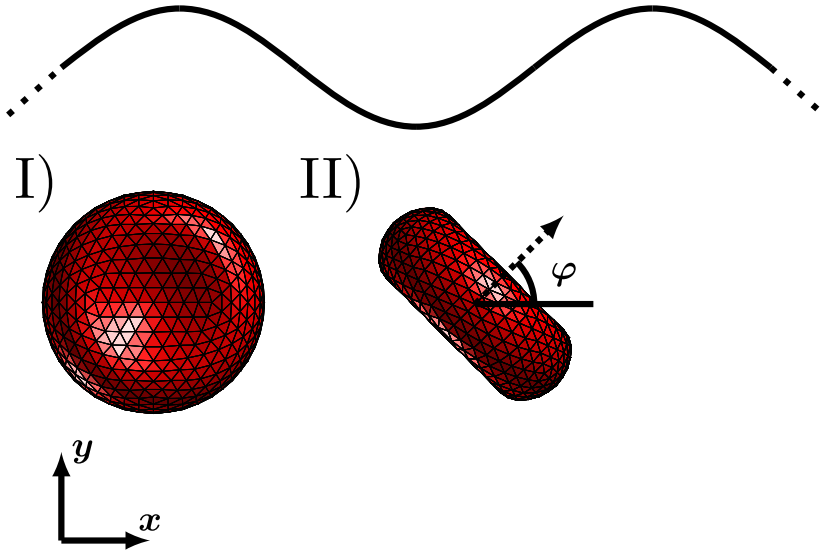

FIG. 4. The two initial orientations of the RBC with respect to the channel which have been used are shown: Whereas in the main text (see Fig. 3) and in Fig. 2, an initial orientation as shown in I) has been applied, in Fig. 3 the RBC's initial rotational symmetry axis is perpendicular to the flow vorticity, as shown in II). In addition, the angle φ which is enclosed by the rotational symmetry axis of the RBC and the channel axis, is varied for this orientation.

DETAILS OF THE USED MODELS

THE MOBILITY MATRIX

As described in the main text, the soft particle's surface is represented by N beads (nodes) , with bead i being located at a position $\mathbf{r_i}$. This is shown in Fig. 5. Their Stokesian dynamics [1] is given by Eq. 3 in the main text

$$\dot{\mathbf{r}}_i = \mathbf{u}(\mathbf{r}_i) + \sum_{j=1}^{N} \mathbf{H}_{ij} \cdot \mathbf{F}_j \ , \tag{1}$$

whereby $\mathbf{F}_j$ is the force (derived from a potential) on the j-th bead and the mobility matrix $\mathbf{H}_{ij}$ describes the hydrodynamic interaction between the beads. We use the Rotne-Prager tensor [2–4] as mobility matrix

$$\mathbf{H}_{ij}(\mathbf{r}_i, \mathbf{r}_j) = \begin{cases} \frac{1}{8\pi\eta r_{ij}} \left[\left(1 + \frac{2a^2}{3r_{ij}^2}\right) \mathbf{1} + \left(1 - \frac{2a^2}{r_{ij}^2}\right) \mathbf{e}_{ij}\mathbf{e}_{ij} \right], & r_{ij} > 2a \\ \frac{1}{6\pi\eta a} \left[\left(1 - \frac{9r_{ij}}{32a}\right) \mathbf{1} + \frac{3r_{ij}}{32a} \mathbf{e}_{ij}\mathbf{e}_{ij} \right], & r_{ij} \leq 2a \end{cases} \tag{2}$$

with $\mathbf{e}_{ij} = \mathbf{r}_{ij}/r_{ij}$ and $\mathbf{r}_{ij} = \mathbf{r}_i - \mathbf{r}_j$; η and a refer to the viscosity and the bead radius, respectively.

THE FORCES AND POTENTIALS

Besides the potentials given in the main text we use the potential of the neo-hookean law [5, 6]

$$V_{\mathrm{NH}} = \frac{G}{2} \left(I_1 - 1 + \frac{1}{I_2 + 1} \right) , \tag{3}$$

whereby G denotes the surface shear elastic modulus and I_1 and I_2 are the in-plane strain invariants, which are related to the local membrane deformation tensor. We also use the potential of the Skalak law [7, 8]

$$V_{\mathrm{sk}} = \frac{\kappa_{\mathrm{s}}}{12} \left(I_1^2 + 2I_1 - 2I_2 \right) + \frac{\kappa_\alpha}{12} I_2^2 \, . \tag{4}$$

Hereby κ_{s} and κ_α means the shear and the area resistance, respectively.

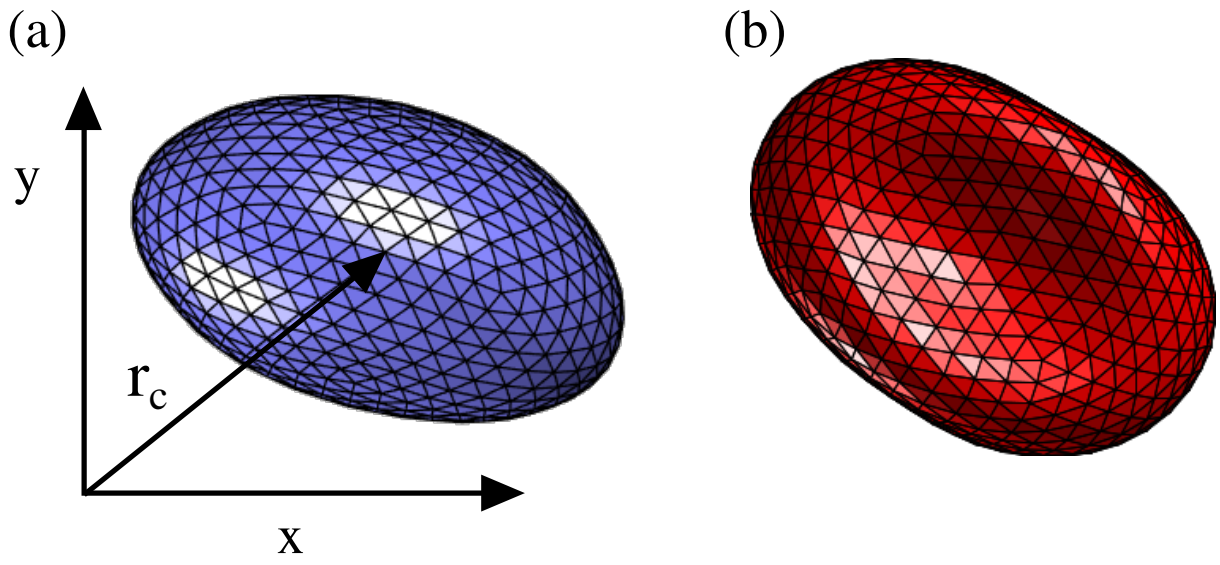

FIG. 5. Snapshots of simulated particle shapes for (a) a deformed capsule and (b) a biconcave red blood cell. Both models are discretized with $N = 642$ beads (nodes) that form triangles. The center of the particle is denoted by $\mathbf{r}_{\mathrm{c}}$.

The equilibrium shape of the red blood cell is given as follows: Assuming rotational symmetry of the shape of the RBC around the z-axis, one has the following relation between

$$z(\varrho) = \pm \frac{\sqrt{1 - \left(\frac{\varrho}{R}\right)^2}}{2} \left(C_0 + C_2 \left(\frac{\varrho}{R}\right)^2 + C_4 \left(\frac{\varrho}{R}\right)^4 \right) \tag{5}$$

and $\varrho := \sqrt{x^2 + y^2}$ whereby the constants C_i define the shape [9]. Their values are $C_0 = 1.62$, $C_2 = 15.66$, $C_4 = -8.78$.

CALCULATION OF THE FLOW PROFILE

Besides the interaction between the particles, also the undisturbed flow $\mathbf{u}(\mathbf{r})$ must be calculated. Thus the pressure driven flow at zero Reynolds number through a channel with walls located at

$$y = \pm h(x) = \pm d \left[1 + \varepsilon \sin(Kx)\right] \tag{6}$$

with the average channel diameter $2d$, the dimensionless modulation amplitude ε and the wave number K is calculated in first order of ε (see e. g. [10]). The Stokes equation

$$\nabla p = \eta \Delta \mathbf{u}$$

with the pressure p and the viscosity η can be rewritten in terms of the stream function $\tilde{\Psi}$, defined by $u_x = \partial_y \tilde{\Psi} = \tilde{\Psi}_y$ and $u_y = -\partial_x \tilde{\Psi} = -\tilde{\Psi}_x$ by

$$0 = \eta \Delta \nabla \times \mathbf{u} \tag{7}$$

$$0 = \Delta \Delta \tilde{\Psi} \ . \tag{8}$$

The boundary conditions are

$$0 = u_x(x, y = \pm h(x)) = \tilde{\Psi}_y(x, y = \pm h(x)) \tag{9}$$

$$0 = u_y(x, y = \pm h(x)) = -\tilde{\Psi}_x(x, y = \pm h(x)) \ . \tag{10}$$

We nondimensionalize the stream function by

$$\Psi = \frac{\tilde{\Psi}}{\tilde{u} d} \tag{11}$$

with the velocity of the flow at the origin $\tilde{u}$. The stream function is expanded in series of ε. We calculate the first order which means

$$\Psi \approx \Psi^{(0)} + \Psi^{(1)} \varepsilon \ . \tag{12}$$

We transform the problem to coordinates with straight boundaries

$$\vartheta = \frac{x}{d} \tag{13}$$

$$\zeta = \frac{y}{h(x)} \tag{14}$$

with boundary conditions

$$\Psi_\vartheta = 0, \ \Psi_\zeta = 0 \text{ at } \zeta = \pm 1 \ . \tag{15}$$

The equation of the stream function in Eq. 8 in the new coordinates reads for the zeroth order

$$\Psi^{(0)}_{\zeta\zeta\zeta\zeta} = 0 \tag{16}$$

The solution is

$$\Psi^{(0)} = \zeta - \frac{\zeta^3}{3} \tag{17}$$

The first order equation is

$$\Psi^{(1)}_{\vartheta\vartheta\vartheta\vartheta} + 2\Psi^{(1)}_{\vartheta\vartheta\zeta\zeta} + \Psi^{(1)}_{\zeta\zeta\zeta\zeta} + 12\zeta h_{\vartheta\vartheta} + \zeta(1 - \zeta^2) h_{\vartheta\vartheta\vartheta\vartheta} = 0 \ . \tag{18}$$

The solution is

$$\Psi^{(1)} = \left[\frac{2\cosh(Kd)\sinh(Kd\zeta) - 2\sinh(Kd)\zeta\cosh(Kd\zeta)}{\cosh(Kd)\sinh(Kd) - Kd} - \zeta(1-\zeta^2)\right]\sin(K\vartheta d)\ . \tag{19}$$

The flow is calculated by the stream function and a transformation back to the Cartesian coordinates. After that a Taylor expansion in ε is necessary because only the first order of ε was calculated. This means the flow fulfills the Stokes equation exactly and the divergence of the flow is zero, but the boundary condition is fulfilled only in first order. The resulting flow is

$$u_x = \tilde{u}\left(1 - \frac{y^2}{d^2} + 2\sin(Kx)\frac{[-K\sinh(Ky)y - \cosh(Ky)]\sinh(Kd) + Kd\cosh(Kd)\cosh(Ky)}{Kd - \cosh(Kd)\sinh(Kd)}\varepsilon\right) \tag{20a}$$

$$u_y = 2\tilde{u}K\cos(Kx)\frac{\sinh(Kd)y\cosh(Ky) - \cosh(Kd)d\sinh(Ky)}{Kd - \cosh(Kd)\sinh(Kd)}\varepsilon \tag{20b}$$

which can be simplified to

$$B_1 = \frac{-\sinh(Kd)}{Kd - \cosh(Kd)\sinh(Kd)}\,,\ B_2 = \frac{Kd\cosh(Kd)}{Kd - \cosh(Kd)\sinh(Kd)}\,,$$

$$u_x = \tilde{u}\Big(1 - \frac{y^2}{d^2} + 2\varepsilon\sin(Kx)\left[B_1 Ky\sinh(Ky) + (B_1 + B_2)\cosh(Ky)\right]\Big) \tag{20c}$$

$$u_y = -2\tilde{u}\varepsilon\cos(Kx)\left[B_1 Ky\cosh(Ky) + B_2\sinh(Ky)\right] \tag{20d}$$

[1] J. K. G. Dhont, *An Introduction to dynamics of colloids* (Elsevier, Amsterdam, 1996).
[2] H. Yamakawa, J. Chem. Phys. **53**, 436 (1970).
[3] J. Rotne and S. Prager, J. Chem. Phys. **50**, 4831 (1969).
[4] E. Wajnryb, K. A. Mizerski, P. J. Zuk, and P. Szymczak, J. Fluid Mech. **731**, R3 (2013).
[5] S. Ramanjuan and C. Pozrikidis, J. Fluid. Mech. **361**, 117143 (1998).
[6] D. Barthès-Biesel, Annu. Rev. Fluid Mech. **48**, 25 (2016).
[7] T. Krueger, M. Gross, D. Raabe, and F. Varnik, Soft Matter **9**, 9008 (2013).
[8] R. Skalak, A. Tozeren, R. P. Zarda, and S. Chien, Biophys. J. **13**, 245 (1973).
[9] E. Evans and Y. Fung, Microvasc. Res. **4**, 335 (1972).
[10] S. Tsangaris and E. Leiter, J. Eng. Math. **18**, 89 (1984).

Publication 2

Cross-stream migration of asymmetric particles driven by oscillating shear
M. Laumann , P. Bauknecht, S. Gekle, D. Kienle and W. Zimmermann,
2017 EPL **117** 44001

DOI: 10.1209/0295-5075/117/44001

epl A Letters Journal Exploring the Frontiers of Physics

February 2017

EPL, **117** (2017) 44001
doi: 10.1209/0295-5075/117/44001

www.epljournal.org

Cross-stream migration of asymmetric particles driven by oscillating shear

M. Laumann[1], P. Bauknecht[2], S. Gekle[2], D. Kienle[1(a)] and W. Zimmermann[1]

[1] *Theoretische Physik I, Universität Bayreuth - 95440 Bayreuth, Germany*
[2] *Biofluid Simulation and Modeling, Universität Bayreuth - 95440 Bayreuth, Germany*

received 23 December 2016; accepted in final form 13 March 2017
published online 6 April 2017

PACS 47.15.G- – Low-Reynolds-number (creeping) flows
PACS 47.57.ef – Sedimentation and migration
PACS 83.50.-v – Deformation and flow

Abstract – We study the dynamics of asymmetric, deformable particles in oscillatory, linear shear flow. By simulating the motion of a dumbbell, a ring-polymer, and a capsule we show that cross-stream migration occurs for asymmetric elastic particles even in linear shear flow if the shear rate varies in time. The migration is generic as it does not depend on the particle dimension. Importantly, the migration velocity and migration direction are robust to variations of the initial particle orientation, making our proposed scheme suitable for sorting particles with asymmetric material properties.

Introduction. – During the recent years, microfluidics has evolved to a cross-disciplinary field, ranging from basic physics to a plethora of biological and technical applications [1–7], including the control of small amounts of fluids, chemical synthesis [8,9], biological analysis [10,11], and the study of the deformation dynamics of droplets, vesicles, capsules, or blood cells [12–40]. An important transport mechanism in microfluidic flows is the cross-stream migration (CSM), where particles move across streamlines and can be sorted due to their particle-specific properties [41,42].

The CSM effect has been first reported in 1961 by Segre and Silberberg for rigid particles at finite Reynolds number in pipes with diameters of several millimeters [43]. When channels approach the micrometer scale, the Reynolds number vanishes (Stokes regime) and fluid inertia does not matter; likewise, for μm-sized particles thermal effects can be discarded. In the Stokes regime, CSM arises in curvilinear [12–15] and rectilinear flow [16–20], if the particle is elastic and, in case of rectilinear flow, the flow's fore-aft symmetry is broken, requiring intra-particle hydrodynamic interaction [16–19]. Such symmetry breaking occurs near boundaries via wall-induced lift forces [19,21–23] or by space-dependent shear rates, so that dumbbells [16–18], droplets [24–26], vesicles and capsules [27–29] exhibit CSM even in unbounded flow. These parity breaking mechanisms may be accompanied by other effects due to viscosity contrast [24,44] or particle chirality [45], which further impact the CSM.

Here we show that a controlled cross-stream migration is possible even in unbounded *linear* shear flow, provided that 1) the particle holds an intrinsic asymmetry (parity breaking), and 2) the shear rate varies in time, causing time-dependent particle deformations. Importantly, the cross-stream migration occurs irrespective of the dimensionality of the particle, accentuating its *generic* nature, as we show by studying particles extending in one (1D), two (2D), and three (3D) dimensions. We demonstrate that the CSM depends on external flow parameters such as switching period, which can be controlled conveniently to achieve an optimized migration.

Model and approach. – To reveal the generic behavior of the CSM in oscillatory shear flow, we use three kinds of particles, which share the common features that they are deformable, asymmetric, and their constituent parts interact hydrodynamically. The first two particle types are a dumbbell (1D) and a ring-polymer (2D), modeled by a sequence of bead-spring units with the i-th bead located at $\mathbf{r}_i$ and connected to its nearest neighbors by linear springs

(a) E-mail: diego.kienle@uni-bayreuth.de (lead author and project coordination)

with an equilibrium bond length b and force constant k. The dumbbell asymmetry is modeled by assigning different friction coefficients ζ_1 and ζ_2 to unequal sized beads 1 and 2 with $r_\zeta = \zeta_2/\zeta_1 = 3$ (fig. 1(a), inset). The asymmetry of the N-bead ring-polymer is realized by a space-dependent bending stiffness $\kappa(\{\mathbf{r}\})$ along the ring contour $\{\mathbf{r}\}$. The third particle is an elastic capsule (3D), the asymmetry of which is implemented likewise by a spatially varying bending stiffness $\kappa(\{\mathbf{r}\})$ along the capsule surface $\{\mathbf{r}\}$. For the purpose of this study, we split the contour/surface of the ring/capsule in equal parts (Janus-particle); the stiff and bendy portion in either case has a bending stiffness of κ_2 and κ_1 with a ratio $r_\kappa = \kappa_2/\kappa_1 = 1.5$ (fig. 1(b) and (c), inset).

The migration behavior of all three particle kinds is obtained from their non-Brownian trajectories. The trajectories for the dumbbell and ring-polymer, exposed to an unperturbed flow field $\mathbf{u}(\mathbf{r})$, are determined by solving the standard Stokesian dynamics for bead-spring models [46],

$$\dot{\mathbf{r}}_i = \mathbf{u}(\mathbf{r}_i) + \sum_{j=1}^{N} \mathbf{H}_{ij} \cdot \left[\mathbf{F}_j^{bo} + \mathbf{F}_j^{be}\right]. \tag{1}$$

$\mathbf{F}_i^{bo}$ and $\mathbf{F}_i^{be}$ refer to harmonic bonding and bending forces, obtained from the potentials $U^{bo} = \sum_{i=1}^{N} \frac{k}{2}(R_i - b)^2$ and $U^{be} = -\sum_{i=1}^{N} \kappa(\mathbf{r}_i) \ln[1 + \cos\alpha_i]$. $R_i = |\mathbf{r}_i - \mathbf{r}_{i+1}|$ denotes the absolute value of the bond vector and $\cos\alpha_i = \mathbf{e}_{R_{i-1}} \cdot \mathbf{e}_{R_i}$ is the angle between the bond vectors $\mathbf{R}_{i-1}$ and $\mathbf{R}_i$ with $\mathbf{e}_{R_i} = \mathbf{R}_i/R_i$ the bond unit vector. The hydrodynamic interaction (HI) between bead i and j, inducing a hydrodynamic backflow (HB), is included in eq. (1) via the mobility matrix $\mathbf{H}_{ij}$ within the Oseen tensor [46],

$$\mathbf{H}_{ij} = \begin{cases} \frac{1}{8\pi\eta R_{ij}} \left[\mathbf{I} + \mathbf{e}_{R_{ij}} \otimes \mathbf{e}_{R_{ij}}\right] & i \neq j, \\ \frac{1}{\zeta_i}\mathbf{I} & i = j \end{cases} \tag{2}$$

with $\mathbf{e}_{R_{ij}} = \mathbf{R}_{ij}/R_{ij}$ and $\mathbf{R}_{ij} = \mathbf{r}_i - \mathbf{r}_j$. The capsule path is calculated using the immersed boundary method in conjunction with the lattice Boltzmann method for the flow [47–49], employing an adapted version of the ESPResSo package [50]. Throughout we assume a time-dependent (td), linear shear flow $\mathbf{u}(x, y) = S(t)y\,\mathbf{e}_x$ along the $\mathbf{e}_x$-axis; the shear rate $S(t)$ has a period T with $S(t) = +\dot{\gamma}$ during the first half-period T_1 and $S(t) = -\dot{\gamma}$ during the second half-period T_2 with $T_1 = T_2 = T/2$. The initial orientation of all three particles is $\phi_0 = 2.0\ \pi$ with the small ζ_1-bead, respectively, the stiff κ_2-contour/surface being located to the left.

Generic behavior. – Figure 1 shows the transverse component of the center of drag $y_c(t)$ (ζ-weighted), scaled with respect to the bond length b of the bead-spring unit or the capsule radius a, as a function of the scaled time $t\dot{\gamma}$ with fixed $\dot{\gamma}$ for all three particles. For symmetric particles ($r_{\zeta,\kappa} = 1.0$), the cross-stream migration is zero at any time (dashed line) [14,17] as parity breaking does not occur irrespective of whether the shear flow is stationary (ss) or time dependent (td). For asymmetric particles ($r_{\zeta,\kappa} > 1.0$) in *stationary* shear flow parity breaking exists, resulting indeed in a temporary CSM, as reflected in the oscillatory behavior of $y_c(t)$, whereas the *net* migration over one shear-cycle is still zero (red solid line). This interim migration of asymmetric particles can be exploited to attain a *net* cross-stream migration, if the shear rate $S(t)$ is made time dependent by switching $S(t)$ at a frequency $1/T$, as shown in fig. 1(a)–(c) by the blue solid

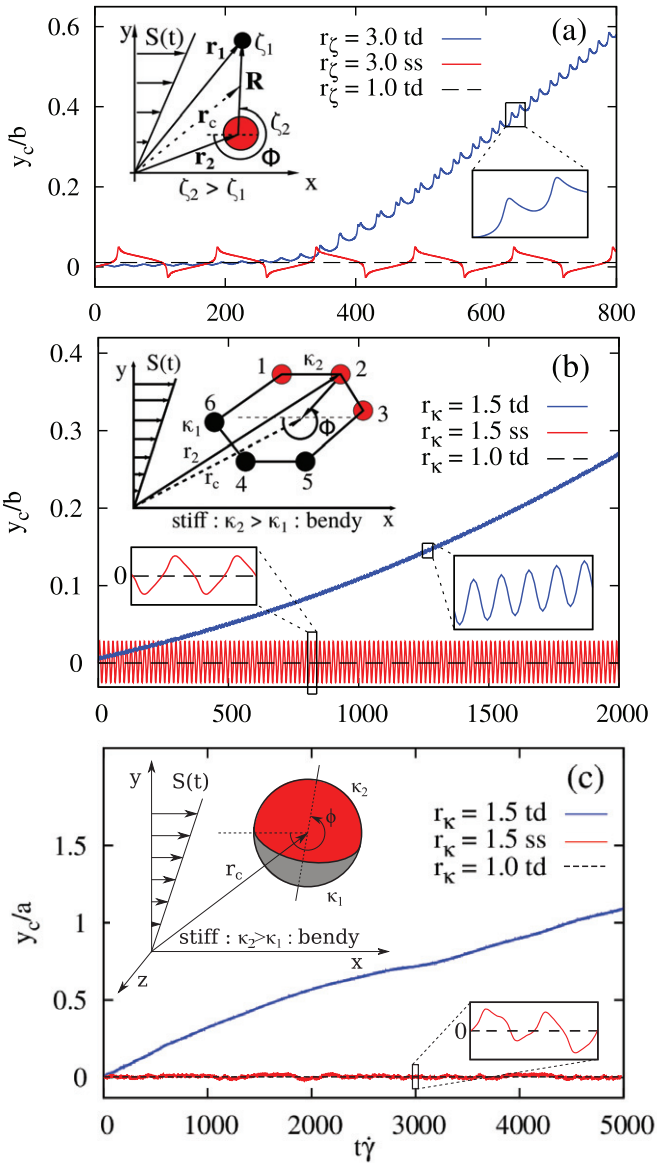

Fig. 1: (Color online) Lateral position $y_c(t)$ *vs.* scaled time $t\dot{\gamma}$ for the asymmetric (a) 1D dumbbell, (b) 2D ring, and (c) 3D capsule, sketches of which are shown in the inset. Irrespective of the model details, all particle types perform a *net* cross-stream migration in linear shear (blue solid), if the shear rate is time-dependent (td). At steady shear (ss), $y_c(t)$ oscillates around a constant mean (red solid), so that the *net* migration vanishes [14,17]. For symmetric particles ($r_{\zeta,\kappa} = 1.0$), the migration is zero. The initial orientation is $\phi_0 = 2.0\ \pi$.

line. The fact that all three particles display cross-stream behavior irrespective of their dimensionality and model details is an indication of a *generic* property[1], which can be attributed to the different *mean* shapes the particle acquires during each half-period, as discussed next.

Migration mechanism. – To understand the CSM mechanism, we take a closer look at the cross-stream dynamics of an asymmetric dumbbell ($r_\zeta > 1$) and an asymmetric ring ($r_\kappa > 1$), consisting of N-bead-spring units; we note that the discussion provided for the ring is general insofar as it applies for the 3D capsule as well where the ring is viewed as a 2D cut through the capsule plane of symmetry. To keep the explanation of the CSM mechanism transparent, we focus in either case on the *steady-state* regime (approached by all three particles after a transient), where the dumbbell and the ring have adopted a stable *mean* orientation $\langle\phi\rangle_{T/2}$ or $\langle\phi\rangle_T$, as determined by averaging their orientation angle $\phi(t)$ over a half or full shear-cycle, respectively.

Starting with the dumbbell, one can derive from eq. (1) a closed-analytical expression for the instantaneous cross-stream velocity $v_m(t)$ of its ζ-weighted center $y_c(t)$, as detailed in footnote [1] and given by

$$v_m(t) = \frac{k}{4\pi\eta}\,\frac{r_\zeta - 1}{r_\zeta + 1}\,\frac{R(t) - b}{R(t)}\,\sin\phi(t), \qquad (3)$$

with η the viscosity, $\phi(t)$ the orientation angle, and $R(t) = |\mathbf{r}_1 - \mathbf{r}_2|$ the distance between bead 1 and 2, as introduced in fig. 1(a). Equation (3) facilitates reading off various, well-known limiting cases: in linear shear flow CSM does not occur at any time ($v_m(t) = 0$), irrespective of whether the flow is stationary or time-dependent, if the dumbbell is i) symmetric ($r_\zeta = 1$), ii) very soft (small k), or iii) if HI is absent (free-draining) or weak, as realized for large bond lengths b [17].

Once the dumbbell is asymmetric ($r_\zeta > 1$) and simultaneously deformable (finite k), $v_m(t) \neq 0$, a *net* migration may be possible. Even though the precise conditions for a net migration step Δy_c during one half-cycle can be obtained only by integrating eq. (3), one can still gain important insights on the CSM mechanism by a qualitative inspection of eq. (3) and how the various terms interplay. First, as long as the switching period T and the shear rate $\dot\gamma$ are not too large to avoid full turnovers, the dumbbell orientation $\phi(t)$ oscillates (after a transient regime) around a mean angle $\langle\phi\rangle_{T/2} = 3\pi/2$ or $\pi/2$, depending on the initial orientation ϕ_0. When $\langle\phi\rangle_{T/2} = 3\pi/2$ ($\pi/2$), we observe that $\sin\phi(t)$ remains negative (positive) over the entire half-cycle and becomes largest once $\phi(t) \approx 3\pi/2$ ($\pi/2$), *i.e.*, the dumbbell is perpendicular to the flow direction, as shown in fig. 2(a). The bond length $R(t)$ oscillates also around the equilibrium bond length b, so that the term $R(t) - b$ in eq. (3) alters its sign (fig. 2(a)), causing the instantaneous CSM velocity $v_m(t) = \dot y_c(t)$ to oscillate (fig. 1(a)). Therefore, the sign of the *net* CSM depends on whether the positive or negative migration increments to Δy_c contribute most during the half-cycle.

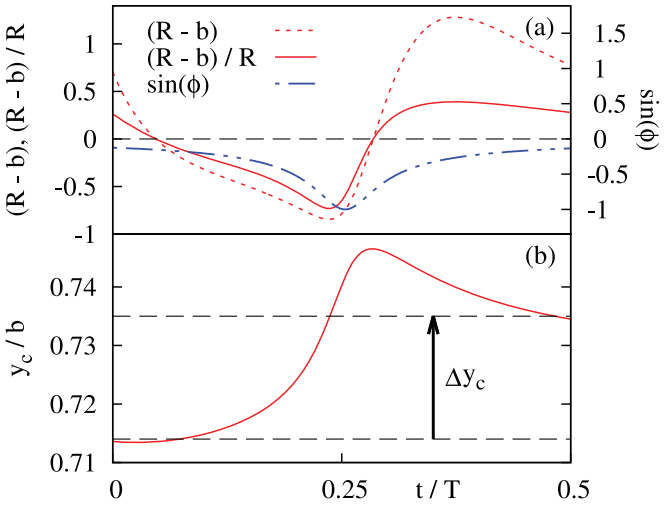

Fig. 2: (Color online) (a) Time dependence of the terms $R(t) - b$, $(R(t) - b)/R(t)$, and $\sin\phi(t)$, appearing in eq. (3), over a half period $T/2$ for the dumbbell orientation oscillating around $\langle\phi\rangle_{T/2} = 3\pi/2$. (b) Evolution of the transverse component of the center of drag $y_c(t)$, obtained by integrating eq. (3), and the *net* migration step $\Delta y_c > 0$ acquired at the end of $T/2$.

Based on eq. (3), one may expect that $\Delta y_c < 0$ because $\sin\phi(t) < 0$ over the whole half-cycle while the deformation $R(t) - b$ is asymmetric such that the dumbbell is stretched more strongly ($R(t) - b > 0$) than being compressed over $T/2$, as demonstrated in fig. 2(a) by plotting the respective terms of eq. (3); the asymmetry of $R(t) - b$ can be ascribed to the larger difference of the flow velocity between and hence larger drag on the beads when the dumbbell is stretched. However, a mean CSM with $\Delta y_c < 0$ is in clear contradiction to our numerical results, shown in fig. 1(a). The origin for the *net* migration step Δy_c being *positive* can be attributed to the non-linear behavior of the hydrodynamic interaction, appearing in eq. (3) via the $1/R(t)$-term, so that deformations of a compressed dumbbell receive a larger *negative* weight; fig. 2(a) displays the respective behavior of $(R(t) - b)/R(t)$, which is amplified furthermore by the peaking of $\sin\phi(t)$ when $R(t) - b < 0$. Hence, the positive contributions during the dumbbell compression outbalance the negative ones when the dumbbell is stretched. Our qualitative analysis, based on eq. (3), indicates that Δy_c is positive (negative) when the dumbbell swings around $\langle\phi\rangle_{T/2} = 3\pi/2$ ($\pi/2$). This qualitative picture is consistent with fig. 2(b), showing the evolution of $y_c(t)$ by integrating eq. (3) with the migration step $\Delta y_c > 0$ at the end of one half-cycle $T/2$, and is in full agreement with our numerical result shown

[1]The Supporting Information (SI) contains further details on the models, a derivation of eq. (4), plots and movies on the generic behavior (including an extension of the orientation robustness) of the dumbbell and capsule (`Movie1.mp4`, `Movie2.mp4`, `Movie3.mp4`, `Movie4.mp4`, `Movie5.mp4`, `Movie6.mp4`, `Movie7.mp4`, `Movie8.mp4`, `Movie9.mp4`, and `Supplementarymaterial.pdf`). A link of the abrupt v_m-drop to the $\langle\phi\rangle_T$-attractors is provided, too.

in fig. 1(a). Finally, we note that for a rigid dumbbell ($\dot{R}(t) = 0$) the migration step $\Delta y_c = 0$ when swinging around $\langle\phi\rangle_{T/2} = 3\pi/2$ ($\pi/2$), as one can show by solving eq. (3) analytically (see footnote [1]).

We now inspect the CSM behavior of the 2D ring and assume again that both the period T and the shear rate $\dot{\gamma}$ are not too large as to prevent the ring dynamics being dominated by tank-treading, causing a net zero migration, as discussed in the following paragraphs. Under this condition and for an initial orientation ϕ_0, the ring adopts (after a transient) one stable *mean* orientation $\langle\phi\rangle_T$ over one shear-cycle T. Specifically, for $\phi_0 = 2.0\ \pi$ the mean orientation of the ring is $\langle\phi\rangle_T \approx 1.75\ \pi$ with the stiff contour located in the upper (left) half-space and referred to below. We note that other initial orientations ϕ_0 may lead to one of the other possible mean orientations with $\langle\phi\rangle_T \approx 1.25\ \pi$, $\approx 0.75\ \pi$, or $\approx 0.25\ \pi$, where the ring (and capsule) displays CSM. Importantly, the explanation of the CSM mechanism provided for the mean orientation $\langle\phi\rangle_T \approx 1.75\ \pi$ and shown in fig. 1(b) applies irrespective of the specific value of $\langle\phi\rangle_T$.

Since a closed semi-analytic expression of the CSM velocity similar to eq. (3) is not possible beyond dumbbell models, we analyze the migration of the ring in terms of the *mean steady-state* CSM velocity $v_m^i = \langle v_m(\infty)\rangle_{T_i}$ (along the y-axis) for each half-period T_i, obtained by averaging the velocity $v_m(t)$ over T_i (see footnote [1]),

$$v_m^i = \langle \mathbf{e}_y \cdot \dot{\mathbf{r}}_c(\infty)\rangle_{T_i} = \frac{1}{N}\sum_{i=1}^{N}\sum_{j\neq i}\langle \mathbf{e}_y \cdot \mathbf{H}_{i,j} \cdot \mathbf{F}_j\rangle_{T_i}. \quad (4)$$

Equation (4) implies that for rectilinear flows with $\mathbf{e}_y \cdot \mathbf{u} = 0$, the cross-stream transport is entirely driven by the particle drag due to the hydrodynamic backflow, induced by the potential forces $\mathbf{F}_j$. Further, the magnitude and direction of each HB (and hence of v_m^i) depend on the particle shape via the force profile $\mathbf{F}(\{\mathbf{r}_j\})$ and the dyadic mobility matrix $\mathbf{H}_{i,j}$. An expression similar to eq. (4) can be used to determine the *mean* HI-induced flow field $\mathbf{v}(\mathbf{r})$ for each half-period (see footnote [1]). The respective 2D backflow $\mathbf{v}(\mathbf{r})$, shown in fig. 3(a) and (b) when $\langle\phi\rangle_T \approx 1.75\ \pi$, corresponds to an *elongational* flow, whose flow lines are reversed (sign change) as a result of the altering ring deformation during the $S(t)$-switching ($+\dot{\gamma} \to -\dot{\gamma}$), and displayed more clearly in fig. 3(c) and (d). The ring asymmetry causes generally a break of the parity symmetry (PS) of the elongational HB, but the extent of the PS violation depends on the strength of the *mean* deformation during each half-cycle T_i (fig. 3(c) and (d)).

Comparing the *mean* deformation for each half-cycle, one observes that the ring asymmetry is *enhanced* during the first T_1 shear-cycle, causing an increased parity break of the elongational HB (fig. 3(c)). But this implies that the *difference* between the mean opposing partial HB-drags at the stiff and bendy side, v_m^s and v_m^b (see footnote [1]: eq. (9) of the SI), becomes larger with $|v_m^s| > |v_m^b|$ since $\kappa_2 > \kappa_1$.

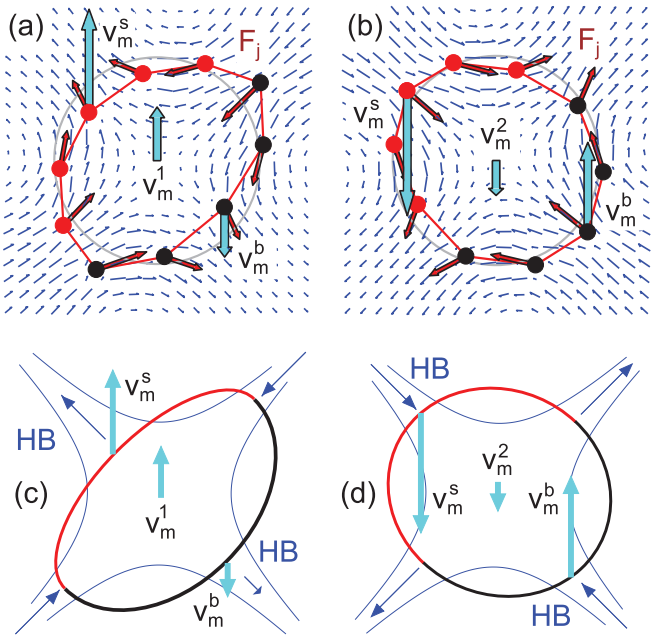

Fig. 3: (Color online) Explanation of the basic migration mechanism by way of the ring. Shown are simulation data for the *mean* ring shape, averaged over the (a) first T_1 and (b) second T_2 shear-cycle, and the potential forces $\mathbf{F}_j$ along the N-bead contour. While the backflow $\mathbf{v}(\mathbf{r})$ (HB) induced within each half-cycle T_i is approximately elongational (blue), its parity is broken due to the particle asymmetry and leads to different mean CSM-driving drags v_m^s and v_m^b at the stiff and bendy side. Panels (c) and (d) show how the parity asymmetry of the HB is enhanced ($|v_m^s| > |v_m^b|$) during the T_1-cycle, while during the T_2-cyle the HB-parity is partially recovered ($|v_m^s| \gtrsim |v_m^b|$), leading to a *net* positive migration $v_m = v_m^1 + v_m^2 > 0$.

Hence, the *mean* migration velocity during the T_1-cycle, $v_m^1 = v_m^s + v_m^b$, is large and *positive*. In turn, during the T_2 shear-cycle the situation is reversed as the ring shape is roughly circular, *i.e.*, the ring asymmetry is *reduced* with the result that the parity of the elongational backflow is partly recovered (fig. 3(b) and (d)), and the opposing partial HBs almost cancel. The reason for the residual backflow is because the HB-drag at the stiff contour part is slightly larger than at the bendy side ($|v_m^s| \gtrsim |v_m^b|$), as a result of the larger stiffness. During the T_2-cycle the *mean* migration step $v_m^2 = v_m^s + v_m^b$ is thus small and *negative*. Over the course of one shear-cycle $T = T_1 + T_2$, the *net* migration $v_m = v_m^1 + v_m^2$ is therefore *positive*, as displayed by all three kinds of particles (fig. 1(a)–(c)).

Orientation robustness. – We now demonstrate that the CSM effect is quite robust against a dispersal of initial orientations by varying the angle ϕ_0, while keeping the orientation axis within the y-x shear plane (tilt angle $\theta_0 = 0$). Figure 4 shows the instantaneous migration velocity of the ring $\langle v_m(t)\rangle_T \tau_b/b$, averaged over one cycle T, *vs.* time $t\dot{\gamma}$ ($\dot{\gamma} = 0.1$ fixed, $\tau_b = \eta b^3/\kappa_1$) for various orientations ϕ_0 within the intervals $I^+ = [1.1; 2.0]\pi$ and $I^- = [0.1; 1.0]\pi$. The interval I^+ (I^-) corresponds to ring

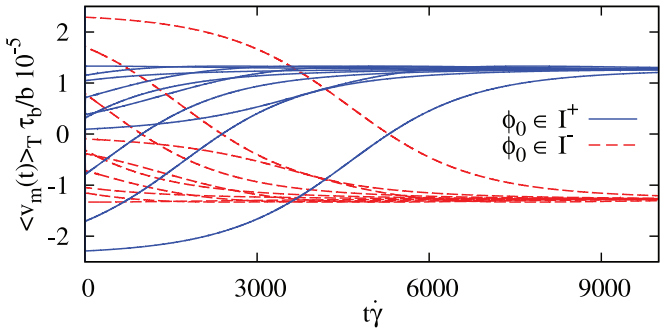

Fig. 4: (Color online) Instantaneous migration velocity $\langle v_m(t)\rangle_T \tau_b/b$ of the ring, averaged over one period T, *vs.* time $t\dot\gamma$ for different initial angles ϕ_0 taken out of the interval $I^+ = [1.1; 2.0]\,\pi$ or $I^- = [0.1; 1.0]\,\pi$. The $\langle v_m(t)\rangle_T$-transient depends on ϕ_0, while the steady-state value $v_m = \langle v_m(\infty)\rangle_T$ is ϕ_0-independent. Parameters: $\dot\gamma = 0.1$, $T = 20$, $r_\kappa = 1.5$.

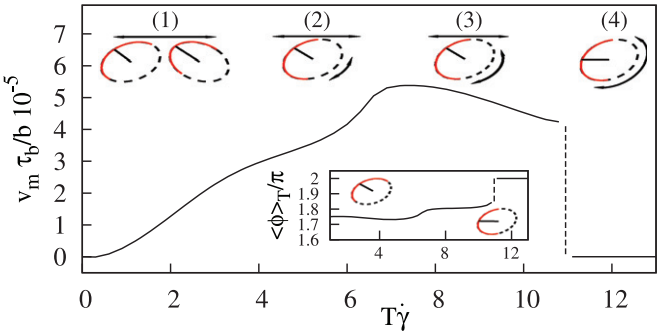

Fig. 5: (Color online) Steady-state migration velocity $v_m\tau_b/b$ of the ring *vs.* switching period $T\dot\gamma$. Four dynamic regimes are identified: (1) oscillatory shear deformation, indicated by the horizontal arrow, at small T; (2) weak tank-treading (TT) superposed with (1), marked by the half-circle arrow; (3) enhanced tank-treading at large T; (4) TT-dominated with zero net migration for $T\dot\gamma > 11$. Inset: T-averaged mean orientation $\langle\phi\rangle_T$ *vs.* $T\dot\gamma$. Parameters: $\phi_0 = 2.0\ \pi$, $\dot\gamma = 0.1$, $r_\kappa = 1.5$.

orientations, where during migration the stiff part lies in the mean within the upper (lower) half-space with the orientation angle $\phi(t)$ oscillating either around the *mean* $\langle\phi\rangle_T \approx 1.75\ \pi$ or $1.25\ \pi$ ($\langle\phi\rangle_T \approx 0.75\ \pi$ or $0.25\ \pi$). As discussed before, this implies that the final, steady-state migration velocity $v_m \equiv \langle v_m(\infty)\rangle_T$, is positive for $\phi_0 \in I^+$ and negative for $\phi_0 \in I^-$, as disclosed in fig. 4 for $t\dot\gamma > 9.0 \cdot 10^3$. Remarkably, the ring migrates always at the same steady-state speed $v_m^{+/-}$ even though the ϕ_0-orientation varies by almost $\Delta\phi_0^{+/-} \approx \pi$, meaning $v_m^{+/-}$ is independent of ϕ_0. In turn, the choice of ϕ_0 determines strongly the short-time dynamics of $\langle v_m(t)\rangle_T$, as shown in fig. 4 for $t\dot\gamma < 9.0 \cdot 10^3$. This imbalance of the magnitude and in part the sign of $\langle v_m(t)\rangle_T$ is a transient signature and exists as the orientation angle $\phi(t)$ is not yet in-phase with the shear signal $S(t)$; the phase synchronization of the angle takes place gradually within the transient regime over many shear-cycles T before a phase-locking is established. The behavior of $\langle v_m(t)\rangle_T$, shown for the ring in fig. 4, is generic and displayed by the other particles types (see footnote [1]).

We note that while the migration persists ($v_m \neq 0$) in most cases when the tilt angle θ_0 between the particle axis and the y-x shear plane is non-zero (accentuating the robustness of the CSM effect), some signatures of the migration alter when $\theta_0 \neq 0$ and depend on the particle type, which we briefly summarize below with more details provided in the SI (see footnote [1]). In case of the dumbbell, the tilt angle $\theta(t)$ always relaxes back towards the y-x shear plane ($\theta(\infty) = 0$) for any value of $\theta_0 \in [0.0; \pi/2[$, so that $\langle\theta\rangle_T^{FP} = 0$ is an asymptotically stable fixed point; only for one tilt angle $\theta_0 = \pi/2$, the dumbbell retains its initial orientation within the z-x plane, in which case $\langle\theta\rangle_T^{FP} = \frac{\pi}{2}$ is a *neutral stable* fixed point and corresponds to a non-migrating state ($v_m = 0$). The dumbbell migration is, therefore, robust against θ_0-variations over the entire interval $\pi/2$. The capsule behaves likewise and exhibits orientational relaxation as well, except that the previous robustness interval for θ_0 is reduced to $[0; \frac{2}{3}]\frac{\pi}{2}$ with $v_m \neq 0$, while the residual interval $]\frac{2}{3}; 1.0]\frac{\pi}{2}$ leads to zero migration, as the capsule axis relaxes to the other stable fixed point $\langle\theta\rangle_T^{FP} = \frac{\pi}{2}$. The ring migration differs from the dumbbell and capsule insofar as *all* tilt angles θ_0 are *neutral stable* fixed points, *i.e.*, $\langle\theta\rangle_T^{FP} = \theta_0 \in [0; \frac{\pi}{2}]$, implying that the ring keeps its initial θ_0-orientation. The non-relaxation of the tilt angle has the consequence that the ring moves at a different (but constant) speed for each value $\theta_0 \in [0; \frac{\pi}{2}[$. Again, the CSM of the ring is robust over the entire θ_0-interval of $\pi/2$.

Frequency dependence. – The migration process is not entirely determined by the material properties of the particle (*e.g.*, stiffness), but can be controlled also by external parameters such as the shear rate $\dot\gamma$ or the switching period T, the latter being discussed next. Figure 5 shows the steady-state migration velocity $v_m\tau_b/b$ for a fixed $\dot\gamma = 0.1$ *vs.* the period $T\dot\gamma$, which sets the time scale for the sign change of the shear rate $S(t)$. When $T\dot\gamma$ is small, the migration speed v_m is rather low (regime (1)) since the quickly alternating shear rate $S(t)$ induces only a small shear deformation of the ring shape, so that the ring has not sufficient time to reorient and to fully develop its mean conformation within each half-period T_1 and T_2, respectively; at these short times tank-treading is still marginal, as sketched in fig. 5. For larger periods T, the ring has now more time within each half-cycle to deform and fully adopt the migration state, so that v_m monotonously grows first (regime (2)), approaching a maximum at $T\dot\gamma \approx 7$. At this stage, a weak partial tank-treading (TT) of the contour is initiated, but the ring dynamics is still dominated by oscillatory shear deformations, driving the CSM. Beyond a value of $T\dot\gamma > 7$ the migration gradually decays since tank-treading becomes increasingly important insofar as a larger fraction of time of each half-cycle T_i is spent on tank-treading.

This implies that a portion of the stiff/bendy contour is now partly shuffled from the upper/lower half-space to the lower/upper one (regime (3)), *i.e.*, the dynamics of the entire shear-cycle takes now place within two half-spaces (with an unequal amount) and each contributes to the CSM with opposite sign. The *net* velocity v_m is still positive, since the *mean* orientation of the ring $\langle\phi\rangle_T \approx 1.75\pi$ (fig. 5, inset) with the stiff/bendy contour part residing on *average* within the upper/lower half-space. Beyond $T\dot{\gamma} > 11$ the CSM comes to a halt since tank-treading dominates now the dynamics within each half-period, so that even a larger fraction of the stiff/bendy contour is reshuffled between the upper-lower half-space. Within this TT-dominated regime, the *mean* orientation flips from $\langle\phi\rangle_T \approx 1.75\ \pi$ ($v_m > 0$) to $\langle\phi\rangle_T \approx 2.0\ \pi$ (fig. 5, inset), which corresponds to a *symmetric* state where equal amounts of the stiff/bendy contour lie in the *mean* within both half-spaces, so that v_m is zero (see footnote [1]). The abrupt v_m-drop is hence inherently connected with the abrupt change of the *mean* orientation $\langle\phi\rangle_T$, which can be understood by inspecting the phase-space $\langle\dot{\phi}(t)\rangle_T$-$\langle\phi(t)\rangle_T$ (see SI in footnote [1] for details). Here we just note that the phase-space features a pattern of discrete, *asymptotically stable* orientations $\langle\phi\rangle_T^{FP}$ (fixed points), which the ring can access. Importantly, the number and value of available $\langle\phi\rangle_T^{FP}$ depend sensitively on the switching period T (see footnote [1]). In our case with $\phi_0 = 2.0\ \pi$, the only stable orientation the ring can adopt is $\langle\phi\rangle_T^{FP} \approx 1.75\ \pi$ as long as $T\dot{\gamma} < 11$ while $\langle\phi\rangle_T \approx 2.0\ \pi$ is unstable[2]. When $T\dot{\gamma} > 11$, the previous fixed point at $1.75\ \pi$ disappears, so that the orientation $\langle\phi(t)\rangle_T \approx 1.75\ \pi$ is acquired only temporarily while a new orientational attractor appears at $\langle\phi\rangle_T^{FP} = 2.0\ \pi$. Since the value $1.75\ \pi$ lies within the (extended) range of the 2π-attractor, the ring locks in to the mean orientation of $\langle\phi\rangle_T = 2.0\ \pi$ (fig. 5, inset), corresponding to a non-migrating state ($v_m = 0$) (see footnote [1]).

Conclusions. – We have shown that deformable particles, which hold an intrinsic asymmetry (parity breaking), display cross-stream migration (CSM) in time-perodic, linear shear flow for medium switching frequencies. The net migration can be attributed uniquely to the particle asymmetry as it leads to an asymmetric force distribution within the periodically deformed particle, inducing asymmetric, non-compensating hydrodynamic backflows (HBs). Since the magnitude and direction of the HBs depend on the actual particle deformation, which is different within the first and second half-period, the HBs averaged over one shear-cycle T are non-zero, thus leading to a finite CSM (fig. 3). The CSM is *generic* inasmuch as it does not depend on the particle dimension nor on the specific details of its asymmetry (fig. 1(a)–(c)). While the migration direction is sensitive to whether the stiff/bendy part of the particle resides during one shear cycle in the mean within the upper or lower half-space, the CSM speed approaches after a transient phase a constant value and is independent of the initial particle orientation (fig. 4).

Given that even a small asymmetry in the bending modulus (factor 1.5 or less) of micron-sized particles can trigger for medium channel lengths a sizable migration velocity of 20 $\frac{\mu\mathrm{m}}{\mathrm{min}}$ under realistic flow conditions with a shear rate of $\dot{\gamma} = 22\ \frac{1}{\mathrm{s}}$ and a period of $T = 1.75\,\mathrm{Hz}$ (see footnote [1]), our proposed scheme facilitates appreciable migration distances in compact microfluidic setups just by independently tuning the amplitude and frequency of the shear rate. Investigating effects due to random material inhomogeneities will be an interesting subject for future studies.

* * *

PB and SG thank the Volkswagen foundation for support and gratefully acknowledge the Leibniz Supercomputing Center Munich for the provision of computing time. ML and WZ acknowledge support by the DFG priority program on Micro- and Nanofluidics.

REFERENCES

[1] Squires T. M. and Quake S. R., *Rev. Mod. Phys.*, **77** (2005) 978.
[2] Whitesides G. M., *Nature*, **442** (2006) 368.
[3] Popel A. S. and Johnson P. C., *Annu. Rev. Fluid Mech.*, **37** (2005) 43.
[4] Graham M. D., *Annu. Rev. Fluid Mech.*, **43** (2011) 273.
[5] Dahl J. B., Lin J.-M. G., Muller S. J. and Kumar S., *Ann. Rev. Chem. Biomol. Eng.*, **6** (2015) 293.
[6] Sackmann E. K., Fulton A. L. and Beebe D. L., *Nature*, **507** (2014) 181.
[7] Amini H., Lee W. and Di Carlo D., *Lab Chip*, **14** (2014) 2739.
[8] Jähnisch K., Hessel V., Löwe H. and Baerns M., *Angew. Chem., Int. Ed.*, **43** (2004) 406.
[9] Elvira K. S., Casadevall i Solvas X., Wootton R. C. R. and deMello A. J., *Nat. Chem.*, **5** (2013) 905.
[10] Yi C., Li C.-W., Ji S. and Yang M., *Anal. Chim. Acta*, **560** (2006) 1.
[11] Chen J., Li J. and Sun Y., *Lab Chip*, **12** (2012) 1753.
[12] Shafer R. H., Laiken N. and Zimm B. H., *Biophys. Chem.*, **2** (1974) 180; Shafer R. H., *Biophys. Chem.*, **2** (1974) 185.
[13] Aubert J. H. and Tirrell M., *J. Chem. Phys.*, **72** (1980) 2694; Aubert J. H., Prager S. and Tirrell M., *J. Chem. Phys.*, **73** (1980) 4103.
[14] Nitsche L. C., *AIChE J.*, **42** (1996) 613.
[15] Ghigliotti G., Rahimian A., Diros G. and Misbah C., *Phys. Rev. Lett.*, **106** (2011) 028101.
[16] Sekhon G., Armstrong R. C. and Jhon M. S., *J. Polym. Sci.*, **20** (1982) 947.
[17] Brunn P. O., *Int. J. Multiphase Flow*, **9** (1983) 187.

[2] We note that whether the system approaches an attractive fixed point does also depend on the *range* of each attractor. In the case of the ring, the 2π-fixed point is unstable for $T\dot{\gamma} = 9.0$, but turns into a stable FP when $T\dot{\gamma} = 10.0$. Since the range of the 2π attractor is quite small, the ring does not approach this FP, but continues to lock in to the orientational attractor $\langle\phi\rangle_T^{FP} \approx 1.8\ \pi$ due to its larger range. More details are provided in the SI (see footnote [1]).

[18] Brunn P. O. and Chi S., *Rheol. Acta*, **23** (1984) 163.
[19] Jhon M. S. and Freed K. F., *J. Polym. Sci.*, **23** (1985) 955.
[20] Agarwal U. S., Datta A. and Mashelkar R. A., *Chem. Eng. Sci.*, **49** (1994) 1693.
[21] Cantat I. and Misbah C., *Phys. Rev. Lett.*, **83** (1999) 880.
[22] Seifert U., *Phys. Rev. Lett.*, **83** (1999) 876.
[23] Ma H. B. and Graham M. D., *Phys. Fluids*, **17** (2005) 083103.
[24] Haber S. and Hetsroni G., *J. Fluid Mech.*, **49** (1971) 257.
[25] Leal L. G., *Annu. Rev. Fuid Mech.*, **12** (1980) 435.
[26] Mandal S., Bandopadhyay A. and Chakraborty S., *Phys. Rev. E*, **92** (2015) 023002.
[27] Kaoui B., Ristow G. H., Cantat I., Misbah C. and Zimmermann W., *Phys. Rev. E*, **77** (2008) 021903.
[28] Danker G., Vlahovska P. M. and Misbah C., *Phys. Rev. Lett.*, **102** (2009) 148102.
[29] Doddi S. K. and Bagchi P., *Int. J. Multiphase Flow*, **34** (2008) 966.
[30] Sibillo V., Pasquariello G., Simeone M., Cristini V. and Guido S., *Phys. Rev. Lett.*, **97** (2006) 054502.
[31] Abkarian M. and Viallat A., *Soft Matter*, **4** (2008) 653.
[32] Dupire J., Abkarian M. and Viallat A., *Phys. Rev. Lett.*, **104** (2010) 168101.
[33] Baroud C. N., Gallaire F. and Dangla R., *Lab Chip*, **10** (2010) 2032.
[34] Deschamps J., Kantsler V., Segre E. and Steinberg V., *Proc. Natl. Acad. Sci. U.S.A.*, **106** (2009) 11444.
[35] Kessler S., Finken R. and Seifert U., *Eur. Phys. J. E*, **29** (2009) 399.
[36] Noguchi H., *Phys. Rev. E*, **81** (2010) 061920.
[37] Zhao M. and Bagchi P., *Phys. Fluids*, **23** (2011) 111901.
[38] Matsunaga D., Imai Y., Yamaguchi T. and Ishikawa T., *J. Fluid Mech.*, **762** (2015) 288.
[39] Zhu L., Rabault J. and Brandt L., *Phys. Fluids*, **27** (2015) 071902.
[40] Cordasco D. and Bagchi P., *J. Fluid Mech.*, **800** (2016) 484.
[41] Sajeesh P. and Sen A. K., *Microfluid. Nanofluid.*, **17** (2014) 1.
[42] Geislinger T. M. and Franke T., *Adv. Colloid Interface Sci.*, **208** (2014) 161.
[43] Segre G. and Silberberg A., *Nature*, **189** (1961) 209.
[44] Farutin A. and Misbah C., *Phys. Rev. Lett.*, **109** (2012) 248106.
[45] Watari N. and Larson R. G., *Phys. Rev. Lett.*, **102** (2009) 246001.
[46] Doi M. and Edwards S. F., *The Theory of Polymer Dynamics* (Oxford University Press, Oxford) 1986.
[47] Krüger T., Varnik F. and Raabe D., *Comput. Math. Appl.*, **61** (2011) 3485.
[48] Guckenberger A., Schraml M. P., Chen P. G., Leonetti M. and Gekle S., *Comput. Phys. Commun.*, **207** (2016) 1.
[49] Bächer C., Schrack L. and Gekle S., *Phys. Rev. Fluids*, **2** (2017) 013102.
[50] Arnold A. *et al.*, *ESPResSo 3.1 - Molecular Dynamics Software for Coarse-grained Models* (Springer, Berlin) 2013.

Cross-stream migration of asymmetric particles driven by oscillating shear

– Supporting Information –

(Dated: March 13, 2017)

The supplementary note provides further details on the models and parameters used to simulate the cross-stream migration (CSM) of the dumbbell (1D), ring-polymer (2D), and capsule (3D) in linear shear flow. The *generic* behavior of the CSM is demonstrated further by complementing the simulations of the ring (shown in Fig. 4 and 5 in the main text) with corresponding plots, cf. Figs. 1 and 2 for the dumbbell and capsule, respectively.

I. DETAILS ON MODELS AND APPROACH

A. Bead-Spring: Dumbbell (1D) and Ring-Polymer (2D)

The dumbbell and the ring polymer are represented by a string of N beads, which overdamped dynamics for each bead i at position $\mathbf{r}_i$ is given by

$$\dot{\mathbf{r}}_i = \mathbf{u}(\mathbf{r}_i) + \sum_{j=1}^{N} \mathbf{H}_{ij} \cdot \left[\mathbf{F}_j^{bo} + \mathbf{F}_j^{be}\right] \tag{1}$$

with $\mathbf{F}_i^{bo} = -\nabla_{\mathbf{r}_i} U^{bo}$ and $\mathbf{F}_i^{be} = -\nabla_{\mathbf{r}_i} U^{be}$ referring to the harmonic bonding and bending forces, obtained from the respective potential

$$U^{bo} = \sum_{i=1}^{N} \frac{k}{2} \left(R_i - b\right)^2 \ , \qquad U^{be} = -\sum_{i=1}^{N} \kappa\left(\mathbf{r}_i\right) \ln\left[1 + \cos\alpha_i\right] \ . \tag{2}$$

The parameters k, b, and R_i denote the force constant, equilibrium bond length, and absolute value of the bond vector $R_i = |\mathbf{R}_i| = |\mathbf{r}_i - \mathbf{r}_{i+1}|$, respectively; $\kappa\left(\mathbf{r}\right)$ refers to the space-dependent bending stiffness and $\cos\alpha_i = \mathbf{e}_{R_{i-1}} \cdot \mathbf{e}_{R_i}$ is the angle between the bond vectors $\mathbf{R}_{i-1}$ and $\mathbf{R}_i$ with $\mathbf{e}_{R_i} = \mathbf{R}_i / R_i$ the bond unit vector.

The mobility matrix $\mathbf{H}_{ij}$ accounts for the hydrodynamic interaction (HI) between bead i and j, which in the Oseen-approximation[1] reads

$$\mathbf{H}_{ij} = \begin{cases} \frac{1}{8\pi\eta R_{ij}} \left[\mathbf{I} + \mathbf{e}_{R_{ij}} \otimes \mathbf{e}_{R_{ij}}\right] & : i \neq j \\ \frac{1}{\zeta_i}\mathbf{I} & : i = j \end{cases} \tag{3}$$

where $\mathbf{e}_{R_{ij}} = \mathbf{R}_{ij}/R_{ij}$ with $\mathbf{R}_{ij} = \mathbf{r}_i - \mathbf{r}_j$, and $\zeta_i = 6\pi\eta a_i$ the Stokes drag coefficient for a single bead with radius a_i.

The unperturbed flow field $\mathbf{u}(\mathbf{r})$ in Eq. (1) is given by the linear shear along the x-axis

$$\mathbf{u}(x, y) = S(t) y \, \mathbf{e}_x \tag{4}$$

with a time-dependent shear rate $S(t)$.

If the dumbbell is exposed to the linear shear flow $\mathbf{u}(x, y)$ only, it will not continuously perform a tumbling and rotational motion, rather rotates as to align with the streamlines along the x-axis. This behavior is known to be unphysical and a consequence of approximating the hydrodynamic interaction to first order only via the Oseen-tensor, assuming point-like particles. In general, this restriction could be lifted by including third-order corrections to the HI and thus reproduce the tumbling/rotational motion for the dumbbell[2]. Instead, we amend the linear shear flow $\mathbf{u}(x, y)$ by the flow-field[3]

$$\mathbf{v}^{\mathrm{rot}}(\mathbf{r}_i) = \frac{1}{2} \left(\frac{a_j}{R_{ji}} \right)^3 (\mathbf{r}_j - \mathbf{r}_i) \times [\nabla \times \mathbf{u}(\mathbf{r}_j)] \ , \tag{5}$$

which accounts for the rotation of finite-sized, spherical beads when being exposed to the shear flow of Eq. (4). In this manner, we capture the correct physics of the torque-induced tumbling and rotation of the dumbbell in the presence of flows with shear gradients.

The inclusion of tumbling and rotation in the dumbbell dynamics, as mediated by $\mathbf{v}^{\mathrm{rot}}(\mathbf{r})$, ensures that the dumbbell can develop a transient dynamics (main text: Fig. 1 (a)), where its orientation $\phi(t)$ is not yet in phase with the external shear signal $S(t)$; the presence of such a transient regime, however, is critical for establishing a phase synchronization of $\phi(t)$ (phase-locking), so that the dumbbell approaches ultimately a mean steady state orientation. Importantly, once the phase is locked the flow-field $\mathbf{v}^{\mathrm{rot}}(\mathbf{r})$ is no longer critical to describe the dumbbell dynamics at steady state. Yet, launching the dumbbell using just Eq. (1) without the $\mathbf{v}^{\mathrm{rot}}(\mathbf{r})$ term would not reproduce the correct transient dynamics, required to reach phase-locking and a mean orientation. We note that in case of the 2D ring and 3D capsule the tumbling and rotation dynamics is naturally captured by their dynamic equation, because both particles are already extended objects, so that the flow field $\mathbf{v}^{\mathrm{rot}}(\mathbf{r})$ does not need to be included in their dynamic equations.

Table I lists the parameters for the two bead-spring particles (bond length b, bead radii a_i, force constant k, bending stiffness $\kappa_{1,2}$), and the shear flow (shear rate $\dot{\gamma}$, period T,

viscosity η) used in the simulation of the 1D dumbbell and the 2D ring-polymer. With these parameters a timescale for the relaxation of the dumbbell and ring can be defined via $\tau = \zeta_1/k$ and $\tau_b = \eta b^3/\kappa_1$, respectively.

TABLE I: Dimensionless parameters used in the simulation of the 1D dumbbell and 2D ring.

particle kind	b	a_i	k	$\kappa_{1,2}$	$\dot{\gamma}$	T	η
dumbbell	2.0	0.1/0.3	1.0	N/A	1.0	30.0	1.0
ring-polymer	2.0	0.3	1.0	16.0/24.0	0.1	20.0	1.0

B. Bead-Spring: General Expression for Migration Velocity

An expression for the *instantaneous* velocity of cross-stream migration $v_m(t)$ can be derived by introducing the ζ-weighted center of drag $\mathbf{r}_c(t) := 1/\tilde{\zeta}\sum_{i=1}^{N}\zeta_i\ \mathbf{r}_i(t)$ for N beads with $\tilde{\zeta} = \sum_{i=1}^{N}\zeta_i$ the total drag coefficient. The velocity of the drag center follows then directly from $\dot{\mathbf{r}}_c(t)$; using Eq. (1) for $\dot{\mathbf{r}}_i(t)$ and taking into account that the sum of the total potential forces $\sum_{i=1}^{N}\mathbf{F}_i = 0$ with $\mathbf{F}_i = \mathbf{F}_i^{bo} + \mathbf{F}_i^{be}$, one obtains

$$\dot{\mathbf{r}}_c(t) = \frac{1}{\tilde{\zeta}}\sum_{i=1}^{N}\zeta_i\left[\mathbf{u}(\mathbf{r}_i) + \sum_{j\neq i}\mathbf{H}_{i,j}\cdot\mathbf{F}_j\right]\ . \tag{6}$$

In case of *rectlinear* flows such as linear shear, the axis of the main flow is *perpendicular* to the migration axis, i.e., $\mathbf{u}\cdot\mathbf{e}_y = 0$, so that the instantaneous velocity of *cross-stream* migration reads

$$v_m(t) = \dot{y}_c(t) = \frac{1}{\tilde{\zeta}}\sum_{i=1}^{N}\sum_{j\neq i}\mathbf{e}_y\cdot\zeta_i\ \mathbf{H}_{i,j}\cdot\mathbf{F}_j\ . \tag{7}$$

From Eq. (7) one can further define the *mean* steady-state CSM velocity, approached in the long-time limit, for each half-cycle, by averaging $v_m(t)$ over a half-period T_i, i.e.,

$$v_m^i = \langle v_m(\infty)\rangle_{T_i} = \frac{1}{T_i}\int_t^{t+T_i} dt'\ v_m(t')\ , \tag{8}$$

so that the *net* CSM velocity over a full shear cycle is simply given by $v_m = v_m^1 + v_m^2$.

For the analysis of the CSM mechanism, as discussed in the main text, it is useful to introduce a *contour-specific* migration velocity $v_m^\alpha(t)$, which can be assigned to the stiff and

bendy contour ($\alpha = s, b$) and defined via Eq. (7) as

$$v_m^\alpha(t) = \dot{y}_c^\alpha(t) = \frac{1}{\tilde{\zeta}} \sum_{i\in\alpha} \sum_{j\neq i} \mathbf{e}_y \cdot \zeta_i \, \mathbf{H}_{i,j} \cdot \mathbf{F}_j \ . \tag{9}$$

The *mean* migration velocity v_m^α of the α-contour can be determined from Eq. (8) by simply replacing $v_m(t)$ with $v_m^\alpha(t)$.

When the beads have the same radius, as in case of the ring, the drag coefficient $\zeta_i \equiv \zeta$ and $\sum_{i=1}^N \zeta_i = N\zeta$, so that Eq. (6) simplifies

$$\dot{\mathbf{r}}_c(t) = \frac{1}{N} \sum_{i=1}^{N} \left[\mathbf{u}(\mathbf{r}_i) + \sum_{j\neq i} \mathbf{H}_{i,j} \cdot \mathbf{F}_j \right] \ . \tag{10}$$

Eqs. (7) and (9) are modified accordingly.

The 2D *mean* HI-backflow $\mathbf{v}(\mathbf{r})$ at position $\mathbf{r}$ can be obtained from the instantaneous flow field

$$\mathbf{v}(\mathbf{r}, t) = \sum_{j=1}^{N} \mathbf{H}(\mathbf{r}, \mathbf{r}_j) \cdot \mathbf{F}_j \tag{11}$$

in a similar manner by using the mean forces, and shown in Fig. 3 (a) and (b) (see main text), demonstrating that the 2D profile of the backflow, as induced in the mean by the ring-forces during each shear-cycle T_i, is *elongational*.

C. Stiff Dumbbell: Zero Mean Migration

The equations of the Stokesian dynamics of bead-spring models, as provided in Section I, natively comprises also the case of an asymmetric dumbbell, composed of two beads of different radii $a_1 < a_2$ (corresponding to different drag coefficients $r_\zeta = \zeta_2/\zeta_1 > 1$) and connected by a linear spring with force constant k.

In this section we show that the *mean* cross-stream migration of a *stiff* asymmetric dumbbell at *steady state* is zero, for which purpose it is useful to rewrite the dumbbell equations in polar coordinates, starting from the full equations for each bead

$$\dot{\mathbf{r}}_1 \ = \ \mathbf{u}(\mathbf{r}_1) - \left[\frac{1}{\zeta_1}\mathbf{I} - \mathbf{H}_{1,2} \right] \cdot \mathbf{f}(R) + \mathbf{v}^{\mathrm{rot}}(\mathbf{r}_1) \ , \tag{12a}$$

$$\dot{\mathbf{r}}_2 \ = \ \mathbf{u}(\mathbf{r}_2) + \left[\frac{1}{\zeta_2}\mathbf{I} - \mathbf{H}_{2,1} \right] \cdot \mathbf{f}(R) + \mathbf{v}^{\mathrm{rot}}(\mathbf{r}_2) \ , \tag{12b}$$

where $\mathbf{u}(\mathbf{r}_{1,2})$ denote the unperturbed external flow at the bead position $\mathbf{r}_{1,2}$, while $\mathbf{v}^{\rm rot}(\mathbf{r}_{1,2})$ are the perturbations of the flow-field due to the shear-induced bead rotation, as given by Eq. (5). The matrix $\mathbf{H}(\mathbf{R}) \equiv \mathbf{H}_{1,2} = \mathbf{H}_{2,1}$ refers to the matrix elements of the Oseen-tensor, accountig for the hydrodynamic screening between the beads

$$\mathbf{H}(\mathbf{R}) = \frac{1}{8\pi\eta R}\left[\mathbf{I} + \mathbf{e}_R \otimes \mathbf{e}_R\right] \ , \tag{13}$$

with the bond unit vector $\mathbf{e}_R = \mathbf{R}/R$, the bond vector $\mathbf{R} = \mathbf{r}_1 - \mathbf{r}_2$ being the bond vector of the beads at position $\mathbf{r}_1$ and $\mathbf{r}_2$, and $R = |\mathbf{R}|$. The force $\mathbf{f}$ of the spring is measured with respect to the equilibrium bond length b

$$\mathbf{f}(R) = k(R-b)\ \mathbf{e}_R = f(R)\ \mathbf{e}_R \ . \tag{14}$$

Using the ζ-weighted center of the dumbbell ($N = 2$), i.e., $\mathbf{r}_c = \left(\zeta_1\mathbf{r}_1 + \zeta_2\mathbf{r}_2\right)/\zeta$ with $\zeta = \zeta_1 + \zeta_2$, the dynamic equations (12a) and (12b) can be rewritten as

$$\dot{\mathbf{r}}_c \ = \ \frac{1}{\zeta}\left[\zeta_1\left[\mathbf{u}_1 + \mathbf{H}(\mathbf{R})\cdot\mathbf{f}(R)\right] + \zeta_2\left[\mathbf{u}_2 - \mathbf{H}(\mathbf{R})\cdot\mathbf{f}(R)\right]\right] + \frac{1}{\zeta}\left(\zeta_1\mathbf{v}_1^{\rm rot} + \zeta_2\mathbf{v}_2^{\rm rot}\right) \ , \tag{15}$$

$$\dot{\mathbf{R}} \ = \ \mathbf{u}_1 - \mathbf{u}_2 + \mathbf{v}_1^{\rm rot} - \mathbf{v}_2^{\rm rot} - \left[\frac{1}{\zeta_1} + \frac{1}{\zeta_2}\right]\mathbf{f}(R) + 2\mathbf{H}(\mathbf{R})\cdot\mathbf{f}(R) \ . \tag{16}$$

Since we are interested in the CSM behavior of the dumbbell when it is at *steady-state*, i.e., *after* it has passed through the *transient regime*, one can drop the non-linear flow-fields $\mathbf{v}_{1,2}^{\rm rot}$ in Eqs. (15) and (16), which simplifies the following CSM analysis of a stiff dumbbell. As mentioned in the 2nd paragraph on Page 2 of Sect. I A, the flow-field $\mathbf{v}^{\rm rot}(\mathbf{r})$ is only required to assure the existence of a transient regime, so that the dumbbell can establish phase-locking and, hence, approach a steady-state *after* passing the transient. Once in steady state, the $\mathbf{v}^{\rm rot}(\mathbf{r})$-terms are no longer essential to describe the dumbbell dynamics.

Using polar coordinates of the radial and azimuthal unit vector, i.e., $\mathbf{e}_R = -(\cos\phi, \sin\phi)$ and $\mathbf{e}_\phi = (\sin\phi, -\cos\phi)$, along with $\mathbf{R} = R\ \mathbf{e}_R$, to project Eqs. (15) and (16) onto the $\mathbf{e}_R$ and $\mathbf{e}_\phi$ direction, exploiting the relation $\mathbf{H}(\mathbf{R})\cdot\mathbf{e}_R = (4\pi\eta R)^{-1}\mathbf{e}_R$ and Eq. (4), one obtains four, coupled, non-linear equations, describing the dumbbell dynamics in polar coordinates

$$\dot{\phi} \ = \ -S(t)\sin^2\phi\,, \tag{17}$$

$$\dot{R} \ = \ \frac{1}{2}S(t)R\sin(2\phi) - f(R)\left[\frac{1}{\zeta_1} + \frac{1}{\zeta_2} - \frac{1}{2\pi\eta R}\right] , \tag{18}$$

$$\dot{y}_c \ = \ \frac{\zeta_2 - \zeta_1}{\zeta_1 + \zeta_2}\frac{f(R)}{4\pi\eta R}\sin\phi \equiv v_m(t)\,, \tag{19}$$

$$\dot{x}_c \ = \ S(t)y_c + \frac{\zeta_2 - \zeta_1}{\zeta_1 + \zeta_2}\frac{f(R)}{4\pi\eta R}\cos\phi\,. \tag{20}$$

Importantly, in the numerical simulation of the dumbbell with the respective results shown in the main text [see Fig. 1 (a)] and in Sections II A, II B, and V A of the SI, the flows $\mathbf{v}^{\mathrm{rot}}(\mathbf{r}_{1,2})$ have been taken into account.

Equation (19) describes the instantaneous migration velocity $v_m(t) \equiv \dot{y}_c(t)$ of the dumbbell and with $f(R) = k(R-b)$, cf. Eq. (14), leads to the final expression of Eq. (3), as given in the main text. The *net* migration step per half period $T/2$ can be obtained by integrating Eq. (19) over a half period

$$\Delta y_c = \int_t^{t+T/2} dt'\ v_m(t') = \frac{k}{4\pi\eta}\frac{r_\zeta - 1}{r_\zeta + 1} \int_t^{t+T/2} dt'\ \frac{R(t') - b}{R(t')}\ \sin\phi(t')\,. \tag{21}$$

When the dumbbell is rigid, the bond length does not change ($\dot{R} = 0$) and is fixed to the equilibrium bond length $R = b$. This condition imposes a constraint on the dumbbell dynamics, resulting in a constraining force $f(R)$ which can be determined from Eq. (18)

$$f(R=b) = \frac{S(t) b \sin 2\phi}{2\left(\frac{r_\zeta+1}{\zeta_2} - \frac{1}{2\pi\eta b}\right)}\,. \tag{22}$$

The shear rate $S(t)$ in Eq. (22) can be replaced via Eq. (17), so that the constraint force $f(b)$, appearing in Eq. (19), can be eliminated. We then obtain an expression for the migration step per half cycle, which depends only on the orientation ϕ_1 and ϕ_2 at the beginning, respectively, end of a half-cycle

$$\Delta y_c = -\underbrace{\frac{1}{8\pi\eta}\frac{r_\zeta - 1}{r_\zeta + 1}\frac{1}{\left(\frac{r_\zeta+1}{\zeta_2} - \frac{1}{2\pi\eta b}\right)}}_{=:C} \int_{\phi_1}^{\phi_2} d\phi \frac{\sin 2\phi}{\sin\phi} = -2C \int_{\phi_1}^{\phi_2} d\phi \cos\phi = 2C\left[\sin\phi_1 - \sin\phi_2\right] \tag{23}$$

Using Eq. (23) one can now determine the *net* migration step for a full shear cycle by simply adding the respective steps for each half cycle. During the first half period $T/2$, the orientation angle ϕ of the dumbbell changes from $\phi_1 \to \phi_2$ where the dumbbell migrates the step

$$\Delta y_c^{(1)} = 2C\left[\sin\phi_1 - \sin\phi_2\right]\ . \tag{24}$$

During the second half of the shear cycle, the dumbbell swings back and reverses its orientation back from $\phi_2 \to \phi_1$, and the dumbbell performs the step

$$\Delta y_c^{(2)} = 2C\left[\sin\phi_2 - \sin\phi_1\right] = -\Delta y_c^{(1)}\ . \tag{25}$$

From Eqs. (24) and (25) follows that the magnitude of the migration steps are the same, but have the opposite sign. Therefore, when the dumbbell is *rigid* the *net* migration over a full shear cycle vanishes, i.e., $\Delta y_c = \Delta y_c^{(1)} + \Delta y_c^{(2)} = 0$.

D. Capsule (3D)

The Lattice-Boltzmann (LB) method is a mesoscopic method for solving fluid problems which is based on a discretization of space and velocities. Over the last years it has become a well-established method and we omit the details which can be found in e.g.[4–6]. We use the D3Q19 scheme as implemented in the ESPResSo package[7,8].

For the elastic capsule, we implemented the immersed boundary method into ESPResSo, following the work of Refs.[9,10]. The surface of the particle is discretized into 1280 triangles and endowed with an elastic shear and a bending resistance. The elastic force is described by the Neo-Hookean law and the bending resistance by a Helfrich Hamiltonian[11]. We add an additional force to ensure volume conservation as in[10].

The x-z periodic LB-grid has a size of $120 \times 180 \times 120$ lattice units and is bounded by walls in the y direction. A linear shear flow is imposed by moving the upper and lower walls in opposite directions with a fixed velocity. The physical length and time scales are chosen such that the grid dimension in SI units is $720 \times 1080 \times 720$ μm^3, the density and kinematic fluid viscosity are 1000 kg/m^3 and 10^{-6} m^2/s, respectively (corresponding to water); the frequency is 1.75 Hz, the shear rate is 22.22 s^{-1}, and the time step is 10.8 μs.

The particle has a radius of 39.6 μm, a bending resistance in the soft half of $9.2 \cdot 10^{-17}$ Nm, and an elastic modulus of $4.4 \cdot 10^{-5}$ N/m. For comparison, the typical values for a red blood cell are 4 μm radius, $2 \cdot 10^{-19}$ Nm bending resistance, and $5 \cdot 10^{-6}$ N/m elastic modulus. A typical timescale for the capsule relaxation can be defined via $\tau_b = \eta a^3/\kappa_2$.

Table II lists the respective parameters for the 3D capsule (radius a, bending stiffness $\kappa_{1,2}$), and the shear flow (shear rate $\dot{\gamma}$, period T, viscosity η) used in the simulation. The conversion of each parameter "Q" between the "SI" units and "sim" units is realized by multiplying Q^{SI} with the powers of the conversion parameters for time C_t, length C_x, and density C_ρ; for example, the dynamic viscosity $\nu^{\mathrm{SI}} = \nu^{\mathrm{sim}} \cdot {\mathrm{C}_x}^2/\mathrm{C}_t$, so that $[\nu] = \mathrm{m}^2/\mathrm{s}$. Here, we choose $\mathrm{C}_x = 6.0 \cdot 10^{-6}$ m, $\mathrm{C}_t = 36.0 \cdot 10^{-5}$ s, and $\mathrm{C}_\rho = 10^3$ kg/m^3 to prescribe a micrometer length scale, and the fluid density and viscosity to resemble that of water.

TABLE II: Parameters used in the simulation of the 3D capsule.

particle kind	a	$\kappa_{1,2}$	$\dot{\gamma}$	T	η
capsule (SI units)	39.6 μm	$9.2 \cdot 10^{-17}/13.8 \cdot 10^{-17}$ Nm	22.22 s^{-1}	0.57 s	10^{-3} Pas
capsule (sim. units)	6.6	1.53/2.3	0.008	1590	10.0

II. GENERIC BEHAVIOR OF CROSS-STREAM MIGRATION (CONTINUED)

A major outcome of this study is that the cross-stream migration of all three kinds of particles behaves *qualitatively* the same, irrespective of the model details and dimensionality of the particle, which lets us conclude that the CSM is a *generic* property.

Here we show that the CSM characteristics in terms of *orientation robustness* and *frequency dependence*, discussed via Fig. 4 and 5 of the main text by example of the ring-polymer (2D), are also displayed by the dumbbell (1D) and the capsule (3D).

A. Orientation Robustness of the Dumbbell (1D) and Capsule (3D)

Figure 1 shows the dependence of the migration velocity $\langle v_m(t)\rangle_T$ of the (left) dumbbell and (right) capsule, averaged over the period T, as a function of time $t\dot{\gamma}$ for different initial orientations ϕ_0. In case of the dumbbell, ϕ_0 is taken from the ϕ_0-intervals $I^+ = [1.1; 2.0]\,\pi$ and $I^- = [0.1; 1.0]\,\pi$, where $I^{+/-}$ denotes the interval leading to a positive or negative v_m, respectively. For the capsule, the corresponding intervals are given by $I^+ = [1.5; 2.25]\,\pi$ and $I^- = [0.5; 1.25]\,\pi$ and quantitatively differ to those of the dumbbell and the ring-polymer.

Similar to the 2D ring (see main text, Fig. 4), the migration velocity $\langle v_m(t)\rangle_T$ of the dumbbell and capsule depends on ϕ_0 within a transient regime and approaches a steady-state, common value $v_m \equiv \langle v_m(\infty)\rangle_T$ in the long-time limit, independent of ϕ_0 in each case. Again, the sign of v_m depends on whether ϕ_0 is taken from the interval I^+ or I^-; the width of both intervals is with $\Delta I^{+/-} \approx \pi$ rather large, so that the terminal CSM velocity v_m of the 1D dumbbell and 3D capsule is quite robust against uncertainties in ϕ_0, consistent with the CSM behavior of the 2D ring (see main text, Fig. 4).

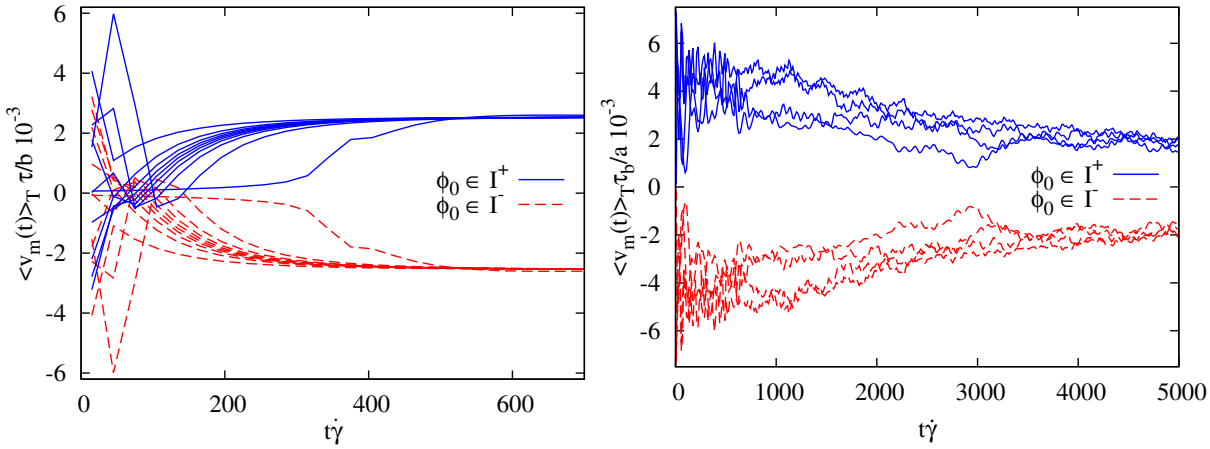

FIG. 1: (Color online) T-averaged migration velocity $\langle v_m(t)\rangle_T$ vs. time $t\dot\gamma$ shown for the 1D dumbbell (left) and 3D capsule (right). In each case, the 2π-range of ϕ_0 can be grouped in two intervals I^+ and I^-, leading to a positive or negative v_m. The intervals $I^{+/-}$ are: (left) dumbbell: $I^+ = [1.1; 2.0]\,\pi$ and $I^- = [0.1; 1.0]\,\pi$, (right) capsule: $I^+ = [1.5; 2.25]\,\pi$ and $I^- = [0.5; 1.25]\,\pi$.

B. Frequency Dependence of the Dumbbell (1D) and Capsule (3D)

Figure 2 shows the dependence of the migration velocity v_m versus the period $T\dot\gamma$ (inverse frequency) with $\dot\gamma$ fixed. Also here, about four dynamic regimes can be identified for the (left) 1D dumbbell and (right) 3D capsule, depending on the period T similar to the 2D ring- polymer (see main text, Fig. 5). The v_m-T behavior of the capsule can be characterized in the same manner as for the ring due to the close resemblance of the two systems, namely a combination of shear deformation at low frequency and a setting in of a tank-treading dynamics at medium and large frequencies.

For the dumbbell, a classification in terms of a shear- and tank-treading dynamics is not adequate, since the "shape" of the dumbbell with $N = 2$ beads can not be associated with a proper contour as opposed to the 2D/3D particles. Instead, the dumbbell dynamics should be described in terms of a *stretch-compress* dynamics of the bond length along with a *pendulous* and *rotational* motion.

The analogy between the 1D and 2D/3D systems consists then in identifying the dumbbell's shear-induced pendulous dynamics (back- and forward swing cycles along with the stretch-compress cycle of the bond length) with the oscillatory shear deformation (low frequency) of the ring and capsule, respectively, and accordingly the dumbbell rotation with tank-treading (medium/large frequency).

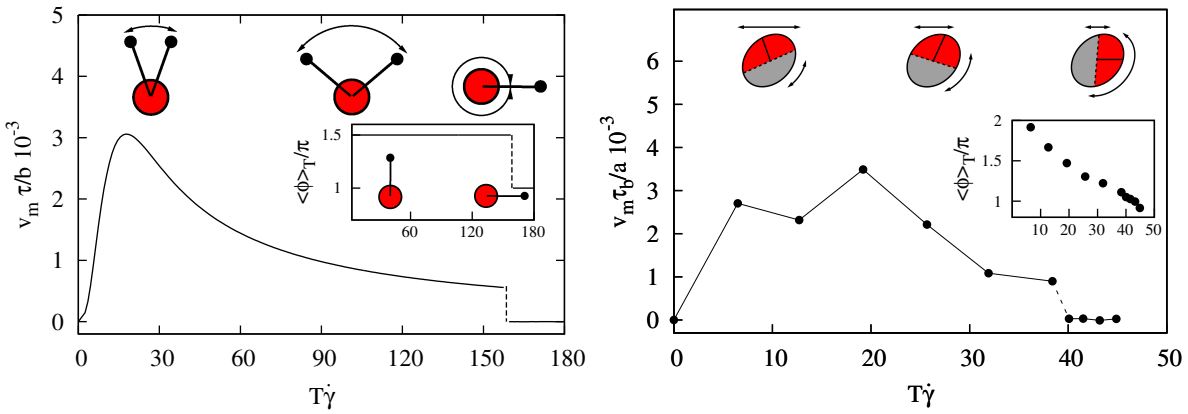

FIG. 2: (Color online) Migration velocity v_m versus switching period $T\dot{\gamma}$ (inverse frequency), shown for the 1D dumbbell (left) and 3D capsule (right) with four dynamic regimes: (1) oscillatory motion (pendular/shear deformation) at small T (high frequency), (2) weak rotational/tank-treading motion superposed with (1) (mid frequency), (3) enhanced rotational/tank-treading dynamics at large T (low frequency), and (4) zero net migration. Insets: T-averaged mean orientation $\langle\phi\rangle_T$ vs. $T\dot{\gamma}$ of the dumbbell and the capsule, respectively. At high frequency, the dumbbell (capsule) orientation $\langle\phi\rangle_T \approx 1.5\pi$ (1.5π), i.e., the small ζ_1 (stiff κ_2-contour) remains in the mean in the upper half-space ($v_m > 0$). Once $T\dot{\gamma} > 160$ (40), the mean orientation flips to $\langle\phi\rangle_T \approx \pi$ (π), i.e., the dumbbell (capsule) orientation has an upper-lower symmetry ($v_m = 0$).

What matters for the cross-stream migration is that the asymmetric parts of each type of particle reside in the *mean* in one of the half-spaces when the frequency is high (small T), whereas at medium and in particular at low frequency (large T) there is a "re-shuffling" of the differing constituents (in terms of friction coefficient or stiffness) between the two half-spaces; whether this re-shuffling occurs via rotation (dumbbell) or tank-treading (ring, capsule) is irrelevant and leads to the *same qualitative*, i.e., generic behavior for all three kinds of particles (see main text: Fig. 4 and 5 and SI: Fig. 1 and 2, respectively).

III. SAMPLE MOVIES: ILLUSTRATION OF MIGRATION REGIMES

The MP4-format movies, cf. Table III, show the shear-induced dynamics for each particle kind in the typical CSM regime with the values for $T\dot{\gamma}$ given in Table III. For each case, these values are chosen in accord with the v_m-$T\dot{\gamma}$ curves of Fig. 5 (main text: 2D ring) and Fig. 2 (SI: 1D dumbbell and 3D capsule), starting with small values of $T\dot{\gamma}$ (high frequency), followed by medium $T\dot{\gamma}$-values (mid frequency), and finally large periods (low

frequency). The movie set M1-M9 visualize how the particle dynamics traverses from the pendulous/deformation (pen/def) regime at high frequency (small $T\dot{\gamma}$) to the rotation/tank-treading (rot/TT) dominated regime at low frequency (large $T\dot{\gamma}$).

TABLE III: MPEG movies M1-M9 visualizing the migration dynamics characteristic for each regime. For each movie "M#:" the value of $T\dot{\gamma}$ used in the simulation is given.

particle kind	pen/def	pen/def+rot/TT	rot/TT
dumbbell	M1: 5	M2: 100	M3: 180
ring	M4: 2	M5: 10	M6: 12
capsule	M7: 6	M8: 26	M9: 45

IV. ORIGIN OF ABRUPT CSM-DROP: $\langle\phi(t)\rangle_T$ PHASE-SPACE ANALYSIS

In this section, we extend our brief discussion of the abrupt v_m-drop (see main text: Fig. 5 and SI: Fig. 2) and provide here a more in-depth analysis. As already discussed in detail in the main text, the cross-stream migration $v_m = \langle v_m(\infty)\rangle_T$ is intimately correlated with the *mean* steady-state orientation $\langle\Phi\rangle_T \equiv \langle\phi(\infty)\rangle_T$, acquired by the particle over the course of *one* shear cycle and can be tuned via the external control parameter $T\dot{\gamma}$. Figure 5 (main text) and Fig. 2 (SI) demonstrate this close relationship for all three particles, how the mean particle orientation is the key controlling factor for the presence or absence of CSM[13]. In case of the ring, cf. Fig. 5 (main text), such a change of v_m occurs once the period $T\dot{\gamma}$ exceeds a critical value $T_c\dot{\gamma} \approx 11$.

In order to gain a better insight on why the particles alter their *stable mean* orientation when the switching period T is varied, we determine numerically the phase-space of the time-dependent *mean* orientation $\langle\dot{\phi}(t)\rangle_T$-$\langle\phi(t)\rangle_T$, obtained by launching the particle at *different* initial orientations ϕ_0 over the entire interval $\phi_0 \in [0.0, 2.0]\ \pi$, and keeping the switching period $T\dot{\gamma}$ fixed. This procedure is then repeated at different (but fixed) values of $T\dot{\gamma}$. Such a phase-plot allows one then to analyze and identify in general the set of *stable* mean orientations (attractors) the particle can adopt[12]. In accord with the discussion in the main text, we use again the ring-polymer as representative particle.

Figure 3 shows such a phase-space plot for the ring (following the above procedure) for three different values of the switching period around the critial value $T_c\dot{\gamma} \approx 11$, where the

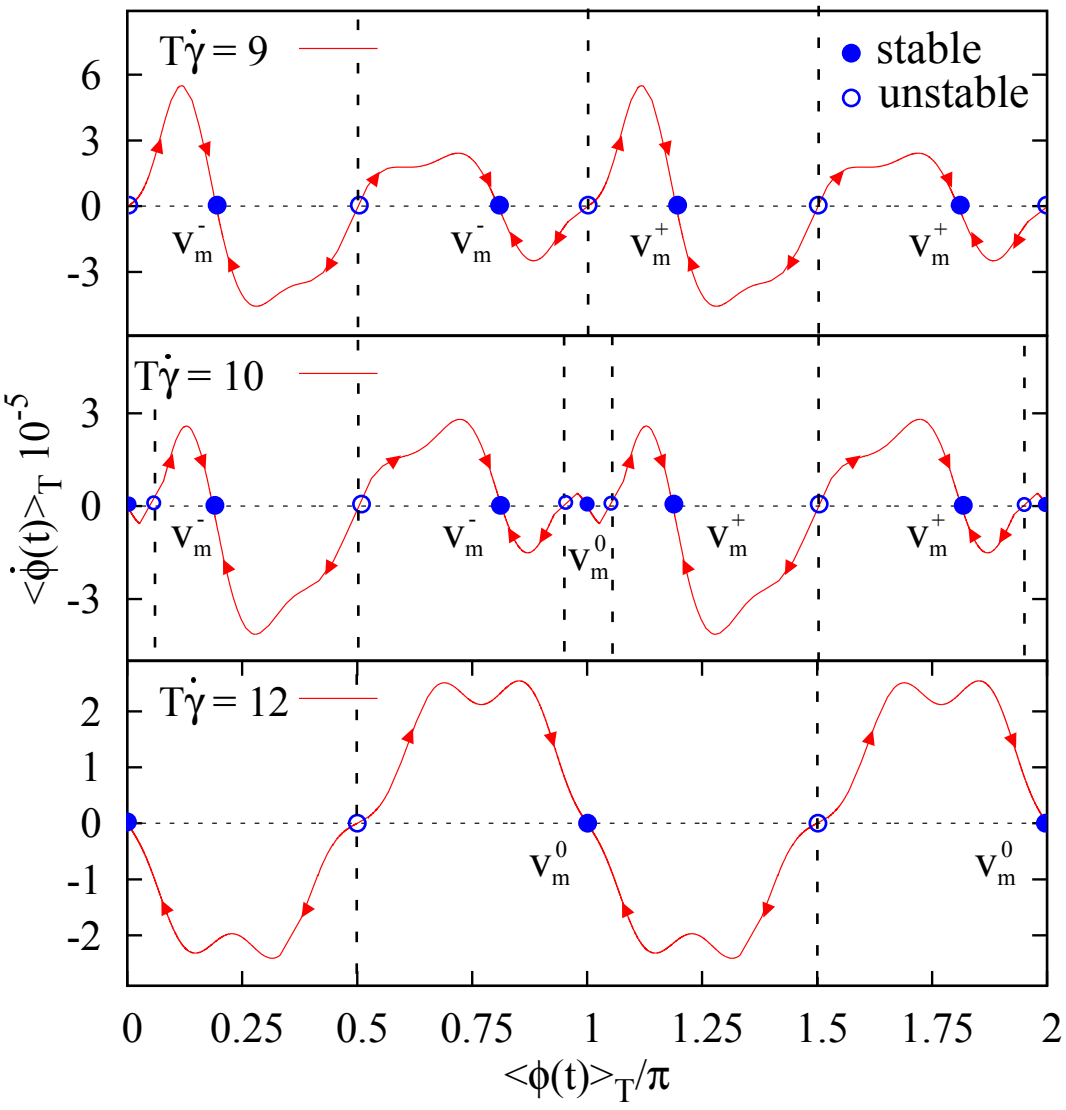

FIG. 3: (Color online) Phase-space of the time-dependent mean orientation $\langle\dot{\phi}(t)\rangle_T - \langle\phi(t)\rangle_T$ for the same ring, as in Fig. 5 (main text) at three different values of the switching period $T\dot{\gamma} = 9$, 10, and 12, around the critical value $T_c\dot{\gamma} \approx 11$, marking the onset of the abrupt change of the ring orientation. For each value of $T\dot{\gamma}$, there is a distinct set of stable (symbol: •) and unstable (symbol: ∘) fixed points ($\langle\dot{\phi}\rangle_T = 0$). The stable fixed points (FP) correspond to non-migrating (v_m^0) orientations with $\langle\phi\rangle_T^0 = \{0.0, 1.0\}$ π or (positive/negative) migrating states ($v_m^{+/-}$) with a mean orientation $\langle\phi\rangle_T^{+/-}$ other than 0.0 π and π. The switching period $T\dot{\gamma}$ sensitively controls whether migrating and non-migrating orientations coexist ($T\dot{\gamma} = 10$) or not ($T\dot{\gamma} = 9$ and 12). The angular interval between neighboring *unstable* FPs define the range of an asymptotically stable FP, as marked by the dashed lines. When the transient angle $\langle\phi(t)\rangle_T$ lies within the range of a specific stable FP, the ring approaches the mean orientation $\langle\phi\rangle_T^{FP}$ of this fixed point.

abrupt change of the mean orientation occurs, i.e., $T\dot{\gamma} = 9$, 10, and 12. From the phase-space plot shown in Fig. 3 one can easily determine the so-called orientation *fixed points* (FP) of the system, which refer to those mean orientations $\langle\phi\rangle_T^{FP}$ where $\langle\dot{\phi}\rangle_T = 0$, as marked by the symbols $\bullet$ and $\circ$ in each case. Whether an FP is *stable* (symbol: $\bullet$) or *unstable* (symbol: $\circ$) depends on the slope $\beta = d\langle\dot{\phi}\rangle_T/d\langle\phi\rangle_T$ near the FP. If $\beta < 0$, the FP is *asymptotically stable* and the orientation $\langle\phi(t)\rangle_T$ moves towards the orientational fixed-point $\langle\phi\rangle_T^{FP}$, as long as $\langle\phi(t)\rangle_T$ lies within the range of the (orientational) attractor, while it moves away from the FP if $\beta > 0$. The respective FP is then *unstable*[12]. Near the fixed point, this behavior can be formally described by $d_t\langle\phi(t)\rangle_T = \langle\dot{\phi}(t)\rangle_T \approx \beta\left[\langle\phi(t)\rangle_T - \langle\phi\rangle_T^{FP}\right]$ with $d_t = d/dt$, reflecting the exponential behavior towards or away from the FP.

Applying these general concepts to the three different phase-space plots of Figure 3, one can identify a total of 8 FPs when $T\dot{\gamma} = 9$, among which the 4 orientations $\langle\phi\rangle_T^{FP} \in I_{FP}^{<} = [0.25, 0.8, 1.25, 1.8]\ \pi$ are asymptotically stable ($\beta < 0$) and the other ones are unstable ($\beta > 0$). Importantly, the *range* of each attractor (marked by the vertical dashed lines) is about 0.5 π, so that for a given initial orientation $\phi_0 \in [0.0, 2.0]\ \pi$ the transient ring orientation $\langle\phi(t)\rangle_T$ evolves towards *one* of these available stable FPs and acquires its affiliated steady-state *mean* orientation $\langle\phi\rangle_T^{FP} \in I_{FP}^{<}$, when $\langle\phi(t)\rangle_T$ lies within the range of this attractor. We note that while in general for any (but fixed) value of $T\dot{\gamma}$ all FPs are available to the particle, it can accept only *one* orientational fixed point for only *one* initial angle ϕ_0. As discussed in the main text, the existence and direction of the CSM depends on the mean steady state particle orientation $\langle\phi\rangle_T = \langle\phi(\infty)\rangle_T$, controlling whether the stiff/bendy contour portions reside in the *mean* within the upper and lower half-space.

When $T\dot{\gamma} = 9$, the ring can only adopt the mean orientations $\langle\phi\rangle_T \in I_{FP}^{<} = [0.25, 0.8, 1.25, 1.8]\ \pi$, which correspond to migrating orientations only with $v_m^{+/-} \neq 0$, cf. Fig. 3 (top). Two of these states, i.e., $\langle\phi\rangle_T^{+} = [1.25, 1.8]\ \pi$, lead to a *positive* migration ($v_m^{+} > 0$) since the stiff/bendy part of the ring contour reside in the mean in the upper/lower half-space (as discussed in the main text.), and vice versa for the two remaining states $\langle\phi\rangle_T^{-} = [0.25, 0.8]\ \pi$. Note that within each class of stable states $\langle\phi\rangle_T^{+/-}$ the CSM steady state velocity v_m is the same, while the respective mean orientation is different.

When the period is further increased to $T\dot{\gamma} = 10$, but still lower than the critical value $T_c\dot{\gamma} = 11$, the previous set of fixed points in terms of their *value* remains, while four new FPs appear at around $[0.1, 0.9, 1.1, 1.9]\ \pi$, all of which are *unstable*, cf. Fig. 3 (middle).

Importantly, the two previously unstable FPs at $\langle\phi\rangle_T^{FP} = \pi$ and 2.0 π reverse their character and become now *stable* fixed points (attractors). Since these mean orientations have an upper-lower symmetry where an equal amount of the stiff and bendy contour are located in the mean within the upper and lower half-space, these states refer to *non-migrating* orientations ($v_m^0 = 0$). For the initial ring orientation of $\phi_0 = 2.0\ \pi$, the ring does not approach the new non-migrating FP $\langle\phi\rangle_T^{FP} = 2.0\ \pi$, but still locks-in to the "old" migrating fixed point $\langle\phi\rangle_T^{FP} = 1.8\ \pi$, as shown in the $\langle\phi\rangle_T$-$T\dot{\gamma}$ plot of Fig. 5 (inset: main text). This occurs because over the course over many shear cycles, the transient angle $\langle\phi(t)\rangle_T$ of the ring does not lie within the narrow range of the 2π-attractor, but is located within the range of the FP $\langle\phi\rangle_T^{FP} = 1.8\ \pi$, which has a broad stability range of about 0.5 π, cf. Fig. 3 (middle).

When the period exceeds the critical value $T\dot{\gamma} > T_c\dot{\gamma} = 11$, the coexistence of migrating and non-migrating states vanishes entirely, and only a total of 4 fixed points remain, as shown in Fig. 3 (bottom). The respective two asymptotically stable FPs with the mean steady-state orientation $\langle\phi\rangle_T^{FP} \in I_{FP}^{<} = [1.0, 2.0]\ \pi$ are all *non-migrating* states v_m^0. Simultaneously, their attractor range has substantially grown from about 0.1 π ($T\dot{\gamma} = 10$) to π ($T\dot{\gamma} = 12$).

The abrupt drop of the migration velocity v_m is therefore a direct consequence of its strong link to the *mean* orientation $\langle\phi\rangle_T$, leading to a discrete sequence of migrating ($v_m^{+,-}$) or non-migrating (v_m^0) states, which may even coexist. The number and type of these stable states $\langle\phi\rangle_T^{FP}$ (attractors) can be externally tuned by the control parameter $T\dot{\gamma}$ with the result that the entire attractor landscape changes, including the appearance/disappearance of new/old FPs or the reversal of stable FPs to unstable ones and vice versa. In case of the ring and an initial orientation of $\phi_0 = 2.0\ \pi$ this means that the orientational attractor $\langle\phi\rangle_T^{FP} = 1.8\ \pi$ disappears once $T\dot{\gamma} > T_c\dot{\gamma} \approx 11$, so that $\langle\phi(t)\rangle_T$ adopts the orientation 1.8 π only transiently while a new stable orientational fixed point emerges at $\langle\phi\rangle_T^{FP} = 2.0\ \pi$. Since the value 1.8 π lies within the (extended) range of the 2π-attractor, the orientation $\langle\phi(t)\rangle_T$ approaches this new fixed point, corresponding to a non-migrating state. Hence, at the critical value of $T_c\dot{\gamma} = 11$, there is a discontinuous transition of the ring mean orientation $\langle\phi\rangle_T^{FP}$ from a v_m^+-migrating state to a v_m^0-non-migrating one, and appears in the v_m-$T\dot{\gamma}$ plot as abrupt drop of v_m, as shown in Fig. 5 (main text).

V. CSM-ROBUSTNESS AGAINST VARIATIONS OF TILT-ANGLE Θ

In Fig. 4 (main text) and in Fig. 1 (SI: Sect. II A) we have shown that $v_m > 0$ when the initial orientation $\phi_0 \in I^+$, and $v_m < 0$ for $\phi_0 \in I^-$. In all these cases we assumed that the *second* angle (tilt angle θ), determining the particle orientation outside the x-y shear plane, is zero, as indicated in the particle sketches of Fig. 1 (a)-(c) (see main text).

In general, however, one must expect that the direction of the CSM (sign of v_m) does not only depend on the initial *in-plane* orientation (specified by $\phi_0 \in I^{\pm}$), but also on the θ_0-orientation outside the y-x shear plane.

In the following sections we show that the cross-stream behavior, as characterized by the finite slope of the lateral position $y_c(t)$ corresponding to a finite migration velocity $v_m \neq 0$, persist and remains *robust* for all three particles, if their initial orientation $\{\phi_0, \theta_0\}$ is allowed to vary also away from the shear plane ($\theta_0 \neq 0.0$).

A. Dumbbell (1D)

Figure 4 (left) shows the lateral position $y_c(t)$ vs. time for the 1D dumbbell at varying tilt-angles $\theta_0 \in [0.0, 0.5]\ \pi$ outside the y-x shear plane and an in-plane initial orientation of $\phi_0 = 2.0\ \pi$. The CSM behavior persist over the entire range of θ_0-orientations with $\theta_0^+ \in I^+ = [0.0, 0.5[\ \pi$, leading to a positive cross-stream migration (v_m^+). Only for the single tilt angle $\theta_0^0 = 0.5\ \pi$, the CSM vanishes as reflected by the zero slope of $y_c(t)$.

Figure 4 (right) shows the respective time-dependence of $\theta(t)$, which approaches $\theta(\infty) \approx 0.0\ \pi$ for long times if $\theta_0^+ \in I^+$. In these cases, the dumbbell reorients back towards the stable orientation $\theta(t) \to 0.0\ \pi$, i.e., the dumbbell axis lies within the y-x shear plane. The tilt angle $\langle\theta\rangle_T^{FP} = 0.0\ \pi$ refers therefore to an *asymptotically stable* fixed point (FP)[12].

In turn, for $\theta_0 = 0.5\ \pi$ the tilt angle remains constant (unstable FP) since the dumbbell lies within the z-x plane (this plane is perpendicular to the shear plane), in which case the shear is ineffective as the dumbbell has no lateral extension (zero thickness) and $v_m = 0$.

Overall, the CSM-effect of the dumbbell is quite *robust* against a broad variation of the initial orientations with regards to ϕ_0 and θ_0.

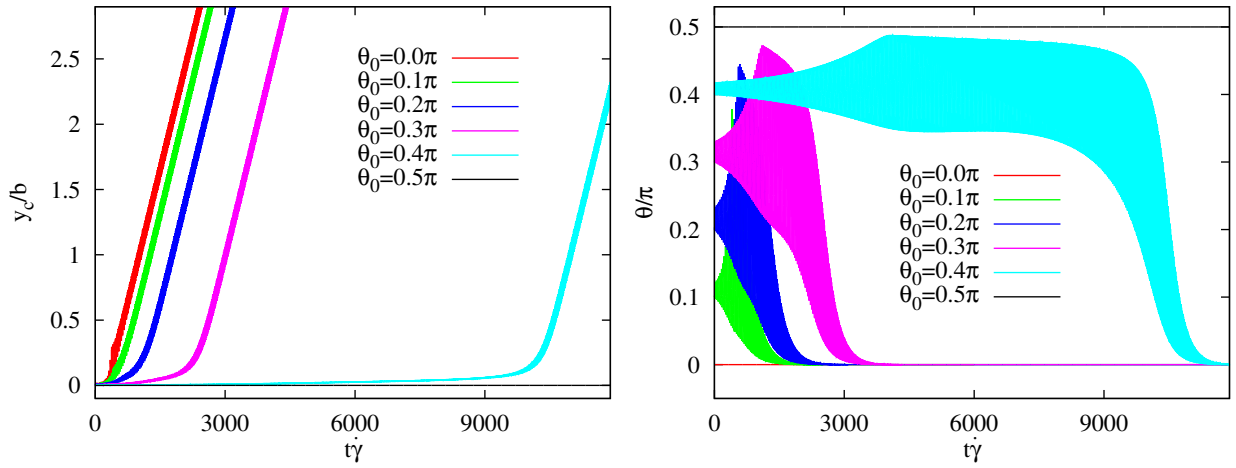

FIG. 4: (Color online) Robustness of the CSM for the 1D dumbbell in regards to variations of the tilt angle θ_0 outside the y-x shear plane with $\theta_0 \in [0.0, 0.5]\ \pi$; the initial in-plane orientation is $\phi_0 = 2.0\ \pi$. Left: Lateral position $y_c(t)$ vs. time $t\dot{\gamma}$, displaying the persistence of the CSM effect ($v_m^+ > 0$) for the entire range of θ_0-orientations with $\theta_0^+ \in I^+ = [0.0, 0.5[\ \pi$. Only for $\theta_0 = 0.5\ \pi$, the CSM is zero. Right: Time-dependence of the respective tilt angle $\theta(t)$, showing how the dumbbell axis reorients back towards the stable orientation within the y-x shear plane ($\theta(\infty) = 0.0\ \pi$) if $\theta_0^+ \in I^+$. When $\theta_0 = 0.5\ \pi$ the dumbbell retains this orientation.

B. Ring (2D)

In contrast to the 1D dumbbell and 3D capsule, both of which have an axis of *high rotational symmetry*, the 2D ring-polymer has only a twofold 180^o-symmetry since it is *planar*, so that the ring can be tilted outside the y-x shear plane in two ways, namely by rotating its plane either along the x- or y-axis.

Figure 5 (left) shows the lateral position $y_c(t)$ vs. time for the 2D ring with its plane being rotated along the x-axis (top) and y-axis (bottom), respectively, at varying tilt-angles $\theta_0^{x,y} \in [0.0, 0.5]\ \pi$ outside the y-x shear plane and an in-plane initial orientation of $\phi_0 = 2.0\ \pi$.

Similar to the dumbbell, the CSM behavior of the ring also persist over the entire range of $\theta_0^{x,y}$-orientations with $\theta_0^+ \in I^+ = [0.0, 0.5[\ \pi$, leading to a positive cross-stream migration ($v_m^+ > 0$), irrespective along which axis the ring plane is rotated. Only for the single tilt angle $\theta_0^0 = 0.5\ \pi$, the ring does not migrate. However, contrary to the dumbbell and capsule, there is no longer a common steady-state migration velocity v_m^+ in the long-time limit, but depends on the initial tilt angle θ_0^+.

Figure 5 (right) shows for either case the respective time-dependence of $\theta^{x,y}(t)$, which

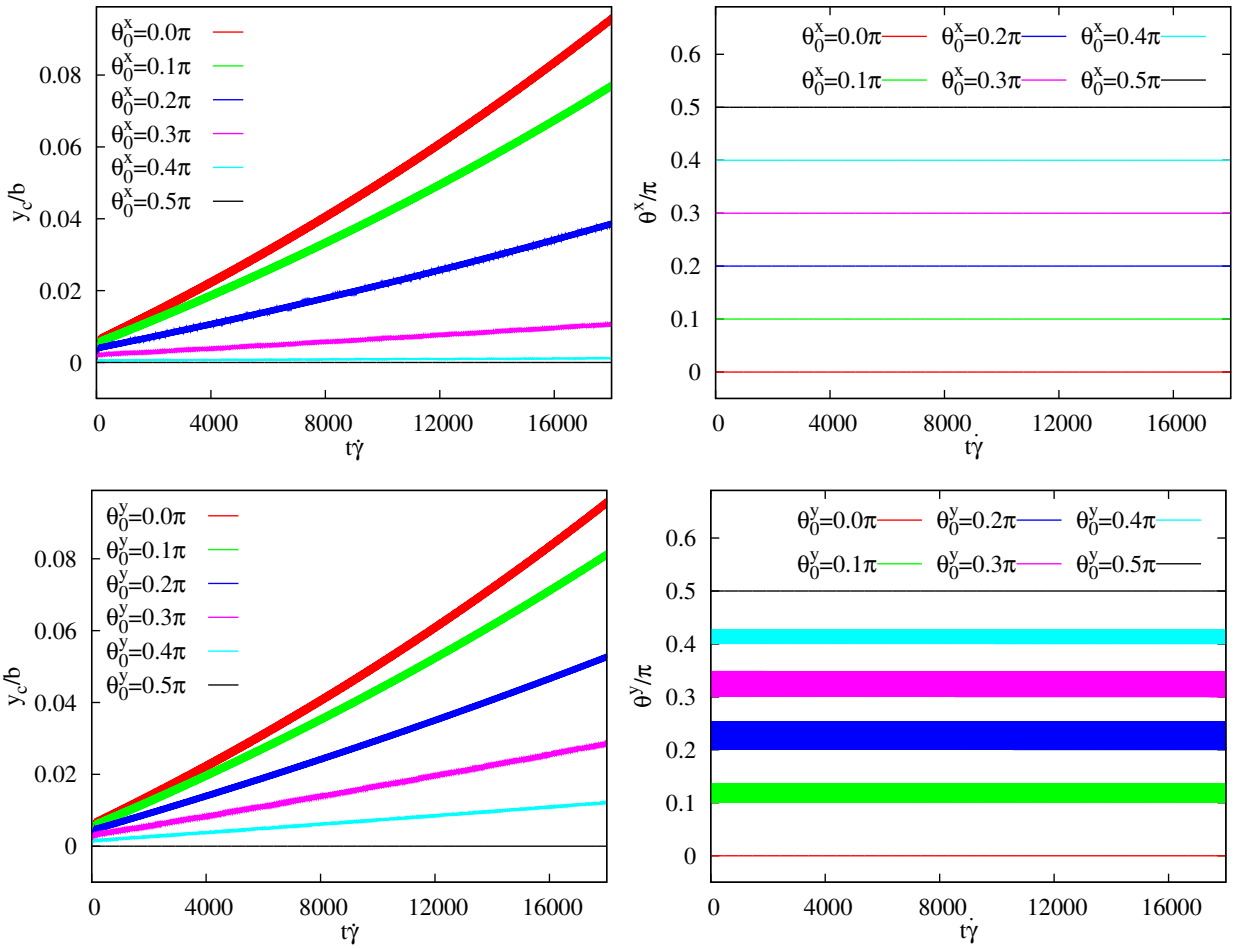

FIG. 5: (Color online) Robustness of the CSM for the 2D ring with respect to θ_0-variations outside the y-x shear plane, and an initial in-plane orientation of $\phi_0 = 2.0\ \pi$ (similar to Fig. 1 (b): see main text). The top panel refers to θ_0^x-orientations, where the ring plane is rotated along the x-axis, and the bottom panel refers to θ_0^y-orientations. Left: Lateral position $y_c(t)$ vs. scaled time $t\dot{\gamma}$, displaying the persistence of the CSM effect ($v_m > 0$) for the entire range of off-plane orientations $\theta_0^{x,y} \in [0.0, 0.5[\ \pi$. Only when $\theta_0^{x,y} = 0.5\ \pi$, the CSM is zero. Right: Time dependence of the respective off-plane orientation $\theta^{x,y}(t)$ starting at $\theta_0^{x,y}$, showing that the off-plane orientation of the ring $\theta^{x,y}(t)$ remains in the mean constant.

remains constant for all times, while the ring continues to migrate within the y-x shear plane. Hence, the ring plane does not reorient back towards the y-x shear plane as the dumbbell and capsule do, but holds its initial orientation $\theta_0^{x,y}$. In this case, all angles $\langle\theta\rangle_T^{FP} = \theta_0^{x,y} \in [0.0, 0.5]\ \pi$ are so-called *neutral stable* fixed points $\langle\dot{\theta}\rangle_T = 0$[12].

Overall, the CSM-effect of the ring is quite *robust* against a broad variation of the initial orientations with regards to ϕ_0 and θ_0.

C. Capsule (3D)

Finally, we show in Fig. 6 (left) the lateral position $y_c(t)$ vs. time for the 3D capsule at varying tilt-angles $\theta_0 \in [0.0, 0.5]\ \pi$ outside the y-x shear plane and an in-plane initial orientation of $\phi_0 = 2.0\ \pi$. Similar to the 1D and 2D particle, the CSM behavior persist also for the 3D capsule over a broad range of θ_0-orientations outside the shear plane with $\theta_0^+ \in I^+ = [0.0, 6/18]\ \pi$, leading to a positive cross-stream migration (v_m^+). When $\theta_0^0 \in I^0 = [7/18, 0.5]\ \pi$, the CSM vanishes in the long-time limit, as reflected by the flattening of $y_c(t)$.

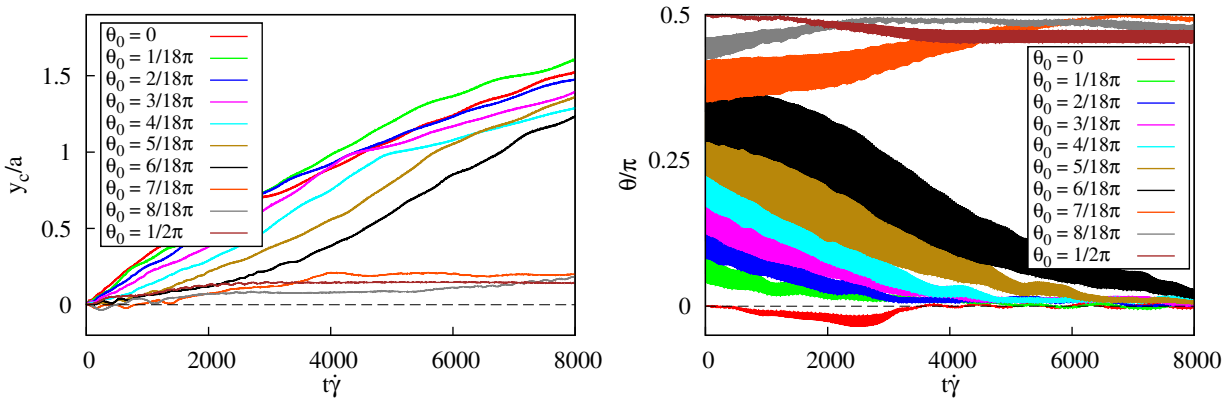

FIG. 6: (Color online) Robustness of the CSM for the 3D capsule in regards to variations of the tilt angle θ_0 outside the y-x shear plane with $\theta_0 \in [0.0, 0.5]\ \pi$; the initial in-plane orientation is $\phi_0 = 2.0\ \pi$. Left: Lateral position $y_c(t)$ vs. time $t\dot{\gamma}$, displaying the persistence of the CSM effect ($v_m^+ > 0$) for a broad range of θ_0-orientations with $\theta_0^+ \in I^+ = [0.0, 6/18]\ \pi$. For other orientations $\theta_0^0 \in I^0 = [7/18, 0.5]\ \pi$ the CSM is nearly zero. Right: Time-dependence of the respective tilt angle $\theta(t)$ showing how the capsule axis reorients back towards the stable orientation within the y-x shear plane ($\theta(\infty) \approx 0.0\ \pi$) if $\theta_0^+ \in I^+$. For $\theta_0^0 \in I^0$ the tilt angle approaches another stable orientation $\theta(\infty) = 0.5\ \pi$, corresponding to a state with an upper-lower symmetry, so that $v_m = 0$.

Figure 6 (right) shows the respective time-dependence of $\theta(t)$, which approaches in the long-time limit towards the steady-state angle $\theta(\infty) \approx 0.0\ \pi$ when the initial tilt angle is $\theta_0^+ \in I^+$. This implies that for these θ_0^+-orientations the capsule preferential stable orientation at steady-state is such that its axis lies within the y-x shear plane. In turn, for $\theta_0^0 \in I^0$ the tilt angle approaches another possible stable orientation $\theta(\infty) \approx 0.5\ \pi$, in which case the capsule axis lies now within the z-x plane (the plane being perpendicular to the

shear-plane). This orientation corresponds to a state with an *upper-lower* symmetry, so that in the mean $v_m = 0$. In case of the capsule, there are now two *asymptotically stable* fixed points (FP) at $\langle\theta\rangle_T^{FP} = 0.0\ \pi$ and $0.5\ \pi$[12].

Overall, the CSM-effect of the capsule is quite *robust* against a broad variation of the initial orientations with regards to ϕ_0 and θ_0.

---

[1] DOI M. and EDWARDS S. F., *The Theory of Polymer Dynamics* (Oxford University Press, Oxford) 1986.

[2] BRUNN P. O., *Int. J. Multiphase Flow*, **9** (1983) 187.

[3] DHONT J. K. G., *An Introduction to Dynamics of Colloids* (Elsevier, Amsterdam) 1996.

[4] SUCCI S., *The Lattice Boltzmann equation for fluid dynamics and beyond* (Clarendon Press, Oxford) 2001.

[5] DÜNWEG B. and LADD J. C. A., *Adv. Polym. Sci.* **221** (2009) 89.

[6] AIDUN C. K. and CLAUSEN J. R., *Annu. Rev. Fluid Mech.* **42** (2010) 439.

[7] ARNOLD A., LENZ O., KESSELHEIM S., WEEBER R., FAHRENBERGER F., ROEHM D., KOSOVAN P. and HOLM C., *ESPResSo 3.1 molecular dynamics software for coarse-grained models* (Springer, Berlin) 2013.

[8] LIMBACH H. J., ARNOLD A., MANN B. A. and HOLM C., *Comput. Phys. Commun.* **174** (2006) 704.

[9] KRÜGER T., VARNIK F. and RAABE D., *Computers and Mathematics with Applications* **61** (2011) 3485.

[10] KRÜGER T., *Computer simulation study of collective phenomena in dense suspensions of red blood cells under shear* (Universität Bochum, Bochum) 2011.

[11] HELFRICH W., *Zeitschrift für Naturforschung* **28c** (1973) 693.

[12] GUCKENHEIMER J. and HOMES P., *Nonlinear Oscillations, Dynamical Systems, and Bifurcations of Vector Fields* (Springer, Berlin) 1989.

[13] We remind that the mean orientation of the particle determines whether CSM exists or not in so far as $\langle\phi\rangle_T$ dictates in turn the location of the stiff and bendy contour part in regards to the upper and lower half-space, as discussed in the main text.

Publication 3

Engineering passive swimmers by shaking liquids
M. Laumann , A. Förtsch, E. Kanso and W. Zimmermann
submitted to New J. Phys. on 2019-03-15 (with referees)
manuscript number NJP-110170
preprint on arXiv (https://arxiv.org/abs/1903.11510)

Engineering passive swimmers by shaking liquids

M Laumann[1], A Förtsch[1], E Kanso[2] and W Zimmermann[1]

Theoretische Physik I, Universität Bayreuth, Bayreuth, Germany[1]
Aerospace and Mechanical Engineering, University of Southern California, Los Angeles, California, USA[2]

E-mail: walter.zimmermann@uni-bayreuth.de

Abstract. The locomotion and design of microswimmers are topical issues of current fundamental and applied research. In addition to numerous living and artificial active microswimmers, a passive microswimmer was identified only recently: a soft, Λ-shaped, non-buoyant particle propagates in a shaken liquid of zero-mean velocity [Jo *et al.* Phys. Rev. E **94**, 063116 (2016)]. We show that this novel passive locomotion mechanism works for realistic non-buoyant, asymmetric Janus microcapsules as well. According to our analytical approximation, this locomotion requires a symmetry breaking caused by different Stokes drags of soft particles during the two half periods of the oscillatory liquid motion. It is the intrinsic anisotropy of Janus capsules and Λ-shaped particles that break this symmetry for sinusoidal liquid motion. Further, we show that this passive locomotion mechanism also works for the wider class of symmetric soft particles, e.g., capsules, by breaking the symmetry via an appropriate liquid shaking. The swimming direction can be uniquely selected by a suitable choice of the liquid motion. Numerical studies, including lattice Boltzmann simulations, also show that this locomotion can outweigh gravity, i.e., non-buoyant particles may be either elevated in shaken liquids or concentrated at the bottom of a container. This novel propulsion mechanism is relevant to many applications, including the sorting of soft particles like healthy and malignant (cancer) cells, which serves medical purposes, or the use of non-buoyant soft particles as directed microswimmers .

Submitted to: *New J. Phys.*

1. Introduction

Biological microswimmers and their artificial counterparts attract a great deal of attention in research both for their fundamental relevance and their potential applications in a variety of physical, biological, chemical or biomedical applications (see e.g., [1, 2, 3, 4, 5]). Several studies focus on the dynamics of soft particles in microflows, such as capsules and red blood cells [6, 7, 8, 9, 10]. Their exploration and understanding inspires, among others, passive microswimmers that are indirectly driven by a time-dependent liquid motion. An example is a recently identified inertia-driven, passive microswimmer: A non-buoyant asymmetric soft microparticle in oscillatory liquid motion of zero mean displacement was studied in [11, 12]. Here we show how this inertia-driven locomotion mechanism can be generalized to the much wider class of homogeneous, soft particles, such as capsules, by engineering an appropriate time-dependent liquid motion.

Mechanisms that underly the propulsion of microswimmers include the propulsion via chemical reactions on the anisotropic surface of Janus particles, by magnetic fields or acoustic fields (see e.g., [4]). Common propulsion mechanisms of microorganisms at low Reynolds number are periodic motions of flagella, cilia or the deformation of the body shape (amoeboid motion) [2, 3, 5, 13, 14, 15, 16]. To achieve a net displacement at these length scales the mechanism has to be non-reciprocal to break Purcell's scallop theorem [2, 17].

The non-reciprocal motion of biological swimmers inspired also passive artificial microswimmers recently. One example is a soft Janus capsule in a temporally periodic linear shear flow at low Reynolds number, whereby the intrinsically asymmetric Janus particle is propelled perpendicular to the streamlines [18]. This type of passive swimming and the theoretical model of a brake controlled triangle [19] are similar to cross-stream migration of droplets and soft particles in stationary low Reynolds number Poiseuille flows [20, 21, 22, 23, 24]. Other recent studies identified the finite inertia of soft particles in oscillatory homogeneous liquid motion as a crucial property for passive swimming [11, 12]. The non-reciprocal body shape and therefore the different Stokes drag in both half periods of the periodic liquid motion is the driving force of these novel locomotion mechanism. The first inertia driven particle locomotion at low Reynolds number was demonstrated for a soft, asymmetric, Λ-shaped particle in a shaken liquid [11]. This was extended to an internally structured capsule with an inhomogeneous mass distribution in a gravitation field [12].

In this work we show that the inertia induced passive swimming of realistic and experimentally available soft particles in oscillatory liquid motion can outweigh gravitation. We show this at first for an Janus capsule with an asymmetric elasticity (see e.g. [25]). We explain that an intrinsic particle asymmetry is not required for passive swimming and we demonstrate that the inertia driven particle propulsion works also for the much wider class of homogeneous and symmetric soft particles, such as soft capsules. This is achieved by appropriately engineering the time-dependence of shaking

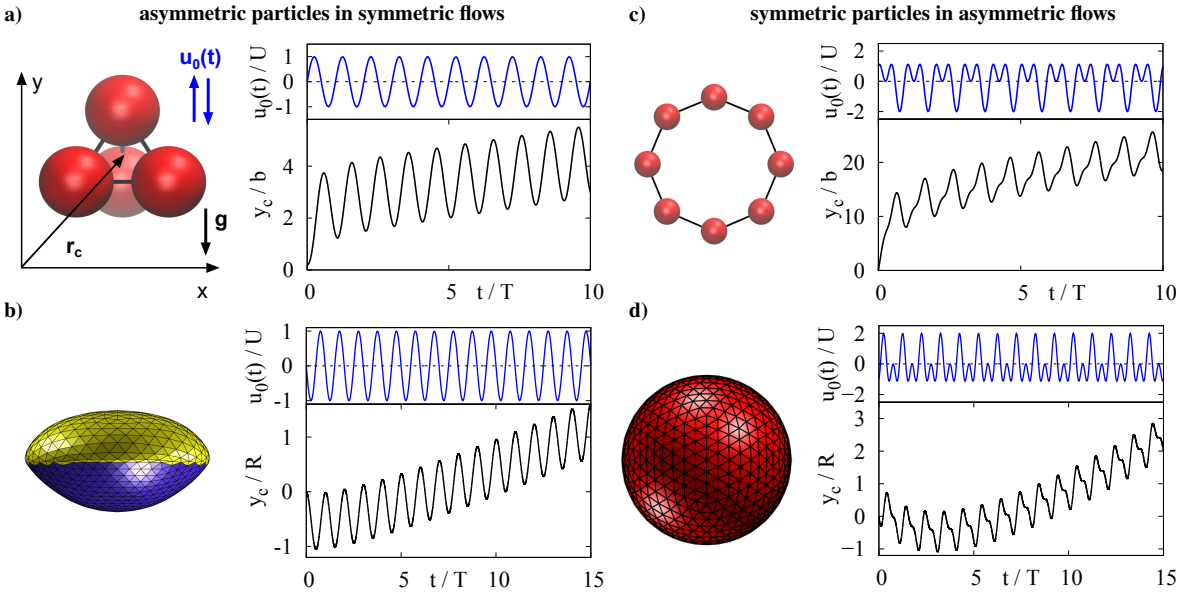

Figure 1. Sketch of four different particles with a mass density different from that of the surrounding liquid. The liquid shaken with the velocity $\mathbf{u}_0(t) = u_0(t)\mathbf{e}_y$ causes an inertia-driven particle locomotion. The actuation is indicated by the motion of the particle's center of mass $\mathbf{r}_c(t) = y_c(t)\mathbf{e}_y$. Part a) shows an asymmetric bead-spring tetrahedron and part b) an asymmetric Janus capsule with different stiffness of each half (soft part yellow). Both asymmetric particles are considered in a sinusoidal velocity of the liquid with period T, as indicated by the upper blue curves in a) and b). We observe for both particles a net motion along the direction of shaking against gravitation, as described by the black curves in a) and b). The ring in c) and the symmetric capsule in d) are shaken by non-symmetric velocities as indicated by the blue curves in part c) and d). Also the ring and the symmetric capsule show a net progress against gravity as indicated by the black curves in c) and d). Parameters are given in sections 2 and 4.

the liquid. The time-dependence of the shaking determines also the direction of passive swimming. This motion is distinct from particle locomotion in oscillatory flows at finite Re, where propulsion is related to streaming flows and a fluid jet in the wake of the swimmer [26].

The work is organized as follows: In section 2 we describe the modeling and simulation of the particles sketched in figure 1. We show in section 3 by an approximate analytical approach, that the locomotion of non-buoyant soft particles in a periodically oscillating fluid motion requires the symmetry breaking caused by different particle deformations and Stokes drags during the two half-periods of the shaking of the liquid. The analytical results are confirmed in section 4 by numerical simulations of the bead-spring models and capsules shown in figure 1. We study an asymmetric bead-spring tetrahedron in a sinusoidal liquid motion and a symmetric semiflexible bead-spring ring in a non-symmetric periodic liquid motion for a wide parameter range. The results of these simulations are complemented and verified by Lattice Boltzmann simulations of realistic soft asymmetric Janus capsules and symmetric capsules. For instance,

we provide parameter ranges where the passive locomotion mechanism outweighs gravitation. Discussions of the results and the conclusions are given in sec. 5.

2. Model and Approach

The dynamics of four deformable particles in a shaken liquid is investigated by taking into account particle inertia. We use two asymmetric particles, namely a bead-spring tetrahedron composed of four beads, and a Janus capsule, as sketched in figures 1 a) and b), respectively. As examples of common symmetric particles we choose a bead-spring ring, as shown in figure 1c), and a symmetric capsule, as shown in figure 1d). The positions and the motion of the beads of the ring are restricted to the (x, y) plane.

The shaking velocity of the liquid is given by

$$\mathbf{u}_0(t) = u_0(t)\hat{e}_y = U\ [\sin(\omega t) + \varepsilon \cos(2\omega t)]\, \hat{e}_y\,, \tag{1}$$

with the frequency $\omega = 2\pi/T$ and a vanishing mean velocity $\langle \mathbf{u}_0(t) \rangle = 0$. For $\varepsilon = 0$ the velocity is sinusoidal and antisymmetric with respect to a shift $t \to t + T/2$, i.e., $\mathbf{u}_0(t) = -\mathbf{u}_0(t + T/2)$. For $\varepsilon \neq 0$ this symmetry is broken and the velocity of the liquid is non-symmetric as indicated by the blue curves in figures 1c) and 1d).

In section 2.1 we describe the modeling of the bead-spring models and the capsules. In section 2.2, we present the equations of motion of the bead spring models, the Maxey and Riley equations [27] for several beads. They take the particle inertia into account and are extended by the hydrodynamic particle-particle interaction via the dynamical Oseen-tensor. The Lattice-Boltzmann-Method (LBM) for the particle simulations is explained in section 2.3.

2.1. Modeling the bead-spring models and the capsules

The beads of the bead-spring models have the mass m_i. Their mass density ρ_i may be different from the mass density of the fluid, $\rho_f \neq \rho_i$. With the gravitational force along the negative y direction, this leads to the buoyancy force

$$\mathbf{F}_{g,i} = -F_{g,i}\mathbf{e}_y, \tag{2}$$

which acts on a particle immersed in the liquid with

$$F_{g,i} = gV_i(\rho_i - \rho_f) = g(m_i - m_f)\,. \tag{3}$$

The tetrahedron in figure 1a) consists of $N = 4$ beads at positions $\mathbf{r}_i$. The beads have the same radius a, but may have different masses. They are connected by springs with the stiffness k. The center of mass is given by

$$\mathbf{r}_c = \frac{1}{\sum_i m_i} \sum_i m_i \mathbf{r}_i\,. \tag{4}$$

Each bead experiences a force that is composed of the buoyancy force $\mathbf{F}_g$ and forces imposed by springs,

$$\mathbf{F}_i^{(P)} = -F_{g,i}\hat{e}_y - \nabla_i V_{spring} \tag{5}$$

with the spring potential

$$V_{spring} = \sum_{i,j\neq i}^{N} k(|\mathbf{r}_i - \mathbf{r}_j| - b)^2 \tag{6}$$

and the undistorted spring length b.

Also for the bead-spring model shown in figure 1c) (with $N = 8$ beads) the neighboring beads are connected by Hookean springs. In addition to equation (5) a bending potential with the stiffness κ is taken into account

$$V_{bend} = -\frac{\kappa}{2} \sum_{i=1}^{N} \ln(1 + \cos\beta_i) \tag{7}$$

where $\mathbf{R}_i = \mathbf{r}_i - \mathbf{r}_{i+1}$ is the the bond vector between the next-neighbor beads i and $i + 1$ and the angle β_i is defined via $\cos\beta_i = \mathbf{e}_{R_{i-1}} \cdot \mathbf{e}_{R_i}$ with the bond unit vectors $\mathbf{e}_{R_j} = \mathbf{R}_j/R_j$. This bending potential causes a circular ring shape in equilibrium.

The capsules are modeled by discretizing their surface with $N = 642$, which is done iteratively as described in more detail in Ref. [28]. We assume that the surface is thin and has a constant surface shear elastic modulus G_s. In this case the relation between the deformation and the forces is given by the neo-Hookean law described by the potential V_{NH} (for details we refer to [29, 30]). Furthermore a bending potential V_b is assumed [31, 32], which is given by

$$V_b = -\frac{\kappa_c}{2} \sum_{i,j} (1 - \cos\beta_{i,j}) \ , \tag{8}$$

where κ_c denotes the bending stiffness and $\beta_{i,j}$ is the angle between the normal vectors of neighboring triangles.

For Janus capsules the stiffness is different in both halves of the capsule, as indicated in figure. 1(c). We use a penalty force to keep the capsule's volume $\mathcal{V}(t)$ close to the reference volume $\mathcal{V}_0$ during the simulations. Its potential V_v is given by

$$V_v = -\frac{k_v}{\mathcal{V}_0}(\mathcal{V}(t) - \mathcal{V}_0)^2 \tag{9}$$

with the rigidity k_v [32]. The complete potential related to the forces acting on the capsule is given by

$$V(\mathbf{r}) = V_{NH} + V_b + V_v. \tag{10}$$

2.2. Maxey and Riley equations, including the dynamic Oseen-Tensor

The dynamics of the beads at small fluid Reynolds number is described by the equations for the particle velocities $\mathbf{v}_i$ of Maxey and Riley [27]. These dynamical equations are derived with the help of the time-dependent Stokes equation, i.e., the advective term of the Navier-Stokes equation is neglected. A bead experiences besides $\mathbf{F}_i^{(P)}$ the inertial force

$$\mathbf{F}_i^{(0)} = m_{f,i} \frac{d\mathbf{u}_i}{dt} \tag{11}$$

caused by the liquid acceleration at the position $\mathbf{r}_i$ of the bead. Note that the liquid velocity includes the externally imposed homogeneous liquid motion $\mathbf{u}_0(t)$ described in equation (1) and the flow perturbations caused by the motion of all other particles with respect to the liquid. Furthermore, the force $\mathbf{F}_i^{(1)}$ created by the difference between the particle velocity $\mathbf{v}_i$ and the liquid velocity $\mathbf{u}_i$ must be considered. This is composed of three contributions, the added mass, the Stokes drag and the Basset force,

$$\begin{aligned}\mathbf{F}_i^{(1)} = & -\frac{1}{2}m_{f,i}\frac{d}{dt}\left(\mathbf{v}_i-\mathbf{u}_i\right)-\zeta_b(\mathbf{v}_i-\mathbf{u}_i)\\ & -6\pi\eta a^2\int_0^t d\tau\frac{\frac{d}{d\tau}\left[\mathbf{v}_i(\tau)-\mathbf{u}_i(\tau)\right]}{\sqrt{\pi\nu(t-\tau)}}\,,\end{aligned} \tag{12}$$

with the Stokes drag coefficient $\zeta_b = 6\pi\eta a$. Alltogether we obtain the dynamical equation for the velocity of the ith bead

$$m_i\frac{d\mathbf{v}_i}{dt} = \mathbf{F}_i^{(0)}+\mathbf{F}_i^{(1)}+\mathbf{F}_i^{(P)}\,. \tag{13}$$

The flow disturbances at $\mathbf{r}_i$ caused by all the other beads are determined via the dynamic Oseen tensor [33], which is the Greens function of the time-dependent linear Stokes equation. This provides the flow at the ith bead

$$\mathbf{u}_i = \mathbf{u}_0(t)+\sum_{j\neq i}\int_0^t dt'\;\mathbf{H}_{i,j}(t')\cdot\mathbf{F}_j^{(1)}(t')\,. \tag{14}$$

For the explicit expression of $\mathbf{H}_{i,j}(t')$ we refer to Appendix A.

Equation (12) is solved numerically for the bead-spring tetrahedron as shown in figure 1a) and for the bead-spring ring shown in figure 1c) by using a Runge-Kutta-scheme of fourth order. The dimensionless parameters given below are used for simulations of equation (13) for the bead-spring tetrahedron and the bead-spring ring. These parameters can be converted to SI units if the dimensionless time is multiplied by the factor $s_t = 1$ ms, the length by $s_l = 50$ μm and mass by $s_m = 5.2\cdot10^{-13}$ kg. This leads to the density and viscosity of water ($\rho_{water} = 1000$ kg/m^3, $\eta_{water} = 1$ mPas) and the correct gravitational acceleration $g \approx 10$ m/s^2.

The Parameters used in simulations of the bead-spring tetrahedron are: number of beads $N = 4$, bead radius $a = 0.1$, equilibrium spring length $b = 0.25$, spring stiffness $k = 15000$, mass density $\rho_i = 3600$ of a bead, mass density of the fluid $\rho_f = 240$, fluid viscosity $\eta = 100.0$, amplitude of the shaking velocity $U = 10.0$ in equation (1), asymmetry parameter $\varepsilon = 0$, shaking period $T = 0.4$, gravitational acceleration $g = 0.21$ and time step $dt = 2.5\cdot10^{-4}$ in numerical integrations of equation (13).

The Parameters used in simulations of the semiflexible bead-spring ring are: number of beads $N = 8$, bead radius $a = 0.1$, equilibrium spring length $b = 0.5$, spring stiffness $k = 2000$, bending stiffness $\kappa = 500$, mass density $\rho_i = 3600$ of a bead, mass density of the liquid $\rho_f = 240$, viscosity of the liquid $\eta = 100$, amplitude $U = 20$ of the shaking velocity in equation (1), asymmetry parameter $\varepsilon = 0.8$, shaking period $T = 0.4$, gravitational acceleration $g = 0.21$ and time step $dt = 2.5\cdot10^{-4}$ in numerical integrations of equation (13).

2.3. The Lattice Boltzmann Method

We utilize the common D3Q19 lattice-Boltzmann method (LBM) to simulate the distribution $f(\mathbf{x},t)$ of the fluid elements on a 3D grid of positions $\mathbf{x}_i = (x,y,z)$ along the discrete directions $\mathbf{c}_i$ $(i = 0,\ldots,19)$ [34]. The lattice constants are $\Delta x = 1$ for spatial and $\Delta t = 1$ for temporal discretization. The evolution of the distribution function is governed by the discrete Boltzmann equation

$$f_i(\mathbf{x}+\mathbf{c}\Delta t, t+\Delta t) = f_i(\mathbf{x},t) + \mathcal{C}, \tag{15}$$

where $\mathcal{C}$ defines the collision operator. Walls are incorporated by the standard bounce back scheme (bb) [35, 36] by adding the contribution $\mathcal{W} = -2w_i\rho\frac{\mathbf{c}_i\cdot\mathbf{u}_w}{c_s^2}$ for wall links to equation (15) [36, 37], where $\mathbf{u}_w$ is the wall velocity. The weighting factor w_i and the speed-of sound c_s are constants for the chosen set of velocity directions [34].

Tetrahedron dynamics: For the simulations of the tetrahedron, the Bhatnagar-Gross-Krook (BGK) collision operator

$$\mathcal{C} = -\frac{1}{\tau}\left[f_i(\mathbf{x},t) - f_i^{eq}(\mathbf{x},t)\right] + \mathcal{F} \tag{16}$$

is extend by the Guo force-coupling $\mathcal{F} = \Delta t\left(1-\frac{1}{2\tau}\right)w_i\left[\frac{c_i\cdot\mathbf{u}}{c_s^2} + \frac{(\mathbf{c_i}\cdot\mathbf{u})}{c_s^4}\mathbf{c}_i\right]\cdot\mathbf{F}^{(e)}$ for external volume forces $\mathbf{F}^{(e)}$ [38]. f^{eq} is an expansion of the Maxwell-Boltzmann distribution and τ is the relaxation parameter. The macroscopic density and momentum are obtained from the first two moments via $\rho = \sum_i f_i$ and $\rho\mathbf{u} = \sum_i \mathbf{c}_i f_i + \frac{\Delta t}{2}\mathbf{F}^{(e)}$, respectively. The viscosity of the fluid is given by $\nu = c_s^2\Delta t\,(\tau - 1/2)$. The hard spheres are implemented as moving walls according to [35], with an additional lubrication-correction for squeezing motion of near particles, as discussed in [39]. This simulations are used to compare the Oseen simulations and the LBM simulations (see also Appendix B).

Capsule dynamics: For the simulations of capsules, an adapted LBM-scheme of the multi-relaxation time LBM for a spatially dependent density is used [40]. The time evolution of the mean density $\rho_0(\mathbf{x},t) = \sum_i f_i + \frac{1}{2}\mathbf{u}\nabla\rho\Delta t$, the local density $\rho(\mathbf{x},t)$ and its gradient $\nabla\rho$ is used as input for the collision operator

$$\begin{aligned}\mathcal{C} = & -S_{il}\left[f_l(\mathbf{x},t) - f_l^{eq}(\mathbf{x},t)\right] \\ & + F_i(\mathbf{x},t) - \frac{1}{2}S_{il}F_l(\mathbf{x},t).\end{aligned} \tag{17}$$

For the collision matrix $\mathbf{S}$ and its corresponding transformation matrix we use the set given in [41]. The correction term $F_i(\mathbf{x},t) = \Delta t\frac{(\mathbf{c}_i-\mathbf{u})}{c_s^2}\cdot\left[\nabla\rho c_s^2(\Gamma_i - w_i) + \mathbf{F}^{(e)}\Gamma_i\right]$ accounts for the density inhomogeneity and external forces, with $\Gamma_i = w_i\left[1 + \frac{\mathbf{e}_i\cdot\mathbf{u}}{c_s^2} + \frac{(\mathbf{c}_i\cdot\mathbf{u})^2}{2c_s^4} - \frac{|\mathbf{u}|^2}{2c_s^2}\right]$ [40]. The fluid velocity is linked to the density ρ via the second moment $\rho\mathbf{u} = \sum_i f_i\mathbf{c}_i + \frac{1}{2}\mathbf{F}^{(e)}\Delta t$. The equilibrium distribution has the form $f_l^{eq}(\mathbf{x},t) = w_i\left[\rho_0 + \rho\left(\frac{(\mathbf{c}_i\cdot u)}{c_s^2} + \frac{(\mathbf{c}_i\cdot\mathbf{u})^2}{2c_s^4} - \frac{|\mathbf{u}|^2}{2c_s^2}\right)\right]$. The capsule mesh is coupled to the LBM-grid via the immersed-boundary method using the four-point stencil [42]. The calculation of the

field for the density $\rho(\mathbf{x},t)$ used in [40] is replaced by tracking nodes inside the capsule and setting $\rho(\mathbf{x},t)$ as $\rho_{capsule}$ inside and ρ_{fluid} outside of the membrane and updating the capsule surface via the membrane-forces.

Oscillating flow. To drive the oscillating flow, an external (volume-)force $\mathbf{F}^{(e)}_{flow} = U\rho\,\omega[\cos(t\omega) - 2\varepsilon\sin(2t\omega)]\hat{\mathbf{e}}_y$ is applied to the LBM. To screen hydrodynamic self-interaction, we use bb walls in x and z-direction with velocity $\mathbf{u}_w(t) = \mathbf{u}(t)$ to ensure Dirichlet boundary conditions of the flow.

Parameters and unit-conversion. The used LBM parameters can be obtained from the SI parameters via the conversion values for length $s_L = 7.57 \cdot 10^{-7}$m, mass $s_M = 4.348 \cdot 10^{-16}$kg and time $s_T = 4.54 \cdot 10^{-8}$s. All LBM simulations are performed with a viscosity $\eta = \eta_{water} = 1$ mPas , gravitational acceleration $g = 9.81\mathrm{m/s}^2$, fluid density $\rho = \rho_{water} = 1000\frac{\mathrm{kg}}{\mathrm{m}}^3$ and $k_v = 2.78 \cdot 10^5 \frac{\mathrm{kg}}{\mathrm{s}^2\mathrm{m}}$. The amplitude of the liquid's velocity is $U = 0.5\frac{\mathrm{m}}{\mathrm{s}}$ and the period is $T = 90\mu$s if not given otherwise. The cubic simulation box has a length of 1.14×10^{-4}m.

3. Inertia driven actuation: Approximate analytical results

Soft particles are periodically deformed in shaken liquids, which causes a time-dependent viscous drag coefficient of the particle. How this deformability drives passive swimming of a particle in a shaken liquid is determined by an approximate analytical approach.

We discuss here a particle with a drag coefficient ζ_{tot}. This already simplifies the dynamical equation (13). We further neglect the Basset force and the added mass in equation (12) but take the force $\mathbf{F}^{(0)}$ and the dominant viscous drag contribution to $\mathbf{F}^{(1)}$ into account. In this case we obtain the approximate dynamical equation for the velocity of a stiff particle

$$M\frac{d\mathbf{v}(t)}{dt} = \zeta_{tot}\left[\mathbf{u}_0(t) - \mathbf{v}(t)\right] + M_f\frac{d\mathbf{u}_0(t)}{dt}\,, \tag{18}$$

with the particle mass M, the displaced fluid mass M_f and the constant Stokes drag coefficient ζ_{tot}. To justify the validity of this approximations we compare them with the full numerical results in the next section.

For a sinusoidal liquid motion $\mathbf{u}_0(t)$ as described by equation (1) with $\varepsilon = 0$ the solution of equation (18) is $\mathbf{v}(t) = v(t)\hat{e}_y$ with

$$v(t) = Ce^{-\frac{\zeta_{tot}}{M}t} + A\sin\left(\omega t + \phi\right)\,, \tag{19}$$

whereby

$$A = U\sqrt{\frac{M_f^2\omega^2 + \zeta_{tot}^2}{M^2\omega^2 + \zeta_{tot}^2}} = U\sqrt{\frac{\left(M_f\omega/\zeta_{tot}\right)^2 + 1}{\left(M\omega/\zeta_{tot}\right)^2 + 1}} \tag{20}$$

is the amplitude of the particle oscillation and the phase shift relative to the time-dependent liquid motion is given by

$$\phi = -\arctan\left(\frac{\zeta_{tot}\omega(M-M_f)}{MM_f\omega^2+\zeta_{tot}^2}\right). \tag{21}$$

The exponential contribution to equation (19) includes the relaxation time $\tau_v = \frac{M}{\zeta_{tot}}$ that the particle needs to adjust its velocity $\mathbf{v}$ to the velocity of the liquid $\mathbf{u}_0$. We approximate this time scale by

$$\tau_v = \frac{M}{\zeta_{tot}} \approx \frac{4m}{4\zeta_b} = \frac{m}{\zeta_b} \tag{22}$$

for the bead spring models and for the capsule by

$$\tau_v = \frac{M}{\zeta_{tot}} = \frac{2R^2\rho}{9\eta} \tag{23}$$

with

$$\zeta_{tot} = 6\pi\eta R\,, \quad V = \frac{4}{3}\pi R^3\,, \quad M = \rho V. \tag{24}$$

We discuss in the following the case $M \geq M_f$ (but also $M < M_f$ is possible). For a high friction or slow frequency, i.e. $\frac{M}{\zeta_{tot}}\omega \ll 1$, the particle velocity adjusts rather quickly to the liquid motion. This means the particle quickly adapts to the motion of the liquid, i.e. $A \to U$ and $\phi \to 0$ (cf. equations (20) and (21)) and the particle's inertia is negligible in this case.

In the range $\frac{M}{\zeta_{tot}}\omega \gtrapprox 1$ the particle's inertia becomes important and it can not follow the liquid velocity, which results in $A < U$, $\phi < 0$. This lag behind of the particle can be used to achieve a non-vanishing mean velocity: If the shape of the deformable particle and therefore the drag is different in each half cycle of the shaking, as indicated in figure 2b), the delay of the particle with respect to the fluid is different in each half cycle. This difference may finally lead to a net motion of the particle with respect to the fluid. Since the liquid does not move in the mean, this relative net motion results in an absolute particle actuation.

In order to gain further analytical insight, we consider an asymmetric, i.e. anisotropic, deformable particle as illustrated in figure 2b). We assume a fixed shape and therefore a fixed Stokes drag during each half period as described by

$$\zeta_{tot}(t) = \begin{cases} \zeta_1 \text{ at } 0 < t < \frac{T}{2}\,, \\ \zeta_2 \text{ at } \frac{T}{2} < t < T\,, \end{cases} \tag{25}$$

and continued analogously in the following periods. These two different constant values of the Stokes drag just mimic the essence of the different time-dependent shapes and Stokes drags of the particles sketched in figure 1. Numerical results of the full equations, i.e. that include the deformations of the particles, are given in the next section.

For a sinusoidal liquid velocity the particle velocities in both half periods are

$$v_{1,2}(t) = C_{1,2}e^{-\frac{\zeta_{1,2}}{M}t} + A_{1,2}\sin\left(\omega t + \phi_{1,2}\right)\,, \tag{26}$$

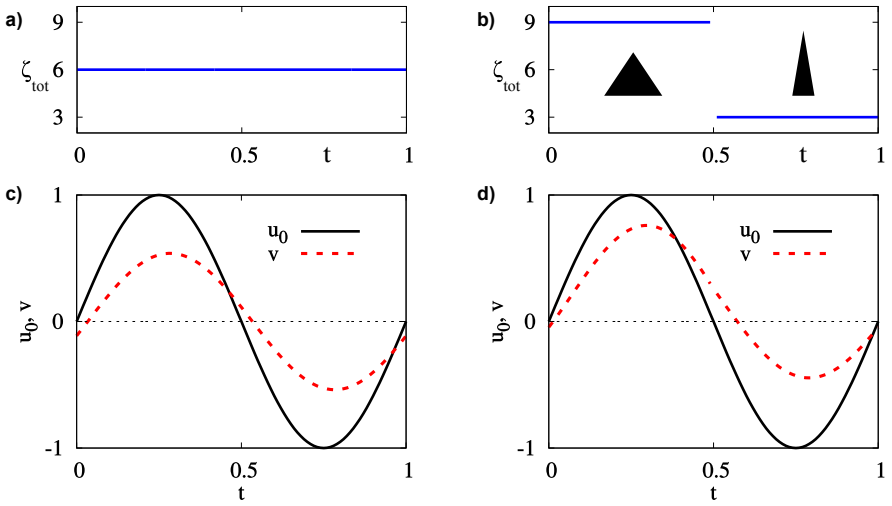

Figure 2. We consider a particle of mass M different from the surrounding liquid of mass M_f for the identical volume. We assume a sinusoidal fluid velocity $u_0(t)$ given by equation (1) for $\varepsilon = 0$, see also solid lines in c) and d). If the shape and the Stokes drag of the particle is constant in time, the particle velocity is also a sinusoidal, but has a smaller amplitude and follows with a small phase shift (dashed line in figure c)). For a different shape and a Stokes drag in both half periods, i.e. $\zeta_1 \neq \zeta_2$, the particle velocity is also differently, as indicated by the dashed line in figure d). This leads to a different mean velocity of the particle in each half cycle. Therefore, the actuation step is different in each half cycle which results in a net particle actuation. Parameters: $U = 1$, $T = 1$, $M_f = 1$, $M = 2$.

whereby A_i and ϕ_i are calculated as given in equations (20) and (21) but with the according value of $\zeta_{tot}(t)$. Due to the periodic liquid motion, the boundary conditions for the particle velocities are

$$v_1(0) = v_2(T), \qquad v_1\left(\frac{T}{2}\right) = v_2\left(\frac{T}{2}\right). \tag{27}$$

This allow the determination of the constants $C_{1,2}$ as

$$C_1 = U\omega\Gamma \frac{(\omega^2 M - \zeta_1\zeta_2)(e^{-\frac{2\zeta_2\pi}{\omega M}} + e^{-\frac{\zeta_2\pi}{\omega M}})}{e^{-\frac{\pi(\zeta_1+2\zeta_2)}{\omega M}} - e^{-\frac{\zeta_2\pi}{\omega M}}}, \tag{28}$$

$$C_2 = U\omega\Gamma \frac{(\omega^2 M - \zeta_1\zeta_2)(1 + e^{-\frac{\zeta_1\pi}{\omega M}})}{e^{-\frac{\pi(\zeta_1+2\zeta_2)}{\omega M}} - e^{-\frac{\zeta_2\pi}{\omega M}}} \tag{29}$$

with the abbreviation

$$\Gamma = \frac{(\zeta_1 - \zeta_2)(M - M_f)}{(\omega^2 M^2 + \zeta_2^2)(\omega^2 M^2 + \zeta_1^2)}. \tag{30}$$

The mean velocity of the particle is then given by

$$\begin{aligned} v_n &= \frac{\int_0^T v(t)dt}{T} \\ &= \frac{U\omega^2 M\Gamma}{2\zeta_1\zeta_2\pi\left(e^{\frac{\pi(\zeta_1+\zeta_2)}{\omega M}} - 1\right)} \left[(\zeta_1+\zeta_2)(\zeta_1\zeta_2 + \omega^2 M^2)\left(1 - e^{\frac{\pi(\zeta_1+\zeta_2)}{\omega M}}\right)\right. \end{aligned}$$

$$+ (\zeta_1 - \zeta_2)(\omega^2 M^2 - \zeta_1\zeta_2)\left(e^{\frac{\zeta_1\pi}{\omega M}} - e^{\frac{\zeta_2\pi}{\omega M}}\right)\Big] . \tag{31}$$

The equations (30) and (31) allows to discuss the requirements of a particle actuation, i.e. a non-vanishing mean velocity v_n. To achieve a mean velocity the factor Γ must not be zero. This means firstly that the mass density of the particle and the surrounding fluid must differ, i.e. $M \neq M_f$. In addition the drag coefficients in both half cycles have to be different, i.e., $\zeta_1 \neq \zeta_2$. This is further illustrated in figure 2.

For an equal mass density of the particle and the liquid, $M = M_f$, the particle follows the fluid motion instantaneously and the mean velocity vanishes. For $M \neq M_f$ but identical drag coefficients in both half periods, as in figure 2a), the fluid velocity $\mathbf{u}_0$ and the particle velocity $\mathbf{v}(t)$ are both sinusoidal as indicated in figure 2c). Both velocities have a different amplitude and there is a relative phase shift, but there is again no net progress of the particle.

If the shape and drag coefficients of the anisotropic particle in figure 2b) are different in both half cycles of the shaking, i.e. $\zeta_1 \neq \zeta_2$, then one has a non-symmetric velocity $\mathbf{v}(t)$ of the particle as shown in figure 2d). This asymmetry of $\mathbf{v}(t)$ causes a net progress of the particle per cycle.

The net progress of a deformable particle depends strongly on the relaxation time τ_v. For a small frequency, i.e., $\tau_v\omega \ll 1$, one obtains only a small actuation because the particle follows the liquid's motion nearly instantaneously, i.e. $\mathbf{v}(t) \approx \mathbf{u}_0$. This means $v_n \to 0$ for $\omega \to 0$ (which follows also with equation (31)).

Hence the requirements of the particle actuation can be discussed with equation (31). Note that it takes the particle inertia into account but the fluid Reynolds number is not important for the actuation.

A time-dependence of the drag coefficient can be achieved with a soft particle in a shaken fluid. The difference in the drag coefficient in both half periods, i.e. $\zeta(t) \neq \zeta(t + T/2)$, (as sketched in figure 2b)) can be achieved with an asymmetric particle in a sinusoidal shaken fluid. In case of a symmetric soft particle a different shape and therefore a different drag coefficient of the particle in each half cycle can be achieved by a non-symmetric periodic fluid velocity $\mathbf{u}_0(t)$ with $\varepsilon \neq 0$ in equation (1). This is further exemplified in the next section.

To compare the approximation in this section for $\mathbf{v}$ and the results from simulations in the next section, gravity must be taken into account. Gravity leads approximately to the additional contribution

$$v_s = \frac{g}{2}\left(\frac{M_f - M}{\zeta_1} + \frac{M_f - M}{\zeta_2}\right) \tag{32}$$

to the mean actuation velocity, cf. equation (31).

4. Numerical Results

In this section, we explore numerically the inertia driven dynamics and locomotion of four soft particles in a shaken liquid, which are sketched in figure 1. The selected

numerical simulations are guided by the results of the previous section i.e., particle locomotion is expected in parameter ranges with different mass densities of the particles and the liquid and the Stokes drag of a particle is is unequal during each half of a shaking period T. Such a time-dependent Stokes drag can be realized by asymmetric particles but also with symmetric ones.

Firstly, the dynamics of the asymmetric particles is investigated for the sinusoidal shaking velocity $\mathbf{u}_0$ in equation (1) with $\varepsilon = 0$. We show simulations of the bead-spring tetrahedron in section 4.1 and compare the results with a more realistic Janus capsule in section 4.2. The intrinsic anisotropic of both particles causes different deformations and Stokes drags during each half period of the sinusoidal velocity $\mathbf{u}_0$.

Secondly, symmetric particles are investigated. To achieve different deformations and Stokes drags during the two halves of the shaking period for these particles as well, we utilize a non-symmetric shaking velocity in equation (1) with $\varepsilon \neq 0$. We discuss the dynamics of a symmetric bead-spring ring and show that a symmetric capsule behaves similar to the ring in section 4.3.

All particles are soft particles with a different mass density than the liquid. They are deformed in shaken liquids, which is taken into account in the numerical simulations. Hence, besides the velocity relaxation time τ_v (cf. equations (22) and (23)) considered in sec. 3, also the shape relaxation time τ_k and especially the ratio T/τ_k are important. The shape relaxation time is given by the time the particles needs to relax to their equilibrium shape after a deformation. To determine the order of the relaxation-time scale, we use as an estimate for the bead spring models

$$\tau_k \approx \sqrt{\frac{m}{k}} \tag{33}$$

with the spring constant k, cf. equation (6), and the bead mass m and for the capsules

$$\tau_k \approx \sqrt{\frac{\rho_{capsule} V}{G}} \tag{34}$$

with the capsule volume V and the surface shear elastic modulus G.

4.1. Actuation of a tetrahedron in a sinusoidally shaken liquid

We investigate at first the motion of asymmetric particles in a sinusoidal shaken fluid. We begin with the simple bead-spring tetrahedron. Two orientations of the bead-spring tetrahedron in a vertically shaken fluid are stable, one with a corner upward (▲), cf. figure 3a), and one with a corner downward (▼). Figure 3a) shows the ▲-tetrahedron at four deformations during one period T of a sinusoidally shaken liquid.

The center of mass of the tetrahedron, $y_c(t)$, follows via the viscous drag the oscillatory motion of the shaken liquid. Moreover, $y_c(t)$ exhibits besides an oscillatory motion also a mean net propulsion as indicated in figure 1a). The resulting mean velocity v_n of the center of mass, which is studied in the following, is determined by fitting a straight line to $y_c(t)$ over a sufficient number of periods after a transient phase. The parameters for the numerical studies are given in section 2.2. We give the mean velocity

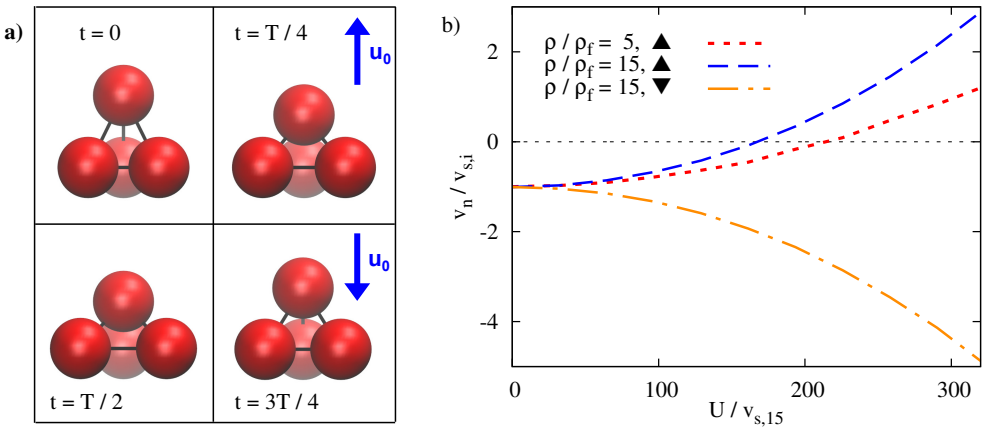

Figure 3. a) shows four snapshots of a deformable, upward oriented tetrahedron(▲) during one period T in a sinusoidally shaken fluid. In b) the mean propulsion velocity v_n of the tetrahedron is given for two ratios between the mass density of the beads and of the fluid, i.e. for $\rho/\rho_f = 5, 15$. v_n is given in units of the related sedimentation velocities $v_{s,i}$, respectively. The ▲-tetrahedron outweighs gravity for $\rho/\rho_f = 15$ in the range $U/v_{s,15} \gtrsim 160$ and rises in the shaken liquid. For $\rho/\rho_f = 5$ the ▲-tetrahedron rises in the range $U/v_{s,15} \gtrsim 210$. The sedimentation velocity of the ▼-tetrahedron is enhanced by liquid shaking as indicated by the dash-dotted line. Parameters: see section 2.2.

v_n and the amplitude U of the shaking velocity in units of the sedimentation velocity (absolute value) denoted by $v_{s,r}$, whereby the index r indicates the ratio of the density of the tetrahedron and the fluid, $\rho/\rho_f = r$. The sedimentation velocities $v_{s,5} = 8.9 \cdot 10^{-3}$ and $v_{s,15} = 3.1 \cdot 10^{-2}$ (absolute values) are determined without a shaking of the liquid (pure sedimentation).

In figure 3b) we show the mean velocity v_n of the tetrahedra in the gravitational field as function of the amplitude U. For the ▲-tetrahedron for two ratios $\rho/\rho_f = 5, 15$ and for the ▼-tetrahedron for $\rho/\rho_f = 15$. The sedimentation velocity $v_{s,r}$ and v_n increase with the density ratio ρ/ρ_f. For ▲-tetrahedra the mean velocity v_n becomes positive for $\rho/\rho_f = 15$ beyond $U/v_{s,15} \gtrsim 160$ and for $\rho/\rho_f = 5$ beyond $U/v_{s,15} \gtrsim 210$. In both ranges the locomotion of a tetrahedron outweighs the downward oriented gravitation and heavy particles can be elevated. Therefore, for smaller mass differences between soft particles and the liquid this locomotion mechanism becomes less effective and a higher velocity amplitude U is required to outweigh gravitation. A downward orientated shaken heavy tetrahedron (▼) will sediment faster than without shaking. Furthermore, a buoyant particle with $\rho/\rho_f = 1$ follows the oscillatory liquid motion and its mean velocity v_n vanishes in agreement with the reasoning given in the previous section. The inertial actuation is also found for tetrahedra lighter than the liquid, i.e. $\rho/\rho_f < 1$. Note that the dependence on the initial condition can be avoided by an asymmetric mass distribution of the beads, because this leads to a reorientation of the tetrahedron. For example with one bead lighter than the other three beads, the lighter bead will point upwards after a certain time. The inertia driven actuation of such a tetrahedron is discussed in Appendix B.

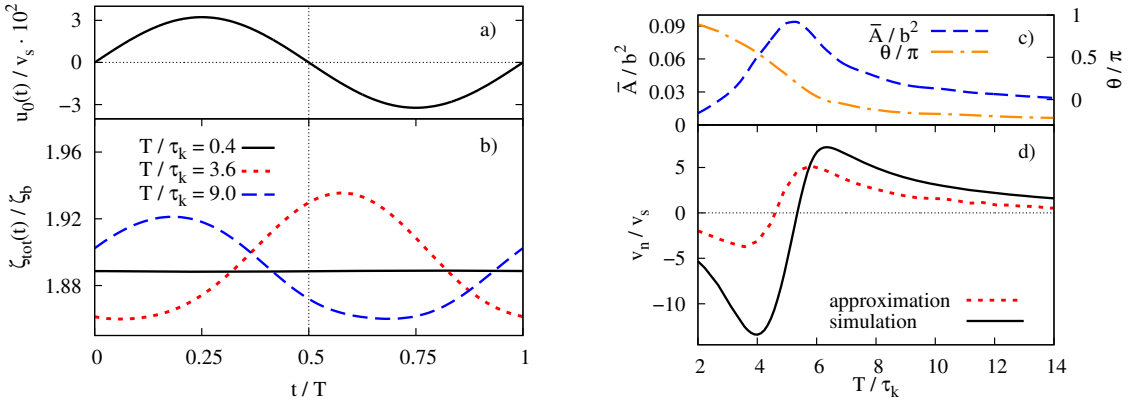

Figure 4. a) shows the shaking velocity $u_0(t)$ with $\varepsilon = 0$ in equation (1) in units of the sedimentation velocity v_s of an upward oriented tetrahedron (▲) with $\rho/\rho_f = 15$. The deformation of a tetrahedron, cf. figure 3a), is accompanied by a time-dependent Stokes drag ζ_{tot} as shown in b) (in units of $\zeta_b = 6\pi\eta a$) for three different ratios T/τ_k. c) shows the time-dependent deviation $\bar{A}$ from the mean area A_0 of the lower triangle of a ▲-tetrahedron, as defined in equation (35), as well as the phase shift Θ/π between the velocity $u_0(t)$ and the deformation. In d) the dependence of the mean velocity v_n/v_s is given as a function of T/τ_k for the velocity amplitude $U/v_s \simeq 32$. The dashed line is obtained by equation (31) with $\zeta_{1,2}$. Parameters: $k = 30000$ and those given in section 2.2.

The mean velocity v_n depends also on ratio between the shaking period T and the bead-spring relaxation time τ_k (cf. equation (33)). This dependence is shown in figure 4d) for a ▲-tetrahedron. This figure shows in part b) also the time-dependence of the drag coefficient of the tetrahedron, $\zeta_{tot}(t)$ (cf. Appendix A), which is caused by the time-dependent deformation. Thus, in addition the deformation amplitude $\bar{A}$ of the bottom triangle of the tetrahedron with area

$$A(t) = \bar{A} \sin\left(\frac{2\pi}{T}t - \Theta\right) + A_0\,, \tag{35}$$

is given in figure 4c). Also the phase shift Θ of the deformation and the flow is shown. The area A(t) is determined by a fit to the data.

If T is considerably smaller than the relaxation time τ_k, the deformation of the tetrahedron cannot follow the liquid oscillation and remains small, as indicated for the deformation amplitude $\bar{A}$ in figure 4c). Consistently, the drag coefficient ζ_{tot} is nearly constant as indicated for $T/\tau_k = 0.4$ in figure 4b). In this case particles just sediment in a shaken liquid. For larger T the tetrahedron becomes deformed during liquid shaking and the drag coefficient $\zeta_{tot}(t)$ shows similar as $u_0(t)$ a sinusoidal time-dependence as indicated for $T/\tau_k = 3.6$ in figure 4b). However, for such short shaking periods the tetrahedron deformation can still not follow the liquid oscillation and ζ_{tot} is nearly in antiphase to $u_0(t)$ as indicated by in figure 4b) and in figure 4c). Due to this phase shift for $T/\tau_k = 3.6$ the Stokes drag in figure 4b) is larger during the downward liquid motion with $u_0(t) < 0$ than during its upward motion. Therefore, the inertia induced locomotion is downward oriented for $T/\tau_k = 3.6$ as also indicated in figure 4d) for the whole range $T/\tau_k \lesssim 5.7$. For $T/\tau_k = 9$ beyond the maximum of v_n/v_s in 4d) the deformation of

the tetrahedron follows $u_0(t)$ more closely with a smaller phase difference Θ and the drag is slightly larger during the upward motion, cf. figure 4b). In this case and in the range $T/\tau_k \gtrsim 5.7$ the locomotion mechanism points into the opposite direction to the gravitation and can even outweigh gravitation for $U/v_s \simeq 32$, i.e., v_n/v_s becomes positive. v_n/v_s remains positive up to about $T/\tau_k \sim 27$ and beyond this ratio the tetrahedron sinks again due to the gravitation.

Besides the shape relaxation time also the velocity relaxation time τ_v (cf. equation (22)) plays a role as stated in section 3. We have chosen similar values of $\tau_v \approx 0.07$ and $\tau_k \approx 0.03$. The period T is in the range $1 \lesssim T/\tau_v \lesssim 6$, so that the particle's inertia is significant.

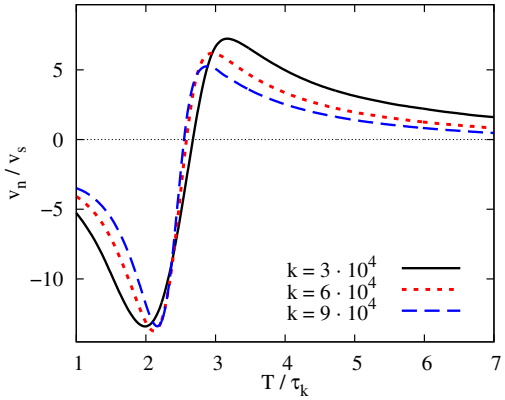

Figure 5. The mean locomotion velocity v_n of the ▲-tetrahedron, cf. figure 3a), is given as a function of T/τ_k for three different values of the spring stiffness k in equation (6) with $\rho/\rho_f = 15$. The minima of the curve occur at similar values of $T/\tau_k \approx 2$ and the maxima at $T/\tau_k \approx 3$ despite different values of k.

One can also use the approximate mean velocity in equation (31) by selecting the drag coefficient ζ_{tot} from simulations of the tetrahedron. We use the maximal drag during each half period for $\zeta_{1,2}$. The resulting dependence of v_n/v_s is indicated in figure 4d). This result confirms that the approximate approach presented in section 3 covers the essential inertia driven locomotion mechanism considered in this work.

In figure 5 the dependence of v_n/v_s on the ratio T/τ_k is shown for different values of the spring constant k of the tetrahedron. The extrema and the zero of v_n/v_s are located at similar values of T/τ_k. Moreover, the magnitudes of the minima and maxima of v_n/v_s differ only slightly for different values of k. This emphasis again the importance of the ratio between shaking period and the particle's relaxation time τ_k

4.2. Actuation of a Janus capsule in a sinusoidally shaken liquid

With a Janus capsule that is composed of two parts of different elasticity we consider in this section a realistic soft anisotropic particle. The four snapshots shown in 6a) highlight the different deformations during a sinusoidal shaking cycle T. An asymmetric Janus particle has also two stable orientations in the shaken liquid: One with the soft

half on top as in figure 6a) (upward oriented Janus capsule ▲), or with the soft part at the bottom (▼).

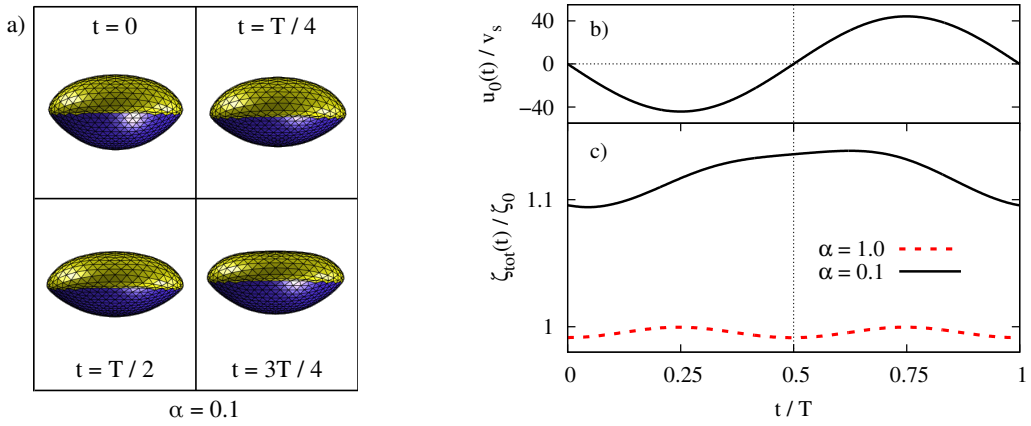

Figure 6. a) shows four snapshots of a deformable, with the soft side upward oriented Janus capsule (▲) during a period T in a shaken fluid with the elasticity ratio $\alpha = 0.1$. Figure b) shows the sinusoidal shaking velocity $u_0(t)/v_s$ in units of the sedimentation velocity v_s of the Janus capsule. The lower part in b) shows the Stokes drag $\zeta_{tot}(t)$ in units of the Stokes drag $\zeta_0 = 6\pi\eta R$ of the undeformed capsule for the elasticity ratio $\alpha = 0.1$ (solid line) and the symmetric capsule with $\alpha = 1$ (dashed line).

The capsule simulations are performed with the LBM and, besides the parameters given in section 2.3, the following values are used: radius of the capsule $R = 10\mu$m, $\rho_{Janus} = 2\rho_{fluid}$, $G^{(0)} = 3.95 \cdot 10^{-3}$kg/s^2 and $\kappa_c^{(0)} = 3,77 \cdot 10^{-13}$kg m^2/s^2. For the elastic properties of the second half of the capsule we set $\kappa_c^{(var)} = \alpha\kappa^{(0)}$ and $G^{(var)} = \alpha G^{(0)}$ with an elasticity ratio $\alpha = 0.1$. This results in the two ratios $T/\tau_k \approx 2$ and $T/\tau_v \approx 2$ (cf. equations (23) and (34), determined with $G^{(0)}$), which ensure that the Janus capsule is deformed during the shaking of the liquid and that the inertia of the capsule is significant.

For Janus capsules neither the deformation nor the Stokes drag ζ_{tot} has a symmetry, i.e. $\zeta_{tot}(t) \neq \zeta_{tot}(t + T/2)$, as indicted for $\alpha = 0.1$ by the snapshots in figure 6a) and in figure 6c), respectively. Therefore the time-dependence of $y_c(t)$ for a ▲ Janus capsule in figure 1b) displays the inertia induced locomotion (cf. figure 1b)). This is not the case for the symmetric capsule with $\alpha = 1.0$: The Stokes drag $\zeta_{tot}(t)$ given in figure 6c) has the symmetry $\zeta_{tot}(t) = \zeta_{tot}(t + T/2)$. Consequently, the symmetric capsule just sinks in a sinusoidally shaken fluid in the presence of gravitation.

The mean velocity of the Janus capsule v_n/v_s is shown in figure 7 as function of the velocity amplitude U. The sedimentation velocity of the ▼ Janus capsule is enhanced by the oscillatory fluid motion as shown by the lower curve in 7a). For a velocity amplitude $U \gtrsim 500\, v_s$ (with $v_s \approx 0.15\frac{\text{mm}}{\text{s}}$) the locomotion of the ▲ capsule outweighs gravitation and moves upward, i.e., $v_n > 0$. This is indicated by the dashed curve in 7a). As for the tetrahedron the locomotion increases with the difference between the mass density of the capsule and the liquid. This also means, the critical amplitude

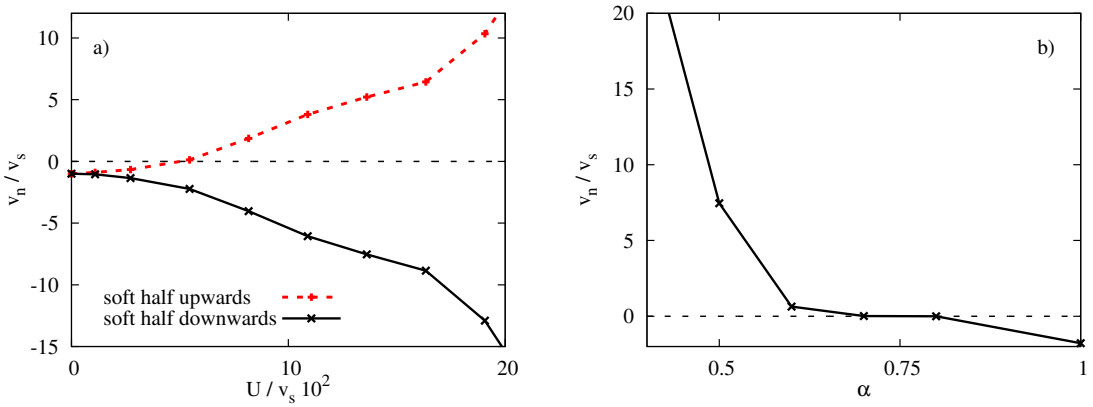

Figure 7. The mean actuation velocity v_n of a Janus capsule is given as a function of the shaking-velocity amplitude U in equation (1) with the soft side either upwards (▲) or downwards (▼). In the ▲-case the capsule locomotion outweighs gravitation if $U \gtrsim 500\, v_s$ and v_n becomes positive. In the ▼-case the shaking of the liquid enhances the sinking velocity. b) shows v_n/v_s for the ▲-capsule as function of the elasticity ratio α. At $\alpha = 1$ the particle sinks. By enhancing the asymmetry (decreasing α) the capsule locomotion outweighs gravitation for $\alpha \lesssim 0.8$.

U to outweigh gravitation is reduced by increasing the ratio $\rho_{capsule}/\rho_{liquid}$. The mean locomotion velocity v_n/v_s for an upward oriented Janus capsule in a gravitational field is also shown as function of elasticity ratio α in figure 7b). This graph shows that the inertia induced locomotion increases with increasing elastic asymmetry (i.e., decreasing α) and outweighs in the range $\alpha \lesssim 0.8$ gravitation for the given parameters. The symmetric capsule with $\alpha = 1.0$ just sinks in the mean.

In figure 7a) the Reynolds number Re in LBM simulations is finite with $0 \leq \mathrm{Re} \lesssim 3$ and an inertia induced capsule locomotion is found at small and intermediate values of the Reynolds number (and also beyond this values). The qualitative behavior of this capsule locomotion is similar as for the tetrahedron in the limit of vanishing Reynolds number.

In this and the following section, we explore the conditions for which also common symmetric soft micro-particles behave in shaken liquids as passive microswimmers. We begin with a symmetric bead-spring ring as sketched in figure 1. The parameters used in simulations are given in section 2.2 and the velocities are given in units of the sedimentation velocity $v_s = 0.031$ (determined without shaking of the liquid).

Figure 8a) shows four snapshots of a bead-spring ring during one period T of a non-symmetric shaking velocity $u_0(t)$ given by equation (1) and as shown in figure 8b) for $\varepsilon = 1$. For a sinusoidally shaken liquid with $\varepsilon = 0$ and $u_0(t) = -u_0(t + T/2)$ the drag coefficient $\zeta_{tot}(t)$ (cf. Appendix A) is the same in both half periods with $\zeta_{tot}(t) = \zeta_{tot}(t + T/2)$, as indicated in figure 8c). In this case the ring exhibits no net actuation and sinks in the gravitational field. For a non-symmetric periodic shaking velocity with $\varepsilon \neq 0$ and $u_0(t) \neq -u_0(t + T/2)$ the drag coefficient of the ring is different in both half periods as shown for $\varepsilon = 1$ in 8c). This leads to the passive swimming as shown in figure 1c).

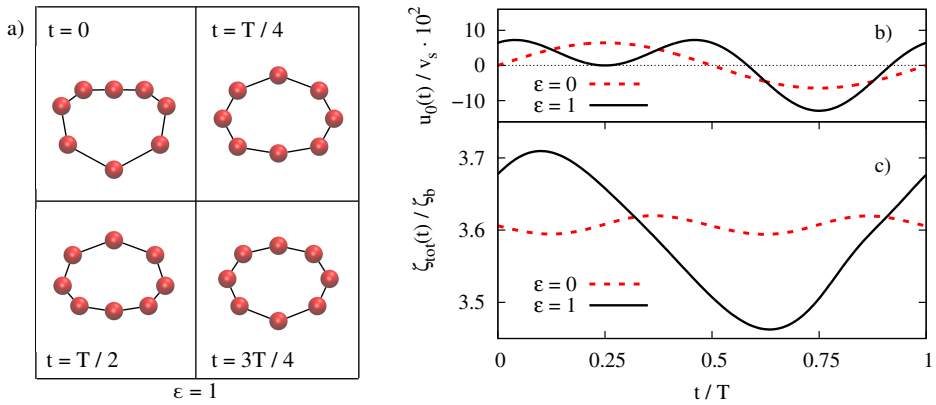

Figure 8. a) shows four snapshots of the bead-spring ring during one period T of the liquid velocity as shown by the solid line in b) and as given by equation (1) for $\varepsilon = 1$. In this case the drag coefficient $\zeta_{tot}(t)$ (in units of $\zeta_b = 6\pi\eta a$) is different in both half periods as shown by the solid line in c), i.e., $\zeta_{tot}(t + T/2) \neq \zeta_{tot}(t)$. This causes a finite mean actuation velocity v_n. For $\varepsilon = 0$ the shaking is sinusoidal, cf. dashed line in b), the drag coefficient is the same in both half periods of the shaking, i.e., $\zeta_{tot}(t) = \zeta_{tot}(t + T/2)$, and $v_n = 0$.

Figure 9 shows the mean velocity v_n of the bead-spring ring as a function of ε. For $\varepsilon \gtrsim 0.05$ the upward directed, inertia induced actuation is sufficiently strong to outweigh gravitation and v_n becomes positive. For $\varepsilon < 0$ liquid shaking enhances the sedimentation velocity. Thus the sign of ε determines the direction of the inertia induced actuation of the semiflexible ring.

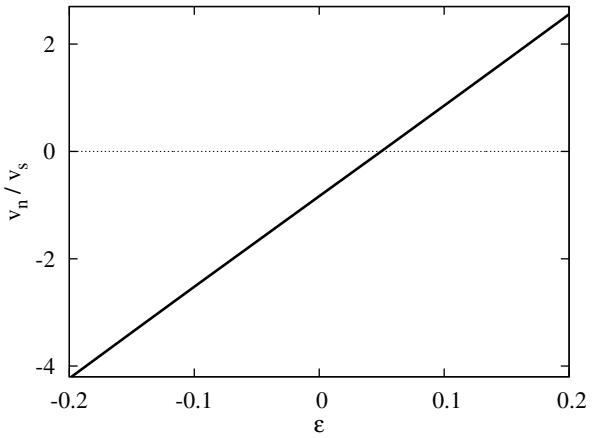

Figure 9. The mean actuation velocity v_n varies linearly with the modulation parameter ε of the shaking velocity in equation (1). For sufficiently positive values $\varepsilon \gtrsim 0.05$ the liquid shaking outweighs gravitation and v_n becomes positive. For sinusoidal shaking with $\varepsilon = 0$ the particle sinks due to gravity and at negative values of ε the inertial actuation leads to an enhanced sedimentation velocity.

The mean velocity v_n is given as function of the amplitude U of the shaking velocity in figure 10. Without shaking at $U = 0$ the ring sinks. With increasing values of U and $\varepsilon = 1$ the sinking velocity slows down until it turns over to an upward motion at larger

values $U \gtrsim 225 v_s$.

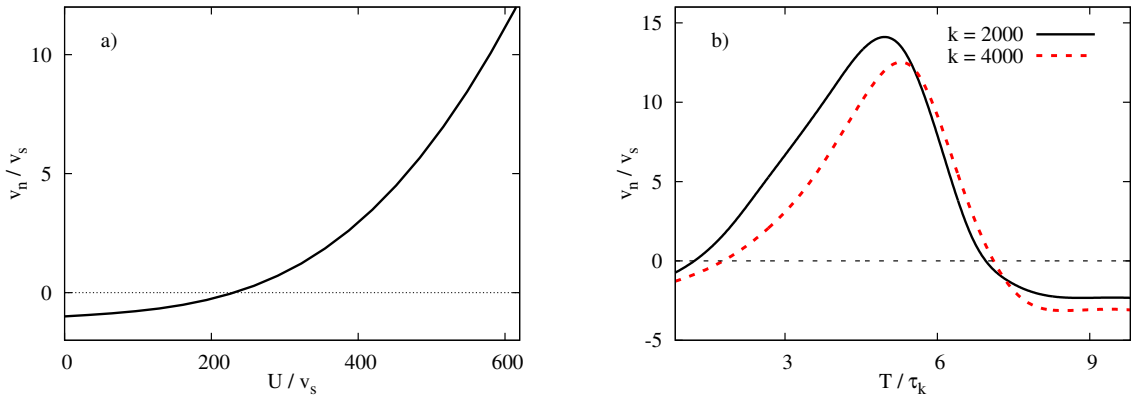

Figure 10. a) shows the mean propulsion velocity v_n as a function of the shaking amplitude U. For positive ε the actuation is upward directed and for $\varepsilon = 1$ it outweighs gravitation in the range $U \gtrsim 225 v_s$, i.e., v_n becomes positive. b) shows the mean velocity of the ring as a function of the ratio T/τ_k for two different values of the spring stiffness k. At small values of T/τ_k the ring can not follow the liquid motion, it is not deformed and just sinking. At intermediate values T/τ_k the mean velocity becomes positive for both values of k with a maximum in the range $T/\tau_k \approx 5$. For longer shaking periods the ring sinks again.

The mean velocity v_n depends also on the ratio between the shaking period and the relaxation time T/τ_k as shown in figure 10b) for two values of the spring stiffness k. At small values of $T/\tau_k \lesssim 0.4$ the ring sinks because the shaking period is too small to cause sufficient deformations and differences between the Stokes drags during the two half periods. For longer periods T and intermediate values of T/τ_k the acceleration induced shape and Stokes drag changes of the ring become sufficiently strong to outweigh gravitation. For both spring constants k the mean velocity becomes positive in a wide range and reaches its maximum at a value of $T/\tau_k \approx 5$ due to the large deformation, as indicated in figure 10b). At higher values of T/τ_k the deformation becomes smaller and therefore the ring sinks again due to gravitation. The values of the shape relaxation time $\tau_k \approx 0.08$ (cf. equation (33)) and the velocity relaxation time $\tau_v \approx 0.07$ (cf. equation (22)) are comparable, so that T/τ_v is in a range where the particle's inertia is important.

4.3. Actuation of a symmetric capsule in a non-symmetrically shaken liquid

In the previous section we demonstrated that a symmetric, semiflexible bead-spring ring is actuated in a liquid that is non-symmetrically shaken with $u_0(t) \neq -u_0(t+T/2)$. This is also the case for a realistic symmetric capsule as we show by LBM simulations in this section. Besides the parameters given in section 2.3, the following ones are used: $R = 10\mu\text{m}$, $\rho_{capsule} = 2\rho_{fluid} = 2000 \frac{\text{kg}}{\text{m}^3}$, $k_v = 2.78 \cdot 10^5 \frac{\text{kg}}{\text{s}^2\text{m}}$, $G = 7.89 \cdot 10^{-4} \frac{\text{kg}}{\text{s}^2}$, $\varepsilon = -1$ and $\kappa_c = 1.51 \cdot 10^{-14} \frac{\text{kg m}^2}{\text{s}^2}$. The shaking period T is chosen so, that the capsule's inertia is significant and the capsule is sufficiently deformed: $T/\tau_v \approx 2$ and $T/\tau_k \approx 0.9$ (cf. equations (23) and (34)).

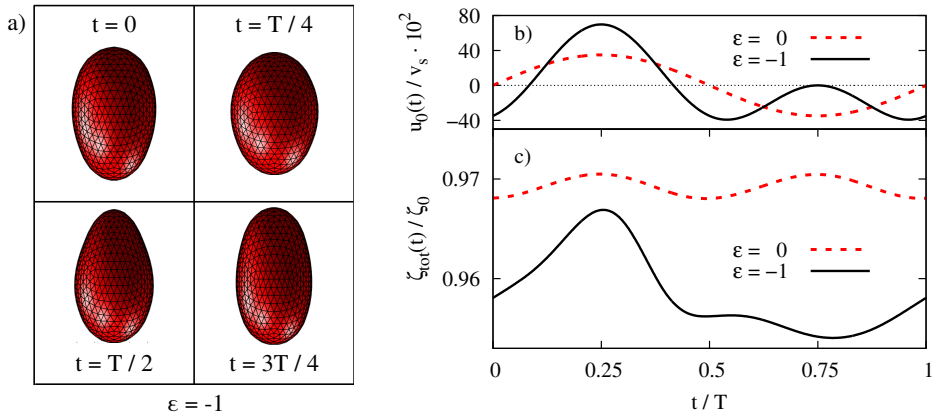

Figure 11. a) shows the capsule's shape at different times in a shaken liquid with a non-symmetric liquid velocity, i.e., $u_0(t+T/2) \neq u_0(t)$, as shown by the solid line in b) and as given by equation (1) for $\varepsilon = -1.0$. In c) the drag coefficient $\zeta_{tot}(t)$ of the capsule is shown in units of $\zeta_0 = 6\pi\eta R$. In a sinusoidally shaken liquid, cf. dashed line in b), $\zeta_{tot}(t)$ is identical in both half periods. For a non-symmetrically shaken liquid also $\zeta_{tot}(t)$ is non-symmetric, cf. solid line and $\varepsilon = -1$, as well as the capsule shapes in a).

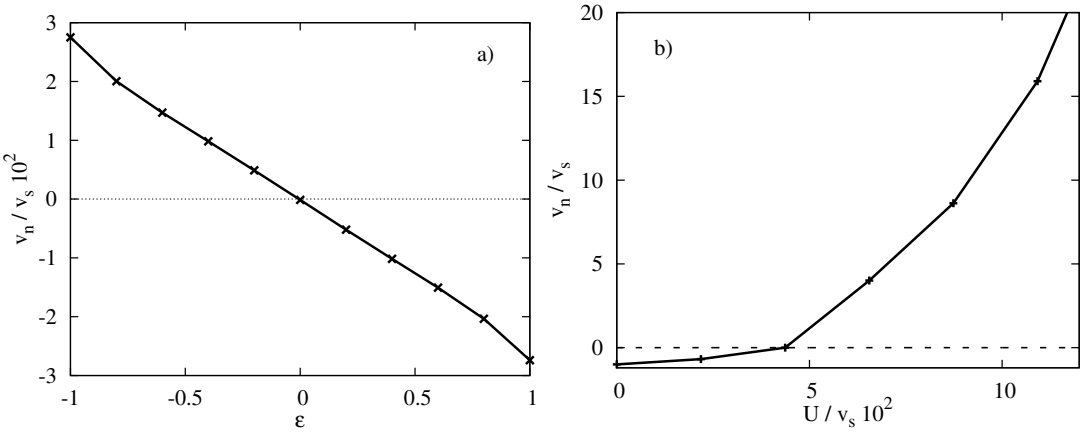

Figure 12. a) shows the mean-propulsion velocity v_n of a homogeneous capsule as a function of the asymmetry parameter ε of the shaking velocity in equation (1). For a sinusoidal shaking with $\varepsilon = 0$ the capsule sinks. At sufficiently negative values $\varepsilon < 0$ the capsule moves upwards and for $\varepsilon > 0$ downwards. This allows to control the direction of v_n via the time-dependence of liquid shaking. In b) v_n is given as function of the amplitude U of the shaking velocity. At low values of U the shaking effect is weak and the capsule sinks. In the range $U \geq 450 v_s$ the actuation induced by the shaking is stronger than the gravity and the capsule moves upwards.

In figure 11a) the shape of the capsule is shown during one period T of the non-symmetric shaking velocity with $u_0(t+T/2) \neq u_0(t)$. For a sinusoidal shaking as displayed in figure 11b), i.e., $\varepsilon = 0$ and $u_0(t) = -u_0(t+T/2)$, the capsule's drag coefficient $\zeta_{tot}(t)$ (cf. Appendix A) shown in figure 11c) is the same during both half periods of the shaking with $\zeta_{tot}(t) = \zeta_{tot}(t+T/2)$. In this case there is no mean actuation and the capsule just sediments due to gravity. If the liquid is shaken non-symmetrically

with $\varepsilon \neq 0$ the drag coefficient differs in both half periods, i.e., $\zeta_{tot}(t) \neq \zeta_{tot}(t + T/2)$. In this case the capsule is actuated by liquid shaking.

Figure 12a) shows how the mean velocity v_n of the capsule depends on the asymmetry parameter ε of the shaking velocity. At sufficient negative values of $\varepsilon \lesssim -0.01$ the upward oriented actuation overcomes gravity and we find a positive mean velocity v_n. Positive values of ε enhance the sedimentation. Thus the direction of the mean capsule actuation can be controlled via the asymmetry parameter ε of the shaking velocity. Note that the mean velocity induced by the shaking also depends on the period T.

Besides the asymmetry ε also a sufficiently high amplitude U of the shaking velocity is required to overcome gravity. Figure 12b) displays the mean velocity v_n as a function of the amplitude U: At low values of U the capsule sinks due to the gravity. For the chosen parameters one finds with $U = 0$ the sedimentation velocity $v_s = 0.19\frac{\text{mm}}{\text{s}}$. For $U \gtrsim 450 v_s$ the mean velocity v_n induced by liquid shaking is stronger than sedimentation and the capsule moves upwards for $\varepsilon = -1.0$. The Reynolds number used in figure 12b) is $0 < \text{Re} \lesssim 2$. Hence, the inertia induced actuation effect is found at small as well as at intermediate values of Re. The qualitative results are comparable to those found for the ring in the previous section in the limit of a vanishing Reynolds number, compare e.g., figure 10a) and figure 12b).

5. Summary and conclusions

We investigated a new kind of microswimmers, so-called passive swimmers. These microswimmers are soft particles with a mass density different from the liquid, which are driven by an oscillating background flow or a shaking of the liquid.

Previous studies focused on the propulsion of intrinsically asymmetric soft particles in sinusoidal liquid motion [11, 12]. With our extension to soft bead-spring tetrahedrons and to asymmetric, soft Janus capsules, we show that the inertia driven propulsion mechanism can even outweigh gravity. Moreover, we show that this novel inertia driven passive swimming mechanism works for the wider class of symmetric soft particles, such as capsules.

By a semi-analytical model calculation we cover the essential properties of the inertia driven propulsion mechanism in liquids shaken periodically with the velocity $\mathbf{u}_0(t + T) = \mathbf{u}_0(t)$. It shows the following requirements: First, the mass densities of the particles and the liquid must be different. Secondly, the Stokes drag during both periods of the shaking with different directions must differ (e.g., due to a deformation). Thirdly, the shaking period T has to be chosen in the order of magnitude of the relaxation time that the particles needs to adjust to the liquid velocity. The essential difference in the drag coefficient during both half periods is achieved by the asymmetry of the particle.

We suggest that this asymmetry can also be achieved by a non-symmetric shaking velocity with $\mathbf{u}_0(t + T/2) \neq \mathbf{u}_0(t)$, as given for instance by equation (1), instead of the intrinsic particle asymmetry. Such a non-symmetric liquid shaking leads to a non-

reciprocal particle deformation and Stokes drag.

This qualitative reasoning and the analytical considerations are verified and supported by simulations. We use symmetric and asymmetric bead spring models and complementary Lattice Boltzmann Simulations of realistic soft symmetric capsules and asymmetric Janus capsules. Asymmetric particles in a sinusoidally shaken fluid have two stable orientations and they exhibit therefore two directions of passive swimming, depending on the initial orientation. In contrast, for the wider class of symmetric particles in non-symmetrically shaken liquids the propulsion direction is determined by the shaking. Therefore the swimming direction can be selected by the engineered time-dependence of liquid shaking.

To provide examples of achievable propulsion velocities for symmetric and asymmetric Janus capsules we chose a realistic capsule size of about 10 μm and a stiffness of $8 \cdot 10^{-4}$ $\frac{\mathrm{N}}{\mathrm{m}}$, which fits the values of common capsules [25, 43, 44]. A higher mass density for capsules than for the liquid can be achieved if salt is dissolved in the liquid inside the capsule [45], whereby water with dissolved salt can reach densities up to three times higher than pure water (without salt). Here we chose the mass density ratio $\rho_{caps}/\rho_{liquid} = 2.0$ and the shaking frequency 10 kHz (see e.g., [46, 47, 48]) of the order of the inverse of velocity relaxation time of about 44μs. For this choice of parameters and a maximal amplitude 0.5 $\frac{\mathrm{m}}{\mathrm{s}}$ of the liquid velocity one obtains for a symmetric capsule with in Lattice Boltzmann simulations an upward swim velocity of about 57 $\frac{\mathrm{mm}}{\mathrm{s}}$. For a Janus capsule one obtains for shaking-velocity amplitude 0.3 $\frac{\mathrm{m}}{s}$ an upward swim velocity of about 15 $\frac{\mathrm{mm}}{\mathrm{s}}$.

Besides the possibility to engineer passive swimmers, the described effects have further applications: The inertia induced actuation may be exploited for separating particles with respect to their different mass and different elasticity (deformability). The separation of two kinds of soft particles with a different stiffness is achieved by choosing a shaking period that fits the shape relaxation time of one type of particles but not of the others. In this case one particle type is stronger actuated and can be accumulated for instance near one container wall. An example are biological cells. They have often a different density than water [49] or other carrier liquids. In addition the stiffness of cells is often an indicator of their health status [50, 51, 52]. In this case healthy cells may be separated for instance from malignant cells by non-symmetric liquid shaking. Our insights about inertia driven particle propulsion might also have impact on further systems studied at finite values of the Reynolds number [53, 54].

6. Acknowledgments

We acknowledge the support by the French-German University (Grant CFDA-Q1-14, program “Living fluids”).

Appendix A. Dynamic Oseen tensor and drag coefficient

Dynamic Oseen tensor. The liquid velocity $\mathbf{u}(\mathbf{r}_i)$ at the particle positions $\mathbf{r}_i$ includes the imposed homogeneous flow $\mathbf{u}_0$ as described by equation (1) and the flow disturbances caused by differences between the particle velocities $\mathbf{v}_j$ and the liquid velocity $\mathbf{u}_0(\mathbf{r}_j)$. For this we use the general solution of the linear part of the Navier-Stokes-equation $\rho_f \frac{\partial \mathbf{u}}{\partial t} = \eta \Delta \mathbf{u} - \nabla p + \mathbf{f}(\mathbf{r}, t)$ for an arbitrary point-like force acting on the fluid. The solution of this problem with a point force $\mathbf{f}(\mathbf{r}, t) = \mathbf{F}(t)\delta(r - r')$ is given by [33]

$$\mathbf{u}_\delta(\mathbf{r}) = \int dt' \; \mathbf{H}(\mathbf{r} - \mathbf{r}', t')\mathbf{F}(t') \,, \tag{A.1}$$

$$\mathbf{H}(\mathbf{r} - \mathbf{r}') = p(r, t)\mathbf{1} - q(r, t)\frac{\mathbf{r} \otimes \mathbf{r}}{r^2} \,, \tag{A.2}$$

$$p(r, t) = \left(1 + \frac{2\nu t}{r^2}\right) f(r, t) - \frac{g(r, t)}{r^2} \,, \tag{A.3}$$

$$q(r, t) = \left(1 + \frac{6\nu t}{r^2}\right) f(r, t) - \frac{3g(r, t)}{r^2} \,, \tag{A.4}$$

$$f(r, t) = \frac{1}{(4\pi\nu t)^{3/2}} \exp\left[\frac{-r^2}{4\nu t}\right] \,, \tag{A.5}$$

$$g(r, t) = \frac{1}{4\pi r}\Phi\left[\frac{r}{(4\nu t)^{1/2}}\right] \,, \tag{A.6}$$

with $\nu = \frac{\eta}{\rho}$, the error function Φ, the unit matrix $\mathbf{1}$ and the dyadic product $\otimes$. This allows to calculate the liquid velocity at a bead position $\mathbf{u}_i = \mathbf{u}(\mathbf{r}_i)$,

$$\mathbf{u}_i = \mathbf{u}_0(t) + \sum_{j \neq i} \int_0^t dt' \; \mathbf{H}_{i,j}(t') \cdot \mathbf{F}_j^{(1)}(t') \tag{A.7}$$

with $\mathbf{H}_{i,j}(t) = \mathbf{H}(\mathbf{r}_i - \mathbf{r}_j, t)$. This velocity is composed of the homogeneous background flow and the liquid velocity changes caused by the differences between the particle velocities and the flow $\mathbf{u}_0$, which are induced by the forces $\mathbf{F}_j^{(1)}$ given in section 2.2.

Determination of the drag coefficient. To calculate the drag $\zeta_{tot}(t)$, we follow the procedure given in [55, 56, 57]. For this, we use the positions of the beads/nodes on the particle surface obtained by simulations. The drag at time t is determined by assuming a fixed shape which implies a constant velocity $\mathbf{v}_i = \mathbf{v} = v\hat{\mathbf{e}}_y$ on each bead/node. We calculate the forces via

$$\mathbf{v}_i = \sum_j \mathbf{H}_{i,j}\mathbf{F}_j^{(P)}, \tag{A.8}$$

where

$$\mathbf{H}_{i,j} = \begin{cases} \mathbf{O}(\mathbf{r}_i - \mathbf{r}_j), \\ \frac{1}{\zeta_b}\mathbf{1} \end{cases} \tag{A.9}$$

is the mobility matrix including the hydrodynamic interaction between particle $\mathbf{r}_i$ and $\mathbf{r}_j$ described by the Oseen tensor $\mathbf{O}(\mathbf{r}) = \frac{1}{8\pi\eta r}\left(\mathbf{1} + \frac{\mathbf{r}\otimes\mathbf{r}}{r^2}\right)$. The drag finally follows with

$$\mathbf{F}_{tot} = \sum_j \mathbf{F}_j = \zeta_{tot}\mathbf{v}. \tag{A.10}$$

The values ζ_1 and ζ_2 (used in equation (25)) are chosen as the maximal value during the first or the second halve period, respectively.

Appendix B. Tetrahedron consisting of beads with different mass

Here we investigate the effects of the mass inhomogeneity on the propulsion velocity of a tetrahedron. If all beads of a tetrahedron have the same mass density, the upward oriented tetrahedron (▲) and the downward oriented one (▼) are both stable. By changing the mass density of one of the four beads then one of both orientations with respect to the gravitational field is preferred, similar as in reference [12]. For example, if the tetrahedron sinks (without liquid shaking) the lighter bead points upwards after a certain time. For this orientation we investigate the effect of a inhomogeneous mass density on the propulsion velocity.

We introduce the density ratio α between one and the other three beads, i.e., $\rho_1 = \alpha\rho_{2,3,4}$, and keep the mean density $\bar{\rho}$ constant:

$$\bar{\rho} = \frac{1}{N}\sum_{i=1}^{N}\rho_i\,, \tag{B.1}$$

$$\rho_1 = \alpha\rho_2,\ \ \rho_2 = \rho_3 = \rho_4\,. \tag{B.2}$$

Figure B1 shows the mean velocity v_n of the tetrahedron and the amplitude of the

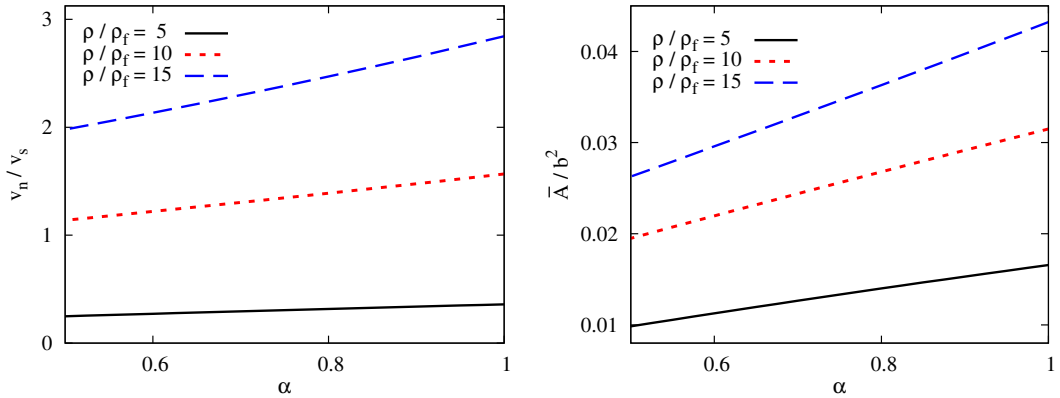

Figure B1. The left part shows the mean propulsion velocity of the tetrahedron for different mass-density ratios $\bar{\rho}/\rho_f$ as function of the density ratio α and the right part the amplitude of the shape deformation $\bar{A}$ as defined in equation (35).

shape deformation $\bar{A}$ (defined in equation (35)) as a function of the mass-density ratio α. The tetrahedron moves slower with an increasing difference of the densities of the beads, which can be explained as follows. A lighter bead can follow the heavier ones

easily and thus the lighter bead moves more in phase with the heavy beads than a bead of the same mass density. This results in smaller spring deformation and in a lower deformation amplitude $\bar{A}$, cf. figure B1. A smaller amplitude $\bar{A}$ leads to smaller temporal changes of the drag coefficient ζ_{tot} and therefore to slower mean velocity.

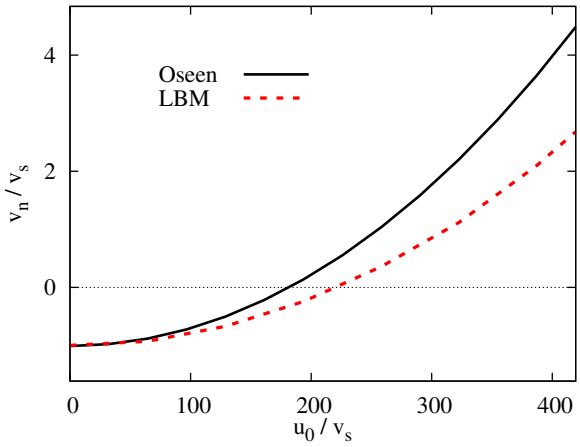

Figure B2. The mean propulsion velocity of a tetrahedron is shown for $\alpha = 0.6$ as a function of the amplitude U of the liquid velocity, obtained by simulations of the Maxey-Riley equations and Lattice Boltzmann simulations.

So far we have used the Maxey and Riley equations and the dynamic Oseen tensor, i.e., we have neglected effects of a finite Reynolds number. Here we compare the results with Lattice Boltzmann simulations of the full Navier-Stokes equation with the tetrahedron. Figure B2 shows the mean velocity of a tetrahedron with $\alpha = 0.6$ as function of the amplitude U of the shaking velocity. Both methods show that the mean velocity increases continuously with the amplitude U. Furthermore both simulations show that at low values of U the tetrahedron sinks and above a critical value of U the tetrahedron rises against gravity. Thus the numerical methods agree qualitatively. This means the LBM simulations, taking effects of a finite Reynolds number into account, and the Maxey and Riley equations including the dynamic Oseen tensor in the limit $Re = 0$ describe inertia induced propulsion of the tetrahedron. This confirms that the mean velocity is the result the temporal change of the drag coefficient $\zeta_{tot}(t)$ and a finite Reynolds number just modifies this result quantitatively.

References

[1] Lauga E and Goldstein R E 2012 *Physics Today* **65** 30

[2] Lauga E and Powers T R 2009 *Phys. Rep.* **72** 096601

[3] Guasto J S, Rusconi R and Stocker R 2012 *Annu. Rev. Fluid Mech.* **44** 373

[4] Bechinger C, Leonardo R D, Löwen H, Reichardt C, Volpe G and Volpe G 2016 *Rev. Mod. Phys.* **88** 045006

[5] Lauga E 2016 *Annu. Rev. Fluid Mech.* **48** 105

[6] Squires T M and Quake S R 2005 *Rev. Mod. Phys.* **77** 978

[7] Sackmann E K, Fulton A L and Beebe D L 2014 *Nature* **507** 181

[8] Dahl J B, Lin J M G, Muller S J and Kumar S 2015 *Ann. Rev. Chem. Biomol. Eng.* **6** 293

[9] Amini H, Lee W and Carlo D D 2014 *Lap Chip* **14** 2739

[10] Secomb T W 2017 *Annu. Rev. Fluid Mech.* **49** 443

[11] Jo I, Huang Y, Zimmermann W and Kanso E 2016 *Phys. Rev. E* **94** 063116

[12] Morita T, Omori T and Ishikawa T 2018 *Phys. Rev. E* **98** 023108

[13] Goldstein R E 2015 *Annu. Rev. Fluid Mech.* **47** 343

[14] Wu H, Thiébaud M, Hu W F, Farutin A, Rafaï S, Lai M C, Peyla P and Misbah C 2015 *Phys. Rev. E* **92** 050701

[15] Wu H, Farutin A, Hu W F, Thibaud M, Rafaï S, Peyla P, Lai M C and Misbah C 2016 *Soft Matter* **12** 7470

[16] Farutin A, Rafaï S, Dysthe D K, Duperray A, Peyla P and Misbah C 2013 *Phys. Rev. Lett.* **111** 228102

[17] Purcell E M 1977 *Am. J. Phys.* **45** 3

[18] Laumann M, Bauknecht P, Gekle S, Kienle D and Zimmermann W 2017 *EPL* **117** 44001

[19] Olla P 2010 *Phys. Rev. E* **82** 015302(R)

[20] Leal L G 1980 *Annu. Rev. Fluid Mech.* **12** 435

[21] Mandal S, Bandopadhyay A and Chakraborty S 2015 *Phys. Rev. E* **92** 023002

[22] Kaoui B, Ristow G H, Cantat I, Misbah C and Zimmermann W 2008 *Phys. Rev. E* **77** 021903

[23] Coupier G, Kaoui B, Podgorski T and Misbah C 2008 *Phys. Fluids* **20** 111702

[24] Doddi S K and Bagchi P 2008 *Int. J. Multiphase Flow* **34** 966

[25] Chen L, An H Z and Doyle P S 2015 *Langmuir* **31** 9228

[26] Klosta D, Baldwin K A, Baldwin R J A, Hill R J A, Bowley R M and Swift M R 2015 *Phys. Rev. Lett.* **115** 248102

[27] Maxey M R and Riley J J 1983 *Phys. Fluids* **26** 883

[28] Krueger T, Varnik F and Raabe D 2011 *Comput. Math. Appl.* **61** 3485

[29] Ramanjan S and Pozrikidis C 1998 *J. Fluid Mech.* **361** 117

[30] Barthès-Biesel D 2016 *Annu. Rev. Fluid Mech.* **48** 25

[31] G Gompper and DM Kroll 1996 *J. Phys. I France* **6** 1305

[32] Krueger T, Gross M, Raabe D and Varnik F 2013 *Soft Matter* **9** 9008

[33] Español P, Rubio M A and Zúñiga I 1995 *Phys. Rev. E* **51** 803

[34] Aidun C K and Clausen J R *Annu. Rev. Fluid. Mech.*

[35] Aidun C K, Lu Y and Ding E J 1998 *J. Fluid Mech.* **373** 287

[36] d'Humières D, Ginzburg I, Krafczyk M, Lallemand P and Luo L S 2002 *Phil. Trans. R. Soc. Lond. A* **360** 437

[37] Ladd A J C 1994 *J. Fluid Mech.* **271** 285

[38] Guo Z, Zheng C and Shi B 2002 *Phys. Rev. E* **65** 046308

[39] Ladd A J C and Verberg R 2001 *J. Stat. Phys.* **104** 1191

[40] Shao J Y and Shu C 2015 *Int. J. Numer. Methods Fluids* **77** 526

[41] Premnath K N and Abraham J 2007 *J. Comput. Phys.* **224** 539

[42] Peskin C S 2002 *Acta Numer.* **11** 479

[43] Sun H, Wong E H H, Yan Y, Cui J, Dai Q, Guo J, Qiao G G and Caruso F 2015 *Chem. Sci.* **6** 3505

[44] Amstad E 2017 *CHIMIA* **71** 334

[45] Koroznikova L, Klutke C, McKnight S and Hall S 2008 *J. S. Afr. Inst. Min. Metall.* **108** 25

[46] Gerlach T, Schuenemann M and Wurmus H 1995 *J. Micromech. Microeng.* **5** 199

[47] Nabavi M and Mongeau L 2009 *Microfluid. Nanofluid.* **7** 669

[48] Roberts D C, Li H, Steyn J, Turner K T, Mlcak R, Saggere L, Spearing S, Schmidt M A and Hagood N W 2002 *Sens. Actuators, A* **97-98** 620

[49] Milo R and Phillips R 2016 *Cell biology by the numbers* (New York, NY: Garland Science)

[50] Karimi A, Yazdi S and Ardekani A M 2013 *Biomicrofluidics* **7** 021501

[51] Cross S E, Jin Y S, Rao J and Gimzewski J K 2007 *Nat. Nanotechnol.* **2** 780

[52] Guck J, Schinkinger S, Lincoln B, Wottawah F, Ebert S, Romeyke M, Lenz D, Erickson H M, Ananthakrishnan R, Mitchell D, Ks J, Ulvick S and Bilby C 2005 *Biophys. J.* **88** 3689

[53] Sorokin V S, Blekhmann I I and Vasilkow V B 2012 *Nonlinear Dyn.* **67** 147

[54] Scholz C, Jahanshai S, Ldov A and Löwen H 2018 *Nature Comm.* **9** 5156

[55] Dhont J K G 1996 *An Introduction to dynamics of colloids* (Amsterdam: Elsevier)

[56] Doi M and Edwards S F 1986 *The Theory of Polymer Dynamics* (Oxford: Clarendon Press)

[57] Leal L G 2007 *Advanced Transport Phenomena* (Cambridge: Cambridge University Press)

Publication 4

Migration reversal of soft particles in vertical flows
A. Förtsch, M. Laumann, D. Kienle and W. Zimmermann
2017 EPL **119** 64003

DOI: 10.1209/0295-5075/119/64003

epl A Letters Journal Exploring the Frontiers of Physics

September 2017

EPL, **119** (2017) 64003 www.epljournal.org
doi: 10.1209/0295-5075/119/64003

Migration reversal of soft particles in vertical flows

Andre Förtsch, Matthias Laumann, Diego Kienle and Walter Zimmermann

Theoretische Physik I, Universität Bayreuth - 95440 Bayreuth, Germany

received 13 June 2017; accepted in final form 13 November 2017
published online 14 December 2017

PACS 47.57.ef – Sedimentation and migration
PACS 83.50.-v – Deformation and flow
PACS 47.15.G- – Low-Reynolds-number (creeping) flows

Abstract – Non-neutrally buoyant soft particles in vertical microflows are investigated. We find for light soft particles in downward Poiseuille flow cross-streamline migration (CSM) to off-center streamlines and for heavy particles CSM to the center. In both cases a reversal of the vertical flow direction and the related shear gradient causes a *reversal* of the migration direction. This gravitational driven CSM of soft particles occurs also in linear shear flows: heavy (light) particles migrate antiparallel (parallel) to the shear gradient. The surprising, flow-induced migration (reversal) is characterized by simulations and analytical approximations, confirming our plausible explanation of the effect. This might be applied for separating particles.

Introduction. – Microfluidics is a rapidly evolving cross-disciplinary field, ranging from basic physics to a large variety of applications in life science and technology [1–3]. The blooming subfield of the dynamics of *neutrally buoyant* soft particles in suspension and their cross-streamline migration (CSM) in rectilinear shear flows plays a central role for blood flow, (blood) cell and DNA sorting or polymer processing among others [2–5]. In contrast, little is known about the dynamics of *non-neutrally buoyant* soft particles in rectilinear flows. We demonstrate in this work a novel migration reversal for such particles.

Segre and Silberberg reported in 1961 on CSM of *neutrally buoyant* rigid particles in finite Reynolds-number flows through pipes [6]. When particles and channels approach the micrometer scale, fluid inertia does not matter and particles follow the Stokesian dynamics. In this limit CSM occurs not for rigid but for soft particles for example in rectilinear flows [7,8], whereby the flows fore-aft symmetry is broken, requiring intra-particle hydrodynamic interaction [7]. Such symmetry breaking occurs also near boundaries via wall-induced lift forces [3,8,9] or by space-dependent shear rates, so that dumbbells [7], droplets [10,11], vesicles and capsules [12–14] exhibit CSM even in unbounded flow. Such parity-breaking mechanisms may be also accompanied by a viscosity contrast [15] or chirality [16]. Recently, CSM was found for asymmetric soft particles in time-dependent linear shear flow [17] and that soft particles are actuated even in a homogeneous but time-dependent flow by taking particle inertia into account [18].

Heavy rigid particles in a finite Reynolds number flow downward or upward in a gravitational field migrate away from or to the tube center, respectively [19]. Effects of axial forces along the tube axis on particles and their CSM in finite Reynolds number flows were studied in refs. [20–22] and effects of axial (electrical) forces on (charged) polymers in Poiseuille flows in refs. [23,24]. In the wide field of sedimentation, characteristic deformations of sedimenting heavy vesicles have been explored only recently [25], but very little is known about the dynamics non-neutrally buoyant soft particles in vertical Stokes flows.

Here we show that during sedimentation in a channel heavy soft microparticles migrate to its center, while rigid particles do not [26]. Moreover, heavy (light) soft particles migrate antiparallel (parallel) to the shear gradient in vertical rectilinear Stokes flows, as shown in fig. 1. This dependence of the CSM-direction on the shear gradient direction is obtained by approximate analytical calculations and by numerical simulations for soft capsules and ring polymers. We also provide a plausible qualitative explanation of CSM of non-neutral particles: It is based on the interplay between the shear-induced orientation of the elliptically shaped soft capsule (ring) together with its anisotropic friction coefficients.

Model and approach. – To investigate the cross-stream migration of non-neutrally buoyant soft particles

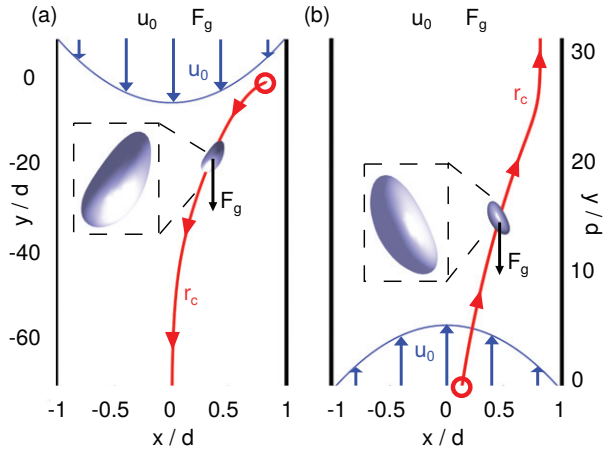

Fig. 1: (Colour online) Impact of the gravitational force $\mathbf{F}_g$ on migration trajectories $\mathbf{r}_c(t)$ of a heavy capsule in a vertical-plane Poiseuille flow $\mathbf{u}_0(x)$ and channel width $2d$. The simulations reveal that the capsule displays (a) a migration to the channel center when $\mathbf{u}_0 \downdownarrows \mathbf{F}_g$ or (b) a migration to the wall when $\mathbf{u}_0 \uparrow\downarrow \mathbf{F}_g$. Parameters: see footnote [1].

under the impact of a vertical gravitational force $\mathbf{F}_g = \mathrm{F}_g\mathbf{e}_y$ in rectilinear flows, we use the capsule and ring as particle representatives, exposed to a vertical 3D, plane Poiseuille flow along the y-axis

$$\mathbf{u}_0(x) = \mathrm{u}_0\left[1-(x/d)^2\right]\mathbf{e}_y \tag{1}$$

with its two confining boundaries at $x_d = \pm d$ and $\mathrm{u}_0 \gtrless 0$ the maximum flow velocity at the channel center.

The capsule and ring are described by a bead-spring model consisting of N beads. The surface of the capsule is triangulated with the beads at the vertices (see `Supplementarymaterial.pdf` given as Supplementary Material (SM)). Their Stokesian dynamics [27] is described by the coupled equations ($1 \le i \le N$),

$$\dot{\mathbf{r}}_i = \mathbf{u}_0(\mathbf{r}_i) + \sum_{j=1}^{N}\mathbf{H}_{ij}\cdot\mathbf{F}_j, \tag{2}$$

whereby the inertia of the beads is neglected due to the small Stokes number (see SM). The particle center is given by $\mathbf{r}_c = \sum_{i=1}^{N}\mathbf{r}_i/N$.

The force on bead j is given by $\mathbf{F}_j = -\nabla_j V(\mathbf{r}) + \mathbf{F}_g$ with $V(\mathbf{r})$ referring to the total potential, and $\mathbf{H}_{ij}$ denoting the mobility matrix, as specified in the following.

For a capsule, the total potential is $V(\mathbf{r}) = V_{NH}+V_b+V_v$ with the Neo-Hookean potential V_{NH}, suited to describe rubber-like materials with a constant surface shear-elastic modulus G [28,29], and a bending potential V_b

$$V_b = -\frac{\kappa_c}{2}\sum_{i,j}\left(1-\cos\beta_{i,j}\right) \tag{3}$$

with bending elasticity κ_c. The angle $\beta_{i,j}$ is formed by the two normal surface vectors of nearest-neighbor triangles with beads at the triangle corners [30]. The potential $V_v = -\frac{k_v}{\mathcal{V}_0}(\mathcal{V}(t)-\mathcal{V}_0)^2$ keeps the capsule's instantaneous volume $\mathcal{V}(t)$ close to the reference volume $\mathcal{V}_0 = \frac{4}{3}\pi R^3$ of a spherical capsule of radius R with volume stiffness k_v.

The total potential of the ring of radius R reads $V(\mathbf{r}) = V_h + V_b$, using a harmonic potential $V_h = \frac{k}{2}\sum_{i=1}^{N}(R_i-b)^2$ with spring constant k, equilibrium bond length b, and $R_i = |\mathbf{R}_i|$ the magnitude of the bond vector $\mathbf{R}_i = \mathbf{r}_i - \mathbf{r}_{i+1}$ of the next-neighbor beads i and $i+1$. The bending potential V_b with a bending stiffness κ_r is given by

$$V_b = -\frac{\kappa_r}{2}\sum_{i=1}^{N}\ln\left(1+\cos\beta_i\right), \tag{4}$$

with the angle β_i defined via $\cos\beta_i = \mathbf{e}_{R_{i-1}}\cdot\mathbf{e}_{R_i}$ by the bond unit vectors $\mathbf{e}_{R_j} = \mathbf{R}_j/R_j$.

The Blake tensor $\mathbf{H}_{ij}$, describing the hydrodynamic interaction (HI) between beads i and j in the presence of a single plane boundary within the yz-plane [31], reads

$$\begin{aligned}\mathbf{H}_{ij}(\mathbf{r}_i,\mathbf{r}_j) = {}& {}^{S}\mathbf{H}_{ij}(\mathbf{r}_i,\mathbf{r}_j) - {}^{S}\mathbf{H}_{ij}(\mathbf{r}_i,\mathbf{r}'_j)\\ & + {}^{D}\mathbf{H}_{ij}(\mathbf{r}_i,\mathbf{r}'_j) - {}^{SD}\mathbf{H}_{ij}(\mathbf{r}_i,\mathbf{r}'_j)\end{aligned} \tag{5}$$

with $\mathbf{r}'_j = (x_j + 2h_j, y_j, z_j)$ the position of the mirror-particle of bead j at a wall distance h_j. The first term in eq. (5) describes the bulk HI via the Oseen tensor [27]

$${}^{S}H_{ij}^{\alpha\beta}(\mathbf{r}_i,\mathbf{r}_j) = \begin{cases}\dfrac{1}{8\pi\eta R_{ij}}\left[\delta_{\alpha\beta}+\mathbf{e}^{\alpha}_{R_{ij}}\mathbf{e}^{\beta}_{R_{ij}}\right], & i\neq j,\\ \dfrac{1}{6\pi\eta a}\delta_{\alpha\beta}, & i=j,\end{cases} \tag{6}$$

with $\mathbf{e}_{R_{ij}} = \mathbf{R}_{ij}/R_{ij}$ and $\mathbf{R}_{ij} = \mathbf{r}_i - \mathbf{r}_j$; η and a refer to the viscosity, respectively, bead radius, and $\alpha,\beta \in \{x,y,z\}$.

The term ${}^{S}\mathbf{H}_{ij}(\mathbf{r}_i,\mathbf{r}'_j)$ is the source singlet due to the HI of the mirror bead j, given by eq. (6) for $i \neq j$ with $\mathbf{R}_{ij}$ replaced by $\bar{\mathbf{R}}_{ij} = \mathbf{r}_i - \mathbf{r}'_j$ and $\bar{\mathbf{e}}_{\bar{R}_{ij}} = \bar{\mathbf{R}}_{ij}/\bar{R}_{ij}$. The last two terms in eq. (5) refer to the Stokes doublet (D)

$${}^{D}H_{ij}^{\alpha\beta}(\mathbf{r}_i,\mathbf{r}'_j) = \frac{h_j^2(1-2\delta_{\beta x})}{4\pi\eta\bar{R}_{ij}^3}\left[\delta_{\alpha\beta}-3\bar{\mathbf{e}}^{\alpha}_{R_{ij}}\bar{\mathbf{e}}^{\beta}_{R_{ij}}\right], \tag{7}$$

and source doublet (SD)

$$\begin{aligned}{}^{SD}H_{ij}^{\alpha\beta}(\mathbf{r}_i,\mathbf{r}'_j) = {}& \frac{1}{4\pi\eta\bar{R}_{ij}^2}h_j\left(1-2\delta_{\beta x}\right)\\ & \times\left[\delta_{\alpha\beta}\bar{\mathbf{e}}^{x}_{R_{ij}} - \delta_{\alpha x}\bar{\mathbf{e}}^{\beta}_{R_{ij}} + \delta_{\beta x}\bar{\mathbf{e}}^{\alpha}_{R_{ij}} - 3\bar{\mathbf{e}}^{\alpha}_{R_{ij}}\bar{\mathbf{e}}^{\beta}_{R_{ij}}\bar{\mathbf{R}}^{x}_{ij}\right].\end{aligned} \tag{8}$$

Screening effects of a second wall are included by superposition of the HI of the single walls, and provide reasonable results for a channel width to particle size ratio larger than 5 [32]. In simulations where wall-HI is turned off, the mobility $\mathbf{H}_{ij}$ in eq. (5) reduces to the Oseen tensor ${}^{S}\mathbf{H}_{ij}$.

We use throughout this work (dimensionless) parameters given in footnote [1]. $\tau_c = \eta R/G$ and $\tau_R = \eta R^3/\kappa_r$ are the typical relaxation time of a capsule and a ring, respectively. In both cases the capillary number $\mathrm{Ca} = \dot{\gamma}\tau$ (with $\tau = \tau_c$ or τ_R) is a measure for the particle deformation, with the shear gradient $\dot{\boldsymbol{\gamma}} = \partial_x u_y \hat{\mathbf{e}}_x$. Further information on the modeling is provided in the SM.

Explanation of $\mathbf{F}_g$-induced CSM. – We provide at first a qualitative picture of the $\mathbf{F}_g$-induced migration, with the generic results of the simulation already shown in fig. 1, and derive subsequently the $\mathbf{F}_g$-induced CSM velocity, obtained for small capsule deformations.

A. Qualitative analysis of CSM. Figure 2 shows how a soft heavy capsule and ring ($\mathrm{F}_g < 0$) are deformed by the local shear gradient $\dot{\gamma}$ of plane Poiseuille flows $\mathbf{u}_0(x)$, whereby the snapshots are from Stokesian dynamics simulations: (a) $\mathbf{u}_0 \downarrow\downarrow \mathbf{F}_g$ and (b) $\mathbf{u}_0 \uparrow\downarrow \mathbf{F}_g$. For moderate $\dot{\gamma}$, their shape is nearly ellipsoidal or elliptic, respectively, with their major axis being inclined at an angle θ with $\mathbf{u}_0$ and $\mathbf{F}_g$; the sign of θ depends on the sign of the local $\dot{\gamma}$ [29], as shown in fig. 2(a) and (b). The drag coefficients $\zeta_{\parallel,\perp}$ of the distorted capsule and ring are different along and perpendicular to their major axis with $\zeta_\parallel < \zeta_\perp$. Therefore a vertical force $\mathbf{F}_g$ acting on the obliquely oriented bodies causes a slanted migration velocity $\mathbf{v}$ with an angle α to $\mathbf{F}_g$ and with its transverse component v_m. The *sign* of v_m and, hence, the CSM direction depends on the sign of the local shear rate $\dot{\gamma}(x_c)$, which is controlled by the direction of $\mathbf{u}_0$. The resulting migration to the center ($v_m < 0$) for down-flow ($\mathbf{u}_0 \downarrow$) or away from center ($v_m > 0$) for up-flow ($\mathbf{u}_0 \uparrow$), is illustrated in fig. 2(a) and (b), respectively.

We note that the $\mathbf{F}_g$-driven CSM of soft particles occurs for any kind of vertical flow with a finite local $\dot{\gamma}$, including *linear* shear flow. This is to be contrasted to the well-known CSM of *neutrally* buoyant soft particles ($\mathbf{F}_g = 0$), where a spatial-dependent shear gradient is required to drive the bulk migration [12,13]. When soft particles migrate towards the wall, the CSM gets balanced by lift forces due to the wall-HI [9], so that the migration stops at a certain wall distance, as shown below.

B. Analytical approximation of CSM. We now derive an analytical expression of the CSM velocity v_m for the case where a total force $\bar{\mathbf{F}}_g = \bar{\mathrm{F}}_g \mathbf{e}_y$ acts on a shear-distorted capsule. Motivated by our simulations, including the snapshots in fig. 2, we approximate the spatially varying $\dot{\gamma}(x)$ by a *constant* $\dot{\gamma}(x_c)$ across the capsule, *i.e.*, the Poiseuille flow is locally replaced by a *linear* shear flow. The assumption of a linear shear flow entails that the capsule shape is an ellipsoid with a major axis.

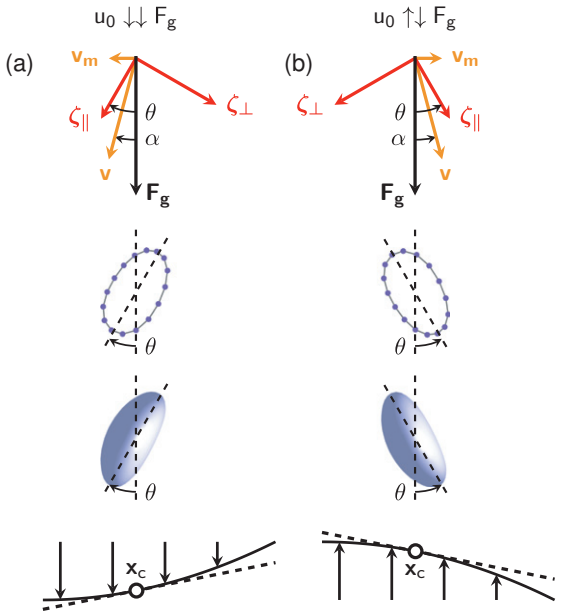

Fig. 2: (Colour online) Explanation of the gravitational ($\mathbf{F}_g$-) driven CSM of a heavy capsule and ring in a vertical Poiseuille flow $\mathbf{u}_0$: (a) CSM to the flow center when $\mathbf{u}_0 \downarrow\downarrow \mathbf{F}_g$ ($v_m < 0$) or (b) away from it for $\mathbf{u}_0 \uparrow\downarrow \mathbf{F}_g$ ($v_m > 0$). The capsule (ring) is deformed by the flow's (local) shear gradient $\dot{\gamma}(\mathbf{r}_c)$ towards an approximate ellipsoid (ellipse) with different drag coefficients $\zeta_\parallel < \zeta_\perp$ along and perpendicular to the major axis, which is inclined to $\mathbf{u}_0$ and $\mathbf{F}_g$ at an angle θ, as depicted. Since $\zeta_\parallel < \zeta_\perp$, the force $\mathbf{F}_g$ on the oblique capsule (ring) leads to a skew migration velocity $\mathbf{v}$ at an angle α and a CSM component v_m. Important: A reversal of $\mathbf{u}_0$ with respect to $\mathbf{F}_g$ *reverses* the CSM direction v_m, as shown in (a) and (b).

Under these prerequisites, the respective anisotropic drag coefficients can be obtained by calculating first the three different axes of a Neo-Hookean capsule from [28,29]

$$r^2 = x^2 + y^2 + z^2 = R^2 + \frac{25}{3}\frac{\mathrm{Ca}}{\dot{\gamma}}\mathbf{r}^T \cdot \mathbf{J} \cdot \mathbf{r} + O(\mathrm{Ca}^2)\,,$$
$$\mathbf{J} = \frac{1}{2}\left[(\nabla \otimes \mathbf{u}_0) + (\nabla \otimes \mathbf{u}_0)^T\right] \qquad (9)$$

with the lengths d_1 of the major and d_3 of the minor axis. They deviate from the radius R of a spherical capsule,

$$d_{1,3} = \left[1 \mp \frac{25}{6}\mathrm{Ca}\right]^{-1/2} R, \qquad d_2 = R, \qquad (10)$$

with the d_1-axis inclined to $\mathbf{u}_0$ at an angle $\theta \approx \pi/4$ [29,33].

To obtain an analytical expression for the drag coefficients, we further assume rotational symmetry along the capsule's major a-axis [33] with $a = d_1$ and approximate the minor axis by $b = (d_2 + d_3)/2$. Using Perrin's formulas [33], the drag coefficients associated with the a-major

[1] Model parameters: a) Flow: $\mathrm{u}_0 = 0.5$, $d = 60$, $\eta = 1.0$; (b) Capsule: $G = 0.1$, $\kappa_c = 0.1$, $k_v = 3.0$, $a = 0.2$, $N = 642$, $b = 1.0$, $R = 6.6$; c) Ring: $a = 0.5$, $k = 0.175$, $\kappa_r = 6.0$, $N = 16$, $b = 2.5$, $R = 6.36$; d) Gravitational force $\mathbf{F}_g = \mathrm{F}_g \mathbf{e}_y$ with $\mathrm{F}_g = -0.03$. We use throughout dimensionless parameters and simulation data can be converted to SI-units by multiplying them by the s-factors for length $s_m = 7.58\,\mu$m, time $s_s = 717\,\mu$s, and mass $s_{\mathrm{kg}} = 5.43 \cdot 10^{-12}$ kg. The parameters above then read in SI-units: $R = 50\,\mu$ m, $G = 1\,\mu$N/m, $\mathrm{u}_0 = 5$ mm/s, $\eta = 1$ mPas, and $\mathrm{F}_g = -0.01$ corresponds via $\bar{\mathrm{F}}_g \equiv N\mathrm{F}_g = gV\Delta\rho$ to a density difference $\Delta\rho$ of about 10% for water.

and b-minor axis are given by

$$\zeta_{\parallel} = 16\pi\eta b \left[\frac{(2\beta^2-1)\ln\left(\frac{\beta+\sqrt{B}}{\beta-\sqrt{B}}\right)}{B^{\frac{3}{2}}} - \frac{2\beta}{B} \right]^{-1}, \quad (11)$$

$$\zeta_{\perp} = 16\pi\eta b \left[\frac{(2\beta^2-3)\ln(\beta+\sqrt{B})}{B^{\frac{3}{2}}} + \frac{\beta}{B} \right]^{-1} \quad (12)$$

with $B = \beta^2 - 1$ and $\beta = a/b$. Decomposing $\bar{\mathbf{F}}_g$ into its components $\bar{\mathbf{F}}_{g,\parallel}$ and $\bar{\mathbf{F}}_{g,\perp}$, parallel and perpendicular to the major a-axis, the CSM velocity along the x-axis is

$$v_m = \mathbf{v}\cdot\mathbf{e}_x \quad \text{with } \mathbf{v} = \frac{\bar{\mathbf{F}}_{g,\perp}}{\zeta_{\perp}} + \frac{\bar{\mathbf{F}}_{g,\parallel}}{\zeta_{\parallel}}. \quad (13)$$

A Ca-expansion of $\zeta_{\parallel,\perp}$ provides the leading order of the Ca-dependence of v_m, and is given by

$$v_m = \frac{5}{96}\frac{\bar{\mathrm{F}}_g}{\pi\eta R}\,\mathrm{Ca} + O(\mathrm{Ca}^2) \quad (14)$$

with $v_m \sim \dot{\gamma}$ being constant in linear shear flow. Equation (14) gives for the spatial-dependent $\mathrm{Ca}(x)$ of a plane Poiseuille flow, $\mathrm{Ca}(x_c) = -\frac{2\mathrm{u}_0 x_c}{d^2}\frac{\eta R}{G}$, the CSM velocity

$$v_m \approx -\frac{5}{48}\frac{\bar{\mathrm{F}}_g \mathrm{u}_0 x_c}{\pi G d^2}, \quad (15)$$

showing how the migration direction can be controlled by the *relative* orientation of $\mathbf{u}_0$ and $\bar{\mathbf{F}}_g = \bar{\mathrm{F}}_g\mathbf{e}_y$, depending on the location of the capsule center $\mathbf{r}_c$ within the channel.

The $\bar{\mathbf{F}}_g$-induced migration velocity $v_y = \mathbf{v}\cdot\mathbf{e}_y$ along the streamlines is determined by the Stokes drag and a deformation dependent correction term $\propto$ Ca. For Poiseuille flow it is given by

$$v_y \approx \frac{\bar{\mathrm{F}}_g}{6\pi\eta R} - \frac{5}{144}\frac{\bar{\mathrm{F}}_g \mathrm{u}_0 x_c}{\pi d^2 G}. \quad (16)$$

When $\mathbf{u}_0 \uparrow\downarrow \bar{\mathbf{F}}_g$ and $\bar{\mathbf{F}}_g$ sufficiently large, the capsule's v_y-velocity can become antiparallel to the flow direction with the onset obtained from $v_y \geq \mathrm{u}_0(x_c, y_c)$, *i.e.*,

$$\tilde{\mathrm{F}}_g \geq \frac{144\pi\eta R d^2 G \mathrm{u}_0}{24 d^2 G - 5R\eta \mathrm{u}_0 x_c}\left[1 - \frac{x_c^2}{d^2}\right]. \quad (17)$$

Simulations of CSM in unbounded flow. – With our basic understanding of the $\mathbf{F}_g$-driven CSM from the previous section, we extend our study of the CSM of non-neutrally buoyant soft particles by Stokesian dynamics simulations of heavy soft capsules and rings ($\mathrm{F}_g < 0$), at first in unbounded Poiseuille flow.

Figure 3 shows for up ($\mathbf{u}_0 \uparrow$) and down flow ($\mathbf{u}_0 \downarrow$) the CSM velocity v_m for a capsule (left panel) and a ring (right panel), extracted from the slope of the transverse trajectory $x_c(t)$, as a function of $x_c \sim$ Ca. Here and in the following sections v_m is a superposition of the conventional CSM and the $\mathbf{F}_g$-induced one. The capsule's

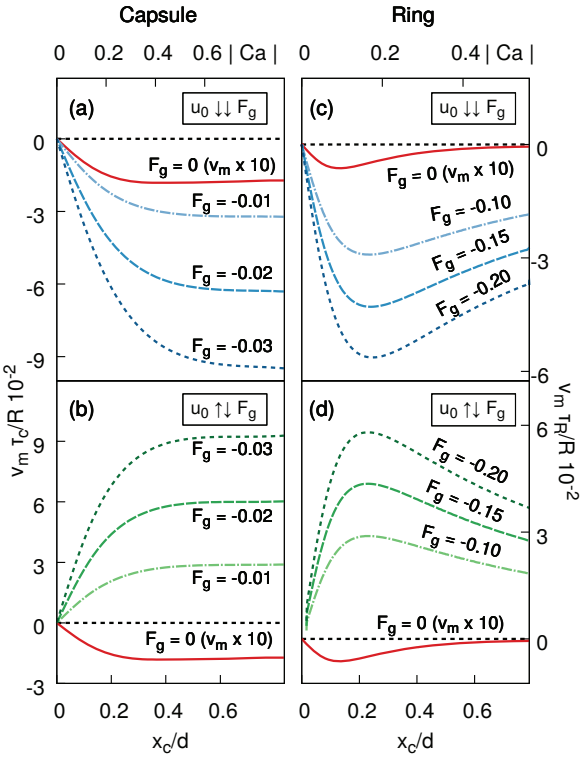

Fig. 3: (Colour online) Migration velocity v_m *vs.* center position $x_c \sim |\mathrm{Ca}|$ for a heavy capsule (left panel) and a ring (right panel), mediated by the interplay between a gravitational force $\mathbf{F}_g$ and an *unbounded* Poiseuille flow, streaming up- ($\mathbf{u}_0 \uparrow$) or downwards ($\mathbf{u}_0 \downarrow$). For both particles, the v_m-Ca characteristics is similar, reflecting the *generic* feature of the $\mathbf{F}_g$-driven CSM. For $\mathbf{u}_0 \downarrow\downarrow \mathbf{F}_g$ ((a) and (c)), the capsule and ring always migrate towards the center ($v_m < 0$), even if $\mathrm{F}_g = 0$; the finite F_g-value just enhances the CSM. For $\mathbf{u}_0 \uparrow\downarrow \mathbf{F}_g$ ((b) and (d)), the CSM can be reversed towards the wall ($v_m > 0$) once F_g exceeds a certain threshold $\mathrm{F}_g^{\mathrm{th}}$. Further parameters: see footnote [1].

$\mathbf{F}_g$-values are varied in the range $[0.01; 0.03]$ and correspond to 10%–30%higher density than the surrounding liquid[2]. Note, that v_m is shown in fig. 3 only in the positive range $0 < x_c < d$, because v_m changes only the sign for $-d < x_c < 0$.

For comparison the conventional CSM velocity for neutrally buoyant particles is also shown in fig. 3(a)–(d) (solid lines), which is directed to the flow center for up and down flow [12–14]. With a parallel force $\mathbf{u}_0 \downarrow\downarrow \mathbf{F}_g$ as in fig. 3(a) and (c) a capsule and a ring exhibit increased center-migration ($v_m < 0$). This is no longer the case when $\mathbf{u}_0 \uparrow\downarrow \mathbf{F}_g$, as in fig. 3(b) and (d), where the capsule and ring migrate away from the flow center, $v_m > 0$, if F_g is sufficiently large. This is the case in the range $\mathrm{F}_g > 0.001$ for the parameters in footnote [1] and a capsule at least 1% heavier than the liquid; otherwise the conventional center migration takes over. Importantly, the $\mathbf{F}_g$-induced CSM

[2] A number of biological cells are about 5%–15% heavier than water [34] and salt-loaded capsules are even heavier.

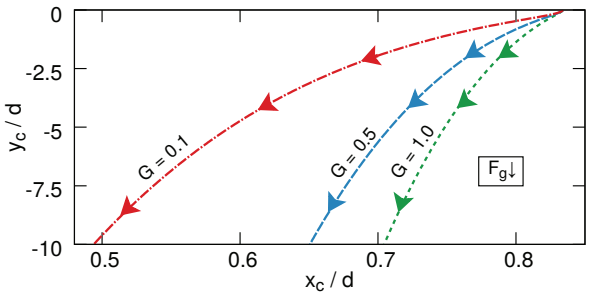

Fig. 4: (Colour online) Dependency of the trajectory $\mathbf{r}_c = (x_c, y_c)$ on the Neo-Hookean stiffness G for a capsule, sedimenting in a resting fluid ($\mathrm{u}_0 = 0$) between walls. Soft capsules (small G), initially located at $x_c/d \approx 0.9$, depart faster from the wall towards the channel center while rigid ones sediment parallel to the wall.

velocity v_m can be by a factor 10 larger than for neutrally buoyant particles (solid lines), as shown in fig. 3.

As explained above, the $\mathbf{F}_g$-driven CSM relies on the interplay between $\mathbf{F}_g$ and the anisotropic friction of soft particles, once they are deformed and obliquely oriented by a local shear gradient. This means firstly that we get a similar dependence of v_m on Ca for soft capsules and rings, which shows the generic feature of the F_g-driven migration. Secondly it means the $\mathbf{F}_g$-driven migration works also in a vertical *linear* shear flow indicated in fig. 2; fig. 3 may also be used to read off the expected CSM velocities v_m for known Ca-values of the linear shear rate.

For a capsule or a ring lighter than the fluid one has $\mathrm{F}_g > 0$, *i.e.*, the migration is reversed for a given $\mathbf{u}_0$, as predicted by eq. (15). The important point to bear in mind is that the direction of the CSM is solely controlled by the *relative* orientation of $\mathbf{u}_0$ and $\mathbf{F}_g$, resulting in a migration towards the center when they are parallel or to the wall in the anti-parallel case.

Wall effects on CSM. – The previous exploration of CSM of heavy particles in unbounded vertical-plane Poiseuille flow allowed us to identify the key mechanism of the $\mathbf{F}_g$-induced CSM in *bulk* flow. In a *bounded* Poiseuille flow lift forces induced by the hydrodynamic wall-interaction (wall-HI) are expected [9] and their effects on CSM are analyzed now.

CSM of a soft sedimenting capsule. We first look at a heavy capsule, freely sedimenting in a vertical-plane channel when $\mathbf{u}_0 = 0$. In the absence of inertia, it is well-known that rigid particles sedimenting between the two walls do not display any CSM [26]. This changes once the particle has a certain softness (measured for a Neo-Hookean capsule by the parameter G) with trajectories y_c-x_c shown in fig. 4 for various values of G; the capsule always migrates away from the wall towards the center. It migrates the faster the softer the capsule is (small G). For example, a capsule of diameter 100 μm and 10% more dense than the liquid migrates from $x_c = 0.36\,\mathrm{mm}$ to $x_c = 0.23\,\mathrm{mm}$ in fig. 4 (red curve) away from the wall, while covering a

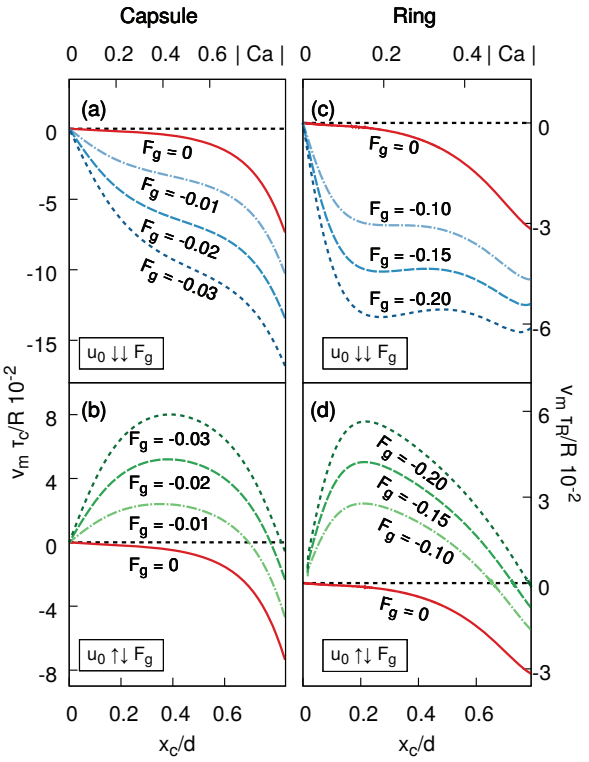

Fig. 5: (Colour online) Migration velocity v_m *vs.* center position $x_c \sim |\mathrm{Ca}|$ for a heavy capsule (left panel) and a ring (right panel), as in fig. 3, but now exposed to a *bounded* Poiseuille flow, showing how the wall-HI modifies the $\mathbf{F}_g$-driven CSM. When $\mathbf{u}_0 \downarrow\downarrow \mathbf{F}_g$ ((a) and (c)), capsules and rings still migrate to the center ($v_m < 0$), but v_m is now *amplified* by the repulsive wall-HI and pronounced near the wall (large Ca). In turn, when $\mathbf{u}_0 \uparrow\downarrow \mathbf{F}_g$ ((b) and (d)), wall-HI *weakens* the outward migration and may even stop ($v_m = 0$) at a finite wall distance, depending on the strength of $\mathbf{F}_g$; near the wall the v_m-reduction is quite strong such that the CSM is reversed from the wall back towards the center ($v_m < 0$). Further parameters as in fig. 3.

vertical distance of $\sim$2.7 mm. Hence, the sedimentation or elevation of heavy and light soft particles leads to particle focusing in the channel center.

It may surprise that the capsule migrates at all, considering that $\mathbf{u}_0 = 0$. Recall, that the $\mathbf{F}_g$-induced CSM requires 1) a particle deformation (leading to an anisotropic friction), accompanied by its inclination andb 2) a finite $\mathbf{F}_g$ driving the oblique particle *relative* to the (resting) flow. Indeed, all these requirements are met: the deformation and inclination of the sedimenting particle is mediated by the wall-HI, which is stronger for those parts of the capsule in proximity to the wall; as a result, the parts further away from the wall experience less wall friction. The different drag forces across the capsule causes its deformation towards an ellipsoid with its major axis being oblique to the wall, while $\mathbf{F}_g$ drives the CSM of the anisotropic body.

CSM in bounded Poiseuille flow. The wall-induced repulsive lift forces cause a sustained center-migration. We

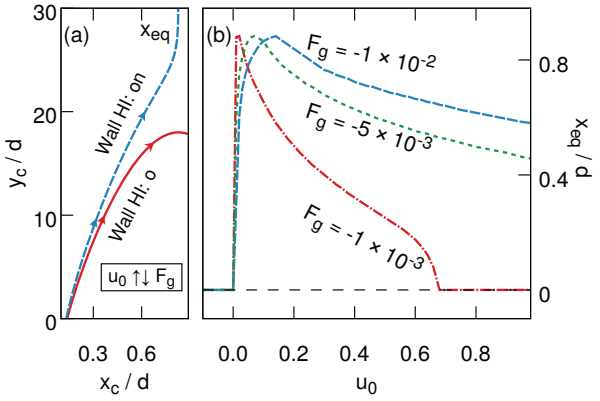

Fig. 6: (Colour online) (a) Trajectories y_c *vs.* x_c when $\mathbf{u}_0 \uparrow\downarrow \mathbf{F}_g$ for a capsule migrating towards the wall with wall-HI turned off (solid) or on (dashed). With wall-HI the capsule migrates towards an equilibrium position x_{eq} at a finite wall distance $x_c/d \approx 0.85$ due to the repulsive lift force. (b) The halt position x_{eq} is tuneable across the channel width d by varying the flow velocity u_0 and the force $\mathbf{F}_g$. With larger $\mathbf{F}_g$ the capsule can be navigated away from the channel center closer to the wall.

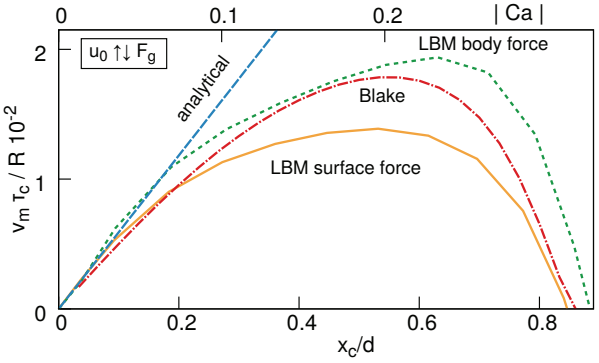

Fig. 7: (Colour online) Comparison of the v_m-x_c behavior for a capsule, obtained analytically through eq. (15) (long-dashed) or numerically by Stokesian dynamics (dash-dotted) and LBM simulations with the gravitational force $\mathbf{F}_g$ acting in the LBM-approach on the volume (short-dashed) or surface (solid) of the capsule. The analytical solution, valid for small capsule deformations, agrees well with the numerics upto Ca $\lesssim 0.1$. Parameters different from footnote [1]: $u_0 = 0.01$, $G = 0.001$, $k_v = 0.01$, $\kappa_c = 0.001$, $\mathbf{F}_g = -10^{-4}\mathbf{e}_y$. LBM parameters: $\tau = 1.0$, $\rho = 1.0$, Grid points $N_x = 120$, $N_{y,z} = 100$.

expect that this affects the interplay of $\mathbf{F}_g$ and $\mathbf{u}_0$, and, therefore, the $\mathbf{F}_g$-induced CSM of soft particles, as shown in fig. 5 for the capsule (left panel) and ring (right panel). When $\mathbf{u}_0 \downarrow\downarrow \mathbf{F}_g$, cf. fig. 5(a) and (c), capsules and rings continue to migrate to the center ($v_m < 0$), but now at a higher CSM velocity as a result of the repulsive wall-HI and distinct in proximity of the wall.

In turn, for $\mathbf{u}_0 \uparrow\downarrow \mathbf{F}_g$ in fig. 5(b) and (d) the migration to the wall of both particles gets slowed down by wall-HI. Moreover, the repulsive lift forces may become strong enough that the CSM halts ($v_m = 0$) at a certain equilibrium distance to the wall, at $x_{eq} < d$, that decreases with decreasing F_g. Figure 6(a) shows the capsule trajectory in an unbounded and bounded Poiseuille flow, in the latter case the capsule approaches its stationary position $x_c = x_{eq} \approx 0.85\ d$. However, both trajectories are rather close as long as the capsule is sufficiently far away from the wall until wall-HI becomes strong enough. Interestingly, the halt position x_{eq} of the CSM can be controlled by the flow strength u_0, as demonstrated in fig. 6(b) for different values of $\mathbf{F}_g$ with x_{eq} being located further away from the wall the larger u_0. For sufficiently small $\mathbf{F}_g$, the ordinary CSM mechanism due to a spatial shear gradient may become dominant, in which case the capsule migrates towards the center $x_{eq} = 0$ when $u_0 > 0.7$.

Comparison of different approaches. – For the $\mathbf{F}_g$-driven CSM of soft particles in (un)bounded Poiseuille flow we relied up to now on assumptions: For the analytics leading to eq. (15), we used a body force. For our Stokesian dynamics the wall-HI is included via a modified mobility matrix in eqs. (5)–(8) [31] and the external forces $\mathbf{F}_g$ act onto the beads on the capsule's surface.

We now check the validity of these approximations. Therefore we compare in fig. 7 the v_m-Ca characteristics of a soft heavy capsule, obtained by both approaches, with results from the Lattice Boltzmann method (LBM) for a sufficiently small Reynolds number Re = 0.8. The LBM solves the Navier-Stokes equation and therefore natively captures wall-HI [35]. We model $\mathbf{F}_g$ within LBM either as a surface (dashed line) or a force on fluid inside the capsule (solid line). This leads to a quantitatively slightly different capsule dynamics, but gives qualitatively a similar migration behavior, as shown in fig. 7.

All approaches in fig. 7 show a good quantitative agreement for small capillary numbers up to Ca $\lesssim 0.1$ with $v_m \propto$ Ca consistent with eq. (15). Beyond linear response the analytical v_m deviates from the simulations as expected. The v_m obtained via Stokesian dynamics and LBM display the same qualitative behavior over the entire range of Ca and, importantly, reproduce the stop of the CSM ($v_m = 0$) due to wall-HI at a similar wall distance $x_c \approx 0.85\ d$.

Conclusions. – We identified and explained a novel cross-streamline migration (CSM) for soft microparticles that is driven by the vertical gravitational force $\mathbf{F}_g$ acting on particles heavier ($\mathbf{F}_g \downarrow$) or lighter ($\mathbf{F}_g \uparrow$) than the fluid in vertical Poiseuille (or linear shear) flows at low Reynolds number. It complements the CSM driven by the spatially varying shear gradient across a soft particle in Poiseuille flow [12–14]. We analyzed this CSM for soft capsules and ring polymers.

The shear gradient in Poiseuille or linear shear flow leads to elliptically shaped soft particles and to their oblique orientation to $\mathbf{F}_g$ and the streamlines. $\mathbf{F}_g$ causes via the anisotropic drag of the particle its CSM velocity v_m and the sign of v_m depends on the shear-gradient direction. The $\mathbf{F}_g$-driven CSM is expected to apply for non-neutrally buoyant soft microparticles in general. Heavy particles in

downward Poiseuille flow ($\mathbf{F}_g \downarrow\downarrow \mathbf{u}_0$) migrate to the flow center and sufficiently light particles ($\mathbf{F}_g \uparrow\downarrow \mathbf{u}_0$) away from it up a stationary point apart from the wall. *Reversing* the downward Poiseuille flow into an upward one *reverses* the migration directions too. This allows a flow-controlled particle positioning in the range $0 < x_c < d$. For small capsule deformations v_m is proportional to the product of F_g and the local capillary number Ca, $v_m \propto \mathrm{F}_g\mathrm{Ca}$. This trend is confirmed by numerical results for finite Ca.

Since the $\mathbf{F}_g$-driven contribution to CSM is considerably larger than the conventional CSM [12–14], it opens efficient strategies for manipulation and sorting methods of non-neutrally buoyant soft particles in fluid flows, complementing those for neutrally buoyant particles of different dynamical properties [36]. For instance, many biological cells have about a 5%–15% higher mass density than water [34]. Healthy or malignant cells often have the same mass density but a different stiffness (different Ca) [37]. Therefore, they can be separated by the $\mathbf{F}_g$-driven CSM. Furthermore, soft particles can be focused at different Ca- (stiffness-) dependent positions x_{eq} between the flow center and the channel wall. This CSM mechanism is expected to work also at finite values of the Reynolds number (see also ref. [22]).

Having a tool of positioning soft particles according to their weight or stiffness along the entire channel cross-section via the vertical flow enables studies *e.g.* on the dynamics of non-neutrally buoyant soft particles under conditions of high or low shear rates via micro-focused synchrotron XSAS or optical microscopy [38].

* * *

We acknowledge exchanges with C. Schaaf and the support by the German French University (DFA/UFA).

REFERENCES

[1] Squires T. M. and Quake S. R., *Rev. Mod. Phys.*, **77** (2005) 978; Popel A. S. and Johnson P. C., *Annu. Rev. Fluid Mech.*, **37** (2005) 43; Sackmann E. K., Fulton A. L. and Beebe D. L., *Nature*, **507** (2014) 181; Dahl J. B., Lin J.-M. G., Muller S. J. and Kumar S., *Annu. Rev. Chem. Biomol. Eng.*, **6** (2015) 293; Amini H., Lee W. and Carlo D. D., *Lab Chip*, **14** (2014) 2739.

[2] Graham M. D., *Annu. Rev. Fluid Mech.*, **43** (2011) 273.

[3] Secomb T. W., *Annu. Rev. Fluid Mech.*, **49** (2017) 443.

[4] Geislinger T. M. and Franke T., *Adv. Colloid Interface Sci.*, **208** (2014) 14; Sajeesh P. and Sen A. K., *Microfluid. Nanofluid.*, **17** (2014) 1.

[5] Misbah C., *J. Fluid Mech.*, **760** (2014) 1; Farutin A., Piasecki T., Slowicka A. M., Misbah C., Wajnryb E. and Ekiel-Jeżewska M. L., *Soft Matter*, **12** (2016) 7307.

[6] Segré G. and Silberberg A., *Nature*, **189** (1961) 209.

[7] Sekhon G., Armstrong R. and Jhon M. S., *J. Polym. Sci.: Polym. Phys.*, **20** (1982) 947; Brunn P. O., *Int. J. Multiphase Flow*, **187** (1983) 202.

[8] Jhon M. S. and Freed K. F., *J. Polym. Sci.: Polym. Phys.*, **23** (1985) 255.

[9] Cantat I. and Misbah C., *Phys. Rev. Lett.*, **83** (1999) 880; Seifert U., *Phys. Rev. Lett.*, **83** (1999) 876; Abkarian M., Lartigue C. and Viallat A., *Phys. Rev. Lett.*, **88** (2002) 068102; Grandchamp X., Goupier G., Srivastav A., Minetti C. and Podgorski T., *Phys. Rev. Lett.*, **110** (2013) 108101.

[10] Leal L. G., *Annu. Rev. Fluid Mech.*, **12** (1980) 435.

[11] Mandal S., Bandopadhyay A. and Chakraborty S., *Phys. Rev. E*, **92** (2015) 023002.

[12] Kaoui B., Ristow G. H., Cantat I., Misbah C. and Zimmermann W., *Phys. Rev. E*, **77** (2008) 021903.

[13] Coupier G., Kaoui B., Podgorski T. and Misbah C., *Phys. Fluids*, **20** (2008) 111702.

[14] Doddi S. K. and Bagchi P., *Int. J. Multiphase Flow*, **34** (2008) 966.

[15] Farutin A. and Misbah C., *Phys. Rev. E*, **89** (2011) 042709.

[16] Watari N. and Larson R. G., *Phys. Rev. Lett.*, **102** (2009) 246001.

[17] Laumann M., Bauknecht P., Gekle S., Kienle D. and Zimmermann W., *EPL*, **117** (2017) 44001.

[18] Jo I., Huang Y., Zimmermann W. and Kanso E., *Phys. Rev. E*, **94** (2016) 063116.

[19] Jeffrey R. C. and Pearson J. R. A., *J. Fluid Mech.*, **22** (1965) 721.

[20] Kim Y. W. and Yoo J. Y., *Lab Chip*, **9** (2009) 1043.

[21] Prohm C. and Stark H., *Lab Chip*, **14** (2014) 2115.

[22] Schaaf C. and Stark H., *Soft Matter*, **13** (2017) 3544.

[23] Zheng J. and Yeung E. S., *Anal. Chem.*, **74** (2002) 4536.

[24] Usta O. B., Butler J. E. and Ladd A. J. C., *Phys. Rev. Lett.*, **98** (2007) 098301.

[25] Huang Z.-H., Abkarian M. and Viallat A., *New J. Phys.*, **13** (2011) 035026; Peltomäki M. and Gompper G., *Soft Matter*, **9** (2013) 8346; Boltz H.-H. and Kierfeld J., *Phys. Rev. E*, **92** (2015) 033003.

[26] Feng J., Hu H. H. and Joseph D. D., *J. Fluid Mech.*, **261** (1994) 95.

[27] Dhont J. K. G., *An Introduction to Dynamics of Colloids* (Elsevier, Amsterdam) 1996.

[28] Barthès-Biesel D., *J. Fluid Mech.*, **113** (1981) 251.

[29] Barthès-Biesel D., *Annu. Rev. Fluid Mech.*, **48** (2016) 25.

[30] Krüger T., Kusumaatmaja H., Kuzmin A., Shardt O., Silva G. and Viggen E. M., *The Lattice Boltzmann Method - Principles and Practice* (Springer, Berlin) 2016.

[31] Blake J. R., *Proc. Cambridge Philos. Soc.*, **70** (1971) 303.

[32] Jones R. B., *J. Chem. Phys.*, **121** (2004) 483.

[33] Happel J. and Brenner H., *Low Reynolds Number Hydrodynamics* (Prentice-Hall, Englewood Cliffs) 1981.

[34] Milo R. and Phillips R., *Cell Biology by Numbers* (Garland, New York) 2016.

[35] Krüger T., Kaoui B. and Harting J., *J. Fluid Mech.*, **751** (2014) 725.

[36] Wang G., Mao W., Byler R., Patel K., Heneger C., Alexeev A. and Sulchek T., *PLOS ONE*, **8** (2013) e75901; Henry E., Holm S. H., Zhang Z., Beech J. P., Tegenfeld J. O., Fedosov D. A. and Gompper G., *Sci. Rep.*, **6** (2016) 34375.

[37] Guck J., Schinkinger S., Lincoln B., Wottawah F., Ebert S., Romeyke M., Lenz D., Erickson H. M., Ananthakrishan R., Mitchell D. and Käs J., *Biophys. J.*, **88** (2005) 3689.

[38] Trebbin M., Steinhauser D., Perlich J., Buffet A., Roth S. V., Zimmermann W., Thiele J. and Förster S., *Proc. Natl. Acad. Sci. U.S.A.*, **110** (2013) 6707.

Migration reversal of soft particles in vertical flows
Supporting information

Andre Förtsch, Matthias Laumann, Diego Kienle, Walter Zimmermann[1]

[1] *Theoretische Physik I, Universität Bayreuth, 95440 Bayreuth, Germany*

(Dated: September 19, 2017)

This supplementary note provides further information about the Stokesian Dynamics and the Lattice Boltzmann Method (LBM) as used in this work for simulations of soft microparticles in vertical flows as well as the modeling of the capsule by a bead-spring model.

STOKESIAN DYNAMICS

At first we give further intermediate steps leading to the equation of motion (2) of the main text (see [6, 7]). We investigate small particles (a capsule and a ring polymer) of μm size immersed in a flow and one has a small Reynolds number. Inertia effects can be neglected (see below) and the Stokes equation is the appropriate approach for calculating the pressure driven flow with an immersed, deformable particle like a capsule or a ring, which are composed of N equally distributed beads over the surface of the capsule or along the circumference of the ring polymer.

The velocity $\dot{\boldsymbol{r}}_i$ of a single spherical particle results from the flow velocity at the bead position, $\boldsymbol{u}(\boldsymbol{r}_i)$, and the force $\boldsymbol{F}_i$ acting on the particle:

$$\dot{\boldsymbol{r}}_i = \frac{1}{6\pi\eta a}\boldsymbol{F}_i + \boldsymbol{u}(\boldsymbol{r}_i) \tag{1}$$

with the Stokes friction $6\pi\eta a$ and the particle radius a.

Moving particles in the neighborhood induce via the Oseen-tensor $\boldsymbol{O}$

$$\boldsymbol{O}(\boldsymbol{r}) = \frac{1}{8\pi\eta r}\left(\mathbf{1} + \frac{\boldsymbol{r}\boldsymbol{r}^T}{r^2}\right) \ . \tag{2}$$

flow perturbations at $\boldsymbol{r}_i$. Taking them into account the dynamical equation takes the following form:

$$\dot{\boldsymbol{r}}_i = \boldsymbol{u}_0(\boldsymbol{r}_i) + \frac{1}{6\pi\eta a}\boldsymbol{F}_i + \sum_{i,j,i\neq j} \boldsymbol{O}(\boldsymbol{r}_i - \boldsymbol{r}_j)\boldsymbol{F}_j \, . \tag{3}$$

This equation is often rewritten in a form as in the main text

$$\dot{\boldsymbol{r}}_i = \boldsymbol{u}_0(\boldsymbol{r}_i) + \sum_{i,j} \boldsymbol{H}_{ij}\boldsymbol{F}_j \tag{4}$$

with the so-called mobility matrix

$$\boldsymbol{H}_{ij} = \begin{cases} \boldsymbol{O}(\boldsymbol{r}_i - \boldsymbol{r}_j) & : i \neq j \\ \frac{1}{6\pi\eta a} & : i = j \end{cases} \tag{5}$$

The effects of walls are taken into account via the Blake tensor as given in the main text.

INERTIA EFFECTS ARE NEGLIGIBLE

The negligibility of particle inertia in Equation (2) can be estimated: Assume a rigid sphere (instead of a deformable capsule) in a fluid with constant flow $\mathbf{u_0}$, initially at rest and accelerated by a force $\mathbf{F}$. We obtain approximately the following equation of motion,

$$m\ddot{\mathbf{r}} = 6\pi\eta a(\mathbf{u_0} - \dot{\mathbf{r}}) + \mathbf{F}\,, \tag{6}$$

with the radius a and the mass $m = \frac{4}{3}\pi a^3 \rho_{intern} = \frac{\pi}{6} d^3 \rho_{intern}$ of the sphere, where ρ_{intern} is the density inside the capsule and $d = 2a$ its diameter [to estimate the effect of inertia we neglect here the Basset history force and the added mass, see M. R. Maxey and J. J. Riley, Phys. Fluids **26**, 883, (1983)]. The solution is

$$\dot{\mathbf{r}}(t) = \left(\mathbf{u_0} + \frac{\mathbf{F}}{6\pi\eta d}\right)\left(1 - e^{-\frac{6\pi\eta a}{m}t}\right)\,. \tag{7}$$

The typical timescale of the velocity changes is therefore $\tau_i = \frac{m}{6\pi\eta a} = \frac{\rho_{intern} V}{3\pi\eta d} = \frac{\rho_{intern} d^2}{18\eta}$. We can neglect inertia, because this timescale is small against all other timescales, which is the timescale of the flow $\tau_f = \frac{1}{\dot{\gamma}}$ and the relaxation time of the capsule $\tau_c = \frac{\eta R}{G}$.

Let's assume typical values of a capsule in a channel to estimate the Stokes number $\mathrm{St} = \tau_i \dot{\gamma}$ for the capsule's diameter $d = 10\,\mu m$, a viscosity $\eta = 1\,mPas$ (water), a density of the capsule 30% higher than water, i. e. $\rho = 1.3 \cdot 10^3 \frac{kg}{m^3}$ (typical value used our work), a channel with diameter $w = 100\mu m$ and a flow velocity of $u_0 = 1\frac{cm}{s}$ which means $\dot{\gamma} \approx 10^2 \frac{1}{s}$. For these parameters one obtains $\tau_f = 10^{-2}\,s$ and $\tau_i \approx 7.2 \cdot 10^{-6}$. This gives $\mathrm{St} = 7.2 \cdot 10^{-4} \ll 1$. A typical relaxation time of a capsule is $\tau_c = 10^{-3} s$, which means $\frac{\tau_i}{\tau_c} \approx 7.2 \cdot 10^{-3} \ll 1$. Therefore, our neglect of the capsule's inertia is well justified.

THE LATTICE-BOLTZMANN METHOD

In order to take boundary effects directly into account, we use as a complementary simulation approach the lattice-Boltzmann method (LBM) in 3D with a standard velocity discretization D3Q19 (see Fig. 1). As model for the collision we utilize the Bhatnagar-Gross-Krook (BGK) collision operator for the evolution of the probability-distribution $f_i(\boldsymbol{r},t)$ in velocity-direction i at position $\boldsymbol{r}$ of the form [3, 5]

$$f_i(\boldsymbol{r}+c_i\Delta t, t+\Delta t) = f_i(\boldsymbol{r},t) - \frac{\Delta t}{\tau}\left(f_i(\boldsymbol{r},t) - f_i^e(\boldsymbol{r},t)\right). \tag{8}$$

Here c_i are the unit vectors along the i-th velocity direction, τ is a typical relaxation time, which is set to $\tau = 1$ as usual, and $f_i^e(\boldsymbol{r},t)$ is the equilibrium distribution at the given position in i-direction:

$$f_i^e(\boldsymbol{r},t) \approx \rho w_i \left[1 + \frac{(\boldsymbol{c}_i\cdot\boldsymbol{u})}{c_s^2} + \frac{(\boldsymbol{c}_i\cdot\boldsymbol{u})^2}{2c_s^4} - \frac{u^2}{2c_s^2}\right] + \mathscr{O}(u^3). \tag{9}$$

The weighting factors w_i as well as the speed $c_s = \frac{1}{\sqrt{3}}$ are chosen as usual [3].

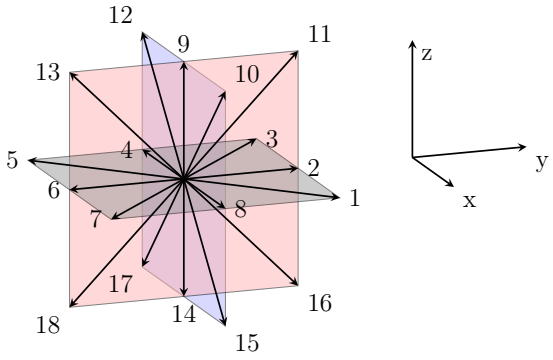

FIG. 1: Graphical representation for the different velocity directions in the D3Q19 model used for lattice-Boltzmann simulations.

The macroscopic density $\rho(\boldsymbol{r},t)$ and mean velocity $\boldsymbol{u}(\boldsymbol{r},t)$ are determined by the leading two moments

$$\rho(\boldsymbol{r},t) = \sum_i f_i(\boldsymbol{r},t), \tag{10}$$

$$\rho(\boldsymbol{r},t)\boldsymbol{u}(\boldsymbol{r},t) = \sum_i \boldsymbol{c}_i f_i(\boldsymbol{r},t). \tag{11}$$

The dynamic fluid-viscosity is given by

$$\nu = c_s^2 \left(\tau - \frac{1}{2} \right) . \tag{12}$$

For simulating a Poiseuille-flow, volume-forces are applied to the fluid-particles and the coupling to the probability-distribution is implemented using the suggested method given in Ref. [4]. To couple the forces acting on the surface of the continuously moving objects to the discrete LBM-mesh, we use the immersed-boundary method [2] with the approximate delta-function $\phi(\Delta \boldsymbol{r}) = \tilde{\phi}(\Delta x)\tilde{\phi}(\Delta y)\tilde{\phi}(\Delta z)$ and

$$\tilde{\phi}(R) = \begin{cases} \frac{1}{4}\left(1 + \cos(\frac{\pi R}{2})\right) & \text{if } |R| \leq 2 \\ 0 & \text{else} \end{cases} , \tag{13}$$

where $\Delta \mathbf{r} = (\Delta x, \Delta y, \Delta z)$ is the distance between the object nodes and the neighboring grid points. This functions is used to couple the force from the Lagrangian system to the neighboring discrete grid nodes of the LBM and to calculate the velocity of the nodes at the position of the nodes of the capsule.

MODEL OF THE CAPSULE

To simulate the capsule via the Stokesian dynamics method and with the LBM we first discretize the surface of the capsule, which is shortly described here.

To discretize the surface of a sphere we begin with a regular icosahedron (see [1]), which consists of 20 equilateral triangles and 12 nodes. This body can be refined by adding new nodes in the middle of each edge and then shifting the new nodes radially outwards to the surface of the sphere. This leads to a greater amount of nodes and triangles. This procedure is repeated until we have $N = 642$ nodes. This scheme is used for the LBM and for the Stokesian dynamics simulations, whereby in case of the Stokesian dynamics the beads are located at the nodes. The resulting capsule discretization is shown in Fig. 2.

The forces on the nodes (LBM) or at the beads (Stokesian Dynamics) are calculated for both simulation methods the same way. We use three forces: A force that ensures volume conservation of the capsule, a force resulting from the bending of the surface and a Neo-Hookean force, which describes rubber-like materials with a constant surface shear-elastic modulus [8–10]. The forces can be calculated by the corresponding potentials via $\mathbf{F}_j = -\nabla_j (V_{NH} + V_b + V_v)$.

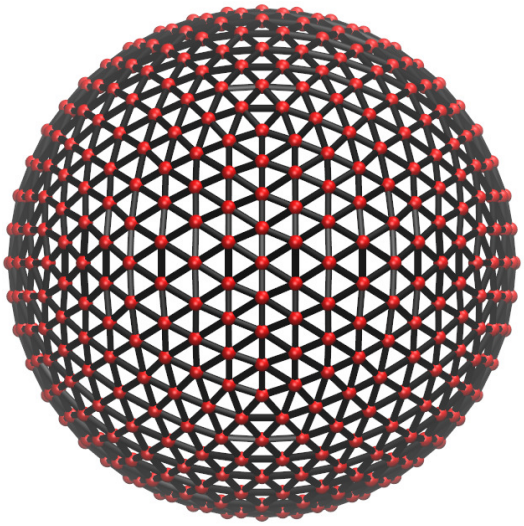

FIG. 2: The used discretization of the capsule model resulting from the subdivision of a regular icosahedron. The $N = 642$ nodes are marked by red dots and the triangles by black lines.

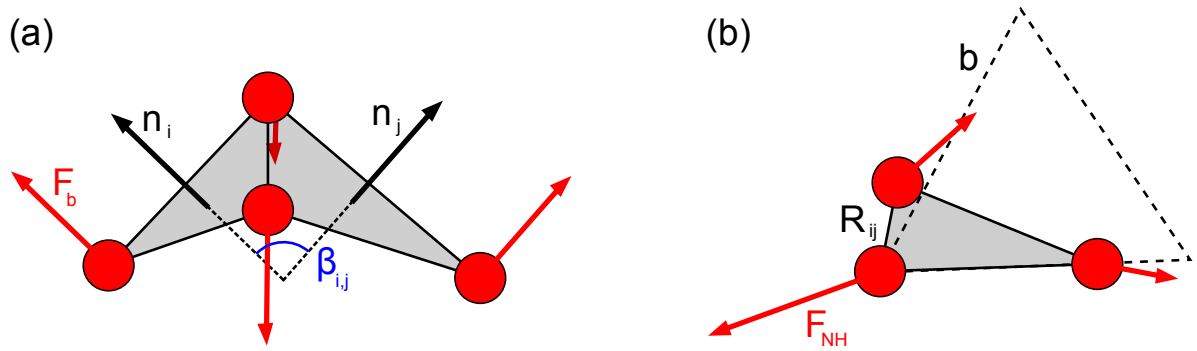

FIG. 3: The modeling of the capsules forces resulting from bending of the surface (a) and deformation (b). The bending force depends on the angle $\beta_{i,j}$ between two normal vectors $\boldsymbol{n}_i$ and $\boldsymbol{n}_j$ of neighbouring triangles. The Neo-Hookean law describes the elastic restoring force of a deformed triangle with side length R_{ij} between bead i and j (solid lines) towards the equilibrium shape with equilateral side length b (dashed line).

The potential $V_v = -\frac{k_v}{\mathcal{V}_0}(\mathcal{V}(t) - \mathcal{V}_0)^2$ keeps the capsule's instantaneous volume $\mathcal{V}(t)$ close to the reference volume $\mathcal{V}_0 = \frac{4}{3}\pi R^3$ of a spherical capsule of radius R with volume stiffness

k_v.

The bending potential is given by

$$V_b = -\frac{\kappa_c}{2} \sum_{i,j} (1 - \cos \beta_{i,j}) \tag{14}$$

and depends on the angle $\beta_{i,j}$ between two normal vectors $\boldsymbol{n}_i$ and $\boldsymbol{n}_j$ of neighbouring triangles (see Fig. 3 (a)). It describes the resistance to bending.

The Neo-Hookean law describes the elastic force that results from the deformation of the equilibrium shape of the triangle and describes the resistance to deformations of the capsule surface.

[1] Krueger T., Varnik F., Raabe D., *Computers & Mathematics with Applications* **61** (2011) 3485.

[2] Peskin C. S., *Acta Numerica*, **11** (2002) 479

[3] Aidun C. K. and Clausen J. R., *Annu. Rev. Fluid Mech.*, **43** (2010) 439-472.

[4] Guo Z. ,Zheng C. and Shi B. , *Phys. Rev. E*, **65** (2002) 046308.

[5] Bhatnagar P. L. , Gross E. P. and Krook M., *Phys. Rev. E*, **3** (1954) 511.

[6] Bird R. B., Curtiss C. F., Armstrong R. C., Hassager G., *Dynamics of Polymeric Liquids II*, (Wiley & Sons, New York), 1987

[7] Dhont J. K. G., *An Introduction to dynamics of colloids* (Elsevier, Amsterdam) 1996.

[8] Barthès-Biesel D., *J. Fluid Mech.* **113** (1981) 251.

[9] Barthès-Biesel D., *Annu. Rev. Fluid Mech.* **48** 2016 25.

[10] Krüger T., Kusumaatmaja H., Kuzmin A., Shardt O., Silva G. , Viggen E. M., *The Lattice Boltzmann Method - Principles and Practice* (Springer, Berlin) 2016.

Publication 5

Measurement of the magnetic moment of single Magnetospirillum gryphiswaldense cells by magnetic tweezers
C. Zahn, S. Keller, M. Toro-Nahuelpan, P. Dorscht, W. Gross, M. Laumann, S. Gekle, W. Zimmermann, D. Schüler and H. Kress,
Sci. Rep. **7**, 3558 (2017)

DOI: 10.1038/s41598-017-03756-z

SCIENTIFIC REPORTS

OPEN

Measurement of the magnetic moment of single *Magnetospirillum gryphiswaldense* cells by magnetic tweezers

Received: 19 January 2017
Accepted: 3 May 2017
Published online: 15 June 2017

C. Zahn[1], S. Keller[1], M. Toro-Nahuelpan[2,3], P. Dorscht[1], W. Gross[1], M. Laumann[4], S. Gekle[5], W. Zimmermann[4], D. Schüler[2] & H. Kress[1]

Magnetospirillum gryphiswaldense **is a helix-shaped magnetotactic bacterium that synthesizes iron-oxide nanocrystals, which allow navigation along the geomagnetic field. The bacterium has already been thoroughly investigated at the molecular and cellular levels. However, the fundamental physical property enabling it to perform magnetotaxis, its magnetic moment, remains to be elucidated at the single cell level. We present a method based on magnetic tweezers; in combination with Stokesian dynamics and Boundary Integral Method calculations, this method allows the simultaneous measurement of the magnetic moments of multiple single bacteria. The method is demonstrated by quantifying the distribution of the individual magnetic moments of several hundred cells of *M. gryphiswaldense*. In contrast to other techniques for measuring the average magnetic moment of bacterial populations, our method accounts for the size and the helical shape of each individual cell. In addition, we determined the distribution of the saturation magnetic moments of the bacteria from electron microscopy data. Our results are in agreement with the known relative magnetization behavior of the bacteria. Our method can be combined with single cell imaging techniques and thus can address novel questions about the functions of components of the molecular magnetosome biosynthesis machinery and their correlation with the resulting magnetic moment.**

The magnetic field of the earth plays a role in the orientation and navigation of a wide variety of organisms including bacteria, algae, bees, pigeons and mice[1]. Magnetic navigation in bacteria was discovered more than 40 years ago[2]. Magnetotactic bacteria, such as the α-proteobacterium *Magnetospirillum gryphiswaldense*[3] synthesize magnetosomes, unique intracellular organelles that comprise membrane-enclosed magnetite (Fe_3O_4) nanoparticles that allow the cells to align and to navigate along the geomagnetic field[4]. *M. gryphiswaldense* generates cuboctahedron-shaped magnetite crystals with a diameter of approximately 30 to 50 nanometers[5]. The magnetosomes assemble into an intracellular chain, which is positioned at midcell by a dedicated cytoskeletal structure, the actin-like MamK filament[6,7]. The bacteria are helically shaped with a length of several micrometers and a diameter of approximately half a micrometer (Fig. 1).

M. gryphiswaldense has been well investigated previously at the molecular and cellular levels. For example, its motility[8], its swimming behavior in magnetic fields[9,10] and its magnetotaxis and aerotaxis[11] have been recently investigated. Furthermore, the molecular mechanisms underlying magnetosome biosynthesis and intracellular alignment have been explored thoroughly[4,5,7,12–20]. However, the fundamental physical property enabling *M. gryphiswaldense* to perform magnetotaxis, its magnetic moment, remains to be elucidated at the single cell level. A characterization of the total magnetic moment of a large and unknown number of bacteria as a function of an external magnetic field showed that the remanent magnetic moment has a value of approximately 40% of the

[1]Biological Physics, Department of Physics, University of Bayreuth, Bayreuth, Germany. [2]Department of Microbiology, University of Bayreuth, Bayreuth, Germany. [3]Department of Molecular Structural Biology, Max Planck Institute of Biochemistry, Planegg-Martinsried, Germany. [4]Theoretical Physics I, Department of Physics, University of Bayreuth, Bayreuth, Germany. [5]Biofluid Simulation and Modeling, Department of Physics, University of Bayreuth, Bayreuth, Germany. Correspondence and requests for materials should be addressed to H.K. (email: holger.kress@uni-bayreuth.de)

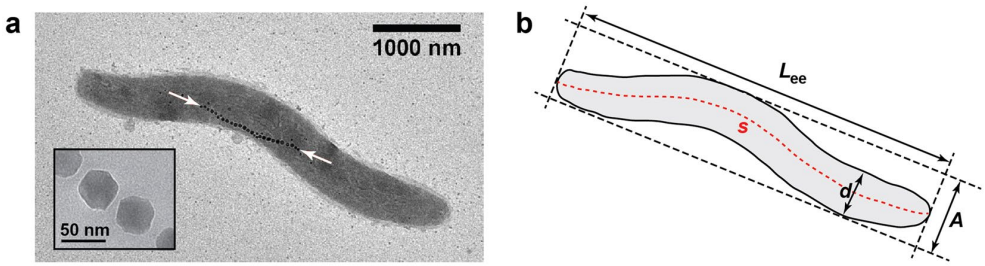

Figure 1. The magnetotactic bacterium *Magnetospirillum gryphiswaldense*. The bacteria possess a helical shape with a length of several micrometers and a diameter of approximately half a micrometer. An intracellular chain of magnetosomes allows them to navigate along magnetic fields. (**a**) Transmission electron microscopy image of a cell with a chain of approximately thirty magnetosomes (white arrows). The inset shows a high resolution image of magnetosomes from another cell. (**b**) We parameterize the helical shape of the cells by the end-to-end length L_{ee}, the diameter d, the arc length s and the amplitude A of the helix.

saturation magnetic moment and that a magnetic moment of approximately 95% of the saturation magnetization is reached at an external field of approximately 100 mT[21].

In several studies the average magnetic moment of multiple *M. gryphiswaldense* cells was measured from a bacterial population. In these cases, it was assumed that the cells were identical in size and their helical shape was simplified as a cylindrical or ellipsoidal geometry. These studies yielded average magnetic moments that differ by more than one order of magnitude[10,22,23] despite the fact that the measurements were performed with external magnetic fields below 2 mT, which should lead to comparable magnetic moments that differ only by approximately 2%[21]. In one of these studies, the average magnetic moment was measured using light scattering and the assumption that the bacteria have a cylindrical shape[23]. This approach yielded an average magnetic moment of $(25 \pm 2) \times 10^{-16}$ A m^2 at external magnetic fields below 0.9 mT. The length of the model cylinder in this study was determined by a fit to the scattering data and had a value of 1.6 µm which was considered by Reufer *et al.*[10] to be "unrealistically short". In their study, Reufer *et al.* determined the average magnetic moment of the bacteria by tracking the motion of nonmotile bacteria in a magnetic field and by assuming that the bacteria had an ellipsoidal shape[10]. This approach yielded a magnetic moment of $(2.0 \pm 0.6) \times 10^{-16}$ A m^2 at a magnetic field of 1.5 mT. In a different type of study the bacterial cell dynamics in rotating magnetic fields was measured to determine the ratio of the magnetic moment of the bacteria to their rotational drag coefficient[9]. For this study, it was stated that a magnetic moment of 43×10^{-16} A m^2 would be in agreement with a bacterium that possesses a rotational drag coefficient of an ellipsoid with a long axis of 4 µm and a short axis of 0.5 µm. The large spread of the reported values for the magnetic moment of *M. gryphiswaldense* raises the question of the underlying reasons for these discrepancies. Possible reasons include the approximation of the helical cell shape by ellipsoids and cylinders, the usage of average cell dimensions instead of the individual dimensions of each measured cell or systematic errors in the used measurement techniques.

Besides the abovementioned studies about the magnetic moment of *M. gryphiswaldense*, there are various other characterizations of the magnetic moments of closely related bacterial species such as *M. magnetotacticum*[24,25] and *M. magneticum*[26]. The latter article addresses the question of potential systematic errors in various measurement techniques and presents a comparison of six different methods to determine the magnetic moments of bacteria. The authors showed that the use of different methods led to magnetic moments that varied by almost one order of magnitude. They found that methods relying on viscous relaxation of the cell orientation gave results that were comparable to magnetosome measurements, whereas methods relying on statistical mechanics assumptions gave systematically lower values. Since living cells were used in the study of Nadkarni *et al.*, the authors suggested that the non-thermal noise induced by the living cells is a potential source of error in measurements of the magnetic moment of bacteria.

In summary, the magnetic moments of *M. gryphiswaldense* ensembles have not yet been measured at the single cell level. Furthermore, there are multiple open questions concerning the large discrepancies between the magnetic moments that were reported so far for these and other magnetotactic bacteria: Is it - in the case of *M. gryphiswaldense* - necessary to take the helical shape of the cells into account or is it sufficient to approximate them with a simplified geometry such as a cylinder or an ellipsoid? Is it necessary to take the dimension of each individual cell into account or is it sufficient to use the average dimensions of a bacterial ensemble? Does the use of dead (chemically fixed) cells that do not induce non-thermal noise lead to more consistent results if different methods are compared?

Here we present a method for measuring the magnetic moments of multiple single cells of magnetotactic bacteria simultaneously by analyzing their dynamics in various magnetic fields. We demonstrate the method by quantifying the magnetic moments of more than 350 individual cells of *M. gryphiswaldense*. Inhomogeneous switchable magnetic fields were created using magnetic tweezers (MT). Magnetic tweezers and the comparable technique of magnetic twisting cytometry are versatile biophysical methods for force and torque generation on small length scales and have been applied in single molecule and cellular studies[27–33]. The translational motion of cells was measured in static magnetic field gradients, whereas the rotational motion of cells was measured in alternating magnetic fields. For each bacterium, these measurements yielded the ratio of its magnetic moment to its translational and rotational viscous drag coefficients, respectively.

The translational and rotational viscous drag coefficients were calculated for each bacterium by two methods in the low Reynolds number limit of Stokes flow, both taking into account the helical shape of the bacteria and their individual dimensions. In a Stokesian dynamics approach the bacterial shape was approximated by several thousand small spheres and the hydrodynamic interaction between the spheres was calculated using the Oseen tensor. The second approach was the Boundary Integral Method (BIM) where the bacterium's surface was discretized as a large set of flat triangles, and no-slip boundary conditions for the flow were used at their surfaces. The flexibility of the two methods allows the application of our approach not only in the case of helically-shaped bacteria but also for the general case of arbitrary cell shapes. In addition to our measurements of the magnetic moments of a large number of bacteria in various external magnetic fields, we also determined the saturation magnetic moment of 50 individual bacterial cells by estimating their magnetosome crystal volume from transmission electron microscopy (TEM) images. Our measurements show that for a typical bacterial population with a length distribution in the range of approximately 2 to 6 μm, the use of mean cell dimensions and the approximation of the cell shape by a simple geometry are sufficient if only population averages of the magnetic moment are needed and if uncertainties on the order of about 10% are acceptable. However this approach leads to an over- or underestimation of up to more than a factor of 2 if it is used to determine the magnetic moment of an individual single bacterium. To determine the magnetic moments of individual single bacteria correctly, their particular shape and size has to be taken into account. Finally, we show that different measurement techniques yield consistent results if dead cells are used, which do not induce non-thermal noise.

Materials and Methods

Cell culture and sample preparation. The *M. gryphiswaldense MSR-1* wild type strain was grown under microoxic conditions in 2% oxygen aerated modified flask standard medium (FSM)[34] containing 50 μM ferric iron citrate. Cultures were incubated at 30 °C with moderate agitation (120 rpm). Exponentially growing cells were fixed in 1.5% formaldehyde for 2 h. Subsequently, 1 ml of culture was centrifuged at 5,000 rpm for 5 min, and the cell pellet was resuspended in a highly viscous solution containing 85% v/v glycerol and 15% v/v water for further analysis.

Polyacrylamide gel preparation. The polyacrylamide (PAA) substrates were prepared according to a protocol that was published previously[35], which we adapted for use in our laboratory[36]. Briefly, 40 × 22 mm sized coverslips (Glaswarenfabrik Karl Hecht, Sondheim v. d. Rhön, Germany) were cleaned by sonicating them successively for 10 minutes in 0.2 M EDTA, 10% w/v hydrogen chloride, and 1% v/v 7X-O-Matic (MP Biomedicals Germany, Eschwege, Germany). After each single sonication step, the coverslips were washed in deionized water (DI). The coverslips were air-dried before surface-activation, which was performed to covalently bind the coverslips to PAA. The details of the reaction were described previously[37]. We spread 20 μl 0.1 M sodium hydroxide by rolling a glass Pasteur pipette over each coverslip. When the coverslips were dry, 15 μl (3-aminopropyl)trimethoxysilane (Sigma-Aldrich, St. Louis, MO) was spread and the coverslips were allowed to dry for 5 minutes. The coverslips were washed 3 times in DI and incubated in 200 μl 0.5% glutaraldehyde solution (from 8% stock solution, Sigma-Aldrich) for 30 minutes and washed in DI 3 times again. The coverslips were stored up to 1 month together with desiccant beads (Neolab Migge Laborbedarf-Vertriebs, Heidelberg, Germany). To cover the gels during polymerization and achieve a flat top surface, we coated coverslips with a diameter of 15 mm (Menzel-Gläser, Braunschweig, Germany) hydrophobically with RainX (Krako Car Care International, Altrincham, WA) according to the manufacturer's protocol to facilitate better detachment of the substrates[38]. To remove dust, the coverslips were cleaned with canned air directly prior to substrate polymerization.

To polymerize PAA substrates, a monomer solution of 5% w/v acrylamide (AA, from 40% w/v stock solution, Sigma-Aldrich) and N,N′methylenebisacrylamide (BIS, from 2% w/v stock solution, Sigma-Aldrich) at a concentration of 0.06% w/v in phosphate-buffered saline (1xPBS, 0.2 g l^{-1} KCl, 8.0 g l^{-1} NaCl, 1.44 g l^{-1} Na_2HPO_4, and 0.24 g l^{-1} KH_2PO_4 in DI) was prepared. N,N,N′,N′-tetramethylethylenediamine (Thermo Fisher Scientific, Waltham, MA) at a final concentration of 1/2000 v/v was added to catalyze the polymerization reaction. The polymerization reaction was started by the addition of 1/200 v/v freshly prepared 10% w/v aqueous ammonium-persulfate (APS) solution.

To prepare thin substrate layers, 15 μl of the monomer solution was pipetted on a RainX-coated coverslip. A surface-activated coverslip was lowered from the top with the activated side facing downwards until surface tension kept both coverslips in place. This sandwich configuration was suspended on a pair of Pasteur pipettes to polymerize at room temperature and high air humidity of approximately 60–80% to minimize evaporation effects. After polymerization, the round coverslips were removed carefully with forceps and the substrates were washed 3 times in 1xPBS to remove unreacted monomers. The substrates had a thickness that ranged from approximately 30 to 110 μm. Even though the thickness of every substrate varied quite significantly the surface still remained horizontal with inclination angles well below 1°, thus not influencing the measurement. Before the measurement, superparamagnetic beads with a diameter of 4.5 μm (Dynabeads® M-450 Epoxy, Thermo Fisher Scientific) were sedimented on the substrates.

Magnetic tweezers setup and calibration. The magnetic tweezers (MT) setup is based on an inverted light microscope (Nikon Eclipse Ti-U, Nikon, Tokyo, Japan) with a 20× magnification objective for calibration measurements (CFI Plan Achromat 20× objective, NA 0.4, Nikon) and a 60× magnification objective (CFI Plan Apochromat λ 60× oil objective, NA 1.40, Nikon) for measurements of the bacteria. Image sequences were acquired with a CMOS camera (Orca-flash 4.0 v2, Hamamatsu, Shizuoka, Japan) under bright-field illumination.

The MT consists of a solenoid with a high permeability soft iron core and a power supply with a maximum output power of 10 A (Elektro Automatik, Viersen, Germany). The coil consists of 1420 turns of a copper wire with a diameter of 0.5 mm and the resulting solenoid has a dimeter of 20 mm and a length of 50 mm. The core

material is the nickel-iron alloy Mumetall (Vacuumschmelze GmbH, Hanau, Germany), which possesses a magnetic permeability up to $\mu_{max} = 250000$. The core has a cylindrical shape and a conical sharp tip with a core length of 163 ± 2 mm and a tip diameter of 35 ± 2 µm. To increase the magnetic permeability of the Mumetall and therefore the magnetic field that can be generated, the rod was annealed in a magnetic field in hydrogen atmosphere at the Vacuumschmelze Hanau. The coil including the soft iron core can be positioned in *x*-, *y*- and *z*-direction using single-axis translation stages (Mitutoyo, Sakado, Japan and Thorlabs, Newton, USA). The inclination angle of the tip within the sample can be adjusted by a manual rotation stage (Suruga Seiki, Tokyo, Japan). Before and after the usage of the MT the remanent magnetization of the core was reduced by a demagnetizer (Analogis, Falkensee, Germany).

The magnetic forces generated by the MT were calibrated by analyzing the movement of super-paramagnetic particles (Dynabeads M-450) with a diameter of $d = 4.5$ µm within a highly viscous fluid consisting of glycerin and water. We determined the exact concentration of the glycerin in the glycerin-water stock solution by measuring the viscosity of the solution with an Ostwald viscometer. At a temperature of 21.1 °C, we measured a viscosity of $\eta_G(21.1\,°C) = 1.23 \pm 1.0$ Pa *s* which corresponds to a glycerin concentration of 99.79%. For sample preparation, 0.012 ml of the particle-water stock solution was suspended in 1.5 ml of the 99.79% glycerin stock solution. The particle concentration of the resulting solution was $3.2 \cdot 10^6$ particles per ml. For the temperature of $T = 22.5 \pm 1.0$ °C at which the MT calibration measurements were performed, we determined a viscosity of $\eta_G = 0.95 \pm 0.25$ Pa *s*. The motion of the particles in the magnetic field was measured by bright-field time-lapse microscopy using the 20× objective and an acquisition rate of 20 frames per second. The particle positions were determined by applying a centroid-based tracking algorithm[39]. The viscous drag force F_d exerted on each particle was calculated by using Stokes law $F_d = 3\pi \cdot \eta_G \cdot d \cdot v$, where v is the velocity of the particle.

Magnetic tweezers experiments. For the characterization of the magnetic moments of single *M. gryphiswaldense* cells with the MT, fixed bacteria suspended in the 85% (v/v) glycerol solution (dynamic viscosity of 135 mPa s at a temperature of 22.5 °C) were placed on a glass coverslip (No. 1, 18 mm diameter, Marienfeld-Superior, Lauda-Königshofen, Germany) which was mounted into a custom-built aluminum holder. The MT tip was immersed into the sample and the bacterial motion in the magnetic field was monitored with bright-field time-lapse microscopy at room temperature with the 60× objective.

For measuring the translational motion of the bacteria in temporally constant magnetic fields, the current through the MT coil was set to $I = 0.1$ A and the image acquisition rate was 20 frames per second. The motion of the center of mass of each bacterium was tracked manually. Only bacteria with a distance of more than 8 µm from the MT tip surface were tracked to ensure positioning within the well-calibrated area of the MT.

For measuring the rotational motion of the bacteria in temporally varying fields, the magnitude of the current through the coil was set to $I = 0.008$ A, and the direction of the current was alternated periodically. The periodicity of the alternations was sufficiently low to allow all rotating bacteria to finish their motion before the current direction was switched. The image acquisition rate was set to 2 frames per second. For bacteria that were rotating mainly in the image plane, the longitudinal axis of the bacteria was identified manually in each image, and the angle θ of the bacterium relative to the magnetic field direction was determined. For bacteria that were rotating mainly perpendicular to the image plane, the time that was need for a full rotation was determined.

Transmission electron microscopy (TEM). For conventional TEM analysis, cells were grown at 28 °C under microaerobic conditions, fixed in formaldehyde (1.5%) and concentrated by centrifugation. Next, unstained cells were absorbed on carbon-coated copper mesh grids (Plano, Wetzlar). Bright-field TEM was performed on a FEI CM200 (FEI; Eindhoven, The Netherlands) transmission electron microscope using an accelerating voltage of 160 kV. Images were captured with an Eagle 4 k CCD camera using EMMenu 4.0 (Tietz) and FEI software. Fiji software was used to obtain data regarding the cell dimensions.

Calculation of the viscous drag coefficients via Stokesian dynamics. The Stokesian dynamics method calculates the flow at zero Reynolds number around an object and its drag by discretizing the surface of the object and by using the flow field of point forces. For details see the Supporting Information and work by Leal[40].

Calculation of the viscous drag coefficients by Boundary Integral Method. The Boundary Integral Method solves the Stokes flow at zero Reynolds number by expressing the flow field as integrals over arbitrarily shaped domain boundaries. For details see the Supporting Information and work by Daddi-Moussa-Ider *et al.*[41] and Guckenberger *et al.*[42].

Results

Magnetic tweezers calibration. The MT system was calibrated using superparamagnetic microparticles with a diameter of 4.5 µm as described in the *Materials and Methods* section. Briefly, the motion of a large number of particles towards the tip of the MT in a highly viscous liquid environment (Fig. 2a) was tracked microscopically using digital image processing. The magnetic forces exerted on the particles as a function of their positions (Fig. 2b) were calculated from the particle velocities and their Stokes drag coefficient (Fig. 2c). At a given electric current I through the coil of the MT, the force F exerted on a particle depends on the distance r between the tip and the particle. The polar angle α of the particle position had no detectable influence on the force-distance relationship $F(r)$ as long as $\alpha \leq 40°$ was fulfilled. The angle $\alpha = 0°$ defines the symmetry axis of the MT (Fig. 2b). We therefore limited the tweezers calibration and the subsequent measurements on bacteria to polar angles of $\alpha \leq 40°$ and considered only the distance of the particles and of the bacteria, respectively, for the subsequent data analysis.

The force-distance relationship $F(r)$ can be described by the equation,

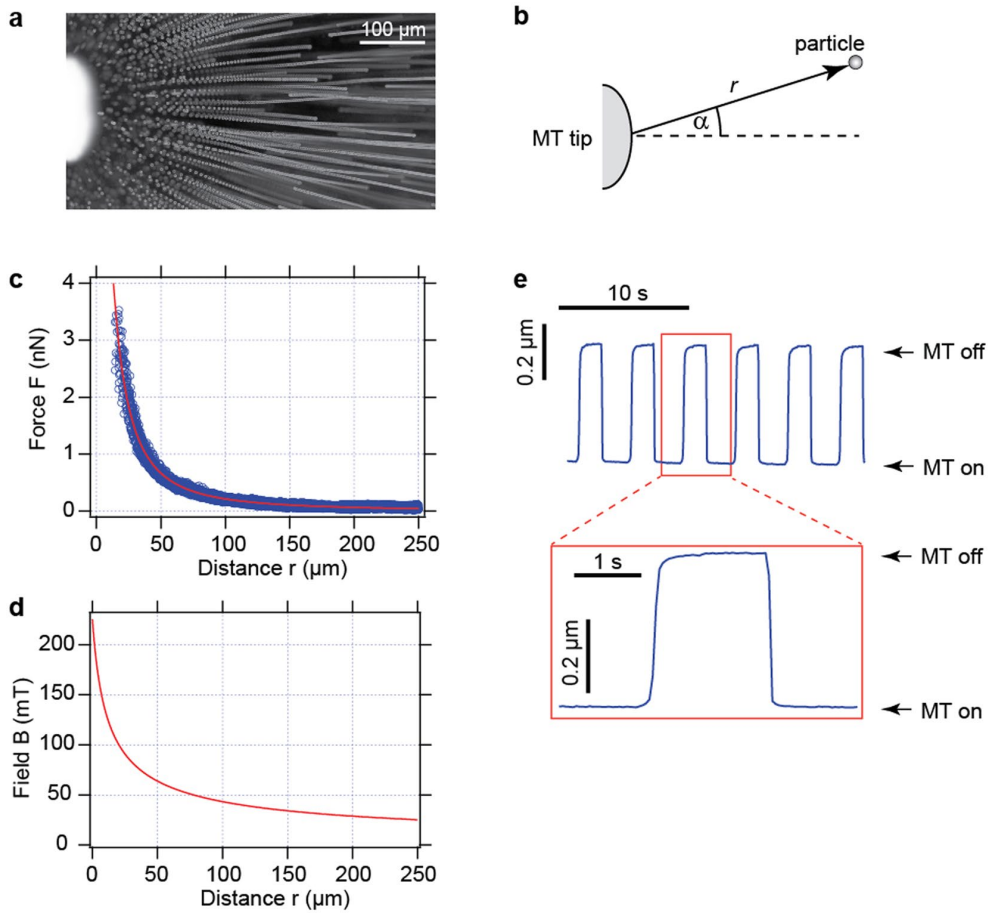

Figure 2. Magnetic tweezers calibration and characterization. The MT were calibrated by tracking the motion of superparamagnetic microparticles towards the MT tip in a highly viscous liquid environment. (**a**) A maximum projection of a time-lapse image sequence with a constant frame rate shows directly the direction of the applied force and the acceleration of the particles towards the tip on the left side. (**b**) The position of a particle is characterized by its distance r from the tip and its polar angle α with respect to the symmetry axis of the MT. (**c**) The data for the force F exerted by the MT on the particles as a function of r are shown by the blue circles. The red line shows the fit of Eq. 1 to the data. The current through the coil of the MT was $I = 0.5$ A in this measurement. (**d**) The known magnetization behavior of the superparamagnetic particles allows the calculation of the magnetic field B as a function of the distance r. (**e**) The field switching time was characterized by tracking the motion of a superparamagnetic particle that was bound to an elastic substrate in a magnetic field that was turned on and off periodically. The data shows the lateral displacement of the bead in the direction of the field. The motion of the particle as a function of time indicated an upper limit for the characteristic times for turning the fields on and off.

$$F(r) = \frac{F_0}{\left[\frac{r}{2r_{0F}} + \frac{1}{2}\right]^{c_F}} \tag{1}$$

a modified version of the force-distance relation described by Kollmannsberger and Fabry[43], which has the property that $F(r_{0F}) = F_0$. For a current of $I = 0.5$ A through the coil of the MT, fitting Eq. 1 to the data yielded $F_0 = 5.5 \pm 0.1$ nN, $r_{0F} = 9.6 \pm 0.2$ µm and $c_F = 1.87 \pm 0.02$ (Fig. 2c).

A particle with a magnetic moment $\boldsymbol{\mu}$ in an inhomogeneous magnetic field $\boldsymbol{B}$ experiences the force

$$\boldsymbol{F} = (\boldsymbol{\mu}\nabla)\boldsymbol{B} \tag{2}$$

The known relationship between the magnitude B of the external field and the magnitude μ of the magnetic moment of the superparamagnetic particles, i.e., the function $\mu(B)$[44] allowed us to derive the magnetic field B as a function of the distance r (Fig. 2d) from the measured relation between the force F and the distance r (Fig. 2c). We found that the equation

$$B(r) = \frac{B_0}{\left[\frac{r}{2r_{0B}} + \frac{1}{2}\right]^{c_B}} \tag{3}$$

is suitable to describe the relationship between the magnetic field and the particle distance. For a current of $I = 0.5$ A through the coil of the MT, the resulting parameters were $B_0 = 147$ mT, $r_{0B} = 7.5$ µm and $c_B = 0.62$. The corresponding field-distance-relation is shown in Fig. 2d. At distances of $r = 10 \ldots 250$ µm, magnetic fields of approximately B = 130 … 25 mT can be achieved. The magnetic H-field of the MT coil scales linearly with the current I. However, the magnetic B-field scales less than linearly with the H-field in our parameter range since the permeability of the annealed Mumetall core material decreases with increasing current for H-fields in the range of approximately 0.1 … 10 A cm^{-1}[45]. With the lowest current ($I = 0.008$ A) that we used, we were able to generate magnetic fields of B = 6 … 55 mT at distances of $r = 10 \ldots 250$ µm.

For experiments in which the magnetic field of the tweezers is abruptly altered (e.g., by changing the direction of the current), it is necessary to know the timescale for changing the field rapidly. To measure an upper limit of this time scale, we placed the tip of the MT close to a superparamagnetic microparticle bound to the surface of an elastic polyacrylamide gel. The MT were turned on and off sequentially and the resulting motion of the particle was tracked microscopically (Fig. 2e). The observed time scale for turning the tweezers on was lower than the time scale for turning them off. An upper limit τ_{max} for the tweezers switching time τ can be defined as the time after which 95% of the total particle displacement is reached. This definition yields $\tau_{max,on} = (100 \pm 10)$ ms and $\tau_{max,off} = (290 \pm 50)$ ms for turning the tweezers on and off, respectively. These time scales represent upper limits for the switching time because they include the finite response time of the gel to a sudden force that is exerted on the gel.

Rotation of bacteria. Bacteria with a given magnetic moment $\boldsymbol{\mu}$ experience a torque $\boldsymbol{T} = \boldsymbol{\mu} \times \boldsymbol{B}$ in a magnetic field $\boldsymbol{B}$ which leads to a rotation of the bacteria if $\boldsymbol{\mu}$ and $\boldsymbol{B}$ are not exactly parallel or antiparallel to each other. Chemically fixed bacteria (i.e. dead and thus incapable of active swimming) were immersed in a highly viscous glycerol-water mixture (85% v/v glycerol) to slow the rotation to a time scale on the order of ten seconds. This step facilitated tracking of the rotation by time-lapse microscopy with an image acquisition rate of 2 Hz. The bacteria aligned with the field of the MT when the tweezers were turned on for the first time in the sample. After the magnetic field direction was switched by changing the direction of the electric current through the coil, the bacteria rotated 180° to align with the new field direction. Although bacteria that are aligned exactly antiparallel to the magnetic field experience no field-induced torque, thermal fluctuations of the orientation lead to deviations from the instable antiparallel equilibrium orientation. For multiple subsequent measurements, we switched the field with periods that were significantly longer than the time period of a full 180° rotation. These measurements were performed at magnetic field strengths between 6 mT and 23 mT. Measurements in such relatively low magnetic fields yield magnetic moments that are close to the remanent moments of the bacteria. The lower boundary of 6 mT was given by the lowest field strength that we generated in the field of view of the microscope. The upper boundary of 23 mT was given by the highest field strength for which we were able to observe rotation of the bacteria. These magnetic fields were sufficiently low to not alter the direction of the magnetic moments of the bacteria with respect to the bacterial orientation. In contrast, upon application of higher magnetic fields with strengths above 23 mT, we observed that the bacteria did not rotate upon field reversal.

The rotation of individual bacteria after switching the magnetic field was measured by bright-field time-lapse microscopy (Fig. 3a). For bacteria that were rotating mainly in the image plane, the angle θ of each bacterium relative to the magnetic field direction was tracked manually, and the resulting time course of the angle $\theta(t)$ (Fig. 3b) was fitted to the solution of the overdamped rotational equation of motion $\mu B \sin\theta = \gamma_{rot} \frac{d}{dt}\theta$:

$$\theta(t) = 2\,\mathrm{arc\,tan}\left[e^{\left(-\frac{\mu \cdot B}{\gamma_{rot}} \cdot t\right)} \cdot \tan\left(\frac{\theta_0}{2}\right)\right] \tag{4}$$

The parameter γ_{rot} is the rotational viscous drag coefficient of the bacterium, and θ_0 is the angle of the bacterium at the beginning of the data acquisition at $t = 0$. The value for γ_{rot} was calculated for each individual bacterium from its shape parameters as described in the *Materials and Methods* section. The remaining free fit parameters were the magnetic moment μ and the value θ_0. An overview over multiple time series of the rotation angle θ as a function of time t and the corresponding fits to Eq. 4 can be seen in Fig. 3c.

For bacteria that were mainly rotating perpendicular to the image plane, the time Δt that was needed for a complete rotation was determined. According to Eq. 4, this time is

$$\Delta t = \frac{\gamma_{rot}}{\mu \cdot B} \cdot \ln\left[\frac{\tan(\theta_e/2)}{\tan(\theta_s/2)}\right] \tag{5}$$

where θ_s is the angle of the bacterium at the start of the rotation, and θ_e is the angle of the bacterium at the end of the rotation (see also Penninga *et al.*[46]). The rotation time Δt diverges for a rotation from 0° to 180°. The limited optical resolution[47] leads to a limited precision in the determination of the orientation of a rotating object[32,33,48,49]. We found that the tracking precision for the orientation of the bacteria was approximately 4°. Consequently orientation angles of up to 4° were indistinguishable from an angle of 0° and orientation angles of down to 176° were indistinguishable from an angle of 180°. We therefore used the boundary values of $\theta_s = 4°$ and $\theta_e = 176°$ for the calculation of Δt. The value for γ_{rot} was also in this case determined for each individual bacterium from its

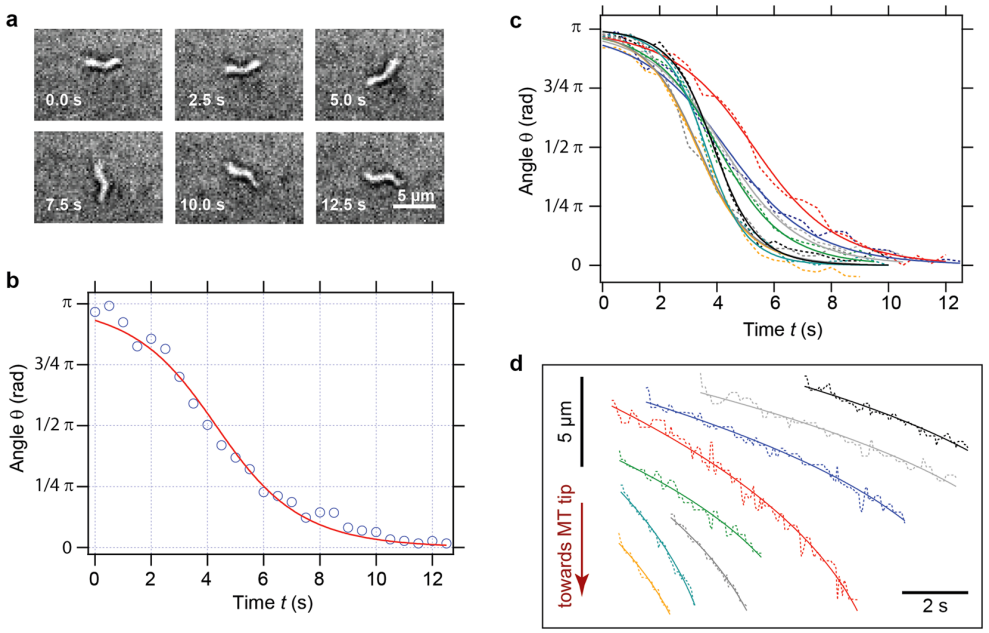

Figure 3. Rotation of *M. gryphiswaldense* in reversed magnetic fields and translation of the bacteria in static magnetic fields. (**a**–**c**) Data for the rotation of bacteria in reversed magnetic fields. (**a**) Frames of a time-lapse microscopy series of a rotating cell. (**b**) Angle $\boldsymbol{\theta}$ of a rotating cell as a function of time t (points) and fit of Eq. 4 to the data (red curve). (**c**) Multiple time series of the rotation angle $\boldsymbol{\theta}$ as a function of time t (dashed curves) and the corresponding fits to Eq. 4 (solid curves). (**d**) Data for the translation of bacteria in static magnetic fields. Multiple time series of the bacterial displacements as a function of time (dashed curves) and the corresponding fits to Eq. 6 (solid curves).

shape parameters, as described in the *Materials and Methods* section and the resulting magnetic moment μ was calculated directly.

The rotation experiments were performed at magnetic field strengths that were sufficiently small to neglect the translational motion of the bacteria in the inhomogeneous field of the MT. The translational motion of the bacteria during their rotation was typically approximately 1 µm, which resulted in changes of the local magnetic fields of approximately 0.1 mT. These changes correspond to relative changes between 2% and 0.4% for the used magnetic fields between 6 mT and 23 mT, which was considered to be negligible. However, for sufficiently large magnetic fields, a strong translational motion of the bacteria along the gradient of the magnetic field was observed. These translational motions were used as a second method for the determination of the magnetic moment of the bacteria.

Translation of bacteria. Bacteria with a magnetic moment $\boldsymbol{\mu}$ experience a force $\boldsymbol{F} = \nabla(\boldsymbol{\mu} \cdot \boldsymbol{B})$ in a magnetic field $\boldsymbol{B}$. For a bacterium with a constant magnetic moment with the absolute value μ, which is aligned along a magnetic field with the magnitude B, the resulting overdamped translational equation of motion is $\nabla B = \gamma_{\text{trans}} \frac{d}{dt} r$, where γ_{trans} is the translational viscous drag coefficient and r is the distance of the bacterium to the MT tip. For the known magnetic field $B(r)$ (Eq. 3) the solution of this equation is

$$r(t) = r_{0\text{B}} + \left[(r_0 - r_{0\text{B}})^{c_\text{B}+2} - \mu B_0 \frac{d_0^{c_\text{B}}}{\gamma_{\text{trans}}} c_\text{B} (c_\text{B} + 2) t \right]^{\frac{1}{(c_\text{B}+2)}} \tag{6}$$

The parameter r_0 is the distance of the bacterium to the MT tip at the beginning of the data acquisition at $t = 0$. This equation was fitted to the experimental data of the bacterial position as a function of time $r(t)$, which was determined by manual tracking of the translational bacterial motion. The value for γ_{trans} was calculated for each individual bacterium from its shape parameters as described in the *Materials and Methods* section. For each bacterium, the remaining free fit parameters were its magnetic moment μ and the value r_0. An overview of multiple time series of the displacement of the bacteria as a function of time and the corresponding fits to Eq. 6 is shown in Fig. 3d. The bacteria were tracked for several seconds, and the displacement during this time was on the order of up to ten micrometers (instead of absolute time- and space-axes, temporal and spatial scale bars were used in this figure to allow the representation of multiple displacement data sets).

These measurements were performed at magnetic fields ranging between 90 mT and 130 mT. The resulting magnetic moments of the bacteria were therefore induced magnetic moments that were expected to have values closer to the saturation moment than to the remanent moment[21]. The upper boundary of 130 mT was given by

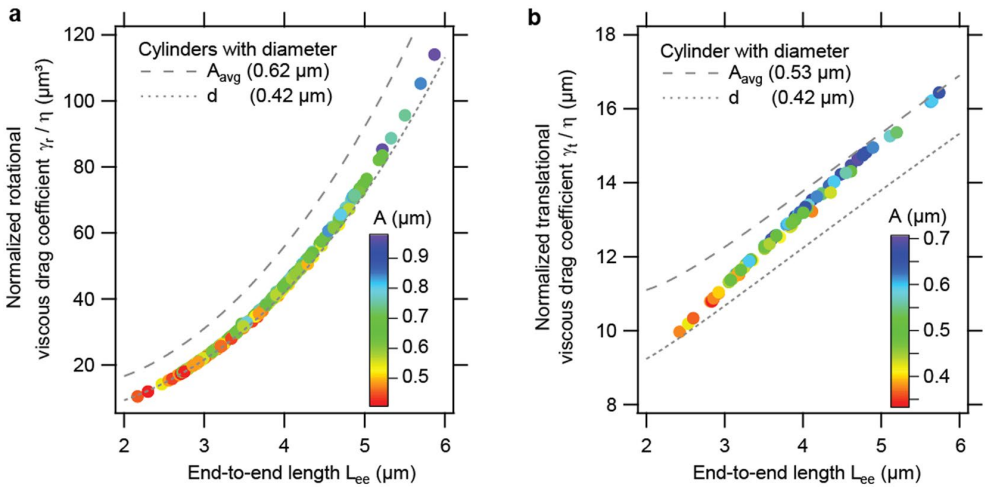

Figure 4. Normalized viscous drag coefficients of individual *M. gryphiswaldense* cells as a function of bacterial dimensions. The rotational (**a**) and translational (**b**) viscous drag coefficients were both calculated with Stokesian dynamics and with a Boundary Integral Method. Shown are the mean values of both methods, which deviate only negligibly from each other. The viscous drag coefficients are normalized by the viscosity of the medium η and plotted as a function of the end-to-end length L_{ee} of the bacteria. The amplitude A of the bacteria is indicated by the color of the data points. For comparison purposes, the normalized viscous drag coefficients of cylinders with various diameters are also shown.

the maximal field strength that was created close to the MT tip, whereas the lower value of 90 mT was set by the boundary condition that a significant translational motion of the bacteria in the highly viscous fluid needed to be detectable within the measurement time.

Viscous drag coefficients. The translational and rotational viscous drag coefficients were determined for each bacterium individually as described in the *Materials and Methods* section. To this end, we used two approaches that both take the helical shape and the dimensions of an individual bacterium into account. The end-to-end-length L_{ee} and the amplitude A (Fig. 1) were determined for each cell individually from light microscopy images. The diameter d of the bacterium is close to the resolution limit of diffraction-limited light microscopy[47]. We therefore analyzed the dimensions of 111 bacteria by TEM, and we found that the spread of the diameter values was very small. The average diameter was 420 nm, and the standard deviation was 30 nm; thus, we considered the mean diameter for the calculation of the drag coefficients of each bacterium. Similarly, the arc length s was difficult to determine by light microscopy. Consequently, we also determined this value from TEM micrographs from a sample of 125 bacteria. We found that the ratio of the arc length to the end-to-end-length was relatively well defined with a value of $s/L_{ee} = 1.1 \pm 0.1$. Thus, we used this value to further calculate the arc length of each bacterium from its light-microscopically determined end-to-end-length: $s = 1.1\, L_{ee}$.

With the given dimensions for each bacterial cell, we determined the translational and rotational drag coefficients in a Stokes flow. Within the Stokesian dynamics, the surface of the bacteria was divided and represented by up to $N = 10{,}000$ particles interacting hydrodynamically via the Oseen tensor. The Boundary Integral Method uses a surface discretization of approximately 24,000 flat triangles and solves the Stokes equation by computing the surface velocities from a specified boundary traction.

The values of the viscous drag coefficients calculated by the two different methods provided quantitatively very similar results for each bacterium. For the rotational viscous drag coefficients, the two methods had an average discrepancy of 0.7% while the translational viscous drag coefficients differed by an average of 1.5%. We therefore used the mean value of the two methods as the drag coefficient for each bacterium. The calculated drag coefficients are shown in Fig. 4 as a function of the end-to-end length of the bacteria. The color code of the data points represents the amplitude A of the bacteria. Longer bacteria, i.e., bacteria with a larger end-to-end length L_{ee} tended to have a larger amplitude. The drag coefficients shown in Fig. 4 are normalized to the viscosity of the liquid η, which varied slightly from experiment to experiment because the temperature in the laboratory varied slightly in the range of 20.8 °C to 23.3 °C.

Both drag coefficients are larger than the drag coefficients of cylinders with a diameter that equals the diameter of the bacteria which had an average value 0.42 µm. For a long cylinder with a length L, a diameter d and $L \gg d/2$, the normalized rotational viscous drag coefficient can be approximated[50] by

$$\frac{\gamma_{\mathrm{rot}}}{\eta} = \frac{1/3 \cdot \pi \cdot L^3}{\ln\left(\frac{L}{d}\right) - 0.66} \tag{7}$$

and the normalized translational viscous drag coefficient can be approximated by

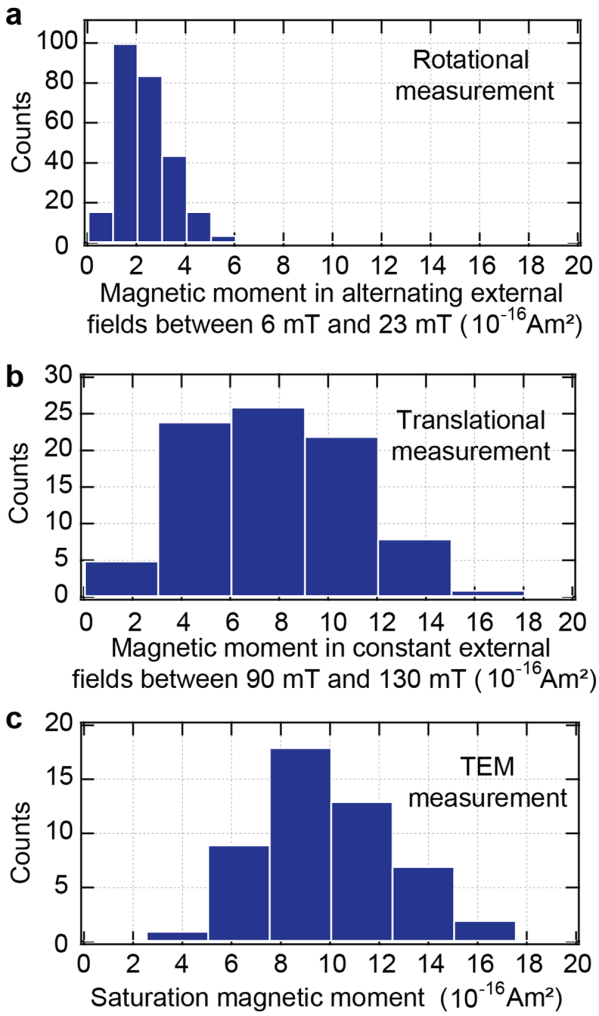

Figure 5. Distributions of the magnetic moments of single *M. gryphiswaldense* cells. (**a**) Magnetic moments determined by measuring the rotation of $N = 265$ cells in alternating magnetic fields. The field strengths ranged from B = 6 mT to 23 mT. (**b**) Magnetic moments determined by measuring the translation of $N = 86$ cells in static magnetic fields. The field strengths ranged from B = 90 mT to 130 mT. (**c**) Saturation magnetic moments of $N = 50$ cells determined by measuring the total magnetosome volume of each cell with TEM.

$$\frac{\gamma_{\text{trans}}}{\eta} = \frac{2\pi \cdot L}{\ln\left(\frac{L}{d}\right) - 0.20} \tag{8}$$

Furthermore, both drag coefficients are always smaller than the drag coefficients of cylinders with a diameter that corresponds to the average value of the amplitude of the bacteria. These average amplitudes were $A_{\text{avg}} = 0.62\,\mu\text{m}$ and $A_{\text{avg}} = 0.53\,\mu\text{m}$ for the bacteria that were investigated in the rotational and translational experiments, respectively.

Magnetic moments. With the calculated rotational viscous drag coefficients, the magnetic moment of each bacterium was determined by fitting Eq. 4 to the tracked rotational motion for the case that the rotation was taking place mainly in the image plane. For the case that the rotation was mainly occurring perpendicular to the image plane, the magnetic moment of each bacterium was calculated by directly applying Eq. 5. As expected, the resulting distributions of magnetic moments were indistinguishable from each other, and we therefore pooled the data. We tracked the rotational motion of $N = 265$ bacteria and found an average magnetic moment of the cells of $\mu = 2.4 \cdot 10^{-16}\,\text{A m}^2$ with a standard deviation of $\sigma_\mu = 1.1 \cdot 10^{-16}$. The maximal magnetic moment was $\mu_{\text{max}} = 6.3 \cdot 10^{-16}\,\text{A m}^2$, and the minimal moment was $\mu_{\text{min}} = 0.58 \cdot 10^{-16}\,\text{A m}^2$. The magnetic field strengths for the rotational measurements were between $B = 6$ mT and $B = 23$ mT. The distribution of the magnetic moments from the rotational measurements is shown in Fig. 5a.

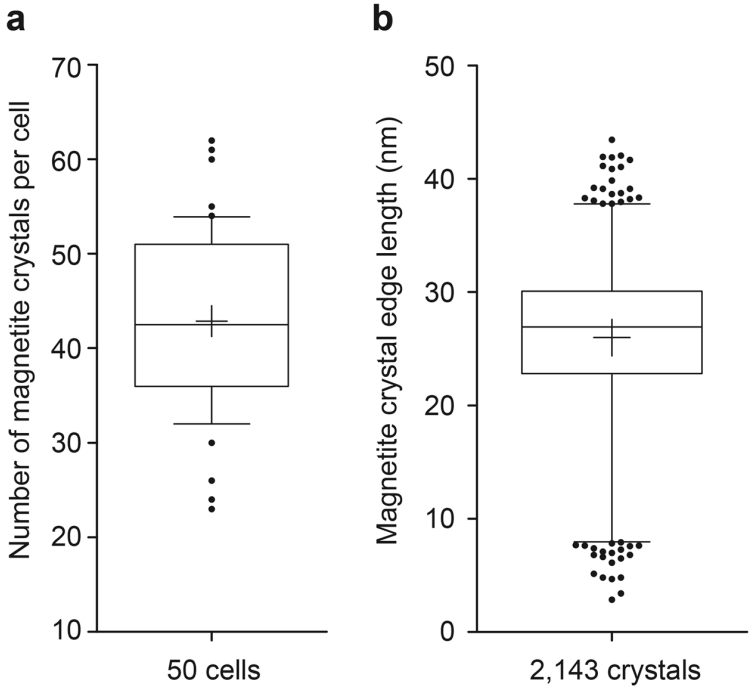

Figure 6. Distributions of the magnetite crystal numbers and sizes in *M. gryphiswaldense* cells. (**a**) Distribution of the number of magnetite crystals per cell. The data from 50 cells are represented in a box and whiskers plot. The box represents 50% of the central data, and the whiskers represent the 10–90 percentile. The central line depicts the median, and the cross indicates the average. (**b**) Distribution of the magnetite crystal edge length of 2,143 crystals from 50 cells. The box represents 50% of the central data and the whiskers show the 1–99 percentile. The central line depicts the median, and the cross indicates the average.

With the calculated translational viscous drag coefficients, the magnetic moment of each bacterium was determined by fitting Eq. 6 to the tracked translation motion. We tracked the translational motion of $N = 86$ bacteria and found an average magnetic moment of the cells of $\mu = 7.7 \cdot 10^{-16}\,\mathrm{A\,m^2}$ with a standard deviation of $\sigma_\mu = 3.4 \cdot 10^{-16}\,\mathrm{A\,m^2}$. The maximal magnetic moment was $\mu_{max} = 16 \cdot 10^{-16}\,\mathrm{A\,m^2}$, and the minimal moment was $\mu_{\mathrm{min}} = 1.2 \cdot 10^{-16}\,\mathrm{A\,m^2}$. The magnetic field strengths for the translational measurements were between $B = 90\,\mathrm{mT}$ and $B = 130\,\mathrm{mT}$. The distribution of the magnetic moments from the translational measurements is shown in Fig. 5b.

For a comparison, we determined the saturation magnetic moment for $N = 50$ bacteria by determining the total magnetosome volume V_{mag} for each cell by TEM. This value was multiplied by the saturation magnetization of magnetite[51] $M = 4.8 \cdot 10^{-22} \frac{\mathrm{A\,m^2}}{\mathrm{nm^3}}$ to determine the saturation magnetic moment for each cell $\mu = V_{\mathrm{mag}} \cdot M$. The average number of magnetite crystals per magnetosome chain was 43 ± 10 ($N = 50$ cells) with chains harboring between 23 and 62 crystals (Fig. 6a). Overall we found magnetosomes with edge lengths between 3 nm and 43 nm with a mean of (26 ± 6) nm for $N = 2{,}143$ crystals (Fig. 6b). The average saturation magnetic moment of the cells was $\mu_{\mathrm{sat}} = 9.9 \cdot 10^{-16}\,\mathrm{Am^2}$ and the standard deviation was $\sigma_{\mu_{\mathrm{sat}}} = 2.6 \cdot 10^{-16}\,\mathrm{A\,m^2}$. The maximal saturation magnetic moment was $\mu_{\mathrm{sat,max}} = 16.7 \cdot 10^{-16}\,\mathrm{Am^2}$ and the minimal moment was $\mu_{\mathrm{sat,min}} = 4.9 \cdot 10^{-16}\,\mathrm{Am^2}$. The distribution of the saturation magnetic moments from the TEM measurements is shown in Fig. 5c. An overview of the magnetic moments determined by the three different methods (bacterial rotation, bacterial translation and magnetosome volume) is shown in Table 1.

Discussion and Conclusions

We present a magnetic tweezers-based method for measuring the magnetic moments of individual bacteria, and we demonstrate the method by quantifying the individual magnetic moments of a large number of *M. gryphiswaldense* cells. Our method takes into account the helical shape of the bacteria and it can be adapted to allow the investigation of arbitrarily-shaped bacteria. Key parameters that describe the size and the shape of the bacteria, their end-to-end length and amplitude, were measured for each individual cell for the determination of its magnetic moment. Furthermore, our method is based on biologically inert (dead) yet well-preserved cells to avoid the non-thermal noise induced by living cells. In addition to characterizing the magnetic moment on a single cell level, our approach can also address various questions concerning the large spread of magnetic moments that were previously reported.

One of these questions was whether it is necessary to take the helical shape of *M. gryphiswaldense* into account or whether it is sufficient to approximate them with a simplified geometry, such as a cylinder. We found (Fig. 4)

B (mT)	μ (10^{-16} A m^2)	Method
6–23	2.4 ± 1.1	Bacterial rotation in alternating fields with a strength ranging between 6 mT and 23 mT
90–130	7.7 ± 3.4	Bacterial translation in constant fields with a strength ranging between 90 mT and 130 mT
∞	9.9 ± 2.6	Magnetosome volume determination by TEM

Table 1. Magnetic moments of the bacteria measured by the three different methods and the corresponding external magnetic fields. Average magnetic moments μ (±standard deviations) determined by the three different experimental methods: Measurement of the bacterial rotation in alternating external magnetic fields, measurement of the bacterial translation in constant external magnetic fields and determination of the magnetosome volume by TEM. The corresponding external field strengths B were in the range between 6 and 23 mT for the rotation measurements and between 90 and 130 mT for the translational measurements. The TEM measurement of the magnetosome volume provides the saturation moment for very large external magnetic fields.

that for the rotational measurements, the measured end-to-end lengths of the bacteria varied from $L_{ee,min} = 2.2\,\mu m$ up to $L_{ee,max} = 5.9\,\mu m$ with a mean value of $\langle L_{ee}\rangle = 3.7 \pm 0.7\,\mu m$. A cylinder with a length of $L = 3.7\,\mu m$ and a diameter of $d = 0.42\,\mu m$ (which is the average diameter according to our TEM measurements) has a normalized rotational viscous drag coefficient of approximately $\frac{\gamma_{rot}}{\eta} = 35.2\,\mu m^3$. Our exact calculations of the viscous drag, which take the helical shape and the individual dimensions of the cells into account, yield an average normalized rotational viscous drag coefficient of $\langle\frac{\gamma_{rot}}{\eta}\rangle = 38.7 \pm 17.0\,\mu m^3$. Therefore, calculating the average magnetic moment of the cells using the mean value $\langle L_{ee}\rangle$ and approximating the cells as cylinders instead of taking the real helical cell shape into account, leads to an error of approximately 9%. Similarly for the translational measurements, the measured end-to-end lengths of the bacteria varied from $L_{ee,min} = 2.4\,\mu m$ up to $L_{ee,max} = 5.7\,\mu m$ with a mean value of $\langle L_{ee}\rangle = 3.8 \pm 0.7\,\mu m$. A cylinder with a length of $L = 3.8\,\mu m$ and a diameter of $d = 0.42\,\mu m$ has a normalized translational viscous drag coefficient of approximately $\frac{\gamma_{trans}}{\eta} = 11.9\,\mu m$. Our exact calculations of the viscous drag, which take the helical shape and the individual dimensions of the cells into account yield an average normalized translational viscous drag coefficient of $\langle\frac{\gamma_{trans}}{\eta}\rangle = 12.8 \pm 1.4\,\mu m$. Therefore, calculating the average magnetic moment of the cells using the mean value $\langle L_{ee}\rangle$ and approximating the cells as cylinders instead of taking their real helical shape into account, leads to an error of approximately 7%. From these observations, we can conclude that for the given bacterial population, the approximation of the cell shapes by a single cylinder with a length and a diameter given by the average length and diameter of the population is a reasonable approach if systematic errors on the order of magnitude of approximately 10% are acceptable.

Another raised question was whether it is necessary to take the dimension of each individual cell into account or whether it is sufficient to use average dimensions of a bacterial ensemble. If the study is purely focused on the average magnetic properties of a bacterial ensemble and if an uncertainty of 10% is acceptable, using the average dimensions is sufficient as stated above. However if individual magnetic moments of single bacteria are relevant, using the individual dimensions of the cells is necessary as discussed below. Figure 4 shows that the individual length and amplitude of the bacteria is important for determining the individual viscous drag and thus the magnetic moment of each bacterium. The rotational viscous drag varies by more than a factor of 10 between the smallest value of $\frac{\gamma_{rot}}{\eta} = 10.5\ \mu m^3$ for the shortest bacterium and the largest value of $\frac{\gamma_{rot}}{\eta} = 114\ \mu m^3$ for the longest bacterium. If the average rotational viscous drag value was used instead of the drag value based on the individual size of the cells, the magnetic moment of the shortest bacterium would be overestimated by +270% and the magnetic moment of the longest bacterium would be underestimated by −64%. In addition, Fig. 4 shows that the translational viscous drag varies between a value of $\frac{\gamma_{trans}}{\eta} = 9.96\,\mu m$ for the shortest bacterium and a value of $\frac{\gamma_{trans}}{\eta} = 16.4\,\mu m$ for the longest bacterium. Thus, if the average translational viscous drag value was used instead of the drag value based on the individual size of the cells, the magnetic moment of the shortest bacterium would be overestimated by +29% and the magnetic moment of the longest bacterium would be underestimated by −22%. The observation that the rotational measurement of the magnetic moment is more sensitive to the length of the bacteria than the translational measurement can be understood by the circumstance that the rotational viscous drag coefficient scales approximately with the cube of the bacteria's length, whereas the translational drag coefficient scales approximately only linearly with the length of the bacteria.

The last question was whether the use of dead cells (ruling out the induction of non-thermal noise) leads to more consistent results than the use of living cells if different methods for determining the magnetic moments are applied. Since we only used dead cells in our measurements, we cannot provide a final answer to this question. However, we are able to contribute to an answer by testing whether the three different methods that were applied in our study are consistent with previous measurements on ensembles of non-motile bacteria. Fischer *et al.* measured the relative magnetization behavior of a large ensemble of dead *M. gryphiswaldense* cells[21]. These measurements provide information about the change of the average magnetic moment of the bacteria as a function of an external magnetic field. Their data indicate that the direction of the bacterial magnetization is reversed if external fields with an absolute value of more than approximately 20 mT are applied in the direction that is antiparallel to the magnetic fields of the bacteria. In agreement with this magnetic coercivity, we observed a rotation of the bacteria after a reversal of the magnetic field direction only for magnetic field strengths of less than 23 mT. For

larger magnetic fields, the bacteria did not rotate suggesting a reversal of the direction of their magnetic moment relative to the orientation of the bacteria.

Furthermore we derived magnetic moments with a mean value of $\mu = 7.7 \cdot 10^{-16}$ A m^2 and a standard deviation of $\sigma = 3.4 \cdot 10^{-16}$ A m^2 from our measurements of the bacterial translation in constant external fields (field strength: 90 mT–130 mT). Given the $N = 86$ translation measurements, the standard error of the mean is therefore $\frac{1}{\sqrt{86}} \cdot 3.4 \cdot 10^{-16}$A m^2 $= 0.4 \cdot 10^{-16}$A m^2. The TEM measurements of the saturation magnetic moment for $N = 50$ cells yielded a mean value of $\mu = 9.9 \cdot 10^{-16}$ A m^2, a standard deviation of $\sigma = 2.6 \cdot 10^{-16}$ A m^2 and therefore a standard error of the mean of $\frac{1}{\sqrt{50}} \cdot 2.6 \cdot 10^{-16}$A m^2 $= 0.4 \cdot 10^{-16}$A m^2. A combination of these two measurements shows that in external magnetic fields in the range between 90 mT and 130 mT the cells have magnetic moments that correspond to a value of 78% ± 5% of the saturation magnetic moment. For these field strengths, the measurements of Fischer *et al.*[21] yielded magnetic moments that correspond to 95% ± 3% of the saturation magnetic moments. Although these measurements are not completely in agreement, they agree relatively well compared to the large discrepancies on the order of one magnitude that were reported so far. Furthermore, our results are in agreement with the work of Reufer *et al.*[10] who investigated *M. gryphiswaldense* and found an ensemble average of the magnetic moment of $(2.0 \pm 0.6) \times 10^{-16}$ A m^2 at a magnetic field of 1.5 mT. Based on the bacterial magnetization behavior[21], an extrapolation of this magnetic moment from an external field of 1.5 mT to external fields in the range of 6 mT to 23 mT would result in a magnetic moment of $(2.7 \pm 1.2) \times 10^{-16}$ A m^2. This value is in very good agreement with the value of $(2.4 \pm 1.1) \times 10^{-16}$ A m^2 that we found for magnetic fields between 6 mT to 23 mT. Altogether, the agreement of our three methods with several previous measurements that were also based on dead cells indicates that the use of such cells leads to more consistent results than the use of living cells.

The possibility of measuring the magnetic moments of a large number of single bacteria by tracking their motion close to the tip of MT and by considering their individual shape and size allows addressing novel questions for the investigation of magnetotactic bacteria. In our study, we used MT in combination with bright-field microscopy. However MT can also be combined with other imaging modes such as fluorescence microscopy. Fluorescence labeling of the magnetosome chain to directly image the chain motion *in vivo* was recently established[7] and can be used in future in combination with the single cell magnetic moment measurements presented here. Moreover, deleting genes that are involved in magnetosome biosynthesis can, for example, be used to investigate quantitatively the effects of these genes on the magnetic moments of the bacteria. Although our results indicate that the use of dead cells provides more robust results that the use of living cells, our MT-based methods can be extended to allow the use of living cells. In this case, our method can be used for example to correlate the magnetic moments of individual bacteria with their behavioral response to obtain a deeper understanding of magnetotaxis as a navigational mechanism.

References

1. Frankel, R. B. Magnetic Guidance of Organisms. *Annu. Rev. Biophys. Bioeng.* **13**, 85–103 (1984).
2. Blakemore, R. Magnetotactic Bacteria. *Science* **190**, 377–379, doi:10.1126/science.170679 (1975).
3. Schleifer, K. H. *et al.* The genus Magnetospirillum gen. nov. Description of Magnetospirillum gryphiswaldense sp. nov. and Transfer of Aquaspirillum magnetotacticum to magnetospirillum magnetotacticum comb. nov. *Syst. Appl. Microbiol.* **14**, 379–385 (1991).
4. Schüler, D. Genetics and cell biology of magnetosome formation in magnetotactic bacteria. *FEMS Microbiol. Rev.* **32**, 654–672, doi:10.1111/j.1574-6976.2008.00116.x (2008).
5. Faivre, D. & Schüler, D. Magnetotactic Bacteria and Magnetosomes. *Chem. Rev.* **108**, 4875–4898, doi:10.1021/cr078258w (2008).
6. Katzmann, E., Scheffel, A., Gruska, M., Plitzko, J. M. & Schüler, D. Loss of the actin-like protein MamK has pleiotropic effects on magnetosome formation and chain assembly in Magnetospirillum gryphiswaldense. *Mol. Microbiol.* **77**, 208–224, doi:10.1111/j.1365-2958.2010.07202.x (2010).
7. Toro-Nahuelpan, M. *et al.* Segregation of prokaryotic magnetosomes organelles is driven by treadmilling of a dynamic actin-like MamK filament. *BMC Biol.* **14**, doi:10.1186/s12915-016-0290-1 (2016).
8. Schultheiss, D., Kube, M. & Schüler, D. Inactivation of the flagellin gene flaA in Magnetospirillum gryphiswaldense results in nonmagnetotactic mutants lacking flagellar filaments. *Appl. Environ. Microbiol.* **70**, 3624–3631, doi:10.1128/aem.70.6.3624-3631.2004 (2004).
9. Erglis, K. *et al.* Dynamics of magnetotactic bacteria in a rotating magnetic field. *Biophys. J.* **93**, 1402–1412, doi:10.1529/biophysj.107.107474 (2007).
10. Reufer, M. *et al.* Switching of Swimming Modes in Magnetospirillium gryphiswaldense. *Biophys. J.* **106**, 37–46, doi:10.1016/j.bpj.2013.10.038 (2014).
11. Popp, F., Armitage, J. P. & Schüler, D. Polarity of bacterial magnetotaxis is controlled by aerotaxis through a common sensory pathway. *Nat. Commun.* **5**, doi:10.1038/ncomms6398 (2014).
12. Grünberg, K., Wawer, C., Tebo, B. M. & Schüler, D. A large gene cluster encoding several magnetosome proteins is conserved in different species of magnetotactic bacteria. *Appl. Environ. Microbiol.* **67**, 4573–4582, doi:10.1128/aem.67.10.4573-4582.2001 (2001).
13. Bazylinski, D. A. & Frankel, R. B. Magnetosome formation in prokaryotes. *Nat. Rev. Microbiol.* **2**, 217–230, doi:10.1038/nrmicro842 (2004).
14. Grünberg, K. *et al.* Biochemical and proteomic analysis of the magnetosome membrane in Magnetospitillum gryphiswaldense. *Appl. Environ. Microbiol.* **70**, 1040–1050, doi:10.1128/aem.70.2.1040-1050.2004 (2004).
15. Scheffel, A. *et al.* An acidic protein aligns magnetosomes along a filamentous structure in magnetotactic bacteria. *Nature* **440**, 110–114, doi:10.1038/nature04382 (2006).
16. Faivre, D., Bottger, L. H., Matzanke, B. F. & Schüler, D. Intracellular magnetite biomineralization in bacteria proceeds by a distinct pathway involving membrane-bound ferritin and an iron(II) species. *Angew. Chem. Int. Ed.* **46**, 8495–8499, doi:10.1002/anie.200700927 (2007).
17. Rong, C. B. *et al.* Ferrous iron transport protein B gene (feoB1) plays an accessory role in magnetosome formation in Magnetospirillum gryphiswaldense strain MSR-1. *Res. Microbiol.* **159**, 530–536, doi:10.1016/j.resmic.2008.06.005 (2008).
18. Jogler, C. & Schüler, D. Genomics, Genetics, and Cell Biology of Magnetosome Formation. *Annu. Rev. Microbiol.* **63**, 501–521, doi:10.1146/annurev.micro.62.081307.162908 (2009).
19. Ding, Y. *et al.* Deletion of the ftsZ-Like Gene Results in the Production of Superparamagnetic Magnetite Magnetosomes in Magnetospirillum gryphiswaldense. *J. Bacteriol.* **192**, 1097–1105, doi:10.1128/jb.01292-09 (2010).

20. Fdez-Gubieda, M. L. *et al*. Magnetite Biomineralization in Magnetospirillum gryphiswaldense: Time-Resolved Magnetic and Structural Studies. *ACS Nano* **7**, 3297–3305, doi:10.1021/nn3059983 (2013).
21. Fischer, H. *et al*. Ferromagnetic resonance and magnetic characteristics of intact magnetosome chains in Magnetospirillum gryphiswaldense. *Earth. Planet. Sci. Lett.* **270**, 200–208, doi:10.1016/j.epsl.2008.03.022 (2008).
22. Erglis, K., Alberte, L. & Cebers, A. Thermal fluctuations of non-motile magnetotactic bacteria in AC magnetic fields. *Magnetohydrodyn* **44**, 223–236 (2008).
23. Logofatu, P. C. *et al*. Determination of the magnetic moment and geometrical dimensions of the magnetotactic bacteria using an optical scattering method. *J. Appl. Phys.* **103**, doi:10.1063/1.2917404 (2008).
24. Bahaj, A. S., James, P. A. B. & Moeschler, F. D. An alternative method for the estimation of the magnetic moment of non-spherical magnetotactic bacteria. *ITM* **32**, 5133–5135, doi:10.1109/20.539514 (1996).
25. Chemla, Y. R. *et al*. A new study of bacterial motion: Superconducting quantum interference device microscopy of magnetotactic bacteria. *Biophys. J.* **76**, 3323–3330, doi:10.1016/s0006-3495(99)77485-0 (1999).
26. Nadkarni, R., Barkley, S. & Fradin, C. A Comparison of Methods to Measure the Magnetic Moment of Magnetotactic Bacteria through Analysis of Their Trajectories in External Magnetic Fields. *Plos One* **8**, doi:10.1371/journal.pone.0082064 (2013).
27. Wang, N., Butler, J. P. & Ingber, D. E. Mechanotransduction Across the Cell Surface and Through the Cytoskeleton. *Science* **260**, 1124–1127, doi:10.1126/science.7684161 (1993).
28. Bausch, A. R., Möller, W. & Sackmann, E. Measurement of local viscoelasticity and forces in living cells by magnetic tweezers. *Biophys. J.* **76**, 573–579 (1999).
29. Fabry, B. *et al*. Scaling the microrheology of living cells. *Phys. Rev. Lett.* **87**, doi:10.1103/PhysRevLett.87.148102 (2001).
30. Tanase, M., Biais, N. & Sheetz, M. In *Cell Mechanics* Vol. 83 *Methods in Cell Biology* (eds Wang, Y. L. & Discher, D. E.) 473–493 (Elsevier Academic Press Inc, 2007).
31. De Vlaminck, I. & Dekker, C. In *Annual Review of Biophysics, Vol 41 Vol. 41 Annual Review of Biophysics* (ed Rees, D. C.) 453–472 (Annual Reviews 2012).
32. Irmscher, M., de Jong, A. M., Kress, H. & Prins, M. W. J. Probing the Cell Membrane by Magnetic Particle Actuation and Euler Angle Tracking. *Biophys. J.* **102**, 698–708, doi:10.1016/j.bpj.2011.12.054 (2012).
33. Irmscher, M., de Jong, A. M., Kress, H. & Prins, M. W. J. A method for time-resolved measurements of the mechanics of phagocytic cups. *J. R. Soc. Interface* **10**, doi:10.1098/rsif.2012.1048 (2013).
34. Heyen, U. & Schüler, D. Growth and magnetosome formation by microaerophilic Magnetospirillum strains in an oxygen-controlled fermentor. *Appl. Microbiol. Biotechnol.* **61**, 536–544, doi:10.1007/s00253-002-1219-x (2003).
35. Wang, J. & Pelham, R. J. Jr. Preparation of a flexible, porous polyacrylamide substrate for mechanical studies of cultured cells. *Methods Enzymol.* **298**, 489–496 (1998).
36. Gross, W. & Kress, H. Simultaneous measurement of the Young's Modulus and the Poisson Ratio of thin elastic layers. *Soft Matter* **13**, 1048–1055 (2017).
37. Aplin, J. D. & Hughes, R. C. Protein-derivatised glass coverslips for the study of cell-to substratum adhesion. *Anal. Biochem.* **113**, 144–148 (1981).
38. Plotnikov, S. V., Sabass, B., Schwarz, U. S. & Waterman, C. M. High-Resolution Traction Force Microscopy. *Methods Cell Biol.* **123**, 367–394, doi:10.1016/b978-0-12-420138-5.00020-3 (2014).
39. Crocker, J. C. & Grier, D. G. Methods of digital video microscopy for colloidal studies. *J. Colloid Interface Sci.* **179**, 298–310, doi:10.1006/jcis.1996.0217 (1996).
40. Leal, L. G. *Advanced Transport Phenomena* (Cambridge University Press, 2007).
41. Daddi-Moussa-Ider, A., Guckenberger, A. & Gekle, S. Long-lived anomalous thermal diffusion induced by elastic cell membranes on nearby particles. *Phys. Rev. E* **93**, doi:10.1103/PhysRevE.93.012612 (2016).
42. Guckenberger, A., Schraml, M. P., Chen, P. G., Leonetti, M. & Gekle, S. On the bending algorithms for soft objects in flows. *Comput. Phys. Commun.* **207**, 1–23, doi:10.1016/j.cpc.2016.04.018 (2016).
43. Kollmannsberger, P. & Fabry, B. High-force magnetic tweezers with force feedback for biological applications. *Rev. Sci. Instrum.* **78**, doi:10.1063/1.2804771 (2007).
44. Fonnum, G., Johansson, C., Molteberg, A., Morup, S. & Aksnes, E. Characterisation of Dynabeads (R) by magnetization measurements and Mossbauer spectroscopy. *J. Magn. Magn. Mater.* **293**, 41–47, doi:10.1016/j.jmmm.2005.01.041 (2005).
45. Hanau, V. (ed Vacuumschmelze Hanau) (Hanau 2002).
46. Penninga, I., Dewaard, H., Moskowitz, B. M., Bazylinski, D. A. & Frankel, R. B. Remanence measurements on individual magnetotactic bacteria using a pulsed magnetic-field. *J. Magn. Magn. Mater.* **149**, 279–286, doi:10.1016/0304-8853(95)00078-x (1995).
47. Jonkman, J. E. N., Swoger, J., Kress, H., Rohrbach, A. & Stelzer, E. H. K. Resolution in optical microscopy. *Methods Enzymol.* **360**, 416–446 (2003).
48. Lipfert, J., Kerssemakers, J. W. J., Jager, T. & Dekker, N. H. Magnetic torque tweezers: measuring torsional stiffness in DNA and RecA-DNA filaments. *Nat. Methods* **7**, 977–U954, doi:10.1038/nmeth.1520 (2010).
49. Mejean, C. O. *et al*. Elastic Coupling of Nascent apCAM Adhesions to Flowing Actin Networks. *Plos One* **8**, doi:10.1371/journal.pone.0073389 (2013).
50. Howard, J. *Mechanics of Motor Proteins and the Cytoskeleton*. (Sinauer Associates, 2001).
51. Haynes, W. M. *CRC Handbook of Chemistry and Physics*. (Taylor & Francis, 2013).

Acknowledgements

We would like to thank Theresa Zwiener for help with the sample preparation. Furthermore we would like to acknowledge support from the Elite Network of Bavaria (ENB), the German Academic Scholarship Foundation (Studienstiftung des deutschen Volkes) and the University of Bayreuth Graduate School. S.G. thanks the Volkswagen Foundation for financial support and the Leibniz Rechenzentrum for computing time on SuperMUC. D.S. thanks the Deutsche Forschungsgemeinschaft (Schu 1080/9-1 and 16-1).

Author Contributions

H.K. and D.S. designed the research; P.D. built the magnetic tweezers setup; C.Z., P.D. and W.G. characterized the magnetic tweezers setup; M.T.-N. prepared the samples and performed the electron microscopy experiments; C.Z. performed the magnetic tweezers experiments; S.K. and C.Z. wrote the data analysis software; C.Z. and M.T.-N. analyzed the experimental data; M.L., W.Z. and S.G. calculated the viscous drag coefficients and analyzed the simulation data; all authors discussed the results and wrote the paper.

Additional Information

Supplementary information accompanies this paper at doi:10.1038/s41598-017-03756-z

Competing Interests: The authors declare that they have no competing interests.

SUPPLEMENTARY INFORMATION

Measurement of the magnetic moment of single *Magnetospirillum gryphiswaldense* cells by magnetic tweezers

C. Zahn[1], S. Keller[1], M. Toro-Nahuelpan[2,3], P. Dorscht[1], W. Gross[1], M. Laumann[4], S. Gekle[5], W. Zimmermann[4], D. Schüler[2], and H. Kress*[1]

[1]Biological Physics, Department of Physics, University of Bayreuth, Germany
[2]Department of Microbiology, University of Bayreuth, Germany
[3]Department of Molecular Structural Biology, Max Planck Institute of Biochemistry, Planegg-Martinsried, Germany.
[4]Theoretical Physics I, Department of Physics, University of Bayreuth, Germany
[5]Biofluid Simulation and Modeling, Department of Physics, University of Bayreuth, Germany
*corresponding author: holger.kress@uni-bayreuth.de

Materials and Methods

Calculation of the viscous drag coefficients via Stokesian dynamics

The centerline $\boldsymbol{r}_{\mathrm{cl}}$ of the bacteria's helix with diameter A, length in axial direction L and helical pitch λ is given by

$$\boldsymbol{r}_{\mathrm{cl}}(u) = \begin{pmatrix} \frac{A}{2}\cos(2\pi\, u) \\ \frac{A}{2}\sin(2\pi\, u) \\ \lambda\, u \end{pmatrix} \tag{1}$$

where u is varied between 0 and $\frac{L}{\lambda}$ to describe the complete helix centerline. Any position $\boldsymbol{r}_{\mathrm{H}}$ on the bacteria's surface, other than the ends, can be described by

$$\boldsymbol{r}_{\mathrm{H}}(u,v) = \boldsymbol{r}_{\mathrm{cl}}(u) + d\, \boldsymbol{D}_{\hat{e}_{\mathrm{t}}}(v)\hat{e}_{\mathrm{n}} \tag{2}$$

since every position has the same distance d to the centerline (except the ends). The unit vector $\hat{e}_{\mathrm{n}}$ is the vector normal to the centerline and $\boldsymbol{D}_{\hat{e}_{\mathrm{t}}}(v)$ denotes the rotation matrix by an angle $v \in [0, 2\pi]$ about an axis in direction of the local unit tangent vector $\hat{e}_{\mathrm{t}}$ of the helix centerline. Through variations in the parameters v and u the bacteria's surface is parameterized. The both ends of the bacteria can be represented, in a similar manner, by fixing $u = 0$ or $u = \frac{L}{\lambda}$ and by varying d and v.

The diameter A is measured directly in the experiment. The quantities L and λ are determined by the experimentally measured arc length s

$$s = \int_0^{L/\lambda} du \left|\frac{\partial \boldsymbol{r}_{\mathrm{cl}}(u)}{\partial u}\right| = \sqrt{(\pi\, A)^2 + \lambda^2}\,(L/\lambda) \tag{3}$$

and the measured end-to-end distance $L_{\mathrm{ee}} = \left|\boldsymbol{r}_{\mathrm{cl}}\left(\frac{L}{\lambda}\right) - \boldsymbol{r}_{\mathrm{cl}}(0)\right|$.

The surface of the helix is divided and represented by N point-like beads with an identical effective radius a. They are located at positions $\boldsymbol{r}_k$ with $= 1, \ldots, N$. A force $\boldsymbol{F}_k$ is required to move the point-like particle at a position $\boldsymbol{r}_k$ through the fluid because the beads have a drag coefficient $\zeta = 6\pi\, \eta\, a$ in a solvent of viscosity η. The beads generate a flow field by moving through the fluid. The flow $\boldsymbol{u}_k(\boldsymbol{r})$ induced by the particle located at $\boldsymbol{r}_k$ at an arbitrary point in space $\boldsymbol{r}$ is given by

$$\boldsymbol{u}_k(\boldsymbol{r}) = \boldsymbol{O}(\boldsymbol{r} - \boldsymbol{r}_k)\boldsymbol{F}_k \tag{4}$$

with the Oseen tensor[1]

$$O_{ij}(\boldsymbol{r} - \boldsymbol{r}_k) = \frac{1}{8\pi\, \eta} G_{ij}(\boldsymbol{r} - \boldsymbol{r}_k)\,. \tag{5}$$

and the tensorial free space Greens function $G_{ij}\,(\boldsymbol{r}) = \frac{1}{r}\left(1 + \frac{r_i\, r_j}{r^2}\right)$. The parameters $i = 1,..3$ and $j = 1,..,3$ denote the entries of the matrices $\boldsymbol{O}$ and $\boldsymbol{G}$.

The flow field $\boldsymbol{u}_k(\boldsymbol{r})$, which is caused by particle k influences via the fluid, respectively via the Oseen tensor, the motion of all other particles at $\boldsymbol{r}_j$ with $j = 1,..,N$ and $j \neq k$. For a helix moving with the velocity $\boldsymbol{v}$, all N beads fixed on its surface move with the same speed $\dot{\mathbf{r}}_k = \boldsymbol{v}$ $(k = 1, \ldots, N)$. Every moving particle influences via the hydrodynamic interaction all other particles. Therefore, the forces $\boldsymbol{F}_1, \ldots, \boldsymbol{F}_N$ required to move the beads with a given velocity $\boldsymbol{v}$ are determined by the N coupled linear equations[1]

$$\boldsymbol{v} = \frac{\boldsymbol{F}_i}{\zeta} + \sum_{k=1,\neq i}^{N} \boldsymbol{O}(\boldsymbol{r}_i - \boldsymbol{r}_k)\, \boldsymbol{F}_k. \tag{6}$$

For one solution with the velocity $\boldsymbol{v}$ nearly parallel to the helical axis and with the total force acting on the helical bacterium, $\boldsymbol{F} = \sum_k \boldsymbol{F}_k$ is parallel to $\boldsymbol{v}$. The friction coefficient γ_{trans} describes the proportionality between both quantities:

$$\gamma_{\mathrm{trans}}\, \boldsymbol{v} = \boldsymbol{F}. \tag{7}$$

For a helix rotating with a frequency ω around the axis of $\boldsymbol{\omega}$ through its center $\boldsymbol{r}_{\mathbf{c}} = \frac{1}{N}\sum_k \boldsymbol{r}_k$, the velocity of each bead is given by

$$\dot{\boldsymbol{r}}_k = (\boldsymbol{r}_k - \boldsymbol{r}_{\mathrm{c}}) \times \boldsymbol{\omega}. \tag{8}$$

Eq. 6 can be used to determine the relation between the bead velocities and the required forces. The torque $\boldsymbol{M}$ acting on the helix can be expressed in terms of the forces: $\boldsymbol{M} = \sum_k (\boldsymbol{r}_k - \boldsymbol{r}_{\mathrm{c}}) \times \boldsymbol{F}_k$. For the case in which the rotational axis is nearly perpendicular to the helix axis, the two vectors $\boldsymbol{\omega}$ and $\boldsymbol{M}$ are related via the rotational friction: $\gamma_{\mathrm{rot}}\, \boldsymbol{\omega} = \boldsymbol{M}$.

Calculation of the viscous drag coefficients by Boundary Integral Method

The Boundary Integral Method (BIM) exploits the fact that the Stokes equation is linear and can therefore be rewritten as an integral equation[2] for the flow velocity $\boldsymbol{u}(\boldsymbol{r})$ at an arbitrary point $\boldsymbol{r}$ inside the infinite and initially quiescent fluid:

$$u_i(\boldsymbol{r}) = \frac{1}{4\pi\,\eta} \oint_S G_{ij}(\boldsymbol{r} - \boldsymbol{y})\, f_j(\boldsymbol{y})\, d\boldsymbol{y}, \tag{9}$$

where summation over the repeated index j is implied, $\boldsymbol{y}$ is a point on the surface S of the bacterium, η is the fluid viscosity and $\boldsymbol{f}$ is the surface traction.

When the observation point $\boldsymbol{r}$ is moved to the surface, Eq. 9 can be converted to a linear system of equations[2] which in our implementation is solved by GMRES[3,4]. The surface integral in Eq. 9 is computed by discretizing the bacterial surface using flat triangles to interpolate between the surface nodes. To allow a direct comparison, the nodes of the triangles are taken at the same positions as in the Stokesian dynamics calculations (see above).

To impose a rotation/translation on the bacterium, each node is coupled by a harmonic spring to an auxiliary anchor point. During the simulation, these imaginary anchor points are translated/rotated with a prescribed (angular) velocity. By distributing the force of these springs over the local area surrounding each node, the force is converted into a surface traction $\boldsymbol{f}$, which is a term in Eq. 9. The solution of the linear system resulting from Eq. 9 then yields the surface velocity $\boldsymbol{u}$ from which the desired drag coefficients γ_{rot} and γ_{trans} and can be directly obtained. The translational/rotational velocities have been chosen to be small enough that the relation between force and velocity remains linear.

References

1 Leal, L. G. *Advanced Transport Phenomena*. (Cambridge University Press, 2007).

2 Pozrikidis, C. *Boundary integral and singularity methods for linearized viscous flow*. (Cambridge University Press, 1992).

3 Saad, Y. & Schultz, M. H. GMRES: A generalized minimal residual algorithm for solving nonsymmetric linear systems. *SIAM J. Sci. Comput.* **7**, 856-869, doi:10.1137/0907058 (1986).

4 Daddi-Moussa-Ider, A., Guckenberger, A. & Gekle, S. Long-lived anomalous thermal diffusion induced by elastic cell membranes on nearby particles. *Phys. Rev. E* **93**, doi:10.1103/PhysRevE.93.012612 (2016).

Publication 6

Focusing and splitting of particle streams in microflows via viscosity gradients

M. Laumann and W. Zimmermann,
submitted to Eur. Phys. J. E on 2019-01-24 (with referees)
manuscript number e190030
preprint on arXiv (https://arxiv.org/abs/1903.11018)

EPJ manuscript No.
(will be inserted by the editor)

Focusing and splitting of particle streams in microflows via viscosity gradients

Matthias Laumann and Walter Zimmermann

Theoretische Physik I, Universität Bayreuth, 95440 Bayreuth, Germany; E-mail: walter.zimmermann@uni-bayreuth.de

Received: date / Revised version: date

Abstract Microflows are intensively used for investigating and controlling the dynamics of particles, including soft particles such as biological cells and capsules. A classic result is the tank-treading motion of elliptically deformed soft particles in linear shear flows, which do not migrate across straight stream lines in the bulk. However, soft particles migrate across straight streamlines in Poiseuille flows. In this work we describe a new mechanism of cross-streamline migration of soft particles. If the viscosity varies perpendicular to the stream lines then particles migrate across stream lines towards regions of a lower viscosity, even in linear shear flows. An interplay with the repulsive particle-boundary interaction causes then focusing of particles in linear shear flows with the attractor stream line closer to the wall in the low viscosity region. Viscosity variations perpendicular to the stream lines in Poiseuille flows leads either to a shift of the particle attractor or even to a splitting of particle attractors, which may give rise to interesting applications for particle separation. The location of attracting streamlines depend on the particle properties, like their size and elasticity. The cross-stream migration induced by viscosity variations is explained by analytical considerations, Stokesian dynamics simulations with a generalized Oseen tensor and Lattice-Boltzmann simulations.

1 Introduction

The success of the interdisciplinary field of microfluidics and its numerous applications in life science and applications are based also on a thorough understanding of the dynamics of particles and their distribution in microflows. [1,2,3,4,5,6] One of the important applications is particle sorting where besides structured channels also optical, electrical or magnetic fields are used.[3] Several sorting strategies rely merely on the interplay between basic hydrodynamics of microflows and particle properties, that cause, for instance, cross-streamline migration (CSM) of particles. CSM may depend on fluid inertia,[5] on particle deformability, [7,8,9,10,11,12,13,14,15,16,17] on channel modulations[18] or on non-Newtonian fluid effects.[19,20, 21,22,23,24] In non-Newtonian flows the action of elastic effects and spatially varying shear viscosity on particles come often simultaneously into play, but little is known about the action of a spatially dependent shear viscosity on the particle dynamics alone. We describe in this work a surprising viscosity-gradient driven CSM and the resulting focusing of soft-particles, which occurs even in linear shear flows as indicated in Fig. 1.

Segré and Silberberg found quite early that rigid particles can migrate across straight streamlines to off-center streamline positions in pipe flows [25]. This type of cross-streamline migration (CSM) is inertia driven in the range of intermediate Reynolds number ($\sim 1 < Re <\sim 100$) and it is extensively used for sorting of rigid particles (see e.g. Ref. [5]). In contrast, deformable particles like capsules or cells show CSM already on the scale of microchannels

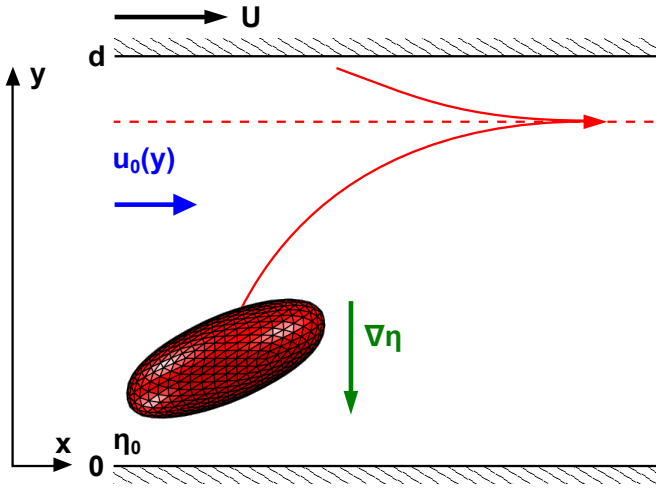

Figure 1. The two solid lines sketch two trajectories of a soft capsule (enlarged) in a shear flow $\mathbf{u}_0(y)$ driven by a moving upper boundary. The shear viscosity of the fluid increases from top to bottom (for instance induced by a temperature gradient) and the capsule migrates towards the region of low viscosity. Along the attractor (dashed line) the migration to a smaller viscosity is in balance with the particle repulsion by the upper boundary.

and in the limit of Stokes flows at very small values of the Reynolds number. The tank-treading motion of vesicles or capsules causes near walls the so-called lift force that drives them away from channel walls in Poiseuille and linear shear flows [7,8,9,10]. Further away from the walls in Poiseuille flows one still has a spatially varying shear rate, which breaks the fore-aft symmetry of deformed particles, so that dumbbells [26,27,28], droplets [11,12], vesicles and capsules [13,14,15,16] exhibit bulk CSM, even in unbounded Poiseuille flows where the interaction with the channel boundaries is neglected. Surprisingly, CSM of soft particles can be driven also by gravitational effects, whereby the migration direction depends on relative directions between the flow and the gravitational force [17]. Migration in Newtonian fluids was also found for non-symmetric soft particles in time-periodic linear shear flows [29] and even shaken liquids when particle inertia is considered [30].

Recent studies of particle CSM use besides Newtonian carrier fluids also visco-elastic fluids. They also break the fore-aft symmetry and may cause already CSM of rigid particles.[24] CSM in viscoelastic liquids is often faster than in Newtonian liquids, which makes non-Newtonian liquids attractive for applications such as in health care or biological and chemical analysis.[19,20,21,22,23,24] Particles in non-Newtonian liquids are sometimes also focused to positions aside of the channel center even in the limit of low Reynolds number flows (see e.g. Ref. [21]). Since in such non-Newtonian liquids shear thinning, leading to a *non-constant viscosity*, comes often simultaneously into play with a fluid elasticity, the specific contribution of a non-constant viscosity to particle CSM is not clear.

Here we study the effects of viscosity gradients on the flow profiles and on the particle dynamics, whereby viscosity gradients may be imposed in a controlled way, for instance, by applying a temperature gradient to fluids [31]. Our modeling approach is described Sec. 2, where also analytical expressions for certain flow profiles and a generalized Oseen tensor are given. In Sec. 3 and Sec. 4 we show by symmetry arguments and numerical simulations, how a viscosity varying perpendicular to the stream lines of a linear shear breaks symmetries and induces CSM of capsules already in simple shear flows, in contrast to liquids with constant viscosity. Two types of viscosity profiles are investigated for plane Poiseuille flows in Sec. 5, where we find also a new scenario for particle stream splitting with interesting applications for particle sorting.

2 Models and Methods

In Sec. 2.1 we consider a constant viscosity gradient perpendicular to the flow lines in linear shear flows and plane Poiseuille flow. We provide for both cases analytical expressions for the flow profile as solutions of the Stokes equation with non-constant viscosity. In Sec. 2.2 we present a generalized Oseen tensor, which takes the first correction of the viscosity gradient into account. It is used in the Stokesian dynamics simulations of the capsule and is derived without the hydrodynamic capsule-wall interactions. The wall effects are taken into account by the Lattice Boltzmann Method described in Sec. 2.3.

2.1 Stokes-flows

We consider fluids between two boundaries located at $y = 0, d$ and a spatially varying viscosity

$$\eta(\mathbf{r}) = \eta_0 + \mathbf{G}_\eta \cdot \mathbf{r} \tag{1}$$

with a constant gradient vector

$$\nabla\eta = \mathbf{G}_\eta \,. \tag{2}$$

We investigate low Reynolds number flows that are determined by the Stokes equation

$$-\nabla p + \nabla \cdot \left\{\eta[\nabla\mathbf{u} + (\nabla\mathbf{u})^{\mathbf{T}}]\right\} = 0 \,, \tag{3}$$

with the pressure p and two choices of boundary conditions at $y = 0, d$.

For a *classical shear cell* with one moving boundary the flow field fulfills the boundary conditions:

$$\mathbf{u}(y=0) = 0 \quad \text{and} \quad \mathbf{u}(y=d) = U\mathbf{e}_x \,. \quad \text{(BC I)} \tag{4}$$

For a pressure driven plane Poiseuille flow with a constant pressure gradient in x-direction, $\nabla p = p_0\mathbf{e}_x$, we use the boundary conditions

$$\mathbf{u}(y=0,d) = 0 \,. \quad \text{(BC II)} \tag{5}$$

If not stated otherwise, we consider further on a viscosity gradient in y-direction

$$\eta(\mathbf{r}) = \eta_0 + G_{\eta,y} y \tag{6}$$

which may be imposed, for instance, by a temperature gradient perpendicular to the two bounding plates. For the viscosity gradient, $G_{\eta,y} \neq 0$, and the solution of the Stokes equation (3) for the boundary conditions BC I gives a nonlinear y-dependence of the velocity in x-direction

$$\mathbf{u}_0(y) = U\frac{\ln[y\,G_{\eta,\mathrm{y}}/\eta_0 + 1]}{\ln[d\,G_{\eta,\mathrm{y}}/\eta_0 + 1]}\mathbf{e}_\mathrm{x} \,. \tag{7}$$

It reduces in the limit $G_{\eta,y} = 0$ to the well known linear shear profile

$$\mathbf{u}_0(y) = U\frac{y}{d}\mathbf{e}_\mathrm{x} \,. \tag{8}$$

For a pressure driven flow between two flat boundaries with the boundary conditions in Eq. (5) the y-dependence of the flow $\mathbf{u}_0(y)$ parallel to the x-axis is given by

$$\mathbf{u}_0(y) = U\frac{Cy - d\ln\left(\frac{G_{\eta,\mathrm{y}}y}{\eta_0}+1\right)}{d\left[1+\ln\left(\frac{C\eta_0}{d\,G_{\eta,\mathrm{y}}}\right)\right] - \frac{C\eta_0}{G_{\eta,\mathrm{y}}}}\mathbf{e}_\mathrm{x} \,,$$
$$\text{with} \quad C = \ln\left(\frac{d\,G_{\eta,\mathrm{y}}}{\eta_0}+1\right) \,. \tag{9}$$

This gives in the limit $G_{\eta,y} = 0$ the well known parabolic profile $\mathbf{u}_0(y) = 4Uyd(d-y)\mathbf{e}_x$.

2.2 Stokesian particle dynamics

The surface of the capsule is discretized with N beads at the positions $\mathbf{r}_i$ $(i = 1, \ldots, N)$. Their Stokesian dynamics is described by[32]

$$\dot{\mathbf{r}}_i = \mathbf{u}_0(\mathbf{r}_i) + \sum_{j=1}^{N} \mathbf{H}_{ij} \cdot \mathbf{F}_j \ . \tag{10}$$

The capsule center is given by $\mathbf{r}_\mathrm{c} = \sum_{i=1}^{N} \mathbf{r}_i/N$. The force on bead j is calculated via $\mathbf{F}_j = -\nabla_j V(\mathbf{r})$ with $V(\mathbf{r})$ denoting the total potential (given in the following) and $\mathbf{H}_{ij}$ means the mobility matrix. The mobility matrix is given by

$$\mathbf{H}_{ij} = \begin{cases} \frac{1}{6\pi\eta_i a}\mathbf{1} & \text{if } i = j\,, \\ \mathbf{O}(\mathbf{r}_i, \mathbf{r}_j) & \text{otherwise}\,. \end{cases} \tag{11}$$

with the Oseen tensor $\mathbf{O}$, the Greens function to the Stokes equation (3). For a spatially varying viscosity, i. e. $\mathbf{G}_\eta \neq 0$, we take the leading correction with respect to the small quantity $\frac{(\mathbf{r}_i - \mathbf{r}_j)\cdot\mathbf{G}_\eta}{\eta_j}$ into account

$$\mathbf{O}(\mathbf{r}_i, \mathbf{r}_j) = \frac{1}{8\pi\eta_j R_{i,j}} \left[\left(1 - \frac{\mathbf{R}_{i,j}\cdot\mathbf{G}_\eta}{2\eta_j}\right) \left(\mathbf{1} + \hat{\mathbf{R}}_{i,j}\hat{\mathbf{R}}_{i,j}\right) + \frac{1}{2\eta_j}\left(\mathbf{R}_{i,j}\mathbf{G}_\eta - \mathbf{G}_\eta\mathbf{R}_{i,j}\right)\right] . \tag{12}$$

Herein we use $\eta_j = \eta(\mathbf{r}_j)$, $\mathbf{R}_{i,j} = \mathbf{r}_i - \mathbf{r}_j$, $r_{i,j} = |\mathbf{R}_{i,j}|$ and $\hat{\mathbf{R}}_{i,j} = \frac{\mathbf{R}_{\mathbf{i,j}}}{r_{i,j}}$. A small value of $\frac{(\mathbf{r}_i - \mathbf{r}_j)\cdot\mathbf{G}_\eta}{\eta_j}$ means that the spatial deviation of the viscosity on the size of the capsule is small compared to the local viscosity at the position of the capsule. It can be estimated by the dimensionless number

$$\widetilde{\mathbf{G}}_\eta = \frac{\mathbf{G}_\eta 2R_\mathrm{c}}{\eta_\mathrm{c}} \tag{13}$$

with the viscosity at the center of the capsule $\eta_\mathrm{c} = \eta(\mathbf{r}_\mathrm{c})$ and the capsule's radius R_c. In this form of the Oseen tensor the interaction with the walls is neglected. The derivation of the expression in Eq. (12) is given in SI.

To calculate the forces and the velocity of the capsule on its surface, which is spherical in its equilibrium shape, it must be discretized (see Fig. 1). We begin with a regular icosahedron, which has 12 nodes, and refine the surface iteratively [33]: We add new nodes at the middle of each edge and shift them to the surface of the sphere, until we obtain a good resolution. With this discretization we can calculate the forces at the surface whereby we use an elastic force, a bending force and a penalty force that ensures volume conservation. The elastic force is modeled by the neo-Hookean law that describes a thin plate with a constant surface shear elastic modulus G_s with a potential V_{NH} (for details see Refs. [34,35]). The bending force follows from the potential V_b [36] with $V_b = \frac{\kappa}{2}\sum_{i,j}(1 - \cos\beta_{i,j})$ whereby κ describes the bending stiffness and $\beta_{i,j}$ denotes the angles of the normal vectors between two neighboring triangles. Furthermore we use a penalty force that ensures that the volume is approximately conserved during the simulations [37]. Its potential is given by $V_v = \frac{k_v}{\mathcal{V}_0}(\mathcal{V}(t) - \mathcal{V}_0)^2$ with the instantaneous volume $\mathcal{V}(t)$, the reference volume $\mathcal{V}_0$ and the rigidity k_v. It is useful to measure the capsule's stiffness with a dimensionless number, the capillary number

$$\mathrm{Ca} = \frac{\eta_0 R_\mathrm{c}}{G_s}\dot{\gamma} \tag{14}$$

with (mean) shear rate

$$\dot{\gamma} = \frac{U}{d}\,. \tag{15}$$

If not stated otherwise we use the following parameters for the Stokesian dynamics. Parameters of the flow: d=50, U=0.5, η_0=3, $\mathbf{G}_\eta = 0.03\,\hat{\mathbf{e}}_\mathrm{y}$. Parameters of the capsule: initial position x_0=0, y_0=d/2, z_0=0, forces: k_v=3.0, κ = 0.2, $G_s = 0.2$ (linear shear flow) and $G_s = 0.4$ (Poiseuille flow), mean bead distance $b = 1.0$, Radius $R_\mathrm{c} = 6.6$, bead radius $a = 0.2$, time step $\Delta t = 0.05$. This leads to Ca ≈ 1, $|\widetilde{\mathbf{G}}_\eta| = 0.18$ at the initial position.

A conversion of the parameters to SI units is obtained by multiplying them with:

$$u_\mathrm{m} = 37.88\,\mu\mathrm{m},\ \ u_\mathrm{s} = 1.89\,\mathrm{ms},\ \ u_\mathrm{kg} = 2.39\cdot 10^{-11}\,\mathrm{kg}\,. \tag{16}$$

The radius of the capsule is $R_\mathrm{c} \approx 250\,\mu$m, and the plate distance is $d \approx 2\,$mm. The viscosity of the fluid at the boundaries (if $\mathbf{G}_\eta \parallel -\hat{\mathbf{e}}_\mathrm{y}$) corresponds to water at $20°C$ with $\eta(y = 0) = 1\,$mPas and $60°C$ with $\eta(y = d) = 0.5\,$mPas [38,39]. This is a temperature gradient comparable to one discussed in Ref. [31]. The maximal velocity is $U = 1\,\mathrm{cm}\ /\ \mathrm{s}$.

2.3 The lattice-Boltzmann method

To investigate the particle dynamics without the constraint of a small viscosity gradient as for the Stokesian dynamics and in order to take also the effects of the boundaries on particle dynamics into account we use the lattice-Boltzmann method (LBM).

We use a LBM with 19 discrete velocity directions (D3Q19), cf. fig. 2 [40], with the Bhatnagar-Gross-Krook (BGK) collision operator [41,42]. The equation of the probability distribution $f_i(\boldsymbol{r}, t)$ in velocity-direction i at position $\boldsymbol{r}$ is then given by

$$f_i(\boldsymbol{r} + c_i\Delta t, t + \Delta t) = f_i(\boldsymbol{r}, t) - \frac{\Delta t}{\tau}\left(f_i(\boldsymbol{r}, t) - f_i^\mathrm{e}(\boldsymbol{r}, t)\right) + \Delta t F_i\,, \tag{17}$$

whereby τ is a typical relaxation time related to the viscosity of the fluid and F_i contains the external forces[43]. $f_i^\mathrm{e}(\boldsymbol{r}, t)$ is the equilibrium distribution:

$$f_i^\mathrm{e}(\boldsymbol{r}, t) \approx \rho w_i \left[1 + \frac{(\boldsymbol{c}_i\cdot\boldsymbol{u})}{c_\mathrm{s}^2} + \frac{(\boldsymbol{c}_i\cdot\boldsymbol{u})^2}{2c_\mathrm{s}^4} - \frac{u^2}{2c_\mathrm{s}^2}\right] + \mathscr{O}(u^3) \tag{18}$$

with the unit vectors c_i along the discrete directions for the i-th velocity. Furthermore we use the equilibrium fluid density ρ_0, the speed of sound in the LBM-system, $c_\mathrm{s} = \frac{1}{\sqrt{3}}$, and the weighting factors w_i [42].

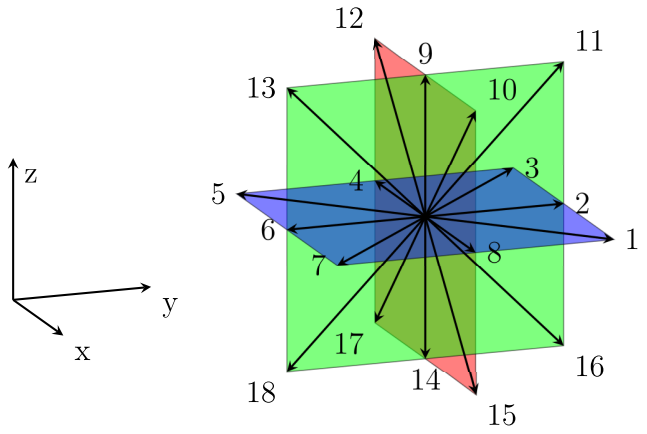

Figure 2. Sketch of the discretized velocity directions of the D3Q19 model for lattice-Boltzmann simulations.

The probability distribution function allows to calculate the density and the velocity of the fluids via

$$\rho(\boldsymbol{r},t) = \sum_i f_i(\boldsymbol{r},t)\,, \tag{19}$$

$$\rho(\boldsymbol{r},t)\boldsymbol{u}(\boldsymbol{r},t) = \sum_i \boldsymbol{c}_i f_i(\boldsymbol{r},t) + \frac{1}{2}\Delta t \boldsymbol{F}(\boldsymbol{r})\,, \tag{20}$$

whereby $\boldsymbol{F}(\boldsymbol{r})$ is the external force density[43]. The viscosity of the fluids is given by

$$\nu(\boldsymbol{r}) = c_\mathrm{s}^2\left(\tau(\boldsymbol{r}) - \frac{1}{2}\right)\Delta t\,. \tag{21}$$

We use a spatial dependent $\tau(\boldsymbol{r})$ to simulate the viscosity gradient given by Eq. (6).

The external forces are coupled to the flow via the immersed boundary method [44]. Thereby one has to consider that the nodes on the membrane of the capsule do not lie on the discrete grid points of the fluid. The force acting on a node of the capsule's surface is distributed to neighbouring fluid nodes with the function $\phi(\Delta\boldsymbol{r}) = \tilde{\phi}(\Delta x)\tilde{\phi}(\Delta y)\tilde{\phi}(\Delta z)$ and

$$\tilde{\phi}(R) = \begin{cases} \frac{1}{4}\left(1+\cos(\frac{\pi R}{2})\right) & \text{if } |R| \le 2 \\ 0 & \text{else} \end{cases}\,. \tag{22}$$

It is also utilized to calculate the velocity at the nodes of the capsule's surface with the velocity of the neighboring fluid nodes. We use periodic boundary conditions in x and z-direction and a standard bounce back scheme at the walls to drive the flow [42].

We use the following parameters for the linear shear flow: Parameters of the flow: density ρ_0=1.0, viscosity $\eta_0 = 1/6$ at $x = 0$, $y = 0$, $z = 0$, viscosity gradient $\mathbf{G}_\eta = 0.002\,\hat{\mathbf{e}}_\mathrm{y}$, velocity of the upper boundary or maximum velocity U=0.005, number of nodes in x-direction N_x=400, number of nodes in z-direction N_z=100, wall distance is $d = 100$. Parameters of the capsule: initial position x_0=0, y_0=51.5 and z_0=49.5, coefficient of the volume preserving force k_v=0.01, bending potential $\kappa = 10^{-4}$, neo-Hookean coefficient $G_\mathrm{s} = 10^{-4}$ node distance $b = 1.0$, which leads to a radius $R = 6.6$, number of nodes $N = 642$ or $R = 13.2$ with $N = 2562$. The time step is $\Delta t = 1.0$. For comparison between LBM and Stokesian dynamics simulations besides the same parameters a bead radius a=0.2 is used.

We use the following parameters for the Poiseuille flow. Parameters of the flow: density ρ_0=1.0, viscosity $\eta_0 = 1/6$ at $x = 0, y = 0, z = 0$, viscosity gradient $|\mathbf{G}_\eta| = 0.009$, velocity of the upper boundary or maximum velocity U=0.15, number of nodes in x-direction N_x=400, number of nodes in z-direction N_z=100, wall distance is $d = 300$. Parameters of the capsule: coefficient of the volume preserving force k_v=0.01, node distance $b = 1.0$ which leads to a Radius $R = 3.3$, number of nodes $N = 162$ or $R = 13.2$ with $N = 2562$, time step $\Delta t = 1.0$, bending potential $\kappa = 0.17$ (large R), bending potential $\kappa = 0.02$ (small R), neo-Hookean coefficient $G_\mathrm{s} = 10^{-3}$ (large R), neo-Hookean coefficient $G_\mathrm{s} = 5 \times 10^{-4}$ (small R).

3 Explanation of $\nabla\eta$-induced CSM

We develop at first a qualitative explanation of the CSM induced by a viscosity gradient perpendicular to stream lines. A viscosity gradient modifies the flow profiles as indicated in Eq. (7) and Eq. (9), i.e. the shear rate across the particle is not constant but is slightly varying. This variation of the shear rate is neglected for the qualitative explanation here. We show that the CSM is directly caused by the $\nabla\eta$-induced modifications of the friction forces acting on the particle's surface and not indirectly by the varying shear rate (this is also confirmed by simulations, cf. SI).

We consider at first a spherical capsule. Without a viscosity gradient, the capsule rotates due to the linear shear flow (see Eq. (8) and Fig. 3 (a)) and its center $\mathbf{r}_\mathrm{c}$ follows a flow line. [32,16,13] The velocity at the capsule's surface in the comoving frame is given by $\tilde{\mathbf{u}}_\mathrm{s}(\tilde{\mathbf{r}}) = \boldsymbol{\omega} \times \tilde{\mathbf{r}}$ with $\tilde{\mathbf{r}} = \mathbf{r} - \mathbf{r}_\mathrm{c}$, $\boldsymbol{\omega} = \frac{1}{2}\nabla \times \mathbf{u}_0$ and the shear flow in the comoving frame $\tilde{\mathbf{u}}_0(\tilde{y}) = U\tilde{y}/d\mathbf{e}_\mathrm{x}$. The friction forces $\mathbf{F}(\tilde{\mathbf{r}})$ between the capsule and the fluid can be calculated by solving Eq. (10) for the forces $\mathbf{F}_j = \mathbf{F}(\tilde{\mathbf{r}}_j)$. In the following we show how this friction force is affected if this rotation is performed in the presence of a viscosity gradient.

A spherical capsule in a linear shear flow without viscosity gradient has symmetries: The spherical capsule is invariant under a reflection at the $\tilde{x}\tilde{z}$- or $\tilde{y}\tilde{z}$-plane. Also the flow's magnitude is equal after these reflections, but the flow changes its sign, cf. Fig. 3 (a). Therefore the velocity and the friction at the surface of the capsule have the same symmetries: At the mirrored position $\tilde{\mathbf{r}}'$ of $\tilde{\mathbf{r}}$ at the $\tilde{x}\tilde{z}$-plane we get $F_\mathrm{x}(\tilde{\mathbf{r}}') = -F_\mathrm{x}(\tilde{\mathbf{r}})$ and $F_\mathrm{y}(\tilde{\mathbf{r}}') = F_\mathrm{y}(\tilde{\mathbf{r}})$ (analogously at the $\tilde{y}\tilde{z}$-plane). The direction of the friction forces from the fluid on the capsule is indicated in Fig. 3

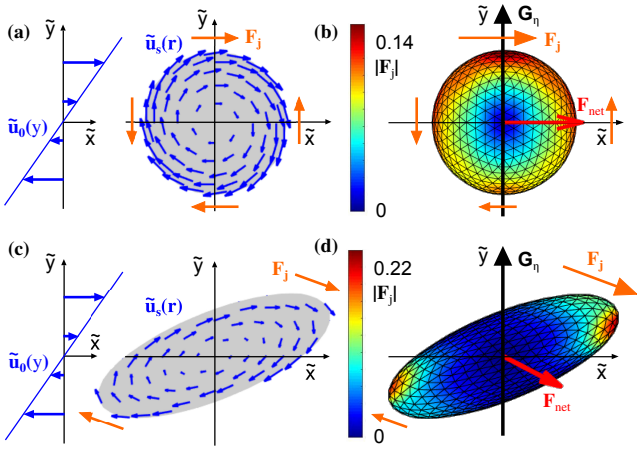

Figure 3. A rigid capsule is rotating due to the shear flow $\tilde{\mathbf{u}}_0(y)$ with velocity $\tilde{\mathbf{u}}_\mathrm{s}(\mathbf{r})$ at its surface (comoving frame, without gradient) (a). This leads to friction forces $\mathbf{F}(\tilde{\mathbf{r}})$ (orange arrows), but the sum of these forces is zero because of the symmetry to the $\tilde{x}\tilde{z}$- and $\tilde{y}\tilde{z}$-plane. This motion in presence of a viscosity gradient $\mathbf{G}_\eta \parallel \hat{\mathbf{e}}_\mathrm{y}$ (black) leads to higher friction forces on one half than on the other (orange arrows and color of surface) (b). This asymmetry causes a net force $\mathbf{F}_\mathrm{net}$ (red) which is oriented in flow direction, i.e. it causes no CSM. A soft capsule is deformed and performs a tank-treading motion (c) in a linear shear flow (shown without a gradient). Due to its ellipsoidal shape it is not symmetric to the $\tilde{x}\tilde{z}$- and $\tilde{y}\tilde{z}$-plane, but has a point symmetry that prevents a net force. A gradient (d) breaks the point symmetry and leads to a net force with a component perpendicular to the flow. This results in a CSM towards regions with a lower viscosity.

(a). As example at the point of the capsule with the highest y-value the friction force points in positive x-direction and at the point with the lowest y-value the force points in negative x-direction and has the same magnitude. This symmetry determines the net force via

$$\begin{aligned} F_\mathrm{net,x} &= \oint F_\mathrm{x} dA = \int_{y>y_\mathrm{c}} F_\mathrm{x} dA + \int_{y<y_\mathrm{c}} F_\mathrm{x} dA \\ &= \int_{y>y_\mathrm{c}} F_\mathrm{x} dA - \int_{y>y_\mathrm{c}} F_\mathrm{x} dA = 0\,, \end{aligned} \tag{23}$$

$$\begin{aligned} F_\mathrm{net,y} &= \oint F_\mathrm{y} dA = \int_{x>x_\mathrm{c}} F_\mathrm{y} dA + \int_{x<x_\mathrm{c}} F_\mathrm{y} dA \\ &= \int_{x>x_\mathrm{c}} F_\mathrm{y} dA - \int_{x>x_\mathrm{c}} F_\mathrm{y} dA = 0\,, \end{aligned} \tag{24}$$

whereby $\int_{y>y_\mathrm{c}} dA$ denotes an integration over the half sphere on the side of the xz-plane with $y > y_\mathrm{c}$. The symmetries show that the force on one half of the sphere has the opposite direction of the force on the other half. Thus the net forces is zero for a constant viscosity. Furthermore the system is symmetric to the $\tilde{x}\tilde{y}$-plane which prevents a force in z-direction:

$$F_\mathrm{net,z} = 0\,. \tag{25}$$

We discuss now the effect of a viscosity gradient oriented perpendicular to the flow direction and in the shear plane, i. e. $\mathbf{G}_\eta \parallel \hat{\mathbf{e}}_\mathrm{y}$ as shown in Fig. 3 (b). With the viscosity gradient the friction at the upper half of a rigid spherical capsule ($y > y_\mathrm{c}$), which is directed in positive x-direction, is higher due to the higher viscosity than at the lower half ($y < y_\mathrm{c}$), which is directed in negative x-direction. Because the magnitude of the friction is not equal at both halves the symmetry used to derive Eq. (23) is broken. Thus a net force is caused by the rotation in presence of the viscosity gradient, even in a linear shear flow.

But the magnitude of the friction still has a symmetry to the $\tilde{y}\tilde{z}$-plane. This can be seen with Fig. 3 (b) by comparing the left part of the capsule ($x < x_\mathrm{c}$) and the right part ($x > x_\mathrm{c}$). Both halves are symmetric because the viscosity increases in y-direction and not in x-direction. Thus the symmetry used in Eq. (23) is broken, but eqs. (24) and (25) are still valid. Therefore, the net force is oriented in x-direction, i.e. $\mathbf{F}_\mathrm{net}$ is parallel to the flow. Thus a rigid sphere shows migration along the flow direction but no CSM. The effects of further possible directions of the viscosity gradient on rigid particles are discussed in SI.

The behavior of a deformable capsule is different. Its tank-treading motion and shape obtained by simulations in a linear shear flow without a viscosity gradient is shown by Fig. 3 (c). The capsule adopts an ellipsoidal shape with its major axis inclined with respect to the flow direction. The capsule's center follows the flow direction. The friction forces are calculated in the same way as for a rigid capsule. The main difference to the rigid capsule is the ellipsoidal shape, which has no mirror symmetries with respect to the $\tilde{x}\tilde{z}$- and $\tilde{y}\tilde{z}$-plane. But the deformed shape and the shear flow have both a point symmetry to the capsules center (see Fig. 3 (c)) and a symmetry to the $\tilde{x}\tilde{y}$-plane. The friction force has the same symmetry. As example the friction force at two points is shown in Fig. 3 (c). At the points with the highest y-value the friction force from the flow on the ellipsoidal, tank-trading particle points in positive x- and negative y-direction. At the mirrored points with the lowest y-value the force points in negative x- and positive y-direction. Thus eqs. (23), (24) and (25) can also be used in case of a deformable capsule, which means $\mathbf{F}_\mathrm{net} = 0$ for a constant viscosity.

We discuss now the effect of a viscosity gradient perpendicular to the flow direction and in the shear plane $\mathbf{G}_\eta \parallel \hat{\mathbf{e}}_\mathrm{y}$ (other orientations: see SI). The symmetry with respect to the center is broken and eqs. (23) and (24) are not valid in this case. This is shown in Fig. 3 (d): The force at the point with the highest y-value at the high viscosity, which points in positive x- and negative y-direction, has a higher magnitude than the mirrored force. This leads to a non-zero net force $\mathbf{F}_\mathrm{net}$ which is oriented in positive x- and negative y-direction. The system still has a symmetry to the $\tilde{x}\tilde{y}$-plane, so that Eq. (25) is still valid and the net force has no z-component. The negative y-component of the net force leads to a CSM towards the lower viscosity. Note that this is different to the rigid capsule, whose symmetry to the $\tilde{y}\tilde{z}$-plane prevents a force in y-direction. Thus a CSM due to a viscosity gradient is found only if the capsule is soft.

4 CSM in a shear flow

Here we confirm by simulations the qualitative reasoning described in the previous section, that a finite viscosity gradient, $\nabla\eta$, causes a CSM of deformable particles already in simple shear flows. We use a generalized Oseen tensor given by Eq. (12), which takes the leading order effects of $\nabla\eta$ into account, and determine in Stokesian-dynamics simulations the capsule's CSM velocity as function of parameters. By LBM simulations of a capsule we evaluate the validity range of these approximate results and we show that capsules in shear flows with $\nabla\eta \neq 0$ are focused to an attractor streamline.

4.1 Numerical results on $\nabla\eta$-induced bulk migration

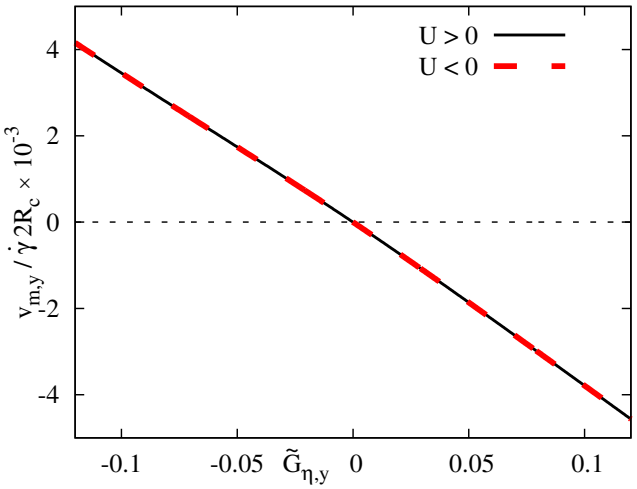

Figure 4. The migration velocity $v_{m,y}$ in units of $2\dot{\gamma}R_c$ as function of the dimensionless viscosity gradient $\tilde{G}_{\eta,y}$. The CSM is directed towards the lower viscosity as sketched in Fig. 3 and it is independent of the sign of U, i. e. independent of the flow direction.

In Stokesian dynamics simulations we use the nonlinear shear flow profile given by Eq. (7) and the generalized Oseen tensor given in Eq. (12). We simulate trajectories $y_c(t)$ of the capsule and determine by linear fits to the slope of capsule trajectories $y_c(t)$ the cross-stream migration velocity $v_{m,y}$. The resulting $v_{m,y}$ of capsules is shown in Fig. 4 as function of the dimensionless viscosity gradient $\widetilde{\mathrm{G}}_{\eta,\mathrm{y}}$. The CSM velocity in Fig. 4 decreases nearly linearly with $|\widetilde{\mathrm{G}}_{\eta,\mathrm{y}}|$ and is oriented as explained in the previous section, cf. Fig. 3. In addition, the migration is directed towards the lower viscosity and does not depend on the flow's direction, i.e. it is independent on the sign of U. The nonlinear y-dependence of the flow velocity in Eq. (7) and therefore the spatially varying velocity gradient causes in Fig. 4 only a slight deviation of v_{m_y} from a linear dependence on $\widetilde{\mathbf{G}}_\eta$ at small values of $|\widetilde{\mathrm{G}}_{\eta,\mathrm{y}}|$ (a more detailed comparison of the CSM in both flow profiles is given in the SI). This justifies the assumption of a constant velocity gradient across the capsule used in the previous section 3.

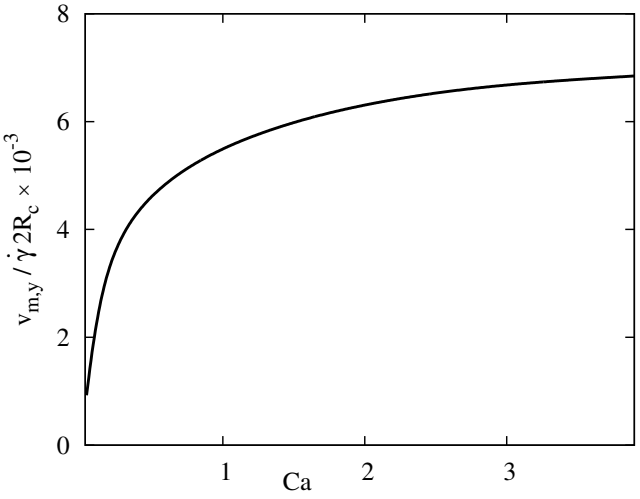

Figure 5. The migration velocity $v_{m,y}$ is given in units of $2\dot{\gamma}R_c$ and as function of the capillary number Ca given by Eq. (14). The migration vanishes at a high capsule-stiffness $\mathrm{Ca} \ll 1$ and increases with Ca.

Fig. 5 shows the dependence of the migration velocity on the stiffness of the capsule: The CSM decreases with increasing stiffness and vanishes at small values of the capillary number $\mathrm{Ca} \ll 1$ given in Eq. (14). This underlines the importance of the deformability of particles for their cross streamline migration (see also Fig. 3).

The generalized Oseen tensor in Eq. (12) takes into account the first order correction with respect to the viscosity gradient, i.e. it is valid for small values of $|\widetilde{\mathbf{G}}_\eta|$. To estimate the validity range of this approximation we compare the CSM velocity $v_{m,y}$ as obtained by Stokesian dynamics simulations using the generalized Oseen tensor in Eq. (12) with that obtained by Lattice-Boltzmann simulations of capsules. In order to keep in LBM simulations the interaction of the capsule with the boundary small, we positioned it in the middle of the flow cell between the two boundaries. In addition we have chosen a small ratio between the capsule's diameter and the wall distance $\frac{2R_c}{d} \approx 0.13$. Furthermore a sufficiently small Reynolds number $\mathrm{Re}=\frac{\rho U R_c}{\eta_0} \approx 0.2$ was chosen in LBM simulations to match the low Reynolds number regime of the Stokesian dynamics simulations. The flow is simulated for the boundary condition given by Eq. (4) and the viscosity gradient points into the direction perpendicular to the boundaries.

The migration velocities resulting from both simulations are shown in Fig. 6. The simulation results for the capsule with the generalized Oseen tensor and those obtained via the LBM agree well in the range of small values of $|\widetilde{\mathbf{G}}_\eta|$ and the deviation increases with $|\widetilde{\mathbf{G}}_\eta|$. For example at $|\widetilde{\mathbf{G}}_\eta| \lessapprox 0.15$ the relative error is below 10% and at $|\widetilde{\mathbf{G}}_\eta| \lessapprox 0.18$ the error is below 20%.

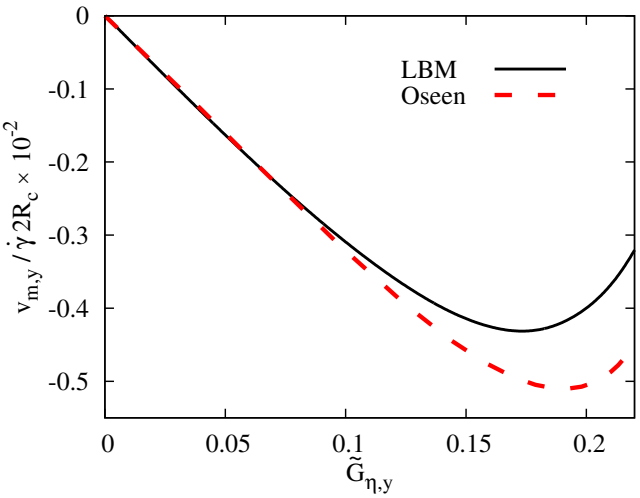

Figure 6. The CSM velocity $v_{m,y}$ is determined by Stokesian dynamics simulations (dashed) and by Lattice-Boltzmann simulations (solid). The expansion up to leading order of the viscosity gradient $\tilde{G}_\eta$, as used in Stokesian dynamics simulations, leads for $v_{m,y}$ to an error less than 10% if $|\tilde{\mathbf{G}}_\eta| \lessapprox 0.15$ compared to the LBM.

4.2 Particle focusing to an attractor streamline

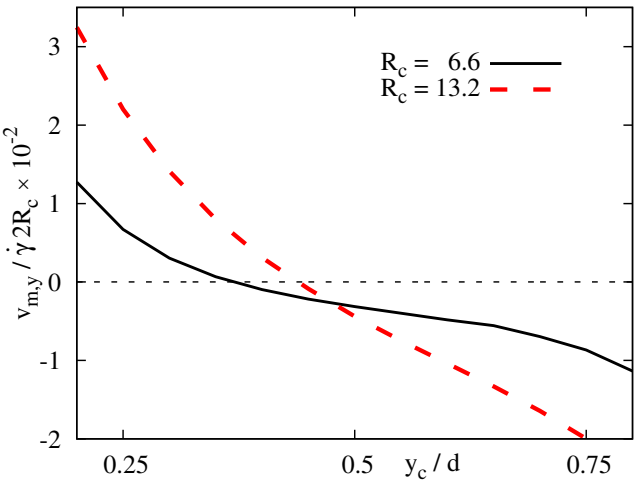

Figure 7. The migration velocity of a soft capsule in a flow with viscosity gradient and the boundary conditions in Eq. (4) is determined by the LBM as function of the initial position y_c for two different particle radii R_c. Far away from the walls the particle migrates due to the viscosity gradient towards the lower viscosity, i.e. towards the plate at $y = 0$. Close to the walls the repulsive wall interaction dominates, which leads to a migration away from the walls. Hence there is a stable position, i.e. an attractor off center, that depends on the particle's size. It is located at $y \approx 0.37d$ with $2R_c/d = 0.13$ and at $y \approx 0.41d$ with $2R_c/d = 0.26$.

The LBM includes the hydrodynamic interaction of the capsule with the walls, which causes a so-called lift force that repels the capsule from walls and that depends on the capsule-wall distance [7,8,9]. The interplay with the lift force causes a y-dependent migration velocity as shown for two capsules with two different radii in Fig. 7. The dimensionless gradient ranges in this case from $G_y = 0.16$ (at $y = 0$) to $\tilde{G}_y = 0.07$ ($y = d$) with $R_c = 6.6$ and with $R_c = 13.6$ from $\tilde{G}_y = 0.14$ to $\tilde{G}_y = 0.32$. The CSM caused by $\nabla\eta$ and the wall repulsion balance each other in the range of the lower viscosity and at this value of y the migration velocity $v_{m,y}$ vanishes. The location of this attractor position depends on the capsule size. We find the attractor at $y \approx 0.37d$ for $2R_c/d = 0.13$ and $y \approx 0.41d$ for $2R_c/d = 0.26$.

5 Simulation of CSM in Poiseuille flow

Capsules and red blood cells migrate in a Poiseuille flow, driven by the spatial varying shear gradient across a soft particle, usually to the center of the flow channel. [13,14, 15,16] If one has a viscosity gradient perpendicular to the boundaries across a plane Poiseuille flow, the $\nabla\eta$ induced migration has in the whole cell the same direction i. e. the $\nabla\eta$ induced migration either supports or acts against the common center directed migration. This interplay is investigated by Stokesian dynamics simulation in unbounded (bulk) Poiseuille flows and by LBM simulations, where boundary effects are included.

If a constant $\nabla\eta$ is used, e.g. induced by a temperature gradient across the flow, then the maximal velocity of a Poiseuille flow is shifted towards the lower viscosity. We study here the migration in such a flow profile. However, also with shear thinning fluids a viscosity gradient can be generated. It is well known from shear thinning fluids, that the viscosity has its maximum in the center of a Poiseuille flow and decreases towards the walls. Particle migration is recently studied also in Non-Newtonian fluids, whereby in these works besides shear-thinning effects also elastic effects are considered to be important. In order to contribute to the understanding of CSM of soft particles in shear thinning fluids, we mimic also shear thinning fluids by studying the effects of a viscosity on the migration behavior of a capsule, where the viscosity has its maximum in the channel center and decays linearly to the boundaries.

5.1 Migration in *unbounded* Poiseuille flow induced by $\nabla\eta = const.$

Here we consider as in the previous section a capsule in a fluid with constant viscosity gradient along the y-axis (e.g. generated by a temperature gradient) given by Eq. (6) but now with a Poiseuille flow profile given by Eq. (9). We simulate the capsule's Stokesian dynamics by using the generalized Oseen tensor given in Eq. (12). With the flow profile in Eq. (9) the simulations focus on the behavior of the capsule in the bulk of a Poiseuille flow, where the hydrodynamic interactions between the capsule and the wall are negligible. This allows a direct comparison between the well known bulk CSM in Poiseuille flow (see e.g. Refs. [14,16]) and the $\nabla\eta$ induced CSM.

Figure 8 shows the migration velocity of the capsule as function of its y position with and without a viscosity gradient. For $\widetilde{G}_{\eta,y} = 0$ the capsule migrates to the center and the related CSM velocity $v_{m,y}$ is indicated by the dashed line.

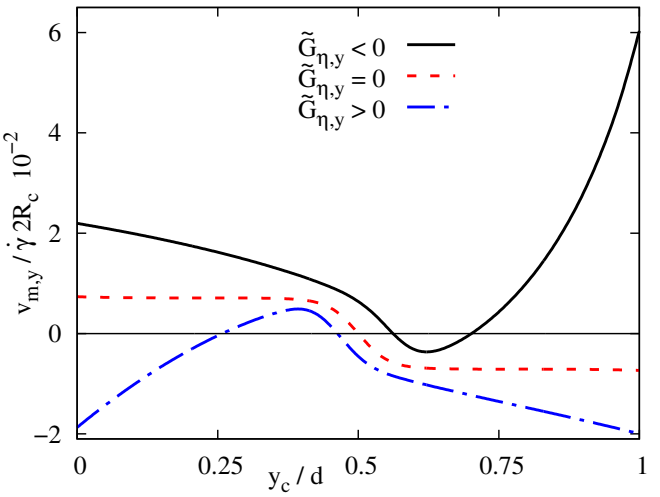

Figure 8. The migration velocity $v_{m,y}/(2\dot{\gamma}R_c)$ of a capsule in the distorted Poiseuille flow profile given by Eq. (9) is shown. It is obtained by Stokesian dynamics simulation as function of the capsule position y/d. The CSM is calculated for two viscosity gradients, one pointing to negative and the other into the positive y-direction as well as with a vanishing viscosity gradient. Without a gradient the capsule migrates towards the center as expected (see e.g. Refs. [14,16]). In the case of a viscosity gradient the capsule migrates again towards the lower viscosity, besides a small region close to the center, where the shear rate of the flow profile in Eq. (9) vanishes.

With a gradient in negative y-direction, i.e. $\widetilde{G}_{\eta,y} < 0$, the viscosity ranges from $\eta(y=0) = 3$ to $\eta(y=d) = 1.5$. The CSM velocity for this case is given by the solid line in Fig. 8. The $\nabla\eta$ effect enhances in a range of smaller y the CSM velocity to the center, i.e. in positive y-direction. Near the channel center at $y = 0.54d$ the flow has its maximal velocity and the shear rate of the flow field given by Eq. (9) vanishes. At this position the $\nabla\eta$ induced migration vanishes too and the migration directed to the channel center dominates. Thus capsules with an initial position $y_0 \lessapprox 0.7\,d$ migrate until they reach the attractor near the center. At initial positions $y_0 \gtrapprox 0.7\,d$ the $\nabla\eta$ induced outward migration dominates and the capsules migrate away from the center. This outward migration is near $y = d$ approximately up to 8 times faster than the center oriented one.

With a gradient in positive y-direction the viscosity ranges from $\eta(y=0) = 3$ to $\eta(y=d) = 4.5$. The situation is similar and the migration is also directed to the region of the lower viscosity, which is now located at the plate at $y = 0$. Therefore we get $v_{m,y} < 0$ again besides the region close to the center. Capsules with an initial position $y_0 \gtrapprox 0.25\,d$ migrate to the attractor close to the center at $y = 0.44\,d$ and capsules with $y_0 \lessapprox 0.25\,d$ migrate to the wall at $y = 0$.

5.2 Migration in *bounded* Poiseuille flow induced by $\nabla\eta = const.$

Here we describe results of LBM simulations of a capsule for $\nabla\eta = const.$ and the flow field boundary conditions given in Eq. (5). Figure 9 (a) shows the spatial dependence of the flow velocity and the linear increase of the viscosity. This demonstrates that the maximum flow velocity in Poiseuille flow is shifted towards the lower viscosity.

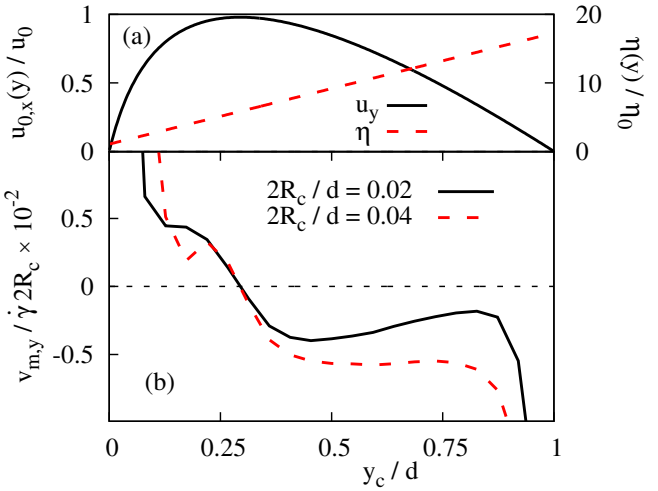

Figure 9. (a) The spatial dependence of the flow velocity $u_{0,x}(y)$ (solid line) and the viscosity for a linear increase of the viscosity between both boundaries (dashed line). The maximal velocity is shifted towards the region with the lower viscosity. (b) The spatial dependence of the migration velocity with wall interaction for two different capsule radii R_c. The attractor with vanishing $v_{m,y}$ is shifted towards the lower viscosity due to the shift of the maximal flow velocity.

The Fig. 9 (b) shows the migration velocity $v_{m,y}$ as function of y_c/d. In contrast to the case without wall interaction (cf. Fig. 8) only the attractor at the maximal flow velocity and no repeller is found. The reason is that wall induced repelling lift force is stronger than the $\nabla\eta$ induced migration to large values of y, even at higher values of $\tilde{G}_y$. The shift of the attractor with $v_{m,y} = 0$ to smaller values of y than the channel center has its origin in the shift of the maximal flow velocity to smaller values of y. Hence, in the presence of walls the capsule migrates always to one attractor that is shifted away from the flow center by the constant viscosity gradient. However, the migration velocity is larger in the presence of the viscosity gradient.

5.3 Particle attractor splitting induced by $\nabla\eta \neq const.$

Here we study the capsules dynamics by LBM simulations in a viscosity profile that is maximal at the channel center and decreases linearly towards the walls, as indicated by the dashed line in Fig. 10 (a). A decay of the shear viscosity in Poiseuille flow is known for shear thinning fluids and the viscosity profile in Fig. 10 (a) is a very simple mimicry

of the shear viscosity of shear thinning fluids. For this viscosity profile one obtains in simulations a Poiseuille flow profile, cf. solid line in Fig. 10 (a), which is flattened near the channel center similar as for shear thinning fluids.

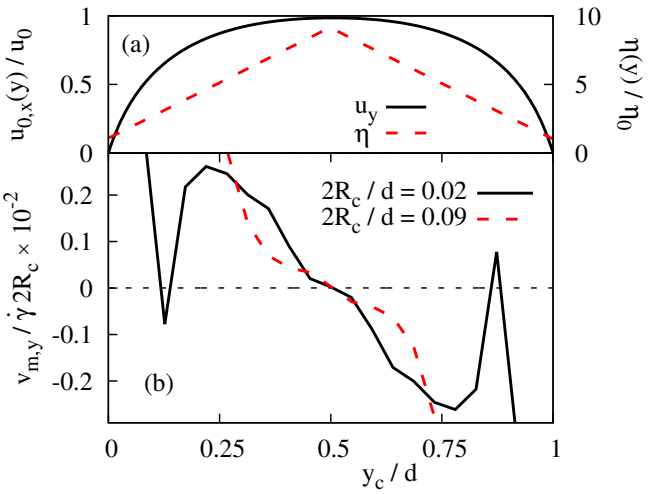

Figure 10. (a) The spatial variations of the shear viscosity (dashed line) and the flattened velocity profile $u_{0,x}(y)$ (solid line). (b) The y-dependence of migration velocity as obtained by LBM simulations of a capsule for two different radii. For the smaller particle radius a second attractor emerges.

The migration velocity of capsules in this viscosity profile is shown in Fig. 10 (b) for two different radii of the capsule. The attractor at the channel center is not shifted by this viscosity profile, because the shear rate vanishes at the channel center and the $\nabla\eta$ induced migration as well. In this region close to the center the center directed migration dominates. However, for the smaller capsule with $2R_c/d = 0.02$ the migration velocity, represented by the solid line in Fig. 10 (b), changes on each side of the channel center two times its sign. At the outer zero of $v_{m,y}$ an additional particle attractor has emerged. It is caused, similar as for the linear shear flow in the previous section 4.2, by the interplay between outward directed $\nabla\eta$ induced migration, which outweighs here the center directed migration, and the wall repulsion. This is similar also to the unbounded flow, where the outward directed $\nabla\eta$ induced migration can overcome the center migration (cf. Fig. 8). Between two neighboring attractors the vanishing migration velocity $v_{m,y}$ marks a particle repeller.

The emergence of the off-center attractors enables interesting applications. If in a viscosity profile, similar as in Fig. 10 (a), particles of different sizes are injected near one boundary, the larger ones migrate to the attractor at the channel center and the smaller ones may stay along the off-center attractor. I. e. at the end of the channel particles of different size or elasticity (cf. Fig. 3 and Fig. 5) are separated. This is a interesting new concept in microfluidics for the separation of different soft particles.

In investigations with viscoelastic fluids a particle migration to off-center attractors has been reported before [19,20,21,22,23,24] and it is not always clear whether this type of migration is driven more by elastic or viscosity effects. Here the mechanisms of an outward directed migration to an off-center attractor, driven by the $\nabla\eta$ effects, are rather clear. Therefore, our model with the viscosity profile shown Fig. 10 (a), may help for an improved understanding of CSM in viscoelastic fluids.

6 Discussion and conclusions

We investigated the effects of a spatially varying viscosity on the flow profile in shear and Poiseuille flow and we described a novel viscosity-gradient driven cross-streamline migration (CSM) of soft capsules, which represents deformable particles. A viscosity gradient in microfluidic devices may be induced, for instance, by a temperature gradient [31].

For the Stokesian dynamics simulations of capsules we determined flow profiles that take a constant viscosity gradient into account. We also derived for these simulations a generalized Oseen tensor that includes the viscosity gradient. These results may be also utilized in other approaches such as the boundary integral method [45] or in simulations of microswimmers [46], polymers [47] and colloids [32].

Rigid and soft particles in liquids of constant viscosity do not migrate across the streamlines in linear shear flows [16]. We have shown by symmetry arguments how the interplay between the particle deformability and the Stokes-friction forces, that vary according to a viscosity gradient across a particle, leads to cross-streamline migration of deformable capsules in simple shear flows towards the region of lower viscosity. This reasoning may also apply to the particle dynamics in non-Newtonian fluid flows, whereby in this case often elastic effects have to be taken into account as well. Our prediction on the basis of symmetry arguments are confirmed by Stokesian dynamics simulations. By Lattice Boltzmann simulations, where the particle wall interactions are taken into account, we also show that the interplay between this viscosity-gradient induced migration and the hydrodynamic wall repulsion causes even in linear shear flows a focusing of particles to an attractor streamline in the low viscosity region as indicated in Fig. 1. The location of the attractor depends on the strength of the viscosity gradient and the particle properties. This predicted focusing may have interesting applications.

We investigated CSM also in Poiseuille flows for two different viscosity gradients. A constant viscosity gradient across plane Poiseuille flow may be induced again by a temperature gradient across a flow cell. CSM in the presence of a viscosity gradient is much faster than without a gradient. As example we showed that the viscosity gradient, that corresponds to water with a temperature difference of 40°C between the boundaries at a distance of 2 mm, can already enhance the migration velocity by up to a factor 8. Such gradients are reported from experiments [31], also higher viscosity gradients can be achieved with e.g. sucrose in water [48]. Besides the faster migration, also the location of the particle attractor in Poiseuille flow is

affected by the viscosity gradient: It is shifted away from the center of a Poiseuille flow. The major reason for this shift is, that the location of the maximum of flow profile and therefore the position of zero shear rate is shifted towards the region of lower viscosity, which also shifts the position of the attractor. Thus the location of the particle attractor can be controlled by the viscosity gradient in a Poiseuille flow as well.

Shear thinning fluids in Poiseuille flows display a variation of the viscosity gradient with a maximum of the viscosity at the channel center. We described the viscosity landscape of shear thinning fluids in a simplified manner. At the channel center we also have chosen the viscosity maximum and a linear decay towards the channel boundaries. In order to focus to the effects of viscosity gradients, we have neglected further possible effects in complex fluids, such as elastic forces. The assumed viscosity landscape changed the CSM velocity as function of the distance from channel center considerably, compared to fluids with constant viscosity. Moreover, the CSM induced by stronger viscosity gradients dominates and drives in a larger off-center region of the channel cross section particles towards the boundaries. In this range the interplay with particle-wall repulsion may even cause, besides the particle attractor at the channel center, two further off-center particle attractors. These attractors are found for smaller but not for larger soft particles. A similar behavior was also found in experiments with visco-elastic liquids [24,21]. Here we can identify the appearance of off-center particle attractors in a unique manner with the viscosity gradient. Our insights may contribute to a further understanding of cross-streamline migration in complex liquids in straight and possibly in wavy channels [18].

The support by the German French University (DFH/UFA) and discussion with A. Förtsch, D. Kienle and W. Schmidt are gratefully acknowledged.

Author contribution statement

ML and WZ designed the research; ML performed the calculations and the simulations; ML and WZ interpreted and discussed the results and wrote the paper.

References

1. T. M. Squires and S. R. Quake, Rev. Mod. Phys. **77**, 978 (2005).
2. A. S. Popel and P. C. Johnson, Annu. Rev. Fluid Mech. **37**, 43 (2005).
3. A. Karimi, S. Yazdi, and A. M. Ardekani, Biomicrofluidics **7**, 021501 (2013).
4. J. B. Dahl, J.-M. G. Lin, S. J. Muller, and S. Kumar, Ann. Rev. Chem. Biomol. Eng. **6**, 293 (2015).
5. H. Amini, W. Lee, and D. D. Carlo, Lap Chip **14**, 2739 (2014).
6. T. W. Secomb, Annu. Rev. Fluid Mech. **49**, 443 (2017).
7. I. Cantat and C. Misbah, Phys. Rev. Lett. **83**, 880 (1999).
8. U. Seifert, Phys. Rev. Lett. **83**, 876 (1999).
9. M. Abkarian, C. Lartigue, and A. Viallat, Phys. Rev. Lett. **88**, 068102 (2002).
10. X. Grandchamp *et al.*, Phys. Rev. Lett. **110**, 108101 (2013).
11. L. G. Leal, Annu. Rev. Fluid Mech. **12**, 435 (1980).
12. S. Mandal, A. Bandopadhyay, and S. Chakraborty, Phys. Rev. E **92**, 023002 (2015).
13. A. Helmy and D. Barthès-Biesel, J. Mecanique theorique appliquee **1**, 859 (1982).
14. B. Kaoui *et al.*, Phys. Rev. E **77**, 021903 (2008).
15. G. Coupier, B. Kaoui, T. Podgorski, and C. Misbah, Phys. Fluids **20**, 111702 (2008).
16. S. K. Doddi and P. Bagchi, Int. J. Multiphas. Flow **34**, 966 (2008).
17. A. Förtsch, M. Laumann, D. Kienle, and W. Zimmermann, EPL **119**, 64003 (2017).
18. M. Schlenk *et al.*, Lab Chip **18**, 3163 (2018).
19. G. D'Avino *et al.*, Comput. Fluids **39**, 709 (2010).
20. D. Yuan *et al.*, Lab Chip **18**, 551 (2018).
21. F. Del Giudice, S. Sathish, G. D'Avino, and A. Q. Shen, Anal. Chem. **89**, 13146 (2017).
22. X. Lu, C. Liu, G. Hu, and X. Xuan, J. Colloid. Interf. Sci. **500**, 182 (2017).
23. M. A. Faridi *et al.*, J. Nanobiotechnol. **15**, 3 (2017).
24. G. D'Avino, F. Greco, and P. L. Maffettone, Annu. Rev. Fluid Mech. **49**, 341 (2017).
25. G. Segré and A. Silberberg, Nature **189**, 209 (1961).
26. G. Sekhon, R. Armstrong, and M. S. Jhon, J. Polymer Sci.:Polymer Phys. **20**, 947 (1982).
27. P. O. Brunn, Int. J. Multiphase Flow **187**, 202 (1983).
28. M. S. Jhon and K. F. Freed, J. Polymer Sci.: Polymer Phys. **23**, 255 (1985).
29. M. Laumann *et al.*, EPL **117**, 44001 (2017).
30. I. Jo, Y. Huang, W. Zimmermann, and E. Kanso, Phys. Rev. E **94**, 063116 (2016).
31. V. Miralles, A. Huerre, F. Malloggi, and M.-C. Jullien, Diagnostics **3**, 33 (2013).
32. J. K. G. Dhont, *An Introduction to dynamics of colloids* (Elsevier, Amsterdam, 1996).
33. T. Krueger, F. Varnik, and D. Raabe, Comput. Math. Appl. **61**, 3485 (2011), mesoscopic Methods for Engineering and Science Proceedings of ICMMES-09.
34. S. Ramanujan and C. Pozrikidis, J. Fluid. Mech. **361**, 117 (1998).
35. D. Barthès-Biesel, Annu. Rev. Fluid Mech. **48**, 25 (2016).
36. G. Gompper and D.M. Kroll, J. Phys. I France **6**, 1305 (1996).
37. T. Krueger, M. Gross, D. Raabe, and F. Varnik, Soft Matter **9**, 9008 (2013).
38. J. Kestin and J. Shankland, J. Non-Equil. Thermody. **6**, 241 (2009).
39. S. Gupta, *Viscosity of Water. In: Viscometry for Liquids* (Springer Series in Materials Science, Cham, 2014).
40. T. Krüger *et al.*, *The Lattice Boltzmann Method - Principles and Practice* (Springer, Berlin, 2016).
41. P. L. Bhatnagar, E. P. Gross, and M. Krook, Phys. Rev. **94**, 511 (1954).
42. C. K. Aidun and J. R. Clausen, Annu. Rev. Fluid. Mech **42**, 439 (2010).
43. Z. Guo, C. Zheng, and B. Shi, Phys. Rev. E **65**, 046308 (2002).
44. C. S. Peskin, Acta Numer. **11**, 479 (2002).

45. C. Pozrikidis, *Boundary Integral and Singularity Methods for Linearized Viscous Flow* (Cambridge University Press, Cambridge, England, 1992).
46. J. Elgeti, R. G. Winkler, and G. Gompper, Rep. Prog. Phys. **78**, 056601 (2015).
47. M. Doi and S. F. Edwards, *The Theory of Polymer Dynamics* (Clarendon Press, Oxford, 1986).
48. V. Telis, J. Telis-Romero, H. Mazzotti, and A. Gabas, Int. J. Food Prop. **10**, 185 (2007).

Focusing and splitting of particle streams in microflows via viscosity gradients
Supplementary Information

Matthias Laumann and Walter Zimmermann
Theoretische Physik I, Universität Bayreuth, 95440 Bayreuth, Germany;
E-mail: walter.zimmermann@uni-bayreuth.de

Abstract

Here we describe the derivation of the generalized Oseen tensor up to the first order correction with respect to the viscosity gradient. In addition we demonstrate that the cross-streamline migration of capsules in a simple shear flow is mainly directly induced by the viscosity gradient and the contribution by the nonlinearity of the flow profile provides only corrections to it. We also discuss the influence of other directions of the viscosity gradient on the migration.

1 Oseen tensor up to first order of the viscosity gradient

We derive in the presence of a viscosity gradient a generalized Oseen tensor that includes first order corrections with respect to viscosity gradient by solving the following two eqns (1a) and (1b)

$$-\nabla p + \nabla \cdot \left\{\eta[\nabla \mathbf{u} + (\nabla \mathbf{u})^{\mathbf{T}}]\right\} + \mathbf{f}\delta(\mathbf{r} - \mathbf{r}_\mathrm{f}) = 0\,, \tag{1a}$$

$$\nabla \cdot \mathbf{u} = 0\,, \tag{1b}$$

whereby $\mathbf{f}\delta(\mathbf{r} - \mathbf{r}_\mathrm{f})$ is a point force located at $\mathbf{r}_\mathrm{f}$. A Taylor expansion of the viscosity around the point $\mathbf{r}_\mathrm{t}$ is used which is given by eqn (2c) with

$$\eta_0 = \eta(\mathbf{r}_\mathrm{t})\,, \tag{2a}$$

$$\mathbf{G}_\eta = \nabla\eta|_{\mathbf{r}=\mathbf{r}_\mathrm{t}}\,, \tag{2b}$$

$$\eta(\mathbf{r}) \approx \eta_0 + \mathbf{G}_\eta \cdot (\mathbf{r} - \mathbf{r}_\mathrm{t})\,. \tag{2c}$$

With eqns (1a) and (2c) one obtains

$$0 = -\nabla p + \mathbf{G}_\eta \cdot [\nabla \mathbf{u} + (\nabla \mathbf{u})^{\mathbf{T}}] + [\underbrace{\eta_0 + \mathbf{G}_\eta \cdot (\mathbf{r}_\mathrm{f} - \mathbf{r}_\mathrm{t})}_{=\eta(\mathbf{r}_\mathrm{f})=\eta_\mathrm{f}} + \mathbf{G}_\eta \cdot (\mathbf{r} - \mathbf{r}_\mathrm{f})]\boldsymbol{\Delta}\mathbf{u} + \mathbf{f}\delta(\mathbf{r} - \mathbf{r}_\mathrm{f})\,,$$

$$0 = -\nabla p + \mathbf{G}_\eta \cdot [\nabla \mathbf{u} + (\nabla \mathbf{u})^{\mathbf{T}}] + [\eta_\mathrm{f} + \mathbf{G}_\eta \cdot (\mathbf{r} - \mathbf{r}_\mathrm{f})]\boldsymbol{\Delta}\mathbf{u} + \mathbf{f}\delta(\mathbf{r} - \mathbf{r}_\mathrm{f}) \tag{3}$$

whereby η_f denotes the viscosity at the location of the point force. Next eqn (3) and eqn (1b) are solved for the velocity field and the pressure. We expand the flow field and pressure as

follows

$$\mathbf{u} = \mathbf{u^{(0)}} + \mathbf{u^{(1)}} + \dots , \tag{4}$$

$$p = p^{(0)} + p^{(1)} + \dots . \tag{5}$$

$\mathbf{u^{(0)}}$ and $p^{(0)}$ denote the velocity and the pressure without a gradient. $\mathbf{u^{(1)}}$ and $p^{(1)}$ are proportional to the gradient. We use the boundary condition that the force does not disturb the fluid at an infinite distance to the force, which means the pressure must vanish at an infinite distance to the force

$$p^{(0)}(\mathbf{r}) \to \mathbf{0} \text{ at } |\mathbf{r} - \mathbf{r}_\mathrm{f}| \to \infty , \tag{6}$$

$$p^{(1)}(\mathbf{r}) \to \mathbf{0} \text{ at } |\mathbf{r} - \mathbf{r}_\mathrm{f}| \to \infty . \tag{7}$$

1.1 The equations of the zeroth order

The equations of the zeroth order are

$$0 = -\nabla p + \eta_\mathrm{f} \Delta \mathbf{u} + \mathbf{f}\delta(\mathbf{r} - \mathbf{r}_\mathrm{f}) , \tag{8}$$

$$0 = \nabla \mathbf{u^{(0)}} . \tag{9}$$

A Fourier-transformation of these linear equations

$$\mathbf{u}(\mathbf{r}) = \frac{1}{(2\pi)^3} \int \mathbf{u}(\mathbf{k}) \mathbf{e^{-ik\cdot r}} \mathbf{d^3 k} , \tag{10}$$

$$\mathbf{u}(\mathbf{k}) = \int \mathbf{u}(\mathbf{r}) \mathbf{e^{ik\cdot r}} \mathbf{d^3 r} . \tag{11}$$

give

$$0 = \mathbf{k} \cdot \mathbf{u^{(0)}} , \tag{12}$$

$$0 = -i\mathbf{k}\mathbf{p^{(0)}} - \eta_\mathrm{f} \mathbf{k^2} \mathbf{u^{(0)}} + \mathbf{f} \mathbf{e^{ik\cdot r_f}} , \tag{13}$$

Solving for $\mathbf{u^{(0)}}$ gives

$$\mathbf{u^{(0)}} = \frac{\mathbf{1}}{\eta_\mathrm{f} \mathbf{k^2}} \left(\mathbf{1} - \hat{\mathbf{k}}\hat{\mathbf{k}} \right) \mathbf{f} \mathbf{e^{ik\cdot r_f}} . \tag{14}$$

The back transformation leads to

$$\mathbf{u^{(0)}} = \frac{1}{(2\pi)^3} \int \frac{1}{\eta_\mathrm{f} k^2} \left(\mathbf{1} - \hat{\mathbf{k}}\hat{\mathbf{k}} \right) e^{-i\mathbf{k}\cdot(\mathbf{r}-\mathbf{r}_\mathrm{f})} d^3 k \cdot \mathbf{f} , \tag{15}$$

$$= \frac{1}{8\pi\eta_\mathrm{f} R} \left(\mathbf{1} + \hat{\mathbf{R}}\hat{\mathbf{R}} \right) \cdot \mathbf{f} \tag{16}$$

with $\mathbf{R} = \mathbf{r} - \mathbf{r}_\mathrm{f}$. The pressure is given by

$$p^{(0)} = \frac{\mathbf{f} \cdot \mathbf{R}}{4\pi R^3} , \tag{17}$$

$$\nabla p^{(0)} = \frac{1}{4\pi R^3} \left(\mathbf{1} - \mathbf{3}\hat{\mathbf{R}}\hat{\mathbf{R}} \right) \cdot \mathbf{f} . \tag{18}$$

The derivation of the zero order Oseen tensor, i.e. without viscosity gradient is e.g. given in Ref. [1].

1.2 The equations at first order

The equations of the first order (the terms proportional to $\mathbf{G}_\eta$) are

$$0 = -\nabla p^{(1)} + \mathbf{G}_\eta \cdot [\nabla \mathbf{u^{(0)}} + (\nabla \mathbf{u^{(0)}})^{\mathbf{T}}] + \eta_\mathrm{f} \mathbf{\Delta u^{(1)}} + \mathbf{G}_\eta \cdot (\mathbf{r} - \mathbf{r}_\mathrm{f}) \mathbf{\Delta u^{(0)}}\,, \tag{19}$$

$$0 = \nabla \mathbf{u^{(1)}}\,. \tag{20}$$

The Fourier-Transformation yields

$$0 = \int \left[-\nabla p^{(1)} + \mathbf{G}_\eta \cdot [\nabla \mathbf{u^{(0)}} + (\nabla \mathbf{u^{(0)}})^{\mathbf{T}}] + \eta_\mathrm{f} \mathbf{\Delta u^{(1)}} + \mathbf{G}_\eta \cdot (\mathbf{r} - \mathbf{r}_\mathrm{f}) \mathbf{\Delta u^{(0)}} \right] e^{i\mathbf{k}\cdot\mathbf{r}} d^3 r\,, \tag{21}$$

$$0 = \mathbf{k} \cdot \mathbf{u^{(1)}}\,. \tag{22}$$

An integration by parts leads to

$$\begin{aligned} 0 =& i\mathbf{k}\mathbf{p^{(1)}}(\mathbf{k}) - \mathbf{i}\mathbf{G}_\eta \cdot [\mathbf{k}\mathbf{u^{(0)}}(\mathbf{k}) + (\mathbf{k}\mathbf{u^{(0)}}(\mathbf{k}))^{\mathbf{T}}] - \eta_\mathrm{f} \mathbf{k^2 u^{(1)}}(\mathbf{k}) \\ &+ \int \mathbf{G}_\eta \cdot (\mathbf{r} - \mathbf{r}_\mathrm{f}) \mathbf{\Delta u^{(0)}} \mathbf{e^{ik\cdot r}} \mathbf{d^3 r}. \end{aligned} \tag{23}$$

To calculate the last term we use the equations of the zeroth order eqn (9) which leads to

$$\Delta \mathbf{u^{(0)}} = \frac{\mathbf{1}}{\eta_\mathrm{f}} \left(\nabla \mathbf{p^{(0)}} - \mathbf{f} \delta(\mathbf{r} - \mathbf{r}_\mathrm{f}) \right)\,. \tag{24}$$

Using this with the last term in eqn(23) one obtains

$$\begin{aligned} &\int \mathbf{G}_\eta \cdot (\mathbf{r} - \mathbf{r}_\mathrm{f}) \mathbf{\Delta u^{(0)}} \mathbf{e^{ik\cdot r}} \mathbf{d^3 r} = \int \mathbf{G}_\eta \cdot (\mathbf{r} - \mathbf{r}_\mathrm{f}) \left[\frac{\mathbf{1}}{\eta_\mathrm{f}} \left(\nabla \mathbf{p^{(0)}} - \mathbf{f} \delta(\mathbf{r} - \mathbf{r}_\mathrm{f}) \right) \right] \mathbf{e^{ik\cdot r}} \mathbf{d^3 r}\,, \\ =& \frac{1}{\eta_\mathrm{f}} \int \mathbf{G}_\eta \cdot (\mathbf{r} - \mathbf{r}_\mathrm{f}) \nabla \mathbf{p^{(0)}} \mathbf{e^{ik\cdot r}} \mathbf{d^3 r} = \frac{\mathbf{1}}{\eta_\mathrm{f}} \int \frac{\mathbf{G}_\eta \cdot \mathbf{R}}{\mathbf{4\pi R^3}} \left(\mathbf{1} - \mathbf{3\hat{R}\hat{R}} \right) \mathbf{e^{ik\cdot r}} \mathbf{d^3 r} \cdot \mathbf{f}\,, \\ =& \underbrace{\frac{1}{\eta_\mathrm{f}} \int \frac{\mathbf{G}_\eta \cdot \mathbf{R}}{4\pi R^3} \left(\mathbf{1} - \mathbf{3\hat{R}\hat{R}} \right) e^{i\mathbf{k}\cdot\mathbf{R}} d^3 R}_{:=\mathbf{M(k)}} \cdot \mathbf{f} \mathbf{e^{ik\cdot r_f}}\,. \end{aligned} \tag{25}$$

Now the Fourier transformation of the tensor $\mathbf{M}$ must be calculated. We use the ansatz

$$\mathbf{M(k)} = \mathbf{a_1 1} + \mathbf{a_2 \hat{k}\hat{k}} + \mathbf{a_3 G_\eta \hat{k}} + \mathbf{a_4 \hat{k} G_\eta} + \mathbf{a_5 G_\eta G_\eta}\,, \tag{26}$$

which follows from the linear dependence on $\mathbf{G}_\eta$ and the right behavior at a transformation of the coordinate system. The coefficients a_i are unknown and must be determined. This ansatz gives

$$\frac{1}{\eta_\mathrm{f}} \int \frac{\mathbf{G}_\eta \cdot \mathbf{R}}{4\pi R^3} \left(\mathbf{1} - \mathbf{3\hat{R}\hat{R}} \right) e^{i\mathbf{k}\cdot\mathbf{R}} d^3 R = a_1 \mathbf{1} + \mathbf{a_2 \hat{k}\hat{k}} + \mathbf{a_3 G_\eta \hat{k}} + \mathbf{a_4 \hat{k} G_\eta} + \mathbf{a_5 G_\eta G_\eta}\,. \tag{27}$$

The coefficients a_i are determined by calculating the trace and tensor contractions of eqn (27) which yields

$$\begin{aligned}
\mathrm{tr}(\mathbf{M}) =& 0 = 3a_1 + a_2 + a_3\mathbf{G}.\eta\hat{\mathbf{k}} + \mathbf{a_4}\hat{\mathbf{k}}\cdot\mathbf{G}_\eta + \mathbf{a_5}\mathbf{G}_\eta\cdot\mathbf{G}_\eta\,,\\
\hat{\mathbf{k}}\cdot\mathbf{M}\cdot\hat{\mathbf{k}} =& 0 = a_1 + a_2 + (a_3+a_4)\hat{\mathbf{k}}\cdot\mathbf{G}_\eta + \mathbf{a_5}\hat{\mathbf{k}}\cdot\mathbf{G}_\eta^{\mathbf{2}}\,,\\
\mathbf{G}_\eta\cdot\mathbf{M}\cdot\hat{\mathbf{k}} =& -i\frac{G_\eta^2 - (\hat{\mathbf{k}}\cdot\mathbf{G}_\eta)^{\mathbf{2}}}{k\eta_\mathrm{f}} = a_1\hat{\mathbf{k}}\cdot\mathbf{G}_\eta + (\mathbf{G}_\eta^{\mathbf{2}}\mathbf{a_5} + \mathbf{a_2})\hat{\mathbf{k}}\cdot\mathbf{G}_\eta + \mathbf{a_3}\mathbf{G}_\eta^{\mathbf{2}} + \mathbf{a_4}(\hat{\mathbf{k}}\cdot\mathbf{G}_\eta)^{\mathbf{2}}\,,\\
\hat{\mathbf{k}}\cdot\mathbf{M}\cdot\mathbf{G}_\eta =& -i\frac{G_\eta^2 - (\hat{\mathbf{k}}\cdot\mathbf{G}_\eta)^{\mathbf{2}}}{k\eta_\mathrm{f}} = G_\eta^2 a_5\hat{\mathbf{k}}\cdot\mathbf{G}_\eta + \mathbf{G}_\eta^{\mathbf{2}}\mathbf{a_4} + \mathbf{a_3}(\hat{\mathbf{k}}\cdot\mathbf{G}_\eta)^{\mathbf{2}}\\
&+ a_1\hat{\mathbf{k}}\cdot\mathbf{G}_\eta + \mathbf{a_2}\hat{\mathbf{k}}\cdot\mathbf{G}_\eta\,,\\
\mathbf{G}_\eta\cdot\mathbf{M}\cdot\mathbf{G}_\eta =& 2i\frac{-G_\eta^2 + (\hat{\mathbf{k}}\cdot\mathbf{G}_\eta)^{\mathbf{2}})\hat{\mathbf{k}}\cdot\mathbf{G}_\eta}{k\eta_\mathrm{f}} = a_1 G_\eta^2 + a_2(\hat{\mathbf{k}}\cdot\mathbf{G}_\eta)^{\mathbf{2}}\\
&+ (a_3+a_4)G_\eta^2\hat{\mathbf{k}}\cdot\mathbf{G}_\eta + \mathbf{a_5}\mathbf{G}^{\mathbf{4}}\,.
\end{aligned} \tag{28}$$

Solving this system of equations gives

$$a_1 = 0,\ a_2 = \frac{2i\hat{\mathbf{k}}\cdot\mathbf{G}_\eta}{k\eta_\mathrm{f}},\ a_3 = -\frac{i}{k\eta_\mathrm{f}},\ a_4 = -\frac{i}{k\eta_\mathrm{f}},\ a_5 = 0\,.$$

With this results and eqn (14), eqn (23) is rearranged to

$$\begin{aligned}
0 =& i\mathbf{k}\mathbf{p}^{(\mathbf{1})}(\mathbf{k}) - \eta_\mathrm{f}\mathbf{k}^{\mathbf{2}}\mathbf{u}^{(\mathbf{1})}(\mathbf{k}) \underbrace{-\frac{i\mathbf{G}_\eta}{k^2\eta_\mathrm{f}}\cdot[\mathbf{k}\mathbf{f} + \mathbf{f}\mathbf{k} - \mathbf{2}(\hat{\mathbf{k}}\cdot\mathbf{f})\hat{\mathbf{k}}\hat{\mathbf{k}}\mathbf{k}]\mathbf{e}^{\mathbf{i}\mathbf{k}\cdot\mathbf{r}_\mathrm{f}}}\\
&+ \underbrace{\left[\frac{2i\hat{\mathbf{k}}\cdot\mathbf{G}_\eta}{k\eta_\mathrm{f}}\hat{\mathbf{k}}\hat{\mathbf{k}} - \frac{i}{k\eta_\mathrm{f}}\mathbf{G}_\eta\hat{\mathbf{k}} - \frac{\mathbf{i}}{\mathbf{k}\eta_\mathrm{f}}\hat{\mathbf{k}}\mathbf{G}_\eta\right]\cdot\mathbf{f}\mathbf{e}^{\mathbf{i}\mathbf{k}\cdot\mathbf{r}_\mathrm{f}}}_{=\mathbf{B}}\,.\\
0 =& i\mathbf{k}\mathbf{p}^{(\mathbf{1})}(\mathbf{k}) - \eta_\mathrm{f}\mathbf{k}^{\mathbf{2}}\mathbf{u}^{(\mathbf{1})}(\mathbf{k}) + \mathbf{B}\,.
\end{aligned} \tag{29}$$

The expression of $\mathbf{B}$ can be simplified:

$$\begin{aligned}
\mathbf{B} =& \left\{-\frac{i}{\eta_\mathrm{f}k}\left[(\mathbf{G}_\eta\cdot\hat{\mathbf{k}})\mathbf{1} + \hat{\mathbf{k}}\mathbf{G}_\eta - \mathbf{2}(\mathbf{G}_\eta\cdot\hat{\mathbf{k}})\hat{\mathbf{k}}\hat{\mathbf{k}}\right]\right.\\
&\left.+\left[\frac{2i\hat{\mathbf{k}}\cdot\mathbf{G}_\eta}{k\eta_\mathrm{f}}\hat{\mathbf{k}}\hat{\mathbf{k}} - \frac{i}{k\eta_\mathrm{f}}\mathbf{G}_\eta\hat{\mathbf{k}} - \frac{\mathbf{i}}{\mathbf{k}\eta_\mathrm{f}}\hat{\mathbf{k}}\mathbf{G}_\eta\right]\right\}\cdot\mathbf{f}\mathbf{e}^{\mathbf{i}\mathbf{k}\cdot\mathbf{r}_\mathrm{f}}\,,\\
=& -\frac{i}{\eta_\mathrm{f}k}\left\{(\mathbf{G}_\eta\cdot\hat{\mathbf{k}})\mathbf{1} + \mathbf{2}\hat{\mathbf{k}}\mathbf{G}_\eta + \mathbf{G}_\eta\hat{\mathbf{k}} - \mathbf{4}(\mathbf{G}_\eta\cdot\hat{\mathbf{k}})\hat{\mathbf{k}}\hat{\mathbf{k}}\right\}\cdot\mathbf{f}\mathbf{e}^{\mathbf{i}\mathbf{k}\cdot\mathbf{r}_\mathrm{f}}\,.
\end{aligned} \tag{30}$$

We calculate the pressure by multiplying (29) with $\mathbf{k}$ and using eqn (22)

$$p^{(1)}(\mathbf{k}) = -\frac{\mathbf{k}\cdot\mathbf{B}}{ik^2}\,, \tag{31}$$

$$= \frac{2}{\eta_\mathrm{f}k^2}\left[\mathbf{G}_\eta - \left(\mathbf{G}_\eta\cdot\hat{\mathbf{k}}\right)\hat{\mathbf{k}}\right]\cdot\mathbf{f}\,. \tag{32}$$

The back transformation is given by

$$p^{(1)}(\mathbf{R}) = \frac{\mathbf{1}}{\mathbf{4}\pi\eta_\mathrm{f}\mathbf{R}}\left[\mathbf{G}_\eta + \left(\mathbf{G}_\eta\cdot\hat{\mathbf{R}}\right)\hat{\mathbf{R}}\right]\cdot\mathbf{f} \tag{33}$$

with $\mathbf{R} = \mathbf{r} - \mathbf{r}_\mathrm{f}$.

We can now calculate the velocity via eqn (29) and and eqn (31). Solving for $\mathbf{u^{(1)}}$ leads to

$$\mathbf{u^{(1)}} = \frac{1}{\eta_\mathrm{f} k^2}\left(\mathbf{1} - \hat{\mathbf{k}}\hat{\mathbf{k}}\right)\cdot\mathbf{B}\,, \tag{34}$$

$$\mathbf{u^{(1)}} = -\frac{i}{k^3\eta_\mathrm{f}^2}\left\{\left(\mathbf{G}_\eta\cdot\hat{\mathbf{k}}\right)\left(\mathbf{1} - \mathbf{2}\hat{\mathbf{k}}\hat{\mathbf{k}}\right) + \mathbf{G}_\eta\hat{\mathbf{k}}\right\}\cdot\mathbf{f}\mathbf{e}^{\mathbf{i}\mathbf{k}\cdot\mathbf{r}_\mathrm{f}}\,. \tag{35}$$

The back transformation is given by

$$\begin{aligned}\mathbf{u^{(1)}} &= \frac{\mathbf{1}}{(\mathbf{2}\pi)^\mathbf{3}}\int -\frac{i}{k^3\eta_\mathrm{f}^2}\left\{\left(\mathbf{G}_\eta\cdot\hat{\mathbf{k}}\right)\left(\mathbf{1} - \mathbf{2}\hat{\mathbf{k}}\hat{\mathbf{k}}\right) + \mathbf{G}_\eta\hat{\mathbf{k}}\right\}e^{-i\mathbf{k}\cdot\mathbf{r}}d^3k\cdot\mathbf{f}\mathbf{e}^{\mathbf{i}\mathbf{k}\cdot\mathbf{r}_\mathrm{f}}\,,\\ &= \underbrace{\frac{1}{(2\pi)^3}\int -\frac{i}{k^3\eta_\mathrm{f}^2}\left\{\left(\mathbf{G}_\eta\cdot\hat{\mathbf{k}}\right)\left(\mathbf{1} - \mathbf{2}\hat{\mathbf{k}}\hat{\mathbf{k}}\right) + \mathbf{G}_\eta\hat{\mathbf{k}}\right\}e^{-i\mathbf{k}\cdot\mathbf{R}}d^3k}_{=\mathbf{O^{(1)}}(\mathbf{R})}\cdot\mathbf{f}\,.\end{aligned} \tag{36}$$

Again we choose the ansatz

$$\mathbf{O^{(1)}}(\mathbf{R}) = \mathbf{a_1}\mathbf{1} + \mathbf{a_2}\hat{\mathbf{R}}\hat{\mathbf{R}} + \mathbf{a_3}\mathbf{G}_\eta\hat{\mathbf{R}} + \mathbf{a_4}\hat{\mathbf{R}}\mathbf{G}_\eta + \mathbf{a_5}\mathbf{G}_\eta\mathbf{G}_\eta \tag{37}$$

and we calculate the trace and the tensor contractions of eqn (36) and eqn (37) to determine the coefficients a_i of the ansatz. This gives

$$\begin{aligned}\mathrm{tr}(\mathbf{O^{(1)}}) =& -\frac{\hat{\mathbf{R}}\cdot\mathbf{G}_\eta}{4\pi\eta_\mathrm{f}^2} = 3a_1 + a_2 + a_3\mathbf{G}.\eta\hat{\mathbf{R}} + \mathbf{a_4}\hat{\mathbf{R}}\cdot\mathbf{G}_\eta + \mathbf{a_5}\mathbf{G}_\eta\cdot\mathbf{G}_\eta\,,\\ \hat{\mathbf{R}}\cdot\mathbf{O^{(1)}}\cdot\hat{\mathbf{R}} =& \frac{\hat{\mathbf{R}}\cdot\mathbf{G}_\eta}{8\pi\eta_\mathrm{f}^2} = a_1 + a_2 + (a_3 + a_4)\hat{\mathbf{R}}\cdot\mathbf{G}_\eta + \mathbf{a_5}\hat{\mathbf{R}}\cdot\mathbf{G}_\eta^\mathbf{2}\,,\\ \mathbf{G}_\eta\cdot\mathbf{O^{(1)}}\cdot\hat{\mathbf{R}} =& -\frac{G_\eta^2 + (\hat{\mathbf{R}}\cdot\mathbf{G}_\eta)^\mathbf{2}}{16\pi\eta_\mathrm{f}^2} = a_1\hat{\mathbf{R}}\cdot\mathbf{G}_\eta + (\mathbf{G}_\eta^\mathbf{2}\mathbf{a_5} + \mathbf{a_2})\hat{\mathbf{R}}\cdot\mathbf{G}_\eta\\ &+ a_3G_\eta^2 + a_4(\hat{\mathbf{R}}\cdot\mathbf{G}_\eta)^\mathbf{2}\,,\\ \hat{\mathbf{R}}\cdot\mathbf{O^{(1)}}\cdot\mathbf{G}_\eta =& \frac{G_\eta^2 - 3(\hat{\mathbf{R}}\cdot\mathbf{G}_\eta)^\mathbf{2}}{16\pi\eta_\mathrm{f}^2} = G_\eta^2a_5\hat{\mathbf{R}}\cdot\mathbf{G}_\eta + \mathbf{G}_\eta^\mathbf{2}\mathbf{a_4} + \mathbf{a_3}(\hat{\mathbf{R}}\cdot\mathbf{G}_\eta)^\mathbf{2}\\ &+ a_1\hat{\mathbf{R}}\cdot\mathbf{G}_\eta + \mathbf{a_2}\hat{\mathbf{R}}\cdot\mathbf{G}_\eta\,,\\ \mathbf{G}_\eta\cdot\mathbf{O^{(1)}}\cdot\mathbf{G}_\eta =& \hat{\mathbf{R}}\cdot\mathbf{G}_\eta\frac{\mathbf{G}_\eta^\mathbf{2} + (\hat{\mathbf{R}}\cdot\mathbf{G}_\eta)^\mathbf{2}}{\mathbf{16}\pi\eta_\mathrm{f}^\mathbf{2}} = \mathbf{a_1}\mathbf{G}_\eta^\mathbf{2} + \mathbf{a_2}(\hat{\mathbf{R}}\cdot\mathbf{G}_\eta)^\mathbf{2}\\ &+ (a_3 + a_4)G_\eta^2\hat{\mathbf{R}}\cdot\mathbf{G}_\eta + \mathbf{a_5}\mathbf{G}^\mathbf{4}\,.\end{aligned}$$

The solution of the system of equations is

$$a_1 = -\frac{\hat{\mathbf{R}}\cdot\mathbf{G}_\eta}{16\pi\eta_\mathrm{f}^2}, a_2 = -\frac{\hat{\mathbf{R}}\cdot\mathbf{G}_\eta}{16\pi\eta_\mathrm{f}^2}, a_3 = -\frac{1}{16\pi\eta_\mathrm{f}^2}, a_4 = \frac{1}{16\pi\eta_\mathrm{f}^2}, a_5 = 0$$

and we find

$$\mathbf{O^{(1)}}(\mathbf{R}) = -\frac{\hat{\mathbf{R}}\cdot\mathbf{G}_\eta}{\mathbf{16}\pi\eta_\mathrm{f}^\mathbf{2}}\mathbf{1} - \frac{\hat{\mathbf{R}}\cdot\mathbf{G}_\eta}{\mathbf{16}\pi\eta_\mathrm{f}^\mathbf{2}}\hat{\mathbf{R}}\hat{\mathbf{R}} - \frac{\mathbf{1}}{\mathbf{16}\pi\eta_\mathrm{f}^\mathbf{2}}\mathbf{G}_\eta\hat{\mathbf{R}} + \frac{\mathbf{1}}{\mathbf{16}\pi\eta_\mathrm{f}^\mathbf{2}}\hat{\mathbf{R}}\mathbf{G}_\eta\,. \tag{38}$$

1.3 The result and discussion

The complete Oseen tensor with the corrections up to first order in the viscosity gradient is given by

$$\mathbf{O^{(0)}} + \mathbf{O^{(1)}} = \frac{1}{8\pi\eta_\mathrm{f} R}\left[\left(1 - \frac{\mathbf{R}\cdot\mathbf{G}_\eta}{2\eta_\mathrm{f}}\right)\left(\mathbf{1} + \hat{\mathbf{R}}\hat{\mathbf{R}}\right) + \frac{\mathbf{1}}{\mathbf{2}\eta_\mathrm{f}}\left(\mathbf{R}\mathbf{G}_\eta - \mathbf{G}_\eta\mathbf{R}\right)\right] \tag{39}$$

With this result the flow field induced by a point force located at $\mathbf{r}_\mathrm{f}$ is up to first order of a Taylor expansion (around point $\mathbf{r}_\mathrm{t}$) with respect to the viscosity gradient given by

$$\mathbf{u} = \mathbf{u^{(0)}} + \mathbf{u^{(1)}} = \left[\mathbf{O^{(0)}} + \mathbf{O^{(1)}}\right]\cdot\mathbf{f} \tag{40}$$

$$= \frac{1}{8\pi\eta_\mathrm{f} R}\left[\left(1 - \frac{\mathbf{R}\cdot\mathbf{G}_\eta}{2\eta_\mathrm{f}}\right)\left(\mathbf{1} + \hat{\mathbf{R}}\hat{\mathbf{R}}\right) + \frac{\mathbf{1}}{\mathbf{2}\eta_\mathrm{f}}\left(\mathbf{R}\mathbf{G}_\eta - \mathbf{G}_\eta\mathbf{R}\right)\right]\cdot\mathbf{f}\,, \tag{41}$$

$$p = p^{(0)} + p^{(1)} = \left[\frac{\mathbf{R}}{4\pi R^3} + \frac{1}{4\pi\eta_\mathrm{f} R}\left\{\mathbf{G}_\eta + \left(\mathbf{G}_\eta\cdot\hat{\mathbf{R}}\right)\hat{\mathbf{R}}\right\}\right]\cdot\mathbf{f} \tag{42}$$

$$\mathbf{R} = \mathbf{r} - \mathbf{r}_\mathrm{f}\,,\ R = |\mathbf{R}|\,,\ \hat{\mathbf{R}} = \frac{\mathbf{R}}{R}, \tag{43}$$

$$\eta_0 = \eta(\mathbf{r}_\mathrm{t})\,,\ \mathbf{G}_\eta = \nabla\eta|_{\mathbf{r}=\mathbf{r}_\mathrm{t}}\,,\ \eta(\mathbf{r}) \approx \eta_\mathbf{0} + \mathbf{G}_\eta\cdot(\mathbf{r} - \mathbf{r}_\mathrm{t})$$

$$\eta_\mathrm{f} = \eta(\mathbf{r}_\mathrm{f}) = \eta_0 + \mathbf{G}_\eta\cdot(\mathbf{r}_\mathrm{f} - \mathbf{r}_\mathrm{t})\,. \tag{44}$$

The expression $\mathbf{u^{(1)}}$ given by eqn (41) and $p^{(1)}$ given by eqn (33) solves the Stokes equation of first order in the gradient, cf. 19) and eqn (20. Furthermore the pressure vanishes at infinite distance to the force, which means the boundary condition eqn (7) is fulfilled.

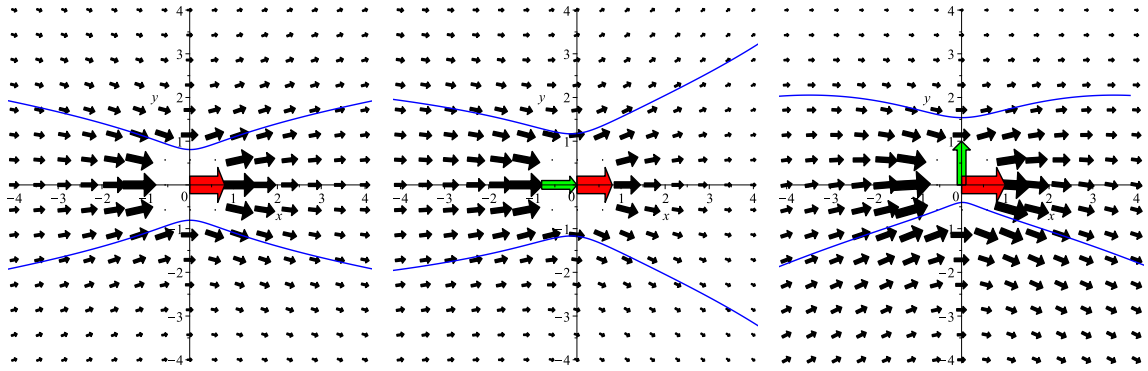

Figure 1: Comparison of the flow field (black) of a point force (red) without (left) and with (middle, right) a nonzero viscosity gradient (green). Also two stream lines are shown (blue). The velocity decays faster in direction of the gradient than in opposite direction and the stream lines are bend towards regions with lower viscosity. Therefore the symmetry of the stream lines is broken if the gradient is included. Parameters: $\eta_0 = 1$, $\mathbf{f} = \hat{\mathbf{e}}_\mathbf{x}$, $\mathbf{r}_\mathrm{t} = \mathbf{r}_\mathrm{f} = \mathbf{0}$, $\mathbf{G}_\eta = -\mathbf{0.2}\hat{\mathbf{e}}_\mathbf{x}$ (left) or $\mathbf{G}_\eta = \mathbf{0.2}\hat{\mathbf{e}}_\mathbf{y}$ (right)

In the main text we describe how we simulate the dynamics of a capsule represented by beads with the Oseen tensor derived here (see eqn (12) main text). We have chosen in the main text $\mathbf{r}_\mathrm{t} = \mathbf{0}$. The force acts on the position of the bead $\mathbf{r}_j$ and the flow is evaluated at the position of another bead $\mathbf{r}_i$ which leads to $\mathbf{r}_\mathrm{f} = \mathbf{r}_j$, $\eta_\mathrm{f} = \eta(\mathbf{r}_\mathrm{f}) = \eta(\mathbf{r}_j) = \eta_j$ and $\mathbf{R} = \mathbf{r}_i - \mathbf{r}_\mathrm{f}$.

We give two examples to illustrate how the gradient influences the flow field. The flow fields of a point force with a viscosity gradient are shown in fig. 1: The velocity of the fluid decays with the distance to the point force. This decay is faster in regions with higher viscosity (in direction of the gradient) than with a lower one (in opposite direction of the gradient). Furthermore the stream lines are bend towards regions with lower viscosity by the gradient, because the fluid can flow more easily at lower viscosity. Moreover, the viscosity gradient breaks the symmetry, which the Oseen tensor has without a gradient: Figure 1 shows that the flow without a gradient has symmetric stream lines: Mirroring both stream lines along the axis parallel or perpendicular to the force (x- and y-direction in the plot) does not change the stream lines. With a gradient the stream lines lose their symmetry axis perpendicular to the gradient.

1.4 Validity range of the approximations

We derived the Oseen tensor in first order of the gradient. Thus we must determine at which conditions this approximation is valid. Therefore we use a nondimensional form of the velocity given by eqn (41). To receive this, we use the magnitude of the force f, the viscosity at the location of the force η_f and a typical length scale L, which is the diameter of the capsule $L = 2R_c$ in the main text. With these quantities we define the dimensionless viscosity gradient $\tilde{\mathbf{G}}_\eta = \frac{\mathbf{G}_\eta L}{\eta_\mathrm{f}}$ and $\tilde{\mathbf{R}} = \frac{\mathbf{R}}{L}$. The velocity is then given by

$$\tilde{\mathbf{u}} = \mathbf{u}\frac{L\eta_\mathrm{f}}{f} = \frac{1}{8\pi\tilde{R}}\left[\left(1 - \frac{\tilde{\mathbf{R}}\cdot\tilde{\mathbf{G}}_\eta}{2}\right)\left(\mathbf{1} + \hat{\mathbf{R}}\hat{\mathbf{R}}\right) + \frac{\mathbf{1}}{\mathbf{2}}\left(\tilde{\mathbf{R}}\tilde{\mathbf{G}}_\eta - \tilde{\mathbf{G}}_\eta\tilde{\mathbf{R}}\right)\right]\cdot\tilde{\mathbf{f}}\,. \tag{45}$$

This allows to discuss the error at locations with $\tilde{R} \approx 1$ or $R \approx L$, i.e. at the surface of the capsule in the main text with $L = 2R_c$. With $\tilde{R} \approx 1$ the error due to the neglected second order is determined by the dimensionless gradient $\tilde{\mathbf{G}}_\eta$. This means the Oseen tensor in first order can be used if

$$\left|\tilde{\mathbf{G}}_\eta\right| \ll 1\,.$$

Another important criterion is that the Taylor expansion of the viscosity must be a good enough approximation of $\eta(\mathbf{r})$. At least the viscosity must not be negative. This means the used Taylor expansion given by eqn (2c) and also the calculated velocity $\mathbf{u}(\mathbf{r})$ (eqn (41)) can only be valid at locations with

$$\eta(\mathbf{r}) \approx \eta_0 + \mathbf{G}_\eta\cdot(\mathbf{r} - \mathbf{r}_\mathrm{t}) > \mathbf{0}\,. \tag{46}$$

2 Influence of the nonlinear shear flow

Driving a flow by a moving plate without a viscosity gradient results in a linear shear flow (eqn (8) main text)

$$\mathbf{u}_0(y) = U\frac{y}{d}\mathbf{e}_\mathrm{x}\,. \tag{47}$$

But if the viscosity gradient has a component in direction from on plate to the other it affects the flow which results in a nonlinear flow

$$\mathbf{u}_0(y) = U\frac{\ln[y\,G_{\eta,\mathrm{y}}/\eta_0 + 1]}{\ln[d\,G_{\eta,\mathrm{y}}/\eta_0 + 1]}\mathbf{e}_\mathrm{x} \tag{48}$$

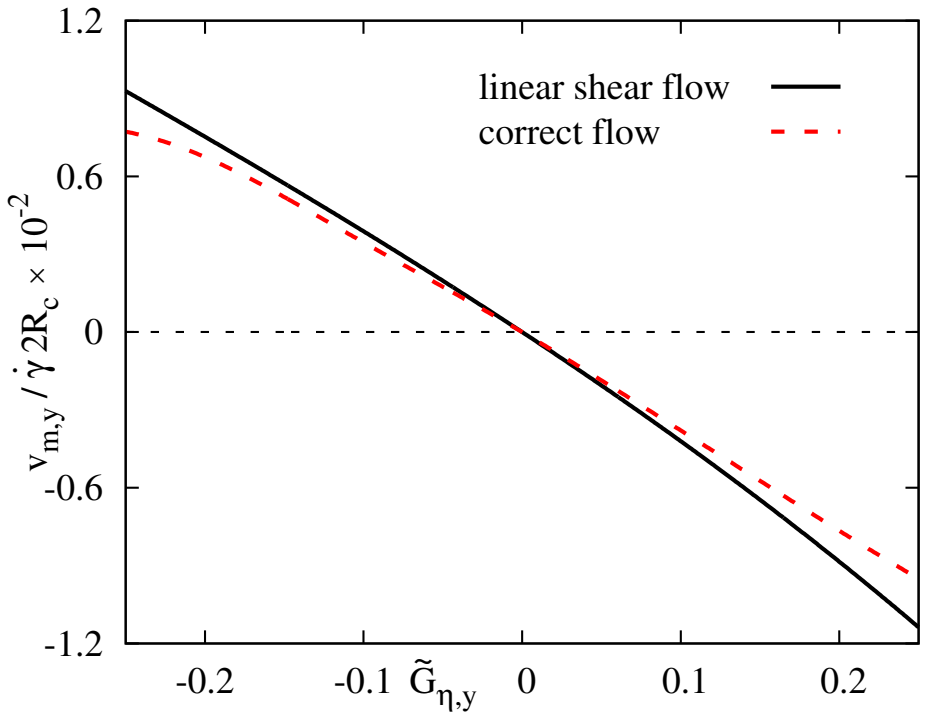

Figure 2: The migration velocity as function of the dimensionless viscosity gradient in the correct, nonlinear flow (which is influenced by the gradient in y-direction) and a linear shear flow. Both simulations show nearly the same migration velocities. Thus the migration is mainly caused directly by the gradient.

given by eqn (7) in the main text.

It is well known that a nonlinear flow with a spatially dependent shear rate can cause a cross-streamline migration (see e.g. Ref. [2]). Therefore we examine whether the migration with the viscosity gradient pointing from one plate to the other is caused directly by the viscosity gradient or indirectly by the nonlinear flow. This is done by comparing the migration in the nonlinear flow with a simulation in a linear flow, where the influence of the gradient on the flow is neglected. Figure 2 shows the migration velocity as function of the viscosity gradient for both the linear and the nonlinear flow. Both simulations give nearly the same velocities at the used magnitudes of $\mathbf{G}_\eta$ so that the migration is mainly caused directly by the viscosity gradient.

3 Explanation of $\nabla\eta$-induced CSM for all directions of $\nabla\eta$

We explain why a particle migrates in a simple shear flow with a viscosity gradient and consider here all directions of the gradient, i.e. firstly a gradient in flow direction, secondly perpendicular to the flow direction and in the shear plane and thirdly perpendicular to the shear plane. As in the main, the effect of the viscosity gradient on the flow is neglected here to show that the migration is caused directly by the gradient (and not indirectly by the influence of the gradient on the flow, cf. fig. 2). We discuss at first the rigid capsule with spherical

shape. The friction force is calculated as explained in the main text

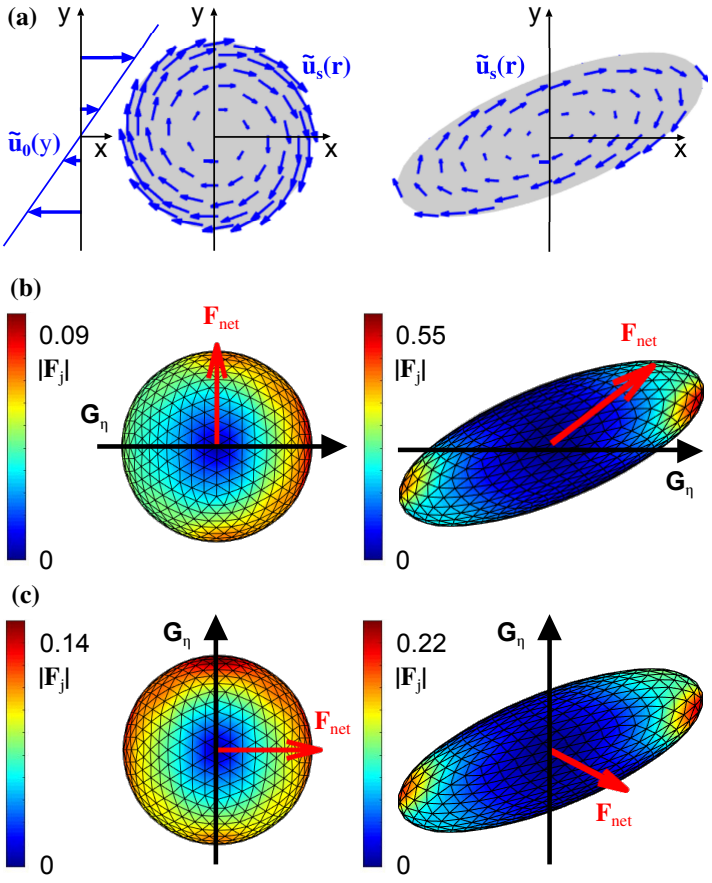

Figure 3: A rigid capsule is rotating due to the shear flow $\tilde{\mathbf{u}}_0(y)$ and a soft capsule performs a tank-treading motion (a) with velocity $\tilde{\mathbf{u}}_s(\mathbf{r})$ at its surface (comoving frame). A viscosity gradient $\mathbf{G}_\eta$ (black) leads to higher friction forces $\mathbf{F}(\mathbf{r})$ between capsule and fluid on the half than on the other (color of surface). This asymmetry causes a net force $\mathbf{F}_{\text{net}}$ (red). If the capsule is rigid then the direction of the viscosity gradient and $\hat{\mathbf{e}}_z$ define a plane of symmetry (see (b) and (c)) and the net force is oriented perpendicular to this plane. This means $\mathbf{G}_\eta \parallel \mathbf{u}_0(\mathbf{r})$ causes a CSM but not $\mathbf{G}_\eta \perp \mathbf{u}_0(\mathbf{r})$ (lateral migration). The soft capsule is deformed and shares therefore no plane of symmetry with the flow. Thus the net force has in both cases (b) and (c) a component perpendicular to the flow, which results in a CSM in both cases.

The system, i.e. the spherical capsule and the shear flow, has symmetries without a viscosity gradient (cf. fig. 3 (a)). The flow does not change if it is mirrored at the xz- or yz-plane and its sign is changed subsequently. Therefore the velocity and the friction at the surface of the capsule have the same symmetries: For example at the mirrored position $\mathbf{r}'$ of $\mathbf{r}$ at the yz-plane we get $F_{\text{x}}(\mathbf{r}') = F_{\text{x}}(\mathbf{r})$, $F_{\text{y}}(\mathbf{r}') = -F_{\text{y}}(\mathbf{r})$ and $F_{\text{z}}(\mathbf{r}') = -F_{\text{z}}(\mathbf{r})$ and analogously

at the xz-plane. This symmetry determines the net force via

$$\begin{aligned} F_{\mathrm{net,x}} &= \oint F_{\mathrm{x}} dA = \int_{y>y_{\mathrm{c}}} F_{\mathrm{x}} dA + \int_{y<y_{\mathrm{c}}} F_{\mathrm{x}} dA \\ &= \int_{y>y_{\mathrm{c}}} F_{\mathrm{x}} dA - \int_{y>y_{\mathrm{c}}} F_{\mathrm{x}} dA = 0 \end{aligned} \tag{49}$$

$$\begin{aligned} F_{\mathrm{net,y}} &= \oint F_{\mathrm{y}} dA = \int_{x>x_{\mathrm{c}}} F_{\mathrm{y}} dA + \int_{x<x_{\mathrm{c}}} F_{\mathrm{y}} dA \\ &= \int_{x>x_{\mathrm{c}}} F_{\mathrm{y}} dA - \int_{x>x_{\mathrm{c}}} F_{\mathrm{y}} dA = 0 \end{aligned} \tag{50}$$

$$\begin{aligned} F_{\mathrm{net,z}} &= \oint F_{\mathrm{z}} dA = \int_{x>x_{\mathrm{c}}} F_{\mathrm{z}} dA + \int_{x<x_{\mathrm{c}}} F_{\mathrm{z}} dA \\ &= \int_{x>x_{\mathrm{c}}} F_{\mathrm{z}} dA - \int_{x>x_{\mathrm{c}}} F_{\mathrm{z}} dA = 0 \end{aligned} \tag{51}$$

whereby $\int_{y>y_{\mathrm{c}}} dA$ denotes an integration over the half sphere on the side of the xz-plane with $y > y_{\mathrm{c}}$ (other integrals analogue). The symmetries show that the force on one half of the sphere is minus the force on the other half, so that the net forces is zero without a gradient. Thus the capsule displays no CSM.

If a gradient is applied the symmetry is broken: If the gradient is oriented parallel to the flow $\mathbf{G}_\eta \parallel \hat{\mathbf{e}}_{\mathrm{x}}$ (cf. fig. 3 (b)) then the friction at the upstream half of the capsule is smaller than at the downstream half. But the magnitude of the friction still has a symmetry plane given by $\hat{\mathbf{e}}_{\mathrm{z}}$ and $\hat{\mathbf{e}}_{\mathrm{x}}$. Thus the symmetry used in eqn (50) is broken, but eqns (49) and (51) still hold true. Therefore the net force is oriented in y-direction $\mathbf{F}_{\mathrm{net}} \parallel \hat{\mathbf{e}}_{\mathrm{y}}$ which is perpendicular to the flow. Hence a net forces acts on a capsule in presence of a gradient if we assume that the capsule moves as it does without gradient. This leads to a CSM. If the viscosity gradient is oriented perpendicular to the flow $\mathbf{G}_\eta \parallel \hat{\mathbf{e}}_{\mathrm{y}}$ the situation is similar (see fig. 3 (c)): The symmetry used in eqn (49) is broken by the gradient but not eqns (50) and (51). Thus the resulting force is parallel to the flow. This leads to a migration in the flow's direction, which means no CSM is found. If the viscosity gradient is oriented perpendicular to the shear plane $\mathbf{G}_\eta \parallel \hat{\mathbf{e}}_{\mathrm{z}}$ the symmetries to the xz- or yz-plane are not broken. Hence all the eqns (49), (50) and (51) hold true in this case and the symmetry prevents a net force.

The behavior of the capsule differs if it is soft. The main difference to the rigid capsule is the elliptical shape, because the deformed shape is not symmetric to the xz- or yz-plane. But the deformed shape and the shear flow have both a point symmetry to the capsules center and a symmetry to the xy-plane. These both symmetries lead also to a symmetry to the z-axis. Thus the friction force has the same symmetry: At the position $\mathbf{r}$ and is mirrored position at the capsules center $\mathbf{r}'$ the friction force fulfills $F_{\mathrm{x}}(\mathbf{r}') = -F_{\mathrm{x}}(\mathbf{r})$ and $F_{\mathrm{y}}(\mathbf{r}') = -F_{\mathrm{y}}(\mathbf{r})$. Thus eqns (49) and (50) can also be used in case of a deformable capsule. Furthermore the flow is invariant in z-direction which prevents a force in z-direction. Thus $\mathbf{F}_{\mathrm{net}} = 0$ without gradient.

If a gradient parallel to the flow $\mathbf{G}_\eta \parallel \hat{\mathbf{e}}_{\mathrm{x}}$ is applied then the point symmetry is broken, eqns (49) and (50) do not apply and a net force with x- and y-component is found. The translational invariance in z-direction is not broken so that the net force has no z-component. Thus we also find a CSM of a soft capsule in y-direction (cf. fig. 3 (b)). Also if the gradient is perpendicular to the flow $\mathbf{G}_\eta \parallel \hat{\mathbf{e}}_{\mathrm{y}}$ the point symmetry is broken and eqns (49) and (50) can not be used: Both the x- and y-component of $\mathbf{F}_{\mathrm{net}}$ are not zero (cf. fig. 3 (c)). The

force is oriented towards the lower viscosity which leads to a CSM towards the lower viscosity. This is different to the rigid capsule whose symmetry prevented a force in y-direction and a CSM. Also the behavior in presence of a gradient perpendicular to the shear plane $\mathbf{G}_\eta \parallel \hat{\mathbf{e}}_\mathrm{z}$ is different. The symmetry to the z-axis exists also with a gradient in z-direction. Therefore eqns (49) and (50) still hold true, so that the net force has no x- and y-component. But $\mathbf{G}_\eta \parallel \hat{\mathbf{e}}_\mathrm{z}$ breaks the translational invariance and the ellipsoidal shape prevents the symmetry to the xz- and yz-plane used in case of the rigid, spherical capsule to derive eqn (51). This makes a net force in z-direction possible.

4 Simulations of CSM in a shear flow driven by a moving plate with different orientations of the gradient

In the main text we showed the results obtained with a gradient in the shear plane and perpendicular to the flow. Here we show also the other orientations, i.e. a gradient parallel to the flow and perpendicular to the shear plane.

The CSM velocity $v_{m,y}$ as function of the gradient is shown in fig. 4. We discuss at first a gradient in flow direction $\widetilde{\mathbf{G}}_\eta = \widetilde{\mathrm{G}}_{\eta,\mathrm{x}}\hat{\mathbf{e}}_\mathrm{x}$. We use here a stiff capsule to demonstrate that in this case also a migration with a rigid capsule is found. The migration velocity is determined at $x_\mathrm{c} = 0$ with $\eta(\mathbf{r}_\mathrm{c}) = \eta_0$. Figure 4 shows that we find a migration of a stiff capsule which is induced by the gradient (cf. fig 3). The direction of the CSM depends on the flow's direction in this case.

Besides the viscosity gradient in flow direction also a gradient perpendicular to the flow can be applied, either in the shear plane (y-direction) or perpendicular to it (z-direction). We use a soft capsule in these cases. For the sake of completeness we use the flow given by eqn (7) if the gradient is pointing from one plate to the other, but the influence of the flow's small nonlinearity on the migration is negligible (see fig. 2). A gradient inside the shear plane and perpendicular to the flow $\widetilde{\mathbf{G}}_\eta = \widetilde{\mathrm{G}}_{\eta,\mathrm{y}}\hat{\mathbf{e}}_\mathrm{y}$ leads also to a CSM inside the shear plane $v_{m,y} \neq 0$ and is directed towards the lower viscosity (see main text). A viscosity gradient perpendicular to the shear plane $\widetilde{\mathbf{G}}_\eta = \widetilde{\mathrm{G}}_{\eta,z}\hat{\mathbf{e}}_\mathrm{z}$ induces a CSM perpendicular to the shear plane $v_{m,z} \neq 0$. The CSM is also directed towards the lower viscosity.

Furthermore fig. 5 shows the dependence of the migration on the stiffness of the capsule for different orientations of the viscosity gradient. If the gradient is parallel to the flow the migration velocity increases with the stiffness. The effect occurs both for stiff, i.e. spherical and soft capsules. This is different in case of a gradient perpendicular to the flow: The CSM decreases with increasing stiffness and vanishes at a high stiffness $\mathrm{Ca} \ll 1$. Thus the deformation is necessary for the migration if the gradient is perpendicular to the flow, but not if the gradient is parallel (cf. fig. 3).

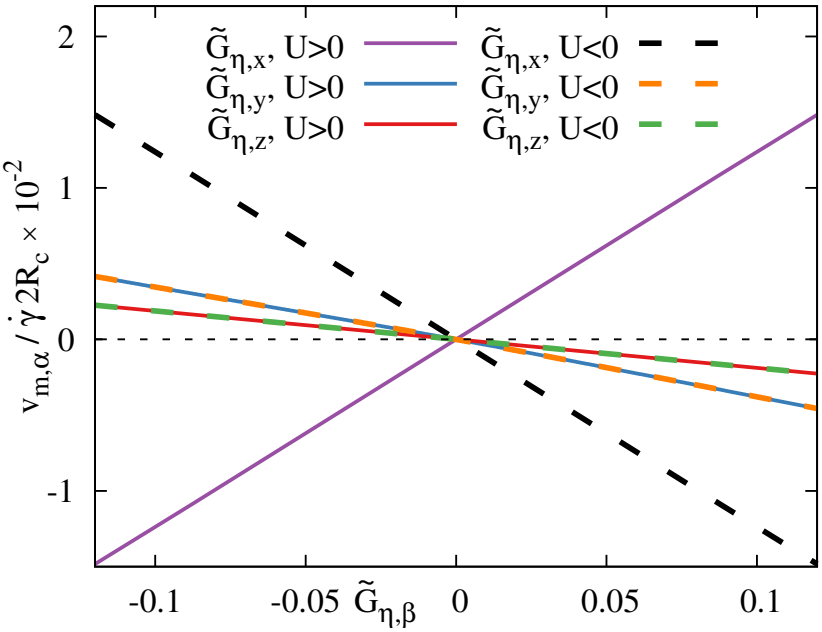

Figure 4: The migration velocity $v_{m,\alpha}$ as function of the viscosity gradient $G_{\eta,\beta}$ in flows in positive and negative x-direction. The plot shows the nonzero component of the CSM velocity. If the gradient is parallel to the flow $\widetilde{\mathbf{G}}_\eta = \widetilde{\mathrm{G}}_{\eta,\mathrm{x}}\hat{\mathbf{e}}_\mathrm{x}$ we find a CSM of a stiff capsule in the shear plane $v_{m,y} \neq 0$ and the sign of $v_{m,y}$ depends on the flow's direction. If the capsule is soft and the gradient is perpendicular to the flow and we find a CSM towards the lower viscosity, which means $v_{m,y} \neq 0$ with $\widetilde{\mathbf{G}}_\eta = \widetilde{\mathrm{G}}_{\eta,\mathrm{y}}\hat{\mathbf{e}}_\mathrm{y}$ and $v_{m,z} \neq 0$ with $\widetilde{\mathbf{G}}_\eta = \widetilde{\mathrm{G}}_{\eta,\mathrm{z}}\hat{\mathbf{e}}_\mathrm{z}$. The direction of the CSM is independent of the flows direction if $\widetilde{\mathbf{G}}_\eta$ is perpendicular to the flow. We use the parameters: $G_s = 0.2$ (soft capsule), $G_s = 10.0$ (stiff capsules)

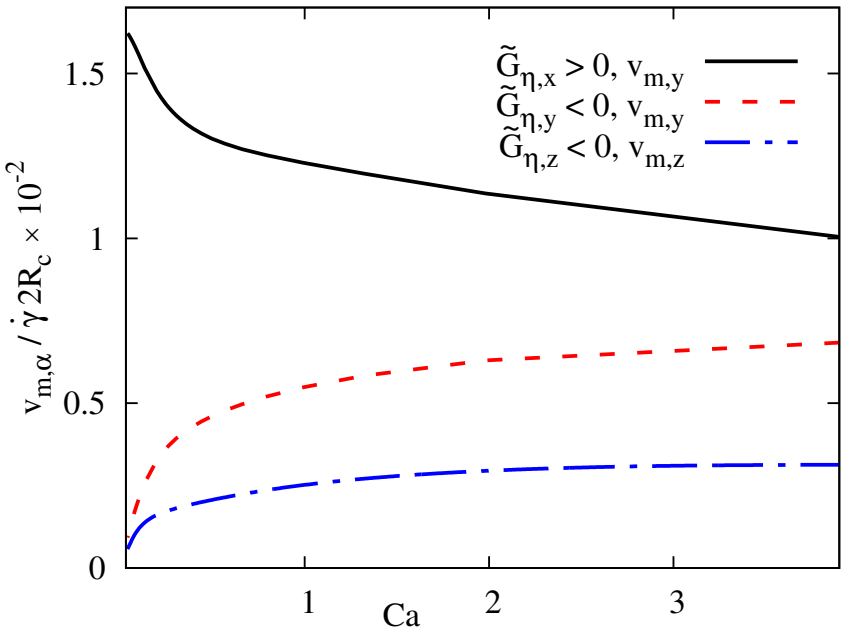

Figure 5: The migration velocity $v_{m,y}$ or $v_{m,z}$ as function of the capillary number Ca (see eqn (14)) of the capsule for different orientations of $\widetilde{\mathbf{G}}_\eta$. If the gradient is parallel to the flow $\widetilde{\mathbf{G}}_\eta = \widetilde{\mathrm{G}}_{\eta,\mathrm{x}}\hat{\mathbf{e}}_\mathrm{x}$ the migration velocity increases with the stiffness and the effect is found for both stiff and soft capsules. If the gradient is perpendicular to the flow ($\widetilde{\mathbf{G}}_\eta = \widetilde{\mathrm{G}}_{\eta,\mathrm{y}}\hat{\mathbf{e}}_\mathrm{y}$, $\widetilde{\mathbf{G}}_\eta = \widetilde{\mathrm{G}}_{\eta,\mathrm{z}}\hat{\mathbf{e}}_\mathrm{z}$) the migration vanishes at a high stiffness $\mathrm{Ca} \ll 1$ (cf. fig. 3).

References

[1] M. Doi and S. F. Edwards, *The Theory of Polymer Dynamics* (Clarendon Press, Oxford, 1986).

[2] S. K. Doddi and P. Bagchi, Int. J. Multiphas. Flow **34**, 966 (2008).

Publication 7

Noise-controlled particle focusing in Poiseuille flows
M. Laumann, S. Schreiber, W. Zimmermann,

draft

Noise-controlled particle focusing in Poiseuille flows

Matthias Laumann, Steffen Schreiber, Walter Zimmermann
Theoretische Physik I, Universität Bayreuth, D-95440 Bayreuth, Germany

Abstract. The dynamics of semi-flexible bead-spring models, which are a model of semi-flexible polymers or fibers, in plane and circular Poiseuille flows is investigated. In unbounded plane Poiseuille flows, semi-flexible polymers migrate either to a stable distance to the center of the flow profile, i.e. to an attractor, or keep migrating away from the center, depending on the initial conditions. This stable distance exists in the limit of small noise only below a certain bending stiffness, which increases with the shear rate. Surprisingly, the parameter range of the existence of the attractors increases with increasing noise strength, what can be explained by the increased deformations of the polymer. If the hydrodynamic interactions with bounding walls are taken into account, additional attractors emerge. In the limit of medium values of the bending elasticity and small noise amplitudes one finds three attractors coexisting in each half of a plane Poiseuille flow. With increasing thermal noise two of these attractors are connected to one so that two attractors are found in this case. Therefore, noise is an essential key to understand the dynamics of semi-flexible polymers and fibers in Poiseuille flows. A possible application of the coexistence of different attractor is the sorting of semiflexible polymers or fibers, e.g., with respect to their stiffness.

1. Introduction

Understanding the behavior of small particles in flows, including spheres, vesicles, fibers and macromolecules plays a central role in fundamental and applied science for a long time. Therefore, many studies deal with inhomogeneous particle distributions in flows. We discuss here a surprising example.

One reason of an inhomogeneous particle distributions was early reported by Silberberg. Particles focus between the wall and the center of the pipe flow [1, 2] due to the so-called Silberberg-effect, which depends strongly on inertia [3, 4, 5]. Furthermore observations about enhanced polymer concentrations near channel walls [6] triggered early polymer kinetic theories for bead-spring chain models in inhomogeneous flows, including hydrodynamic interactions between beads, but not accounting for the change in hydrodynamic interactions due to the presence of walls [7, 8, 9]. For the overdamped motion of vesicles near walls in shear flows lift forces were predicted [10, 11] and measured [12] and later on also for flexible polymers in simulations [13] and experiments [14]. In the range where wall effects can be neglected, droplets are expect to migrate away from the center of an unbounded Poiseuille flow [15], whereas for vesicles it was shown that they migrate to the center [16].

There are also many examples of particles that migrate in a Poiseuille flow to a stable distance to the center. For vesicles also a symmetry breaking transition to the so-called slipper state was found with the center of mass slightly aside the center of the Poiseuille flow [17]. For Brownian fibers a small off-center concentration peak was predicted [18, 19] and recently an off-center distribution of actin filaments was reported [20, 21]. The distribution of the center of mass of semi-flexible polymers with off-center distribution maxima were found in simulations [22, 23, 24, 25] where the boundary effects are expected to be important for the location of these maxima.

Also non-Brownian flexible fibers of constant length display a cross-stream migration in a planar Poiseuille flow [26, 27, 28]. The fibers migrate to one of up to two stable off-center attractor stream lines (two in each half of the channel). It is possible that the presence of a thermal noise affects the migration of the fibers. Furthermore some polymers and certain fibers are extensible and can change their lengths [29]. Therefore it is an important question from the fundamental point of research as well as with regards to applications how the migration of semi-flexible fibers and polymers to defined distances to the center of a Poiseuille flow is affected by thermal noise and whether the extensibility influences the migration.

To answer these questions, we simulate Brownian fibers or polymers with a bead-spring model. This is explained in section 2.

We explore in section 3.1 the cross-stream migration of a semi-flexible bead-spring model in unbounded Poiseuille flow. In the absence of boundary effects it either reaches a stationary distance to the center of the plane Poiseuille flow or keeps migrating away from the center, depending on the initial condition. We show that this attractor exists only below a threshold of the bending stiffness without or with small thermal noise

but exists at a large range of values of the bending stiffness with higher thermal noise. Hence the thermal noise can extend the range of existence of an attractor. Besides this attractor we find surprisingly at low noise a repeller. We furthermore show how the attractor and repeller depend on the parameters by varying the thermal noise, the bending stiffness and the flow velocity. Furthermore we show that the bending angle determines the migration direction, which allows to explain the number of attractors and repellers.

In section 3.2 we show the existence of three attractors (in each half of the channel) in presence of walls in Poiseuille flows at low noise. Also the dependence of all attractors on the bending stiffness is shown, as well as the vanishing of an attractor in case of stronger noise.

2. Model

We analyze the motion and the shape deformation of a single semi-flexible polymer, moving freely either in a plane Poiseuille flow in $\hat{\boldsymbol{x}}$ direction:

$$\boldsymbol{u}(\boldsymbol{r}) = u_0 \left(1 - \frac{z^2}{d^2}\right) \hat{\boldsymbol{x}} \tag{1}$$

with two planes at $z = \pm d$ or in circular Poiseuille flow

$$\boldsymbol{u}(\boldsymbol{r}) = u_0 \left(1 - \frac{y^2 + z^2}{d^2}\right) \hat{\boldsymbol{x}} \tag{2}$$

through a pipe with radius d.

For the N beads at the positions of the bead spring model

$$\mathbf{r}_i = (x_i, y_i, z_i) = r_i \hat{\mathbf{r}}_i \quad \text{with} \quad r_i = |\mathbf{r}_i| \quad (i = 1 \dots N)\,, \tag{3}$$

we assume a harmonic potential with respect to the distances between next nearest-neighbor beads along a chain,

$$V_{\text{str}} = \frac{k}{2} \sum_{i=1}^{N-1} [b - r_{ij}]^2 \qquad \text{with} \qquad j = i + 1 \tag{4}$$

This includes the bead-bead connection vector

$$\mathbf{r}_{ij} = \mathbf{r}_i - \mathbf{r}_j\,, \tag{5}$$

and the related bead-bead distance $r_{ij} = |\mathbf{r}_i - \mathbf{r}_j|$, the spring constant k and the equilibrium distance b between two neighboring beads.

A semi-flexible bead-spring model resists bending and we describe this by the bending potential [30]

$$V_{\text{b}} = -\frac{\kappa}{2} \sum_{i=2}^{N-1} \ln\left(1 + \cos\beta_i\right) \tag{6}$$

with the bending constant κ and relaxation time $\tau = \zeta b^2/\kappa$, the inner product

$$\cos(\beta_i) = \hat{\boldsymbol{r}}_{(i-1)i} \cdot \hat{\boldsymbol{r}}_{i(i+1)} \tag{7}$$

and the unit vectors $\hat{\mathbf{r}}_i = \mathbf{r}_i/|\mathbf{r}_i|$. In addition, a truncated Lennard-Jones potential [30, 31]

$$V_{\mathrm{LJ}} = \varepsilon \sum_{i=1}^{N-1} \sum_{j=i+1}^{N} \left[\frac{1}{2} \left(\frac{r_{LJ}}{r_{ij}} \right)^{12} - \left(\frac{r_{LJ}}{r_{ij}} \right)^{6} \right] \Theta(r_{LJ} - r_{ij}) \tag{8}$$

with the strength ε and the cut-off length r_{LJ} is used in order to avoid overlapping beads.

These potentials are the sources of the three deterministic forces, i.e., the stretching force $\boldsymbol{F}_j^{\mathrm{str}}$, the bending force $\boldsymbol{F}_j^{\mathrm{b}}$, and the short range repulsion force $\boldsymbol{F}_j^{\mathrm{LJ}}$ which act on the beads. Together with the flow field $\mathbf{u}(\mathbf{r}_i)$ at the bead-positions $\mathbf{r}_i$ the over-damped dynamics of the bead spring model is described by the Langevin equations

$$\dot{\boldsymbol{r}}_i = \boldsymbol{u}(\boldsymbol{r}_i) + \mathsf{H}_{ij} \left[\boldsymbol{F}_j^{\mathrm{str}} + \boldsymbol{F}_j^{\mathrm{b}} + \boldsymbol{F}_j^{\mathrm{LJ}} \right] + \boldsymbol{F}_j^{\mathrm{s}} \tag{9}$$

with the mobility matrix H_{ij} and the stochastic contribution $\boldsymbol{F}_j^{\mathrm{s}}$ as described in the following.

In the presence of a plane wall with no-slip boundary condition for the fluid at the wall, we use the mobility matrix as given by the Blake tensor [32]

$$\mathsf{H}_{ij}(\boldsymbol{r}_i, \boldsymbol{r}_j) = {}^{S}\mathsf{H}_{ij}(\boldsymbol{r}_i, \boldsymbol{r}_j) - {}^{S}\mathsf{H}_{ij}(\boldsymbol{r}_i, \boldsymbol{r}'_j) + {}^{D}\mathsf{H}_{ij}(\boldsymbol{r}_i, \boldsymbol{r}'_j) - {}^{SD}\mathsf{H}_{ij}(\boldsymbol{r}_i, \boldsymbol{r}'_j)\,, \tag{10}$$

where $\boldsymbol{r}'_j = (x_j, y_j, -z_j)$ is the position of the mirror image of a bead j at the opposite side of the boundary. The first contribution to H_{ij} accounts for the hydrodynamic interaction (HI) in the bulk of an unbounded domain described by the Oseen tensor [33],

$${}^{S}\mathsf{H}_{ij}^{\alpha\beta}(\boldsymbol{r}_i, \boldsymbol{r}_j) = \begin{cases} \frac{1}{8\pi\eta r_{ij}} \left(\delta_{\alpha\beta} + \dfrac{r_{ij}^{\alpha} r_{ij}^{\beta}}{r_{ij}^2} \right) & \text{for } i \neq j\,, \\ \frac{1}{6\pi\eta a}\, \delta_{\alpha\beta} & \text{for } i = j \end{cases} \tag{11}$$

with $\alpha, \beta = x, y, z$, the viscosity η and the Stokes friction coefficient $\zeta = 6\pi\eta a$. The second contribution to the HI between the beads includes the mirror images of the beads

$${}^{S}\mathsf{H}_{ij}^{\alpha\beta}(\boldsymbol{r}_i, \boldsymbol{r}'_j) = \frac{1}{8\pi\eta\tilde{r}_{ij}} \left(\delta_{\alpha\beta} + \frac{\tilde{r}_{ij}^{\alpha} \tilde{r}_{ij}^{\beta}}{\tilde{r}_{ij}^2} \right)\,. \tag{12}$$

with the distances

$$\tilde{\boldsymbol{r}}_{ij} = \boldsymbol{r}_i - \boldsymbol{r}'_j = \tilde{r}_{ij} \hat{\tilde{\boldsymbol{r}}}_{ij} \tag{13}$$

between the beads and their mirror images, where the components of the vectors $\boldsymbol{r}_{ij}$ and $\tilde{\boldsymbol{r}}_{ij}$ are denoted by r_{ij}^{α} and $\tilde{r}_{ij}^{\alpha}$ with $\alpha = x, y, z$. In eq. (10) the contribution

$${}^{D}\mathsf{H}_{ij}^{\alpha\beta}(\boldsymbol{r}_i, \boldsymbol{r}'_j) = \frac{1}{4\pi\eta\tilde{r}_{ij}^3}\, z_j^2 (1 - 2\delta_{\beta z}) \left(\delta_{\alpha\beta} - 3\frac{\tilde{r}_{ij}^{\alpha} \tilde{r}_{ij}^{\beta}}{\tilde{r}_{ij}^2} \right) \tag{14}$$

is the Stokes doublet (D) and

$${}^{SD}\mathsf{H}_{ij}^{\alpha\beta}(\boldsymbol{r}_i, \boldsymbol{r}'_j) = \frac{z_j(1 - 2\delta_{\beta z})}{4\pi\eta\tilde{r}_{ij}^3} \left(\delta_{\alpha\beta}\tilde{r}_{ij}^{z} - \delta_{\alpha z}\tilde{r}_{ij}^{\beta} + \delta_{\beta z}\tilde{r}_{ij}^{\alpha} - 3\frac{\tilde{r}_{ij}^{\alpha} \tilde{r}_{ij}^{\beta} \tilde{r}_{ij}^{z}}{\tilde{r}_{ij}^2} \right) \tag{15}$$

is the source doublet (SD). In our numerical calculations higher order corrections to H_{ij} due to the finite size of the spheres are included via the method of reflections and Faxén's law [33, 34, 35, 36].

In order to take the effects of hydrodynamic interactions with two opposing parallel and no-slip walls into account in a plane Poiseuille flow, we consider the linear superposition of the effects of two single walls. According to [37], this is a reasonable approximation, when the ratio between the wall-wall distance and the particle extension becomes larger than 5.

The thermal noise [33, 38, 39] has a vanishing mean value and the amplitude is determined by the fluctuation dissipation theorem [40, 41]

$$\left\langle \boldsymbol{F}_j^{\mathrm{s}}(t) \right\rangle = 0\,, \qquad \left\langle \boldsymbol{F}_i^{\mathrm{s}}(t) \boldsymbol{F}_j^{\mathrm{s}}(t') \right\rangle = 2k_{\mathrm{B}} T \mathsf{H}_{\mathrm{ij}} \delta(\mathsf{t} - \mathsf{t}') \tag{16}$$

with Boltzmann's constant k_B and the temperature T.

We choose the effective bead radii $a = 1$, the equilibrium bead-bead distance $b = 5$, the bending constant $\kappa = 8$ and the Hookean spring constant $k = 5$. Furthermore, we set the Stokes friction coefficient $\zeta = 0.5$, which implies the viscosity $\eta = \frac{1}{12\pi}$ of the fluid. For the parabolic flow profile, we use the maximal flow velocity $u_0 = 900$ and $d = 100$ as the half width of the channel, respectively the channel radius. The typical chain lengths in our considerations are $2b$ with $N = 3$. For the cut-off length of the Lennard-Jones potential we have chosen $r_{LJ} = 1.1$ an for the strength $\varepsilon = 100$ in order to prevent overlapping of the beads. We solve the equations numerically with an Euler algorithm with a timestep of $\Delta t = 0.0005$. If not stated otherwise we use these parameters.

It is useful to utilize dimensionless parameters. The bending stiffness κ acts against the bending caused by the curvature of the flow profile, which is given by $c = |\partial_y^2 u_0(y)| = 2u_0/d^2$. Therefore a dimensionless measure of the bending stiffness is given by

$$S = \frac{\kappa}{\zeta b^3} \frac{2u_0}{d^2}\,. \tag{17}$$

It is varied via κ in this study. The strength of the thermal noise is given by $E_T = k_b T/\kappa$ (determined with the reference value $\kappa = 8$) and is varied with $k_b T$.

Since the major focus of this work is the exploration of the cross-stream migration, we restrict the bead dynamics for reasons of simplicity to the shear plane in the case of a plane Poiseuille flow. However, the chains are free to move in all directions in the case of an unbounded circular Poiseuille flow.

3. Results on cross-stream migration of semi-flexible bead-spring polymers

In section 3.1 the cross-stream migration of semi-flexible bead-spring models, which are a model of semi-flexible polymers and fibers, are investigated in absensence and in the presence of noise. We show the migration to a stable distance to the center, how this distance depends on the presence of low or high noise and we explain the direction of the migration with the maximal deformation of the particle. The effects of hydrodynamic interactions between the particle and the boundaries on the cross-stream migration are analyzed in section 3.2.

3.1. Cross-stream migration in unbounded Poiseuille flow

Figure 1 (a) shows the lateral position $y_c\,/\,2b$ as a function of time with the noise amplitude $E_T = 1.3 \cdot 10^{-12}$ for three different lateral initial positions. A particle initially oriented parallel to the flow lines becomes inclined due to the thermal noise. This inclination leads to a flip of the particle because of the shear rate. These flips cause a cross stream line migration: Particles with initial positions closer to the center migrate to an attractor located at $y_c\,/\,2b \approx 2$. Particles located further away from the center of an unbounded parabolic flow migrate even further away from it. The positions where particles migrate to the attractor or just further away from the flow center are separated by an repeller at $y_c\,/\,2b \approx 6$. Particles initially started in the other half of the flow profile

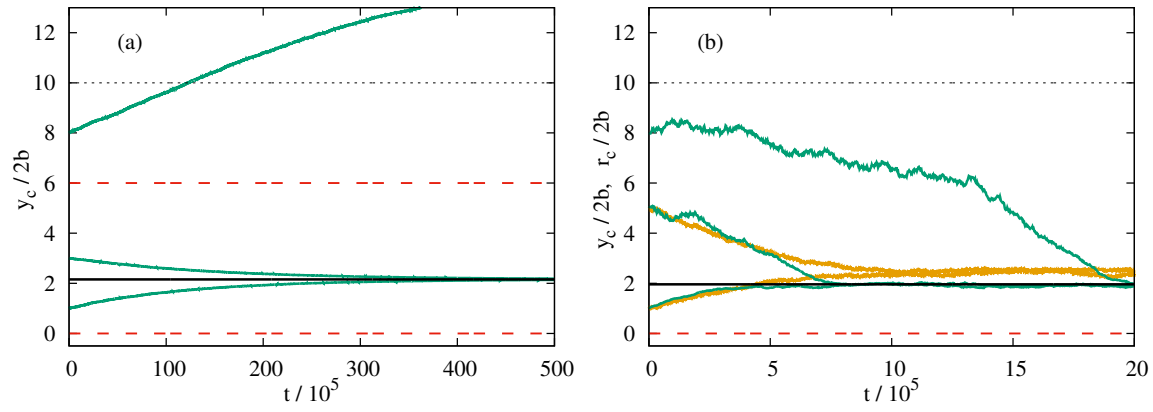

Figure 1. The lateral position $y_c\,/\,2b$ of a bead-spring model as a function time in parabolic flow profiles is shown for three different initial positions (green ——) with $S = 0.48$. (a) shows the motion at lower thermal noise $E_T = 1.3 \cdot 10^{-12}$. The both particles closer to the center migrate to an attractor located at $y_c\,/\,2b \approx 2$ (black ——). The particles further away migrate even further away from the center. This shows the existence of an off-center repeller (red - - - -), which is located at $y_c\,/\,2b \approx 6$. (b) shows a different behavior in case of higher thermal noise $E_T = 6 \cdot 10^{-8}$ (green ——). All initial positions lead to a migration to the attractor at $y_c\,/\,2b \approx 2$ (black - - - -line) and the off-center repeller does not exist at a higher thermal noise. Also the radial positions $r_c\,/\,2b$ (yellow ——) in a circular tube flow are shown. The attractor is slightly shifted but the qualitative behavior is the same as in a planar flow.

(at $y_c < 0$) migrate to an attractor located at $y_c\,/\,2b \approx -2$ due to the symmetry (or migrate further away from the center). This implies that the center is also a repeller.

Figure 1 (b) shows a different behavior in case of a higher thermal noise $E_T = 6 \cdot 10^{-8}$. All initial positions lead to a migration to the attractor at $y_c\,/\,2b \approx 2$. This means the off-center repeller does not exist in case of the higher thermal noise. We also show the radial position $r_c\,/\,2b$ in case of a circular tube flow. The attractor is slightly shifted away from the center but the qualitative behavior is similar to a planar flow. Thus the result is robust and does not rely on the planar Poiseuille flow.

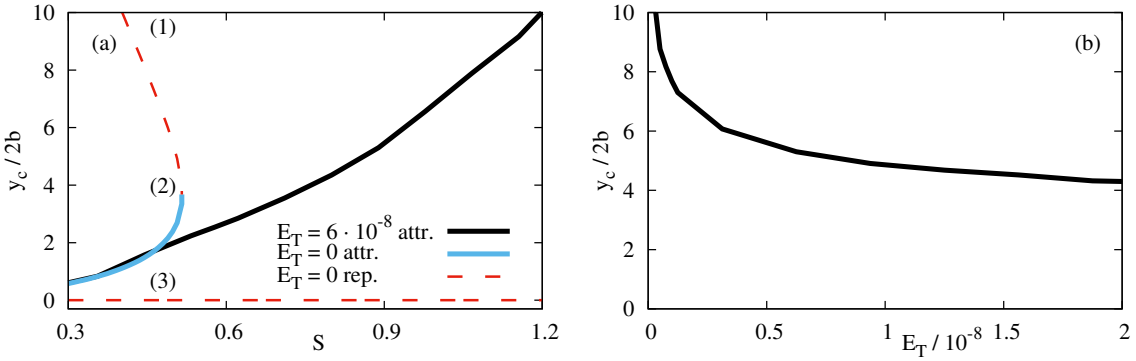

Figure 2. (a) shows the position $y_c\,/\,2b$ of the attractor (blue ——) and the repellers (red - - - -) in an unbounded plane Poiseuille flow as a function of the stiffness S without thermal noise and with a higher thermal noise $E_T = 6 \cdot 10^{-8}$ (black ——). Without thermal noise, the attractor and the off-center repeller exist only below a critical value $S < S_c$ with $S_c \approx 0.5$. The dynamics of particle at the positions marked by (1)-(3) are shown in figure 3. Particles with a stiffness above S_c migrate at all positions away from the center. With $E_T = 6 \cdot 10^{-8}$, no off-center repeller is found and the attractor is found at all values of S. (b) shows how the attractor with $S = 0.7$ depends on the noise strength E_T: The attractor is shifted towards the center with increasing noise amplitude.

We further investigate how the position of the attractor and repeller depend on the parameters. In case of low thermal noise or without thermal noise, the position of the attractor and the repeller can be determined with single flips. At higher values of the thermal noise the position is determined with full trajectories, as shown in figure 1 (cf. Appendix A.1). The position of the attractor and repellers in dependence of S are depicted in figure 2 (a). We discuss at first the case without thermal noise: With increasing values of S the attractor's distance to the center increases and the off-center repeller's distance to the center decreases. Above a critical value of $S > S_c \approx 0.5$ the attractor and off-center repeller vanishes and the particles migrate at all positions away from the center. This behavior changes with an increased value of $E_T = 6 \cdot 10^{-8}$. We find no off-center repeller and the attractor exists at all values of S. The positions of the attractor and the repellers without noise agree with lower thermal noise $E_T = 1.3 \cdot 10^{-12}$ (used in figure 1).

Figure 2 (b) shows how the attractor with $S = 0.7$ depends on the noise strength E_T: With increasing values of E_T the attractor is shifted towards the center. This

means the strength of the noise has a high influence on the migration of the particle.

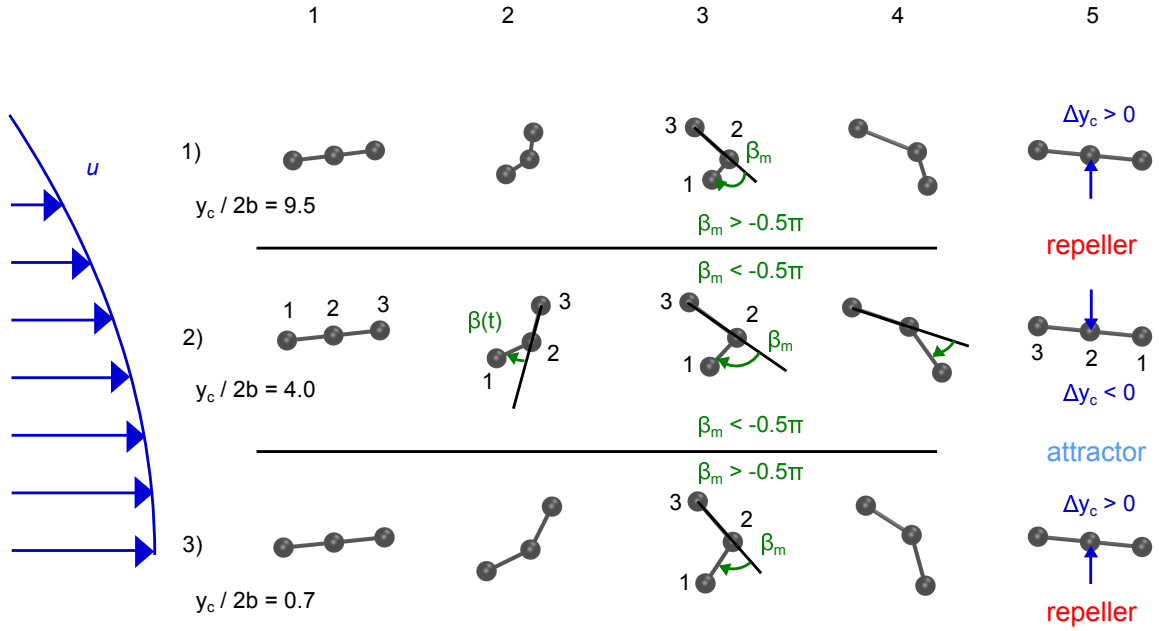

Figure 3. The stages of a flip for different initial positions without thermal noise with $S = 0.48$ (cf. figure 2). Also the angle β is given that measures the deformation and its maximal value β_m during the flip. The particle turns around and is bent by the spatially dependent shear rate. At $y_c\,/\,2b = 0.7$ we find $\beta_m = -0.45\pi$ and a migration away from the center, at $y_c\,/\,2b = 4.0$ we get $\beta_m = -0.55\pi$ and a step towards the center and $y_c\,/\,2b = 9.5$ results in $\beta_m = -0.47\pi$ and a step away from the center. This reflects the migration to the attractor or away from the repeller shown in figure 2. The reason of the different migration steps are the different maximal deformation angles β_m.

We further give an explanation why the attractor and the off-center repeller vanishes at high values of S. For this purpose, we study the deformation of the particle during a flip without thermal noise. Figure 3 shows the stages of a flip of a particle for three different initial positions: below the attractor, above the attractor and above the off-center repeller (marked in figure 2). The shear rate rotates the particle which has initially a small inclination. The spatially dependent shear rate leads also to a bending of the particle and not merely to a simple rotation. We number the beads to describe the rotation whereby bead 1 is the closest to the center (cf. figure 3). At the beginning of a flip bead 3 moves behind bead 2 in x-direction due to the lower flow velocity at its position. The difference of the flow velocity of bead 1 and 2 is lesser than of bead 3 and 2 because of the spatially dependent shear rate. This leads to a bending of the particle. The bending potential acts against the bending by moving bead 1 past bead 2. At the end of the flip all beads are aligned with the streamline.

To measure the deformation we define the angle β as shown in the figure, which measures the deviation from a straight line. The angle β_m is defined as the value of $\beta(t)$ with the maximal absolute value during the flip. We find that the values of the maximum

deformation angle β_m are closely connected to the direction of the migration. The values of β_m and the migration direction at the three initial positions (with increasing distance to the center) are $\beta_m = -0.45\pi$ with a migration away from the center, $\beta_m = -0.55\pi$ with a migration towards the center and $\beta_m = -0.47\pi$ with a migration away from the center. We get a migration away from the center if approximately $-0.5\pi \lessapprox \beta_m \lessapprox 0$ and a migration towards the center if $\beta_m \lessapprox -0.5\pi$. In the other half of the flow profile (at $y_c < 0$) β_m is positive and the direction of the migration follows from the symmetry of the flow profile. This results in

$$\begin{aligned} &\Delta y_c > 0 \text{ at } -0.5\pi \lessapprox \beta_m \lessapprox 0 \;,\; 0.5\pi \lessapprox \beta_m \,, \\ &\Delta y_c < 0 \text{ at } \beta_m \lessapprox -0.5\pi \qquad\quad ,\; 0 \lessapprox \beta_m \lessapprox 0.5\pi \,. \end{aligned} \tag{18}$$

This means the migration is directed away from the center at small deformations $|\beta_m| < 0.5\pi$ and towards the center at high deformations $|\beta_m| > 0.5\pi$.

This interplay between the maximum deformation angle β_m and the sign of the migration step is shown in figure 4. The figure shows the angle β_m of the maximum deformation and the migration step after one flip Δy_c as function of the initial position of y_c. With $S = 0.35 < S_c$ (see figure 4 (a)), the bending angle β_m is small $|\beta_m| < 0.5\pi$ close to the center and the particle migrates away from the center. Further away from the center the deformation is larger with $|\beta_m| > 0.5\pi$ and the migration step Δy_c is directed towards the center. This explains the attractor. Also the behavior with the high value of S can be understood with this criterion (see figure 4 (b)). Due to high value of $S = 0.58 > S_c$ the deformation is always small and $|\beta_m| < 0.5\pi$ holds true at all initial positions. This means that the migration is always directed away from the center. This explains that the attractor vanishes at high values of the stiffness S.

We can now compare $S = 0.58 > S_c$ with and without thermal noise (see figure 4 (b) and (c)). With thermal noise we calculate the average of the maximal deformation $\langle \beta_m \rangle$ with a sufficient number of flips. The deformation during the flip is increased by the noise: Values of $|\langle \beta_m \rangle| > 0.5\pi$ occur, despite of $S = 0.58 > S_c$, which lead to the attractor.

If the number N of the beads is increased we find similar dynamics of the particle (see supplementary information).

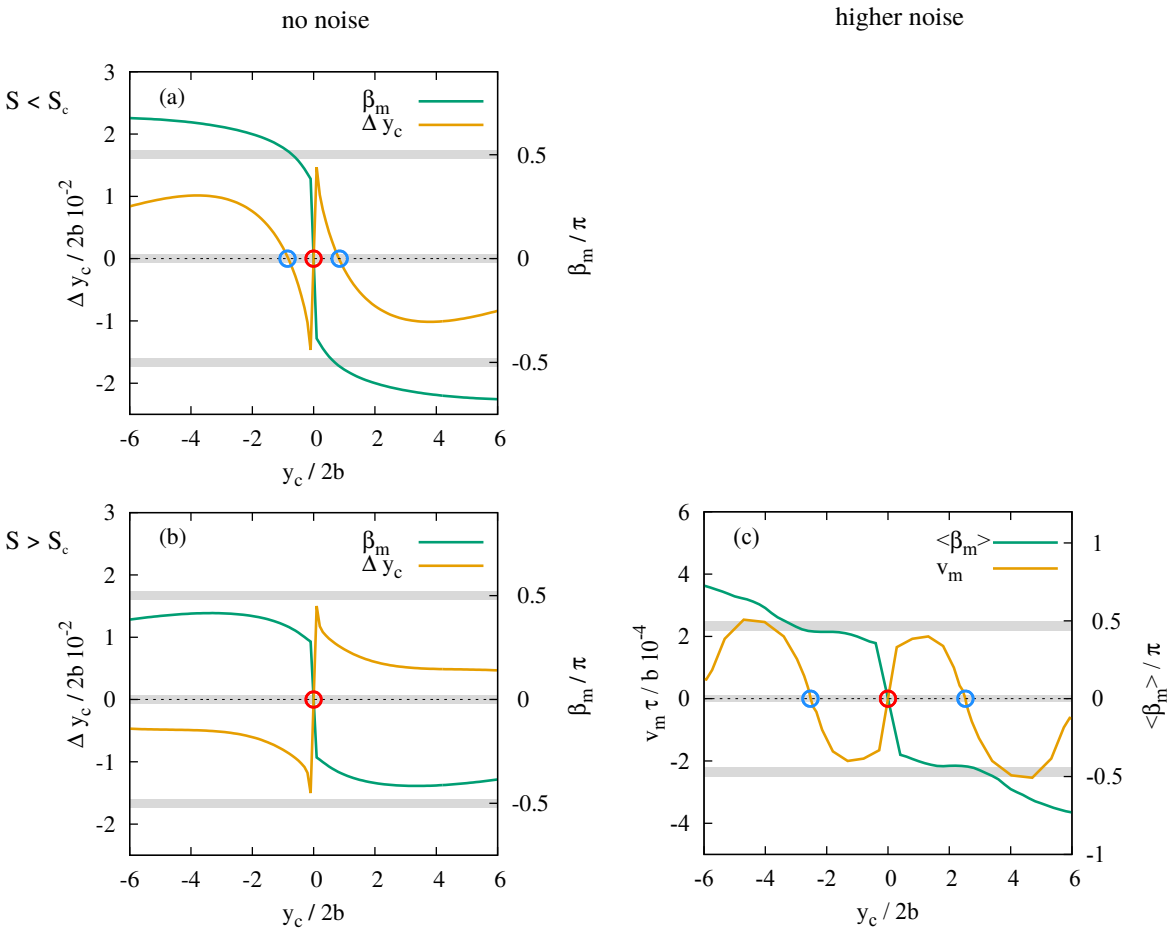

Figure 4. The angle β_m (green ——, cf. figure 3) and the migration step Δy_c (yellow ——) after one flip as function of y_c with $S = 0.35 < S_c$ (a) and $S = 0.58 > S_c$ (b) without thermal noise. With $S < S_c$ (a) the deformation is small with $|\beta_m| < 0.5\pi$ close to the center and the migration is directed away from the center. Further away the deformation is strong with $|\beta_m| > 0.5\pi$ and the migration is directed towards the center. This produces the attractors at $y_c/b \approx \pm 0.8$ (blue circle) and the repeller at the center (red circle). Figure (b) shows the dynamics with high value of $S > S_c$ which lead to small deformations at all positions, i.e. $|\beta_m| < 0.5\pi$. Hence the migration is always directed away from the center and the attractor vanishes. (c) shows the migration velocity v_m (linear fit to $y_c(t)$) with noise $E_T = 6.3 \cdot 10^{-8}$ and $S = 0.58 > S_c$ and the averaged angle $\langle \beta_m \rangle$. The thermal noise increases the deformation during the flip: High values of $|\langle \beta_m \rangle| > 0.5\pi$ occur, despite $S > S_c$, which lead to the attractor.

3.2. Cross-stream migration including the effects of walls

In the previous section 3.1 we found at certain parameters a migration out of the channel without wall interaction, e.g. above the off-center repeller without thermal noise (see figure 1 and figure 2). In this section we include the wall interaction, which is repulsive [10, 11, 12, 13, 42]. Hence the wall interaction prevents a migration out of the channel, which therefore could be expected to lead to one new attractor in the case without thermal noise.

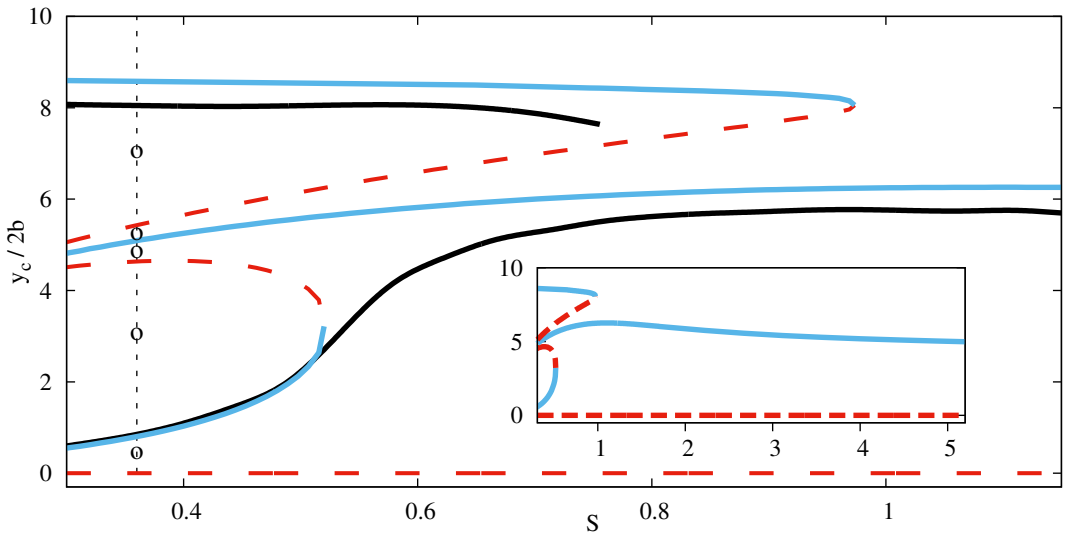

Figure 5. The lateral position $y_c\,/\,2b$ of the attractor (blue ——) and the repeller (red - - - -) in a bounded plane Poiseuille flow as a function of S with $E_T = 1.3 \cdot 10^{-12}$ is shown. Also the attractor with higher thermal noise $E_T = 1.3 \cdot 10^{-9}$ (black ——) is shown. The motion at positions marked with o are shown in figure 6. Without noise we find surprisingly two new attractors and a new repeller compared to the case without wall-interaction. The attractors closest to the wall and closest to the center exist only at values of S below a threshold. The dynamics of the particle at point marked by o are shown in figure 6. At higher thermal noise only two attractors are found. Two attractors at lower noise are connected to one attractor at higher noise.

Surprisingly we find up to two new attractors. The attractors and repellers are determined the same way as in the previous section. Figure 5 shows the lateral position $y_c\,/\,2b$ of the attractor and the repeller in a bounded plane Poiseuille flow as a function of the dimensionless bending stiffness S with lower thermal noise and with higher thermal noise. In case of a lower noise we find three attractors and three repellers. The attractors closest to the wall and closest to the center exist only at values of S below thresholds. The attractor in the middle of the others is found at all values of S and its position changes less with increasing values of S. The attractors with lower thermal noise agree well with the ones without thermal noise.

At higher thermal noise only two attractors are found, i.e. only one new attractor compared to the case without wall. It is close to the wall and matches the one found with a lower noise. The other attractor at higher noise closer to the center corresponds to the attractor found without wall interaction. But different from the unbounded flow it does not leave the channel due to the repulsive wall interaction. Here two attractors at lower noise are connected to one attractor at higher noise. The attractor at $y_c\,/\,2b \approx 5$ at small values of S and at lower noise is not found with higher noise. It is close to two repellers which means its basin of attraction is very small. The higher thermal noise $E_T = 1.3 \cdot 10^{-9}$ is strong enough to move the particles out of the basin of attraction and the attractor vanishes.

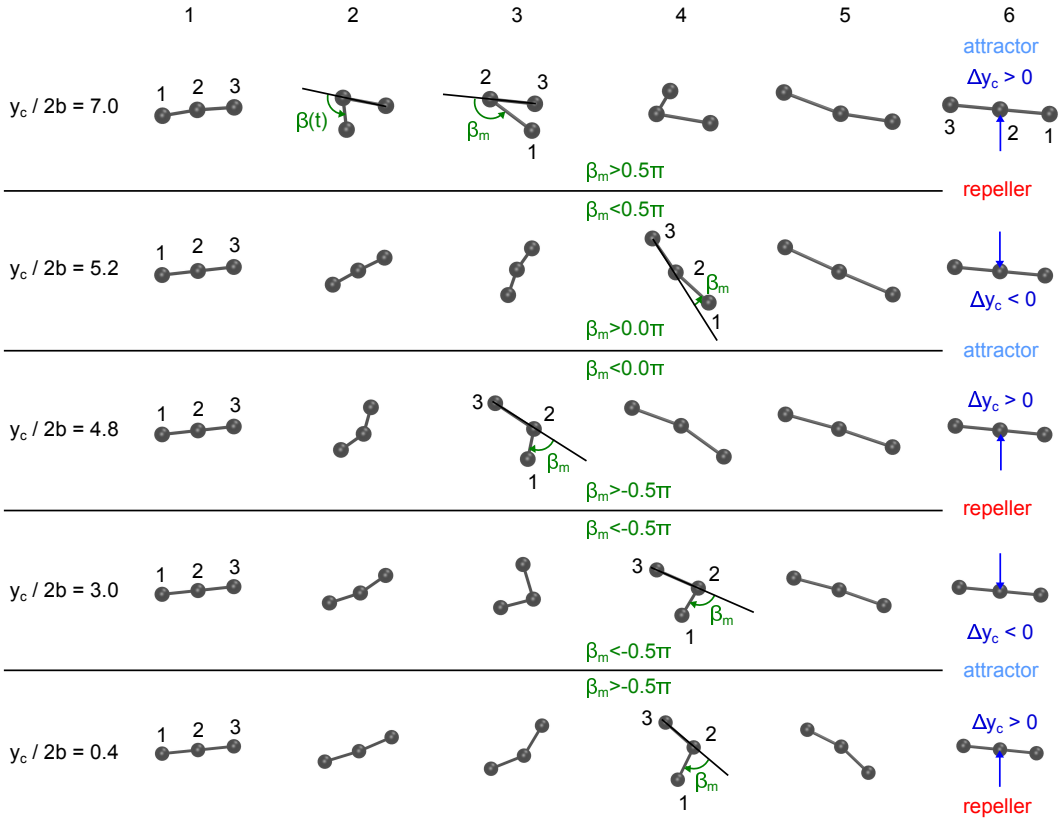

Figure 6. The stages of a flip for different initial positions (marked in figure 5) without thermal noise and with wall interaction. The angle β_m measures the maximal deformation during a flip. The initial positions $y_c\,/\,2b = 0.4$ and $y_c\,/\,2b = 3.0$ behave as in case without wall due to the high distance to the wall (compare figure 3). Bead 3 passes at first bead 2 (before bead 1) and the particle is bent due to the spatially dependent shear rate, which results in angles $\beta_m < -0.5\pi$ and $-0.5\pi \lessapprox \beta_m \lessapprox 0$. But at initial positions closer to the wall bead 3 is slowed due to the wall interaction. At positions close enough to the wall bead 3 passes bead 2 after bead 1 does what results in positive angles $0 \lessapprox \beta_m \lessapprox 0.5\pi$ and even $0.5\pi \lessapprox \beta_m$. According to eq. (18) this leads to attractors and repellers at $\beta_m = -0.5\pi, 0, 0.5\pi$. Very close the the wall (above the third attractor at $y_c \approx 8$) the particle moves towards the center despite $0.5\pi \lessapprox \beta_m$. The wall interaction is stronger than the migration due to the bending of the particle, which results in the third attractor.

The existence of up to three attractors and their location can be explained as in the case without the wall interaction (cf. section 3.1) by the motion of the particle during a flip and the angle β_m for different initial positions, which is shown in figure 6. The migration step and the maximal bending angle as function of the initial position is shown in figure 7. We discuss only one half of the channel with $y_c > 0$ due to the symmetry. The initial positions $y_c\,/\,2b = 0.4$ and $y_c\,/\,2b = 3.0$ behave as in the case without wall due to the high distance to the wall (compare figure 3). Bead 3 falls behind bead 2 and the particle becomes bent due to the spatially dependent shear rate. At $y_c\,/\,2b = 0.4$ we get $-0.5\pi \lessapprox \beta_m \lessapprox 0$ and according to eq. (18) a migration to the wall. At $y_c\,/\,2b = 3.0$

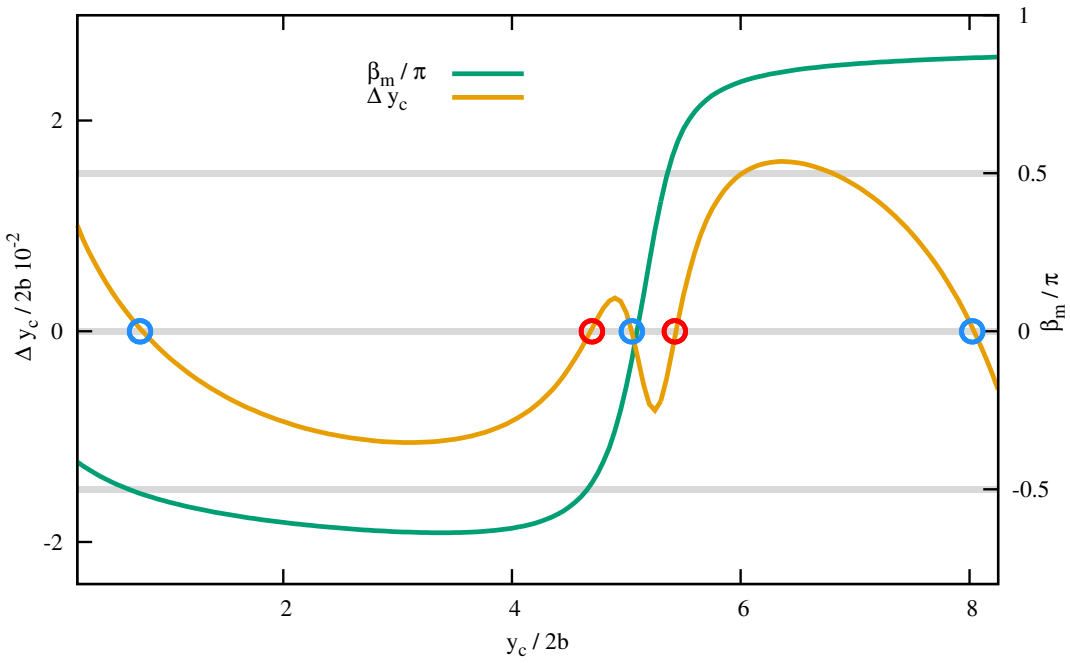

Figure 7. The angle β_m (green ——, cf. figure 3) and the migration step Δy_c (yellow ——) after one flip as function of the initial position of y_c. In the region close to the center, at $y_c/2b \lessapprox 5$, the particle behaves like in the case without wall (cf. figure 4). At higher values of $y_c/2b \lessapprox 5$ the flip of the particle is affect by the wall and the angle β_m increases from $\beta_m < -0.5\pi$ to $\beta_m > 0.5\pi$ (cf. figure 6). The direction of the migration follows then with eq. (18) which explaines the attractors (blue) and repellers (red). Hence the wall interaction influences the migration by affecting β_m. Close to the wall at $y_c/2b \gtrapprox 8$ the particle migrates away from the wall despite $\beta_m > 0.5\pi$. This shows the direct influence of the wall repulsion, i.e. the wall interaction is stronger than the migration due to spatially dependent shear rate.

the shear rate is higher and we get with $\beta_m \lessapprox -0.5\pi$ a migration to the center. This explains the first attractor (marked by a circle) which is also found in case without wall interaction. But already at $y_c\,/\,2b = 4.8$ the behavior differs from the case without wall. Bead 3 is closer to the wall and is hindered by the wall interaction. Thus, bead 3 falls behind bead 2 but much slower than without the walls (cf. figure 3) and nearly as fast as bead 1 passes bead 2. Hence the motion is much closer to a simple rotation and the particle becomes lesser bent with β_m closer to zero and $-0.5\pi \lessapprox \beta_m \lessapprox 0$. This means again a migration to the wall. At even closer distances to the wall $y_c\,/\,2b = 5.2$ bead 3 becomes even slower due to the wall interaction. Here bead 1 passes bead 2 before bead 3 falls behind bead 2. This means β_m becomes positive with $0 \lessapprox \beta_m \lessapprox 0.5\pi$ and the migration direction becomes negative. This is the second attractor. This effect becomes stronger at $y_c\,/\,2b = 7.0$. Here bead 1 passes bead 2 and comes very close to bead 3 before bead 3 can overcome the wall interaction and falls behind bead 2. Therefore β_m becomes large with $0.5\pi \lessapprox \beta_m$ and the migration becomes positive. Closer to the walls the migration becomes negative because the wall interaction becomes stronger than the

migration due to the spatially dependent shear rate and the particle is repelled by the wall, which explains the third attractor.

If the number N of the beads of the polymer model is increased the attractor and the repeller are shifted to different values but the qualitative behavior is similar (As in case of the unbounded flow). This is shown in the supplementary information.

4. Summary and discussion

In this work we investigated the dynamics and the cross-streamline migration of semiflexible bead-spring chains, which are a model of polymers and fiber, in Poiseuille flows. We carried out simulations for bead spring models without and with wall interaction as well as in the cases of very weak and medium noise amplitudes.

In parabolic flow profiles, we find in the absence of noise a migration towards an off-center attractor streamline (one attractor in each half of the flow profile), with initial positions between the flow center and an off-center repeller. If the polymers are initially positioned beyond the off-center repeller then they keep migrating away from the center. Above a critical value of the bending rigidity both the attractor and the repeller vanish and the particles migrate at all positions away from the center of the parabolic flow profile. We find that noise stabilizes this attractor in unbounded parabolic flow, i.e. the attractor persists at higher values of the bending rigidity. The off-center repeller does not exist with sufficiently high noise amplitudes, which means the polymers migrate to the attractor independently of the initial position.

This behavior can be explained by the bending of the semiflexible polymer because the direction of the migration is connected with the bending. The maximal bending angle during a flip decides about the direction of cross-streamline migration. We find that a small bending leads to a migration away from the center and a strong bending leads to a migration towards the center. This explains that the attractor vanishes at high values of the bending rigidity. If the particle is stiff it is less bent and the migration is directed away from the center. The thermal noise increases the bending angle, so that despite of high values of the bending rigidity the deformation is large and the migration is directed towards the center. Therefore the attractor is stabilized by the noise.

Considering semiflexible polymers in wall bounded flow and without thermal noise we find up to three attractors (in each half of the channel). Two of them vanish at high values of the bending stiffness. With thermal noise we find only two attractors and one vanishes at a high bending stiffness.

These results and especially the dynamics (e.g. the turning procedure in the shear flow) bears resemblance to the tumbling motion of polymers in Poiseuille flow as for example shown in [20, 21, 23, 24, 25] and may thus be useful to analyze cross-stream migration in that case. The effects described in this work can be also compared to the simulations of fibers, which show off-center attractors or peaks of their distribution [19, 28]. The presented results for the simple bead-spring model indicate, that the migration may strongly depend on the dimensionless stiffness S and on the ratio between

the polymer length and the diameter of a pipe flow (due to the shown wall interaction).

The attractors found with thermal noise and the importance of the bending on the migration agree with [28], even though [28] uses a constant length of the bead model and we allow a small extension of the springs. Hence we conclude that a change in the length does not change the qualitative behavior. Furthermore, it is interesting that the results with noise agree with [28], despite that [28] does not include thermal noise. However, [28] uses a rotation of the beads which creates a nonlinear flow field. We assume that the rotation of many beads has a similar effect as the thermal noise included in our simulations, which may explain this agreement. This is also a possible explanation that the results without noise differs much from [28], e.g. the repeller without wall or the three attractors with walls found here. Thus we conclude that thermal noise can have a high influence of the qualitative behavior of the polymers and fibers, e.g. by extending the range of existence of attractors and the location of the attractor.

The lateral migration may be exploited to separate polymers or fibers with different properties, e.g stiffness, because the existence and the positions of the attractors depend strongly on the parameters.

5. Acknowledgments

M. L and W.Z. acknowledge the support of the French-German University (Grant CFDA-Q1-14, program "Living fluids").

Appendix A. Supplementary information

Appendix A.1. Determination of the position of the attractor and the repellers

We determine the position of the attractors and reppelers as follows: Every trajectory in figure 1 (a) is the result of a sequence of turns and related migration steps of the particles. The trajectories in part (a) are very smooth and every subsequent migration step is directed in the same direction. In that sense the noise with $E_T = 1.3 \cdot 10^{-12}$ is small. It just inclines the particle out of the orientation parallel to the stream line but does not disturb the dynamics of the flip and the direction of the migration. As these turns are the foundation of the cross-stream migration, the essential information about the direction of the migration in case of a weak thermal noise can be obtained by studying single turns of the particles without noise for continuously varied initial positions across the channel, at which the objects are slightly inclined with respect to the flow direction. In this way we determine for different initial positions $y_c/2b$ the direction of the migration step during one turn in the flow. The stationary points are located at positions leading to a vanishing migration step. The migration steps can lead to a movement towards or away from these stationary points, which allows to distinguish between attractors and repellers.

In case of higher thermal noise $E_T = 6 \cdot 10^{-8}$ the noise disturbs the dynamics and the direction of the migration. Figure 1 (b) shows that the trajectories move up and down in y-direction, which means that subsequent flips do not lead to a migration in the same direction. Hence at high noise we can not study single deterministic flips and therefore the position of the attractor must be determined directly from the trajectories.

Appendix A.2. Results with five beads

We show here that we find with a higher resolution of the particle with five beads similar results as with only three beads. We use wall interactions and the following parameters: number of beads $N = 5$, viscosity $\eta = \frac{1}{12\pi}$, wall to center distance $d = 100.0$, flow velocity $u_0 = 900.0$, Stokes friction coefficient $\zeta = 0.5$, bending constant $\kappa = 7.8$, spring constant $k = 5.0$, equilibrium bead distance $b = 2.5$ (Length $l = 10$), strength of the Lennard-Jones potential $\varepsilon = 100.0$, cutoff radius of the Lennard-Jones potential $r_c = 1.1$, bead radius $a = 1.0$, and Euler step width $\Delta t = 0.0005$.

The results with five beads shown in figure A1 and the findings with three beads given in figure 5 are similar: Both models with three and five beads show three attractors at low values of the bending stiffness. Two of them vanish if the bending stiffness is increased above threshold values. The position of the attractor in the middle changes its position less in dependence of the bending stiffness and is found at all values of S.

We find with three beads that the migration is determined by the maximal bending angle during one flip of the particle which is given by eq. (18) and figure 7. A similar criterion can be given with the five beads, but one has to consider that the bending of the five bead particle is not determined by one angle. Instead we measure the bending

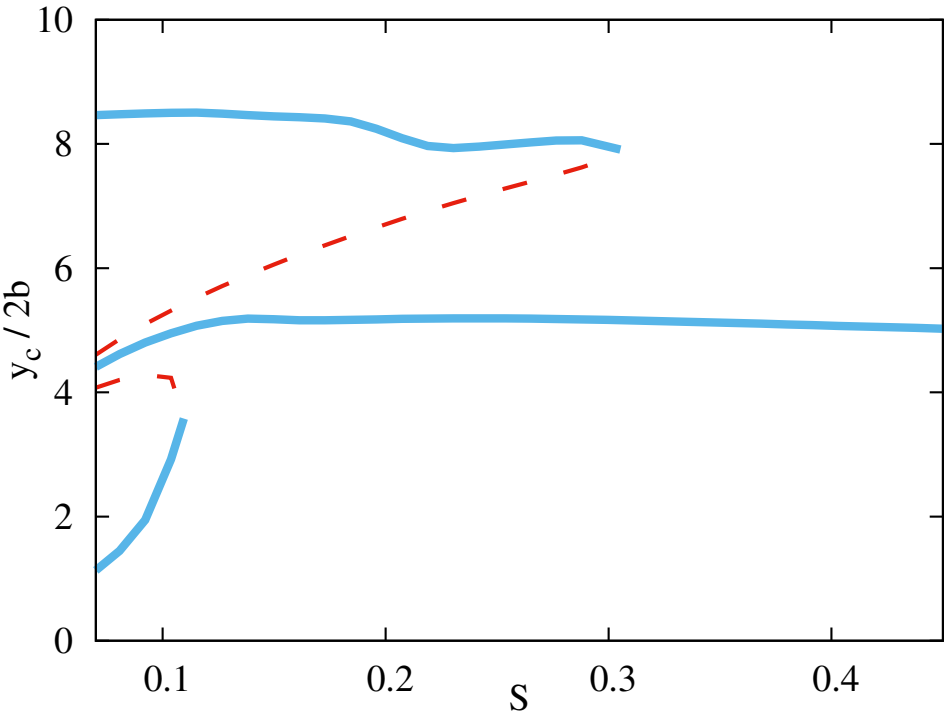

Figure A1. Attractors (blue ——) and repellers (red - - - -) for $N = 5$ beads with wall interaction and without thermal noise. Up to three attractors exist. Two vanish above critical values of the bending stiffness and one is found at all values which is located between the center and the wall.

of the particle by utilizing a parabolic function through the both beads at the ends and the one in the middle, i.e. we use the curve

$$\boldsymbol{r}(y) = \begin{pmatrix} ay^2 + by + c \\ y \\ 0 \end{pmatrix} \tag{A.1}$$

This allows to calculate the curvature C of the particle via

$$C = \pm \frac{|\partial_y \boldsymbol{r} \times \partial_y^2 \boldsymbol{r}|}{|\partial_y \boldsymbol{r}|^3} \tag{A.2}$$

whereby the sign means a curvature to the left or right and we evaluate the expression at the position of the bead in the middle. We measure the curvature in units of the particle length l. Similar to the bending angle in case with three beads the curvature determines the migration direction. This is shown in figure A2 without noise. The migration step and the maximal bending as function of the lateral coordinate of the particle's center is similar to the case with three beads shown in figure 7. If the particle has a curvature with $Cl < -12$ and $0 < Cl < 12$ we find a migration towards the center and at $-12 < Cl < 0$ and $12 < Cl$ we find a migration towards the wall.

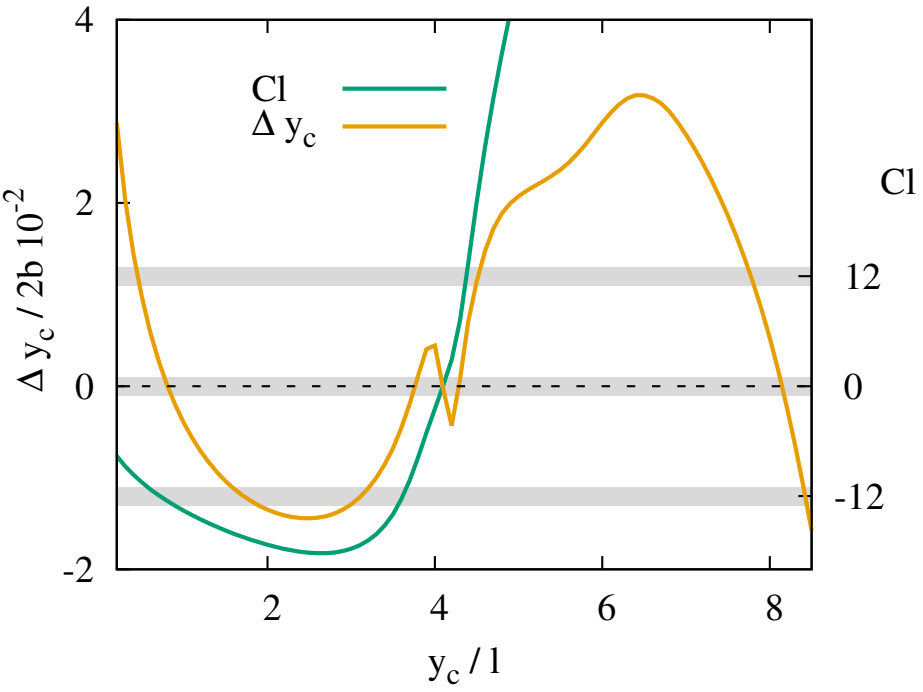

Figure A2. The curvature C of the maximum deformation and the migration step Δy_c after one flip as function of the initial position of y_c with $S = 0.27 < S_c$ without thermal noise and with wall interaction. Similar to the results with three beads (see figure 7) the migration steps changes its direction at certain values of the curvature, namely at $Cl = -12, 0, 12$. Close to the wall, at $y_c/l > 8$, the wall repulsion is stronger than the migration induced by the bending. The migration is directed away from the wall despite the high values of the curvature.

[1] G. Segré and A. Silberberg, Nature **189**, 209 (1961).
[2] G. Segré and A. Silberberg, J. Fluid Mech. **14**, 115 (1962).
[3] J. A. Schonberg and E. J. Hinch, J. Fluid Mech. **203**, 517 (1989).
[4] B. H. Yang *et al.*, J. Fluid Mech. **540**, 109 (2005).
[5] D. D. Carlo *et al.*, Phys. Rev. Lett. **102**, 094503 (2009).
[6] U. S. Agarwal, A. Dutta, and R. A. Mashelkar, Chem. Eng. Sci. **49**, 1693 (1994).
[7] P. O. Brunn and P. N. Kaloni, J. Chem. Phys. **83**, 2497 (1985).
[8] P. O. Brunn, J. Polym. Sci. Polym. Phys. **23**, 89 (1985).
[9] O. du Roure, A. Lindner, E. N. Nazockdast, and M. J. Shelley, Annu. Rev. Fluid Mech. **5**, 539 (2019).
[10] U. Seifert, Phys. Rev. Lett. **83**, 876 (1999).
[11] I. Cantat and C. Misbah, Phys. Rev. Lett. **83**, 880 (1999).
[12] M. Abkarian, C. Lartigue, and A. Viallat, Phys. Rev. Lett. **88**, 068102 (2002).
[13] H. Ma and M. D. Graham, Phys. Fluids **17**, 083103 (2005).
[14] D. Stein, F. J. J. von der Heyden, J. A. Koopmans, and C. Dekker, Proc. Natl. Acad. Sci. (USA) **103**, 15853 (2006).
[15] L. G. Leal, Annu. Rev. Fluid Mech. **12**, 435 (1980).
[16] B. Kaoui *et al.*, Phys. Rev. E **77**, 021903 (2008).
[17] B. Kaoui, G. Biros, and C. Misbah, Phys. Rev. Lett. **103**, 188101 (2009).
[18] L. C. Nitsche and E. J. Hinch, J. Fluid Mech. **332**, 1 (1997).
[19] R. L. Schiek and E. S. G. Shaqfeh, J. Fluid Mech. **332**, 23 (1997).
[20] D. R. Steinhauser, *"Actin filaments and bundles in flow"*, *PhD dissertation* (University of Göttingen, Germany, 2008).
[21] D. R. Steinhauser, S. Köster, and T. Pfohl, ACS Macro Lett. **1**, 541 (2012).
[22] D. Saintillan, E. S. G. Shaqfeh, and E. Darive, J. Fluid Mech. **557**, 297 (2006).
[23] R. Chelakkot, R. G. Winkler, and G. Gompper, EPL **91**, 14001 (2010).
[24] R. Chelakkot, R. G. Winkler, and G. Gompper, J. Phys. Cond. Mat **23**, 184117 (2011).
[25] S. Reddig and H. Stark, J. Chem. Phys. **135**, 165101 (2011).
[26] A. Farutin *et al.*, Soft Matter **12**, 7307 (2016).
[27] A. M. Słowicka, M. L. Ekiel-Jeżewska, K. Sadlej, and E. Wajnryb, J. Chem. Phys. **136**, 044904 (2012).
[28] A. M. Słowicka, E. Wajnryb, and M. L. Ekiel-Jeżewska, Eur. Phys. J. E **36**, 31 (2013).
[29] X. Liu and G. H. Pollack, Biophys J. **83**, 2705 (2002).
[30] J. Hendricks, T. Kawakatsu, K. Kawasaki, and W. Zimmermann, Phys. Rev. E **51**, 2658 (1995).
[31] G. S. Grest and K. Kremer, Phys. Rev. A **33**, 3628 (1986).
[32] J. R. Blake, Proc. Camb. Philos. Soc. **70**, 303 (1971).
[33] J. K. G. Dhont, *An Introduction to dynamics of colloids* (Elsevier, Amsterdam, 1996).
[34] H. Yamakawa, J. Chem. Phys. **53**, 436 (1970).
[35] J. Rotne and S. Prager, J. Chem. Phys. **50**, 4831 (1969).
[36] E. Wajnryb, K. A. Mizerski, P. J. Zuk, and P. Szymczak, J. Fluid Mech. **731**, R3 (2013).
[37] R. B. Jones, J. Chem. Phys. **121**, 483 (2004).
[38] J. Honerkamp, *Stochastic dynamical systems* (VCH, New York, NY, 1994).
[39] N. G. van Kampen, *Stochastic Processes in Physics and Chemistry* (Elsevier, Amsterdam, 2007).
[40] C. W. Gardiner, *Handbook of stochastic methods for physics, chemistry and the natural sciences*, *Springer series in synergetics* (Springer, Berlin, 1983).
[41] H. C. Öttinger, *Stochastic processes in polymeric fluids* (Springer, Berlin, 1996).
[42] J. P. Hernández-Ortiz, H. Ma, J. J. de Pablo, and M. D. Graham, Phys. Fluids **18**, 123101 (2006).

Publication 8

Understanding Cross-Stream Migration with Basic Bead-Spring Models
M. Laumann, M. Holzinger, and W. Zimmermann,

draft

Unterstanding Cross-Stream Migration with Basic Bead-Spring Models

M. Laumann, M. Holzinger, and W. Zimmermann
Theoretische Physik I, Universität Bayreuth, 95440 Bayreuth, Germany
(Dated: April 10, 2019)

Bead-spring models are often used to describe the dynamics of deformable particles in microfluidic flows: The variety of these models ranges from basic models, like a tetrahedron which allows to demonstrate elementary principles in a lucid way, to more complex but efficient models of flexible fibers, vesicles, capsules and red blood cells. In this work we give most simple models, e.g. a triangle or a ring, to describe the cross-stream migration (CSM) of an elastic particle in a flow and discuss the minimal requirements that a model must fulfill to describe CSM. We give furthermore a simple model of a capsule and discuss the different models. This bead capsule shows also quantitative agreement with other, more complex methods. After we demonstrated that the bead-spring models can describe the migration well, we show that a bead capsule is helpful for semi-analytical calculations: It allows to give a simple explanation why cross-stream migration occurs. We show in an easy way that the tank-treading motion and the spatial dependence of the flow lead to forces that drive the migration, what agrees with previous results. Also the finite size of the capsule can lead to a CSM in curved flows. Furthermore we give an semi-analytical approximation of the migration velocity of a capsule in an arbitrary flow at small deformations, which allows to discuss the general requirements of cross-streamline migration.

I. INTRODUCTION

Microfluidics is a fast developing field with a wide spectrum ranging from basic physics to many applications in life science and technology [1–9]. A large branch of Microfluidics deals with the dynamics of soft particles in suspension and especially their cross-streamline migration (CSM) at small Reynolds numbers. Here important results are obtained in understanding blood flow, sorting (blood) cells and DNA or processing polymers, among many others examples [8–13].

The first example of CSM was reported in 1961 by Segré and Silberberg who studied the motion of rigid particles in finite Reynolds-number flows through pipes [14]. But micrometer sized particles often have negligible Reynolds numbers, which means inertial effects can be discarded and CSM occurs on this length scale not for rigid but for soft particles. Examples are particles immersed in curved flows [15–17] or in rectilinear flows [18–20]. In rectilinear flows however, the flows fore-aft symmetry must be broken to observe a CSM which requires hydrodynamic interaction [18, 19]. The symmetry is broken e.g. by near boundaries via wall-induced lift forces [9, 20–24]. But even without walls a symmetry breaking can occur due to spatially dependent shear rates: Examples are dumbbells [18, 19], droplets [25, 26], vesicles and capsules [27–30]. This may be also accompanied by a viscosity contrast [31] or chirality [32].

To understand this multi-faceted phenomenon of CSM it can be desirable to use most simple models, which focus on the essentials. Such an approach was e.g. used by Watari and Larson to describe the above mentioned effect of chirality [32]: They showed that particles with an intrinsic chirality already migrate in an linear shear flow by using an elementary bead-spring tetrahedron, which showed the effect in a lucid way. But bead spring models are not only limited to easy models used in [16, 32]. It was shown recently that bead spring models can describe the dynamics of vesicles (even with a viscosity contrast) [13, 33], of capsules [34] and even of red blood cells [35] in an efficient way. Further recent examples of the usefulness of bead spring models in microfluidic simulations are the description of DNA [36], cilia [37], flexible filaments [38], proteins [39, 40], general colloidal particles [41] and microswimmers [42–44]. Also conceptual work was done in the last years to improve bead models further [45, 46].

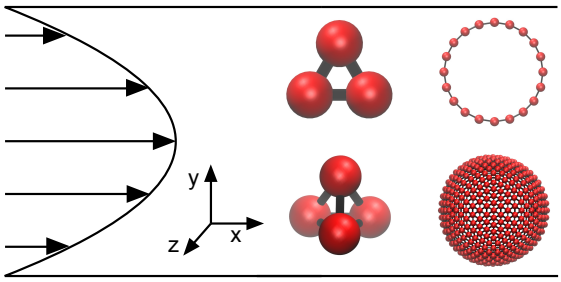

FIG. 1. (color online) The dynamics and the cross-stream migration of bead models in increasing complexity is investigated in Poiseuille flow and compared: The used models are a triangular and a ring shaped bead-spring model (two-dimensional), a tetrahedron and a capsule (three-dimensional). The capsule is also used to semi-analytically calculate the migration velocity in an arbitrary flow (with translational invariance in one direction), which allows to discuss the mechanism of migration and the general requirements.

In this work we show at first minimal bead spring models, e.g. a triangle or a ring sketched in Fig. 1, which display a CSM in a Poiseuille flow and demonstrate that they are sufficient to determine the basic properties of CSM. Furthermore they allow to determine the minimal requirements that a bead model must fulfill to display a CSM (compare [19]). We then give a simple but improved bead model of a more realistic particle, a capsule and

show that it agrees quantitatively well with other more complex methods like the work of Helmy and Barthès-Biesel [27, 47] or the Lattice-Boltzmann method (LBM). We are thus able to give an overview of models ranging from the basic triangle to a capsule and discuss the advantages of each model. Note that we focus in this work on the basic effects, which may be modified e.g. by viscosity contrasts in vesicles, capsules or red blood cells or slip condition in drops. Beyond that we show a further advantage of bead-spring models: They allow semi-analytical calculations. We derive the migration velocity of an elastic, spherical bead particle (e.g. the capsule) in an arbitrary flow (with translational invariance in one direction) at small deformations. This allows to calculate also the forces that drive the migration in an arbitrary, unbounded flow: The calculations show in an easy way that the spatial dependence of the flow and the tank-treading motion lead to forces which are the source of CSM in a rectilinear flow. Up to now the CSM and the driving forces are analytically calculated with more exact models but in special flows, e.g. for capsules in a pipe flow [27], drops in unidirectional flows [48] or vesicles in Poiseuille flows between flat walls [49] among many other examples.

II. MODELS

A. Bead Spring Models

To describe the cross-stream migration of soft particles (without viscosity contrast) in a most simple way, we use bead spring models: A triangle, a ring, a tetrahedron and a bead-spring capsule as particle representatives (see fig. 1). The models are exposed to a vertical 3D, plane Poiseuille flow along the x-axis

$$\mathbf{u}_0(y) = U\left[1-(y/d)^2\right]\mathbf{e}_x \tag{1}$$

with its two boundaries at $y = \pm d$. The maximum flow velocity at the channel center is given by U. We also use a pipe flow

$$\mathbf{u}_0(r) = U\left[1-(r/d)^2\right]\mathbf{e}_x,\ r=\sqrt{y^2+z^2} \tag{2}$$

with a wall at $r = d$ and a maximal velocity U and a linear shear flow, which is given by

$$\mathbf{u}_0(y) = \dot{\gamma} y \mathbf{e}_x \tag{3}$$

with the shear rate $\dot{\gamma}$.

The bead-spring models consist of N beads located at $\mathbf{r}_i$ and the particle's center is given by $\mathbf{r}_c = \sum_{i=1}^{N}\mathbf{r}_i/N$. We use the Stokesian dynamics model [50] to describe the motion of the models. The equation of motion of the beads is given by the coupled equations ($1 \le i \le N$),

$$\dot{\mathbf{r}}_i = \mathbf{u}_0(\mathbf{r}_i) + \sum_{j=1}^{N}\mathbf{H}_{i,j}\cdot\mathbf{F}_j\ , \tag{4}$$

The force acting on bead j is given by $\mathbf{F}_j = -\nabla_j V(\mathbf{r})$ where $V(\mathbf{r})$ denotes to the total potential, and $\mathbf{H}_{i,j}$ means the mobility matrix, as specified in the following.

The triangle model uses springs between the three beads and the used potential is given by $V(\mathbf{r}) = V_h = \frac{k}{2}\sum_{i=1}^{N}(R_i - b)^2$ with spring constant k, equilibrium bond length b, and $R_i = |\mathbf{R}_i|$ the magnitude of the bond vector $\mathbf{R}_i = \mathbf{r}_i - \mathbf{r}_{i+1}$ of the next-neighbor beads i and $i+1$.

The total potential of the ring reads $V(\mathbf{r}) = V_h + V_b$. It consists of the harmonic potential V_h also used by the triangle and a bending potential V_b given by

$$V_b = -\frac{\kappa_r}{2}\sum_{i=1}^{N}\ln\left(1+\cos\beta_i\right), \tag{5}$$

with the bending stiffness κ_r. The angles β_i are defined via $\cos\beta_i = \mathbf{e}_{R_{i-1}}\cdot\mathbf{e}_{R_i}$ with the bond unit vectors $\mathbf{e}_{R_j} = \mathbf{R}_j/R_j$.

The total potential of the capsule is $V(\mathbf{r}) = V_{NH} + V_b + V_v$ with the Neo-Hookean potential V_{NH} [47, 51] which describes rubber-like materials with a constant surface shear-elastic modulus G_s, and a bending potential V_b [52, 53]

$$V_b = \frac{\kappa_c}{2}\sum_{i,j}\left(1-\cos\beta_{i,j}\right) \tag{6}$$

with bending elasticity κ_c. The angle $\beta_{i,j}$ is formed by the two normal surface vectors of adjacent triangles with beads at the triangle corners. The penalty potential $V_v = \frac{k_v}{\mathcal{V}_0}(\mathcal{V}(t)-\mathcal{V}_0)^2$ [53] with volume stiffness k_v ensures that the capsule's instantaneous volume $\mathcal{V}(t)$ remains close to the reference volume $\mathcal{V}_0 = \frac{4}{3}\pi R^3$ of a spherical capsule of radius R. To treat the capsule as a bead model we have to discretize the surface of a sphere to determine the equilibrium positions of the beads. To receive a homogeneous distribution of beads on the surface of a sphere we begin with a regular icosahedron [54]. A icosahedron consists of 20 equilateral triangles and 12 nodes. The discretization is then refined iteratively: We add new nodes in the middle of each edge and shift them radially outwards to the surface of the sphere. We receive a greater amount of nodes and triangles. We repeat this until we have $N = 642$ nodes. The result is shown in fig. 1.

The mobility matrix $\mathbf{H}_{i,j}$ consists of the Oseen tensor [50] or the Blake tensor [55]. The Oseen tensor describes the hydrodynamic interaction (HI) of the beads i and j immersed in an unbounded fluid and the Blake tensor takes also the interaction with a flat wall into account.

The Blake tensor $\mathbf{H}_{i,j}$ reads

$$\begin{aligned}\mathbf{H}_{i,j}(\mathbf{r}_i,\mathbf{r}_j) = {}^{S}\mathbf{H}_{i,j}(\mathbf{r}_i,\mathbf{r}_j) - {}^{S}\mathbf{H}_{i,j}(\mathbf{r}_i,\mathbf{r}'_j)\\ + {}^{D}\mathbf{H}_{i,j}(\mathbf{r}_i,\mathbf{r}'_j) - {}^{SD}\mathbf{H}_{i,j}(\mathbf{r}_i,\mathbf{r}'_j)\end{aligned} \tag{7}$$

where $\mathbf{r}'_j = (x_j, y_j + 2h_j, z_j)$ is the position of the mirror-particle of bead j with a wall distance h_j. The first term in eq. (7) denotes the Oseen tensor, which describes the

HI without walls

$$ {}^{S}H^{\alpha\beta}_{i,j}(\mathbf{r}_i,\mathbf{r}_j) = \begin{cases} \frac{1}{8\pi\eta R_{i,j}}\left[\delta_{\alpha\beta}+\mathbf{e}^{\alpha}_{R_{i,j}}\mathbf{e}^{\beta}_{R_{i,j}}\right](1-\delta_{i,j}) \\ \frac{1}{6\pi\eta a}\delta_{\alpha\beta}\delta_{i,j} \end{cases} \quad (8) $$

with the unit vector $\mathbf{e}_{R_{i,j}} = \mathbf{R}_{i,j}/R_{i,j}$, the bead distance $\mathbf{R}_{i,j} = \mathbf{r}_i - \mathbf{r}_j$, the viscosity η, the bead radius a and $\alpha,\beta \in \{x,y,z\}$.

The further terms in eq. (7) describe the wall interaction. The ${}^{S}\mathbf{H}_{i,j}(\mathbf{r}_i,\mathbf{r}'_j)$ is the source singlet, which means the HI with the mirror bead j and is given by Eq. (8) for $i \neq j$ with $\mathbf{R}_{i,j}$ replaced by $\bar{\mathbf{R}}_{i,j} = \mathbf{r}_i - \mathbf{r}'_j$ and $\bar{\mathbf{e}}_{\bar{R}_{i,j}} = \bar{\mathbf{R}}_{i,j}/\bar{R}_{i,j}$. The last two terms in Eq. (7) refer to the Stokes doublet (D)

$$ {}^{D}H^{\alpha\beta}_{i,j}(\mathbf{r}_i,\mathbf{r}'_j) = \frac{h_j^2(1-2\delta_{\beta y})}{4\pi\eta\bar{R}^3_{i,j}}\left[\delta_{\alpha\beta}-3\bar{\mathbf{e}}^{\alpha}_{R_{i,j}}\bar{\mathbf{e}}^{\beta}_{R_{i,j}}\right], \quad (9) $$

and source doublet (SD)

$$ {}^{SD}H^{\alpha\beta}_{i,j}(\mathbf{r}_i,\mathbf{r}'_j) = \frac{1}{4\pi\eta\bar{R}^2_{i,j}}h_j\,(1-2\delta_{\beta y}) \quad (10) $$
$$ \times\left[\delta_{\alpha\beta}\bar{\mathbf{e}}^{y}_{R_{i,j}} - \delta_{\alpha y}\bar{\mathbf{e}}^{\beta}_{R_{i,j}} + \delta_{\beta y}\bar{\mathbf{e}}^{\alpha}_{R_{i,j}} - 3\bar{\mathbf{e}}^{\alpha}_{R_{i,j}}\bar{\mathbf{e}}^{\beta}_{R_{i,j}}\bar{\mathbf{R}}^{y}_{i,j}\right]. $$

The effects of a second wall are described by superposition of the HI of the single walls, which leads to reasonable results for a channel width to particle size ratio larger than 5 [56]. In simulations with neglected wall-HI, the mobility $\mathbf{H}_{i,j}$ in Eq. (7) reduces to the Oseen tensor ${}^{S}\mathbf{H}_{i,j}$. In the free draining case, where also the HI between the beads is neglected only the diagonal part of ${}^{S}\mathbf{H}_{i,j}$ is taken into account, which describes the Stokes friction.

In case of the triangle and the tetrahedron we use a correction of the Oseen-tensor, which takes the finite size of the beads into account: The Rotne-Prager-Yamakawa tensor [57, 58]. It is given by

$$ H^{\alpha\beta}_{i,j}(\mathbf{r}_i,\mathbf{r}_j) = \quad (11) $$
$$ \begin{cases} \frac{1}{8\pi\eta R_{i,j}}\left[(1+\frac{2a^2}{3R^2_{i,j}})\delta_{\alpha\beta}+(1-\frac{2a^2}{R^2_{i,j}})\mathbf{e}^{\alpha}_{R_{i,j}}\mathbf{e}^{\beta}_{R_{i,j}}\right], & R_{i,j} > 2a \\ \frac{1}{6\pi\eta a}\left[(1-\frac{9R_{i,j}}{32a})\delta_{\alpha\beta}+\frac{3R_{i,j}}{32a}\mathbf{e}^{\alpha}_{R_{i,j}}\mathbf{e}^{\beta}_{R_{i,j}}\right], & R_{i,j} \leq 2a \end{cases} \quad (12) $$

The Rotne-Prager tensor is useful if the beads come close to each other, i.e. at high deformations.

In the simulations with the two dimensional models we suppress the degrees of freedom of the particle perpendicular to the shear plane and restrict its dynamics to the $x-y$ plane. This allows to regard them as a cross-section of a 3D particle.

As not stated otherwise, we use the (dimensionless) parameters:

(a) Plane flow and pipe flow: $U = 3, 4$ and 5, $d = 70$, $\eta = 1$

(b) Triangle $a = 5$, $k = 5$, $N = 3$, $b = 11$, $R = 6.4$ $y_0 = 35$;

(c) Ring: $a = 0.75$, $k = 12$, $\kappa_r = 180.0$, $N = 20$, $b = 2$, $R = 6.4$, $y_0 = 35$;

(d) Tetrahedron: $a = 5.0$, $k = 15.0$, $N = 4$, $b = 11.0$, $R = 6.7$ $y_0 = 35$;

(e) Capsule: $G_s = 5.0$, $\kappa_c = 0.1$, $k_v = 3.0$, $a = 0.3$, $N = 642$, $b = 1.0$, $R = 6.6$, $y_0 = 35$;

Here y_0 denotes the initial position. The values of b are chosen so that all models have approximately the same equilibrium radius R, which means in case of triangle and tetrahedron the radius of the circumcircle or circumsphere. The dimensionless capillary number $\mathrm{Ca}=|\dot{\gamma}|\tau$ is a measure for the particle deformation. The relaxation time τ depends on the model, so that the capillary numbers are denoted by Ca_{tri}, Ca_r and Ca_{tet} for the triangle, the ring and the tetrahedron respectively. The capillary number of the capsule is termed Ca. The relaxation times are denoted with the same indexes and are given by $\tau_{tri} = \frac{6\pi\eta a}{k} = 18.8$ (triangle), $\tau_r = \frac{6\pi\eta R}{k} = 10.0$ (ring), $\tau_{tet} = \frac{6\pi\eta a}{k} = 6.3$ (tetrahedron), $\tau = \frac{\eta R}{G_s} = 1.3$ (capsule). The shear rate is given by $\dot{\gamma} = \frac{\partial u_0}{\partial y} = -2u_0\frac{y}{d}$ in a plane flow or $\dot{\gamma} = \frac{\partial u_0}{\partial r} = -2u_0\frac{y}{r}$ in a pipe flow.

B. Lattice Boltzmann Method

In order to compare the bead-spring models with another model we use a second method, the lattice-Boltzmann method (LBM) [59]. We choose a 3D LBM with a standard velocity descretization D3Q19. The collision are described by the Bhatnagar-Gross-Krook (BGK) collision operator [60, 61]. The evolution of the probability-distribution $f_i(\boldsymbol{r},t)$ in velocity-direction i at position $\boldsymbol{r}$ is given by

$$ f_i(\boldsymbol{r}+c_i\Delta t, t+\Delta t) = $$
$$ f_i(\boldsymbol{r},t) - \frac{\Delta t}{\tau_{LBM}}\left(f_i(\boldsymbol{r},t) - f^e_i(\boldsymbol{r},t)\right). \quad (13) $$

Here c_i denote the unit vectors, τ_{LBM} is a typical relaxation time (which is set to $\tau_{LBM} = 1$ as usual) and $f^e_i(\boldsymbol{r},t)$ is the equilibrium distribution

$$ f^e_i(\boldsymbol{r},t) \approx \rho_0 w_i\left[1+\frac{(\boldsymbol{c}_i\cdot\boldsymbol{u})}{c_s^2}+\frac{(\boldsymbol{c}_i\cdot\boldsymbol{u})^2}{2c_s^4}-\frac{u^2}{2c_s^2}\right], \quad (14) $$

with the equilibrium density ρ_0, the weighting factors w_i and $c_s = \frac{1}{\sqrt{3}}$ [61].

The local density $\rho(\boldsymbol{r},t)$ and mean velocity $\boldsymbol{u}(\boldsymbol{r},t)$ are given by the leading two moments

$$ \rho(\boldsymbol{r},t) = \sum_i f_i(\boldsymbol{r},t), \quad (15) $$
$$ \rho(\boldsymbol{r},t)\boldsymbol{u}(\boldsymbol{r},t) = \sum_i \boldsymbol{c}_i f_i(\boldsymbol{r},t). \quad (16) $$

The dynamic fluid-viscosity is given by

$$ \nu = c_s^2\left(\tau_{LBM}-\frac{1}{2}\right). \quad (17) $$

To drive the Poiseuille-flow we apply volume-forces. The coupling to the probability-distribution is implemented using the method given in [62].

We use further the immersed-boundary method [63] to couple the forces acting on the particle to the LBM-mesh. The delta-function used here is given by $\phi(\Delta \boldsymbol{r}) = \tilde{\phi}(\Delta x)\tilde{\phi}(\Delta y)\tilde{\phi}(\Delta z)$ and

$$\tilde{\phi}(R) = \begin{cases} \frac{1}{4}\left(1+\cos(\frac{\pi R}{2})\right) & \text{if } |R| \leq 2 \\ 0 & \text{else} \end{cases} . \qquad (18)$$

This method allows to couple the force from the Lagrangrian system to the neighbouring discrete grid nodes of the LBM and to calculate the velocity of the nodes at the position of the nodes of the capsule.

The Lattice Boltzmann simulations requires $U \ll c_s$ and $\tau_{LBM} \approx 1$ ensures a stable simulation, hence we choose the parameters:

Plane Flow: $U = 0.01$, $d = 70$, $\eta = \frac{1}{6}$

LBM: $\tau_{LBM} = 1$, $\rho = 1.0$

Capsule: $G_s = 10^{-4}$, $\kappa_c = 10^{-4}$, $k_v = 10^{-3}$, $a = 0.3$, $N = 642$, $b = 1.0$, $R = 6.6$;

III. CROSS-STREAM MIGRATION OF A TRIANGULAR AND A RING-LIKE BEAD-SPRING MODEL

In this section we show that simple models, a triangle and a ring of beads, can qualitatively describe the cross-streamline-migration and discuss the minimal requirements that a model must fulfill to display a CSM. We furthermore compare the models qualitatively with the two dimensional vesicle presented in [28].

A. Triangle

Figure 2 shows the evolution of the lateral coordinate of the triangle's center, $y_c(t)$ in an unbounded plane Poiseuille flow. The triangle is initially positioned off-center at $y_c/d = 0.9$. It moves over time to the center of the flow at $y = 0$, where a stable position is reached. Thus the triangle displays a cross-stream migration to the center of the flow. The figure shows also the dynamics with three different bead radii a and with and without hydrodynamic interaction (HI), i.e. the flow disturbance due to the presence of the particle. In the free-draining limit (HI is neglected) the center $y_c(t)$ is constant as indicated in Fig. 2, i. e. there is no cross-streamline-migration (CMS) in the free draining limit. If we include HI the triangle migrates and moves towards the center of the flow at $y = 0$. When the ratio a/b between the effective bead radius a and the equilibrium bead-bead distance b is increased, then HI effects are enhanced and simultaneously the cross-stream migration is faster. This illustrates the hydrodynamic interaction is necessary to describe the cross-streamline migration of a particle in a Poiseuille flow.

A magnification of Fig. 2 shows oscillations around a mean value. This oscillation vanishes with an increasing number of beads and is not important for the analysis of the net migration.

We also simulated the triangle in a linear shear flow. In this case no migration is found, which means that the spatial-dependent shear rate is crucial to the migration in a flow with parallel stream lines, which corresponds to the findings in [19].

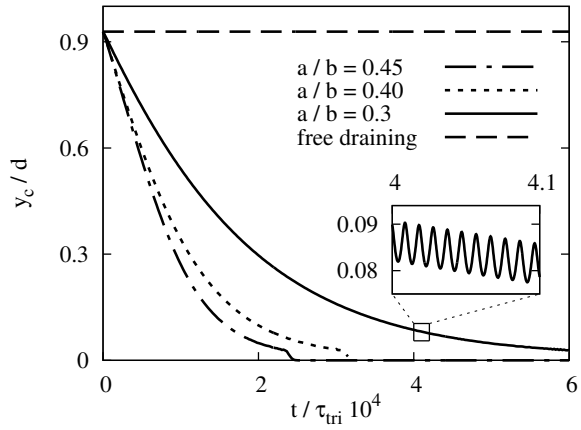

FIG. 2. The temporal evolution of the lateral position $y_c(t)$ of the center of a triangular bead-spring model for three different bead radii and with and without hydrodynamic interaction (HI) at $U\frac{\tau_{tri}}{R} = 3$. In the simulations including HI the particle moves from its initial position close to a wall to the center of the flow at $y = 0$: Thus a migration is found. This migration is faster with higher ratios of the bead radii a to the equilibrium bead distance b. The particle with the ratio $a/b = 0.45$ reaches the center faster than the one with $a/b = 0.4$ and with $a/b = 0.3$. In the free-draining limit (no HI) the triangle follows the flow completely and no migration occurs.

After we found a CSM in a Poiseuille flow, we investigate how it depends on the parameters. The cross-streamline migration velocity $v_{m,y}$ is obtained by the slope of a straight line fitted to $y_c(t)$. Figure 3 shows how the velocity depends on the lateral position and therefore the local capillary number $\mathrm{Ca}_{tri} = \tau_{tri}|\dot{\gamma}|$. At all positive values of the position of the triangle $v_{m,y}$ is negative, which means a migration towards the center of the flow at $y = 0$. At the center the velocity vanishes $v_{m,y} = 0$. At positions with $y_c < 0$ (not shown in fig. 3), i.e. in the other half of the channel, the migration is positive and has the same absolute value as at the positions shown here (with $y_c > 0$). Thus the migration is everywhere directed to the center. Figure 3 also shows the migration velocity as function of Ca_{tri}. It's absolute value $|v_{m,y}|$ vanishes at $\mathrm{Ca}_{tri} = 0$, grows for small values of Ca_{tri} linearly with Ca_{tri} and reaches a maximum at $\mathrm{Ca}_{tri} \approx 0.5$. At values of $\mathrm{Ca}_{tri} \gtrapprox 0.5$ the migration velocity's magnitude $|v_{m,y}|$ decreases with increasing values of Ca_{tri} and vanishes at $\mathrm{Ca}_{tri} \gg 1$. This behavior is found at all used values of the flow velocity $U\frac{\tau_{tri}}{R} = 9, 12, 15$. The dependence of the migration velocity on U at an initial

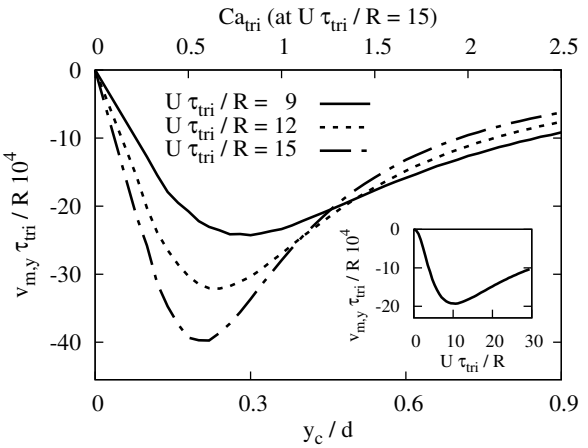

FIG. 3. The cross-stream migration velocity $v_{m,y}$ for the triangle is given as a function of the lateral position of its center and therefore of its local capillary number $\mathrm{Ca}_{tri} = |\dot{\gamma}|\tau_{tri}$ for three different values of the flow velocity U. The migration velocity is negative which means a migration to the center. The migration velocity's magnitude $|v_{m,y}|$ is maximal at $\mathrm{Ca}_{tri} \approx 0.5$ (shown for $U\frac{\tau_{tri}}{R} = 15$) and vanishes for values of $\mathrm{Ca}_{tri} \approx 0$ and $\mathrm{Ca}_{tri} \gg 1$. The inset shows the migration velocity of the triangle as function of the flow velocity at a constant initial position $y_c/d = 0.5$. The migration velocity's magnitude $|v_{m,y}|$ is maximal at $U\frac{\tau_{tri}}{R} \approx 10$ at $y_c/d = 0.5$ and becomes smaller at increasing distance to $U\frac{\tau_{tri}}{R} \approx 10$.

position $y_c/d = 0.5$ is shown at the inset of fig.3. The migration velocity's magnitude grows with increasing values of U up to $U\frac{\tau_{tri}}{R} \approx 10$ reaches a maximal magnitude at $U\frac{\tau_{tri}}{R} \approx 10$ and becomes smaller again at growing values of U at $U\frac{\tau_{tri}}{R} \gtrapprox 10$.

Hence already the easy triangle allows to determine the three main requirements of cross-streamline migration in a flow with parallel stream lines: At first the particle must be deformable, i.e. the capillary number must be larger than zero. Second, the shear rate must change over the size of the particle: We find a migration in a Poiseuille flow, but not in a linear shear flow. Third the flow disturbance due to the particle, the HI, is necessary.

We can compare this results qualitatively with the two dimensional vesicle in a Poiseuille flow given in [28]: Also the vesicle must be deformable, i.e. needs a capillary number larger than zero to migrate. It needs a varying shear rate across its size and it also disturbs the flow (includes HI). Thus the requirements to find a migration is the same for the easy triangle and the vesicle. We can also compare the direction of the migration and the quantitative dependence on the capillary number: The migration velocity of the vesicle [28] is directed to the center and it shows, as function of Ca, a linear increase at small values of Ca until a nearly constant value of the migration velocity is reached at higher values of Ca. The triangle model reproduces the migration to the center. It also displays a nearly linear increase of $v_{m,y}$ at low values of Ca_{tri}. But at high values of Ca_{tri} the migration becomes slower with increasing Ca_{tri} which is different to the vesicle. The reason is that the vesicle model includes an area conservation, which limits the deformations at high values of Ca. This is not used in the triangle model, which leads to high deformations at $\mathrm{Ca}_{tri} > 1$. This means the very simple triangle can reproduce the qualitative features of a deformable particle: The requirements of the migration, the migration direction and the quantitative dependence on the capillary number (linear growth) as long as too high deformations, i.e. too high values of Ca are avoided.

B. Ring

We investigate the cross-streamline migration of a further simple model, the ring of beads. In a linear shear flow no migration is found, hence we use the Poiseuille flow. We also find in a Poiseuille flow without the HI no migration, therefore we include the HI (compare [19]). Figure 4 shows the migration velocity of the ring as function of the lateral position of its center and the according local capillary number for three different values of the flow velocity. Also the ring displays a migration to the center. The migration velocity's magnitude $|v_{m,y}|$ increases with the distance to the center until a value of the local capillary number $\mathrm{Ca}_r \approx 1$ is reached. At higher distances to the center, i.e. higher values of Ca_r, the migration velocity's magnitude becomes nearly constant. The inset of fig. 4 shows also $v_{m,y}$ as function of the flow velocity: The migration's magnitude increases with the flow velocity. Also the deformation of the ring is shown in fig. 4. At low shear rates, i.e. close to the center, the ring is nearly undeformed. Closer to the wall the ring adopts approximately more and more the shape of an ellipse with the long half axis roughly oriented with an angle of $\frac{\pi}{4}$ to the stream lines.

This means also the ring shows the three requirements for cross-streamline migration in a flow with parallel stream lines: deformability, spatial-dependent shear rate and HI. Thus the migration of the ring and the triangle are qualitatively similar, because they show the same requirements and both display a motion to the center of the flow. But the triangle displays a maximum at $\mathrm{Ca}_{tri} \approx 0.5$, whereas the ring does not show a maximum when $v_{m,y}$ is plotted against Ca_r. The reason is that the triangle undergoes very high deformations. In case of the ring this is prevented by the bending potential. This holds true as long as the capillary number of the bending is not too high, i.e. as long as $Ca_r^\kappa = \frac{6\pi\eta R^3}{\kappa}|\dot{\gamma}|$ is not much higher than one. Here the highest value was $Ca_r^\kappa = 4$ with $U\frac{\tau_r}{R} = 8$ at $y = d$.

The result of the simple ring model is similar to the behavior of the vesicle described in [28]. It has the same conditions for the migrations. Also the qualitative dependence on the capillary number is similar: The migration of the vesicle grows almost linear with Ca_r until it reaches a plateau at higher values of Ca_r, which is also found with the ring model. This is case despite the area

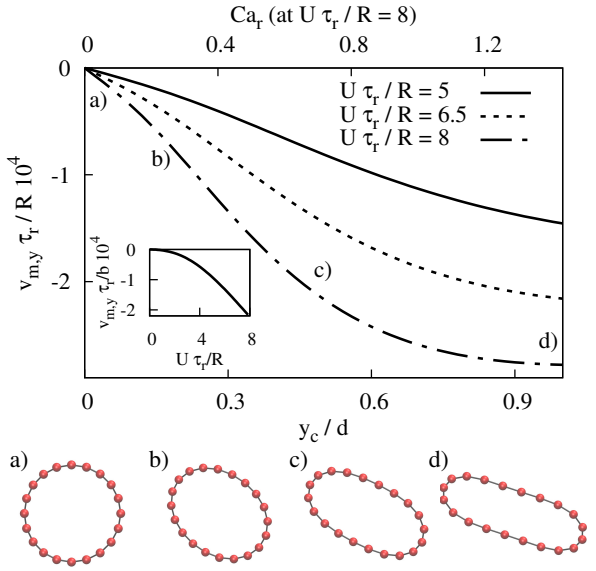

FIG. 4. (color online) The cross-stream migration velocity $v_{m,y}$ for the ring of beads is given as a function of the lateral position of its center and therefore of its local capillary number for three different values of the flow velocity U. The migration velocity increases with the rings distance to the center up to $\mathrm{Ca}_r \lessapprox 1$ and remains approximately constant at $\mathrm{Ca}_r \gtrsim 1$ (shown for $U\frac{\tau_r}{R} = 8$). The inset shows $y_c/d = 0.5$ that the migration velocity of the ring increases with increasing flow velocity. Also the shape of a bead-spring ring-model is shown at different positions along $y_c(t)$ in Poiseuille flow, as indicated by a)-d): Close to the channel center, at a), the ring is less deformed due to the low shear rate. The ring becomes the more deformed the closer it is to the wall. Its shape is then nearly elliptic and the long half axis forms roughly an angle of $\frac{\pi}{4}$ with the stream lines.

and circumference conservation used in [28] is missing in case of the ring of beads.

The simple ring also agrees qualitatively well with the results found with the capsule (see fig. 9), which allows to regard the ring as a cross-section of the capsule.

IV. CROSS-STREAM MIGRATION OF A TETRAHEDRON AND A CAPSULE

We show a simple tree dimensional model that allows to investigate the cross-streamline migration of a deformable particle qualitatively: The bead spring tetrahedron. We also give an example of how a realistic particle, a capsule, can be described easily with a bead model. We also show that we receive a quantitative agreement with other methods: For this purpose we compare the results of the bead capsule with the results of Helmy and Barthès-Biesel (see [47] and [27]) and a lattice-Boltzmann simulation.

A. Tetrahedron

Here we show the cross-stream migration of a most simple three dimensional particle, the tetrahedron. Also the tetrahedron shows no migration in a linear shear flow, hence we use a Poiseuille flow in the following. Furthermore no migration in a Poiseuille flow is found in the free draining limit, therefore we include the HI (compare [19]).

Figure 5 shows the migration velocity of the bead-spring tetrahedron in a plane Poiseuille flow in dependence of the lateral position and the corresponding local capillary number Ca_{tet}. The migration of the tetrahedron is everywhere directed to the center of the flow, which can be seen with $v_{m,y} < 0$ at the shown half of the channel with $y > 0$. The CSM vanishes at the center at $y_c = 0$ and $\mathrm{Ca}_{tet} = 0$. It becomes stronger at increasing values of Ca_{tet} up to $\mathrm{Ca}_{tet} \approx 0.3$, where it reaches a maximum. At higher values $\mathrm{Ca}_{tet} \gtrsim 0.3$ to migration becomes slower. The inset of fig. 5 displays the migration velocity at $y = 0.5d$ as function of the flows velocity U. A maximum of the migration's absolute value is found at $U\frac{\tau_{tet}}{R} \approx 5$ and the migration vanishes at very high or low values of U.

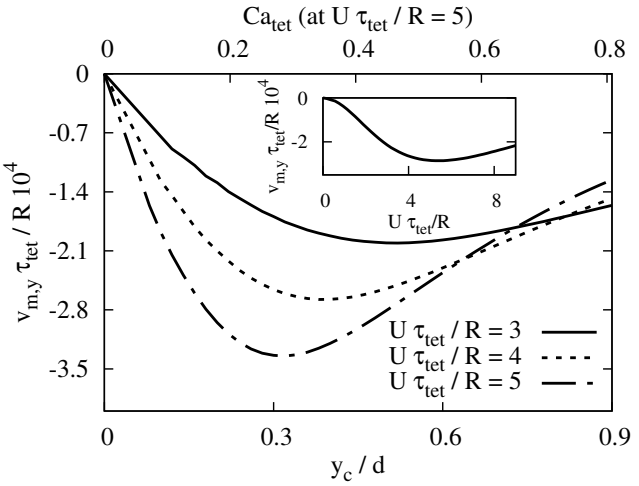

FIG. 5. The migration velocity $v_{m,y}$ of the tetrahedron in a plane Poiseuille-flow is given as a function of the lateral position of its center and therefore of its local capillary number Ca_{tet} for three different values of the flow velocity U. The migration speed vanishes at $\mathrm{Ca}_{tet} = 0$ and at $\mathrm{Ca}_{tet} \gg 1$ and displays a maximum at $\mathrm{Ca}_{tet} \approx 0.3$ (shown for $U\frac{\tau_{tet}}{R} = 5$). The inset shows the migration velocity of the tetrahedron as function of the flow velocity at $y_c/d = 0.5$. A maximum is found at $U\frac{\tau_{tet}}{R} \approx 5$.

We also determined the migration velocity of a tetrahedron in case of a pipe flow, which is shown in fig. 6. The only difference to the planar flow is that the migration velocity is higher, approximately by a factor of 1.5 (compare fig. 6 with fig. 5). The reason is that the flow profile is not only curved in radial direction due to the parabolic flow profile, but the pipe has a second curva-

ture due to the cylindrical shape of the pipe. But the results in a pipe flow are qualitatively very similar to the results in a plane Poiseuille flow shown in fig. 5.

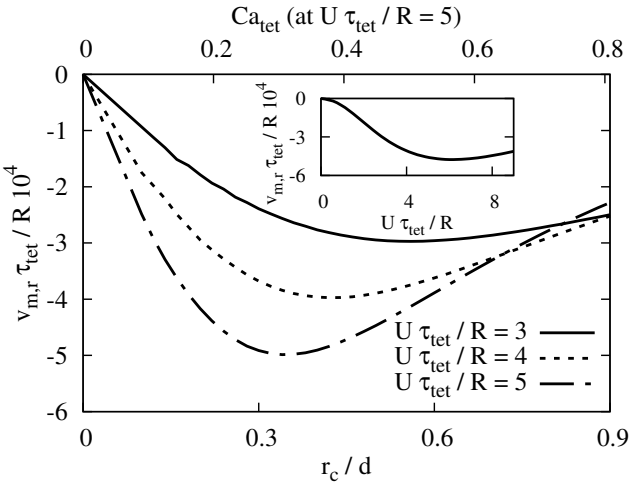

FIG. 6. The migration velocity $v_{m,r}$ for the tetrahedron in a pipe flow is given as a function of the lateral position of its center and therefore of its local capillary number for three different values of the flow velocity U. The inset shows the migration velocity of the tetrahedron as function of the flow velocity. The result is qualitatively similar to the results in a plane Poiseuille flow (compare fig. 5). The migration velocity is approximately 1.5 times faster in the pipe flow than in the plane flow but otherwise the curves have a very similar shape.

Thus the migration of a simple tetrahedron is qualitative very similar to the one of the triangle (compare figs. 3, 5 and 6).

B. Capsule

1. *Migration in Bulk and comparison with results of Barthès-Biesel*

We show that the migration of a capsule in a plane Poiseuille flow and a pipe flow can be described well with an easy bead model. To proof this, we compare our results with the analytical work of Barthès-Biesel.

At first we show that the deformation of our simple bead capsule gives the correct results by comparing our results with the analytical expression given in [47], which describes the deformation of a capsule in a linear shear flow. To describe the deformation the Taylor parameter D= $\frac{L-B}{L+B}$ is used whereby L and B are the long and the short half axis of the deformed capsule. This measure of the deformation is given analytically as function of the capillary number as D = $\frac{25}{12}$Ca in case of small deformations in [47], i.e. as long as D< 0.15. We can now compare the bead capsule model with this analytical results. We simulated the capsule in a linear shear flow and determined the values of D in dependence of

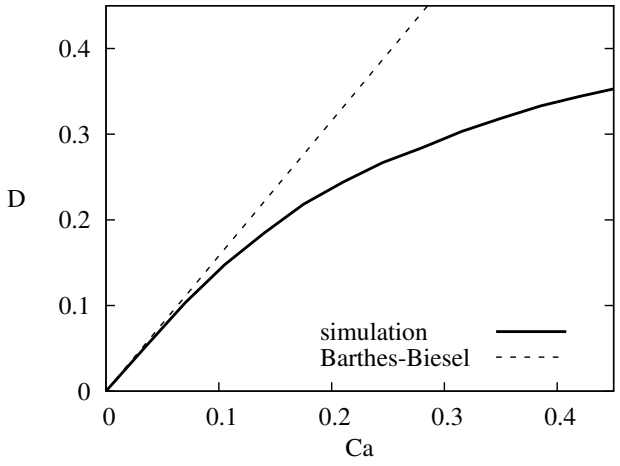

FIG. 7. A benchmark of the bead capsule model: The Taylor parameter D, which measures the deformation of the capsule, as function of the capillary number Ca. Barthès-Biesel has shown [47], that D is given by D = $\frac{25}{12}$Ca in case of small deformations, i.e. D$\lessapprox$ 0.15. Our simulations of the bead capsule agree very well with this result at small deformations.

Ca by varying the shear rate. Both the simulations and the analytical expression is shown in fig. 7. One can see that the simulations and the analytical expression of Barthès-Biesel agree well in case of the assumed small deformations at D$\lessapprox$ 0.15. Thus we see that the simple bead model gives the right values of the deformation of a capsule.

We show now that also the migration of a capsule can be described well with the bead model. We find no migration in a linear shear flow and no migration in a Poiseuille flow, if the HI is neglected (compare [19]). Therefore we investigate the migration in a plane Poiseuille flow and a pipe flow with HI. We can compare the migration with the results of Helmy and Barthès-Biesel, who calculated the cross-stream migration velocity of a capsule in a pipe flow in case of small deformations [27]. For a Neo-Hookean capsule the migration velocity in radial direction is given in [27] as

$$v_{m,r} = -\frac{29}{36}\frac{\eta U^2 R^3 r_c}{G_s D^4} \tag{19}$$

at small deformations, whereby r_c denotes the radial distance of the capsule's center to the center of the flow. A negative velocity means a migration to the center of the flow. We can compare now the simulations of a capsule with eq. (19). We determine therefore the migration velocity as function of the initial position (and also of the local capillary number) at three different values of the flow velocity U and also as function of U. The comparison of the simulations and the analytical expression (19) is shown in fig. 8 at a value of $U\frac{\tau}{R} = 1$. At small deformations the simulation and eq. (19) agree well, hence we see that the simple bead capsule model can correctly

describe the migration velocity.

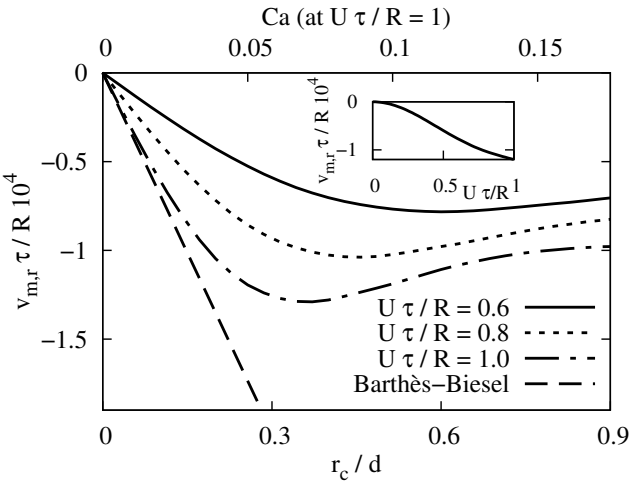

FIG. 8. The migration velocity $v_{m,r}$ of the capsule in a pipe flow is given as a function of the lateral position of its center and therefore of its local capillary number for three different values of the flow velocity U. The negative values of $v_{m,r}$ mean a migration to the center. Also the analytical calculation of Barthès-Biesel for small values of Ca is given as a benchmark of the model for $U\frac{\tau}{R} = 1$. Both simulations and the analytical expression agree well. The migration is also shown at higher values of Ca: The migrations magnitude increases linearly with an increasing value of Ca at Ca$\lessapprox$ 0.06, shows a maximum at Ca$\approx$ 0.06 and then a constant value at Ca$\gtrapprox$ 0.15 (shown for $U\frac{\tau}{R} = 1$). The inset shows at $r_c/d = 0.5$ that $|v_{m,r}|$ increases with the flow velocity U.

We also determined the migration velocity of the capsule at higher values of Ca. With increasing distance to the center the migration's absolute value increases at first linearly. Then the migration's magnitude displays a maximum at Ca$\approx$ 0.06 and becomes smaller at Ca$\gtrapprox$ 0.06 until the migration becomes approximately constant at values of Ca$\gtrapprox$ 0.15. Figure 8 shows also the migration velocity as function of the flow velocity U: The migration's absolute value increases with U. We also see that the migration is always directed to the center.

We determine also the migration of the capsule in a plane Poiseuille flow so that we can on the one hand compare the pipe flow and the plane flow and on the other hand the capsule model with the tetrahedron and the two dimensional ring. The migration velocity of a capsule in a plane flow is given in fig. 9 as function of the lateral position, the local capillary number and in the inset as function of the flow velocity U. Here the migration's absolute value also increases linearly at small deformations, i. e. low values of Ca, and becomes constant at larger values of Ca$\gtrapprox$ 0.1. This is the same behavior as found for a vesicle given in [28] or a capsule given in [30] (Note that [30] defines Ca differently). The inset of fig. 9 shows that the migration becomes faster with increasing values of U. The migration is directed towards the center.

Figure 9 shows also the shape of the capsule at different lateral positions and local capillary numbers. The cross section of the capsule is close to a circle at low values of Ca and becomes more and more an ellipsis at higher values of Ca.

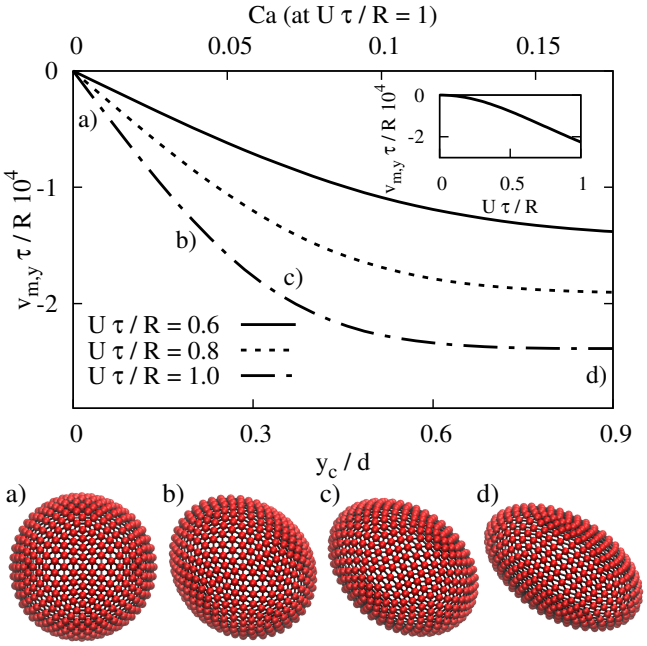

FIG. 9. (color online) The migration velocity $v_{m,y}$ of the capsule in a plane Poiseuille flow is given as a function of the lateral position of its center for three different values of the flow velocity U. The migration's absolute value grows almost linear with Ca until it reaches a plateau at higher values of Ca$\gtrapprox$ 0.15 (shown for $U\frac{\tau}{R} = 1$). The inset shows at $y_c/d = 0.5$ that the migration's absolute value increases with the flow velocity U. Also the shape of the capsule is shown at different positions along $y_c(t)$ in Poiseuille flow, as indicated by a)-d). The higher the value of Ca is the more the cross section of the capsule is deformed to an ellipse.

These results are similar compared with the pipe flow, where the migration's magnitude as function of Ca also increases linearly at low values of Ca and reached a constant value at higher values of Ca. The only difference is that in a plane flow no maximum is found and that the migration velocity in a plane flow is faster than in pipe flow approximately by a factor of two (compare figs. 8 and 9).

We can now compare the other models with the capsule in plane flow, at first with the tetrahedron and the triangle and secondly with the two dimensional ring. The tetrahedron and the capsule displayed both a migration to the center and showed the same three requirements of the occurrence of a migration in a flow with parallel stream lines: The particle must be deformable, the shear rate must vary across the particle and the HI is needed. Furthermore both particles showed a linear increase of the migration's magnitude with the capillary number at low values of the capillary number. Thus both models

showed qualitatively the same results for small deformations. But at larger values of Ca_{tet} we found with the tetrahedron a maximum of the migration's absolute value at $\mathrm{Ca}_{tet} \approx 0.3$ and a vanishing migration at high values of Ca_{tet}. Here the result is different to the capsule, which displayed a constant migration velocity at higher values of $\mathrm{Ca} \gtrapprox 0.15$. Thus in general both models display a migration to the center and show a qualitative agreement as long as the capillary number is not too high. At high capillary numbers the details of the dependency of the migration velocity on the capillary number is different for both models. The reason is that the volume of the capsule is conserved, whereas the tetrahedron is only connected by springs and can undergo very high deformations at large values of Ca_{tet}. This constant migration at high values of Ca is also reported in case of a 2D vesicle [28] or a 3D capsule [30] with area or volume conservation, so that the bead capsule is more comparable to a realistic particle at high values of Ca. The behavior of the triangle is similar to the tetrahedron.

Secondly, we can also compare the migration velocity as function of the capillary number found for capsule with the results of the ring (compare figs. 4 and 9). We find in both cases the same three requirements of the migration in a flow with parallel stream lines and that the migration is directed to the center. We see also that the migration's magnitude as function of the capillary number grows linearly at small values of the capillary number and becomes constant at higher values. This agrees qualitatively well with the vesicle described in [28] or the capsule given in [30]. Furthermore figs. 4 and 9 show the shapes of ring and the capsule. Both ring and capsule show a similar deformation: The ring becomes nearly an ellipse at off center positions and also the capsule displays an elliptic cross section at values of Ca$>$ 0. Thus the ring gives qualitatively the same results as the capsule for both the migration velocity and the shape and can be seen in this sense as a cross section of the capsule.

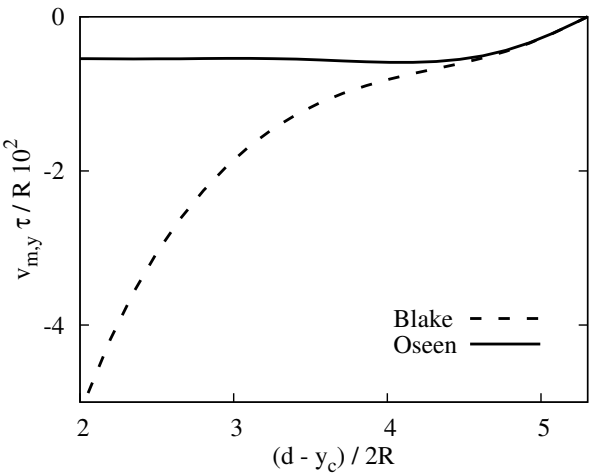

FIG. 10. The migration velocity $v_{m,y}$ of the capsule in a bounded and unbounded flat Poiseuille-flow is given as a function of the lateral distance to the wall. The simulations are conducted with the bead model with the Oseen tensor without wall interaction and with Blake tensor with wall interaction. At distances to the wall lesser then three diameters of the capsule the migration to the center with wall interaction (Blake) is much higher than with neglected wall interaction (Oseen). Thus the wall is repulsive and this repulsion is clearly dominant compared with the bulk migration described by the Oseen tensor. At distances higher then 4 diameters the wall repulsion is negligible and the bulk migration is dominant: Blake and Oseen tensor approximately lead to the same migration velocity.

2. including Wall-repulsion and a comparison with lattice-Boltzmann simulations

Up to now we neglected the wall interaction. Here we show that the wall interaction can easily be taken into account with a bead model. We discuss also how the wall influences the migration and at which distance to the wall the influence of the wall can be neglected. This is done by comparing simulations with the Blake tensor, which includes the wall interaction with simulations with the Oseen tensor, which neglects the wall. We also give a third benchmark of the bead model by comparing the bead capsule with a full lattice Boltzmann simulation.

At first we discuss the differences between the bead models with and without wall interaction: Figure 10 shows the migration velocity as function of the distance to the wall. One sees that up to a distance of approximately three diameters distance to wall the wall interaction is dominant: The migration to the center with wall interaction is more than two times faster than without the wall. This repulsion of the wall decays with the distance to the wall. At a distance of approximately four diameters away from the wall the difference in the velocities is less than 10% and the wall Hi becomes negligible. This strong wall repulsion was also reported in [30].

We can also compare the result of the bead model with a Lattice-Boltzmann simulation. As described in sec. II the lattice Boltzmann simulation solves the full Navier-Stokes Equation on a grid and the moving capsule is coupled with this grid via the immersed boundary method. In contrast the bead model uses point particles and solves the stokes equation with the Blake tensor, which is an approximation of the wall interaction. This means also that in one case the Reynolds Number is 0 for the bead model and for the LBM simulation the Reynolds Number is small but finite with a value of Re=0.78. Despite these differences in the modeling of the capsule the results agree well, which is shown in fig. 11: It shows the migration velocity in dependence of the distance of the capsule center and the wall. Both models show the strong wall repulsion close to the wall, the slower migration in bulk further away from the wall, which vanishes at the center. Thus the results are similar.

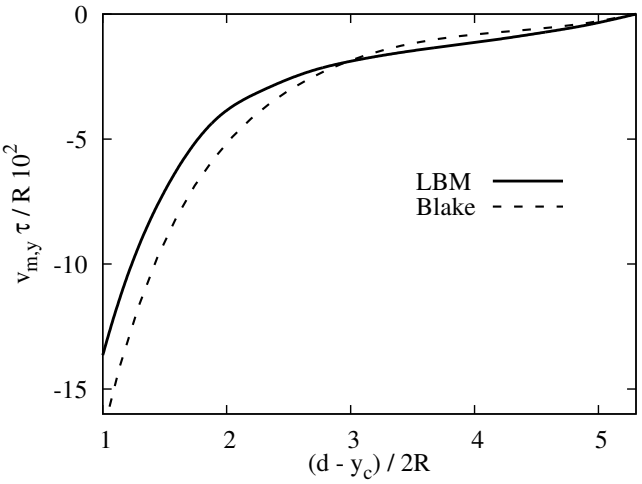

FIG. 11. Top: A comparison of the Blake simulations (dashed) with a Lattice Boltzmann simulation (solid). The plot shows the migration velocity as function of the distance to the wall. Both methods show a strong repulsion close to the wall. Further away from the wall the simulations show a slower migration in bulk. Thus the qualitative behavior is the same in both simulations. Also the quantitative agreement is good, which is between 0% and 35%.

V. MIGRATION MECHANISM EXPLAINED BY BEAD-SPRING MODELS AND SEMI-ANALYTICAL RESULTS

Here we give an explanation of the migration of deformable particles with the help of bead-spring models. At first, in section V A, we explain the basic mechanism: We show that the migration is driven by forces due to the tank-treading motion and the spatial dependence of the flow and by the particle's finite size if the stream lines are not parallel. We also compare these results with [27].

In section V B we give an analytic expression for the migration velocity of the bead capsule and explain the approximations used to derive the expression. This allows to determine the conditions under which a migration of this capsule model occurs: We show that a cross-streamline migration is found in flow with parallel stream lines if the flow has a finite first and second spatial derivative and if Hi is included (compare [19]). The finite shear rate means a finite capillary number and the second derivative means a shear rate that changes over the size of the particle, so that this agrees with the numerical findings in the Poiseuille flow. We further show that also non-parallel stream lines can lead to a migration. In this case the HI is not necessary. The used plausible approximations are then justified by a comparison and a good agreement with the numeric simulations.

A. The mechanism of cross-streamline migration in bulk

Here we explain the main migration mechanism of a spherical and deformable bead-spring particle in an arbitrary, unbounded flow, e.g. the capsule described in sec II. Let

$$\mathbf{p}(\phi,\theta,t) = \rho(\phi,\theta,t)\hat{\mathbf{e}}_r + \mathbf{r}_c(t) \tag{20}$$

describe the surface of the particle. It is chosen in a way, that all beads are located on $\mathbf{p}$. Here $\mathbf{r}_c(t)$ is its center at

$$\mathbf{r}_c(t) = \frac{1}{N}\sum_i \mathbf{r}_i(t) \tag{21}$$

and $\rho(\phi,\theta)\hat{\mathbf{e}}_r$ describes the distance between the center and the surface in spherical coordinates. Also the coordinates $\phi_i(t)$ and $\theta_i(t)$ of a bead are time-dependent due to its motion. The velocity of a bead located at $\mathbf{r}_i$ is therefore given by

$$\dot{\mathbf{r}}_i = \frac{d}{dt}\mathbf{p}(\phi_i(t),\theta_i(t),t) \tag{22}$$

$$= \underbrace{\frac{d}{dt}\left[\rho(\phi_i(t),\theta_i(t))\hat{\mathbf{e}}_r\right]}_{=\mathbf{v}_i^{tt}} + \dot{\mathbf{r}}_c(t) \tag{23}$$

$$= \mathbf{v}_i^{tt} + \dot{\mathbf{r}}_c(t)\,, \tag{24}$$

If the temporal change of the surface $\frac{\partial\rho}{\partial t}$ is negligible then $\mathbf{v}^{tt}$ is a motion parallel to the surface, the so-called tank-treading motion, and $\dot{\mathbf{r}}_c(t)$ is the motion of the center of the particle. This derivative $\frac{\partial\rho}{\partial t}$ vanishes if the shape is approximately stationary. This is the case e.g. in a plane Poiseuille flow, where the shape changes only due to the lateral migration, which is magnitudes smaller than the motion in flow direction (compare e.g. [30] or fig. 9).

We use the equation of motion (4) and eq. (24), which leads to

$$\mathbf{v}_i^{tt} + \dot{\mathbf{r}}_c(t) = \mathbf{u}_i + \sum_j \mathbf{H}_{i,j}\mathbf{F}_j\,. \tag{25}$$

We further assume an external force $\mathbf{F}^{ext}$ (e.g. a buoyancy force). Therefore the sum of all forces is $\mathbf{F}^{ext}$, because the sum of the internal forces must vanish. We receive with this definition

$$\sum_j \mathbf{H}_{i,j}\mathbf{F}_j = \dot{\mathbf{r}}_c - \mathbf{u}_i + \mathbf{v}_i^{tt}\,, \tag{26}$$

$$\sum_i \mathbf{F}_i = \mathbf{F}^{ext}\,, \tag{27}$$

This set of linear equations allows to determine the origin of the forces $\mathbf{F}_i$. To see this we have a closer look at eq.

(26) and define the forces

$$\sum_j \mathbf{H}_{i,j}\mathbf{F}_j^{tr} = \dot{\mathbf{r}}_c - \mathbf{u}_m\,, \tag{28}$$

$$\sum_j \mathbf{H}_{i,j}\mathbf{F}_j^{u} = -\left(\mathbf{u}_i - \mathbf{u}_m\right)\,, \tag{29}$$

$$\sum_j \mathbf{H}_{i,j}\mathbf{F}_j^{tt} = \mathbf{v}_i^{tt}\,, \tag{30}$$

$$\text{with } \mathbf{u}_m = \frac{1}{N}\sum_i \mathbf{u}_i\,,\ \mathbf{u}_i = \mathbf{u}_0(\mathbf{r}_i). \tag{31}$$

This implies that eq. (26) is fulfilled and yields

$$\mathbf{F}_i = \mathbf{F}_i^u + \mathbf{F}_i^{tr} + \mathbf{F}_i^{tt}\,, \tag{32}$$

so the force acting on the particle consists of three contributions: The source of three contributions $\mathbf{F}_i^u$, $\mathbf{F}_i^{tr}$, $\mathbf{F}_i^{tt}$ are the right hand side of eqs. (28), (29) and (30): The force $\mathbf{F}_i^{tr}$ describes the Stokes friction of the particle that occurs if the particles velocity differs from the mean external flow velocity. The force $\mathbf{F}_i^u$ is a modification of the stokes friction and describes how the stokes friction is changed if the external flow changes at the surfaces of the particle, i.e. if the flow is not homogeneous. The last force $\mathbf{F}_i^{tt}$ describes the friction force between the fluid and the particle due to the particle's tank-treading motion.

With the definition $\sum \mathbf{F}_i^{tr} = \mathbf{F}^{tr}$ (other forces analogue) and the linearity of eq. (28) we can express the solution as

$$\mathbf{F}^{tr} = \boldsymbol{\zeta}(\dot{\mathbf{r}}_c - \mathbf{u}_m)\,, \tag{33}$$

which represents the stokes friction with the friction matrix $\boldsymbol{\zeta}$.

The sum over all forces (over eq. (32) with eqs. (27), (33)) can now be written as

$$\mathbf{F}^{tr} + \mathbf{F}^{u} + \mathbf{F}^{tt} = \mathbf{F}^{ext} \tag{34}$$

$$\boldsymbol{\zeta}(\dot{\mathbf{r}}_c - \mathbf{u}_m) = -\mathbf{F}^{u} - \mathbf{F}^{tt} + \mathbf{F}^{ext} \tag{35}$$

$$\dot{\mathbf{r}}_c = \mathbf{u}_m + \boldsymbol{\zeta}^{-1}(-\mathbf{F}^{u} - \mathbf{F}^{tt} + \mathbf{F}^{ext}) \tag{36}$$

$$\dot{\mathbf{r}}_c = \mathbf{u}_m + \underbrace{\mathbf{u}_u}_{=-\boldsymbol{\zeta}^{-1}\mathbf{F}^u} + \underbrace{\mathbf{u}_{tt}}_{=-\boldsymbol{\zeta}^{-1}\mathbf{F}^{tt}} + \boldsymbol{\zeta}^{-1}\mathbf{F}^{ext} \tag{37}$$

This means the force due to the spatial dependence of the flow $-\mathbf{F}^u$ and the force due to the tank treading $-\mathbf{F}^{tt}$ contribute to the motion of the particle in the same way as the external force $\mathbf{F}^{ext}$. We can define the migration velocity $\mathbf{v}_m$ as the difference of the particle velocity to the flow velocity at its center

$$\mathbf{v}_m = \dot{\mathbf{r}}_c(t) - \mathbf{u}(\mathbf{r}_c) \tag{38}$$

$$= \mathbf{u}_m - \mathbf{u}(\mathbf{r}_c) + \boldsymbol{\zeta}^{-1}(\mathbf{F}^{ext} - \mathbf{F}^{u} - \mathbf{F}^{tt}) \tag{39}$$

The eq. (39) allows to identify the three mechanism of migration in bulk: The first term $\mathbf{u}_m - \mathbf{u}(\mathbf{r}_c)$ means that a particle can migrate if the average velocity over its surface is not the same as the velocity at its center. If all streamlines of the flow are parallel and the flow is directed everywhere in the same direction, it follows that $\mathbf{u}_m$ is parallel to $\mathbf{u}(\mathbf{r}_c)$. This means in this case $\mathbf{u}_m$ can not contribute to the cross-streamline-migration. But it can contribute if the flow's direction is spatially dependent, which means if the streamlines are non-parallel. This term is caused by the finite size of the particle, which means its motion is influenced by the flow on its complete surface, not on its center. The second term in eq.

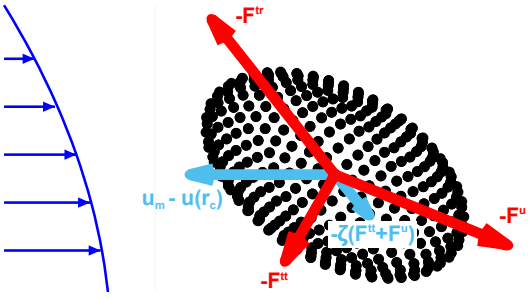

FIG. 12. The forces $-\mathbf{F}^{tr}$, $-\mathbf{F}^{tt}$ and $-\mathbf{F}^{u}$ (red) acting on a capsule in a plane Poiseuille flow (sketched in blue). Both the tank-treading and the spatial dependence of the flow lead to a force, which leads to the migration to the center $-\zeta(\mathbf{F}^{tt}+\mathbf{F}^{u})$ (blue, scaled by a factor 10^3, see eq. (39)). Together with the force due to the translation of the particle the sum of all forces is zero. The contribution of the mean flow to the migration $\mathbf{u}_m - \mathbf{u}(\mathbf{r}_c)$ (see eq. (39)) leads to a migration (shown in blue) anti-parallel to the flow direction, a lag behind, and does not contribute to the cross-streamline migration (compare also [30]). The forces and velocities are determined by simulations and with eqs. (28), (29), (30), (40) and (41) (with $U\frac{\tau}{R} = 1$, $y_c = 65$ and $\mathbf{F}^{ext} = 0$, compare fig. 9).

(39) describes that a spatially dependent flow can exert a force $\mathbf{F}^u$ on the particle, even if the particle moves with the mean velocity of the flow. This force leads to the velocity $-\boldsymbol{\zeta}^{-1}\mathbf{F}^u$. This term vanishes in a homogeneous flow (see eq. (29)). The third term describes the motion due to the force $\mathbf{F}^{tt}$ caused by the friction of the tank-treading motion, which leads to the velocity $-\boldsymbol{\zeta}^{-1}\mathbf{F}^{tt}$. The last term $\boldsymbol{\zeta}^{-1}\mathbf{F}^{ext}$ describes the motion due to an external force with the the stokes friction matrix $\boldsymbol{\zeta}$.

The forces $\mathbf{F}^{tr}$, $\mathbf{F}^{tt}$ and $\mathbf{F}^{u}$ and the contribution of the mean velocity $\mathbf{u}_m - \mathbf{u}(\mathbf{r}_c)$ to the migration velocity (see eq. (39)) can now be calculated with numerical data: With $\mathbf{r}_i$ and $\dot{\mathbf{r}}_i$ determined with simulations one can use eqs. (21) and (24) which yield

$$\dot{\mathbf{r}}_c = \frac{1}{N}\sum_i \dot{\mathbf{r}}_i, \tag{40}$$

$$\mathbf{v}_i^{tt} = \dot{\mathbf{r}}_i - \dot{\mathbf{r}}_c \tag{41}$$

and the equations (28), (29) and (30) to determine $\mathbf{u}_m$, $\mathbf{F}^{tr}$, $\mathbf{F}^{u}$, $\mathbf{F}^{tt}$ and $\boldsymbol{\zeta}$ with the help of the numerical data. Figure 12 gives an example of these forces in case of a capsule in a plane Poiseuille flow. One can see clearly

that both the tank treading and the spatial dependence of the flow lead to the forces $\mathbf{F}^u$ and $\mathbf{F}^{tt}$, which cause the migration to the center in the plane Poiseuille flow. The contribution of the mean flow $\mathbf{u}_m - \mathbf{u}(\mathbf{r}_c)$ is parallel to the flow and leads to a migration in flow direction (a lag behind, compare also [30]).

We did not assume a certain flow. This allows to compare this results with the analytical calculation of Helmy and Barthès-Biesel given in [27], where the cross stream migration velocity was calculated in a pipe flow at small deformations. They also give a force as reason of the migration, which is caused by the interaction of the flow and the particle. The Poiseuille flow is of course spatially dependent and the calculation of [27] considers the tank-treading motion, so that the force found by Helmy and Barthès-Biesel is in this sense comparable to the forces $\mathbf{F}^u$ and $\mathbf{F}^{tt}$ given here. As stated above the term $\mathbf{u}_m - \mathbf{u}(\mathbf{r}_c)$ does not contribute to the cross-streamline migration in case of a pipe flow, due to the parallel streamlines. Conformable to this result Helmy and Barthès-Biesel do not give a contribution like $\mathbf{u}_m - \mathbf{u}(\mathbf{r}_c)$ to the cross-stream migration. Thus the explanation of the migration in a pipe flow given here agree with the results of Helmy and Barthès-Biesel.

Note that the source of these forces $\mathbf{F}^u$, $\mathbf{F}^{tt}$ is the hydrodynamic interaction, which means these forces are caused by the flow disturbance of the particle. This can be seen as follows: Without HI the equation of motion (4) becomes

$$\dot{\mathbf{r}}_i = \mathbf{u}_0(\mathbf{r}_i) + \frac{1}{6\pi\eta a}\mathbf{F}_i \,, \tag{42}$$

If the equation is averaged over all beads and if we consider that the sum of all forces is zero (assuming no external force) we get

$$\dot{\mathbf{r}}_c = \frac{1}{N}\sum_i \mathbf{u}_0(\mathbf{r}_i) \,, \tag{43}$$

$$\dot{\mathbf{r}}_c = \mathbf{u}_m \,. \tag{44}$$

and

$$\mathbf{v}_m = \mathbf{u}_m - \mathbf{u}(\mathbf{r}_c) \,. \tag{45}$$

This is similar to the migration velocity with HI given by eq. (39), but without the forces $\mathbf{F}^u$, $\mathbf{F}^{tt}$ that drive the migration in flows with parallel stream lines. Therefore in case of parallel stream lines the HI is necessary to receive a cross-streamline migration. As explained above the term $\mathbf{u}_m - \mathbf{u}(\mathbf{r}_c)$ can only lead to a migration in flows with non-parallel stream lines, so that for non-parallel stream lines a migration can also occur without HI, which means due to the undisturbed flow.

B. Semi-analytical approximation of the migration velocity

We have showed in the previous section that the migration is caused in general by three contributions: the finite size of the particle and the forces due to the tank-treading and spatially dependent flow. We now calculate the migration velocity with approximations and give an expression of these contributions in dependence of the flow. This allows also to determine under which conditions a migration occurs. We give here just the used assumptions and the result. The complete calculation can be found in the appendix.

1. *Derivation of the migration velocity and assumptions*

We use a flow with translational invariance in one direction, but otherwise arbitrary. This means the flow is 3D but depends only on two coordinates, we choose on x and y. We assume at first that the flow changes slightly at the size of the particle, so that we can represent it by a Taylor expansion of second order

$$\mathbf{u}_0 \approx \sum_{n=0}^{2} \frac{1}{n!}\left[(x-x_c)\partial_x + (y-y_c)\partial_y\right]^n_{x=x_c,y=y_c}\mathbf{u}_0 \,, \tag{46}$$

$$= \sum_{k,l=0}^{k+l\leq 2} \mathbf{b}_{k,l}(x-x_c)^k(y-y_c)^l \,. \tag{47}$$

The $\mathbf{b}_{k,l}$ represent the Taylor coefficients of the flow. We use σ as an abbreviation of m,k,l and define

$$a_\sigma := (\mathbf{a}_{k,l})_m = R^{k+l}(\mathbf{b}_{k,l})_m \,, \tag{48}$$

whereby $(\mathbf{a}_{k,l})_m$ denotes the m-component of $\mathbf{a}_{k,l}$ and R the radius of the particle. We determine now approximately the particles velocity $\dot{\mathbf{r}}_c$ as function of the a_σ. At first we assume that no external torque is applied, which means the particle is torque free. In this case the tank-treading motion can be approximated with the rotation of the flow (see e.g. [27])

$$\boldsymbol{\omega} = \frac{1}{2}\,\nabla\times\mathbf{u}_0|_{\mathbf{r}=\mathbf{r}_c} \,. \tag{49}$$

Thus the tank-treading motion of all beads $\mathbf{v}_i^{tt}$ has the same axis $\boldsymbol{\omega}$ with the same angular velocity $|\boldsymbol{\omega}| = \dot{\phi}$. The angle θ_i is chosen to be the angle between $\mathbf{r}_i - \mathbf{r}_c$ and $\boldsymbol{\omega}$ hence θ_i is not changed by the rotational motion. With this we get for the expression of the tank-treading motion eq. (23)

$$\mathbf{v}_i^{tt} = \frac{d}{dt}\left[\rho(\phi_i(t),\theta_i)\hat{\mathbf{e}}_{r,i}\right] \tag{50}$$

$$= \dot{\phi}\frac{\partial}{\partial\phi}\left[\rho(\phi,\theta_i)\hat{\mathbf{e}}_r\right]_{\phi=\phi_i} \tag{51}$$

$$= \dot{\phi}\,\rho(\phi_i,\theta_i)\,\sin\theta\hat{\mathbf{e}}_{\phi,i} + \dot{\phi}\left.\frac{\partial\rho}{\partial\phi}\right|_{\phi=\phi_i}\hat{\mathbf{e}}_{r,i} \tag{52}$$

$$= \boldsymbol{\omega}\times(\mathbf{r}_i - \mathbf{r}_c) + \dot{\phi}\left.\frac{\partial\rho}{\partial\phi}\right|_{\phi=\phi_i}\hat{\mathbf{e}}_{r,i} \tag{53}$$

Furthermore we assume that the equilibrium shape is a sphere with radius R and that the deformation of the sphere is small. Therefore we define

$$\mathbf{r}_i = \mathbf{r}_i^{(0)} + \Delta\mathbf{r}_i + \mathbf{r}_c, \quad \text{with } |\Delta\mathbf{r}_i| \ll R \tag{54}$$

The $\mathbf{r}_i^{(0)}$ are the equilibrium positions at the spherical shape without deformations. We also need an equation that relates the deformation and the forces on the sphere. Due to the small deformations we assume that elastic restoring forces of the particle are linear, hence we can assume that beads are connected with springs. We use a Taylor expansion around small deformations of the springs. But springs between the beads alone do not lead to a stable shape, e.g. it is possible to reduce the volume to zero without changing the length of the springs. In the simulations this is prevented by the conserved volume and the bending force (see sec. II). We therefore add a spring between the bead and its equilibrium position, which leads to a stable shape and mimics in this sense the effect of a bending force. This leads to

$$\mathbf{F}_i^{int} = -f_k \sum_j \hat{\mathbf{b}}_{i,j}\hat{\mathbf{b}}_{i,j} \cdot (\Delta\mathbf{r}_i - \Delta\mathbf{r}_j) - f_b \frac{\Delta\mathbf{r}_i}{N}\,, \tag{55}$$

$$\hat{\mathbf{b}}_{i,j} = \frac{\mathbf{r}_i^{(0)} - \mathbf{r}_j^{(0)}}{|\mathbf{r}_i^{(0)} - \mathbf{r}_j^{(0)}|}\,, \tag{56}$$

whereby the summation is over next neighbors. The spring stiffness of the springs to the equilibrium position is scaled with N, because the number of springs and therefore the restoring force to the equilibrium position is proportional to the number of the beads. For the sake of simplicity we chose $f_b = f_k$, so that both forces have approximately the same magnitude. Furthermore the springs connected with the equilibrium position ensures that the average deformation is zero, because sum of the internal forces is zero

$$0 = \sum_i \mathbf{F}_i^{int} = -f_b \sum_i \frac{\Delta\mathbf{r}_i}{N} \;\Rightarrow\; \frac{1}{N}\sum_i \Delta\mathbf{r}_i = 0 \tag{57}$$

This means the average deformation is zero and the internal forces do not shift the center of the particle.

These spring forces are internal forces. As above the entire external force is given by $\mathbf{F}^{ext}$ and the force on a bead by

$$\mathbf{F}_i = \mathbf{F}_i^{int} + \mathbf{F}_i^{ext},\; \mathbf{F}_i^{ext} = \frac{1}{N}\mathbf{F}^{ext} \tag{58}$$

Thus the external force is equally distributed over the surface of the particle. The same assumption was made in [34] to describe the effect of an external force in simulations.

This allows to determine under which conditions the deformations are small. The deformation is caused by the change of the external flow velocity on the scale of the particle, which is measured by a_σ. The force resulting from the external flow on the particle is also determined by the viscosity. This must be compared with the spring stiffness, because a high spring stiffness leads to a small deformation. A dimensionless number Df that measures the deformation due to the flow is therefore

$$\mathrm{Df} = \frac{\eta}{f_k} \sum_{\sigma,k+l>0} |a_\sigma|\,. \tag{59}$$

The constant part of the flow $\mathbf{a}_{0,0}$ is not included in the sum because it does lead to a deformation. The Df in a linear shear flow represents the usual definition of the capillary number. The deformation is small if $\mathrm{Df} \ll 1$. Also the external force deforms the sphere, which is measured by

$$\mathrm{Df}^{ext} = \frac{|\mathbf{F}^{ext}|}{f_k R}\,. \tag{60}$$

Also Df^{ext} must be small enough to avoid large deformations $\mathrm{Df}^{ext} \ll 1$. We can also compare the friction forces due to the flow and the external force with the number

$$\mathrm{V} = \frac{|\mathbf{F}^{ext}|}{\eta R \sum\limits_{\sigma,k+l>0} |a_\sigma|}\,. \tag{61}$$

We consider only small external forces and neglect the deformation caused by the external force. This means the external force is assumed to be much smaller than the friction due to the flow, i.e. we assume

$$\mathrm{V} \ll 1\,, \tag{62}$$

which is equal to $\mathrm{Df}^{ext} \ll \mathrm{Df}$ (A similar assumption was made in [34]). We neglect contributions of higher than first order of these numbers Df and Df^{ext}.

The small deformations allow furthermore a Taylor expansion of the Oseen tensor around the equilibrium positions of the beads

$$\mathbf{H}_{i,j} = \mathbf{O}(\mathbf{r}_i^{(0)} - \mathbf{r}_j^{(0)} + \underbrace{\Delta\mathbf{r}_i - \Delta\mathbf{r}_j}_{\boldsymbol{\varepsilon}})\,,\; i \neq j \tag{63}$$

$$\approx \mathbf{O}(\mathbf{r}_i^{(0)} - \mathbf{r}_j^{(0)}) + \sum_p \mathbf{O}_{i,j}^p \varepsilon_p \tag{64}$$

$$= \mathbf{O}(\mathbf{r}_i^{(0)} - \mathbf{r}_j^{(0)}) + \sum_p \mathbf{O}_{i,j}^p \left(\Delta\mathbf{r}_i - \Delta\mathbf{r}_j\right)_p \tag{65}$$

$$= \mathbf{H}_{i,j}^{(0)} + \sum_p \mathbf{H}_{i,j}^p \left(\Delta\mathbf{r}_i - \Delta\mathbf{r}_j\right)_p \tag{66}$$

$$\mathbf{O}_{i,j}^p = \frac{\partial}{\partial\varepsilon_p}\mathbf{O}(\mathbf{r}_{0,i} - \mathbf{r}_{0,j} + \boldsymbol{\varepsilon})\Big|_{\boldsymbol{\varepsilon}=0} \tag{67}$$

With these assumptions and the eqs. (26) and (27) we

get a set of equations

$$\sum_j \mathbf{H}_{i,j}\mathbf{F}_j = \dot{\mathbf{r}}_c - \mathbf{u}_i + \mathbf{v}_i^{tt}\,, \tag{68}$$

$$\sum_i \mathbf{F}_i = \mathbf{F}^{ext},\ \mathbf{F}_i = \mathbf{F}_i^{int} + \frac{1}{N}\mathbf{F}^{ext},\ \sum_i \mathbf{F}_i^{int} = 0 \tag{69}$$

$$\mathbf{F}_i^{int} = -\,f_k \sum_j \hat{\mathbf{b}}_{i,j}\hat{\mathbf{b}}_{i,j}\cdot(\Delta\mathbf{r}_i - \Delta\mathbf{r}_j) - f_b\frac{\Delta\mathbf{r}_i}{N} \tag{70}$$

$$\boldsymbol{\omega} = \frac{1}{2}\,\nabla\times\mathbf{u}_0|_{\mathbf{r}=\mathbf{r}_c}\,,\ \dot{\phi} = |\boldsymbol{\omega}| \tag{71}$$

$$\mathbf{v}_i^{tt} = \boldsymbol{\omega}\times\left(\mathbf{r}_i^{(0)} + \Delta\mathbf{r}_i\right) + \dot{\phi}\frac{\partial r_i}{\partial\phi}\hat{\mathbf{e}}_{r,i} \tag{72}$$

This set of equations allows to determine the forces, the shape and the tank-treading and translational motion. But due to the product of the Oseen Tensor and the forces the system is nonlinear. We solve it therefore in an iterative way. The shape and the resulting hydrodynamic forces are calculated alternating, which can be done until all equations are fulfilled. This leads to a system of linear equations, which can be solved (semi-) analytically. A similar approach is used in [64], where also the shape and the forces are calculated alternating until a self-consistent solution is found, but with a purely numerical boundary integral method. We use only one iteration step for the analytical calculation, which already agrees with the simulations in case of small deformations (what we show in the following sections). The full calculation is given in the SI. Here we show the result

$$\dot{\mathbf{r}}_c = \mathbf{u}_m + \mathbf{u}_u + \mathbf{u}_{tt} + \boldsymbol{\zeta}^{-1}\mathbf{F}^{ext}\,,\ \mathbf{v}_m = \dot{\mathbf{r}}_c - \mathbf{u}(\mathbf{r}_c) \tag{73}$$

$$\mathbf{u}_m = \sum_{k,l}\mathbf{a}_{k,l}\left(\ {}_{mean}M_{k,l} + \frac{\eta}{f_k}\sum_{\sigma'} a_{\sigma'}\ {}_{mean}M_{k,l,\sigma'}\right) \tag{74}$$

$$\mathbf{u}_u = \frac{\eta}{f_k}\sum_{\sigma,\sigma'}\ {}_u\mathbf{M}_{\sigma,\sigma'}\ a_\sigma a_{\sigma'} \tag{75}$$

$$\mathbf{u}_{tt} = \frac{\eta}{f_k}\sum_{\sigma,\sigma'}\ {}_{tt}\mathbf{M}_{\sigma,\sigma'}\ a_\sigma a_{\sigma'} \tag{76}$$

$$\boldsymbol{\zeta}^{-1} = \underbrace{0.0527}_{\approx\frac{1}{6\pi}}\frac{1}{\eta R}\mathbf{1} + \frac{1}{f_k R}\sum_\sigma a_\sigma\ {}_\zeta\mathbf{M}_\sigma\,, \tag{77}$$

The velocity of the particle is given by the terms $\mathbf{u}_m$, $\mathbf{u}_u$, $\mathbf{u}_{tt}$, $\boldsymbol{\zeta}^{-1}$ which represents the contribution of the mean flow, the spatial dependency of the flow, the tank treading motion and the stokes friction (cf. eq. (37)). This solution is a polynomial in the Taylor coefficients of the flow. The dimensionless prefactors ${}_{mean}M_{k,l}$, ${}_u\mathbf{M}_{\sigma,\sigma'}$, ${}_{tt}\mathbf{M}_{\sigma,\sigma'}$ and ${}_\zeta\mathbf{M}_\sigma$ are calculated numerically. Their values are given in the appendix (sec. 1.3).

2. Results: Requirements for cross streamline migration and direction of the migration

With the help of the eqs. (73), (74), (75), (76), (77) and the prefactors given in the appendix (sec. 1.3) we can determine under which conditions a CSM occurs and in in which direction it takes place (in an unbounded flow with translational invariance in one direction and in case of small deformations).

The term $\mathbf{u}_m$ represents the undisturbed flow averaged over the surface of the particle. Therefore it can not contribute to the cross-streamline migration if all streamlines are parallel: In this case the term points in flow direction. Furthermore it can only contribute to the migration if the flow depends nonlinear on the spatial coordinates. In an linear flow the averaged velocity over the surface is exactly the velocity at the particle's center, i.e. $\mathbf{u}_m - \mathbf{u}(\mathbf{r}_c) = 0$ (compare eq. (39)). Thus this term leads to a migration in a spatially nonlinear flow with non-parallel stream lines. As we have seen with the help of eq. (45) this term also occurs without HI, therefore it is an effect of the undisturbed flow. Furthermore it does not require a deformation of the particle, but is affected by it.

The migration due to the spatially dependence of the flow $\mathbf{u}_u$ and the migration due to tank-treading $\mathbf{u}_{tt}$ occur only if the flow has both a non vanishing first and second derivative (in other cases the prefactors ${}_u\mathbf{M}_{\sigma,\sigma'}$ ${}_{tt}\mathbf{M}_{\sigma,\sigma'}$ are zero in eq. (75), see SI sec. 1.3). As example if the flow has one non vanishing first derivative given by b_σ and one non vanishing second derivative $b_{\sigma'}$ the eqs. (75) and (76) becomes

$$\mathbf{u}_u + \mathbf{u}_{tt} = (\ {}_u\mathbf{M}_{\sigma,\sigma'} + \ {}_{tt}\mathbf{M}_{\sigma,\sigma'})\ \underbrace{\frac{\eta R}{f_k}b_\sigma}_{=\mathrm{Ca}}\ \underbrace{R^2\ b_{\sigma'}}_{=C}\,, \tag{78}$$

$$= \mathrm{Ca}\,C\quad \underbrace{(\ {}_u\mathbf{M}_{\sigma,\sigma'} + \ {}_{tt}\mathbf{M}_{\sigma,\sigma'})}_{=\text{const. given in appendix}}\quad, \tag{79}$$

$$\Rightarrow (\mathbf{u}_u + \mathbf{u}_{tt}) \propto \mathrm{Ca}\,C\,, \tag{80}$$

whereby $\mathrm{Ca} = \frac{\eta R}{f_k}b_\sigma$ represents the capillary number and $C = R^2\ b_{\sigma'}$ measures the flow profile's curvature (which means the second derivative) of the flow on the size of the particle (note that Ca and C include here the sign of the shear rate b_σ and the flow profile's curvature $b_{\sigma'}$). Thus in general the migration is proportional to the capillary number and the flow profile's curvature. If the flow has more than one non vanishing first and second derivative more terms in the sum in eq. (75) contribute, whereby each term is proportional to its corresponding capillary number and flow profile's curvature. The direction of the migration is given by the symmetry of the flow. An examples is given in the SI sec. 1.4:

These requirements of the migration are similar to the numerically found conditions given in sec. III and IV and the ones found in [19]. With the numeric results we found three requirements for migration in a flow with parallel

stream lines: The particle must be deformable, i.e. Ca must be larger than zero. This is also found with this calculation here, because the migration is proportional to Ca (see. eq. (80)). The numeric solution showed also that the shear rate must vary across the particle. This is also the case here, because the migration is proportional the flow profile's curvature and this curvature means a spatially dependent shear rate. At last we have seen with the simulations that the HI is important in the Poiseuille flow. As discussed above also the semi-analytical calculation includes the Oseen-tensor. The only term that does appear without is the finite size contribution $\mathbf{u}_m$ (see eq. (45)), which can only lead to a migration with non-parallel stream lines, but not in flow with parallel stream lines as the Poiseuille flow. Thus the general requirements here are the same as found numerically for the Poiseuille flow.

3. Comparison of the semi-analytical results and the simulations

We made various assumptions to derive the expression of the migration velocity (eq. (73)). To justify these assumptions we compare the result with simulations and with the results of Helmy and Barthès-Biesel [27].

For the semi-analytical results we used a linearized dependence of the force on the deformation with stiffness f_k, whereas capsules are described by the Neo-Hookean law with stiffness G_s. Therefore we have to find the right value of f_k to compare the calculations with a Neo-Hookean capsule. To do this we compare the deformations in a shear flow. The complete deformation, which means the displacement of each bead, is not given here, because of the large number of coefficients due to the high amount of beads. We give instead the Taylor parameter in a linear shear flow. It is defined as $D = \frac{L-B}{L+B}$ with the length of the long and the short half axis. We find for the semi-analytical model

$$D = 4.7910\ \dot{\gamma}\eta R/f_k \tag{81}$$

(see appendix). This can be compared with the values of a capsule with the Neo-Hookean law with surface shear elastic modulus G_s given by

$$D = \frac{25}{12}\ \dot{\gamma}\eta R/G_s \tag{82}$$

(given in [47] and cf. fig. 7). It allows to determine a value of f_k that leads to the same Taylor parameter as that of a capsule

$$f_k = 2.2997\ G_s\,. \tag{83}$$

This allows to compare Neo-Hookean capsules with this model, because both models show with this choice similar deformations in case of a small capillary number.

(i) linear shear flow: At first we show the results of the migration velocity in a linear shear flow given by eq. (3) and compare it with the simulations to justify the assumptions used to derive the migration velocity eq. (73). The values of a_σ (see eq. (48)) are $(\mathbf{a}_{0,0})_1 = \dot{\gamma}y_c$, $(\mathbf{a}_{0,1})_1 = \dot{\gamma}R$ and zero else. The contributions of $\mathbf{u}_m$, $\mathbf{u}_{tr}$, $\mathbf{u}_{tt}$ and $\boldsymbol{\zeta}^{-1}$ are in this case (with eqs. (73), (83) and appendix sec. 1.3)

$$\mathbf{u}_m = \dot{\gamma}y_c\,, \tag{84}$$
$$\mathbf{u}_u = 0\,, \tag{85}$$
$$\mathbf{u}_{tt} = 0\,, \tag{86}$$
$$\boldsymbol{\zeta}^{-1} = \frac{0.0527}{\eta R}\mathbf{1} + \frac{\dot{\gamma}}{G_s}\begin{pmatrix} 0 & 0.0194 & 0 \\ 0.0194 & 0 & 0 \\ 0 & 0 & 0 \end{pmatrix} \tag{87}$$

with the coefficients given in the appendix in sec 1.3. Thus the particle's velocity is with eq. (73)

$$\dot{\mathbf{r}}_c = \dot{\gamma}y_c\hat{\mathbf{e}}_x + \left[\frac{0.0527}{\eta R}\mathbf{1} + \frac{\dot{\gamma}}{G_s}\begin{pmatrix} 0 & 0.0194 & 0 \\ 0.0194 & 0 & 0 \\ 0 & 0 & 0 \end{pmatrix}\right]\mathbf{F}^{ext} \tag{88}$$

Here one can see, that in a linear shear flow no migration is found, which means that the tank-treading motion and the spatially dependent flow does not contribute to the particles translational velocity. This fits the simulations of the capsule in sec IV B, where also no migration was found in a linear shear flow. We can also compare the stokes friction matrix with known values. The Stokes friction without deformation, at $\dot{\gamma} = 0$ is given by $\frac{0.0527}{\eta R}$ in eq. (88) differs from the correct value $\frac{1}{6\pi\eta R}$ less than one percent, which means the Stokes friction without deformation is well reproduced. Furthermore the Stokes friction matrix in case of deformation at $\dot{\gamma} \neq 0$ has off-diagonal elements, which reflects the ellipsoidal shape of the particle. Here the stokes drag depends on the direction of the force (see e.g. [65] for the drag of an ellipsoid). These off-diagonal elements are the stronger the higher the shear rate is because the deformation towards an ellipsoid increases with the shear rate.

(ii) plane Poiseuille flow: Here we give the migration velocity in a plane Poiseuille flow derived with eq. (73) and compare it with the simulations. In a Poiseuille flow at the particles center position y_c (given by eq. (1)) the values of a_σ (see eq. (48)) are

$$(\mathbf{a}_{0,0})_1 = U\left(1 - \frac{y_c^2}{d^2}\right), \quad (\mathbf{a}_{0,1})_1 = -2U\frac{y_c}{d^2}R, \tag{89}$$
$$(\mathbf{a}_{0,2})_1 = -U\frac{1}{d^2}R^2\,, \tag{90}$$

which results (with eqs. (73), (83) and appendix sec. 1.3)

in

$$\mathbf{u}_m = \hat{\mathbf{e}}_x U \left[1 - \frac{y_c^2}{d^2} - 0.3333\frac{R^2}{d^2}\right] , \tag{91}$$

$$\mathbf{u}_u = -\,0.7212\; U^2 \frac{\eta y_c R^3}{G_s d^4}\hat{\mathbf{e}}_y , \tag{92}$$

$$\mathbf{u}_{tt} = -\,0.1663\; U^2 \frac{\eta y_c R^3}{G_s d^4}\hat{\mathbf{e}}_y , \tag{93}$$

$$\boldsymbol{\zeta}^{-1} = \frac{0.0527}{\eta R}\mathbf{1} - \frac{U y_c}{G_s d^2}\begin{pmatrix} 0 & 0.0388 & 0 \\ 0.0388 & 0 & 0 \\ 0 & 0 & 0 \end{pmatrix} . \tag{94}$$

Thus the migration velocity is with eq. (73)

$$v_{m,x} = -\,0.3333\frac{UR^2}{d^2} + 0.0527\frac{F_x^{ext}}{\eta R} - 0.0388\frac{U y_c F_y^{ext}}{G_s d^2} , \tag{95}$$

$$v_{m,y} = -\,0.8875\; U^2 \frac{\eta y_c R^3}{G_s d^4} + 0.0527\frac{F_y^{ext}}{\eta R} - 0.0388\frac{U y_c F_x^{ext}}{G_s d^2} , \tag{96}$$

$$v_{m,z} = 0.0527\frac{F_z^{ext}}{\eta R} . \tag{97}$$

This equation describes the migration well. Without an external force the migration velocity in flow direction is negative: This is the lag behind due to $\mathbf{u}_m$,i.e. the finite size of the particle, and the parabolic flow profile, as also found e.g. in [30]. Furthermore the migration perpendicular to the flow without external force is proportional to $-y_c$ which results in the migration to the center of the flow at $y = 0$. Moreover we can see the effect of an external force: A force in flow direction leads to an additional motion perpendicular to the flow, because of the ellipsoidal shape of the particle and the anisotropic friction coefficients. A force in flow direction leads to a faster migration to the center and a strong enough force anti-parallel to the flow leads to a migration to the walls. This effect was also reported in [34], where the velocity due to the external flow $v_{ext,y}$ was calculated with different approximations. It is given as

$$v_{ext,y} = -\,\frac{5}{48\pi}\frac{U y_c F_x^{ext}}{G_s d^2} \approx -0.0332\frac{U y_c F_x^{ext}}{G_s d^2} , \tag{98}$$

which agrees well with eq. (97) despite the different methods.

We can now compare the analytical result eq. (97) with the simulations above by using eq. (83). Figure 13 shows the migration velocity as function of the lateral position of the capsule for both the simulations and calculated with the eq. (97). The eq. (97) agrees well with the simulations and shows the linear dependency of the migration velocity of the lateral positions. Simulation and the analytical eq. (97) corresponds in case of small values of Ca because of the assumed small deformations.

Figure 14 shows the migration velocity as function of the flows velocity at the center U for both simulations and eq. (97). Again the dependency of $v_{m,y} \propto U^2$ is shown both by the simulations and the eq. (97), so that the eq. (97) agrees with the simulations. Again the error between simulations and eq. (97) is small at small values of U which means at small deformations.

Thus the simulation shows the same dependencies on the parameters as the eq. (97), which means the analytical eq. (97) can describe the motion of the capsule.

(iii) pipe flow: At last we give the migration velocity in a pipe flow derived with eq. (73) and compare it the simulations and with the results of Helmy and Barthès-

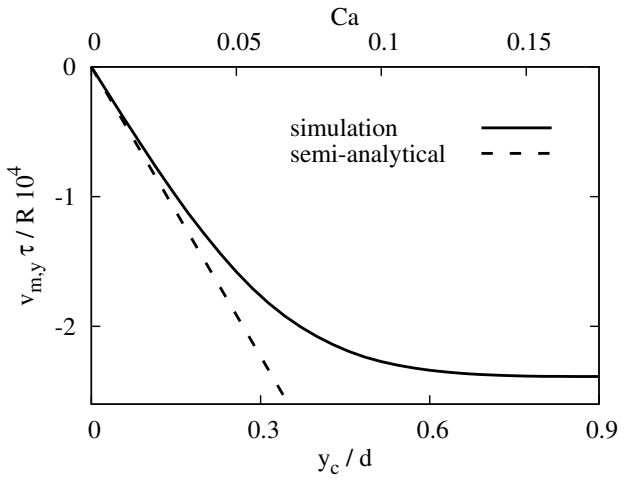

FIG. 13. The migration velocity $v_{m,y}$ of a capsule in a plane Poiseuille flow with $U\frac{\tau}{R} = 1$ as function of its lateral coordinate y_c obtained by simulations (compare fig. 9) and eq. (97). Both simulations and eq. (97) display at small deformations a linear dependency of $v_{m,y}$ on y_c and agree well.

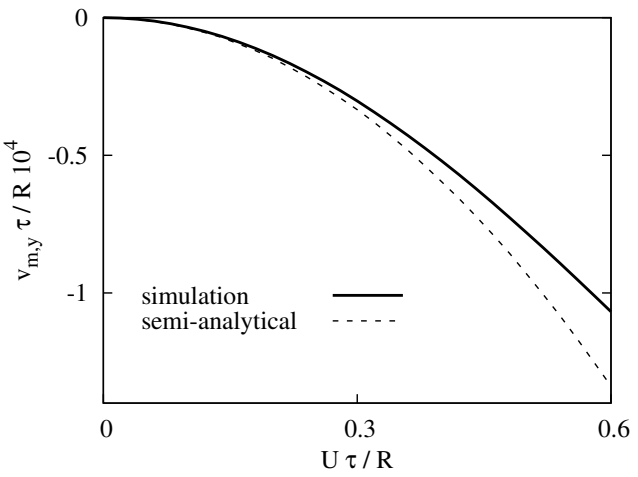

FIG. 14. The migration velocity $v_{m,y}$ of a capsule in a plane Poiseuille flow in dependence of the flow velocity at the center U for simulations (compare fig. 9) and the eq. (97). The eq. (97) shows $v_{m,y} \propto U^2$ which is confirmed by the simulations: Both simulations and eq. (97) corresponds well at small deformations, i.e. small values of U.

Biesel given in [27], which allows to justify the assumptions used to derive eq. (73). The pipe flow is given by eq. (2). We chose the particles center position at $x_c = 0$, so that the radial direction is the y-direction.The a_σ (see eq. (48)) are in this case

$$(\mathbf{a}_{0,0})_3 = U\left(1 - \frac{y_c^2}{d^2}\right), \quad (\mathbf{a}_{0,1})_3 = -2U\frac{y_c}{d^2}R, \tag{99}$$

$$(\mathbf{a}_{2,0})_3 = -U\frac{1}{d^2}R^2, \quad (\mathbf{a}_{0,2})_3 = -U\frac{1}{d^2}R^2\,, \tag{100}$$

We get the migration velocity with eq. (73), appendix sec. 1.3 and with eq. (83), which allows to use G_s instead of f_k. We get

$$v_{m,x} = 0.0527\frac{F_x^{ext}}{\eta R} \tag{101}$$

$$v_{m,y} = -0.8706\ U^2\frac{\eta y_c R^3}{G_s d^4} + 0.0527\frac{F_y^{ext}}{\eta R} - 0.0388\frac{U y_c F_z^{ext}}{G_s d^2} \tag{102}$$

$$v_{m,z} = -0.6667\frac{UR^2}{d^2} + 0.0527\frac{F_z^{ext}}{\eta R} - 0.0388\frac{U y_c F_y^{ext}}{G_s d^2} \tag{103}$$

As expected, we see that without an external force the

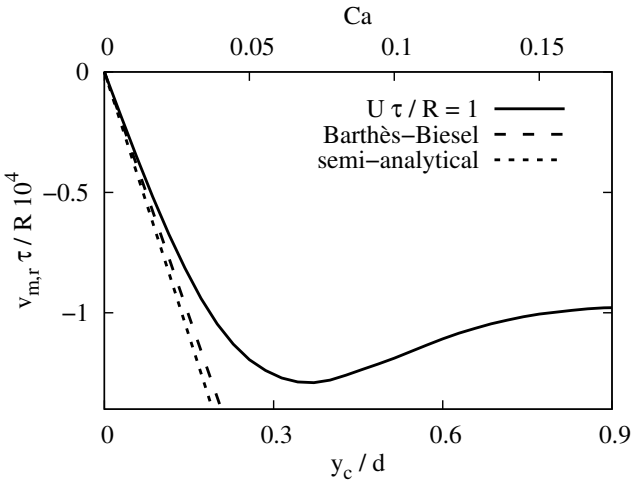

FIG. 15. The migration velocity $v_{m,r}$ of a capsule in a pipe flow with $U\frac{\tau}{R} = 1$ as function of its position y_c (with $x_c = 0$) obtained by simulations (see fig. 8) and the eq. (103). Both simulations and the eq. (103) display a linear dependency of $v_{m,r}$ on y_c and agrees well at small deformations. Also the expression (103) agrees well with the analytical results derived by Helmy and Barthès-Biesel for capsules in pipe flow (given in [27]).

migration velocity in flow direction is negative: This is the lag behind $\mathbf{u}_m$ due the finite size of the particle and the parabolic flow profile, as also found e.g. in [30]. Also the migration perpendicular to the flow meets the expectations: Without external force the cross streamline migration is proportional to $-y_c$ which results in the migration to the center of the flow at $y = 0$.

We can compare this result in case of no external force with eq. (19), i.e. with the result of Helmy and Barthès-Biesel given in [27]

$$v_{m,y} = -\frac{29}{36}\ U^2\frac{\eta y_c R^3}{G_s d^4} = -0.8056\ U^2\frac{\eta y_c R^3}{G_s d^4}\,. \tag{104}$$

Both results agree well and show the same dependence on the parameters and have less than ten percent difference. We can compare this result also with the simulations (without external forces), which is shown in fig. 15. The expression (103) agrees well with the simulations as long as the capillary number is small.

VI. CONCLUSIONS

We showed that elementary bead spring models can describe the migration of deformable particles (without viscosity contrast) well. To show this we investigated the migration of simple bead-spring models in an (at first) unbounded Poiseuille flow. Very easy models like three beads connected by springs or a ring of beads display already a cross-streamline migration to the center of a Poiseuille flow. They also allow to determine the requirements of a cross-streamline migration in an unbounded flow with parallel stream lines (compare [19]): The particle must be deformable, the shear rate must vary across the particle and the model must include the flow disturbance due to the particle. We compared the models with the two dimensional, more complex vesicle model given in [28]: The vesicle showed the same requirements of the migration. Also the dependence of the migration on the capillary number can be compared: The migration velocity of the vesicle as function of the capillary number displayed at first a linear increase with the capillary number and reached then a constant value at higher capillary numbers. This behavior was also found with the ring of beads, which means that a simple bead-spring ring can describe the migration qualitatively well.

We also showed a three dimensional easy bead model of a capsule. Here we compared the results also with [30] and quantitatively with the analytical calculations of Barthès-Biesel [27] and [47]. We received a good agreement. We also included the interaction of the capsule with the walls and compared the results with the results of a lattice-Boltzmann simulation, which also showed a good agreement.

After we demonstrated that the elementary bead-spring models can describe cross-streamline migration we gave a simple analytical explanation why deformable particles migrate in an arbitrary flow (with translational invariance in one direction) with the help of bead models. We showed that in an arbitrary flow there are three contributions to the migration: A contribution due to the finite size of the particle and forces caused by the tank-treading motion and by the spatial dependency of the flow, which drive the migration. This explanation fits the explanation found in case of a pipe flow given in [27]

well, where the driving forces and the migration was calculated with a more exact model, but in a special flow. This allows a more detailed explanation of the migration than the often used discussion on the basis of the symmetry alone, e.g. given in [28].

We also gave an analytical expression for the migration of a capsule in an unbounded, arbitrary flow (with translational invariance in one direction) for small capillary numbers. We used plausible approximations, which are justified by a good agreement with the results of the simulations. We compared the results also with the results of Barthès-Biesel for a pipe flow and found a good agreement with a small deviation of 10% due to the made approximations. The results showed that one has to distinguish between flows with parallel stream lines and non-parallel stream lines. In flows with non-parallel stream lines we find a migration due to the finite size of the particle, even if the particle is rigid and even without hydrodynamic interaction. In flows with parallel stream lines a cross-streamline migration can occur if the particle is deformable, if HI is included and if the shear rate changes on the size of the particle, which fits the results of [19]. The calculations showed that in this case the migration (at small deformations) is proportional to the product of the capillary number, which measures the deformation, and the second spatial derivative of the flow, which measures how the shear rate varies across the particle's size.

ACKNOWLEDGMENTS

We acknowledge the support by the German French University (DFH/UFA).

[1] T. M. Squires and S. R. Quake, Rev. Mod. Phys. **77**, 977 (2005).
[2] B. J. Kirby, *Micro- and Nanoscale Fluid Mechanics* (Cambridge University Press, Cambridge, England, 2010).
[3] N.-T. Nguyen and S. T. Wereley, *Fundamentals and Applications of Microfluidics* (Artech House, Boston, 2010).
[4] A. S. Popel and P. C. Johnson, Annu. Rev. Fluid Mech. **37**, 43 (2005).
[5] E. K. Sackmann, A. L. Fulton, and D. J. Beebe, Nature **507**, 181 (2014).
[6] J. B. Dahl, J.-M. G. Lin, S. J. Muller, and S. Kumar, Annu. Rev. Chem. Biomol. Eng. **6**, 293 (2015).
[7] H. Amini, W. Lee, and D. D. Carlo, Lab Chip **14**, 2739 (2014).
[8] M. D. Graham, Annu. Rev. Fluid Mech. **43**, 273 (2011).
[9] T. W. Secomb, Annu. Rev. Fluid Mech. **49**, 443 (2017).
[10] T. M. Geislinger and T. Franke, Adv. Colloid Interface Sci. **208**, 161 (2014).
[11] P. Sajeesh and A. K. Sen, Microfluid. Nanofluid. **17**, 1 (2014).
[12] C. Misbah, J. Fluid Mech. **760**, 1 (2014).
[13] A. Farutin, T. Piasecki, A. M. Slowicka, C. Misbah, E. Wajnryb, and M. L. Ekiel-Jeżewska, Soft Matter **12**, 7307 (2016).
[14] G. Segré and A. Silberberg, Nature **189**, 209 (1961).
[15] R. H. Shafer, Biophy. Chem. **2**, 185 (1974).
[16] L. C. Nitsche, AIChE J. **42**, 613 (1996).
[17] G. Ghigliotti, A. Rahimian, G. Biros, and C. Misbah, Phys. Rev. Lett. **106**, 028101 (2011).
[18] G. Sekhon, R. Armstrong, and M. S. Jhon, J. Polym. Sci., Polym. Phys. Ed. **20**, 947 (1982).
[19] P. O. Brunn, Int. J. Multiphase Flow **9**, 187 (1983).
[20] M. S. Jhon and K. F. Freed, J. Polym. Sci., Polym. Phys. Ed. **23**, 955 (1985).
[21] I. Cantat and C. Misbah, Phys. Rev. Lett. **83**, 880 (1999).
[22] U. Seifert, Phys. Rev. Lett. **83**, 876 (1999).
[23] M. Abkarian, C. Lartigue, and A. Viallat, Phys. Rev. Lett. **88**, 068103 (2002).
[24] X. Grandchamp, G. Goupier, A. Srivastav, C. Minetti, and T. Podgorski, Phys. Rev. Lett. **110**, 108101 (2013).
[25] L. G. Leal, Annu. Rev. Fluid Mech. **12**, 435 (1980).
[26] S. Mandal, A. Bandopadhyay, and S. Chakraborty, Phys. Rev. E **92**, 023002 (2015).
[27] A. Helmy and D. Barthès-Biesel, J. Mecanique theorique appliquee **1**, 859 (1982).
[28] B. Kaoui, G. H. Ristow, I. Cantat, C. Misbah, and W. Zimmermann, Phys. Rev. E **77**, 021903 (2008).
[29] G. Coupier, B. Kaoui, T. Podgorski, and C. Misbah, Phys. Fluids **20**, 111702 (2008).
[30] S. K. Doddi and P. Bagchi, Int. J. Multiphase Flow **34**, 966 (2008).
[31] A. Farutin and C. Misbah, Phys. Rev. E **89**, 042709 (2014).
[32] N. Watari and R. G. Larson, Phys. Rev. Lett. **102**, 246001 (2009).
[33] I. Mourad and L.-L. Aline, Int. J. Numer. Methods Fluids **76**, 835 (2014).
[34] A. Förtsch, M. Laumann, D. Kienle, and W. Zimmermann, EPL **119**, 64003 (2017).
[35] S. Lingling, P. Tsorng-Whay, and G. Roland, Int. J. Numer. Methods Fluids **68**, 1393 (2012).
[36] H. Pandey and P. T. Underhill, Phys. Rev. E **92**, 052301 (2015).
[37] B. Nasouri and G. J. Elfring, Phys. Rev. E **93**, 033111 (2016).
[38] A. G. Bailey and C. P. Lowe, Phys. Rev. E **96**, 062417 (2017).
[39] P. M. Blanco, M. Via, J. L. Garcés, S. Madurga, and F. Mas, Entropy **19**, 105 (2017).
[40] E. Chow and J. Skolnick, Biophys. J. **112**, 2261 (2017).
[41] J. W. Swan and G. Wang, Phys. Fluids **28**, 011902 (2016).
[42] N. Watari and R. G. Larson, Biophys. J. **98**, 12 (2010).
[43] M. Kong, Y. Wu, G. Li, and R. G. Larson, Soft Matter **11**, 1572 (2015).
[44] N. Küchler, H. Löwen, and A. M. Menzel, Phys. Rev. E **93**, 022610 (2016).
[45] K. A. Mizerski, E. Wajnryb, P. J. Zuk, and P. Szymczak, J. Chem. Phys. **140**, 184103 (2014).
[46] P. J. Zuk, E. Wajnryb, K. A. Mizerski, and P. Szymczak, J. Fluid Mech. **741**, R5 (2014).

[47] D. Barthès-Biesel, Annu. Rev. Fluid Mech. **48**, 25 (2016).
[48] P. C.-H. Chan and L. G. Leal, J. Fluid Mech. **92**, 131 (1979).
[49] A. Farutin, S. Rafaï, D. K. Dysthe, A. Duperray, P. Peyla, and C. Misbah, Phys. Rev. Lett. **111**, 228102 (2013).
[50] J. K. G. Dhont, *An Introduction to Dynamics of Colloids* (Elsevier, Amsterdam, 1996).
[51] S. Ramanujan and C. Pozrikidis, J. Fluid Mech. **361**, 117 (1998).
[52] G. Gompper and D. M. Kroll, J. Phys. I (France) **6**, 1305 (1996).
[53] T. Krueger, M. Gross, D. Raabe, and F. Varnik, Soft Matter **9**, 9008 (2013).
[54] T. Krueger, F. Varnik, and D. Raabe, Comput. Math. Appl. **61**, 3485 (2011).
[55] J. R. Blake, Proc. Camb. Philos. Soc. **70**, 303 (1971).
[56] R. B. Jones, J. Chem. Phys. **121**, 483 (2004).
[57] J. Rotne and S. Prager, J. Chem. Phys. **50**, 4831 (1969).
[58] H. Yamakawa, J. Chem. Phys. **53**, 436 (1970).
[59] T. Krüger, H. Kusumaatmaja, A. Kuzmin, O. Shardt, G. Silva, and E. M. Viggen, *The Lattice Boltzmann Method - Principles and Practice* (Springer, Berlin, 2016).
[60] P. L. Bhatnagar, E. P. Gross, and M. Krook, Phys. Rev. **94**, 511 (1954).
[61] C. K. Aidun and J. R. Clausen, Annu. Rev. Fluid. Mech **42**, 439 (2010).
[62] Z. Guo, C. Zheng, and B. Shi, Phys. Rev. E **65**, 046308 (2002).
[63] C. S. Peskin, Acta Numer. **11**, 479 (2002).
[64] H.-H. Boltz and J. Kierfeld, Eur. Phys. J. **225**, 2269 (2016).
[65] J. Happel and H. Brenner, *Low Reynolds Number Hydrodynamics* (Prentice-Hall, Englewood Cliffs, 1981).

1 Supplementary information

1.1 Calculation of the migration velocity

In the main text, sec. V, we derived equations (eqs. (68), (69), (70), (71) and (72)) and approximations which allow to calculate the migration velocity of a deformable particle in an arbitrary flow (with translational invariance in one direction) at small deformations. We gave only the results in the main text. Here we show the complete calculation.

The equations

For the sake of completeness we list at fist the equations (given main text) which allow to calculate the migration velocity. The flow is given as eq. (47) in the main text as the Taylor expansion of a flow with translational invariance in one direction

$$\mathbf{u}_0 \approx \sum_{n=0}^{2} \frac{1}{n!} \left[(x-x_c)\partial_x + (y-y_c)\partial_y\right]^n_{x=x_c,y=y_c} \mathbf{u}_0 \,, \tag{1}$$

$$= \sum_{k,l=0}^{k+l\leq 2} \mathbf{b}_{k,l} (x-x_c)^k (y-y_c)^l \,. \tag{2}$$

The $\mathbf{b}_{k,l}$ represent the Taylor coefficients of the flow. We use further the definition eq. (48) given in the main text

$$a_\sigma := (\mathbf{a}_{k,l})_m = R^{k+l} (\mathbf{b}_{k,l})_m \,, \tag{3}$$

where σ as an abbreviation of m, k, l and $(\mathbf{a}_{k,l})_m$ denotes the m-component of $\mathbf{a}_{k,l}$.

We solve approximately eqs. (53), (54), (68), (69), (70), (71) and (72) of the main text, which are there given as

$$\sum_j \mathbf{H}_{i,j} \mathbf{F}_j = \dot{\mathbf{r}}_c - \mathbf{u}_i + \mathbf{v}_i^{tt} \,, \tag{4}$$

$$\sum_i \mathbf{F}_i = \mathbf{F}^{ext}, \ \mathbf{F}_i = \mathbf{F}_i^{int} + \frac{1}{N}\mathbf{F}^{ext}, \ \sum_i \mathbf{F}_i^{int} = 0 \,, \tag{5}$$

$$\mathbf{F}_i^{int} = - f_k \sum_j \hat{\mathbf{b}}_{i,j} \hat{\mathbf{b}}_{i,j} \cdot (\Delta\mathbf{r}_i - \Delta\mathbf{r}_j) - f_k \frac{\Delta\mathbf{r}_i}{N} \,, \tag{6}$$

$$\mathbf{r}_i = \mathbf{r}_i^{(0)} + \Delta\mathbf{r}_i + \mathbf{r}_c \,, \tag{7}$$

$$\boldsymbol{\omega} = \frac{1}{2} \nabla \times \mathbf{u}_0|_{\mathbf{r}=\mathbf{r}_c} \,, \ \dot{\phi} = |\boldsymbol{\omega}| \,, \tag{8}$$

$$\mathbf{v}_i^{tt} = \boldsymbol{\omega} \times \left(\mathbf{r}_i^{(0)} + \Delta\mathbf{r}_i\right) + \dot{\phi} \left.\frac{\partial \rho}{\partial \phi}\right|_{\phi=\phi_i} \hat{\mathbf{e}}_{r,i} \,. \tag{9}$$

Before we solve the equations we simplify them. To do this we show a first that the mean tank-treading velocity is zero. We use here

$$\frac{1}{N}\sum_i^N \mathbf{v}_i^{tt} \approx \frac{1}{N}\int_1^N \mathbf{v}^{tt}\mathrm{d}n\,, \tag{10}$$

whereby $\mathrm{d}n$ means the number of beads located in a surface element $\mathrm{d}A$. With the density of the beads ρ we get $\mathrm{d}n = \rho\mathrm{d}A$. If the surface of the particle is deformed the number of beads stays the same, only the density of the beads changes due to the assumed small deformations. This means $\mathrm{d}n = \rho\mathrm{d}A = \rho^{(0)}\mathrm{d}A^{(0)}$ whereby $\rho^{(0)}$ and $\mathrm{d}A^{(0)}$ is the density and the surface element in the non deformed state. Here the beads are distributed equally and the shape is a sphere which means $\rho^{(0)} = \frac{N}{A}$ with the number of beads N and $\mathrm{d}A^{(0)} = R^2\sin\theta$. So we get

$$\mathrm{d}n = \rho\mathrm{d}A = \rho^{(0)}\mathrm{d}A^{(0)} = \frac{N}{A^{(0)}}R^2\sin\theta\mathrm{d}\phi\mathrm{d}\theta \tag{11}$$

With the tank-trading motion given in eq. (51) (main text) we get finally

$$\frac{1}{N}\sum_i^N \mathbf{v}_i^{tt} \approx \frac{1}{N}\int_1^N \mathbf{v}^{tt}\mathrm{d}n = \frac{R^2\dot{\phi}}{A^{(0)}}\int_0^{\pi}\sin\theta\int_0^{2\pi}\frac{\partial}{\partial\phi}\left[\rho(\phi,\theta)\hat{\mathbf{e}}_r\right]\mathrm{d}\phi\,\mathrm{d}\theta = 0 \tag{12}$$

So the mean tank-treading velocity is zero if the discretization of the surface is dense enough, so that it can be approximated by the integral.

Now we can simplify the equations. Averaging eq. (4) over all beads yields with eq. (5)

$$\begin{aligned}
\dot{\mathbf{r}}_c =& \frac{1}{N}\sum_p \mathbf{u}_p + \frac{1}{N}\sum_{p,j}\mathbf{H}_{p,j}\mathbf{F}_j && (13)\\
=& \frac{1}{N}\sum_p \mathbf{u}_p + \frac{1}{N}\sum_{p,j,p\neq j}\mathbf{H}_{p,j}\mathbf{F}_j + \frac{1}{N}\sum_p \underbrace{\mathbf{H}_{p,p}}_{=\zeta^{-1}}\mathbf{F}_p && (14)\\
=& \frac{1}{N}\sum_p \mathbf{u}_p + \frac{1}{N}\sum_{p,j,p\neq j}\mathbf{H}_{p,j}\mathbf{F}_j + \frac{\mathbf{F}^{ext}}{\zeta N} && (15)
\end{aligned}$$

Substituting this in eq. (4) results in

$$\sum_j \mathbf{H}_{i,j}\mathbf{F}_j = \frac{1}{N}\sum_p \mathbf{u}_p + \frac{1}{N}\sum_{p,j,p\neq j}\mathbf{H}_{p,j}\mathbf{F}_j + \frac{\mathbf{F}^{ext}}{\zeta N} - \mathbf{u}_i + \mathbf{v}_i^{tt} \tag{16}$$

$$\sum_j\left[\left(\mathbf{H}_{i,j} - \frac{1}{N}\sum_{p,p\neq j}\mathbf{H}_{p,j}\right)\mathbf{F}_j\right] = \frac{1}{N}\sum_p \mathbf{u}_p - \mathbf{u}_i + \frac{\mathbf{F}^{ext}}{\zeta N} + \mathbf{v}_i^{tt} \tag{17}$$

This ensures that the sum of all forces is given by $\mathbf{F}^{ext}$, which can be seen by a summation of eq. (17) over all beads i

$$\sum_{i,j}\left[\left(\mathbf{H}_{i,j}-\frac{1}{N}\sum_{p,p\neq j}\mathbf{H}_{p,j}\right)\mathbf{F}_j\right]=\frac{\mathbf{F}^{ext}}{\zeta} \tag{18}$$

$$\sum_i \mathbf{H}_{i,i}\mathbf{F}_i=\frac{\mathbf{F}^{ext}}{\zeta} \tag{19}$$

$$\frac{1}{\zeta}\sum_i \mathbf{F}_i=\frac{\mathbf{F}^{ext}}{\zeta} \tag{20}$$

$$\sum_i \mathbf{F}_i=\mathbf{F}^{ext} \tag{21}$$

So eqs. (13) and (17) are equivalent to eqs. (4) and (5). The set of equation we want to solve consists of eqs. (13) and (17) and eqs. (6), (8), (9).

But these equations are nonlinear and are therefore solved in an iterative way (see main text and compare [1]). The iteration step is denoted by $^{(s)}$. This leads to the equations

$$\begin{aligned}&\sum_j\left[\left(\mathbf{H}_{i,j}^{(s-1)}-\frac{1}{N}\sum_{p,p\neq j}\mathbf{H}_{p,j}^{(s-1)}\right)\mathbf{F}_j^{(s)}\right]\\&=\frac{1}{N}\sum_p \mathbf{u}_p^{(s-1)}-\mathbf{u}_i^{(s-1)}+\frac{\mathbf{F}^{ext}}{\zeta N}+\mathbf{v}_i^{tt,(s-1)}\end{aligned} \tag{22}$$

$$\mathbf{F}_i^{(s),int}=-f_k\sum_j \hat{\mathbf{b}}_{i,j}\hat{\mathbf{b}}_{i,j}\cdot\left(\Delta\mathbf{r}_i^{(s)}-\Delta\mathbf{r}_j^{(s)}\right)-f_k\frac{\Delta\mathbf{r}_i^{(s)}}{N} \tag{23}$$

$$\mathbf{r}_i^{(s)}=\mathbf{r}_i^{(0)}+\Delta\mathbf{r}_i^{(s)}+\mathbf{r}_c \tag{24}$$

$$\dot{\mathbf{r}}_c^{(s)}=\frac{1}{N}\sum_i \mathbf{u}_i^{(s)}+\frac{1}{N}\sum_{i,j}\mathbf{H}_{i,j}^{(s)}\mathbf{F}_j^{(s)}\,, \tag{25}$$

$$\boldsymbol{\omega}=\frac{1}{2}\,\nabla\times\mathbf{u}_0\big|_{\mathbf{r}=\mathbf{r}_c}\,,\ \dot{\phi}=|\boldsymbol{\omega}| \tag{26}$$

$$\mathbf{v}_i^{tt,(s)}=\boldsymbol{\omega}\times\left(\mathbf{r}_i^{(0)}+\Delta\mathbf{r}_i^{(s)}\right)+\dot{\phi}\frac{\partial r_i^{(s)}}{\partial\phi}\hat{\mathbf{e}}_{r,i} \tag{27}$$

This means the forces are determined approximately with the shape of the previous iteration step (eq. 22). With the known forces the shape is calculated (eq. 23) and with the forces and the shape follows the new velocity of the particle (eq. 25). After this a new iteration can be started which can be done until a self-consistent solution is reached. But we assume here only small deformations. So we can assume that the force distribution does not change due to the small deformations and use only one iteration step. This approximation is justified by a comparison with the numeric simulations.

Because we assume small deformations we start the iteration with zero deformation, which results in

$$\Delta \mathbf{r}_i^{(0)} = 0 \tag{28}$$

$$\begin{aligned}\mathbf{v}_i^{tt,(0)} &= \boldsymbol{\omega} \times \mathbf{r}_i^{(0)} = \frac{1}{2} \begin{pmatrix} (\mathbf{b}_{0,1})_3 \\ -(\mathbf{b}_{1,0})_3 \\ (\mathbf{b}_{1,0})_2 - (\mathbf{b}_{0,1})_1 \end{pmatrix} \times \begin{pmatrix} x_{0,i} \\ y_{0,i} \\ z_{0,i} \end{pmatrix} \\ &= \frac{1}{2} \begin{pmatrix} -(\mathbf{b}_{1,0})_3 z_{0,i} - [(\mathbf{b}_{1,0})_2 - (\mathbf{b}_{0,1})_1] y_{0,i} \\ [(\mathbf{b}_{1,0})_2 - (\mathbf{b}_{0,1})_1] x_{0,i} - (\mathbf{b}_{0,1})_3 z_{0,i} \\ (\mathbf{b}_{0,1})_3 y_{0,i} + (\mathbf{b}_{1,0})_3 x_{0,i} \end{pmatrix}\end{aligned} \tag{29}$$

With these start values the first iteration reads

$$\begin{aligned}&\sum_j \left[\left(\mathbf{H}_{i,j}^{(0)} - \frac{1}{N} \sum_{p,p\neq j} \mathbf{H}_{p,j}^{(0)} \right) \mathbf{F}_j^{(1)} \right] \\ &= \frac{1}{N} \sum_p \mathbf{u}_p^{(0)} - \mathbf{u}_i^{(0)} + \frac{\mathbf{F}^{ext}}{\zeta N} + \mathbf{v}_i^{tt,(0)} ,\end{aligned} \tag{30}$$

$$\mathbf{F}_i^{(1),int} = - f_k \sum_j \hat{\mathbf{b}}_{i,j} \hat{\mathbf{b}}_{i,j} \cdot \left(\Delta \mathbf{r}_i^{(1)} - \Delta \mathbf{r}_j^{(1)} \right) - f_k \frac{\Delta \mathbf{r}_i^{(1)}}{N} , \quad \mathbf{r}_i^{(1)} = \mathbf{r}_i^{(0)} + \Delta \mathbf{r}_i^{(1)} \tag{31}$$

$$\dot{\mathbf{r}}_c^{(1)} = \frac{1}{N} \sum_i \mathbf{u}_i^{(1)} + \frac{1}{N} \sum_{i,j,} \mathbf{H}_{i,j}^{(1)} \mathbf{F}_j^{(1)} , \tag{32}$$

In the following we drop the superscript $^{(1)}$ of the first iteration step.

Calculation of the internal forces

Equation (30) allows to determine the internal forces. By using eq. (30) and the equation of the flow (2) we get

$$\begin{aligned}&\sum_j \left[\left(\mathbf{H}_{i,j}^{(0)} - \frac{1}{N} \sum_{p,p\neq j} \mathbf{H}_{p,j}^{(0)} \right) \mathbf{F}_j^{int} \right] \\ &= \sum_{k,l} \left(-\mathbf{b}_{k,l} x_{0,i}^k y_{0,i}^l + \frac{1}{N} \sum_j \mathbf{b}_{k,l} x_{0,j}^k y_{0,j}^l \right) + \mathbf{v}_i^{tt,(0)} + \frac{\mathbf{F}^{ext}}{\zeta N}\end{aligned} \tag{33}$$

We define $\mathbf{r}_i^{(0)} = R \mathbf{r}_i'^{(0)}$, whereby the values of $\mathbf{r}_i'^{(0)}$ are dimensionless and represent discrete points on the unit sphere. We use the same discretization as used for the simulations in the main text (see sec. II). Especially the values of $\mathbf{r}_i'^{(0)}$ do not depend on any parameter or on the flow. This allows in the following to calculate occurring

sums numerically. The mobility matrix is then expressed as

$$\text{for } i \neq j: \ \mathbf{H}_{i,j}^{(0)} = \frac{1}{8\pi\eta|\mathbf{r}_i^{(0)} - \mathbf{r}_j^{(0)}|}\left(\mathbf{1} + \hat{\mathbf{e}}_{i,j}^{(0)}\hat{\mathbf{e}}_{i,j}^{(0)}\right) = \frac{1}{R\eta}\frac{1}{8\pi|\mathbf{r}_i'^{(0)} - \mathbf{r}_j'^{(0)}|}\left(\mathbf{1} + \hat{\mathbf{e}}_{i,j}'^{(0)}\hat{\mathbf{e}}_{i,j}'^{(0)}\right)$$
$$= \frac{1}{R\eta}\mathbf{H}_{i,j}'^{(0)}\,, \tag{34}$$

$$\text{for } i = j: \ \mathbf{H}_{i,j}^{(0)} = \frac{1}{6\pi\eta a} = \frac{1}{R\eta}\frac{1}{6\pi v_a} = \frac{1}{R\eta}\mathbf{H}_{i,j}'^{(0)}\,, \text{ with } v_a = \frac{a}{R} \tag{35}$$

whereby also $\mathbf{H}_{i,j}'^{(0)}$ does not depend on any parameter. We determine v_a as follows: The surface of the sphere is $4\pi R^2$, which means the average area per bead is $\frac{4\pi R^2}{N}$ and the average distance to a neighbor bead is approximate $b = \sqrt{\frac{4\pi}{N}}R$. We chose the same ratio $\frac{a}{b}$ as in the simulations in the main text (see sec. II) $a = 0.3b = 0.042R = v_a R$. With this definitions and eq. (29) we get the equation

$$\sum_j \left[\left(\mathbf{H}_{i,j}'^{(0)} - \frac{1}{N}\sum_{p,p\neq j}\mathbf{H}_{p,j}'^{(0)}\right)\mathbf{F}_j^{int}\right] = \sum_\sigma R\eta a_\sigma(\ {}_u\mathbf{C}_{\sigma,i} + \ {}_{tt}\mathbf{C}_{\sigma,i}) + \frac{\mathbf{F}^{ext}}{6\pi v_a N} \tag{36}$$

with

$${}_u\mathbf{C}_{\sigma,i} = \left(x_{0,i}'^k y_{0,i}'^l - \frac{1}{N}\sum_j x_{0,j}'^k y_{0,j}'^l\right)\hat{\mathbf{e}}_m\,, \tag{37}$$

$${}_{tt}\mathbf{C}_{\sigma,i} = -\frac{1}{2}\begin{pmatrix} -\delta_{k,1}\delta_{l,0}\delta_{m,3}z'_{0,i} - (\delta_{k,1}\delta_{l,0}\delta_{m,2} - \delta_{k,0}\delta_{l,1}\delta_{m,1})y'_{0,i} \\ (\delta_{k,1}\delta_{l,0}\delta_{m,2} - \delta_{k,0}\delta_{l,1}\delta_{m,1})x'_{0,i} - \delta_{k,1}\delta_{l,0}\delta_{m,3}z'_{0,i} \\ \delta_{k,0}\delta_{l,1}\delta_{m,3}y'_{0,i} - \delta_{k,1}\delta_{l,0}\delta_{m,3}x'_{0,i} \end{pmatrix}. \tag{38}$$

With the assumption eq. (62) given in the main text we get

$$\frac{|\mathbf{F}^{ext}|}{\sum_\sigma \eta R|a_\sigma|} \ll 1 \tag{39}$$

$$\Rightarrow |\mathbf{F}^{ext}| \ll \sum_\sigma \eta R|a_\sigma| \tag{40}$$

$$\Rightarrow \frac{|\mathbf{F}^{ext}|}{6\pi v_a N} \ll \sum_\sigma \eta R|a_\sigma| \tag{41}$$

Therefore we can neglect the external force in eq. (36). Equation (36) is a linear system of equations, which allows to determine the forces in dependence of the Taylor coefficients of the flow. We can regard $\left(\mathbf{H}_{i,j}'^{(0)} - \frac{1}{N}\sum_{p,p\neq j}\mathbf{H}_{p,j}'^{(0)}\right)$ as one large matrix with entries i, j. This matrix depend only on the $\mathbf{r}_i'^{(0)}$ and not on any parameter. This allows to invert the complete matrix numerically. We denote the inverse matrix as $\mathbf{M}'$

with the entries $\mathbf{M}'_{i,j}$. So the complete solution of the forces can be expressed as

$$\mathbf{F}_i^{int} = \sum_\sigma R\eta a_\sigma \Big(\underbrace{\sum_j \mathbf{M}'^{(0)}_{i,j}\ {}_u\mathbf{C}_{\sigma,j}}_{=:\ {}_u\mathbf{A}_{\sigma,i}} + \underbrace{\sum_j \mathbf{M}'^{(0)}_{i,j}\ {}_{tt}\mathbf{C}_{\sigma,j}}_{=:\ {}_{tt}\mathbf{A}_{\sigma,i}} \Big) \tag{42}$$

$$\mathbf{F}_i^{int} = R\eta \sum_\sigma a_\sigma (\underbrace{{}_u\mathbf{A}_{\sigma,i} + {}_{tt}\mathbf{A}_{\sigma,i}}_{:=\mathbf{A}_{\sigma,i}} \tag{43}$$

$$\mathbf{F}_i^{int} = R\eta \sum_\sigma a_\sigma \mathbf{A}_{\sigma,i} \tag{44}$$

This is a linear relation between the forces acting on the beads and the coefficients of the Taylor expansion of the flow. The coefficients $\mathbf{A}_{\sigma,i}$ depend only on $\mathbf{r}_i'^{(0)}$ and not on any parameter or the flow, which allows to calculate them numerically: The summation over j in eq. (42) can be calculated numerically. Due to the high number of beads, we do not give here each value of $\mathbf{A}_{\sigma,i}$ (we show instead in the next section how the Taylor parameter depends on the variables in a linear shear flow). The terms proportional to ${}_u\mathbf{A}_{\sigma,i}$ describe the forces due to the translational motion and the ones proportional to ${}_{tt}\mathbf{A}_{\sigma,i}$ the forces due to the tanktreading.

Calculation of the deformation of the particle

The eq. (31) gives the relation of the internal forces and the deformation. Because we know the forces on each bead we have now a system of linear equations which be solved for the deformations. By solving eq. (31) for the deformations we get

$$\Delta\mathbf{r}_i = \frac{1}{f_k} \sum_q \mathbf{M}^{(\Delta r)}_{i,q} \mathbf{F}^{int}_q \,, \tag{45}$$

whereby the $\mathbf{M}^{(\Delta r)}_{i,q}$ are numerical coefficients that does not depend on any parameter (analogue to the solution of the system of linear equations of the forces). This allows to determine the deformation with eqs. (44) and (45)

$$\Delta\mathbf{r}_i = \frac{R\eta}{f_k} \sum_\sigma a_\sigma \underbrace{\sum_q \mathbf{M}^{(\Delta r)}_{i,q} \mathbf{A}_{\sigma,q}}_{=\mathbf{B}_{\sigma,i}} \,, \tag{46}$$

$$\Delta\mathbf{r}_i = \frac{R\eta}{f_k} \sum_\sigma a_\sigma \mathbf{B}_{\sigma,i} \,. \tag{47}$$

This shows that the dimensionless number

$$\mathrm{Df} = \frac{\eta}{f_k} \sum_{\sigma, k+l>0} |a_\sigma| \tag{48}$$

given in the main text as eq. (59) measures the deformation (compared the the radius, i.e. $\frac{|\Delta\mathbf{r}_i|}{R}$) as stated in the main text.

Calculation of the velocity of the particle

With the known forces, the shape and the Taylor expansion of $\mathbf{H}_{i,j}$ (as given in eq. (66) in the main text) the velocity of the particle can be calculated by eq. (32)

$$\dot{\mathbf{r}}_c = \frac{1}{N}\sum_i \left[\mathbf{u}_0(\mathbf{r}_i) + \sum_j \mathbf{H}_{i,j}\left(\mathbf{F}_j^{int} + \frac{\mathbf{F}^{ext}}{N}\right)\right] \tag{49}$$

$$= \frac{1}{N}\sum_i \mathbf{u}_0(\mathbf{r}_i) + \frac{1}{N}\sum_{i,j}\left(\left[\mathbf{H}_{i,j}^{(0)} + \sum_p \mathbf{H}_{i,j}^p \left(\Delta\mathbf{r}_i - \Delta\mathbf{r}_j\right)_p\right]\left(\mathbf{F}_j^{int} + \frac{\mathbf{F}^{ext}}{N}\right)\right) \tag{50}$$

$$= \underbrace{\frac{1}{N}\sum_i \mathbf{u}_0(\mathbf{r}_i)}_{I} + \underbrace{\frac{1}{N}\sum_{i,j}\mathbf{H}_{i,j}^{(0)}\left(\mathbf{F}_j^{int} + \frac{\mathbf{F}^{ext}}{N}\right)}_{II} \tag{51}$$

$$+ \underbrace{\frac{1}{N}\sum_{i,j,p}\mathbf{H}_{i,j}^p \left(\Delta\mathbf{r}_i - \Delta\mathbf{r}_j\right)_p\left(\mathbf{F}_j^{int} + \frac{\mathbf{F}^{ext}}{N}\right)}_{III} \tag{52}$$

In the following we calculate the terms I to III. The first term I represents the averaged undisturbed flow $\mathbf{u}_m$ over the surface of the particle. It is given as

$$\mathbf{u}_m = I = \frac{1}{N}\sum_i \mathbf{u}_0(\mathbf{r}_i) \tag{53}$$

$$= \frac{1}{N}\sum_i [\mathbf{b}_{0,0} + \mathbf{b}_{1,0}R(x_i - x_c)' + \mathbf{b}_{0,1}R(y_i - y_c)' \tag{54}$$

$$+ \mathbf{b}_{2,0}R^2(x_i - x_c)'^2 + \mathbf{b}_{1,1}R^2(x_i - x_c)'(y_i - y_c)' + \mathbf{b}_{0,2}R^2(y_i - y_c)'^2] \tag{55}$$

$$= \mathbf{a}_{0,0} + \frac{1}{N}\sum_i \big[\mathbf{a}_{2,0}(x_i - x_c)'^2$$

$$+ \mathbf{a}_{1,1}(x_i - x_c)'(y_i - y_c)' + \mathbf{a}_{0,2}(y_i - y_c)'^2\big] \tag{56}$$

Here we give the calculation for the term proportional $\mathbf{a}_{2,0}$ (the other parts are calculated analogously)

$$\frac{\mathbf{a}_{2,0}}{N}\sum_i (x_i - x_c)'^2 = \frac{\mathbf{a}_{2,0}}{N}\sum_i (x'_{0,i} + \Delta x'_i)^2 \tag{57}$$

$$= \frac{1}{N}\sum_i (\mathbf{a}_{2,0} x'^2_{0,i} + 2\mathbf{a}_{2,0} x'_{0,i}\Delta x'_i + \underbrace{\mathbf{a}_{2,0}\Delta x'^2_i}_{\approx 0}) \tag{58}$$

$$= \mathbf{a}_{2,0}\Big(\underbrace{\sum_i \frac{x'^2_{0,i}}{N}}_{=:\ {}_{mean}M_{2,0}} + \frac{\eta}{f_k}\sum_{\sigma'} a_{\sigma'} \underbrace{\sum_i 2\frac{x'_{0,i}}{N}(\mathbf{B}_{\sigma',i})_1}_{=:\ {}_{mean}M_{2,0,\sigma'}} \Big) \tag{59}$$

$$= \mathbf{a}_{2,0}\left({}_{mean}M_{2,0} + \frac{\eta}{f_k}\sum_{\sigma'} a_{\sigma'}\ {}_{mean}M_{2,0,\sigma'} \right), \tag{60}$$

where we have neglected the terms of second order in Df. The coefficients ${}_{mean}M_{k,l}$ and ${}_{mean}M_{k,l,\sigma'}$ do not depend on the parameters and can be calculated numerically. Their values are given in sec. 1.3. In total $\mathbf{u}_m$ (eq. (53)) can be expressed as results in

$$\mathbf{u}_m = \sum_{k,l} \mathbf{a}_{k,l}\left({}_{mean}M_{k,l} + \frac{\eta}{f_k}\sum_{\sigma'} a_{\sigma'}\ {}_{mean}M_{k,l,\sigma'} \right) \tag{61}$$

The second term II yields

$$II = \frac{1}{N}\sum_{i,j} \mathbf{H}_{i,j}\left(\mathbf{F}^{int}_j + \frac{\mathbf{F}^{ext}}{N} \right) \tag{62}$$

$$= \underbrace{\frac{1}{N}\sum_{i,j} \mathbf{H}_{i,j}\mathbf{F}^{int}_j}_{IIA} + \underbrace{\frac{1}{N}\sum_{i,j} \mathbf{H}_{i,j}\left(\frac{1}{N}\mathbf{F}^{ext} \right)}_{IIB} \tag{63}$$

$$IIA = \sum_\sigma \frac{1}{N} a_\sigma \sum_{i,j} \mathbf{H'}_{i,j}\mathbf{A}_{\sigma,i} \tag{64}$$

$$IIB = \frac{1}{\eta R}\left(\frac{1}{N^2}\sum_{i,j} \mathbf{H'}_{i,j} \right)\mathbf{F}^{ext} \tag{65}$$

Again the sums can be calculated numerically. One gets

$$IIA = 0 \tag{66}$$

$$IIB = \frac{0.0527}{\eta R}\mathbf{F}^{ext} \tag{67}$$

The third term III is

$$III = \frac{1}{N} \sum_{i,j,p,\sigma} \mathbf{H}^p_{i,j} \left(\Delta \mathbf{r}_i - \Delta \mathbf{r}_j\right)_p \left(\eta Ra_\sigma \left({}_u\mathbf{A}_{\sigma,j} + {}_{tt}\mathbf{A}_{\sigma,j} \right) + \frac{1}{N} \mathbf{F}^{ext} \right) . \tag{68}$$

We calculate at first the term proportional to ${}_u\mathbf{A}_{\sigma,j}$, which is named $\mathbf{u}_u$ in the following

$$\begin{aligned}
\mathbf{u}_u =& \frac{1}{N} \sum_{i,j,p,\sigma} \mathbf{H}^p_{i,j} \left(\Delta \mathbf{r}_i - \Delta \mathbf{r}_j\right)_p \left(\eta Ra_\sigma \, {}_u\mathbf{A}_{\sigma,j} \right) && (69)\\
=& R\eta \sum_\sigma a_\sigma \sum_{i,j,p} \mathbf{H}^p_{i,j} \left(\Delta \mathbf{r}_i - \Delta \mathbf{r}_j\right)_p \frac{1}{N} \, {}_u\mathbf{A}_{\sigma,j} && (70)\\
=& \frac{\eta}{f_k} \sum_{\sigma,\sigma'} a_\sigma a_{\sigma'} \underbrace{\sum_{i,j,p} \mathbf{H}'^p_{i,j} \left(\mathbf{B}_{\sigma',i} - \mathbf{B}_{\sigma',j}\right)_p \frac{1}{N} \, {}_u\mathbf{A}_{\sigma,j}}_{:= \, {}_u\mathbf{M}'_{\sigma,\sigma'}} && (71)\\
=& \frac{\eta}{f_k} \sum_{\sigma,\sigma'} a_\sigma a_{\sigma'} \, {}_u\mathbf{M}'_{\sigma,\sigma'} . && (72)
\end{aligned}$$

The values of the coefficients are given in sec. 1.3. The term in III proportional to ${}_{tt}\mathbf{A}_{\sigma,j}$ are named $\mathbf{u}_{tt}$ and are calculated analogously

$$\begin{aligned}
\mathbf{u}_{tt} =& \frac{1}{N} \sum_{i,j,p,\sigma} \mathbf{H}^p_{i,j} \left(\Delta \mathbf{r}_i - \Delta \mathbf{r}_j\right)_p \left(\eta Ra_\sigma \, {}_{tt}\mathbf{A}_{\sigma,j} \right) && (73)\\
=& R\eta \sum_\sigma a_\sigma \sum_{i,j,p} \mathbf{H}^p_{i,j} \left(\Delta \mathbf{r}_i - \Delta \mathbf{r}_j\right)_p \frac{1}{N} \, {}_{tt}\mathbf{A}_{\sigma,j} && (74)\\
=& \frac{\eta}{f_k} \sum_{\sigma,\sigma'} a_\sigma a_{\sigma'} \underbrace{\sum_{i,j,p} \mathbf{H}'^p_{i,j} \left(\mathbf{B}_{\sigma',i} - \mathbf{B}_{\sigma',j}\right)_p \frac{1}{N} \, {}_{tt}\mathbf{A}_{\sigma,j}}_{:= \, {}_{tt}\mathbf{M}'_{\sigma,\sigma'}} && (75)\\
=& \frac{\eta}{f_k} \sum_{\sigma,\sigma'} a_\sigma a_{\sigma'} \, {}_{tt}\mathbf{M}'_{\sigma,\sigma'} . && (76)
\end{aligned}$$

The values of the coefficients are given in sec. 1.3. The term in III proportional to

$\mathbf{F}^{ext}$ is

$$\frac{1}{N}\sum_{i,j,p}\mathbf{H}^{p}_{i,j}\left(\Delta\mathbf{r}_i-\Delta\mathbf{r}_j\right)_p\frac{1}{N}\mathbf{F}^{ext} \tag{77}$$

$$=\sum_{i,j,p}\mathbf{H}^{p}_{i,j}\left(\Delta\mathbf{r}_i-\Delta\mathbf{r}_j\right)_p\frac{1}{N^2}\mathbf{F}^{ext} \tag{78}$$

$$=\frac{1}{f_kR}\sum_{\sigma}a_\sigma\underbrace{\sum_{i,j,p}\mathbf{H}'^{p}_{i,j}\left(\mathbf{B}_{\sigma,i}-\mathbf{B}_{\sigma,j}\right)_p\frac{1}{N^2}}_{:=\ {}_\zeta\mathbf{M}_\sigma}\mathbf{F}^{ext} \tag{79}$$

$$=\frac{1}{f_kR}\sum_{\sigma}a_\sigma\ {}_\zeta\mathbf{M}_\sigma\mathbf{F}^{ext} \tag{80}$$

It represents the change in the stokes friction matrix due to small deformations. The values of ${}_\zeta\mathbf{M}_{m,k,l}$ are given in sec. 1.3 So in total the velocity of the particle is

$$\dot{\mathbf{r}}_c=\mathbf{u}_m+\frac{1}{6\pi\eta R}\mathbf{F}^{ext}+\mathbf{u}_u+\mathbf{u}_{tt}+\frac{1}{f_kR}a^{(m')}_{k',l'}\mathbf{M}_{m',k',l'}\mathbf{F}^{ext} \tag{81}$$

$$=\mathbf{u}_m+\underbrace{\left(\frac{1}{6\pi\eta R}\mathbf{1}+\frac{1}{f_kR}a^{(m')}_{k',l'}\mathbf{M}_{m',k',l'}\right)}_{\boldsymbol{\zeta}^{-1}}\mathbf{F}^{ext}+\mathbf{u}_u+\mathbf{u}_{tt} \tag{82}$$

$$=\mathbf{u}_m+\mathbf{u}_u+\mathbf{u}_{tt}+\boldsymbol{\zeta}^{-1}\mathbf{F}^{ext} \tag{83}$$

The migration velocity is obtained by subtracting the velocity at the center of the particle

$$\mathbf{v}_m=\dot{\mathbf{r}}_c-\mathbf{u}(\mathbf{r}_c)=\mathbf{u}_m-\mathbf{a}_{0,0}+\mathbf{u}_u+\mathbf{u}_{tt}+\boldsymbol{\zeta}^{-1}\mathbf{F}^{ext} \tag{84}$$

These are the results given in the main text (eq. (73) in the main text).

Note that we simplify the eqs (72) and (76) to reduce the number of coefficients. We can define

$${}_u\mathbf{M}_{\sigma,\sigma'}={}_u\mathbf{M}'_{\sigma,\sigma'}+{}_u\mathbf{M}'_{\sigma',\sigma} \tag{85}$$

$${}_u\mathbf{M}_{\sigma',\sigma}=0 \tag{86}$$

$${}_{tt}\mathbf{M}_{\sigma,\sigma'}={}_{tt}\mathbf{M}'_{\sigma,\sigma'}+{}_{tt}\mathbf{M}'_{\sigma',\sigma} \tag{87}$$

$${}_{tt}\mathbf{M}_{\sigma',\sigma}=0 \tag{88}$$

so that eqs. (72) and (76) do not change

$$\mathbf{u}_u=\frac{\eta}{f_k}\sum_{\sigma,\sigma'}a_\sigma a_{\sigma'}\ {}_u\mathbf{M}'_{\sigma,\sigma'}=\frac{\eta}{f_k}\sum_{\sigma,\sigma'}a_\sigma a_{\sigma'}\ {}_u\mathbf{M}_{\sigma,\sigma'}\,, \tag{89}$$

$$\mathbf{u}_{tt}=\frac{\eta}{f_k}\sum_{\sigma,\sigma'}a_\sigma a_{\sigma'}\ {}_{tt}\mathbf{M}'_{\sigma,\sigma'}=\frac{\eta}{f_k}\sum_{\sigma,\sigma'}a_\sigma a_{\sigma'}\ {}_{tt}\mathbf{M}_{\sigma,\sigma'}\,. \tag{90}$$

This means hat each pair of $a_\sigma a_{\sigma'}$ occuring in the sum has only one nonzero coefficient, which reduces the number of nonzero coefficients ${}_u\mathbf{M}_{\sigma',\sigma}$ and ${}_{tt}\mathbf{M}_{\sigma',\sigma}$. Note further that all the prefactors are calculated 20 times with a discretization $\mathbf{r}_i'^{(0)}$ rotated around the z-Axis to minimize the discretization errors.

1.2 Measurement of the deformation

Here we give a measurement of the deformation of the particle in a linear shear flow with the shear rate $\dot{\gamma}$, which is show in fig. 1. The Taylor parameter is defined as $D = \frac{L-B}{L+B}$, whereby L and B are the length of the long and the short half axis. The shape is calulated with eq. (47). We find here

$$D = 4.7910\ \dot{\gamma}\eta R/f_k\,. \tag{91}$$

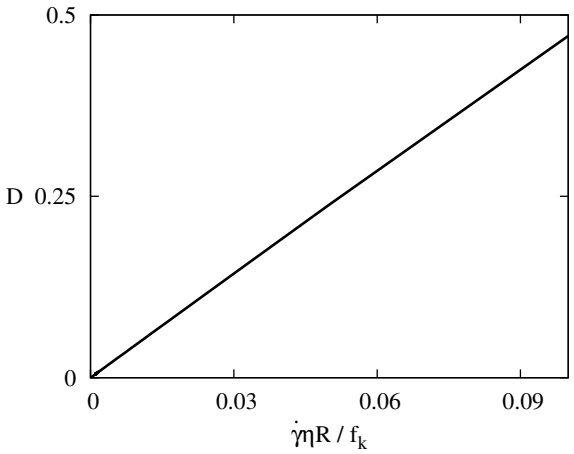

Figure 1: The Taylor parameter as function of $\dot{\gamma}\eta R/f_k$ in a linear shear flow. It grows linear and is described by $D = 4.7910\ \dot{\gamma}\eta R/f_k$. The shape is calculated with eq. (47).

This can be compared with e.g. a capsule described with the neo-hookean law with surface shear elastic modulus G_s. In this case one finds (see [2])

$$D = \frac{25}{12}\ \dot{\gamma}\eta R/G_s\,. \tag{92}$$

This means one receives the same Taylor parameter in a linear shear flow if one chooses

$$f_k = 2.2997\ G_s\,, \tag{93}$$

which allows to compare the spring's stiffness f_k used in the calculation and G_s used in the simulations.

1.3 Numerically determined coefficients

Here we give a table of the numerically calculated prefactors. All entries not listed here are zero.

k	l	$_{mean}M_{k,l}$
0	0	1
0	2	0.333333
2	0	0.333333

k	l	m'	k'	l'	$_{mean}M_{k,l,\sigma'}$
2	0	1	1	0	24.594873
2	0	2	0	1	20.149046
1	1	1	0	1	2.222914
1	1	2	1	0	2.222914
0	2	1	1	0	20.149046
0	2	2	0	1	24.594873

m	k	l	m'	k'	l'	$_{tt}\mathbf{M}_{\sigma,\sigma'}$			
1	0	1	1	0	2	(0	, -0.191180	, 0	)
1	0	1	1	1	1	(-0.286938	, 0	, 0	)
1	0	1	1	2	0	(0	, 0.382696	, 0	)
1	0	1	2	0	2	(-0.382696	, 0	, 0	)
1	0	1	2	1	1	(0	, 0.286938	, 0	)
1	0	1	2	2	0	(0.191180	, 0	, 0	)
2	1	0	1	0	2	(0	, 0.191180	, 0	)
2	1	0	1	1	1	(0.286938	, 0	, 0	)
2	1	0	1	2	0	(0	, -0.382696	, 0	)
2	1	0	2	0	2	(0.382696	, 0	, 0	)
2	1	0	2	1	1	(0	, -0.286938	, 0	)
2	1	0	2	2	0	(-0.191180	, 0	, 0	)
3	0	1	1	1	1	(0	, 0	, -0.287106	)
3	0	1	2	0	2	(0	, 0	, -0.382696	)
3	0	1	2	2	0	(0	, 0	, 0.191516	)
3	0	1	3	0	2	(0	, -0.191180	, 0	)
3	0	1	3	2	0	(0	, -0.191516	, 0	)
3	1	0	1	0	2	(0	, 0	, 0.191516	)
3	1	0	1	2	0	(0	, 0	, -0.382696	)
3	1	0	2	1	1	(0	, 0	, -0.287106	)
3	1	0	3	0	2	(-0.191516	, 0	, 0	)
3	1	0	3	2	0	(-0.191180	, 0	, 0	)

m	k	l	m'	k'	l'	${}_u\mathbf{M}_{\sigma,\sigma'}$			
1	0	1	1	0	2	(0	, -0.829265	, 0	)
1	0	1	1	1	1	(0.503804	, 0	, 0	)
1	0	1	1	2	0	(0	, 0.623211	, 0	)
1	0	1	2	0	2	(1.388603	, 0	, 0	)
1	0	1	2	1	1	(0	, -0.070072	, 0	)
1	0	1	2	2	0	(-1.211625	, 0	, 0	)
1	0	1	3	1	1	(0	, 0	, 0.238674	)
1	1	0	1	0	2	(-0.425331	, 0	, 0	)
1	1	0	1	1	1	(0	, -0.594487	, 0	)
1	1	0	1	2	0	(0.845778	, 0	, 0	)
1	1	0	2	0	2	(0	, 0.426584	, 0	)
1	1	0	2	1	1	(1.431865	, 0	, 0	)
1	1	0	2	2	0	(0	, 0.022939	, 0	)
1	1	0	3	0	2	(0	, 0	, -0.449524	)
1	1	0	3	2	0	(0	, 0	, 0.027824	)
2	0	1	1	0	2	(0.022939	, 0	, 0	)
2	0	1	1	1	1	(0	, 1.431865	, 0	)
2	0	1	1	2	0	(0.426584	, 0	, 0	)
2	0	1	2	0	2	(0	, 0.845778	, 0	)
2	0	1	2	1	1	(-0.594487	, 0	, 0	)
2	0	1	2	2	0	(0	, -0.425331	, 0	)
2	0	1	3	0	2	(0	, 0	, 0.027824	)
2	0	1	3	2	0	(0	, 0	, -0.449524	)
2	1	0	1	0	2	(0	, -1.211625	, 0	)
2	1	0	1	1	1	(-0.070072	, 0	, 0	)
2	1	0	1	2	0	(0	, 1.388603	, 0	)
2	1	0	2	0	2	(0.623211	, 0	, 0	)
2	1	0	2	1	1	(0	, 0.503804	, 0	)
2	1	0	2	2	0	(-0.829265	, 0	, 0	)
2	1	0	3	1	1	(0	, 0	, 0.238674	)
3	0	1	1	1	1	(0	, 0	, 0.785233	)
3	0	1	2	0	2	(0	, 0	, 1.393488	)
3	0	1	2	2	0	(0	, 0	, -0.176978	)
3	0	1	3	0	2	(0	, -0.824381	, 0	)
3	0	1	3	1	1	(-0.515218	, 0	, 0	)
3	0	1	3	2	0	(0	, 0.206054	, 0	)
3	1	0	1	0	2	(0	, 0	, -0.176978	)
3	1	0	1	2	0	(0	, 0	, 1.393488	)
3	1	0	2	1	1	(0	, 0	, 0.785233	)
3	1	0	3	0	2	(0.206054	, 0	, 0	)
3	1	0	3	1	1	(0	, -0.515218	, 0	)
3	1	0	3	2	0	(-0.824381	, 0	, 0	)

m	k	l	$\zeta\mathbf{M}_\sigma$
1	0	1	$\begin{pmatrix} 0 & 0.044642 & 0 \\ 0.044642 & 0 & 0 \\ 0 & 0 & 0 \end{pmatrix}$
1	1	0	$\begin{pmatrix} -1.586555 & 0 & 0 \\ 0 & -1.675839 & 0 \\ 0 & 0 & -1.675839 \end{pmatrix}$
2	0	1	$\begin{pmatrix} -1.675839 & 0 & 0 \\ 0 & -1.586555 & 0 \\ 0 & 0 & -1.675839 \end{pmatrix}$
2	1	0	$\begin{pmatrix} 0 & 0.044642 & 0 \\ 0.044642 & 0 & 0 \\ 0 & 0 & 0 \end{pmatrix}$
3	0	1	$\begin{pmatrix} 0 & 0 & 0 \\ 0 & 0 & 0.044642 \\ 0 & 0.044642 & 0 \end{pmatrix}$
3	1	0	$\begin{pmatrix} 0 & 0 & 0.044642 \\ 0 & 0 & 0 \\ 0.044642 & 0 & 0 \end{pmatrix}$

1.4 Direction of the migration

Furthermore we can discuss the direction of the migration. If the stream lines are straight lines the migration is always directed in the direction in which the flow has no symmetry at the position of the particle. As an example the Poiseuille flow given by eq. (1) in the main text does not depend on the x- or the z-coordinate, hence if we transform the coordinates (with respect top the center of the particle) $x - x_c \longrightarrow -(x - x_c)$ or $z - z_c \longrightarrow -(z - z_c)$ the flow does not change. Thus positive and negative x and z- direction can not be distinguished. But a transformation $y - y_c \longrightarrow -(y - y_c)$ does change the flow, therefore it has no symmetry with respect to y. This leads to an asymmetric shape and to the migration in y-direction. A y-symmetry is only found at $y_c = 0$, where no migration occurs. Generally the migration in a flow with straight stream lines is directed in the direction with no symmetry, which can be seen by comparing all the Taylor coefficients of the flow and the resulting migration directions given in the SI (see sec. 1.3).

If the flow is two dimensional the stream lines lie in a plane. If the stream lines have an axis of symmetry in this plane then the migration is directed along this axis. In this case the flow left and right to the symmetry axis can not be distinguished.

We give here as an example the migration in a Taylor-Couette flow (the flow between two rotating cylinders). The flow is given by

$$\mathbf{u} = \left(Ar + \frac{B}{r}\right)\hat{\mathbf{e}}_\phi = \left(A + \frac{B}{x^2 + y^2}\right)\begin{pmatrix} -y \\ x \end{pmatrix} . \tag{94}$$

Without the loss of generality we assume that the particle is located at $x_c = 0$, so that the radial direction is the y-Axis. This leads to the Taylor coefficients

$$\mathbf{b}_{0,0} = \begin{pmatrix} -Ay_c - \frac{B}{y_c} \\ 0 \end{pmatrix}, \mathbf{b}_{1,0} = \begin{pmatrix} 0 \\ A + \frac{B}{y_c^2} \end{pmatrix}, \tag{95}$$

$$\mathbf{b}_{0,1} = \begin{pmatrix} -A + \frac{B}{y_c^2} \\ 0 \end{pmatrix}, \mathbf{b}_{2,0} = \begin{pmatrix} \frac{B}{y_c^3} \\ 0 \end{pmatrix}, \tag{96}$$

$$\mathbf{b}_{1,1} = \begin{pmatrix} 0 \\ -\frac{2B}{y_c^3} \end{pmatrix}, \mathbf{b}_{0,2} = \begin{pmatrix} -\frac{B}{y_c^3} \\ 0 \end{pmatrix} \tag{97}$$

We get now the migration velocity with the help of eqs. (73), (74), (75), (76), (77) in the main text and the prefactors given sec. 1.3. We find

$$\mathbf{u}_m = \mathbf{b}_{0,0} - 8.8917\frac{B^2R^3\eta}{y_c^5 f_k}\hat{\mathbf{e}}_y \tag{98}$$

$$\mathbf{u}_u + \mathbf{u}_{tt} = 3.1852\frac{B^2R^3\eta}{y_c^5 f_k}\hat{\mathbf{e}}_y\,, \tag{99}$$

$$\dot{\mathbf{r}}_c = \mathbf{u}_m + \mathbf{u}_u + \mathbf{u}_{tt}\,,\ \mathbf{v}_m = \dot{\mathbf{r}}_c - \mathbf{b}_{0,0}\,. \tag{100}$$

Thus indeed the migration caused by $\mathbf{u}_u + \mathbf{u}_{tt}$ is directed in y-direction (radial direction), because the stream lines are symmetric to the y-Axis. We can also see that the

averaged flow $\mathbf{u}_m$ is not completely directed in direction of $\mathbf{u}_0(\mathbf{r}_c) = \mathbf{b}_{0,0}$ and therefore also leads to a migration. The reason is that the stream lines are curved and the flow is nonlinear in the coordinates.

In an arbitrary flow the sums in the eqs. (75) and (76) (main text) can have many contributions. The direction of each contribution is given by the symmetry of the flow which consists only of the parts including the contributions of a_σ and $a_{\sigma'}$. This means of the flow

$$\begin{aligned}\mathbf{u}_{0,part} =&(\mathbf{b}_{k,l})_m (x-x_c)^k (y-y_c)^l \hat{\mathbf{e}}_m \\ &+ (\mathbf{b}_{k',l'})_{m'} (x-x_c)^{k'} (y-y_c)^{l'} \hat{\mathbf{e}}_{m'}\end{aligned} \tag{101}$$

which is a part of the flow that leads to a migration. This flow can be one or two dimensional. If this part of the flow contributes to the migration (i.e. has non-vanishing values of ${}_u\mathbf{M}_{\sigma,\sigma'}$ or ${}_{tt}\mathbf{M}_{\sigma,\sigma'}$) it has a nonzero first and second derivative. This leads to a symmetry axis (even if the complete flow may has none). This symmetry axis defines the direction of the migration, which is caused by this part of the flow.

References

[1] H.-H. Boltz and J. Kierfeld, Eur. Phys. J. **225**, 2269 (2016).

[2] D. Barthès-Biesel, Annu. Rev. Fluid Mech. **48**, 25 (2016).

Eidesstattliche Versicherung

Hiermit versichere ich an Eides statt, dass ich die vorliegende Arbeit selbstständig verfasst und keine anderen als die von mir angegebenen Quellen und Hilfsmittel verwendet habe.

Weiterhin erkläre ich, dass ich die Hilfe von gewerblichen Promotionsberatern bzw. -vermittlern oder ähnlichen Dienstleistern weder bisher in Anspruch genommen habe, noch künfig in Anspruch nehmen werde.

Zusätzlich erkläre ich hiermit, dass ich keinerlei frühere Promotionsversuche unternommen habe

Bayreuth, den _____

Unterschrift _____